EDITED and PUBLISHED quarterly at the offices of The American Society of Mechanical Engineers, United Engineering Center, 345 E. 47th St., New York, N. Y. 10017. Cable address, "Mechaneer," New York. Second-class postage paid at New York, N. Y., and at additional mailing offices.
CHANGES OF ADDRESS must be received at Society headquarters seven weeks before they are to be effective. Please send old label and new address.
PRICES: To members, $25.00, annually; to nonmembers, $50.00. Single copies, $15.00 each. Add $1.50 for postage to countries outside the United States and Canada.
STATEMENT from By-Laws. The Society shall not be responsible for statements or opinions advanced in papers or . . . printed in its publications (B 13, Par. 4).

INDEXED by the Engineering Index, Inc.

transactions of the ASME

Published Quarterly by
The American Society of
Mechanical Engineers
Volume 99 • Series C • Number 3
AUGUST 1977

journal of heat transfer

(Contents continued on page 373)

CONTENTS (CONTINUED)

DISCUSSION

ERRATUM

Hsiang-Cheng Kung
Senior Research Scientist, Factory Mutual Research Corp., Norwood, Mass.
Mem. ASME

Cooling of Room Fires by Sprinkler Spray

Cooling of combustion products and the room by vaporizing water droplets appears to be a promising mechanism in sprinkler control of residential fires. An experimental procedure coupled with an energy balance scheme has been developed to obtain the heat absorption rate of a sprinkler spray. A test room was constructed, 3.05 × 3.66 × 2.45 m high, with a window. Hexane pool fires were selected to simulate room fires. The key parameters of investigation were water-discharge rate and drop size. For the room tested, a correlation has been established between the heat-absorption rate by the sprinkler water and the relative median drop size of the sprinkler spray. It is found that the rate of sprinkler water evaporated is directly proportional to the heat release rate and the water discharge rate, and varies as the minus 0.73 power of the relative median drop size. An extinction criterion for the hexane pool fire in the enclosure, based on the water evaporation rate at the time of sprinkler operation, has also been established.

1 Introduction

The control of fires by automatic sprinkler systems may be accomplished according to the following three mechanisms, singly or combined: (1) cooling of the combustion products and the room to reduce the heat feeding the combustible elements; (2) direct contact of water droplets with the burning material to prevent the further generation of combustible vapor by cooling the burning fuel; and (3) prewetting the combustible material to prevent further fire spread. Associated with the first mechanism are two other effects: (1) inerting of the gas mixture inside the room by the evaporated water; and (2) the displacement of large volumes of air from the room by steam.

The relative effectiveness of the various mechanisms differs between residential buildings and industrial properties. The design of residential sprinkler systems is still based on information available for industrial systems and, therefore, systems possibly more costly than necessary have been the result.

A residence is generally subdivided into many small rooms. The initial stage of fire growth and heat generation is usually limited and confined within a single room. As a large portion of the combustible material in the room becomes involved, hot combustion products move out of the room and into adjacent rooms to ignite other combustible materials. It is essential to limit the fire to the room of origin for purposes of life safety and property conservation. To achieve this, the combustion products must be cooled considerably to prevent them from igniting combustibles in the adjacent rooms. The relatively low ceiling and small size of individual rooms enhance the convective and radiative heat transfer from combustion products to the rest of the combustible materials in the room. Sufficient cooling of combustion products by evaporating water droplets not only prevents fire spread to adjacent rooms but also prevents ignition of other combustible items within the room. Hence the cooling of combustion products and the room by vaporizing water droplets appears to be a promising mechanism in control of residential fires by use of water [1].[1]

A few attempts have been directed to the study of fire extinguishment by means of water. Salzberg, et al. [2, 3] conducted experiments to determine the amount of water required to suppress building fires by either hand extinguishers or water hoses. Rasbash, et al. [4, 5] studied the extinction of pool fires with water sprays by cooling of the burning liquid fuel and correlated extinction times with the rate of application, drop size, and the flash point of the liquid.

This paper presents an experimental study of the cooling of both the combustion products and the room by sprinkler sprays. An experimental procedure coupled with an energy balance scheme has been developed to obtain the heat absorption rate of sprinkler spray.

Hexane pool fires were selected to simulate fire sources to avoid the complexity encountered in fires with solid fuels. Such complexity results from interaction among the cooling and other control mechanisms, i.e., prewetting of combustibles to prevent further fire spread and direct extinction by contact of water droplets with the burning surface.

Key experimental parameters were the water discharge rate and the orifice diameter. It has been shown [6, 7] that the volume median

Contributed by the Heat Transfer Division for publication in the JOURNAL OF HEAT TRANSFER. Manuscript received by the Heat Transfer Division November 1, 1976.

[1] Numbers in brackets designate References at end of paper.

diameter[2] of the drop-size distribution generated by geometrically similar sprinklers varies as the $-1/3$ power of the water pressure and $2/3$ power of the sprinkler orifice diameter. The median drop size of the sprinkler spray can then be varied by changing the water pressure and orifice diameter while the discharge rate is maintained constant. In other words, the key parameters in this study can be interpreted as the drop size and the discharge rate. The extinguishment of hexane pool fires by water evaporation has also been investigated.

2 Experimental Facility and Instrumentation

2.1 Experimental Facility. The test room was built inside a larger (12.2- × 18.3- × 10.1-m high) burn facility. The size of the test room was 3.05-m wide, 3.66-m long, and 2.45-m high. The test room was elevated 0.61 m above the ground. The walls, floor, and ceiling were made of 6.35-mm thick asbestos-cement boards attached to a steel channel frame. Detailed dimensions of the room are shown in Fig. 1. Steel sheets 3.18-mm thick were placed underneath the asbestos-cement floor.

Five geometrically similar sprinklers were fabricated for the program, based on the proportions of a commercial design. The orifice diameters, D, of these five sprinklers are 11.10, 8.36, 6.96, 5.54, and 4.17 mm. The linear-scale ratios, referenced to the largest sprinkler, are 1, 3/4, 5/8, 1/2, and 3/8. Detailed dimensions of the 3/4-scale sprinkler are shown in Fig. 2. The sprinkler was installed at the center of the ceiling with the orifice 53.5 mm below the ceiling, and the plane of the supporting rods for the deflector perpendicular to the window plane.

A flow meter and a pressure gage were installed in the sprinkler piping system to give accurate readings of water discharge rate and water pressure.

2.2 Instrumentation. The test room has been instrumented with a total of 79 data channels; these include 68 thermocouple measurements, six measurements of the gas flow velocity through the window, measurements of CO, CO_2, and O_2 concentration at a single location in the window, one radiation measurement in the window, and a continuous weight loss measurement of the fuel.

Of the 68 thermocouples, 50 were employed in 25 pairs to measure the outside and inside surface temperatures of the walls, ceiling, and floor. These measurements provided information on heat storage in the walls, ceiling, and floor and heat loss to the ambient from the outside surface of the test room. The locations of these 25 thermocouple pairs are shown in Fig. 3.

Twelve thermocouples were installed inside the room to measure gas temperature; their locations are shown in Fig. 1. The remaining six thermocouples were utilized to obtain a temperature profile in the window. Fig. 4 shows the locations of all instrumentation in the window (thermocouples, velocity probes, gas sampling port, and radiometer).

All the thermocouples were fabricated from 30-gage chromel-alumel wire. The thermocouples measuring the surface temperatures of the walls, ceiling, and floor were mounted in shallow grooves (25-mm long) filled with an appropriate high-temperature adhesive such that the thermocouple bead was flush with the surface. The gas-temperature-measuring thermocouples inside the room were shielded from direct water impingement during sprinkler operation by two small metal plates, as shown in Fig. 1. (A metal bracket from a thermocouple connector was convenient to use for the shield; hence, the two plates.) To shield the thermocouples in the window from direct water impingement, the beads were simply placed between the pressure-transmitting tubes of the velocity probes (Fig. 4).

Gas velocities through the windows were monitored by six bidirectional, differential pressure flow tubes [9] located in the plane of the window. Their locations are shown in Fig. 4. These tubes can sense and indicate flows in opposite directions with equal sensitivity. Pressure differences were measured with an electronic manometer (Datametrics Barocel); the probe-manometer system had a response time significantly less than 1 s and was sufficiently sensitive to measure velocities reliably down to 0.3 m/s. A gas sampling port was placed

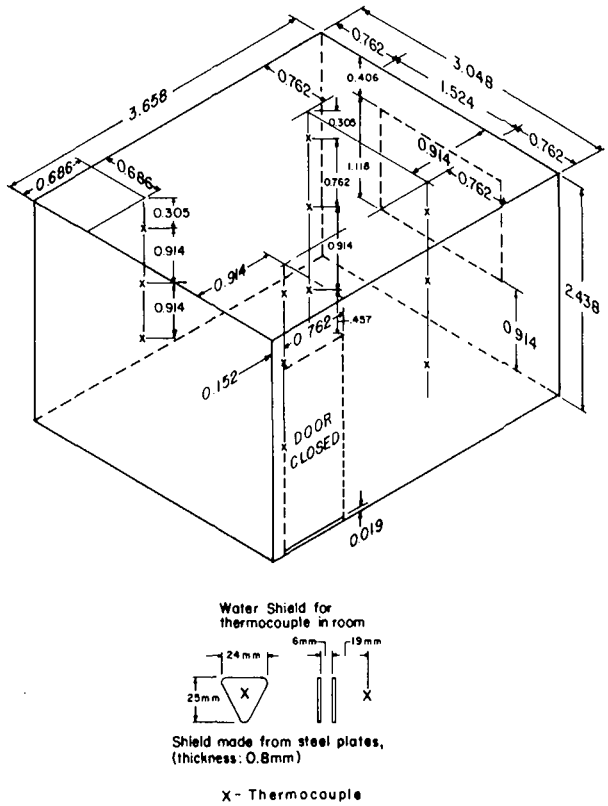

Fig. 1 Dimensions of the test room and locations of gas-temperature measuring thermocouples inside the test room

[2] The volume median diameter [8] has been chosen to characterize sprays produced by sprinklers and is defined as the diameter which divides the total volume of the spray into two equal parts; one part containing drops smaller than the median diameter and the other part containing drops larger than the median diameter.

Nomenclature

C_{pw} = specific heat of water (J/g°C)
d_r = relative volume median drop diameter $(\Delta p/\Delta p_0)^{-1/3}(D/D_0)^{2/3}$
D = sprinkler orifice diameter (mm)
D_0 = 11.10 mm
$E = (Q - L)/\{\dot{m}_w[H_{evap} + C_{pw}(T_{evap} - T_w)]Q\}$ (MW^{-1})
$E' = (Q - L)/\{\dot{m}_w[H_{evap} + C_{pw}(T_{evap} - T_w)]\}$
H_{evap} = latent heat of evaporation of water (J/g)
L = the sum of heat loss rates defined in Section 5 (MW)
$\dot{m}_w$ = water discharge rate (g/s)
$\dot{M}_{air}$ = air inflow rate through the window (g-mole/s)
$\dot{M}_{evap}$ = estimated generation rate of steam by evaporation (g-mole/s)
$\dot{M}_{hex}$ = burning rate of hexane (g-mole/s)
Δp = water pressure (kPa)
Δp_0 = 17.2 kPa
Q = heat-release rate of the fire (MW)
Q_b = heat-release rate of the fire before sprinkler operation (MW)
$R = \dot{M}_{evap}/(\dot{M}_{evap} + \dot{M}_{hex} + \dot{M}_{air})$
T_{evap} = water evaporation temperature (°C)
T_w = initial water temperature (°C)

0.076 m beneath the top edge of the window as shown in Fig. 4. The gas sample was passed through a condenser, glass wool filter, and desiccant prior to entering the analyzing instrument. The sample was analyzed for CO, CO_2, and O_2. Oxygen was analyzed by means of magnetic susceptibility, CO_2 and CO by means of infrared absorption. All gas analysis instruments were Beckman analyzers.

A wide-angle radiometer was placed at one location of the window plane as shown in Fig. 4 (Medtherm, water cooled, black thermopile behind Irtran window, purged with nitrogen, half-angle = 57.5 deg).

During all the tests, a continuous weight measurement was made of the hexane pool. Measurement was made by means of a load transducing platform (BLH Electronics), placed below the test room and fitted with a load-transferring frame that passed through small holes in the test room floor.

The 79 data signals were monitored by a data acquisition system with a HP 2100S computer. Every 2 s the system scanned each of the 79 data channels ten times within half a second and logged the average value of each data channel on magnetic tape.

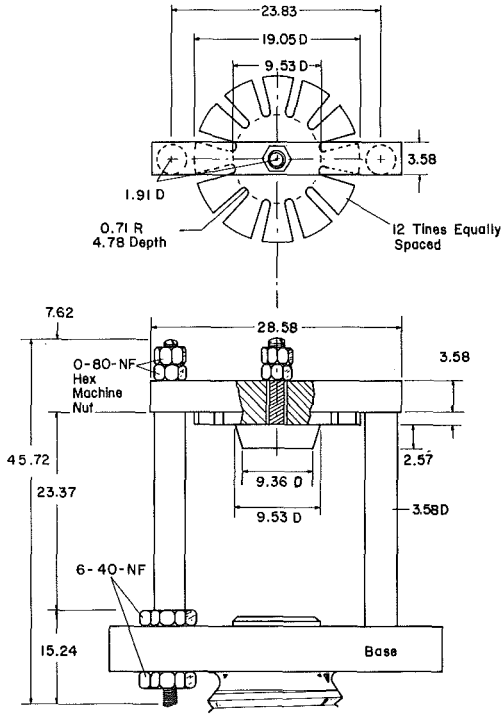

(a) deflector and supporting rods

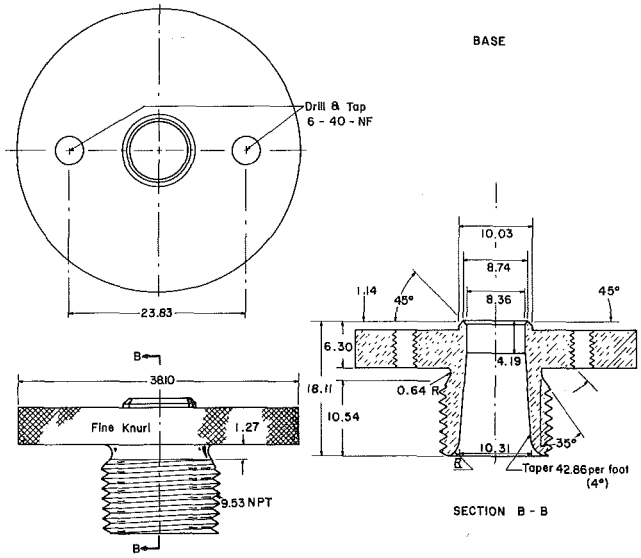

(b) base and orifice

Fig. 2 Detailed dimensions of the 3/4-scale sprinkler

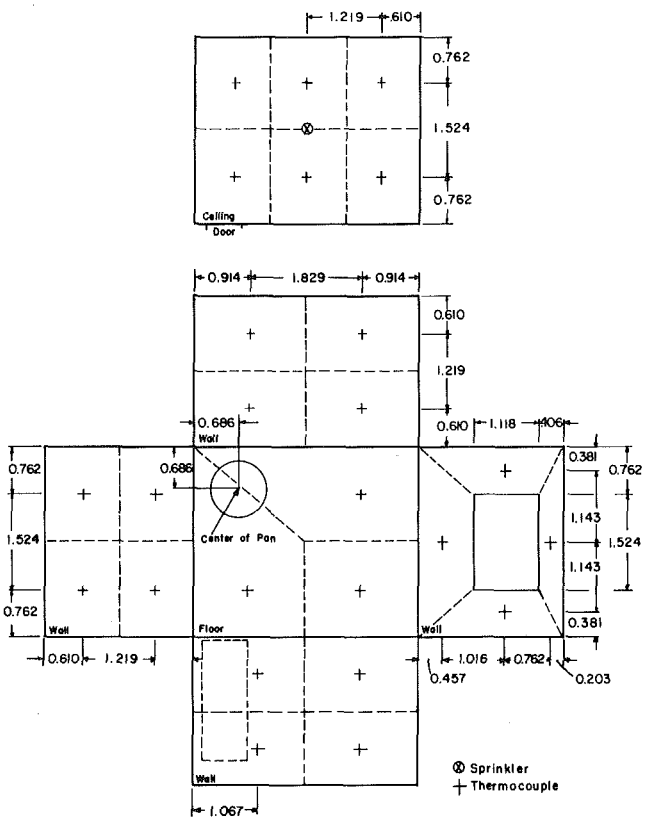

Fig. 3 Thermocouple locations on walls, floor, and ceiling

3 Experimental Procedure

Pan sizes of 0.914- and 0.762-m dia were selected, both with a depth of 0.152 m. The distance from the bottom of the pan to the floor was 0.06 m. In all the tests, the pan was filled with water 76-mm deep. Liquid fuel was then poured into the pan to a depth of 16 or 19 mm on top of the water. The purpose of the water was to prevent the pan from becoming excessively hot. Hexane was chosen as the fuel, because it is immiscible with and has a lower density and boiling point than water. During sprinkler operation, some water droplets were expected to penetrate the plume, pass through the hexane layer, and mix with the water already in the pan. Since hexane has a lower boiling point than water, the water droplets passing through the hexane layer could not turn to steam.

In all the tests reported here,[3] the window was full open but the door was closed. The hexane pool was located at the corner of the room (see Fig. 3). Ignition was achieved by an "electric match." The experimental sprinkler was manually activated at a preselected sprinkler operation delay time. Water discharge rate was maintained constant. The source fire either was extinguished or continued to burn until the hexane was totally consumed.

[3] A few tests were conducted with both window and door open [1]; however, the instrumentation was too limited to allow analyses of the kind presented in this paper.

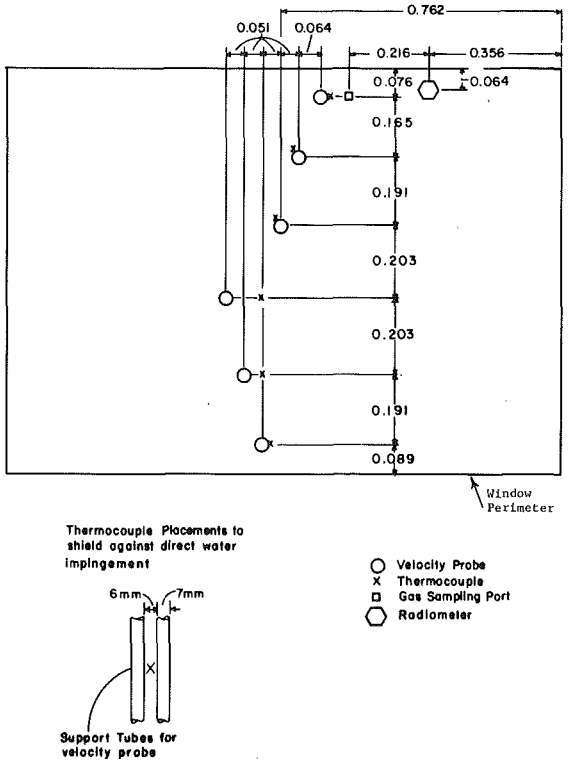

Fig. 4 Locations of velocity probes, thermocouples, gas sampling port, and radiometer in the window

4 Method of Analysis

The heat-release rate of the fire in the test room before sprinkler operation was obtained from the direct measurement of the burning rate by the load platform, coupled with the heat of combustion. The heat of combustion was determined through a species concentration balance from a dry exhaust gas analysis at the window for CO, CO_2, and O_2, subject to the assumptions that C and CO were the only incomplete combustion products [1].

For the nonextinguished fires, the heat-release rate of the fire during the period of sprinkler operation was derived by the following indirect measurement of the burning rate: during sprinkler operation, some water droplets penetrate the plume and accumulate in the pan. At the moment the remaining hexane has burned off, the load platform will give the total amount of water delivered to the pan by the sprinkler. This provides an average rate of water delivery to the pan. The algebraic difference between the measured rate of weight change and the average water-delivery rate gives the burning rate of hexane fuel. The heat-release rate of the fire is derived by coupling the burning rate with the calculated heat of combustion.

The following energy terms were computed for each test on an IBM370 computer: (1) the rate of heat storage in the walls, ceiling, and floor, (2) the heat-transfer rate to the ambient air from the outside surfaces of the room, (3) the net convective-heat exchange rate through the window opening, (4) the radiative heat loss through the window, and (5) the rate of change of the gas internal energy inside the room.

The ceiling, walls, and floor were divided into sections corresponding to the thermocouple pairs monitoring inside and outside surface temperatures shown in Fig. 3. It was assumed that the inside and outside surface temperatures of each section were uniform and represented by the temperatures monitored by a pair of surface thermocouples on the section. For each section, the one-dimensional transient heat conduction equation was solved numerically to obtain the time-dependent temperature profiles and, hence, the rates of heat storage in, and heat loss from, the walls, ceiling, and floor. A linear temperature profile was assumed to exist, not for all times, but only at the time of ignition (when inside and outside surface temperatures differ by only a few degrees C) as the initial condition for the partial differential equation. The following thermal-property values of the asbestos-cement board were used in the computation:

density = 1.525 g/cm^3

specific heat = 0.27 cal/g-°C;

and thermal conductivity = 0.00155 cal/s-cm-°C [10].

The net convective-energy exchange rate through the window was calculated by dividing the window opening into full-width areas corresponding to the six bidirectional probes [11]. The individual heights of these sections, top to bottom, were 0.152, 0.178, 0.203, 0.203, 0.203, and 0.178 m. In each section, the velocity and temperature were assumed constant over the sectional area. Perfect gas behavior was also assumed but temperature dependence of the specific heat was incorporated. The molecular weight and the temperature dependence of the constant-pressure specific heat of the gases flowing out of the window were assumed to be the same as those of air [12].

The radiative heat flux measured by the wide-angle radiometer at one location of the window opening was assumed to represent the average value through the window. Thus, the total radiative heat loss through the window was given by the measured radiative flux multiplied by the area of the window. Since the total radiation flux through the window accounts for less than 1.5 percent of the total energy-release rate, this approximation is acceptable.

To evaluate the change of total internal energy of the gases inside the room, perfect-gas behavior was assumed along with the assumptions that the molecular weight and the temperature dependence of the constant-volume-specific-heat of the gases were the same as for air. The volume of the room was divided into 12 subvolumes, four 1.53- × 1.83- × 0.61-m high subvolumes next to the ceiling, and eight 1.53- × 1.83- × 0.92-m high subvolumes for the middle and lower portions of the room. The temperature of the gases in each subvolume was measured by one thermocouple. The rate of change of internal energy of the gases in each subvolume was computed separately, and then summed to obtain the net change of total internal energy.

Due to the fluctuation of the turbulent flow, all the energy terms have been averaged for every 10-s period.

5 Results

Table 1 summarizes the combination of test variables used and indicates whether extinguishment occurred or not. The fire was either extinguished by the evaporated water from the sprinkler (E) or continued to burn until the hexane was totally consumed (N).

The water pressures, Δp (immediately upstream of the sprinkler in a 52.5-mm (2-in. nominal) dia pipe), associated with the three discharge rates, $\dot{m}_w$, using the five geometrically similar sprinklers are listed in Table 2. To aid interpretation, the relative volume median drop diameter, $d_r (d_r \equiv (\Delta p/\Delta p_0)^{-1/3} (D/D_0)^{2/3})$, is also listed in Table 2 which is directly proportional to the volume median drop size of the sprinkler spray. Δp_0 and D_0 are reference conditions given by 17.2 kPa and 11.10 mm, respectively.

The results in Table 1 indicate that, for a given discharge rate from the sprinkler and decreasing orifice diameter, an orifice diameter is

Table 1 Results of hexane fire extinguishment (window open, door closed, pan at the corner)

Fuel Pan Dia (m)	Sprinkler Delay Time (sec)	Water Discharge Rate (g/sec)	Sprinkler Orifice Diameter (mm) 11.0	8.36	6.96	5.57	4.17
0.914	60	1080	N	E	E		
0.914	60	707	N	N	N	E	
0.914	60	448			N	N	E
0.762	75	448		N	N	N	N

N - not extinguished

E - extinguished; see Table IV for extinction times

Table 2 Water pressure and relative drop size

Water Discharge Rate $\dot{m}_w$ (g/sec)		Sprinkler Orifice Dia, D, (mm) 11.10	8.36	6.96	5.54	4.17
1080	Water Pressure, Δp, (kPa)	81.7	244	600	-	-
	Relative Volume Median Drop Dia, d_r	0.598	0.342	0.224	-	-
707	Water Pressure, Δp, (kPa)	37.2	110	283	668	-
	Relative Volume Median Drop Dia, d_r	0.774	0.447	0.288	0.186	-
448	Water Pressure, Δp, (kPa)	17.2	45.5	121	269	680
	Relative Volume Median Drop Dia, d_r	1	0.599	0.382	0.252	0.153

Notes:

Δp : Water Pressure

D : Orifice Diameter

d_r : $(\Delta p/\Delta p_o)^{-1/3}(D/D_o)^{2/3}$

Δp_o : 17.2 kPa

D_o : 11.10 mm

eventually reached for which the fire is extinguished completely. Evidently, the decreasing orifice diameter causes a decreasing drop size (Table 2) which allows an increasing fraction of the water flux to evaporate and eventually extinguish the fire.

Before sprinkler operation, the conservation of energy requires that the calculated heat loss rate agree with the heat release rate of the fire. Results show that the ratios of calculated heat loss rate to heat release rate before sprinkler operation are within the range of 0.89–1.14. This agreement between Q and L is reasonably satisfactory and probably cannot by improved significantly without extensive additional instrumentation.

For the nonextinguished fire, the heat absorption rate by the sprinkler spray was obtained by the difference between Q, the heat release rate of the fire, and L, the sum of the heat loss rates due to heat storage in the walls, ceiling, and floor, the heat lost from the outside surface of the room, the convective and radiative heat loss through the window, and the change of total internal energy of the gases inside the room. The term L does not include the heat of vaporization, the sensible heat of the evaporated sprinkler water, and the heat absorbed by the nonevaporated water. The enthalpy and the internal energy of the steam generated by evaporation (referenced at ambient temperature) were accounted for in terms of the convective heat loss through the window and the change of the total internal energy of gases inside the room, respectively.

For the nonextinguished fire tests, Table 3 presents the heat release rate, Q; the total heat loss rate, L; the heat absorption rate, $Q - L$; the fraction of the maximum possible heat absorption rate actually absorbed; E' ($E' = (Q - L)/[\dot{m}_w[H_{evap} + C_{pw}(T_{evap} - T_w)]]$); and the fraction of heat release rate absorbed by water, $(Q - L)/Q$. H_{evap} is the latent heat of evaporation of water, C_{pw} is the specific heat of water, T_{evap} the water evaporation temperature, and T_w the initial water temperature. Both the heat release rate, Q, and the heat loss rate, L, were averaged over a period of 60 s starting either 45 or 50 s after sprinkler operation, while the fire remained in an approximate quasi-steady state.

The heat absorption rate by sprinkler water, $Q - L$, is expected to be a function of: the heat release rate, Q; the water discharge rate, $\dot{m}_w$; the relative median drop size, d_r; and other variables such as room geometry, fuel location, sprinkler location, etc. In the tests conducted, the room geometry, fuel location, and sprinkler location were maintained constant; thus, the heat absorption rate, $Q - L$, should depend only on the variables Q, $\dot{m}_w$, and d_r.

Examination of the results in Table 3 shows that E' is essentially independent of $\dot{m}_w$ at constant Q and d_r; the comparison of two pairs of tests, Tests 1, 11 and Tests 6, 9, indicates this independence. The

Table 3 Rates of heat absorption by sprinkler water ($Q - L$) for nonextinguished hexane fires

1. *Fuel Pan Diameter: 0.914 m; Sprinkler Delay Time: 60 sec*

Water Discharge Rate $\dot{m}_w$ (g/sec)		Sprinkler Orifice Dia D (mm) 11.10	8.36	6.96	5.57
1080	Test No.	1			
	Q(MW)†	0.77	-	-	-
	L(MW)†	0.42			
	Q-L(MW)	0.35	-	-	-
	E'	0.12			
	(Q-L)/Q	0.45	-	-	-
	E(MW^{-1})	0.16			
	d_r	0.598			
707	Test No.	4	5	6	
	Q(MW)†	1.33	0.81	0.78	-
	L(MW)†	0.97	0.46	0.34	-
	Q-L(MW)	0.36	0.35	0.44	-
	E'	0.20	0.19	0.24	
	(Q-L)/Q	0.27	0.43	0.57	-
	E(MW^{-1})	0.15	0.23	0.31	
	d_r	0.774	0.447	0.288	
448	Test No.			8	9
	Q(MW)†	-	-	1.19	0.81
	L(MW)†	-	-	0.85	0.52
	Q-L(MW)	-	-	0.34	0.29
	E'			0.30	0.24
	(Q-L)/Q	-	-	0.29	0.36
	E(MW^{-1})			0.25	0.30
	d_r			0.382	0.252

Table 3 (Cont'd)

2. Fuel Pan Diameter: 0.762 m; Sprinkler Delay Time: 75 sec

Water Discharge Rate $\dot{m}_w$ (g/sec)		Sprinkler Orifice Dia D (mm) 8.36	6.96	5.57	4.17
448	Test No.	11	12	13	14
	Q(MW)§	0.78	0.74	0.58	0.42
	L(MW)§	0.64	0.59	0.34	0.22
	Q-L(MW)	0.14	0.15	0.24	0.20
	E'	0.12	0.13	0.20	0.17
	(Q-L)/Q	0.18	0.20	0.42	0.48
	E(MW^{-1})	0.15	0.17	0.35	0.41
	d_r	0.599	0.382	0.252	0.153

Q : Heat Release Rate

L : Total Heat Loss Rate

Q-L : Heat Absorption Rate by Sprinkler Spray

E' : $(Q-L)/[\dot{m}_w[H_{evap} + C_{pw}(T_{evap} - T_w)]]$

E : $(Q-L)/[\dot{m}_w[H_{evap} + C_{pw}(T_{evap} - T_w)]Q]$

d_r : $(\Delta p/\Delta p_o)^{-1/3}(D/D_o)^{2/3}$

Δp : Water Pressure

Δp_o : 17.2 kPa

D_o : 11.10 mm

H_{evap} : Latent Heat of Evaporation of Water

C_{pw} : Specific Heat of Water

T_{evap} : Water Evaporation Temperature

T_w : Initial Water Temperature

†Average value over a 60-sec period starting at 50 sec after sprinkler operation

§Average value over a 60-sec period starting at 45 sec after sprinkler operation

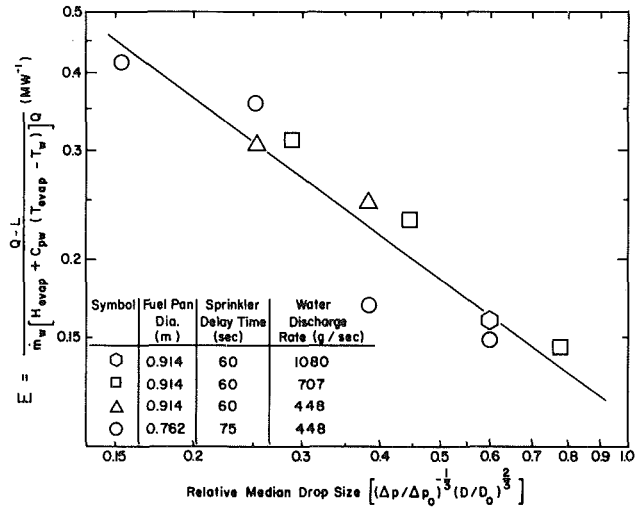

Fig. 5 The heat absorption rate by water spray versus the relative median drop size of the water spray

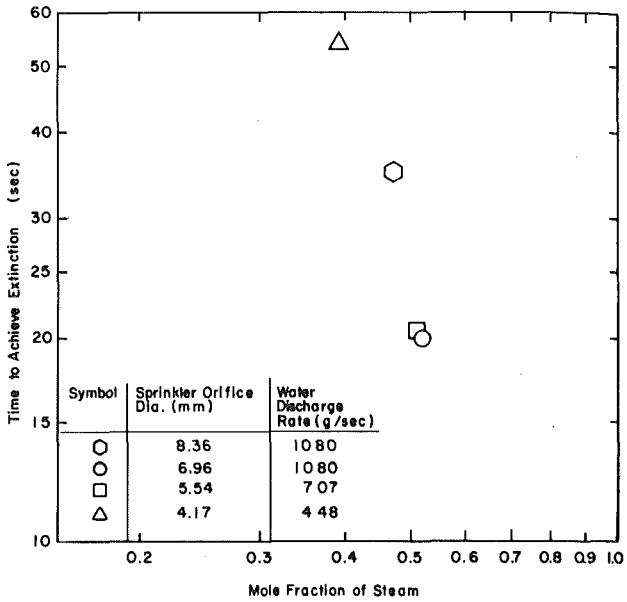

Fig. 6 Time to achieve extinction versus the mole fraction of steam generated by evaporation at the time of sprinkler activation

two tests in each pair have nearly common values of Q and d_r but different values of $\dot{m}_w$; the values of E' are observed to be the same for the paired tests. This suggests that E' is independent of $\dot{m}_w$ but may depend upon Q and d_r. Thus,

$$E' \equiv (Q - L)/\{\dot{m}_w[H_{\text{evap}} + C_{pw}(T_{\text{evap}} - T_w)]\} = f(Q, d_r) \quad (1)$$

Next, the functional dependence of E' on Q for common values of d_r is investigated for three relative median drop diameters (d_r = 0.598, 0.382, and 0.288). The quantities of E' and Q for these drop diameters either were taken directly from Table 3 or were obtained indirectly by linear interpolation between two neighboring tests for constant $\dot{m}_w$. The linear dependence of E' on Q is not inconsistent with the data. With the limited number of data points and their associated scatter, it is felt that the best estimate of functional dependence is thus:

$$E' = Q \cdot g(d_r) \quad (2)$$

Equations (1) and (2) together imply that the heat absorption rate, $(Q - L)$, is directly proportional to the water discharge rate, $\dot{m}_w$, and the heat release rate, Q; this observed dependency leads to the quantity

$$E \equiv (Q - L)/\{\dot{m}_w[H_{\text{evap}} + C_{pw}(T_{\text{evap}} - T_w)]Q\} = h(d_r) \quad (3)$$

as a possible correlating function. The quantity E has been included in Table 3 and plotted versus d_r in Fig. 5; also shown in Fig. 5 is the best-fit correlation obtained for the tests conducted:

$$E(MW^{-1}) = (0.11)d_r^{-0.73} \quad (4)$$

This correlation implies that the rate of sprinkler water evaporated is directly proportional to the heat release rate and the water discharge rate, and varies as the minus 0.73 power of the relative median drop size. The coefficient 0.11 is a property of the particular test enclosure, sprinkler location, and fire location employed. The correlation is somewhat limited by the range of parameters tested.

For sprays consisting of uniform drops, having sufficiently low relative velocity with respect to the surrounding gases, the evaporation rate is inversely proportional to the square of the drop diameter [13, 14]. When the relative velocity is appreciable, the evaporation rate varies as the minus 1.5 power of the drop size and 0.5 power of the relative velocity [13, 14]. In this study, sprays with nonuniform drop size distribution were employed and a significant portion of the drops were intercepted by the hot wall surfaces. Since evaporation from the hot surface probably was insensitive to the drop size, the variation of heat absorption rate as the minus 0.73 power of the median drop size is not unreasonable.

For the extinguished fires, the heat absorption rate just after the time when the sprinkler was activated can be estimated through equation (4) with the heat release rate at 5 s before sprinkler activation,[4] the water discharge rate, and the relative median drop diameter. The water evaporation rate, $\dot{M}_{\text{evap}}$, is approximated by the ratio of the heat absorption rate versus the sum of the heat of vaporization and the sensible heat of water. The approximate water evaporation rate ($\dot{M}_{\text{evap}}$), the measured burning rate of hexane[4] ($\dot{M}_{\text{hex}}$) and the measured air inflow rate[4] ($\dot{M}_{\text{air}}$), 5 s before sprinkler activation, for the four extinguished fires conducted in this study are listed in Table 4. The mole fractions of the steam, R [$R = \dot{M}_{\text{evap}}/(\dot{M}_{\text{evap}} + \dot{M}_{\text{hex}} + \dot{M}_{\text{air}})$], and the time to achieve extinguishment by sprinkler operation, t_{ext}, are also presented in Table 4. The extinction time, plotted against the steam mole fraction in Fig. 6, is very sensitive to the mole fraction

Table 4 Mole fractions of the steam generated by evaporation at the time of sprinkler activation and extinction times

Test No.	3	2	7	10	14
Fuel Pan Dia, (m)	0.914	0.914	0.914	0.914	0.762
Delay Time of Sprinkler Operation, (sec)	60	60	60	60	75
Water Discharge Rate, $\dot{m}_w$ (g/sec)	1080	1080	707	448	448
Sprinkler Orifice Dia, D (mm)	8.36	6.96	5.54	4.17	4.17
Relative Median Drop Dia, $(\Delta p/\Delta p_o)^{-1/3}(D/D_o)^{2/3}$	0.342	0.224	0.186	0.153	0.153
Heat Release Rate Before Sprinkler Operation, Q_b (MW)	1.44	1.40	1.66	1.53	0.92
Steam Generated by Evaporation, $\dot{M}_{\text{evap}}$ (g-mole/sec)	21.5	27.9	24.5	16.4	9.9
Burning Rate of Hexane, $\dot{M}_{\text{hex}}$ (g-mole/sec)	0.44	0.43	0.44	0.44	0.29
Air Inflow Rate Through The Window, $\dot{M}_{\text{air}}$ (g-mole/sec)	23.9	25.4	22.9	24.7	22.8
Mole Fraction of Steam, $R = \dot{M}_{\text{evap}}/(\dot{M}_{\text{evap}}+\dot{M}_{\text{hex}}+\dot{M}_{\text{air}})$	0.47	0.52	0.51	0.39	0.30
Extinction Time (sec)	35	20	21	53	Not Extinguished

[4] Averaged over a 10-s period starting 10 s before sprinkler activation.

of steam generated by evaporation at the time of sprinkler activation.

Table 4 also presents the estimated steam mole fraction,[5] R, of a nonextinguished fire (Test 14) which has the same water discharge rate and relative median drop size as Test 10 in Table 4. However, the heat release rate Q_b of Test 14 before sprinkler activation (Q_b = 0.92 MW) was 40 percent less than that of Test 10 (Q_b = 1.53 MW). This smaller heat release rate resulted in a smaller amount of steam generation; the consequent smaller steam mole-fraction proved inadequate to extinguish the fire.

Table 4 indicates that the minimum mole fraction of steam generated by evaporation at the time of sprinkler activation necessary to extinguish the hexane fire would be greater than 0.30 but less than 0.39. A uniformly mixed, stoichiometric heptane-air mixture at 100°C requires steam in the amount of 30 volume-percent of the heptane-air-water vapor mixture in order to render the mixture nonflammable [15]. In this study, the mixtures were nonuniform and at temperatures much higher than 100°C; it is expected, therefore, that more than 30 percent of steam would be required to extinguish the fire.

6 Conclusion

The cooling of combustion products and the room by vaporizing water droplets appears to be a promising mechanism in control of residential fires. In order to allow improved definition of the role played by vaporization of water in sprinkler control of fires, an experimental procedure coupled with an energy balance scheme has been developed to obtain the heat absorption rate of sprinkler water.

The water discharge rate, the median drop size of the water spray, and the heat release rate of the fire source have been recognized as the important parameters in the cooling of enclosure fires by water spray. For the pool fires tested, the ratio of the heat-absorption rate versus the maximum possible heat-absorption rate, divided by the heat release rate of the fire, varies as the minus 0.73 power of the median drop size. An extinction criterion for the hexane pool fire in the enclosure, based on the water evaporation rate at the time of sprinkler operation, has also been established.

[5] Based on the average values over a 10-s period starting 15 s before sprinkler activation.

Acknowledgments

The work was supported in part by the National Bureau of Standards, Department of Commerce, Contract No. 4-36097.

Special thanks are extended to Mr. R. E. Greene, who was involved in various phases of this program including construction of the test room, instrumentation, and execution of the experimental program.

Valuable discussions with Drs. G. Heskestad and P. A. Croce are sincerely appreciated.

References

1 Kung, H. C., "Residential Sprinkler-Protection Study," Technical Report RC75-T-41, Serial No. 22442, Factory Mutual Research Corp., Norwood, Mass., Nov. 1975.

2 Salzberg, F., Maatman, G. L., and Vodvarka, F. J., "An Approach to Trans-Attack Fire Suppression in Urban Areas," Final Report, IITRI Project No. N-6005, IIT Research Institute, Chicago, Ill., 1964.

3 Salzberg, F., Modvarka, F. J., and Maatman, G. L., "Minimum Water Requirements for Suppression of Room Fires," *Fire Technology*, Vol. 6, Feb., 1970, p. 22.

4 Rasbash, D. J., and Rogowski, Z. W., "Extinction of Fires in Liquids by Cooling With Water Sprays," *Combustion and Flame*, Vol. 1, 1957, p. 453.

5 Rasbash, D. J., Rogowski, Z. W., and Stark, G. W. V., "Mechanics of Extinction of Liquid Fires With Water Sprays," *Combustion and Flame*, Vol. 4, 1960, p. 223.

6 Dombrowski, N., and Wolfsohn, D. L., "The Atomization of Water by Swirl Spray Pressure Nozzles," *Trans. Instn. Chem. Engrs*, Vol. 50, 1972, p. 259.

7 Dundas, P. H., "The Scaling of Sprinkler Discharge: Prediction of Drop Size," Progress Report No. 10 in "Optimization of Sprinkler Fire Protection," Technical Report RC73-T-40, Factory Mutual Research Corporation, June 1974.

8 Marshall, W. R., "Atomization of Spray Drying," CEP Monograph, 1954.

9 Heskestad, G., "Bidirectional Flow Tube for Fire-induced Vent Flows," Appendix K of Technical Report RC74-T-31, Serial No. 21011.4, Factory Mutual Research Corporation, Norwood, Mass., July 1974.

10 Johns-Manville Asbestos-Cement Building Products Technical Bulletin.

11 Croce, P. A., and Emmons, H. W., "The Large-Scale Bedroom Fire Test, July 11, 1973," Technical Report RC74-T-31, Serial No. 21011.4, Factory Mutual Research Corporation, Norwood, Mass., July 1974.

12 *Handbook of Heat Transfer*, Rohsenow, W. M., and Hartnett, J. P., eds., McGraw-Hill, New York 1972, pp. 2-91.

13 Ranz, W. E., and Marshall, W. R., Jr., "Evaporation of Drops—Part I," *Chemical Engineering Progress*, Vol. 48, No. 3, Mar. 1952, p. 141.

14 Ranz, W. E., and Marshall, W. R., Jr., "Evaporation of Drops—Part II," *Chemical Engineering Progress*, Vol. 48, No. 4, Apr. 1952, p. 173.

15 Zabetakis, M. G., "Flammability Characteristics of Combustible Gases and Vapors," U. S. Department of The Interior, Bureau of Mines, Pittsburgh, Pa., 1965, p. 35.

E. M. Sparrow
R. J. Krowech

Department of Mechanical Engineering,
University of Minnesota,
Minneapolis, Minn.

Circumferential Variations of Bore Heat Flux and Outside Surface Temperature for a Solar Collector Tube

An analysis is made of the heat transfer processes in a solar collector tube subjected to large circumferential heat flux variations on its outer surface. The analysis is carried out for a collector plate configuration in which the tubes are situated in embossments in the otherwise flat surface of the plate. The solar energy absorbed by the collector plate is conducted to the tubes and gives rise to large heat flux spikes at discrete circumferential locations on the outer surface of a tube. The two-region heat conduction problem encompassing the embossed portion of the collector plate and the tube is solved by a novel procedure which provides closed form solutions of high numerical accuracy. The influence of system dimensions, thermal properties, and tube bore convection is examined by means of five dimensionless parameters, of which the Biot number was found to be the most important. The results showed that for realistic dimensions and thermal properties of the plate and tube, circumferential variations of the outside surface temperature and bore heat flux can be neglected, provided that the tube flow is laminar. For turbulent flow conditions, the variations in bore heat flux are substantially greater than for laminar flow.

Introduction

A solar collector plate is an important contemporary example of a fin and tube array wherein the tubes are subjected to large circumferential heat flux variations. From the standpoint of a typical tube, the adjacent portion of the collector plate acts like a longitudinal fin which delivers relatively large amounts of heat to discrete circumferential locations on the outer surface of the tube. These circumferential nonuniformities in outside surface heat flux can give rise to circumferential variations both in the convective heat flux at the bore of the tube and in the outside surface temperature. For tube and duct flows, circumferential variations in the heat flux at the bore can cause variations in the convective heat transfer coefficient, e.g., [1–5]. Furthermore, temperature variations on the outside surface of the tube will lead to circumferential nonuniformities in the heat loss. The ramifications of the nonuniformities in outside surface heat flux have heretofore not been considered in the solar energy literature nor, for that matter, in the literature dealing with finned heat exchanger tubes.

The present study was undertaken to analyze the response of a solar collector tube (or of a similar heat exchanger tube) to circumferentially nonuniform outside surface heat flux. There are, of course, a large variety of tube and plate configurations that are being employed or proposed for solar collector plates. For the present investigation, a model configuration was adopted which contains the essential features of practical collector systems and which is amenable to analysis by innovative methods.

The configuration to be studied is illustrated schematically in the left-hand diagram of Fig. 1. As pictured there, the collector plate is fabricated with semicircular embossments in which are situated the fluid-carrying tubes. The thermal bonding between the contiguous surfaces of the tube and the embossment is assumed to have negligible contact resistance, as would be the case in a high-performance collector design. Solar energy is incident on the collector plate from above, whereas the undersides of the plate and the tubes are insulated. The entire collector plate is made up of a succession of modules of the type illustrated in the figure. The part of the collector plate that extends between adjacent tubes will be referred to as the fin and is of length $2L$. The half length L (from a tube to a point midway between tubes) is shown in the figure.

For typical values of the tube diameter and of the fin length $2L$, the solar flux absorbed by the fin portion of the collector plate comprises the major portion of the energy delivered to the working fluid. Correspondingly, the heat flux density at the cross section where the fin

[1] Numbers in brackets designate References at end of paper.

Contributed by the Heat Transfer Division for publication in the JOURNAL OF HEAT TRANSFER. Manuscript received by the Heat Transfer Division April 9, 1976.

connects with the semicircular embossment in the collector plate is very large compared with the flux density at any other point on the semicircle. The effect of such a highly nonuniform distribution on the heat flux at the tube bore and on the outside surface temperatures of the embossment and the tube is the focus of this investigation.

The working diagram for the analysis, showing dimensional nomenclature and coordinates, is pictured at the right of Fig. 1. The tube ($r_1 < r < r_2$) and the semicircular embossment ($r_2 < r < r_3$) in the collector plate are, respectively, identified by t and p. For generality, the tube and plate materials may be different (i.e., different thermophysical properties), as may their thicknesses. The fin portion of the collector plate is not shown in this diagram. Rather, an angle θ_0 is indicated such that the fins connect to the semicircular embossment along the arcs $\theta_0 < \theta < \pi/2$ and $-\pi/2 < \theta < -\theta_0$. The heat collected by the fins passes through these arcs and is dispersed and distributed by a two-dimensional conduction process, ultimately finding its way into the working fluid. Solar energy absorbed at the outer surface of the embossment along the segment $-\theta_0 < \theta < \theta_0$ also reaches the tube bore via two-dimensional conduction.

The problem may be formulated at various levels of complexity. At the extreme degree of complexity, three distinct aspects of the problem have to be considered: (a) coupled, two-region heat conduction for the configuration shown in the right-hand diagram of Fig. 1, with heat inputs from the incident solar radiation, (b) heat losses through the cover system of the collector and through the back-side insulation, and (c) circumferential variations of the convective heat transfer coefficient at the tube bore. Part (a) alone, taken together with a uniform heat transfer coefficient at the tube bore, is a nonelementary heat conduction problem involving a minimum of five independent dimensionless parameters. The inclusion of part (b), even for a relatively simple model, makes the problem nonlinear and involves a large number of additional parameters including actual temperature levels, radiation properties, separation distances between the cover plates, tilt angle of the collector, wind speed, effective sky temperature, insulation thickness and conductivity, etc. Part (c), even when simple models such as those of [1–3, 5] are used, requires simultaneous solution with part (a).

It is evident from the foregoing that it is wise to delay treating the problem in its entirety (i.e., parts (a), (b), and (c)) if useful results can be obtained from analyzing a simplified version. As will be discussed more fully in the final section of the paper, the predicted circumferential variations of the bore heat flux and outside surface temperature are enhanced when the convective heat transfer coefficient is uniform and when heat losses are neglected. Therefore, solutions corresponding to these conditions provide an upper bound for the actual circumferential variations. From these solutions, values of the operating parameters can be identified for which the circumferential variations are negligible, and this information can be applied directly to collector design. In addition, such solutions enable identification of the parameter ranges where consideration has to be given to parts (b) and/or (c).

The present paper is concerned with solutions which give upper bounds for the circumferential variations.

Analysis

Before proceeding with the description of the analysis, it remains to consider the distribution of the incoming solar radiation. One candidate distribution is that depicted schematically in the left-hand diagram of Fig. 1; namely, a uniform flux of solar energy crossing a plane parallel to that of the collector plate. Such a distribution gives rise to temperature and heat flow symmetry with respect to the $\theta = 0$ position defined by the coordinates in the right-hand diagram of Fig. 1.

If the solar flux arrives at an angle of inclination, then strict symmetry no longer exists, and it would appear that an additional parameter (the sixth of the problem) has to be employed to characterize the degree of asymmetry. It should be noted, however, that even when the solar flux is inclined, the unshadowed parts of the fins are uniformly irradiated. Furthermore, for realistic values of the dimensions r_3 and L, the extent of the shadowing is not significant even at moderately large angles of inclination. Since the energy collected by the fins is the dominant heat input in the problem, departures from symmetry should, therefore, be small.

In view of the foregoing, it is reasonable to expect that the results for the symmetry case should continue to be valid for moderate solar inclinations. The present analysis will, therefore, be carried out for the symmetry case. There are no essential difficulties in extending the analytical model to accommodate asymmetry, aside from the penalty of having to deal with another independent parameter.

Let e_i denote the uniform solar flux passing per unit time and area through a plane parallel to the collector plate and α_s be the solar absorptance of the plate surface. With these, and neglecting heat losses for reasons discussed in the Introduction, the energy input per unit time and per unit area at the external surface of the embossment can be expressed as

$$q_{\mathrm{I}} = \alpha_s e_i \cos\theta, \qquad -\theta_0 < \theta < \theta_0 \tag{1a}$$

$$q_{\mathrm{II}} = \frac{\alpha_s e_i (L + r_3(1 - \sin\theta_0))}{r_3(\tfrac{1}{2}\pi - \theta_0)}, \qquad -\pi/2 < \theta < -\theta_0 \text{ and } \theta_0 < \theta < \pi/2 \tag{1b}$$

Region I represents the arc $-\theta_0 < \theta < \theta_0$ along which the solar energy is directly incident on the embossment, whereas Region II encompasses the arcs of contact, $-\pi/2 < \theta < -\theta_0$ and $\theta_0 < \theta < \pi/2$, between the fins and the embossment. The numerator of equation (1b) is the energy collected by the fins, and the denominator is the contact arc length. The quantity $r_3(1 - \sin\theta_0)$ that appears in the numerator takes account of the fact that the front-face length of the fin is very slightly greater than the back-face length L.

If plotted, the q versus θ distribution of equations (1) would display a relatively gradual downsloping portion between $\theta = 0$ and $\theta = \theta_0$, at which point there is an abrupt step increase to a flat plateau which extends from θ_0 to $\pi/2$. The height of the flat plateau is much, much greater than that at any point along the downsloping portion.

The total rate of energy input to a collector-plate module consisting of an embossment and its flanking fins can be written directly as

Nomenclature

Bi = Biot number, hr_1/k_t
e_i = incoming solar flux
h = convection coefficient at bore
k = thermal conductivity
L = half length of fin between adjacent tubes, Fig. 1
Q = rate of energy input per module, per unit axial length
q = local surface heat flux
$\bar{q}$ = average bore heat flux, $Q/2\pi r_1$
r = radial coordinate
r_1 = radius of tube bore
r_2 = outer radius of tube
r_3 = outer radius of embossment
T = temperature
T_b = fluid bulk temperature
T^* = wall temperature based on convective resistance alone, equation (20)
α_s = solar absorptance
η = dimensionless coordinate, r/r_1
η_2 = dimensionless outer radius of tube, r_2/r_1
η_3 = dimensionless outer radius of embossment, r_3/r_1
η_L = dimensionless length of extended surface, L/r_1
θ = angular coordinate, Fig. 1
θ_0 = angle at junction of extended surface and embossment, Fig. 1
σ = sigma factor, equation (8)
ϕ = dimensionless temperature, $(T - T_b)/(Q/k_p)$

Subscripts

p = embossed plate
t = tube

$$Q = 2\alpha_s e_i (r_3 + L) \tag{2}$$

where Q is per unit length in the axial direction. Equation (2) can also be obtained by integration of equations (1a) and (1b).

With the heat input thus specified, consideration can be given to the broad outlines of the solution for the temperature field. Numerical methods were considered but not employed because of the difficulties in handling the sharp turning of the heat flow lines in the neighborhood of $\theta_0 < \theta < \pi/2$. Instead, an analytical method was devised which yields highly accurate closed-form solutions.

The first step is to obtain a solution representation for the outer semicircular region p and, in this connection, an alternative to Fourier series is used to fit the heat inputs specified by equations (1). Next, a solution representation for the inner region t (i.e., the tube) is obtained. Then, the solution representations are matched along the interface between the tube and the embossment. In the matching, account is taken of the fact that the angular ranges of the two regions are different and that the functions which appear in the two representations have different periods. The matching is supplemented by an adiabatic boundary condition at the underside of the tube. The matching and the supplemental boundary condition enable a set of linear algebraic equations to be generated for the unknown coefficients in the inner and outer representations. The solution of these equations provides all that is necessary to evaluate the desired heat flux and temperature results.

To minimize the number of independent parameters, dimensionless quantities are introduced as follows

$$\phi = (T - T_b)/(Q/k_p), \qquad \eta = r/r_1 \tag{3a}$$

$$\eta_2 = \frac{r_2}{r_1}, \qquad \eta_3 = \frac{r_3}{r_1}, \qquad \eta_L = \frac{L}{r_1}, \qquad \mathrm{Bi} = \frac{hr_1}{k_t}, \qquad \frac{k_p}{k_t} \tag{3b}$$

in which T_b and h are, respectively, the local bulk temperature of the working fluid and the convective heat transfer coefficient at the bore. Q is the overall heat transfer rate defined by equation (2).

Outer and Inner Solution Representations. The temperature field in the embossed plate p is governed by Laplace's equation. A solution representation which is symmetric about $\theta = 0$ and which satisfies an adiabatic boundary condition along the back-side edges ($\theta = \pm\pi/2$, $r_2 < r < r_3$) is

$$\phi_p = A_0 + B_0 \ln \eta + \sum_{n=1} (A_n \eta^{2n} + B_n \eta^{-2n}) \cos 2n\theta \tag{4}$$

where the temperature variable that appears in ϕ_p is $T_p(r, \theta)$. The constants A_0, B_0, A_n, and B_n are to be chosen to fit the conditions along the inner and outer semicircular arcs.

Along the outer arc ($\eta = \eta_3$), the heat flux is specified (equations (1)), so that it is appropriate to differentiate equation (4) to obtain

$$\frac{q(\eta_3, \theta)}{(Q/r_1)} = \frac{B_0}{\eta_3} + \sum_{n=1} \left(\frac{2n}{\eta_3}\right) (A_n \eta_3^{2n} - B_n \eta_3^{-2n}) \cos 2n\theta \tag{5}$$

In view of equation (5), it appears natural to expand the given heat flux distribution, equations (1), in a Fourier series of the form

$$\frac{q(\eta_3, \theta)}{(Q/r_1)} = \Omega_0 + \sum_{n=1} \Omega_n \cos 2n\theta \tag{6}$$

where, in determining Ω_0 and Ω_n, cognizance has to be taken of the fact that $q(\eta_3, \theta)$ is specified by different algebraic representations in the circumferential Regions I and II. Therefore,

$$\Omega_0 = \frac{2}{\pi(Q/r_1)} \left[\int_0^{\theta_0} q_{\mathrm{I}} d\theta + \int_{\theta_0}^{\pi/2} q_{\mathrm{II}} d\theta \right] = \frac{1}{\pi\eta_3} \tag{6a}$$

$$\Omega_n = \frac{4}{\pi(Q/r_1)} \left[\int_0^{\theta_0} q_{\mathrm{I}} \cos 2n\theta d\theta + \int_{\theta_0}^{\pi/2} q_{\mathrm{II}} \cos 2n\theta d\theta \right] \tag{6b}$$

The integrals appearing in equation (6b) are easily carried out, so that Ω_n can be regarded as known.

Although it is common knowledge that a Fourier series averages the ordinates at a point of discontinuity such as $\theta = \theta_0$, other responses of the series to a discontinuity are somewhat less well known. In particular, the series overshoots at the top of the discontinuity and undershoots at the bottom (Gibbs' phenomenon). Other features were revealed when the series representation (6) was plotted and compared with the given heat flux distribution, equations (1). It was noted that the series representation was wavy along the entire range of the θ variable, as if the aforementioned overshoot and undershoot had propagated away from the discontinuity in the directions of both increasing and decreasing θ. This qualitative behavior persisted as the number of terms in the series was varied, although there were differences in detail with respect to the amplitude and the frequency of the waviness.

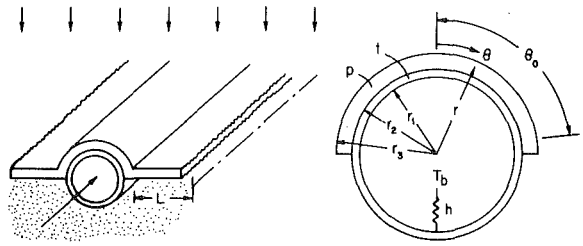

Fig. 1 Collector plate configuration (left) and working diagram for the analysis (right)

In view of the foregoing, an alternative representation for the given heat flux distribution was sought and found. Lanczos [6, 7] has devised a little-known series representation which is especially well suited for handling functions which have discontinuities. The representation given by Lanczos is for a solution domain and eigenvalues different from those of the present problem, necessitating an independent derivation, the end result of which is

$$\frac{q(\eta_3, \theta)}{(Q/r_1)} = \Omega_0 + \sum_{n=1}^{N} \Omega_n \sigma_n \cos 2n\theta \tag{7}$$

The Ω_0 and Ω_n are the conventional Fourier coefficients already defined by equation (6), while σ_n is the sigma factor whose definition depends on the solution domain and on the eigenvalues. For the present problem,

$$\sigma_n = \frac{1}{n\pi/(N+1)} \sin\left(\frac{n\pi}{N+1}\right) \tag{8}$$

For values of N that are fairly large (say, ~50), it is seen that $\sigma_n \approx 1$ for the initial terms of the series (small n) and that $\sigma_n \ll 1$ for the final terms. Therefore, the σ factor representation converges much more rapidly than a conventional Fourier series.

Inspection of graphs of $q(\eta_3, \theta)$ evaluated from equation (7) showed that the sigma factor representation rounds the corners of a discontinuity more than does a Fourier series, but exhibits only very slight overshoot or undershoot. Furthermore, in the region away from the discontinuity, the sigma factor representation is altogether free of waviness and ripples.

From a comparison of coefficients in equations (5) and (7), there follows

$$B_0 = \eta_3 \Omega_0 = 1/\pi \tag{9a}$$

$$B_n = A_n \eta_3^{4n} - \Omega_n \sigma_n \eta_3^{2n+1}/2n \tag{9b}$$

With these, the solution representation (4) for ϕ_p becomes

$$\phi_p = A_0 + (1/\pi) \ln \eta + \sum_{n=1}^{N} A_n (\eta^{2n} + \eta_3^{4n} \eta^{-2n}) \cos 2n\theta - \sum_{n=1}^{N} [\Omega_n \sigma_n \eta_3^{2n+1} \eta^{-2n}/2n] \cos 2n\theta \tag{10}$$

where the constants A_0 and A_n still remain to be determined.

In the forthcoming numerical evaluation of the solution, results will be obtained on the basis of both the Fourier series and sigma factor representations. To facilitate this, the quantity σ_n that appears in

equation (10) will be set equal to one for the former evaluation and taken from equation (8) for the latter evaluation.

The temperature field in the tube wall t is also governed by Laplace's equation. If the convective boundary condition

$$-k_t(\partial T/\partial r) = h(T_b - T) \tag{11}$$

is imposed at the tube bore ($r = r_1$ and $\eta = 1$), the solution takes the form

$$\phi_t = C_0(1 + \text{Bi} \ln \eta) + \sum_{m=1}^{M} C_m\left[\eta^m + \left(\frac{m - \text{Bi}}{m + \text{Bi}}\right)\eta^{-m}\right] \cos m\theta \tag{12}$$

where ϕ_t contains $T_t(r, \theta)$ and Bi is the Biot number defined by equation (3b). The constants C_0 and C_m await determination.

Continuity and Supplementary Boundary Conditions. The physical constraints which remain to be satisfied by the solution are:

(a) heat flow and temperature continuity at the embossment/tube interface, $r = r_2$ and $-\pi/2 < \theta < \pi/2$

(b) no heat flow at the underside of the tube, $r = r_2$ and $\pi/2 < \theta < 3\pi/2$

Since neither temperature nor heat flux continuity is, in itself, a sufficient boundary condition, both are needed in (a). On the other hand, the adiabatic condition of (b) is fully sufficient, and no additional boundary condition is needed along that part of the arc.

The conditions stated in (a) and (b) can be expressed as

$$q_t(r_2, \theta) = \begin{cases} q_p(r_2, \theta), & -\pi/2 < \theta < \pi/2 \\ 0, & \pi/2 < \theta < 3\pi/2 \end{cases} \tag{13}$$

$$T_t(r_2, \theta) = T_p(r_2, \theta), \qquad -\pi/2 < \theta < \pi/2 \tag{14}$$

Equations (13) and (14) may be recast in dimensionless form and ϕ_p and ϕ_t introduced from (10) and (12). The resulting equations, when properly employed, provide a means for determining the unknown A and C coefficients. With respect to the use of these equations, it should be noted that the periods of the cosines which appear on the right- and left-hand sides are not the same. Therefore, orthogonality does not hold for both sides of each equation. As a result, no one coefficient can be determined independently of the others (in contrast to a Fourier series, where each coefficient is independent of the others). Rather, all the coefficients have to be determined simultaneously.

There are two approaches that might be considered for generating the simultaneous algebraic equations needed for determining the coefficients. One approach is collocation (i.e., point matching), whereby equations (13) and (14) are applied at each of a discrete set of θ values, with each application yielding an algebraic equation that interrelates the unknowns. The collocation procedure has two drawbacks when applied to the present problem. First, owing to the possible sharp variations in heat flux and/or temperature in the neighborhood of $\theta_0 < \theta < \pi/2$, the selection of the locations of the matching points may affect the accuracy of the solution. Second, the algebraic equations generated by employing the adiabatic condition on the underside of the tube (i.e., second part of equation (13)) can be solved to yield the C coefficients without involvement of the other constraints of equations (13) and (14). This is an undesirable feature in that the values of the coefficients should reflect all the constraints.

The other approach, which consists of mimicking the procedures for Fourier series, does not suffer from either of these drawbacks. The basis of the approach is to integrate equations (13) and (14) over their respective ranges of applicability, using appropriate multiplicative weighting functions prior to the integration. Thus, for equation (13), one can write

$$2\int_0^{\pi} q_t(r_2, \theta)d\theta = 2\int_0^{\pi/2} q_p(r_2, \theta)d\theta + 2\int_{\pi/2}^{\pi} 0\, d\theta \tag{15a}$$

$$2\int_0^{\pi} q_t(r_2, \theta)\cos \ell\theta\, d\theta = 2\int_0^{\pi/2} q_p(r_2, \theta)\cos \ell\theta\, d\theta + 2\int_{\pi/2}^{\pi} 0\cos \ell\theta\, d\theta \tag{15b}$$

where ℓ is any integer ≥ 1. From (15a), there follows

$$C_0 = (k_p/k_t)/2\pi\text{Bi} \tag{16a}$$

whereas (15b) yields

$$C_\ell = \frac{k_p}{k_t}\left[\Gamma_{0\ell} + \sum_{n=1}^{N} \Gamma_{n\ell} + \sum_{n=1}^{N} \chi_{n\ell}A_n\right] \tag{16b}$$

where the $\Gamma_{0\ell}$, $\Gamma_{n\ell}$, and $\chi_{n\ell}$ are abbreviations for simple, but somewhat lengthy, algebraic expressions. Note that each C_ℓ is related to all of the A_n.

A similar procedure is employed for equation (14). First, equation (14) is integrated from $\theta = -\pi/2$ to $\pi/2$ (or, alternatively, from $\theta = 0$ to $\pi/2$). Next, equation (14) is multiplied by $\cos 2j\theta$ ($j \geq 1$) and then integrated over the same range. These operations yield

$$A_0 = -(\ln \eta_2)/\pi + C_0(1 + \text{Bi} \ln \eta_2) + \sum_{m=1}^{M} \Phi_{m0}C_m \tag{17a}$$

$$A_j = \Lambda_j + \sum_{m=1}^{M} \Phi_{mj}C_m \tag{17b}$$

where Φ_{mo}, Φ_{mj}, and Λ_j are, once again, abbreviations for algebraic expressions. Equations (17) indicate that each A is related to all of the C's.

Suppose that the respective series for ϕ_p and ϕ_t are truncated after the same number of terms, i.e., $N = M$. Furthermore, let ℓ take on successive values of $1, 2, \ldots, N$ and, similarly, let j take on successive values of $1, 2, \ldots, N$. In this way, equations (16b) and (17b) can be employed to generate $2N$ linear, inhomogeneous algebraic equations for A_1 through A_N and C_1 through C_N.

The solution of the resulting system of linear algebraic equations was carried out on a CDC CYBER 74 computer. Preliminary computational experiments were performed to examine the effect of the number of terms and of the influence of the sigma factor versus the Fourier series representation. The final solutions were obtained for a 90-equation system ($N = 45$) in which the sigma factor representation is employed.

Representation of the Results. As was noted earlier, the primary focus of this study is on the heat flux distribution at the tube bore and on the outside surface temperatures of the embossment and the tube. In connection with the former, it is convenient to introduce the average bore heat flux $\bar{q}$

$$\bar{q} = Q/2\pi r_1 \tag{18}$$

Then, upon noting that the local convective heat flux q at the bore is given by $h(T - T_b)$, it follows that

$$q/\bar{q} = 2\pi\,\text{Bi}(k_t/k_p)\,[\phi_t(\theta)]_{\eta=1} \tag{19}$$

where ϕ_t is expressed by equation (12). The departures of $q/\bar{q}$ from unity provide a convenient measure of the circumferential nonuniformity of the heat flux at the bore.

In considering possible reference quantities for the surface temperature results, it may be noted that current practice in collector design is to ignore temperature variations across the metallic walls. Instead, a wall-to-bulk temperature difference is evaluated on the basis of the convective resistance at the tube bore. If $(T^* - T_b)$ represents such a temperature difference, then

$$T^* - T_b = Q/h2\pi r_1 \tag{20}$$

With $(T^* - T_b)$ as a reference quantity, the temperature variation at the exposed surface of the embossed plate ($r = r_3$ and $\eta = \eta_3$) can be written as

$$\frac{T_p(r_3, \theta) - T_b}{T^* - T_b} = 2\pi\,\text{Bi}(k_t/k_p)\,[\phi_p(\theta)]_{\eta 3} \tag{21}$$

with ϕ_p from equation (10). Similarly, for the back side of the tube ($r = r_2$ and $\eta = \eta_2$)

$$\frac{T_t(r_2, \theta) - T_b}{T^* - T_b} = 2\pi \, \mathrm{Bi}(k_t/k_p) \, [\phi_t(\theta)]_{\eta 2} \qquad (22)$$

Results and Discussion

In view of the fact that the problem is governed by five independent parameters (equation (3*b*)), care must be taken in the parameter value selection so that the results can be presented coherently in a reasonable space. Values of r_2/r_1 in the range of 1.2 to 1.4 are typical for small diameter pipes and tubes. However, since the results indicated that very little additional information would be gained by going beyond $r_2/r_1 = 1.3$, computations for the $r_2/r_1 = 1.4$ case were not performed. Rather, to satisfy a curiosity about the extent of the circumferential variations for very thin-walled tubes, results were obtained for $r_2/r_1 = 1.1$.

For each of the three tube-wall radius ratios r_2/r_1 (1.3, 1.2, and 1.1), r_3/r_1 was varied so that the thickness of the embossment was, respectively, half, equal to, and twice that of the tube wall. The length of the extended surface, which has a direct influence on the magnitude of the heat spike on the surface of the embossment, was assigned values L/r_1 of 5, 10, and 20.

In selecting values of the conductivity ratio k_p/k_t, consideration was given to the lowest and highest thermal conductivity values (those for steel and copper, respectively) among the various metals that are candidates for collector applications. The Biot number was deduced from the Nusselt number and the ratio of the thermal conductivities of the working fluid (water or a water-glycol mixture) and the tube wall. For most collector applications involving a liquid working fluid, the flow is laminar and the Nusselt number has a value of approximately four. For the main body of the solutions, the Biot number was evaluated for laminar flow conditions, but some computations were also performed for Biot numbers corresponding to moderate Reynolds number turbulent flow.

Laminar Flow Results. Circumferential distributions of the heat flux at the tube bore and of the outside surface temperatures of the embossment and the tube are presented in Figs. 2–4. The successive figures correspond, respectively, to tube-wall radius ratios r_2/r_1 of 1.3, 1.2, and 1.1. These results are for an extended surface length $L/r_1 = 20$, which is the largest among the L/r_1 values employed here (the effect of L/r_1 will be examined shortly in more detail). The Biot numbers for these figures correspond to laminar flow.

Each figure is subdivided into three graphs. The lower graph depicts a case where the embossment plate and the tube are of the same relatively low-conductivity material (e.g., steel). For the middle graph, the embossment and the tube are both of a high conductivity material (e.g., copper). The upper graph corresponds to the case where the tube is highly conducting (e.g., copper) compared with the embossment (e.g., steel). The ordinate variables and scales of the middle and upper graphs are the same as those of the lower graph.

Each graph is, in turn, subdivided into two parts. The upper part shows the circumferential heat flux distribution at the tube bore. The lower part gives the temperature distribution results in terms of the dimensionless ratios that appear on the left-hand sides of equations (21) and (22). It is seen that the temperature curves consist of two disconnected segments. The left-hand segment is the temperature distribution on the exposed surface of the embossment, whereas the right-hand segment is the temperature distribution on the back side of the tube. In each graph, the curves are parameterized by the embossment radius ratio r_3/r_1.

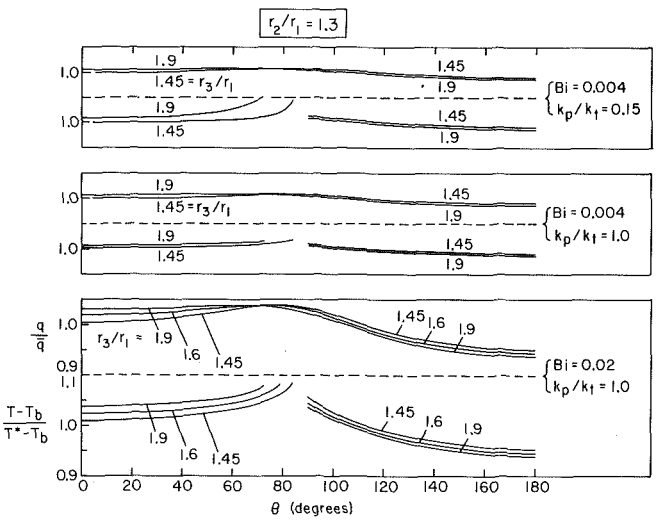

Fig. 2 Circumferential distributions of bore heat flux and outside surface temperature for laminar flow, $r_2/r_1 = 1.3$, $1.45 \leq r_3/r_1 \leq 1.9$, $L/r_1 = 20$

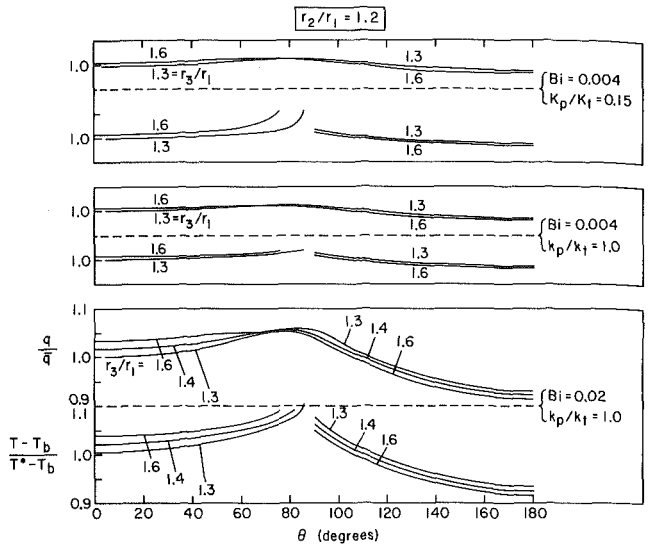

Fig. 3 Circumferential distributions of bore heat flux and outside surface temperature for laminar flow, $r_2/r_1 = 1.2$, $1.3 \leq r_3/r_1 \leq 1.6$, $L/r_1 = 20$

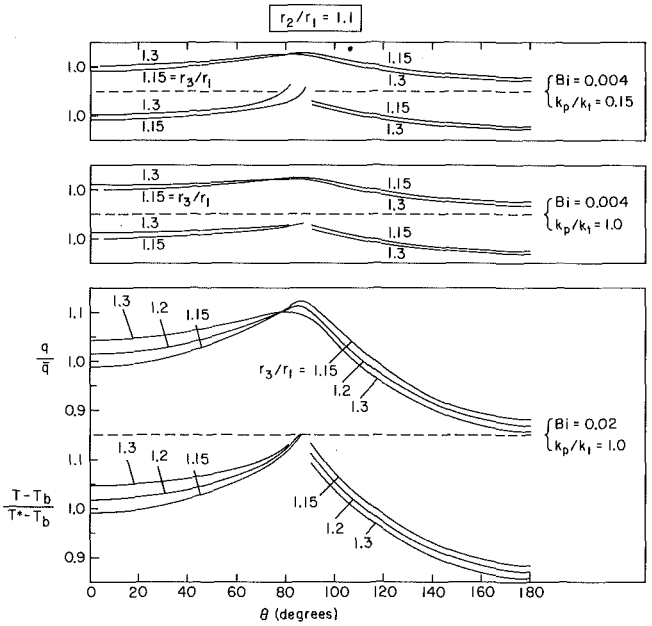

Fig. 4 Circumferential distributions of bore heat flux and outside surface temperature for laminar flow, $r_2/r_1 = 1.1$, $1.15 \leq r_3/r_1 \leq 1.3$, $L/r_1 = 20$

From an overall view of the results, it is seen that the circumferential variations are remarkably small. For a tube wall radius ratio $r_2/r_1 = 1.3$ (Fig. 2), the extreme departure of $q/\bar{q}$ from unity is about 6 percent, and this is for the case where both the embossment and the tube are of the same relatively low conductivity metal. For the other two cases in Fig. 2, the deviations from circumferential heat flux uniformity are almost imperceptible. The temperature distributions shown in the figure display a degree of uniformity comparable to that of the $q/\bar{q}$ distributions, but with a tendency to peak somewhat more sharply.

As the tube wall becomes relatively thinner (i.e., decreasing r_2/r_1), the circumferential nonuniformities tend to increase but still continue to be small. For $r_2/r_1 = 1.2$ (Fig. 3), the deviations from uniformity for the low conductivity case (lower graph) are about 2 percent larger than those for $r_2/r_1 = 1.3$, whereas for the other cases the distributions are even less affected by r_2/r_1. For the radius ratio $r_2/r_1 = 1.1$ (Fig. 4), which corresponds to thinner walls than are available in standard small diameter pipes and tubes, the results for the low conductivity case show deviations from unity as high as 12–15 percent; however, the other cases are, for all practical purposes, circumferentially uniform.

From the foregoing, it may be concluded that for standard tube dimensions and for laminar flow, the convective heat flux at the tube bore and the outside surface temperatures can be taken to be circumferentially uniform. In fact, as will be discussed in the final section of the paper, the accounting of heat losses and of circumferential variations in the convective heat transfer coefficient would diminish the nonuniformities relative to those indicated by the present computational model.

The fact that the calculated circumferential nonuniformities are small is physically plausible. In this connection, consider the heat current which is ducted to the external boundary of the embossment by the extended surfaces. Lying directly ahead of this inflowing stream of heat is the tube bore. If the convection coefficient at the bore were relatively high, the major portion of the heat would be drawn directly into the fluid, and relatively little would flow circumferentially through the walls of the tube and the embossment. Under these circumstances, the circumferential distribution of the bore heat flux would be very nonuniform, with a high peak in the region of attachment of the extended surface.

On the other hand, if the convection coefficient were relatively low, the heat stream would encounter a formidable resistance to its direct passage into the fluid. Instead, it is easier for the heat to flow circumferentially through the walls before entering the fluid. Consequently, the heat flux at the bore would be relatively free of circumferential nonuniformities.

Plausibility arguments similar to the foregoing can be employed to explain the circumferential temperature distributions.

The preceding discussion indicates that low heat transfer coefficients promote circumferential uniformity and high heat transfer coefficients promote circumferential nonuniformity. Since laminar flows are characterized by relatively low heat transfer coefficients (i.e., $\mathrm{Bi} \ll 1$), it is plausible that the associated circumferential nonuniformities are small, as was demonstrated by the results of Figs. 2–4. By the same token, it is to be expected that larger nonuniformities will be associated with turbulent flows, since they have relatively high heat transfer coefficients.

In addition to the foregoing, other interesting trends can be identified in Figs. 2–4. For instance, for a fixed tube-wall radius ratio, the effect of increasing the thickness of the embossment plate is both to elevate and flatten the $q/\bar{q}$ distribution on the upper portion of the tube, with similar effects on the temperature distribution. On the other hand, both the level of $q/\bar{q}$ and of the temperature distribution are diminished on the lower portion.

The results presented thus far have been for extended surface lengths $L/r_1 = 20$. The influence of L/r_1 has been examined for the full range of the parameter values of Figs. 2–4. Inasmuch as the effects are qualitatively identical for all cases, it is only necessary to present a single figure to illustrate the results. In Fig. 5, circumferential distributions of bore heat flux and surface temperature are plotted in a similar format to that of Figs. 2–4, except that now the curve parameter is L/r_1 covering the range from 5 to 20. The figure corresponds to the intermediate tube and plate dimensions $r_2/r_1 = 1.2$ and $r_3/r_1 = 1.4$.

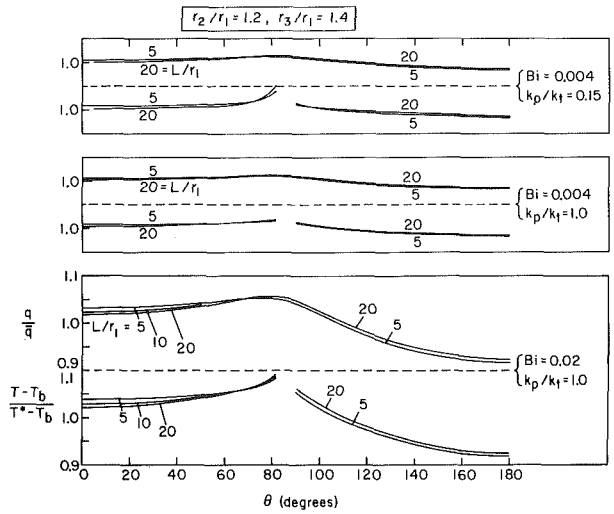

Fig. 5 Circumferential distributions of bore heat flux and outside surface temperature for laminar flow, $r_2/r_1 = 1.2$, $r_3/r_1 = 1.4$, $5 \leq L/r_1 \leq 20$

Inspection of the figure shows that the dimensionless heat flux and surface temperature distributions are insensitive to L/r_1 so that, in effect, L/r_1 is an inactive parameter. The reason for this outcome is that the energy collected by the extended surfaces is the dominant heat input in the problem for the entire range of L/r_1 that was investigated. Varying L/r_1 serves only to vary the degree of this dominance, for example, from 76 to 92 percent of the total heat input over the range from $L/r_1 = 5$ to 20. Although the dimensionless distributions are insensitive to L/r_1, the corresponding dimensional distributions would be highly responsive since both $\bar{q}$ and $(T^* - T_b)$ vary with L/r_1.

Turbulent Flow Results. On the basis of the results that have been presented, it appears that the Biot number is the most significant parameter in affecting the circumferential variations of the bore heat flux and surface temperature distributions. It is, therefore, of interest to examine how these distributions respond to a higher Biot number such as would correspond to a moderate Reynolds number turbulent flow. To this end, Fig. 6 has been prepared. This figure is the counterpart of Fig. 3, except that the respective Biot numbers are now higher by a factor of 40. The corresponding Nusselt number is that for a turbulent pipe flow at a Reynolds number of about 20,000 and a Prandtl number of 10.

In appraising Fig. 6, cognizance should be taken of the ordinate scales, which now range from zero to two or three in contrast to the range from 0.9 to 1.1 in Fig. 3. Clearly, the dimensionless circumferential variations have markedly increased. This is especially so in the cases where both the embossed plate and the tube are of low-conductivity materials (lower graph) and where the plate itself is of low conductivity (upper graph). In these cases, it appears that in view of the larger ordinate values that are attained, the temperature distributions are more markedly affected than the bore heat flux distributions. A major cause of these relatively large values is that the convective resitance, embodied in $(T^* - T_b)$, is relatively small when the flow is turbulent.

To provide further perspective on the temperature variations, it is illuminating to estimate the value of $(T^* - T_b)$ by employing equations (2) and (20). For the aforementioned turbulent flow conditions, $(T^* - T_b) \sim 0.25°\mathrm{F}$ (0.15°C), which is reflective of the low convective resistance that was noted previously. In the most extreme case depicted in Fig. 6, $(T - T_b)/(T^* - T_b)$ ranges from 3.75 to 0.2, which gives a corresponding variation of $(T - T_b)$ from about 1 to

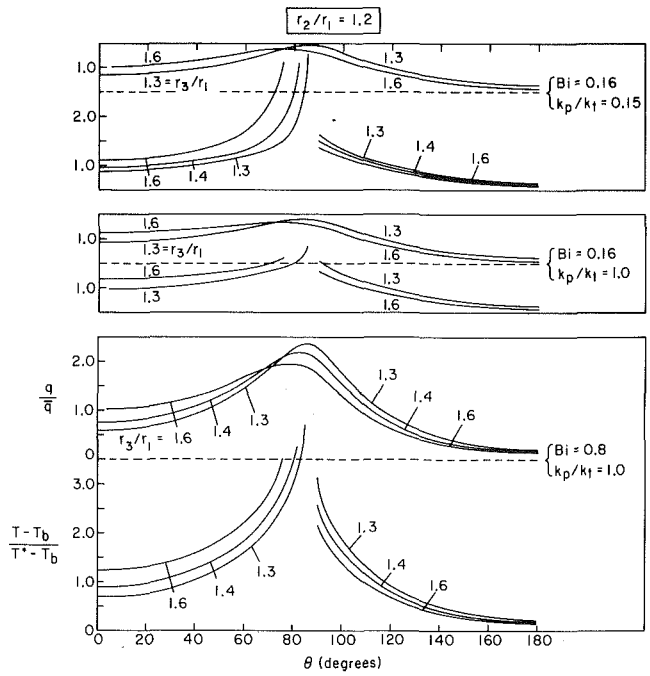

Fig. 6 Circumferential distributions of bore heat flux and outside surface temperature for turbulent flow, $r_2/r_1 = 1.2$, $1.3 \leq r_3/r_1 \leq 1.6$, $L/r_1 = 20$

0.05°F (0.55–0.03°C). As far as heat loss calculations are concerned, such a temperature variation can be regarded as negligible. Therefore, even though they appeared to be large on a percentage basis, the circumferential temperature variations are small in the absolute.

An appraisal of the effects of the bore heat flux variations shown in Fig. 6 is a more difficult task which lies beyond the scope of the present paper. The variations in the convective heat transfer coefficient at the bore that are induced by such heat flux variations can be estimated by employing the analytical results as given in equation (17) and Table 1 of [5].

Concluding Remarks

The results of the present analysis indicate that for realistic plate and tube dimensions and materials, circumferential variations of outside surface temperature and bore heat flux can be neglected, provided that the tube flow is laminar. This conclusion is strengthened by the fact that the analytical model tends to exaggerate the circumferential variations by neglecting heat losses and assuming a uniform heat transfer coefficient at the tube bore.

All of the available information on circumferentially nonuniform heating of a pipe flow [1–5] indicates that the highest convective coefficients are encountered at the least heated circumferential positions, and vice-versa. Therefore, if circumferential variations of the convective heat transfer coefficient were to be taken into account, the bore heat flux variations would be smaller than those corresponding to a uniform coefficient. Furthermore, if heat losses were included in the analysis, the largest losses would occur at circumferential positions having the highest outside surface temperature and the smallest losses at positions of lowest temperature. Thus, the accounting of the losses would tend to make the surface temperature more uniform.

As a final note, brief mention may be made of the numerical accuracy of the results. Auxiliary solutions obtained using a system containing half the number of equations and unknowns (i.e., 46 instead of 90) yielded curves indistinguishable from those of Figs. 2–6. Only in the neighborhood of the highest peaks were there slight deviations, the extent of which was about the width of a pencil line. In addition, results based on the sigma factor and on the Fourier series representations were found to be coincident within the scale of the figures except, again, for a very slight deviation at the highest peaks.

References

1 Reynolds, W. C., "Heat Transfer to Fully Developed Laminar Flow in a Circular Tube With Arbitrary Circumferential Heat Flux," JOURNAL OF HEAT TRANSFER, TRANS. ASME, Series C, Vol. 82, 1960, pp. 108–112.

2 Reynolds, W. C., "Turbulent Heat Transfer in a Circular Tube With Variable Circumferential Heat Flux," *International Journal of Heat and Mass Transfer*, Vol. 6, 1963, pp. 445–454.

3 Sparrow, E. M., and Lin, S. H., "Turbulent Heat Transfer in a Tube With Circumferentially Varying Temperature or Heat Flux," *International Journal of Heat and Mass Transfer*, Vol. 6, 1963, pp. 866–867.

4 Black, A. W., and Sparrow, E. M., "Experiments on Turbulent Heat Transfer in a Tube With Circumferentially Varying Thermal Boundary Conditions," JOURNAL OF HEAT TRANSFER, TRANS. ASME, Series C, Vol. 89, 1967, pp. 258–268.

5 Gartner, D., Johannsen, K., and Ramm, H., "Turbulent Heat Transfer in a Circular Tube With Circumferentially Varying Thermal Boundary Conditions," *International Journal of Heat and Mass Transfer*, Vol. 17, 1974, pp. 1003–1018.

6 Lanczos, C., *Applied Analysis*, Prentice-Hall, Englewood Cliffs, N. J., 1956.

7 Lanczos, C., *Discourse on Fourier Series*, Oliver and Boyd, Edinburgh and London, 1966.

J. C. Koh
J. L. Dutton
B. A. Benson
The Boeing Co., Seattle, Wash.

A. Fortini
NASA-Lewis Research Center, Cleveland, Ohio

Friction Factor for Isothermal and Nonisothermal Flow Through Porous Media[1]

Measurements were performed to determine the pressure drops for gaseous flow through porous materials of different microstructures, porosities, and thickness under isothermal and nonisothermal conditions at various temperature levels. Results were satisfactorily correlated by a simple equation relating the friction factor to the Reynolds number and porosities.

Introduction

Pressure drop for fluid flow through a porous material has been a subject of study for many years because of its application in mining, petroleum processes, chemical industries, and transpiration cooling. Due to the complex geometry of most porous media and the associated irregular flow patterns, study has been limited to experimental measurements and correlations of test data. The well-known correlations are by Ergun (reference [1][2]) and by Carman-Kozeny (reference [2]) for the pressure drop in a packed bed of particles. However, these correlations fail to represent pressure drop in geometeries other than the packed bed of particles. In fact, there exist no valid correlations for flow through a porous material having a complex microstructure such as those used for transpiration cooling. Also, the validity of the use of the room temperature and isothermal test data for nonisothermal conditions at high temperature level is still unknown. This is a very important question that must be answered because in many engineering applications, such as the design of heat exchangers, transpiration cooling system, gas cleaning scrubbers, and other process plants, the flow is highly nonisothermal and at a very high temperature level. For this reason, this study was aimed at the generation of data on pressure drop through different porous materials at various porosities under isothermal and nonisothermal conditions having different temperature levels. Isothermal tests were performed at different temperature levels from 278 to 1120 K. Nonisothermal tests were accomplished at an incident heat flux up to 2.45×10^7 W/m^2. The fluids were gaseous hydrogen and nitrogen. The purpose of this paper is to report the experimental data together with the correlations.

Experimental Apparatus and Test Procedures

Specimen. Three porous metal types were chosen for investigation. They were: (1) 304L stainless steel "rigimesh" wire form, (2) 304L stainless powder form, and (3) OFHC (oxygen free high conductivity) copper powder form. These porous metals were fully characterized to determine the contaminate level, bulk porosity, degree of interconnected porosity, uniformity of microstructure, mean hydraulic pore diameter, surface area per unit volume, and chemical composition of the parent wrought metal. The characterization procedures and results are given in references [6–8].

Fig. 1 shows a typical rigimesh specimen mounted for testing. This design is a result of the consideration of structural strength requirements and minimal conduction to maintain one-dimensional flow. The mount is machined from a 1.27-cm thick disk of 304L stainless steel, 6.35 cm in diameter. The mount has a slightly tapered hole 1.905 cm in diameter located on the disk center line. The rigimesh specimen is machined to a tapered cylinder to match the mount hole. The specimen/mount assemblies were then joined by electron beam welding. The weld yields a metal fusion joint over the entire specimen/mount interface.

Thermal isolation of the test specimen was accomplished by interrupting the conduction path between the specimen and the support structure heat sink. The mount material was removed in a cylindrical configuration around the specimen. Only a thin flange and four stiffening webs remained in contact with the porous specimen. This increased the effective thermal resistance between the porous specimen and the heat sink. After fabrication of the rigimesh test assemblies the parts were cleaned by exposure to a hot trichlorethylene degreasing bath and subsequent "bake-out" in a hard vacuum.

The porous powder materials were produced by Nuclear Metals Division of Whittaker Corporation. Complete details of the manufacture and characterization of the porous powders is given in references [7, 8]. Fig. 2 shows a typical powder specimen mounted and ready for test. Unlike the rigimesh specimens, the powders proved very difficult to electron beam weld to their holders. The primary

[1] This research is sponsored by NASA-Lewis Research Center under contract No. NAS 3-12012.
[2] Numbers in brackets designate References at end of paper.
Contributed by the Heat Transfer Division for publication in the JOURNAL OF HEAT TRANSFER. Manuscript received by the Heat Transfer Division December 14, 1976.

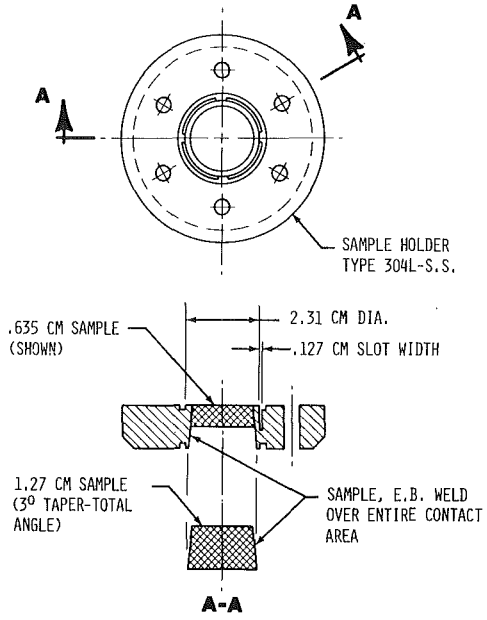

Fig. 1 Rigimesh specimen, mounted for test

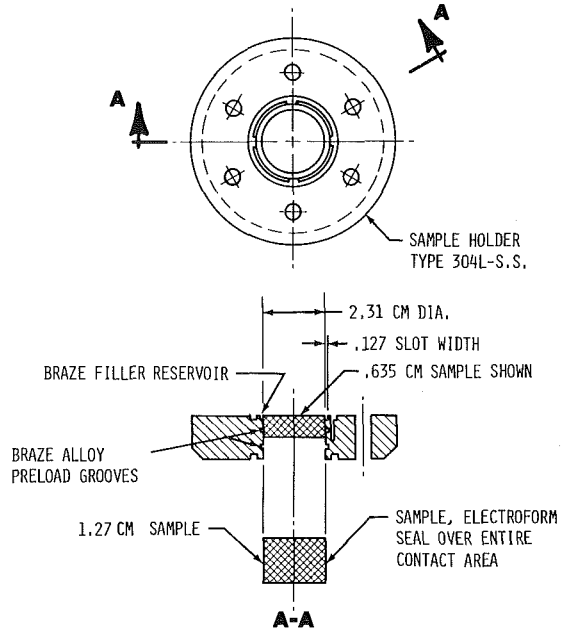

Fig. 2 Powder specimens, mounted for test

problem encountered with the weld joints centered around the low strength of the porous material, especially in the copper material and in the high porosity specimens. This problem was solved by a brazing technique. A braze alloy was preloaded into two small grooves in the holder and the assembly was heated in a vacuum furnace to produce a braze joint. The porous powder specimens were sealed on their outside circumferential surfaces to prevent braze alloy penetration during the oven heat cycle. This was accomplished by electroplating a thin layer of material on the circumferential surface of the specimens. The porous powder test assembly was cleaned by flushing with distilled water and X-ray inspected prior to testing to check for any possible braze infiltration.

Isothermal Facility. The isothermal test system is shown schematically in Fig. 3. It consists of three basic components: the hydrogen supply and control network, the hydrogen heater, and the system instrumentation.

A hydrogen supply system utilizes a bottle farm made up of 28 bottles with a charge pressure of 4.1×10^7 N/m^2 having a total hydrogen capability of 372 m^3 at standard conditions.

A regulator at the manifold end of the bottle farm gives a controlled supply pressure of 1.38×10^7 N/m^2 during a test run. The hydrogen flow rate was controlled by manually regulating the pressure drop across the porous specimen.

A hydrogen heater capable of meeting the test requirements was developed as shown in Fig. 4. The unit was driven by an electrical resistance heated core of molybdenum wire, helically wound in a dense array supported by beryllia insulators.

The resistance heater assembly was 3.81 cm in diameter and approximately 46-cm long. Concentric with the heater core was a cylindrical heat exchanger device. This device was constructed from a 152-cm long, 0.635-cm dia stainless tube of 0.0508-cm wall thickness. The stainless tube was wound over a bar to form a cylinder 5.08 cm in diameter in the same manner as a coil spring. The seam between adjacent coils of tube was welded along the entire coil length to form a sealed cylinder. When installed in the pressure vessel the heat exchanger and resistance core were arranged so that the incoming hydrogen flowed through the heat exchanger before passing over the resistance heater core. Also, the system was equipped with a valve, external to the pressure vessel, which allowed a bypass flow of hydrogen directly from the supply to the resistance core. This arrangement yielded a heater with a very wide operating range. For tests where the mass flow was very small, essentially all the heat transfer takes place in the tube coil. On the other hand, for the high flow rate tests, the heat exchanger was partially bypassed to avoid excessive pressure drop, and velocity in the core was sufficient to accomplish the required heat transfer. The resistance core temperature ranged between 1400 and 2200 K (lengthwise average) depending on test conditions, while the stainless tub coil ranged from 940 to 1400 K.

Isothermal Test Instrumentation. The hydrogen mass flow was measured by "short radius" ASME orifice plates, with six different diameters required for the total flow range. The pressure level and pressure differential across a plate were measured with strain gage

Nomenclature

d = hydraulic diameter or diameter
f = friction factor
g = gravitational constant
H = length of cylinders
k = viscous permeability
L = thickness of porous material
$\dot{m}$ = mass flux
p = pressure
$\Delta p = (P_{up} - P_{dn})$
R = gas constant
s = internal surface area per unit volume
Re = Reynolds number
T = temperature
x = coordinate axis
α = pressure drop coefficient due to viscous force
β = pressure drop coefficient due to inertia force
μ = viscosity
ξ = porosity—voil volume/total volume
ρ = density of coolant

Subscripts

c = cylinders
dn = downstream
p = particle
up = upstream

Superscript

$\bar{}$ = mean value

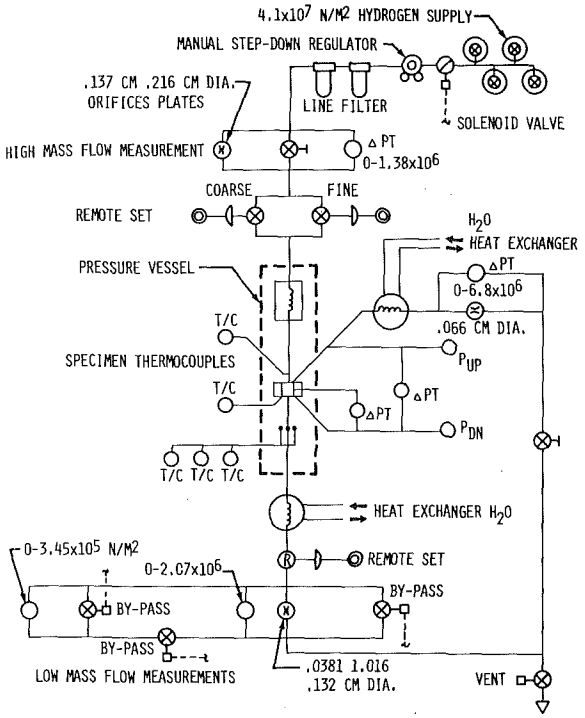

Fig. 3 Schematic of isothermal test setup

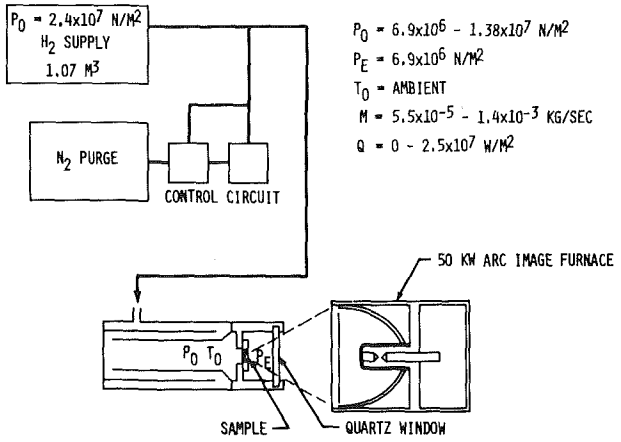

Fig. 5 Diabatic test schematic

transducers. For pressure differential across the orifice plates, the transducers used were $0–3.45 \times 10^5$ N/m^2 and $0–2.07 \times 10^6$ N/m^2. The overall error in the mass flow measurement system was less than ±3 percent. For the pressure level and pressure differential across the porous specimen, the transducers used were $0–6.9 \times 10^6$ N/m^2 and $0–1.38 \times 10^7$ N/m^2. The error in pressure measurements is less than ±1½ percent.

Temperature measurements were made with chromel-alumel thermocouples. The gas temperature was measured directly upstream of the test specimen with a shield thermocouple and again downstream of the specimen. The specimen material temperature was measured in three locations at the downstream surface. The three locations were at the center, the edge, and midradius on the specimen. These surface thermocouples were spring loaded, yielding a high surface contact force.

Nonisothermal Test Hardware. The general layout of the heat transfer test system is shown schematically in Fig. 5. The major test system components are the hydrogen supply which is essentially the same as that for isothermal test, arc-image furnace and light pipe, and the test chamber and instrumentation.

Arc-Image Furnace. A comprehensive description of the development and calibration of the arc-image furnace is given in reference [9]. A special feature of the lamp is its small (6-mm) arc gap. The small gap provides the high radiance and source geometry required to yield the desired irradiance at the target with the 56 cm collector. The lamp was designed and built by the Tamarack Scientific Company.

A light pipe was used to obtain a more uniform heat flux distribution at the test section. A typical heat flux scan with the light pipe is shown in Fig. 6.

Heat Transfer Test Instrumentation. Test temperature at the orifice location and the upstream gas and specimen temperature were measured with chromel alumel thermocouples referenced at 340 K.

Tests with multiple thermocouples located on various test specimens showed that there existed only very small radial temperature gradients in the porous specimens. Therefore, a surface temperature measurement made at the specimen edge would yield nominally the same data as a measurement made at the center. The material surface temperatures were measured by spot welding a small (0.0127-cm dia wire) thermocouple junction at each specimen edge.

The hot side gas temperature was measured by a probe shown in Fig. 7. The probe is basically two tubes, one copper and the other stainless steel. The stainless tube has a coolant flow of gaseous nitrogen which flowed down the tube interior and returned via a smaller tube within the stainless tube. The copper tube runs parallel with the stainless tube in such a way that it is in the shadow of the cooled stainless tube at the entrance to the light pipe. The arrangement reduces the heat load on the copper tube by protecting it with the cooled stainless tube. The copper tube terminates 0.635 cm from the heated

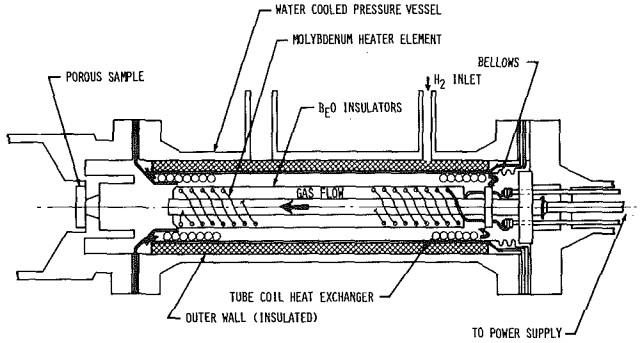

Fig. 4 Isothermal hydrogen heater

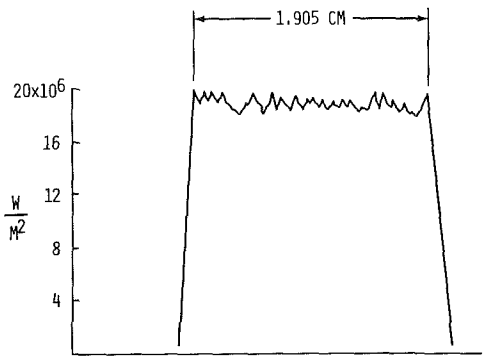

Fig. 6 Typical high-power scan with light pipe

Table 1 Test variables and ranges

Porous materials:	Stainless steel rigimesh, stainless steel sintered spherical particles, OFHC sintered spherical particles
Porosities:	10–40 percent
Thickness:	0.635–1.27 cm
Temperature (isothermal):	278–1120 K
Incident radiation:	up to 2.45×10^7 W/m^2
Temperature gradient (nonisothermal):	0–10^5 K/m
Pressure level:	1.52×10^5 N/m^2–11×10^7 N/m^2
Mass flux:	0.5–84 kg/m^2-s
Gas:	H_2, N_2

specimen surface. A small (0.0625-cm dia) sheathed thermocouple was located within the copper tube, and held on the center line by small spacers. Due to a positive pressure, a sample of the heated hydrogen flows through the copper tube and past the thermocouple junction yielding the desired temperature data. The pressure drop available for this flow is largely spent at the thermocouple junction and near vicinity. Therefore, the velocity at the junction is quite high and the thermocouple setup has a high recovery factor.

Results. Tests have been performed over a wide range of variables. A summary of variables and their ranges are presented in Table 1. Detailed test conditions and results are reported in reference [6]. Only graphical results are presented here.

Correlation of Results

Basic Equations. All published experimental data showed that the pressure drop for flow through porous media can be represented as the sum of two terms, one linear in the velocity (viscous contribution) and the second quadratic in the velocity (inertia contribution) (references [1–5, 11]). Thus, all the pressure drop data are correlated in a form derived from the following equation.

$$-\frac{dp}{dx} = \alpha \frac{\mu \dot{m}}{\rho g} + \beta \frac{\dot{m}^2}{\rho g} \tag{1}$$

Using the equation of state for ideal gas, $\rho = p/RT$, equation (1) can be integrated to give:

$$\bar{\rho} \Delta p = \alpha \frac{\mu \dot{m} L}{g} + \beta \frac{\dot{m}^2 L}{g} \tag{2}$$

where

$$\bar{\rho} = \frac{\bar{p}}{RT} = \frac{P_{up} + P_{dn}}{2RT}$$

$$\Delta P = P_{up} - P_{dn}$$

Equation (2) may be rewritten in terms of the more familar parameters, friction factor f, and Reynolds number Re, as follows:

$$f\mathrm{Re}^2 = 2\alpha \frac{d}{s} \mathrm{Re} + 2\beta \frac{1}{s} \mathrm{Re}^2 \tag{3}$$

where

$$f = \frac{\bar{\rho} \Delta p}{\frac{1}{2} \frac{\dot{m}^2}{g} sL} \tag{4}$$

$$\mathrm{Re} = \frac{\dot{m} d}{\mu} \tag{5}$$

Characteristic Length

The characteristic length used in the Reynolds number and friction factor are the hydraulic diameter d and the reciprocal of the internal surface area per unit volume s. The numerical values of d and s, as taken from the mercury penetration measurements of references [6, 8], are given by the following expressions:

$$d = \begin{cases} 1.28 \times 10^{-3}\, \xi^{1.68} \text{ (rigimesh)} \\ 2.2 \times 10^{-4}\, \xi^{1.16} \text{ (sintered stainless steel powders)} \\ 1.51 \times 10^{-4}\, \xi^{1.16} \text{ (sintered OFHC copper powders)} \end{cases} \tag{6}$$

$$s = \begin{cases} 3.2 \times 10^{2}\, \xi^{-0.58} \text{ (rigimesh)} \\ 1.69 \times 10^{3}\, \xi^{-0.16} \text{ (sintered stainless steel powders)} \\ 2.46 \times 10^{3}\, \xi^{-0.16} \text{ (sintered OFHC copper powders)} \end{cases} \tag{7}$$

For the packed bed of spheres and cylinders, the surface area per unit volume is given by:

$$s \begin{cases} \frac{6}{d_p}(1 - \xi) & \text{spherical particles} \\ \frac{2(1-\xi)}{d_c} \frac{d_c}{H} + 2 & \text{cylinders} \end{cases} \tag{8}$$

The hydraulic diameter is calculated from:

$$d = \frac{4\xi}{s} \tag{9}$$

Correlation Equations

When the isothermal test data are plotted in a log-log format, it is found that $f\mathrm{Re}^2$ can be represented by a set of parallel lines. For nonisothermal cases, the same correlation is valid provided that the property values $\bar{\rho}$ and μ are evaluated at the log mean temperature defined as:

$$T_{LM} = T_1 \frac{\frac{T_2}{T_1} - 1}{\ln \frac{T_2}{T_1}} \tag{10}$$

where T_1 and T_2 are the gas temperature at the inlet and outlet surfaces, respectively. It may be pointed out that the log mean temperature is the true average temperature of the gas when the temperature is an exponential function of x, the distance through the specimen. No attempts were made to determine the temperature distribution in the porous media in this study. However, it was shown in reference [14] that the temperature in porous media varies exponentially along the flow direction. It was for this reason that the log mean temperature was employed for the evaluation of the property values in nonisothermal cases.

It was found that the coefficient α and β in equations (2) and (3) are functions of material structure and porosity. For each material structure, the correlation can be simply represented by:

$$f\mathrm{Re}^2 = C_1 y(1 + C_2 y)$$

where:

$$y = \frac{\mathrm{Re}}{\xi(1 - \xi)^n} \tag{11}$$

and C_1, C_2, n are constants.

For the material in this study and the data on packed beds of spheres, cylinders, and cubes [12, 13], the constants C_1, C_2, and n are given in Table 2. A comparison of test data and correlations is shown in Figs. 8–11.

Fig. 8 shows a comparison between the correlation (equation (11)) and the test data for sintered 304L wire mesh (rigimesh). The porosity of the material was from 0.095 to 0.408 and the temperature was from 278 to 1120 K. Both isothermal and nonisothermal data are shown. For the nitrogen gas, only isothermal tests were performed. Clearly, Fig. 8 shows that the correlation given by equation (11) represents the data satisfactorily.

Fig. 9 shows a comparison between the correlation equation and the test data for sintered 304L stainless spherical powders at various porosities. The incident heat flux was up to 2.45×10^7 W/m^2 and the

Table 2 C_1, C_2, and n of various porous structures

Porous structures	C_1	C_2	n	Porosities	Re	Ref. source
Woven and sintered wire mesh (rigimesh)	1.99	7.39×10^{-5}	3.9	0.087 – 0.40	0.7 – 870	10
Sintered 304L stainless spherical powder	3.42	8.88×10^{-5}	3.8	0.1 – 0.31	0.5 – 150	10
Sintered OFHC copper powder	10.7	7.55×10^{-4}	2.8	0.1 – 0.31	0.35 – 96	10
Packed bed of spherical particles, cylinders, or cubes	22.8	1.17×10^{-3}	2	0.359 – 0.478	30 – 1100	12 & 13

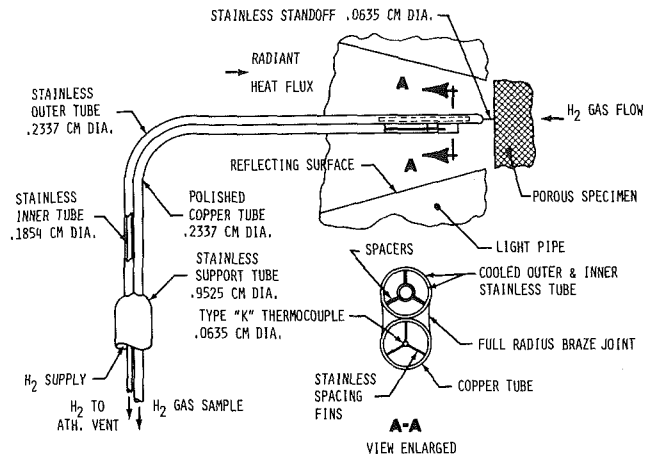

Fig. 7 Gas temperature measurement probe

temperature level up to 1100 K. Again, the correlation appears to represent the data quite well.

Fig. 10 shows a comparison between the correlation equation and the test data of sintered OFHC copper spherical powders. Again, it may be concluded from Fig. 10 that the correlation equation (11) represents the experimental data of OFHC copper powders very well.

Fig. 11 shows a comparison between the correlation equation and the test data for a packed bed of spherical particles, cylinders, or cubes [12, 13]. The porosity was from 0.357 to 0.478. Even though the microstructures vary quite considerably, the correlation equation represents the test data quite well.

In reference [4], experimental data on pressure drop for compressible gas flows in a foametal specimen at 0.95 porosity were reported. The data are replotted in Fig. 12. Since there is no detailed information on the microstructures of the foametal, the variables in Fig. 12 are similar but not identical to those in Figs. 8–11. Clearly, Fig. 12 shows that the data are neatly represented by a simple line. This indeed gives another check on the validity of the correlation form given by equation (11).

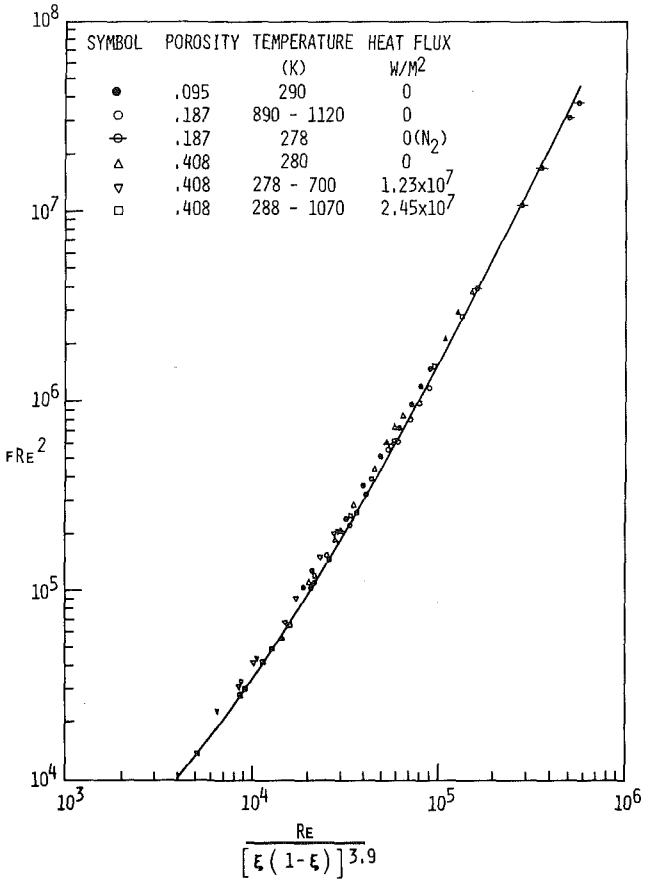

Fig. 8 Pressure drop characteristics for flow through sintered 304L wire mesh (rigimesh)

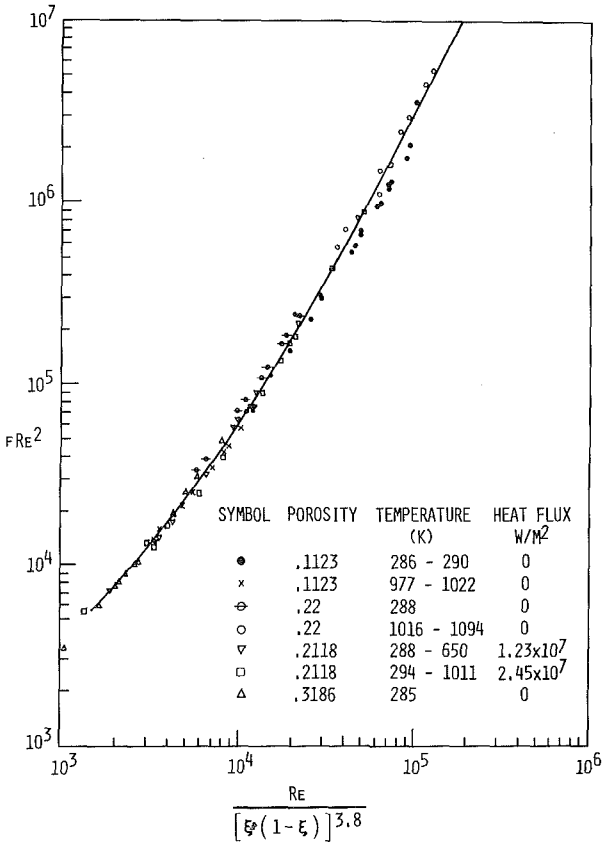

Fig. 9 Pressure drop characteristics for flow through sintered 304L stainless special powders

In reference [5], isothermal pressure drops through porous materials at several temperature levels were reported. Insufficient information is provided for replotting the data in the form given by equation (11).

An examination of Figs. 8–11 shows that the correlation given by equation (11) represents all the test data at various porosities and geometry quite well. Also, since the correlation includes the data for both hydrogen and nitrogen, it may be concluded that the correlation is equally valid for other gases. Finally, since the data includes room temperature gas, high temperature gas, and isothermal and nonisothermal conditions, it is clear that the correlation is valid for both isothermal and nonisothermal flow at all temperature levels of practical interest provided that the property values of the gases are evaluated at a log mean temperature.

Conclusions

Pressure drops for gaseous flow through porous materials of different microstructures, porosities, and thicknesses have been measured under isothermal and nonisothermal conditions at various temperature levels. The significance of this study includes:

1 Friction factor for flow through porous media under room temperature and isothermal conditions is applicable for high-temperature and nonisothermal conditions provided the property values of fluid are evaluated at a log mean temperature between the inlet and exit planes.
2 Friction factor as a function of Reynolds number is independent of gas type (N_2, H_2, etc.) and temperature levels.
3 For flow through rigimesh, sintered powder, and packed bed of particles, the pressure drop can be computed from the equations presented in this paper.
4 For flow through porous media having microstructures other than those studied herein, simple isothermal tests are required

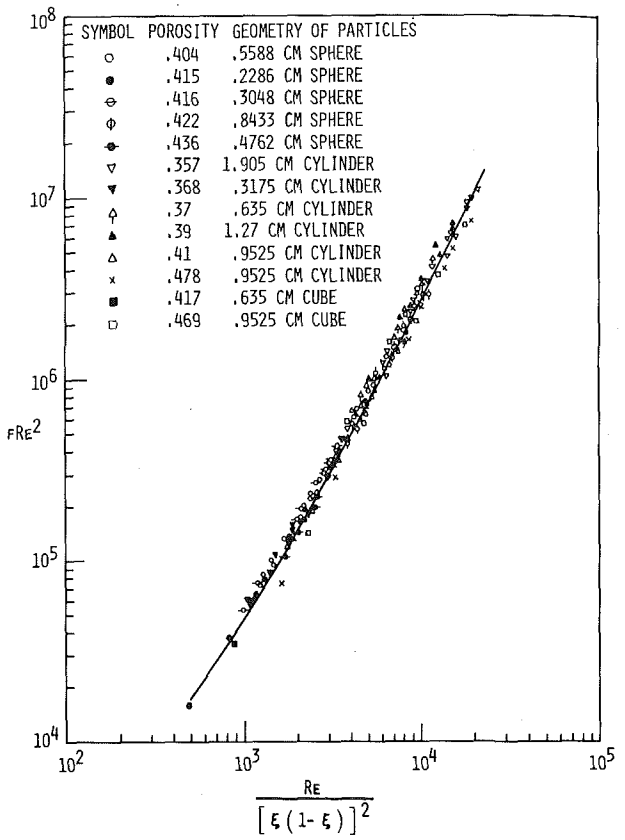

Fig. 11 Pressure drop characteristics for flow through a packed bed of spherical particles, cylinders, or cubes

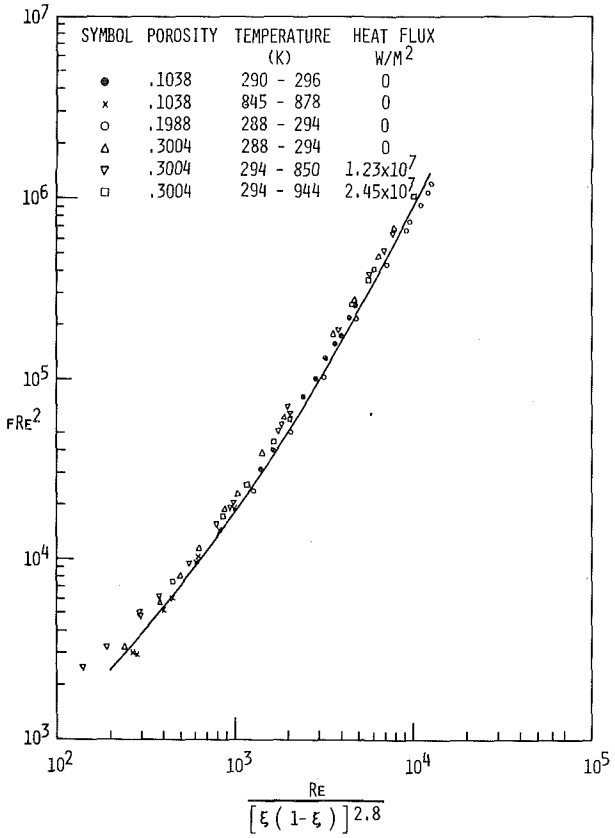

Fig. 10 Pressure drop characteristics for flow through sintered OFHC copper spherical powders

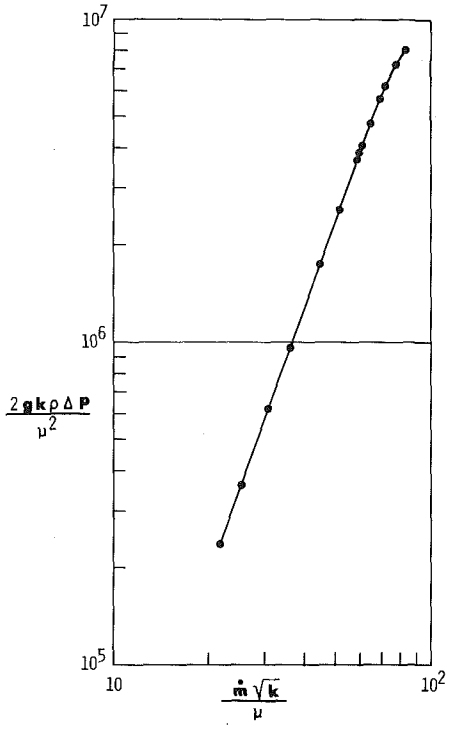

Fig. 12 Pressure drop characteristics for flow through foametal (porosity = 0.95, k = 2.04 × 10^{-4} cm^2 [4])

to determine the correlation constants C_1, C_2, and n in equation (11).

References

1 Eckert, E. R. G., and Drake, R. M., Jr., *Heat and Mass Transfer*, McGraw-Hill, New York, 1959, p. 252.

2 Beavers, G. S., Sparrow, E. M., and Rodenz, D. E., "Influence of Bed Size on the Flow Characteristics and Porosity of Randomly Packed Beds of Spheres," *Journal of Applied Mechanics*, Vol. 40, 1973, pp. 655–660.

3 Beavers, G. S., and Sparrow, E. M., "Non-Darcy Flow Through Fibrous Porous Media," *Journal of Applied Mechanics*, Vol. 36, 1969, pp. 711–714.

4 Masha, B. A., Beavers, G. S., and Sparrow, E. M., "Experiments on the Resistance Law for Non-Darcy Compressible Gas Flows in Porous Media," *Journal of Fluid Engineering*, Vol. 96, 1974, pp. 353–357.

5 Boffa, C. V., "Experimental Investigation of Gas Flow Characteristics in Transpiration-Cooled Porous Matrices," Fifth International Heat Transfer Conference, Vol. 5, 1974, pp. 88–92.

6 Regan, R. E., "Characterization of Porous Matrices for Transpiration Cooled Structures," NASA CR-72699, 1970.

7 Friedman, G., "Fabrication, Characterization and Thermal Conductivity of Porous Copper and Stainless Steel Materials," NASA CR-72755, 1971.

8 Regan, R. E., "Characterization of Porous Powder Metal Matrices for Transpiration Cooled Structures," NASA CR-72994, 1971.

9 Lunde, A. R., "Development of a High Irradiance Source," *Proceedings of the Sixth Space Simulation Conference*, NASA-SP-298, 1972.

10 Koh, J. C. Y., Dutton, J. L., Benson, B. A., "Fundamental Study of Transpiration Cooling," Final Report, NASA CR-134523, 1973.

11 Green, L., Jr., and Duwez, P., "Fluid Flow Through Porous Metals," *Journal of Applied Mechanics*, Vol. 18, No. 1, 1951, pp. 39–45.

12 Gamson, B. W., Thodos, G., and Hougen, O. A., "Heat, Mass and Momentum Transfer in the Flow of Gases through Granular Solids," *AIChE Trans.*, Vol. 39, No. 1, 1943, pp. 1–35.

13 Glaser, M. B., and Thodos, G., "Heat and Momentum Transfer in the Flow of Gases through Packed Beds," *AIChE Journal*, Vol. 4, No. 1, 1958, pp. 63–74.

14 Koh, J. C. Y., and DelCasal, E. P., "Heat and Mass Flow Through Porous Matrices for Transpiration Cooling," *Proceedings of the 1965 Heat Transfer and Fluid Mechanics Institute*, 1965, pp. 261–281.

A. Bejan
Miller Research Fellow,
Department of Mechanical Engineering,
University of California,
Berkeley, Calif.
Assoc. Mem. ASME

The Concept of Irreversibility in Heat Exchanger Design: Counterflow Heat Exchangers for Gas-to-Gas Applications

The thermal design of counterflow heat exchangers for gas-to-gas applications is based on the thermodynamic irreversibility rate or useful power no longer available as a result of heat exchanger frictional pressure drops and stream-to-stream temperature differences. The irreversibility (entropy production) concept establishes a direct relationship between the heat exchanger design parameters and the useful power wasted due to heat exchanger nonideality. The paper presents a heat exchanger design method for fixed or for minimum irreversibility (number of entropy generation units N_S). In contrast with traditional design procedures, the amount of heat transferred between streams and the pumping power for each side become outputs of the N_S design approach. To illustrate the use of this method, the paper develops the design of regenerative heat exchangers with minimum heat transfer surface and with fixed irreversibility N_S.

Introduction

Traditionally, counterflow heat exchangers are designed to accommodate the transfer of a certain amount of heat between two fluids at given flow rates and inlet temperatures with specified amounts of pumping power for each stream. Actual design techniques are presented in detail in many thermal engineering texts [1, 2].[1]

By specifying the amount of heat to be transferred from stream to stream, the designer specifies the heat exchanger effectiveness or, in effect, the size of the stream-to-stream ΔT across which the heat transfer is to take place. At the same time, by specifying the amounts of pumping power invested in pushing each stream through the heat exchanger, one specifies the frictional ΔP allowed for each side. It is important to realize that the heat transfer across the stream-to-stream ΔT and the frictional ΔP experienced by each stream represent two different facets of one single aspect of the heat exchanger, namely, its degree of thermodynamic irreversibility.

Therefore, it seems natural to base the design process on the specification of how irreversible the resulting unit can be instead of specifying the allowable ΔT and ΔP's. Once the irreversibility level is selected, the heat exchanger geometric parameters can be chosen to achieve this level. Features such as the heat exchanger effectiveness (i.e., the amount of heat transferred between streams) and the pumping power needed for each stream become outputs of the design method.

The objective of this paper is to propose a heat exchanger design method based on the concept of thermodynamic irreversibility (entropy generation). The class of gas-to-gas counterflow heat exchangers was selected to illustrate the method. For the sake of clarity, the discussion focuses on nearly ideal (small ΔT, small ΔP's) and nearly balanced ($C_{\min} \simeq C_{\max}$) counterflow heat exchangers of the shell-and-tube type.

Entropy Generation Analysis

In an engineering system in steady state, the rate of thermodynamic irreversibility $\dot{I}$ is directly related to the lost (wasted) useful power [3],

$$\dot{I} = \dot{W}_{\text{reversible}} - \dot{W}_{\text{actual}} \tag{1}$$

In power systems, $\dot{I}$ represents that fraction of the maximum theoretical power output no longer available due to system irreversibilities. In refrigeration systems, $\dot{I}$ is power required in addition to the minimum theoretical power input. Quantitatively, the system irreversibility rate $\dot{I}$ is equal to the product of the environment absolute temperature T_0 and the net entropy generation rate for the system [3],

$$\dot{I} = T_0 \Sigma \dot{S} \tag{2}$$

[1] Numbers in brackets designate References at end of paper.

Contributed by the Heat Transfer Division for publication in the JOURNAL OF HEAT TRANSFER. Manuscript received by the Heat Transfer Division November 17, 1976.

In equation (2), the summation is carried over all irreversible components present in the system. Thus, by estimating the rate of entropy generation $\dot{S}$ of one system component such as a heat exchanger, one determines the degree to which that component contributes to the total useful power wasted by the system. The analysis which follows is based on calculating the rate of entropy generation $\dot{S}$ in the heat exchanger.

The design approach presented here applies primarily to regenerative-type heat exchangers used in gas turbine power cycles and low temperature refrigeration/liquefaction plants. The number of entropy generation units N_S design method recognizes the fact that regenerators serve the function of isolating the hot end of the cycle from the cold end. For example, the key function of a Brayton cycle regenerator is not to transfer a given amount of heat from one stream to another but rather to allow the extreme temperature ends of the cycle to exchange dense fluid for less dense fluid in the most reversible way possible. A similar observation can be made relative to the purpose of the blood counterflow present in the legs of wading birds.

Irreversibility analyses of heat exchangers designed to transfer a certain, specified, amount of heat between streams have been reported in the literature [4]. It seems that the method of designing for specified irreversibility or for minimum irreversibility has so far been used only in low-temperature engineering, especially in the thermal design of large-scale superconducting systems for power conversion, transmission, and storage. In particular, this technique was applied to the thermodynamic optimization of heat exchangers for load-carrying supports of large superconducting systems [5–8].

Counterflow Heat Exchangers for Gas-to-Gas Applications

Consider the counterflow heat exchanger shown schematically in Fig. 1. For each of the two ideal gas streams the following quantities are given:

—inlet temperatures, T_1 and T_2,

—inlet pressures, P_1 and P_2,

—capacity rates, $(\dot{m}c_p)_1 = C_{\min}$ and $(\dot{m}c_p)_2 = C_{\max}$.

Note that no assumption is made at this point concerning the relative magnitude of the inlet temperatures, the stream-to-stream ΔT's and the frictional ΔP's. The counterflow of Fig. 1 is the most general arrangement, although for ease of orientation, subscript 1 was assigned to the quantities referring to the stream with the smaller of the two capacity rates. While following the analytical development of the irreversibility method, the reader will find useful the sketch of Fig. 5. The regenerative heat exchanger of Fig. 5 will eventually be discussed in the design example which concludes the presentation.

We will now take a close look at the rate of thermodynamic irreversibility present in the heat exchanger and see how it is affected by changes in the heat exchanger geometry. The time rate of entropy production in the heat exchanger as an open system is calculated by performing an entropy flux analysis on the control volume of Fig. 1:

$$\dot{S} = \dot{m}_1(s_{\text{out}} - s_{\text{in}})_1 + \dot{m}_2(s_{\text{out}} - s_{\text{in}})_2 \tag{3}$$

In equation (3), the heat transfer across the exchanger outerwalls was assumed negligible. Expressing the ideal gas entropy changes in terms of the end pressures and temperatures [9, 10], equation (3) becomes

$$\dot{S} = C_{\min}[\ln (T_{1_{\text{out}}}/T_1) + (R/c_p)_1 \ln (P_1/P_{1_{\text{out}}})] + C_{\max}[\ln (T_{2_{\text{out}}}/T_2) + (R/c_p)_2 \ln (P_2/P_{2_{\text{out}}})] \tag{4}$$

where the stream outlet properties depend on the actual geometry chosen for the heat exchanger. The first law of thermodynamics for the control volume of Fig. 1,

$$C_{\min}(T_1 - T_{1_{\text{out}}}) + C_{\max}(T_2 - T_{2_{\text{out}}}) = 0 \tag{5}$$

coupled with the definition of heat exchanger effectiveness [1],

$$\epsilon = (T_{1_{\text{out}}} - T_1)/(T_2 - T_1) \tag{6}$$

allows us to eliminate $T_{1_{\text{out}}}$, $T_{2_{\text{out}}}$, expressing $\dot{S}$ solely in terms of the given parameters and ϵ, $(\Delta P/P)_1$ and $(\Delta P/P)_2$.

Defining the *number of entropy production units* N_S as

$$N_S = \dot{S}/C_{\max} \tag{7}$$

the heat exchanger rate of entropy production formula (4) takes the following nondimensional form

$$N_S = \frac{C_{\min}}{C_{\max}} \ln\left[1 + \epsilon\left(\frac{T_2}{T_1} - 1\right)\right] + \ln\left[1 - \frac{C_{\min}}{C_{max}}\epsilon\left(1 - \frac{T_1}{T_2}\right)\right] - \frac{C_{\min}}{C_{\max}}\left(\frac{R}{c_p}\right)_1 \ln\left(1 - \frac{\Delta P_1}{P_1}\right) - \left(\frac{R}{c_p}\right)_2 \ln\left(1 - \frac{\Delta P_2}{P_2}\right) \tag{7a}$$

Expression (7*a*) shows a separation of the entropy production contribution due to the stream-to-stream temperature difference ΔT (the first two terms) from the contribution due to frictional pressure drops (the last two terms). The former, however, mixes together the ΔT effect caused by capacity rate imbalance ($C_{max} > C_{min}$) with the ΔT effect caused by the availability of only a finite amount of heat transfer area (finite N_{tu} or $\epsilon < 1$). A simpler, much more instructive form of the entropy production expression (7*a*) is obtained if one considers counterflow heat exchangers in the following limiting conditions.

Nomenclature

a = imbalance coefficient, equation (21)
A = heat transfer area
A_c = flow cross section
b = imbalance coefficient, equation (23)
B = ideal gas constants ratio, equation (24)
c_p = specific heat at constant pressure
C = capacity rate
D_i = tube inside diameter
D_0 = tube outside diameter
f = friction factor
g = dimensionless mass velocity, $G/(2\rho P)^{1/2}$
G = mass velocity
$\dot{I}$ = rate of thermodynamic irreversibility
L = flow length
$\dot{m}$ = mass flow rate
N_{Pr} = Prandtl number
N_{Re} = Reynolds number
N_S = number of entropy generation units
$N_{S,\Delta P}$ = N_S due to friction ΔP in the channel
$N_{S,\Delta T}$ = N_S due to heat transfer across a finite ΔT
N_{St} = Stanton number
N_{tu} = number of heat transfer units
P = pressure, absolute
r_h = hydraulic radius
R = ideal gas constant
s = specific entropy
$\dot{S}$ = rate of entropy production
T = temperature, absolute
U = overall heat transfer coefficient
Vol = heat exchanger volume per side
$\dot{W}$ = mechanical power
Δ = difference
ϵ = heat exchanger effectiveness
ρ = gas density
τ = temperature span parameter, equation (22)

Subscripts

0 = environment
1 = low capacity rate side
2 = high capacity rate side

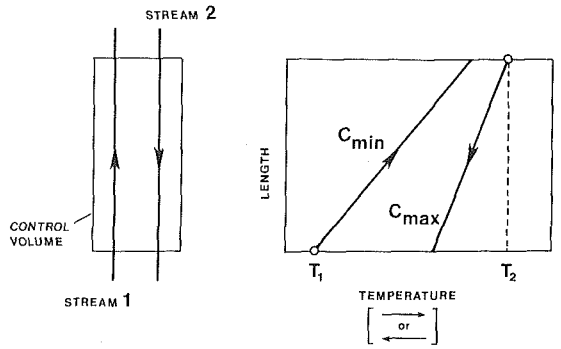

Fig. 1 Schematic of temperature distribution in a counterflow heat exchanger

I Nearly Ideal Heat Exchangers. This limit is characterized by small stream-to-stream ΔT's and small frictional ΔP's such that the following inequalities hold:

$$1 - \epsilon \ll 1 \tag{8a}$$

and

$$(\Delta P/P)_{1,2} \ll 1 \tag{8b}$$

Rewriting expression (7) in the limit (a, b) and expressing ϵ in terms of N_{tu},

$$N_S \simeq \frac{C_{\min}}{C_{\max}} \ln \frac{T_2}{T_1} + \frac{C_{\max}}{C_{\min}} \ln \left[1 - \frac{C_{\min}}{C_{\max}} \left(1 - \frac{T_1}{T_2} \right) \right] + \left(\frac{C_{\min}}{C_{\max}} \right)^2 \left(1 - \frac{C_{\min}}{C_{\max}} \right) \frac{\left(1 - \frac{T_1}{T_2} \right)^2}{1 - \frac{C_{\min}}{C_{\max}} \left(1 - \frac{T_1}{T_2} \right)} \frac{\exp \left[-N_{tu} \left(1 - \frac{C_{\min}}{C_{\max}} \right) \right]}{1 - \frac{C_{\min}}{C_{\max}} \exp \left[-N_{tu} \left(1 - \frac{C_{\min}}{C_{\max}} \right) \right]} + \frac{C_{\min}}{C_{\max}} \left(\frac{R}{c_p} \right)_1 \left(\frac{\Delta P}{P} \right)_1 + \left(\frac{R}{c_p} \right)_2 \left(\frac{\Delta P}{P} \right)_2 \tag{9}$$

Form (9) was obtained by linearly approximating the logarithms containing ϵ and the ΔP's, using the expansion $\ln (1 + y) \simeq y - y^2/2 + \ldots$, in which $y \ll 1$. The higher order terms neglected by each of the linear approximations amount to less than 10 percent if

$$\epsilon > 1 - (0.18) \frac{T_{1,2}}{|T_1 - T_2|} \tag{10a}$$

and

$$(\Delta P/P)_{1,2} < 0.2. \tag{10b}$$

Conditions (10a) and (10b) are met by a wide range of regenerative-type heat exchangers used in power and low-temperature refrigeration cycles (see numerical example at end of paper).

In equation (9), N_{tu} is the conventional number of heat transfer units [1] $AU/C_{\min}$ where A is the total heat transfer area and U the overall heat transfer coefficient based on A. The first two terms in the N_S expression (9) represent the contribution from capacity rate imbalance, the third is the contribution due to finite N_{tu}, and the last two are the contributions due to fluid friction in the heat exchanger passages.

The N_S contribution due to capacity rate imbalance,

$$N_{S,\text{imbalance}} = \frac{C_{\min}}{C_{\max}} \ln \frac{T_2}{T_1} + \ln \left[1 - \frac{C_{\min}}{C_{\max}} \left(1 - \frac{T_1}{T_2} \right) \right] \tag{11}$$

is shown graphically in Fig. 2. As expected, the number of entropy generation units increases as the imbalance becomes more pronounced. $N_{S,\text{imbalance}}$ is the only contribution left even in the "ideal" design characterized by infinite heat transfer area and zero core pressure drop. Hence, for an imbalanced counterflow heat exchanger, the size of $N_{S,\text{imbalance}}$ tells the designer when he has reached the point of diminishing returns in trying to reduce the overall number of entropy generation units N_S by increasing the N_{tu} and decreasing the frictional ΔP's.

***II* Nearly Balanced Capacity Rate.** In many gas-to-gas applications the counterflow heat exchangers of the type discussed here must handle balanced streams ($C_{\min} = C_{\max}$) or almost balanced streams ($C_{\min} \simeq C_{\max}$). The former case is typical of regenerative heat exchangers for gas turbine cycles; the latter most notably appears in the design of helium gas heat exchangers for low temperature refrigerators and helium liquefaction systems.

Applying the calculus of limits as $C_{\min} \to C_{\max}$, the number of entropy production units (9) reduces to

$$N_S \simeq N_{S,\text{imbalance}} + \left(\sqrt{\frac{T_2}{T_1}} - \sqrt{\frac{T_1}{T_2}} \right)^2 \frac{1}{N_{tu}} + \frac{C_{\min}}{C_{\max}} \left(\frac{R}{c_p} \right)_1 \left(\frac{\Delta P}{P} \right)_1 + \left(\frac{R}{c_p} \right)_2 \left(\frac{\Delta P}{P} \right)_2 \tag{12}$$

Expressing the overall N_{tu} in terms of the N_{tu} for each side of the heat transfer surface,

$$\frac{1}{N_{tu}} = \frac{1}{N_{tu_1}} + \frac{C_{\min}}{C_{\max}} \frac{1}{N_{tu_2}} \tag{13}$$

the overall number of entropy production units N_S is divided into three separate contributions:

$$N_S \cong N_{S,\text{imbalance}} + N_{S_1} + N_{S_2} \tag{14}$$

In the limit $C_{\min} \to C_{\max}$ the imbalance term given by equation (11) reduces to

$$N_{S,\text{imbalance}} = \left(\frac{C_{\max}}{C_{\min}} - 1 \right) \left(\frac{T_2}{T_1} - 1 - \frac{C_{\min}}{C_{\max}} \ln \frac{T_2}{T_1} \right) \tag{15}$$

Clearly, if $C_{\min} = C_{\max}$, the imbalance term vanishes. Except for the capacity rate ratio which is close to unity and acts as an imbalance correction factor, the number of entropy production units for each side has an identical form

$$N_{S_1} = \left(\sqrt{\frac{T_2}{T_1}} - \sqrt{\frac{T_1}{T_2}} \right)^2 \frac{1}{N_{tu_1}} + \frac{C_{\min}}{C_{\max}} \left(\frac{R}{c_p} \right)_1 \left(\frac{\Delta P}{P} \right)_1 \tag{16}$$

$$N_{S_2} = \frac{C_{\min}}{C_{\max}} \left(\sqrt{\frac{T_2}{T_1}} - \sqrt{\frac{T_1}{T_2}} \right)^2 \frac{1}{N_{tu_2}} + \left(\frac{R}{c_p} \right)_2 \left(\frac{\Delta P}{P} \right)_2 \tag{17}$$

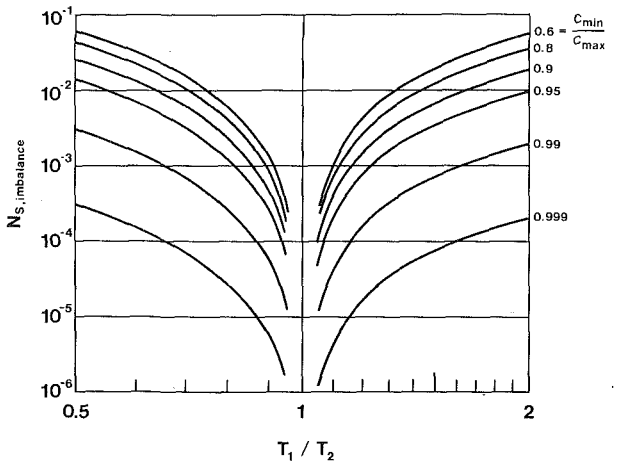

Fig. 2 Number of entropy generation units due to capacity rate imbalance versus the ratio of stream inlet temperatures

$N_{S_{1,2}}$ appears now as the sum of one contribution due to heat transfer across the heat exchanger ΔT and one contribution due to frictional ΔP losses,

$$N_{S_{1,2}} = N_{S,\Delta T_{1,2}} + N_{S,\Delta P_{1,2}} \tag{18}$$

Expressions (16)–(18) point out how increasing the number of heat transfer units and/or reducing the frictional pressure drop amounts to reducing the degree of irreversibility of that side.

The uncoupled form (16)–(18) is the reward for having considered the two successive limits, I and II. We will now analyze the manner in which the design parameters of one side of the heat transfer surface affect the number of entropy production units per side, $N_{S_{1,2}}$.

Number of Entropy Generation Units for One Side

From a design standpoint, we are interested in those combinations of hydraulic radii (r_{h_1}, r_{h_2}), minimum free-flow areas (A_{c_1}, A_{c_2}), and flow lengths (L_1, L_2) leading to an acceptable number of entropy generation units selected for the heat exchanger. For the limiting cases under consideration, the first thing we must do is to express N_S in terms of the actual flow parameters. However, since the one-side contributions (16) and (17) have a similar outlook, we will perform this transformation once, for one side only.

First, from the definitions of number of heat transfer units and friction factor for one side we have [1]

$$N_{tu_{1,2}} = (L/r_h)N_{St} \tag{19a}$$

$$(\Delta P/P)_{1,2} = f(L/r_h)G^2/(2\rho P) \tag{19b}$$

where the notation, the same as in reference [1], is explained in the Nomenclature. In writing equations (18) and (19) we have limited the discussion to bare surfaces and pressure drop dominated by core friction losses, respectively. In this analysis the group $G/(2\rho P)^{1/2}$ appearing in equation (19) is treated as a dimensionless mass velocity, g. Substituting equations (19a) and (19b) into equations (16) and (17) yields

$$N_{S_{1,2}} = \frac{a\tau}{(L/r_h)N_{St}} + bBf(L/r_h)g^2 \tag{20}$$

where

$$a_1 = 1; \qquad a_2 = C_{min}/C_{max} \tag{21}$$

$$\tau = (\sqrt{T_2/T_1} - \sqrt{T_1/T_2})^2 \tag{22}$$

$$b_1 = C_{min}/C_{max}; \qquad b_2 = 1 \tag{23}$$

$$B_1 = (R/c_p)_1; \qquad B_2 = (R/c_p)_2 \tag{24}$$

The Stanton number N_{St} and the friction factor f are both functions of the Reynolds number N_{Re}. Thus, the number of entropy generation units for one side $N_{S_{1,2}}$ is a function of three independent flow parameters, N_{Re}, L/r_h, and g. Since the mass flow rate for each side is given, specifying these parameters is equivalent to selecting the three geometric unknowns per side, r_h, A_c, and L.

The dependence of $N_{S_{1,2}}$ on N_{Re}, L/r_h, and g, equation (20), is shown qualitatively on the three-dimensional logarithmic plot of Fig. 3. The construction of Fig. 3 is actually based on turbulent flow inside round tubes, where both N_{St} and f vary as $Re^{-0.2}$; one can construct qualitatively similar three-dimensional plots for other common heat exchanger surfaces.

For a given L/r_h and N_{Re}, the number of entropy generation units generally increases as g increases. Unlike g, the ratio L/r_h plays a definite trade-off role: for a fixed g and N_{Re}, there exists an optimum L/r_h for which the resulting $N_{S_{1,2}}$ is a minimum. Large values of L/r_h lead to irreversibilities dominated by fluid friction in the heat exchanger passages. Conversely, small values of L/r_h lead to large stream-to-stream ΔT's and overall irreversibilities dominated by heat transfer across these ΔT's. The optimum ratio L/r_h can be calculated by mimimizing the function $N_{S_{1,2}}$ given by equation (20),

$$\left(\frac{L}{r_h}\right)_{opt} = \frac{1}{g}\left(\frac{a\tau}{bBfN_{St}}\right)^{1/2} \tag{25}$$

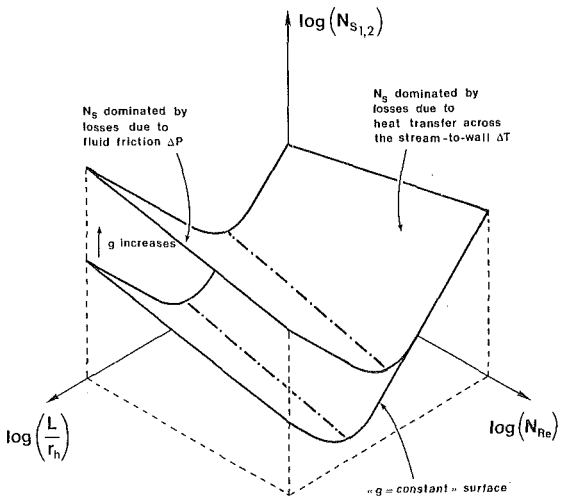

Fig. 3 Number of entropy generation units per side, as a function of L/r_h, g, and N_{Re}

The minimum number of entropy production units corresponding to $(L/r_h)_{opt}$ for each side is

$$N_{S_{1,2}}{}^{min} = 2g(ab\tau Bf/N_{St})^{1/2} \tag{26}$$

An interesting aspect of the N_S method is that it establishes a one-to-one correspondence between the mass velocity g present on one side of the heat transfer surface and the minimum number of entropy production units obtainable for that side. In other words, the selection of a mass velocity g fixes the minimum number of entropy production units per side. As illustrated later, $N_{S_{1,2}}{}^{min}$ is proportional to the mass velocity g and depends only weakly on the Reynolds number in the heat exchanger passages N_{Re}.

Heat transfer and pressure drop data are available in the form of plots of f and $(N_{St}N_{Pr}{}^{2/3})$ versus N_{Re}. Result (26) can be written in a form which brings out the N_{Re} and g dependence of $N_{S_{1,2}}{}^{min}$,

$$N_{S_{1,2}}{}^{min} = 2g\left(\frac{C_{min}}{C_{max}}\tau BN_{Pr}{}^{2/3}\frac{f}{N_{St}N_{Pr}{}^{2/3}}\right)^{1/2} \tag{27}$$

As one would expect from the analogy between momentum transfer and heat transfer, the group $[f/(N_{St}N_{Pr}{}^{2/3})]^{1/2}$ is relatively insensitive to changes in N_{Re}. The weak dependence of $N_{S_{1,2}}{}^{min}$ on N_{Re} is illustrated in Fig. 4 for four bare surfaces commonly encountered in shell-and-tube counterflow heat exchangers. The dotted lines correspond to three different arrangements of flow normal to a staggered tube bank while the solid line corresponds to flow inside circular tubes. The surface description and the origin of the data are shown in Fig. 4. The minimum number of entropy production units for one side is proportional to the gas mass velocity for that side provided L/r_h is the optimum given by equation (25).

Design Constraints

The three dimensionless unknowns for one side of the heat exchanger, (L/r_h), g, and N_{Re}, define a three-dimensional space of possible design conditions. If the degree of thermodynamic irreversibility of each side $N_{S_{1,2}}$ is specified a priori, then, via equation (20), the number of degrees of freedom for each side is reduced to two. If $N_{S_{1,2}}$ is not specified but, for a given g and N_{Re}, the ratio L/r_h is picked such that $N_{S_{1,2}}$ is a minimum, the number of degrees of freedom per side is again reduced to two.

In practice, the number of independent design parameters may be less than two per side due to additional design constraints. It would be unrealistic to attempt a review of all the design constraints which may be present. Instead we will list two frequent examples.

1 **Heat Transfer Area.** This constraint is based on economic considerations since a larger heat transfer area means increased

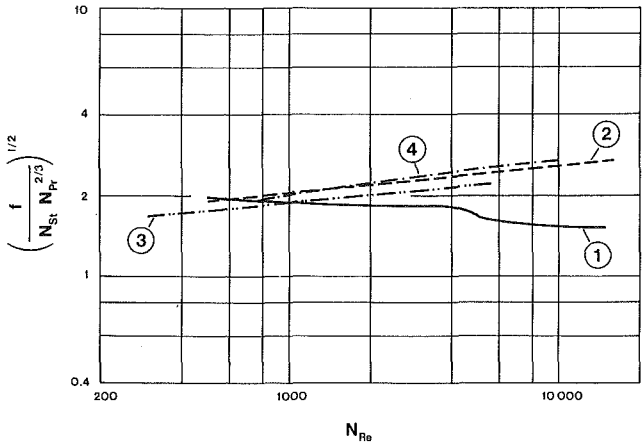

Fig. 4 $N_{S_{1,2}}{}^{min}$ **versus** N_{Re} **for four common heat exchanger surfaces [1]: (1) surface ST − 1, flow inside circular tubes; (2) surface** $S1.50 - 1.25$**, flow normal to staggered tube bank; (3) surface** $S1.25 - 1.25$**, flow normal to staggered tube bank; (4) surface** $S1.50 - 1.50$**, flow normal to staggered tube bank**

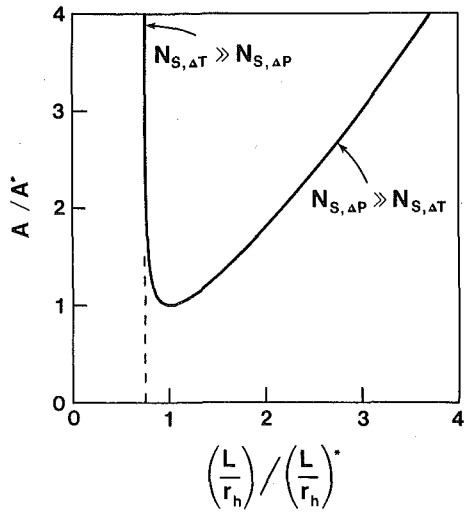

Fig. 5 Dependence of heat transfer area on L/r_h**, for a given** N_{Re} **and fixed** N_S **per side**

production costs, weight, shipping difficulties, etc. In an actual design it may be required to minimize the size of the heat transfer surface or to hold it constant at a level specified in advance. The area constraint has a double impact: once the size of the heat transfer area is selected for one side, the area for the other side is roughly the same. In the shell-and-tube example used so far, the ratio A_2/A_1 is equal to the tube diameters ratio, D_0/D_i, assuming that side 2 is the shell side. For many tube sizes the ratio D_0/D_i is approximately constant (slightly larger than unity). Once a value of A is selected, it serves as constraint for both sides of the heat exchanger.

In terms of the design terminology used in this paper, the heat transfer area A is

$$A = (L/r_h)A_c \tag{28}$$

or

$$A(2\rho P)^{1/2}/\dot{m} = (L/r_h)/g \tag{29}$$

2 Heat Exchanger Volume. The total volume occupied by the heat exchanger is an important constraint in space-limited applications. The volume of one side of the heat exchanger is given by

$$\text{Vol} = LA_c \tag{30}$$

In terms of the three dimensionless design parameters g, (L/r_h), and N_{Re}, the volume constraint can be written as

$$\text{Vol}\,(8\rho P)/(\mu\dot{m}) = N_{Re}(L/r_h)/g \tag{31}$$

Design for Minimum Area and Fixed N_S

In this section we will apply the N_S method to a concrete design case. Suppose we want to design a shell-and-tube regenerative heat exchanger for minimum heat transfer area and subject to a fixed number of entropy generation units for each side. The mathematical tools required by this design example are equations (20) and (29).

Consider only side 1 of the heat exchanger surface. Due to constraints (20) and (29), only one of the three unknowns g, L/r_h, and N_{Re} can be specified independently. The area A is not a function of N_{Re}, equation (29). At the same time, as shown by equation (20) and Fig. 3, $N_{S_{1,2}}$ depends only weakly on N_{Re}. Therefore, it is convenient to treat N_{Re} as the independent parameter since its specific value will have little impact on N_S and A. As shown in the numerical example which concludes this discussion, the selection of a particular N_{Re} is tied to other design considerations such as the availability and cost of a certain size of heat exchanger tubing.

Combining equations (20) and (29) to eliminate g, the area A becomes a function of L/r_h,

$$A\frac{(2\rho P)^{1/2}}{\dot{m}} = \frac{(L/r_h)^2(bBf)^{1/2}}{[N_{S_1}(L/r_h) - a\tau/N_{St}]^{1/2}} \tag{32}$$

where all quantities refer to side 1 of the surface. The area A reaches its minimum when the ratio L/r_h assumes the value

$$\left(\frac{L}{r_h}\right)^* = \frac{4}{3}\frac{a\tau}{N_{St}N_{S_1}} \tag{33}$$

The minimum area corresponding to equation (33) is

$$A^*\frac{(2\rho P)^{1/2}}{\dot{m}} = \frac{16}{3^{3/2}}N_{S_1}{}^{-2}\left(\frac{a\tau}{N_{St}}\right)^{3/2}(bBf)^{1/2} \tag{34}$$

The mass velocity corresponding to equation (33) and constant N_{S_1} is

$$g^* = \frac{3^{1/2}}{4}N_{S_1}\left(\frac{N_{St}}{a\tau bBf}\right)^{1/2} \tag{35}$$

As shown in Fig. 5, the selection of L/r_h is quite critical. For ratios L/r_h much larger than the optimum $(L/r_h)^*$, the fixed N_{S_1} is due primarily to frictional ΔP losses while the required area is much larger than the minimum given by equation (34). If $(L/r_h) < (L/r_h)^*$ the heat transfer surface increases sharply due to the necessary decrease in mass velocity dictated by the constant N_{S_1} condition.

As expected, the crucial design input in calculating $(L/r_h)^*$ and g^* is the number of entropy production units allowed for each side. The mass velocity number g^* is almost independent of N_{Re} (see Fig. 4). The ratio $(L/r_h)^*$ and A^* are both weak functions of N_{Re}, especially in the range $N_{Re} > 3000$. In general, A^* and $(L/r_h)^*$ will slowly decrease as N_{Re} decreases. However, since the mass velocity is practically constant, N_{Re} is reduced only by minimizing the hydraulic radius, a process which soon runs into construction limitations.

The selection of L/r_h and g for the other side of the surface is done using equations (33) and (35) with quantities referring to side 2. This time the design faces the additional constraint imposed by $A_1{}^*$, calculated previously. As mentioned in the preceding section, in shell-and-tube applications the ratio A_2/A_1 has a value close to unity. Thus, the Reynolds number N_{Re_2} becomes a dependent parameter which, using equation (35), has to be adjusted such that the resulting $A_2{}^*$ properly matches $A_1{}^*$.

The design procedure outlined in this section constitutes one example of how the N_S method can be applied. One can develop similar sizing procedures for counterflow heat exchangers facing other constraints, such as the volume constraint, of equation (31). The following numerical example illustrates the use of the simple relations developed in this section.

Numerical Example: Regenerator for a Brayton Cycle

Consider the regenerative heat exchanger for a Brayton cycle heat engine operating between a maximum temperature $T_{max} = 1100$ K and a minimum temperature $T_{min} = 300$ K $= T_0$. The cycle is sketched on the temperature-entropy diagram of Fig. 6. The isoentropic efficiency of both expander and compressor is 80 percent. The working fluid is helium. The helium pressure (absolute) at the compressor outlet is $P_H = 70$ atm ($7.09\ 10^6$ N/m^2) while the pressure at the expander outlet is $P_L = 35$ atm ($3.55\ 10^6$ N/m^2). Since the N_S method yields a design on a per unit mass flow basis, the helium mass flow rate $\dot{m}$ need not be specified at this point.

The object of this exercise is to design a shell-and-tube regenerative heat exchanger with minimum heat transfer area and fixed irreversibility rate. It is proposed to design a unit in which the lost useful power [irreversibility rate $\dot{I}$, equation (1)] equals 20 percent of the net power output of a cycle employing a reversible regenerator ($\dot{W}_{net}$). In other words, the net power output of a heat engine equipped with the designed unit is allowed to drop to 80 percent of the maximum power output possible when the regenerator is theoretically loss-free (reversible).

Further, it is assumed that the high-pressure stream is placed on the tube side (surface 1, Fig. 4) while on the shell side the flow is normal to a staggered tube bank (surface 2, Fig. 4). In the following calculations subscripts 1 and 2 are used for the high-pressure side and low-pressure side, respectively.

We begin with estimating the constants entering the design relations. The extreme temperatures seen by the regenerator are $T_1 = 419$ K and $T_2 = 888$ K, hence, $\tau = 0.59$. The capacity rates are balanced; therefore, $a_1 = a_2 = b_1 = b_2 = 1$. For helium, $B = 0.4$ and $N_{Pr} = 0.67$. The helium properties are estimated at an average temperature of 650 K: $\rho_1 = (5.2)10^{-3}$ g/cm^3, $\rho_2 = (2.6)10^{-3}$ g/cm^3, $\mu_1 = \mu_2 = (3.4)10^{-4}$ g/(cm s).

The design is executed in three steps:

I The number of entropy generation units N_S is determined from equations (7) and (2),

$$N_S = \frac{\dot{W}_{net}}{\dot{m}c_pT_0}\frac{\dot{I}}{\dot{W}_{net}} \tag{36}$$

The ratio $\dot{W}_{net}/(\dot{m}c_pT_0) = 0.31$ is the net power output per unit mass flow rate, assuming the regenerator is reversible. The second ratio is given, $\dot{I}/\dot{W}_{net} = 0.20$. Distributing the number of entropy generation units equally among the two sides of the heat exchanger surface, we obtain

$$N_{S_1} = N_{S_2} = \frac{1}{2}N_S = 0.031 \tag{37}$$

It will be shown that the choice $N_{S_1} = N_{S_2}$ leads to practically similar channel geometries r_h, L, for both sides of the heat transfer surface.

II The nondimensional parameters g, L/r_h, and N_{Re} are subject to the selection of N_{Re} for one of the two surfaces. For example, let us start with

$$N_{Re_1} = (2)10^4 \tag{38}$$

Consulting the heat exchanger surface data of reference [1] and using equations (35) and (33) we get

$$g_1^* = (0.65)N_{S_1} = 0.0202 \tag{39}$$

$$(L/r_h)_1^* = 240/N_{S_1} = 7730 \tag{40}$$

N_{Re_2} is determined from the area matching condition $A_2/A_1 = D_0/D_i$. Writing equation (34) for both surfaces and dividing side by side leads to

$$\left[\frac{(N_{St}N_{Pr}^{2/3})^{3/2}}{f^{1/2}}\right]_2 = \frac{A_1}{A_2}\left(\frac{\rho_1P_1}{\rho_2P_2}\right)^{1/2}\left[\frac{(N_{St}N_{Pr}^{2/3})^{3/2}}{f^{1/2}}\right]_1 \tag{41}$$

which, for $A_2/A_1 = 1.2$, determines

$$N_{Re_2} = (1.42)10^4 \tag{42}$$

Again, using equations (35) and (33) we obtain

$$g_2^* = (0.38)N_{S_2} = 0.0118 \tag{43}$$

$$(L/r_h)_2^* = 84.4/N_{S_2} = 2722 \tag{44}$$

III The physical dimensions r_h, L, and A_c follow immediately from the nondimensional parameters:

$$r_{h_1} = N_{Re_1}\mu_1/(4G_1) = 1 \text{ mm}, \quad \text{i.e., } D_i = 4 \text{ mm} \tag{45}$$

$$L_1 = r_{h_1}(L/r_h)_1^* = 7.73 \text{ m} \tag{46}$$

$$A_{c_1} = \dot{m}/G_1 = (0.058\,\dot{m})\text{s cm}^2/\text{g} \tag{47}$$

Similarly, $r_{h_2} = 2.5$ mm, $L_2 = 6.8$ m, and $A_{c_2} = (0.2\,\dot{m})$ s cm^2/g. Thus, the flow cross section is proportional to the mass flow rate while the flow channel geometry r_h, L, is independent of $\dot{m}$. Consequently, large mass flow rates require an increased number of identical channels placed in parallel.

Among the outputs of this design we can calculate the heat exchanger effectiveness ϵ and the ΔP on each side. Using equations (13), (16), and (20) we find that $\epsilon = 0.927$ and $(\Delta P/P)_1 = (\Delta P/P)_2 = 0.0194$. These values are well within the limitations imposed by the nearly ideal heat exchanger approximation (8*a*) and (8*b*) and (10*a*) and (10*b*).

If the calculated D_i is too small, then the last two steps II and III will have to be repeated using a larger N_{Re_1}. If due to assembly constraints L_2 must be considerably shorter than L_1, the overall N_S will have to be distributed unequally between the two sides such that $N_{S_1} < N_{S_2}$.

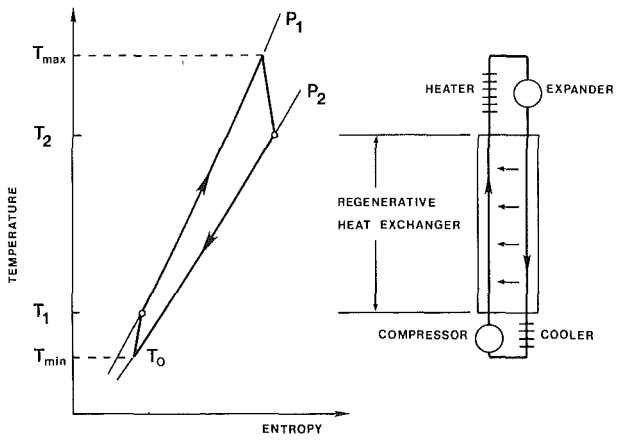

Fig. 6 Regenerative heat exchanger for a Brayton cycle heat engine

Concluding Remarks

The number of entropy generation units N_S method provides a simple and direct means of relating the heat exchanger design possibilities to the thermodynamic efficiency of the designed unit. Unlike traditional design techniques, the irreversibility method presented here is based on trading heat exchanger size and production costs directly for savings in otherwise lost useful power due to the heat exchanger irreversibilities (finite stream-to-stream temperature difference and frictional pressure drops). This method is in tune with the contemporary emphasis on approaching the engineering design issue from an energy-saving point of view, based on the limitations imposed by the second law of thermodynamics [11].

As a brief summary to the N_S method for counterflow heat exchangers, the following observations should be stressed. The number of entropy generation units for one side of the heat transfer surface $N_{S_{1,2}}$ is a strong function of the flow channel aspect ratio L/r_h and mass velocity g. $N_{S_{1,2}}$ is relatively insensitive to changes in N_{Re}. For a given g and N_{Re}, there exists an optimum ratio L/r_h for which $N_{S_{1,2}}$

is a minimum. At the optimum, the entropy production of one side is proportional to the mass velocity and relatively insensitive to the Reynolds number.

The number of entropy generation units criterion can be used in conjunction with other design constraints. As an example, we presented the design of shell-and-tube regenerators which minimizes the heat transfer area subject to a fixed N_S. This example pointed out explicitly a well known characteristic of heat exchangers, namely, highly efficient units require large heat transfer areas. In fact, from equation (34), the heat transfer area scales up with the square of $1/N_{S_{1,2}}$. In an entirely similar manner we could have presented a design which minimizes the heat exchanger volume while keeping N_S constant. Although not shown here, the volume per side of a unit designed this way scales up with the cube of $1/N_{S_{1,2}}$. Thus, we may regard $1/N_{S_{1,2}}$ as a characteristic dimension ℓ describing the size of each side of the heat exchanger, i.e.,

$$\text{heat transfer area} \sim \ell^2,$$

$$\text{volume} \sim \ell^3.$$

In conclusion, a large heat exchanger (large ℓ) is what renders a thermodynamically effective unit (small N_S).

Acknowledgments

The author thanks Prof. C. L. Tien, Chairman, Department of Mechanical Engineering, University of California, Berkeley, for encouragement and many helpful discussions. The author thanks Prof. W. M. Rohsenow, Department of Mechanical Engineering, Massachusetts Institute of Technology, for bringing reference [14] to his attention. This work was made possible by a postdoctoral research fellowship awarded by the *Miller Institute for Basic Research in Science,* University of California, Berkeley.

References

1 Kays, W. M., and London, A. L., *Compact Heat Exchangers,* McGraw-Hill, New York, 1964.

2 Fraas, A. P., and Ozisik, M. N., *Heat Exchanger Design,* Wiley, New York, 1963.

3 Van Wylen, G. J., and Sonntag, R. E., *Fundamentals of Classical Thermodynamics,* Wiley, New York, 1973, pp. 276, 277.

4 McClintock, F. A., "The Design of Heat Exchangers for Minimum Irreversibility," Paper No. 51-A-108, presented at the 1951 ASME Annual Meeting.

5 Bejan, A., and Smith, J. L., Jr., "Thermodynamic Optimization of Mechanical Supports for Cryogenic Apparatus," Cryogenics, Vol. 14, Mar. 1974, pp. 158–163.

6 Bejan, A., and Smith, J. L., Jr., "Heat Exchangers for Vapor-Cooled Conducting Supports of Cryostats," *Advances in Cryogenic Engineering,* Vol. 21, Plenum, New York, 1976, pp. 247–256.

7 Hilal, M. A., and Boom, R. W., "Optimization of Mechanical Supports for Large Superconductive Magnets," *Advances in Cryogenic Engineering,* Vol. 22, Plenum, New York, 1976, pp. 224–232.

8 Bejan, A., "Discrete Cooling of Low Heat Leak Supports to 4.2 K," *Cryogenics,* Vol. 15, May 1975, pp. 290–292.

9 Reynolds, W. C., and Perkins, H. C., *Engineering Thermodynamics,* McGraw-Hill, New York, 1970, pp. 215.

10 Holman, J. P., *Thermodynamics,* McGraw-Hill, New York, 1974, p. 169.

11 Socolow, R. H., et al, "Efficient Use of Energy", *Physics Today,* Aug. 1975, pp. 23–33.

K. H. Chen
Post Doctoral Research Engineer.

G. J. Trezek
Professor.

Department of Mechanical Engineering,
University of California,
Berkeley, Calif.

The Effect of Heat Transfer Coefficient, Local Wet Bulb Temperature and Droplet Size Distribution Function on the Thermal Performance of Sprays

Energy balance considerations indicate that the droplet heat transfer coefficient, local wet bulb temperature, and droplet size distribution function are the basic parameters affecting spray system thermal performance. Within the range of available experimental data, results indicate that the Ranz-Marshall correlation gives an agreement to within ±5.0 percent of measured droplet temperatures at the pond surface for a medium wind range of between 2.5 and 5 m/s. The local wet bulb temperature is taken as the arithmetic mean of the initial and final wet bulb temperatures. For wind speeds greater than 3.5 m/s, the local wet bulb can be taken as the ambient. The modified log normal distribution of Mugele and Evans provides the best description of the droplet size distribution. Further, through the introduction of a correction term, the Spray Energy Release (SER) can be deduced from single droplet information.

Introduction

Recently, increased effort has been directed toward improving the thermal performance predictions of direct contact open atmosphere spray cooling systems. Justification is particularly due to the fact that these systems offer a flexible and economic means for providing various aspects of power plant cooling. A number of thermal performance models, recently reviewed in part by Ryan and Myers [1],[1] ranging from being purely empirical to semiempirical in nature, have been developed. Further, these models can be classified according to the approach used in their derivation; namely, beginning with either a single drop, a single spray unit, or the spray system.

The spray system model is an example of an empirical approach in which the test result of one system is assumed to be valid for the design of another system. A representative model is that due to Berman [2].

On the other hand, the single unit model is an example of the semiempirical approach. Here the single spray unit is experimentally evaluated, and through the knowledge of the unit performance, the whole system performance is estimated. Examples of this technique are the NTU models of Hoffman [3], Porter and Chen [4], and the SER model of Chen and Trezek [5].

The single drop, transferring heat and mass along its trajectory, has been used by Elgahwary [6] and Chen [7] as a basis for modeling spray system performance. Here an experimentally determined entrainment factor is introduced as a means of accounting for the local air humidity variation. Soo [8, 9] studied the performance parameters of the open atmosphere spray system through the consideration of a single drop of suitable mean size. His investigation was aimed at evaluating and improving the spray system rather than at the accuracy of predicting the system performance.

Three basic parameters, the droplet heat transfer coefficient (h_c)), the local wet bulb temperature (T_{wb}), and the size distribution ($f_N(D)$) of the spray droplets, have been identified as being critical in the evaluation of spray system performance. This work considers some of the common relations used to model the foregoing three parameters. The motivation is to ascertain how these various individual parameter models affect spray system performance so that further insight into increasing the accuracy of predictive techniques can be achieved.

[1] Numbers in brackets designate References at end of paper.

Contributed by the Heat Transfer Division for publication in the JOURNAL OF HEAT TRANSFER. Manuscript received by the Heat Transfer Division March 3, 1977.

Basic Parameters

Neglecting any effects of the initial water sheet leaving the nozzle, the thermal performance of a spray can be ascertained by evaluating the energy transfer from the droplets. The formulation of the energy balance provides a means of identifying the essential parameters controlling the energy transfer process as well as delineating their interrelationship. Thus, utilizing the assumption of a completely mixed spherical drop, the usual form of the energy balance can be written; namely,

$$\rho_w \frac{c_w D}{6}\frac{dT}{dt} = h_c(T - T_d) + K_m h_{fg}\left(\frac{x_0 - x_\infty}{1 - x_0}\right) + (T^4 - T_r{}^4) \quad (1)$$

The condition of equilibrium results from the fact that as $dT/dt \to 0$, $T \to T_e$, and $x_0 \to x_e$ or in terms of equation (1)

$$h_c(T_e - T_d) + K_m h_{fg}\left(\frac{x_e - x_\infty}{1 - x_e}\right) + \epsilon\sigma(T_e{}^4 - T_r{}^4) = 0 \quad (2)$$

Equation (1) can be rearranged into the following form:

$$\rho_w \frac{c_w D}{6}\frac{dT}{dt} = h_c(T - T_e) + K_m h_{fg}\frac{x_0 - x_e}{1 - x_0} + \epsilon\sigma(T^4 - T_e{}^4) + h_c(T_e - T_d) + K_m h_{fg}\frac{x_e - x_\infty}{1 - x_0} + \epsilon\sigma(T_e{}^4 - T_r{}^4) \quad (3)$$

Thus, from equations (2) and (3) it follows that the energy balance can be considered more conveniently in terms of the equilibrium temperature, i.e.,

$$\rho_w \frac{c_w D}{6}\frac{dT}{dt} \simeq h_c(T - T_e) + K_m h_{fg}\frac{x_0 - x_e}{1 - x_0} + \epsilon\sigma(T^4 - T_e{}^4) \quad (4)$$

Linearizing the radiation term and assuming the air vapor as an ideal gas yields:

$$\rho_w \frac{c_w D}{6}\frac{dT}{dt} = (h_c + h_r)(T - T_e) + K_m h_{fg}\left(\frac{p_0 - p_e}{p - p_0}\right) \quad (5)$$

The quantity p_0 in the denominator of the last term of equation (5) can be neglected as small compared to p. Introducing the Clausius-Clapeyron relation allows equation (5) to be cast into the following form:

$$\frac{d\theta}{dt} = \frac{6}{\rho_w c_w D}\left[1 + \frac{K_m}{h_c + h_r}\frac{p_e}{p}A_T h_{fg}\right](h_c + h_r)\theta \quad (6)$$

where

$$A_T = \left[\operatorname{Exp}\frac{h_{fg}}{R}\left(\frac{1}{T_e} - \frac{1}{T}\right) - 1\right] \Big/ (T - T_e)$$

and $\theta = (T - T_e)$. The initial condition at $t = 0$ is given by $\theta = (T_{c0} - T_e)$.

Further, the average temperature of the entire spray at the end of the trajectory is given by

$$T_{sp} = \int_0^\infty D^3 T_{sp}(D) f_N(D) dD / D_v{}^3 \quad (7)$$

Consequently, it can be seen from equations (6) and (7) that the accuracy of prediction will be influenced by the quantities K_m, $h_c + h_r$, T_e, and $f_N(D)$.

Although the radiation effect can be on the order of ±9 percent for extreme conditions [10], it will not be considered in the present discussion of the basic parameter behavior. Thus, assuming $h_r \ll h_c$, it follows that $T_e \to T_{wb}$, $p_e \to p_{wb}$ and $c_s K_m/(h_c + h_r) \to (L_e)^{-2/3}$. Equation (6) then takes the form

$$\frac{d\eta}{dt^*} = \frac{6 h_c t_f}{\rho_w c_w D}\left[1 + (\mathrm{Le})^{-2/3}\left(\frac{P_{wb}}{p}\right)\left(\frac{A_T h_{fg}}{c_s}\right)\right]\eta \quad (8)$$

where $\eta = (T - T_{wb})/(T_{c0} - T_{wb})$, $t^* = t/t_f$, and the initial condition at $t^* = 0$ becomes $\eta = 1$. In this form the basic parameters of h_c, T_{wb}, and $f_N(D)$ are readily distinguishable.

Heat Transfer Coefficient

The Ranz and Marshall [11] correlation

$$\mathrm{Nu} = 2.0 + 0.6\,\mathrm{Re}^{1/2}\mathrm{Pr}^{1/3} \quad (9)$$

has been used in the prediction of open atmosphere spray cooling systems [6, 7]. This correlation is established for a stationary drop with a Reynolds number up to 200 and can be used up to a Reynolds number of 1000 according to the authors. Yao and Schrock [12] experimentally investigated the heat and mass transfer of freely falling

Nomenclature

c_s = air vapor heat capacity or humid heat
c_w = specific heat of liquid water
C_D = droplet drag coefficient
D = drop diameter
D_ℓ = mean length diameter
D_m = maximum diameter
D_s = mean surface diameter
D_v = mean volume diameter
D_{vs} = Sauter mean diameter
f_M = mass distribution function
f_N = number distribution function
g = heat transfer correlation correction factor of Yao and Schrock
$\vec{g}$ = body force per unit mass
h_c = heat transfer coefficient
$\bar{h}_c$ = statistical time average heat transfer coefficient
h_{fg} = latent heat of vaporization
h_r = radiation heat transfer coefficient ($h_r = \epsilon\sigma(T^4 - Te^4)/(T - Te)$)
K_m = mass transfer coefficient
L = mass spray rate
Le = Lewis number
N = total number of drops
NTU = Number of Transfer Units
Nu = Nusselt number
p = total pressure
p_e = vapor pressure at equilibrium temperature
p_0 = vapor pressure at saturated temperature
p_{wb} = vapor pressure at wet bulb temperature
P = nozzle pressure
Pr = Prandtl number
R = gas constant
Re = Reynolds number
SER = Spray Energy Release
t = time
$\bar{t}$ = average residence time of spray
t^* = nondimensional time
t_f = residence time of a drop
T = droplet temperature
T_{c0} = spray temperature at nozzle
T_d = dry bulb temperature
T_e = equilibrium temperature
T_r = a reference temperature
T_{sp} = spray temperature at the end of the trajectory (experimental)
T_{sp}' = spray temperature at the end of the trajectory (predicted)
T_{wb} = local wet bulb temperature
T_{wbf} = final wet bulb temperature
$T_{wb\infty}$ = ambient wet bulb temperature
u_∞ = ambient wind speed
$\vec{U}$ = air vapor velocity
$\vec{U}_p$ = particle or drop velocity
x = falling distance of drop; wet bulb temperature weighting factor
x_e = mole fraction at equilibrium temperature
x_0 = mole fraction at saturation temperature
x_∞ = mole fraction at ambient condition
y = as defined
ΔSER = slope of the SER versus wind speed curve

Subscripts

δ = a spray distribution parameter
ϵ = emissivity
ν = kinematic viscosity
ρ = air vapor density
ρ_w = water density
σ = Stephan-Boltzmann constant
θ = spray exit angle

water drops with a size range from 3 to 6 mm in diameter. They found that the Ranz and Marshall correlation had to be modified for the falling height and drop size according to

$$(\mathrm{Nu} - \mathrm{Nu}_{R\&M})/0.6\ \mathrm{Pr}^{1/3}\mathrm{Re}^{1/2} = (g - 1) \tag{10}$$

where $g = 25.0\ (D/x)^{0.7}$, and x is the distance the drop falls which is taken to be greater than zero. Soo [2] used the solid sphere correlation

$$\mathrm{Nu} = 0.37\ \mathrm{Re}^{0.6} \tag{11}$$

in his investigation.

Unfortunately, none of the foregoing correlations are consistent with the droplet cooling phenomenon in a spray. The dynamical effects experienced by the droplet in its trajectory such as acceleration and deceleration, vibration, rotation and internal circulation which influence the heat and mass transfer process are not completely considered. Further, it is likely that the heat transfer coefficient will both decrease and increase as a droplet decelerates and accelerates during the course of its trajectory. Therefore, the adoption of any of the correlations is a matter of convenience and the subsequent model must be subjected to experimental verification.

Local Wet Bulb Temperature

The air humidity within the spray field is a function of the ambient wind conditions and location in the spray. Thus, the temperature driving potential $(T - T_{wb})$ for each drop is different and varies with time and location. Soo [2] gives two limiting conditions for determining the local air vapor humidity for an assumed homogeneous air vapor flow under the spray. At zero or low wind conditions, the local humidity can be obtained through a solution of the diffusion equation neglecting convective effects. For high ambient wind having a mass flow value equal or greater than the evaporation rate (critical wind condition), all the vapor produced will be removed so that the local air vapor humidity can be taken as the ambient value. Below the critical wind condition the local air vapor humidity is not readily defined and a suitable average value has to be used.

Spray Distribution Function

Since sprays generated by typical nozzles used in cooling systems are not mono-dispersed, thermal performance calculations require a description of the spray distribution function. Basically, this is due to the fact that the spray average temperature is the statistical average temperature of all the drops, and the loss in momentum of the ambient wind going through the spray is due to the total drag forces of all the drops suspended in air. Mugele and Evans [13], in their discussion of the validity of various distribution functions, point out that the established functions are not representative of all the general situations. In other words, a particular situation has to be matched with a particular function(s).

It is also important that the selected distribution function, even though it may fit the size distribution data, yield the correct values of subsequently computed parameters such as mean diameters, etc. An example is seen in the comparison of two distribution functions with cumulative distribution data for a typical nozzle. Data from a Spraco 1751 nozzle was selected [14]. Fig. 1 illustrates the comparison of the cumulative distributions generated by a modified Rosin-Rammler function of the form

$$R_v = A_1 \exp(-A_2 D^{-A_3}) \tag{12}$$

where $A_1 = 275.75$, $A_2 = 446.5$, and $A_3 = 0.7116$ and a modified log-normal distribution or "upper limit" equation (13) given by

$$\frac{dR_v}{dD} = \frac{\delta}{\sqrt{\pi}} e^{-\delta^2 y^2} \frac{dy}{dD} = f_M \tag{13}$$

where $y = \ln [aD/(D_m - D)]$, $\delta = 1.1247$, $a = 1.6312$, and $D_m = 6578\mu$. Even though both relations provide a good fit to the data, only the upper limit relation as seen in Table 1 gives a reasonably good comparison of the various computed mean diameters.

Table 1 Comparison of mean diameters

Mean dia (μ)	Modified Rosin Rammler	Upper limit law	Test data
D_v	252.6	1131.4	1127.6
D_s	1022.8	867.4	955.8
D_{vs}	15.4	1924.7	1573.0
D_ℓ	753.7	625.0	793.4

The fact that the Rosin-Rammler relation is valid for the range $0 < D < 6000\mu$ while the integration limit for computing the mean diameters if $0 < D < \infty$ would tend to yield a smaller volume mean diameter and a larger surface mean diameter.

Prediction Results

The quantitative evaluation of the effect of the heat transfer correlations and local wet bulb temperature variation on the spray performance will be considered. Predictions will be compared with the Rancho-Seco spray pond thermal performance test data [15]. The procedure for calculating the appropriate droplet temperature is given previously and the number and mass distributions are related by the following:

$$Nf_N dD = \frac{L\bar{t}f_M dD}{\rho_w \dfrac{\pi}{6} D^3} \tag{14}$$

Different heat transfer coefficients along the drop trajectories can readily be obtained from equations (9)–(11) in conjunction with the solution of the following drop momentum equation:

$$\frac{d\vec{U}_p}{dt} = \frac{3}{4}\left(\frac{\rho}{\rho_w}\right)\left(\frac{C_D}{D}\right)|\vec{U} - \vec{U}_p|(\vec{U} - \vec{U}_p) + \vec{g}\left(1 - \frac{\rho}{\rho_w}\right) \tag{15}$$

The particle drag coefficient C_D, a function of particle Reynolds number defined as $\mathrm{Re} = |\vec{U} - \vec{U}_p|D/\nu$, has the following correlation for water drops [16]:

$$C_D = \frac{24}{\mathrm{Re}} + \frac{6}{1 + \sqrt{\mathrm{Re}}} + 0.27 \quad 1 < \mathrm{Re} \le 1000 \tag{16}$$

and

$$C_D = 0.6649 - 0.2712 \times 10^{-3}\mathrm{Re} + 1.220 \times 10^{-7}\mathrm{Re}^2 - 10.919 \times 10^{-12}\mathrm{Re}^3 \quad 1000 \le \mathrm{Re} \le 3600 \tag{17}$$

Equation (15) is subject to the initial condition

$$\vec{U}_p = \sqrt{2P/\rho_w}(\vec{i}\cos\theta + \vec{j}\sin\theta) \tag{18}$$

where the ambient air flow $\vec{U} = -u_\infty \vec{i}$. Here, the ambient wind velocity is assumed to be always in the opposite direction to the horizontal

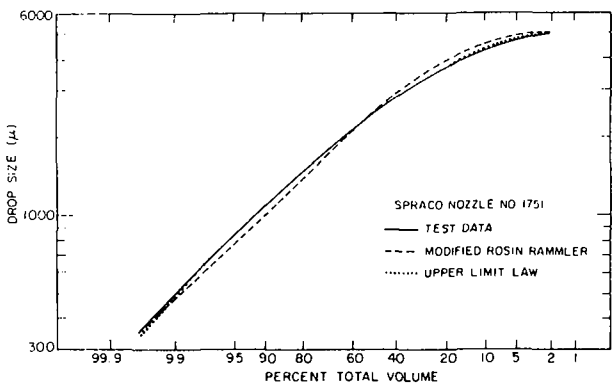

Fig. 1 Cumulative volume distribution curves

velocity component of the drop in order to obtain the value of the heat transfer coefficient. The trajectory is completely traversed by the drop when it hits the water surface, which in the present case, is 1.52 m below the spray nozzle. The Yao and Schrocks' correction factor $g = (25.0(D/x)^{0.7})$ was modified by replacing x, which is the falling distance of the drop, with s, which is the distance of the trajectory from the spray nozzle. The heat transfer coefficients along the trajectory corresponding to three drop sizes, of 1, 3, and 6 mm, in diameter are shown in Fig. 2. All the heat transfer coefficients obtained from the different correlations have the same general trend of high initial values. This is especially true with the Yao and Schrock correlation where the correction factor is proportional to the 0.7th power of $(s)^{-1}$ so that for very small $s(<D)$, h_c is necessarily large. The value of h_c computed from the solid sphere and the Ranz and Marshall correlations have the same trend of varying with the drop relative velocity. The lowest value is seen at the highest point of the trajectory, which is qualitatively consistent with the physical situation. The Yao and Schrock correlation gives a continuously decreasing value as is expected from the inverse variation of h_c with the trajectory distance. Of the three correlations, the highest and lowest values are given by solid sphere and the Yao and Schrock correlations respectively except in the case of the latter for a short distance (or time) after the drop leaves the nozzle. It is also anticipated that the smaller the drop the larger the heat transfer coefficient. The results shown in Fig. 2 suggest that either the solid sphere or the Ranz and Marshall correlation gives a proper trend for the cooling of a drop along the trajectory, while the Yao and Schrock correlation, modified as above, does not.

The quantitative evaluation of the applicability of the different correlations is carried out in two steps: assuming the correlations are valid, the spray temperature at the end of the trajectory is computed using equations (7), (8), (13), and (14) with the local wet bulb temperature equal to either: (*a*) the ambient value, or (*b*) the arithmetic mean value of the initial and the final wet bulb temperatures as deduced from the test data [16]. Thus, the final wet-bulb temperature or wet-bulb change across the spray was obtained from laboratory test results. The results are shown in Fig. 3 in terms of the error of prediction (temperature deviation as a function of wind speed. Not shown in the figure is the modified Yao and Schrock correlation which consistently gives a high positive error (under cooling). The solid sphere correlation does not give a good prediction except in the narrow region of 4.5–5.5 m/s wind speed, where the local wet bulb temperature is assumed to be equal to the ambient value. However, when the local wet bulb temperature is taken as in case (*b*) in the foregoing, the range is improved and the error is under ±5.0 percent in the range 4.0 to 5.5 m/s. The Ranz and Marshall correlation has a wider range of applicability. For the assumed local wet bulb temperature equal to the ambient, the prediction error is within ±5.0 percent for wind speeds of 3.5 m/s and upward. Below that, this correlation predicts excessive cooling. When the local wet bulb temperature is taken as the arithmatic mean, the prediction is within ±5.0 percent in the range of 2.5 to 5 m/s. Below the lower wind speed limit, the deviation is high, although it is better than the case assuming an ambient atmosphere as local.

Because the single drop correlation has some deficiency in predicting thermal performance, the above results suggest a classification of the spray thermal performance in terms of three wind speed ranges, in which the Ranz and Marshall correlation, together with a proper modification of the local wet-bulb temperature, may be used as a good predicting model for the spray system. Thus, a suggested method, based on the conditions observed within our system, for expressing the local wet bulb temperature can be given as

$$T_{wb} = T_{wbf} - x(T_{wbf} - T_{wb\infty}) \tag{19}$$

where

$$x < 0.5, \qquad u_\infty < 2.5 \text{ m/s}$$

$$x = 0.5, \qquad 2.5 \le u_\infty \le 3.5 \text{ m/s}$$

$$x = 1.0, \qquad u_\infty \ge 3.5 \text{ m/s}$$

Since the foregoing is not a generalized method, the appropriate choice of x for $u_\infty < 2.5$ m/s other than the conservative choice of $x = 0$ will depend on experimental or operating experience. Thus, at low to intermediate wind speeds the thermal performance is significantly affected by the proper choice of the local wet bulb temperature. Again, the choice of the wind speed ranges were suggested by our results.

Spray Energy Release (SER)

The concept and details of dealing with the thermal performance of a spray system in terms of the net energy released (SER) have been previously given [5, 16]. Of interest here is the possibility of obtaining a spray unit SER through the consideration of the single drop. This in turn would reduce the amount of experimental work necessary in determining single spray unit thermal performance.

The spray characteristic SER is given by

$$\text{SER} \equiv 6\frac{\bar{\bar{h}}_c\bar{t}}{c_s\rho_w D_{vs}} \tag{20}$$

where

$$\bar{\bar{h}}_c\bar{t} = \int_0^\infty \int_0^t D^2 h_c(D, t) f_N(D)\, dt\, dD/D_s{}^2 \tag{21}$$

The SER computed from the above relation is shown in Fig. 4 as a function of wind speed along with SER values obtained from experimental data. Although the solid sphere correlation gives a closer prediction, the trend is not correct. The Ranz and Marshall correlation gives a curve parallel to that of the experiment; however, it deviates by a value of about 0.36. This suggests that when the single drop heat

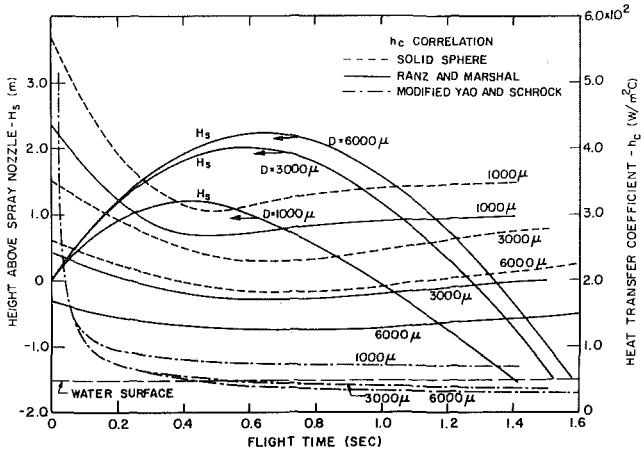

Fig. 2 Variation of heat transfer coefficients along the drops' trajectories

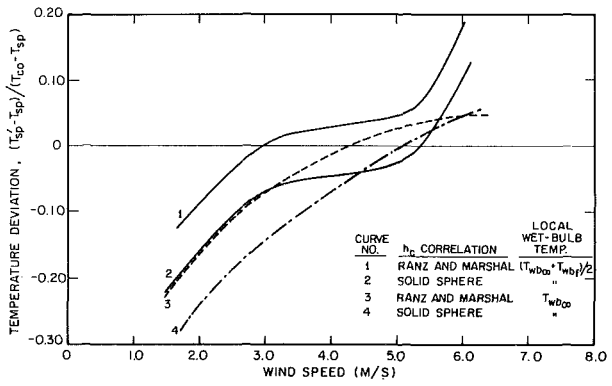

Fig. 3 Predicted final spray temperature deviation for different heat transfer coefficients and local wet-bulb temperatures

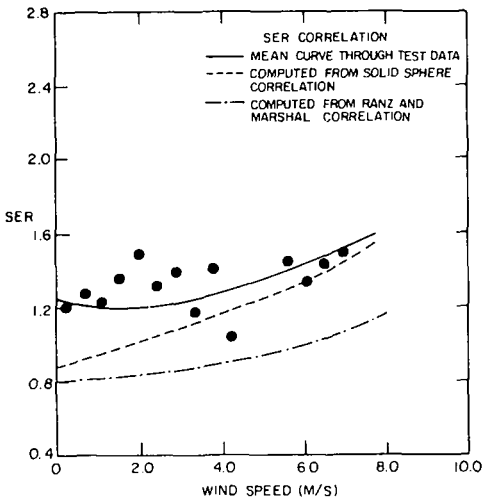

Fig. 4 SER versus wind speed for Spraco nozzle no. 1751 at 0.48 bar

transfer correlation of Ranz and Marshall is used, the SER relation may assume the following modified form:

$$\text{SER} \cong \frac{6\bar{\bar{h}}_c \bar{t}}{c_s \rho_w D_{vs}} + b/\cos\theta \tag{22}$$

where in terms of the data under consideration, $b = 0.36$, and $\theta = \tan^{-1}(\Delta\text{SER}/\Delta u_\infty)$. Because of the lack of comprehensive spray system thermal performance data, additional experimentation, comparable to that of the Rancho-Seco tests, is needed in order to completely establish the validity of the foregoing approach.

Conclusion

In light of the fact that an experimental determination of the heat and mass transfer from a droplet along a trajectory comparable to that encountered in a spray unit does not exist, correlations obtained for other more easily measured conditions are adapted in the spray system thermal models. The present investigation has shown that for the drop size range ($\leq$6 mm), the Ranz and Marshall heat-mass transfer correlation yields a valid prediction of thermal performance provided that the proper choice of the local wet-bulb temperature and spray distribution function are made. If it is possible to obtain the variation of local wet bulb temperature as a function of wind speed, the single drop approach of analyzing the spray system performance will be more assuring with these quantities properly chosen.

The results also indicate that there is a wind speed range where T_{wb} does not significantly influence the heat transfer coefficient (h). In this range the prediction using the Ranz and Marshal correlation will be slightly high. Accordingly the SER predicted with the higher value of h given by the Ranz and Marshal correlation will be smaller. At lower winds T_{wb} does have an influence on h. Even if T_{wb} was selected correctly the use of the Ranz and Marshal relation in predicting h would result in a subsequently lower SER so that SER values predicted by use of the Ranz-Marshal relation can always be expected to be below the experimental data.

The single unit approach of analyzing the spray system is more accurate and practical at this stage of development. The economy and relatively simple approach coupled with the possible reduction in experimental work for spray unit thermal testing through the single drop analysis, makes the single unit method more attractive. Finally, the system approach of a purely empirical method, though not advisable for extrapolation for larger system design, can be used as a helpful guide in spray system development.

References

1 Ryan, P. J., and Myers, D. M., "Spray Cooling: A Review of Thermal Performance Models," presented in the Spray Cooling Workshop, 38th American Power Conference, Chicago, Apr. 20-22, 1976.

2 Berman, L. D., *Evaporative Cooling of Circulating Water*, Pergamon Press, New York, 1961.

3 Hoffman, D. P., "Spray Cooling for Power Plants," *Proceedings of the American Power Conference*, Vol. 35, 1973, p. 702.

4 Porter, R. W., and Chen, K. H., "Heat and Mass Transfer of Spray Canals," JOURNAL OF HEAT TRANSFER, TRANS. ASME, Series C, Vol. 96, No. 3, Aug. 1974.

5 Chen, K. H., and Trezek, G. J., "Spray Energy Release (SER) Approach to Analysing Spray System Performance," presented in the Spray Cooling Workshop, 38th American Power Conference, Chicago, Apr. 20-22, 1976.

6 Elgawhary, A. M., "Spray Pond Mathematical Model for Cooling Fresh Water and Brine," PhD dissertation, Oklahoma State University, Stillwater, Aug. 1969.

7 Chen, K., "Heat and Mass Transfer From Power Plant Spray Cooling Ponds," PhD dissertation, University of California, Berkeley, 1975.

8 Soo, S. L., "Power Spray Cooling—Unit and System Performance," ASME Paper No. 75-WA/Pwr-8, 1975.

9 Soo, S. L., "Systems Considerations in Spray Cooling and Evaporation," presented in the Spray Cooling Workshop, 38th American Power Conference, Chicago, Apr. 20-22, 1976.

10 Porter, R. W., Lavan, Z., and Weinstein, H., "Progress on Research on Open Circulating Water Cooling Systems for Large Electric Power Plants," Waste Energy Management Report No. 1, Illinois Institute of Technology, Chicago, Oct. 1975.

11 Ranz, W., and Marshall, W., Jr., "Evaporation From Drops," *Chemical Engineering Progress*, Vol. 48, 1952, pp. 141-146, 137-180.

12 Yao, S-C., and Schrock, V. E., "Heat and Mass Transfer From Freely Falling Drops," JOURNAL OF HEAT TRANSFER, TRANS. ASME, Series C, Vol. 98, No. 1, Feb. 1976.

13 Mugele, R. A., and Evans, H. D., "Droplet Size Distribution in Sprays," *Industrial and Engineering Chemistry*, Vol. 43, No. 6, June 1951, pp. 13-17.

14 Private Communication with Spray Engineering Company, 100 Cambridge St., Burlington, Ma.

15 Schrock, V. E., and Trezek, G. J., "Rancho Seco Nuclear Service Spray Ponds Performance Evaluation," Waste Heat Management Report No. WHM-4, University of California, Berkeley, July, 1973.

16 Chen, K. H., "Heat and Mass Transfer of Multi-Spray Unit Cooling System in Open Atmosphere," PhD dissertation, University of California, Berkeley, 1976.

J. J. Williams
Manager, Applied Sciences,
Development Department,
Hoffmann-La Roche Inc.,
Nutley, N. J.

W. H. Giedt
Associate Dean-Graduate Study,
College of Engineering,
University of California,
Davis, Calif.

Experimental and Predicted Recovery Temperature Distributions in a Rocket Nozzle With Gaseous Film Cooling

The adiabatic wall temperature distribution in nozzles with gas injection through a peripheral slot at the entrance was investigated. Experimental wall temperature distributions were measured in a series of hot gas (hydrogen-air combustion as the primary source) tests with three geometrically different channels—a constant area duct, a gradually converging nozzle, and a rapidly converging nozzle. Cooling effectiveness was found to be significantly higher for the rapidly converging geometry. Prediction of recovery temperature distributions under the test conditions with available boundary layer computer programs was then investigated. Predicted results were consistently higher than measured. Significantly improved agreement between predicted and measured results was achieved by introducing effective initial temperature profiles in the injectant to account for gross mixing between the injectant gas (nitrogen) and free stream gas at the injection station.

Introduction

Initial studies of gaseous film cooling dealt primarily with flows over flat plates [1–6][1] and, for the most part, experiments were conducted using small temperature differences between the free stream and injected gases. More recently, investigators have examined the effect of flow acceleration e.g., [7–10]. These were primarily laboratory studies in which the injectant fluid flowed along a flat surface. The role of streamline curvature with no pressure gradient was investigated by Mayle, et al. [11]. Some experimental measurements have been made in rocket motors [12–14]. However, there are still only limited data for flows of practical interest where there is simultaneous free stream acceleration and wall radius change.

Therefore, this study was undertaken to investigate the combined effect of flow acceleration and streamline curvature. Tests were conducted with two converging-diverging nozzles. The first had a gradual contraction and a throat approach radius of 10.16 cm (4 in.). The second converged rapidly, having a throat approach radius of 2.54 cm (1.0 in.). Recovery temperature distributions were measured in these two nozzles, with peripheral injection of nitrogen just prior to the beginning of convergence, and along a constant area duct. The main stream consisted of the combustion products of hydrogen and air. The experimental program is described in the following sections. The results are then compared with predictions from two finite difference boundary layer computer programs.

Experimental Apparatus

The assembled components of the test apparatus are depicted in Fig. 1. This consisted of a concentric-tube hydrogen injector, an uncooled combustion tube, a radial flow mixer, an uncooled extension tube, an annular coolant flow injector, and an instrumented nozzle. The assembly was designed to operate at a nominal stagnation pressure of 1.379×10^6 Pa (200 psia) with air and hydrogen mass flow rates of 0.91 and 0.0045 kg/s, respectively. The hydrogen-air mixture ratio was selected to provide a temperature of 540°C for the combustor gas which entered the nozzle at a velocity of 19 m/s. Operating conditions correspond to a nominal thrust of 890 N (200 lb_f) and throat Reynolds number of 1.5×10^6 (based on the throat diameter of 2.54 cm as the characteristic dimension). A hot-wire probe was used to measure free stream turbulence downstream of the flow mixer, with ambient temperature air flowing in the system. Since it is believed that the flow mixer is the major source of turbulence, the measured value of 10 percent is considered representative of the intensity present during the high temperature tests.

The nitrogen film coolant, at a temperature of 25°C, was injected upstream of the nozzle convergent section. Details of the nitrogen

[1] Numbers in brackets designate References at end of paper.

Contributed by the Heat Transfer Division for publication in the JOURNAL OF HEAT TRANSFER. Manuscript received by the Heat Transfer Division March 18, 1976.

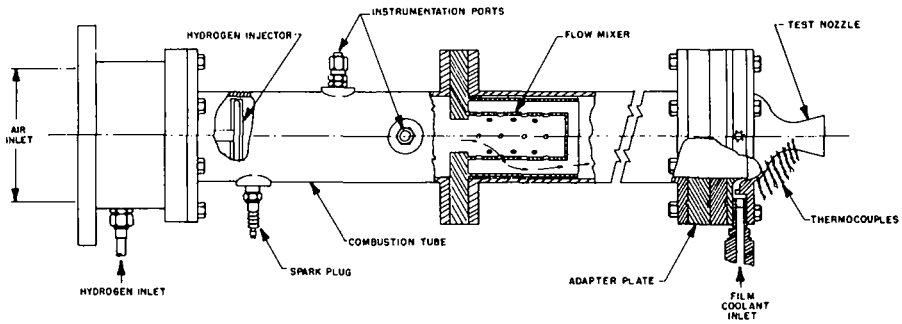

Fig. 1 Test assembly

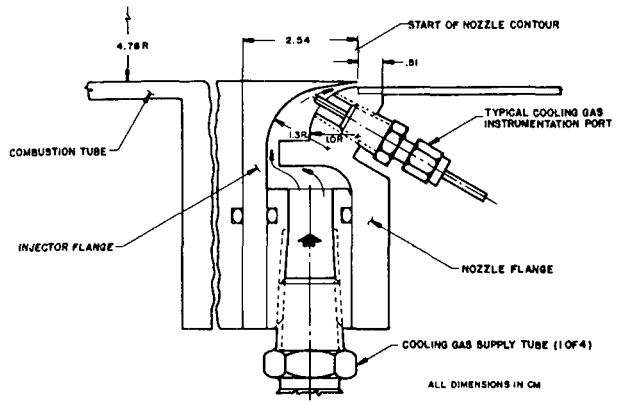

Fig. 2 Injection section details

Table 1 Injector slot heights

Nozzle[a]	Injector Flange	Slot Height (cm.)
N_1	I_1	0.064
N_1	I_2	0.089
N_1	I_3	0.140
N_3	I_1	0.076
N_3	I_2	0.102
N_3	I_3	0.152
N_4	I_1	0.064
N_4	I_2	0.089
N_4	I_3	0.140

[a] Nozzle numbers were assigned according to the approximate throat approach radius of curvature measured in inches. An extensive description of the experimental apparatus, as well as a tabulation of the operating conditions and measurements made, is given in Reference 15.

injection system are shown in Fig. 2. The measured slot height for each nozzle flange combination is shown in Table 1. Since "clean" slot geometries were desired, the slot lips were made as sharp as possible so that the step-heights between the injected fluid and the mainstream were negligible. Special effort was also made to align the final injectant flow passage with the mainstream to reduce initial mixing. Results indicated that certain injectors were more satisfactory in this respect than others.

The test nozzles were spun from 0.124-cm thick, type 304 stainless steel sheets. The internal contours are shown in Figs. 3(*a*) and 3(*b*). Thermal instrumentation consisted of twelve 30-gage Chromel-Alumel thermocouples spot-welded on the outside surface of each nozzle. The ratios of injected mass flux to free-stream mass flux and the ratios of injectant velocity to free-stream velocity are shown in Table 2 for selected configurations. Additional details of the test apparatus and conditions are given in references [15, 16].

Experimental Results and Discussion

The change in adiabatic wall temperature accomplished by injecting a film of fluid along the nozzle wall is described in terms of an effectiveness defined by the following relationship:

$$\eta = \frac{T_{aw} - T_{aw'}}{T_{aw} - T_c} \tag{1}$$

equation (1) involves the recovery temperature distribution T_{aw} without film cooling. This was based on a recovery factor computed from the following relationship:

$$RF = (\text{Prandtl number})^{1/3} \tag{2}$$

A value of 0.65 was used for the Prandtl number. The local free stream static temperature was based on isentropic flow of the combustion products with a constant ratio of specific heats ($\gamma = 1.35$ was used in all cases). Values for the adiabatic wall temperature, $T_{aw'}$, were determined from wall temperature measurements by correcting for conduction effects as described in the Appendix.

Effectiveness values were plotted versus dimensionless length so that they could be compared with flat-plate data which are usually presented in this manner. The dimensionless length (x/ms) was computed using the measured mass flows, slot height, and distance along the surface from the point of injection. The mass flux ratio, m, given in the dimensionless length is based on conditions at the point of injection and, therefore, is constant for any one test.

Representative results are shown in Figs. 4–7. A reference curve labelled "zero-pressure gradient correlation" was also drawn on each plot to facilitate comparison between configurations. The data in Fig.

Nomenclature

E = exponent defining stagnation temperature profile

m = mass flux ratio of injectant to mainstream fluid

$\dot{m}$ = mass flow rate

s = gas injection slot height

T_c = coolant injection temperature

T_0 = local stagnation temperature

T_{aw} = adiabatic wall temperature without film cooling

$T_{aw'}$ = adiabatic wall temperature with film cooling

$T_{0,\infty}$ = free stream stagnation temperature

x = distance along wall

y = normal distance from wall

η = cooling effectiveness

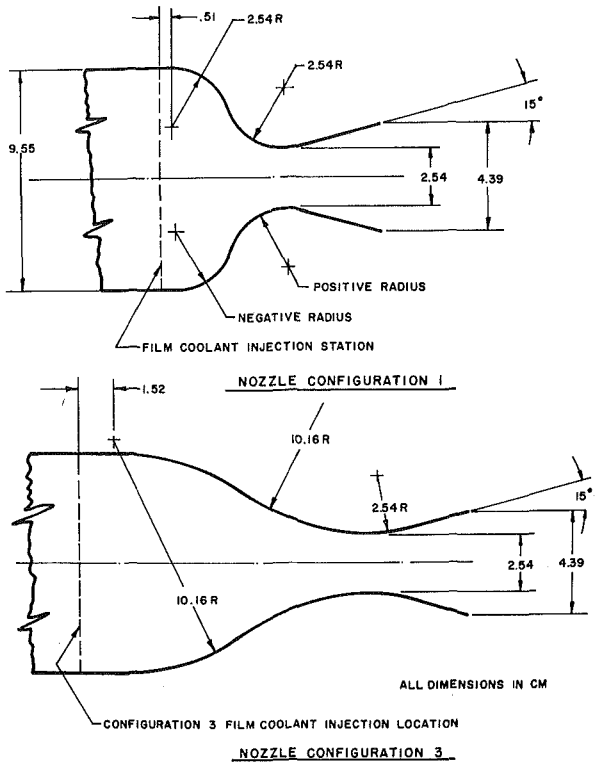

Fig. 3 Nozzle configurations

Table 2 Test parameters

Test	Ratio of Injected Mass to Free Stream Mass (Percent)	Ratio of Average Injectant Velocity to Free Stream Velocity	Ratio of Average Injectant Mass Flux to Free Stream Mass Flux Evaluated at Injection Location
335	10.84	1.051	2.913
336	7.85	0.784	2.109
337	5.53	0.572	1.486
338	2.59	0.292	0.696

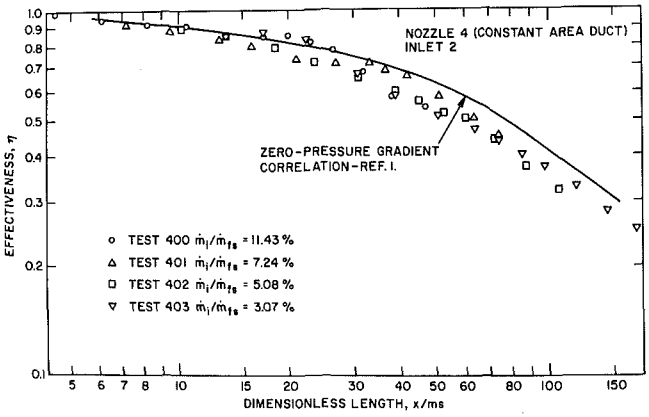

Fig. 4 Film cooling effectiveness for configuration $N_4 l_2$

4 (constant area duct) show the normally expected trends for flow without a pressure gradient. Although the results shown in Figs. 5–7 for the converging channels drop below the flat plate curve, it must be recognized that a constant value of m is not valid in these cases because the free-stream mass flux is not constant. The trend of rapidly decreasing effectiveness near the nozzle throat is apparent in Figs.

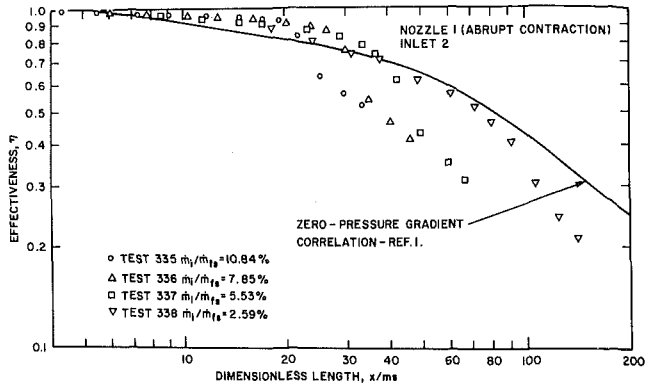

Fig. 5 Film cooling effectiveness for configuration $N_1 l_2$

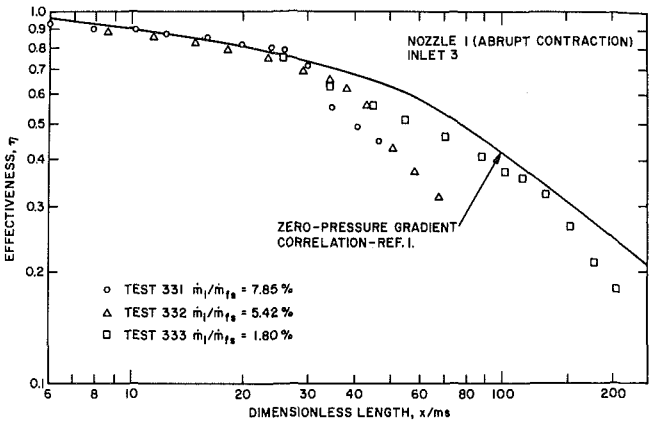

Fig. 6 Film cooling effectiveness for configuration $N_1 l_3$

5–7.

The data presented in Figs. 5 and 6 illustrate the variation in effectiveness distributions associated with different injectors. Values obtained with Injector 3 (Fig. 6) are lower by as much as 10 percent than those obtained with Injector 2 in the region immediately downstream of injection. However, as the nozzle throat is approached,[2] values for Injector 2 decrease more rapidly to about the same values as those for Injector 3 for comparable ratios of injectant to free-stream flow rates. A comparison of results obtained with Injectors 2 and 3 in Nozzle 3 shows almost identical trends [15]. In view of the comparatively large difference in temperature between the free-stream and nitrogen injectant and the small magnitude of the corrections to measure wall temperatures (see Appendix), the differences between results with these two injectors are considered real and not attributable to experimental error.

The effect of nozzle area contraction rate on effectiveness is demonstrated in Fig. 8. For equal injection flow rates, the cooling effectiveness values are significantly higher at all locations in Nozzle 1 than at the corresponding area ratio locations in the more gradual contour of Nozzle 3. At the throat of Nozzle 1, the effectiveness is twice that of Nozzle 3. This indicates that distance from the injection location has the major influence on the change of effectiveness rather than flow acceleration or wall radius, and shows that a rapid contraction would be preferable for rocket motor protection.

The effect of injectant mass flow rate on effectiveness near the throat of Nozzle 1 is shown in Fig. 9. This plot indicates only a slight decay in the slope of the effectiveness curve at the higher mass flows.

[2] The nozzle throat is located between the second and third data points from the downstream end.

It may be concluded, therefore, that effectiveness values higher than those measured may be obtained at the expense of additional film coolant.

As plotted in Figs. 5–7, the results show essentially the variation of effectiveness with dimensionless distance x/s since m is constant. With Inlet 2, values of effectiveness immediately downstream of injection fall on or are slightly above the zero-pressure gradient curve, while with Inlet 3, they tend to coincide. Before the throat is reached, however, they began to decrease markedly and fall below the zero-pressure gradient curve. The latter behavior is consistent with the observations of previous investigators of the influence of strong favorable pressure gradients and streamline curvature [10, 11]. However, the trends reported herein, immediately downstream of injection and in the converging section of the nozzles, differ from previous studies in that effectiveness values are as high or higher than for the zero-pressure gradient curve. This may be partly due to the fact that the measurements were made along a curved wall rather than along a flat surface. It is also likely that a strong laminarizing effect resulted from the flow acceleration in the relatively rapidly converging nozzles. The extent of this effect probably depends on the magnitude of the initial turbulence level and, therefore, may be more significant with the relatively high levels in our experiments than for other investigations.

Finite Difference Boundary Layer Predictions

The applicability of currently available finite difference boundary layer programs for predicting the experimental measurements was next investigated. The numerical solution methods selected were those presented by Beckwith and Bushnell [17] and by Patankar and Spalding [18]. Both computer programs solve the compressible nonsimilar-boundary-layer equations for continuity, mean momentum, and mean total enthalpy for an ideal gas with constant or variable specific heat capacity. The turbulent-flux terms are modeled by means of eddy-diffusivity and mixing-length concepts. The magnitude and distribution of the mixing length across the boundary layer are determined from the computed characteristics of the boundary layer.

Calculations were performed using the values recommended in references [17–19] for the turbulent Prandtl number, turbulent Schmidt number, and other program parameters. Illustrative results are shown as the curve labelled "nominal" in Fig. 10 for Nozzle 1 (Inlet 2) with a ratio of injected to free stream velocity of 0.572 ($\dot{m}_i/\dot{m}_{fs}$ = 5.53 percent). This nozzle inlet combination was selected because it was considered to be a configuration for which mixing at the injection station was minimal and, therefore, would be most appropriate for comparison with the analysis which did not include mixing. The curve labelled "nominal" shows the results of calculating effectiveness values, assuming that the temperature in the boundary layer between the nozzle wall and the lip of the injector was equal to the injectant temperature. Between the injector lip and the edge of the boundary layer, it was assumed that the temperature was equal to the free stream value. Also, the computer calculations were made using the velocity at the edge of the boundary layer based on one-dimensional, isentropic, duct flow. It was interesting to find that the results from both programs were essentially the same and yielded effectiveness values that were higher than measured over the entire length of the nozzle.

The fact that the experimental values of effectiveness fall below the predicted curve in the constant area duct region suggests some mixing of the free and injectant streams (which is not included in either program) and/or some preheating of the nitrogen in the injectant passage. As a means of accounting for this, the following relationship was investigated for representing the temperature profile just downstream of the injection location:

$$\frac{T_{aw} - T_0}{T_{aw} - T_{0,\infty}} = 1 - [1 - (y/s)^2]^E \tag{3}$$

Curves corresponding to different values of E are plotted in Fig. 11. Note that for $E = 0$, a constant temperature profile is obtained. This

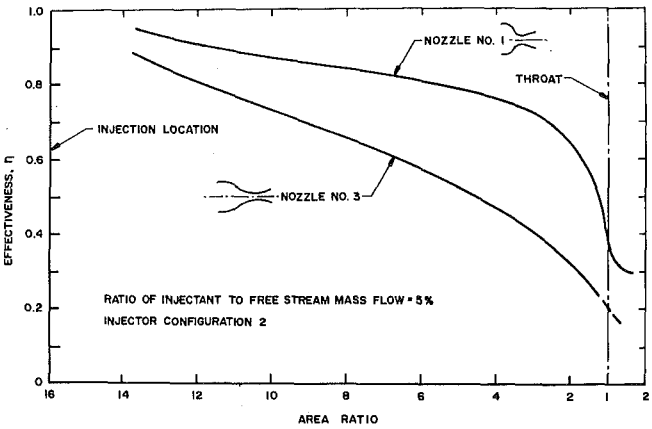

Fig. 8 Effect of area contraction rate on effectiveness

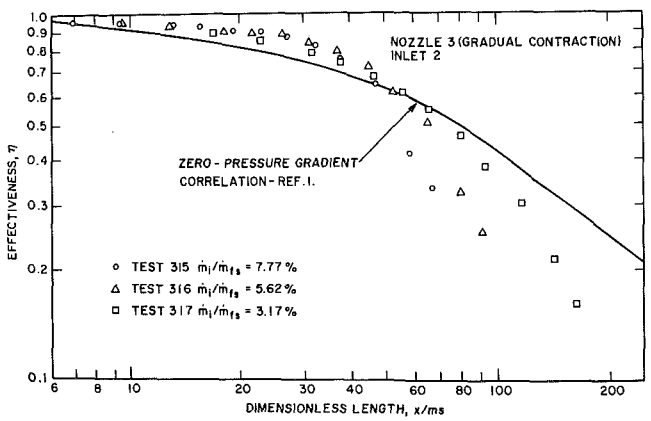

Fig. 7 Film cooling effectiveness for configuration $N_3 I_2$

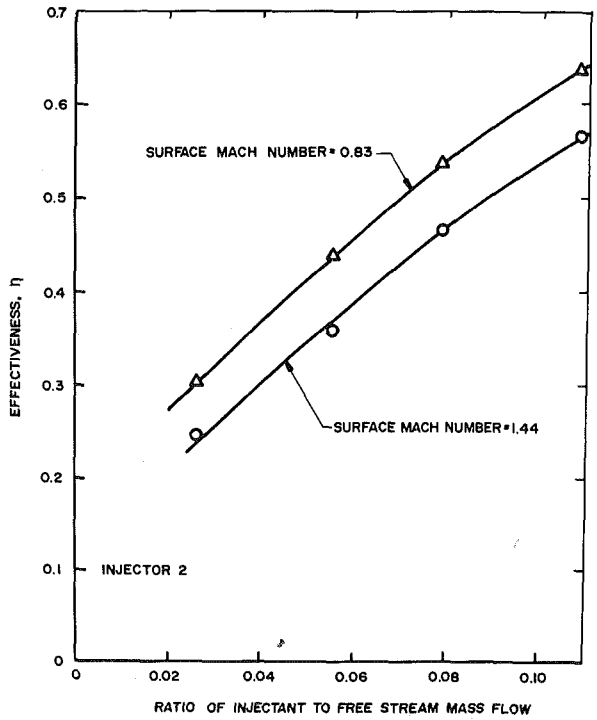

Fig. 9 Effect on injectant flow on effectiveness at the throat for Nozzle 1

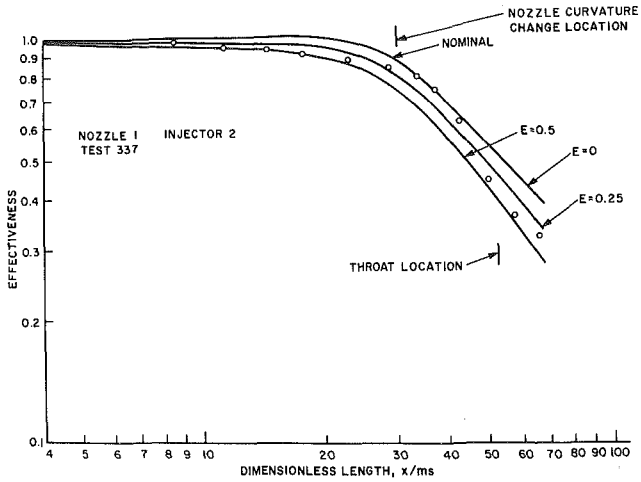

Fig. 10 Comparison of predicted and measured effectiveness variations

would represent the ideal situation at the injection location.

In actual flows, the velocity distribution at the injection location will not be uniform and sudden mixing between the free-stream and injectant will occur because of the velocity discontinuity, free-stream turbulence (which was comparatively high in the present tests), and possible nonalignment of the two flows. The effect of this mixing (and possibly preheating of injectant) would be a temperature profile such as shown in Fig. 11 for values of E greater than zero. Assuming that the injectant temperature profile at the injector station could be represented by the relationship of equation (3), calculations were made for a range of values of the parameter E (again with both programs).

Significantly improved agreement with the measured results was obtained with $E = 0.25$, as can be seen in Fig. 10. This tends to verify the applicability of the assumed initial temperature profile (equation (3)) for this nozzle and injector combination. However, it is noted that, in the region where the nozzle cross-sectional area is changing the most rapidly (values of x/ms between 22 and 40), measured values of effectiveness are as much as 12 percent higher than those predicted. A strong laminarization effect is suggested. Beyond this region, effectiveness values drop sharply and fall below the predicted curve. Similar trends were observed for other test runs.

The possibility of correcting the finite difference boundary layer calculations for flow acceleration and streamline curvature effects was also investigated. A procedure for modifying the eddy viscosity to account for flow acceleration has been proposed by Cebeci, et al. [20]. This method predicts a decrease in eddy viscosity and yields values of effectiveness higher than predicted by the unmodified boundary layer programs. Since the experimental results were below the unmodified boundary layer calculations, this procedure was not successful.

According to Bradshaw [21], the effect of streamline curvature on the turbulent mixing length is an increase in mixing length in a concave section and an increase in a convex section of a channel. Although the curvature changes in the subsonic section of the nozzles used in this study, this entire section would be concave in the sense that the flow along the wall is turned in the same direction all the way to the throat. Only after leaving the throat does the direction of radial velocity along the wall change. Thus the effect of streamline curvature predicted by reference [21] would be an increase in turbulent mixing length in the subsonic sections of the nozzles. However, very little effect is predicted just downstream of injection because there is little change in curvature. At the location of maximum curvature change, the data show a retarded rate of decrease in effectiveness rather than an accelerated decrease (suggesting, as mentioned earlier, a laminarization effect). It therefore appears that currently available analytical methods are not applicable for predicting the film cooling results reported.

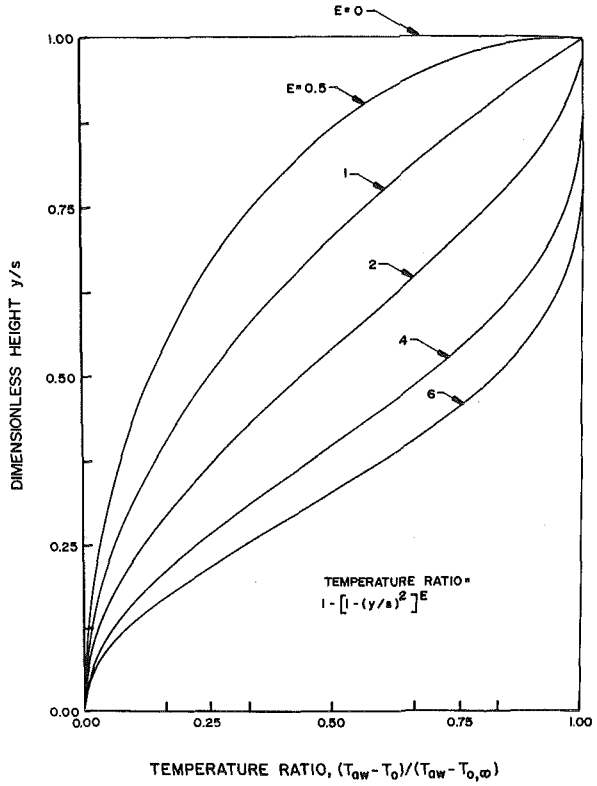

Fig. 11 Temperature profiles to account for injectant and free-stream mixing

Conclusions

This study demonstrated that cooling effectiveness in a converging channel is influenced by the rate of convergence. Results suggest that, even with a clean injector entrance, gross mixing of the injectant and free-stream fluid occurs at the injection station.

Comparison of measured effectiveness distributions with those predicted from finite difference models indicates that initial mixing, fluid acceleration and flow laminarization, and wall curvature affect the mixing process. However, the exact nature of how these effects enter cannot as yet be clearly specified.

References

1 Hartnett, J. P., Birkebak, R. C., and Eckert, E. R. G., "Velocity Distributions, Temperature Distributions, Effectiveness and Heat Transfer for Air Injected Through a Tangential Slot Into a Turbulent Boundary Layer," JOURNAL OF HEAT TRANSFER, TRANS. ASME, Series C, Vol. 83, 1961, pp. 293–306.

2 Wieghardt, K., "Über das Ausblasen von Warmluft für Enteiser," ZBW Research Report No. 1900 (AAF Translation Rest. No. F-TS-919-Re, Wright Field, 1946).

3 Tribus, M., and Klein, J., "Forced Convection From Non-Isothermal Surfaces," Symposium on Heat Transfer, University of Michigan, 1962.

4 Papell, F. S., and Trout, A. N., "Experimental Investigation of Air Film Cooling Applied to an Adiabatic Wall by Means of an Axially Discharging Slot," NASA TN:D-9, 1959.

5 Hatch, J. E., and Papell, F. S., "Use of a Theoretical Flow Model to Correlate Data for Film Cooling or Heating an Adiabatic Wall by Tangential Injection of Gases of Different Fluid Properties," NASA TN:D-130, 1959.

6 Papell, F. S., "Effect on Gaseous Film Cooling of Coolant Injection Through Angled Slot and Normal Holes," NASA TN:D-299, 1960.

7 Seban, R. A., and Back, L. H., "Effectiveness and Heat Transfer for a Turbulent Boundary Layer With Tangential Injection and Variable Free Stream Velocity," JOURNAL OF HEAT TRANSFER, TRANS. ASME, Series C, Vol. 84, 1962, pp. 235–244.

8 Hartnett, J. P., Birkebak, R. C., and Eckert, E. R. G., "Velocity Distributions, Temperature Distributions, Effectiveness and Heat Transfer in Cooling of a Surface With a Pressure Gradient," *International Developments in Heat Transfer, Proceedings of the 1961–1962 Heat Transfer Conference*, ASME, 1963, pp. 682–689.

9 Carlson, L. W., and Talmor, L. W., "Gaseous Film Cooling at Various Degrees of Hot Gas Acceleration and Turbulence Levels," AIChE Report 31, 1968.

10 Pai, B. R., and Whitelaw, J. H., "The Influence of Strong Pressure Gradients on Film Cooling Effectiveness," *Heat Transfer 1970*, Vol. II, Elsevier Publishing Co., Amsterdam.
11 Mayle, R. E., and Kopper, F. C., "Effect of Streamline Curvature on Film Cooling," ASME Paper No. 76-GT-90.
12 Lucas, J. G., and Golladay, R. L., "An Experimental Investigation of Gaseous-Film Cooling of a Rocket Motor," NASA Technical Note D-1988, 1963.
13 Lucas, J. G., and Golladay, R. L., "Gaseous-Film Cooling of a Rocket Motor With Injection Near the Throat," NASA TN:D-3836, Feb. 1967.
14 Colucci, S. E., "Film Cooling Progress for Solid Rocket Nozzles," Aerojet-General Corporation Technical Paper 116 SRP, Apr. 20, 1962.
15 Williams, J. J., "The Effect of Gaseous Film Cooling on the Recovery Temperature Distribution in Rocket Nozzles," PhD thesis, University of California at Davis, May 1969.
16 Williams, J. J., and Giedt, W. H., "The Effect of Gaseous Film Cooling on the Recovery Temperature Distribution in Rocket Nozzles," ASME Paper No. 70-HT/SPT-42, June 1970.
17 Beckwith, I. E., and Bushnell, D. M., "Calculation by a Finite-Difference Method of Supersonic Turbulent Boundary Layers With Tangential Slot Injection," NASA TN:D-6221, Apr. 1971.
18 Patankar, S. V., and Spalding, D. B., "Heat and Mass Transfer in Boundary Layers," *International Textbook*, London, 1970.
19 Hixon, B. A., Beckwith, I. E., and Bushnell, D. M., "Computer Program for Compressible Laminar or Turbulent Nonsimilar Boundary Layers," NASA TM:X-2140, Apr. 1971.
20 Cebeci, Tuncer, "Calculation of Compressible Turbulent Boundary Layers With Heat and Mass Transfer," AIAA Paper No. 70-741, presented at the AIAA 3rd Fluid and Plasma Dynamics Conference, Los Angeles, Calif., June 29–July 1, 1970.
21 Bradshaw, P., "Effects of Streamline Curvature on Turbulent Flow," AGARD-AG-169, Aug. 1973.
22 McAdams, W. H., *Heat Transmission*, Third ed., McGraw-Hill, New York.
23 Bobco, R. P., "Radiation Heat Transfer in Semigray Enclosures With Specularly and Diffusely Reflecting Surfaces," JOURNAL OF HEAT TRANSFER, TRANS. ASME, Series C, Vol. 86, 1964.

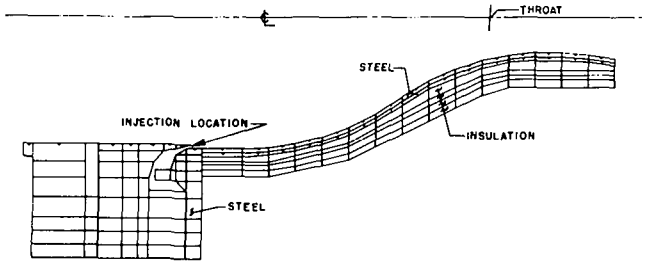

Fig. A1 Thermal model used for conduction analysis of nozzle configuration 3

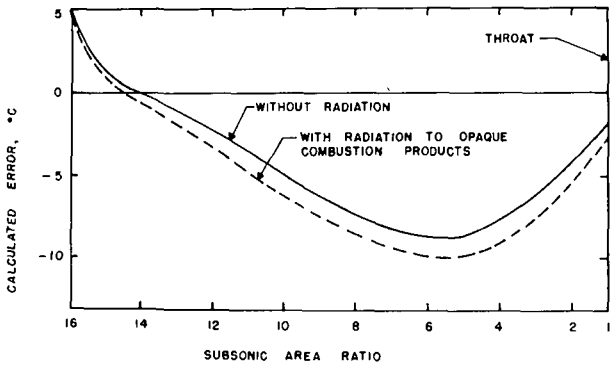

Fig. A2 Calculated measurement error for nozzle configuration 3

APPENDIX

Procedure for the Determination of Adiabatic Recovery Temperatures

Analyses were made to determine the differences between experimentally measured wall temperatures and the reported adiabatic wall temperatures.[3] Results from these analyses were used to correct the measured wall temperatures for conduction effects to arrive at the reported adiabatic temperature distributions. The overall procedure used was as follows:

1 Two-dimensional finite difference thermal models such as shown in Fig. A1 were formulated.
2 The heat transfer coefficient distribution was estimated from the measured transient temperatures.
3 The gas recovery temperature distribution was approximated by the measured steady-state wall temperature distribution.
4 The thermal response of each model using the foregoing assumptions was calculated from the start of heating until a quasi-steady state condition was reached.
5 The difference between the assumed gas recovery temperature distribution and the calculated wall temperature distribution at the quasi-steady state condition was then taken as the measurement error. This difference is plotted as a function of nozzle area ratio in Fig. A2.
6 Measured temperatures were corrected to the reported adiabatic wall temperatures by the following relationship:

$$\text{Reported adiabatic wall temperature} = \text{Measured wall temperature} - \text{Measurement error}$$

Because of the low value for maximum error (9°C out of a difference of 515°C between the combustion gas temperature and the initial coolant temperature), it was not considered necessary to recalculate the wall temperature distribution using the newly determined adiabatic temperatures.

To obtain an estimate of the maximum measurement error associated with radiation from the combustion products, each conduction analysis was repeated assuming the gas radiated as a black body at its local static temperature. The increase in predicted error associated with this assumption is also shown in Fig. A2. As can be seen, the added error is one degree or less at all locations.

For the combustion of hydrogen and air, the only effective radiating component of the chamber gas will be water vapor. At a mixture ratio of 200 and a chamber pressure of 1.4×10^6 Pa, the total water vapor pressure will be about one atmosphere. If an effective beam length of 10 cm is assumed, the emissivity of the water vapor is on the order of 0.1 [22]. One nozzle configuration (No. 1) was analyzed to evaluate steady-state radiation effects assuming nozzle surfaces with an emissivity of 0.5 and a transparent gas.

The analysis was performed by dividing the nozzle into a series of conical elements, determining the gray body view factors by the method of reference [23], and performing an energy balance that included convection and radiation effects to determine the equilibrium element temperatures. Again, the predicted effect of radiation was negligible in comparison with the temperature change caused by coolant injection.

[3] This difference is defined as the measurement error which is negative for a measured temperature lower than the adiabatic wall temperature (a negative error would thus be a positive correction to the measured wall temperature).

D. R. Pitts
Professor. Mem. ASME

H. C. Hewitt
Professor. Mem. ASME

B. R. McCullough
Graduate Assistant.

Tennessee Technological University, Cookeville, Tenn.

Heat Transfer Controlled Collapse of a Cylindrical Vapor Bubble in a Vertical Isothermal Tube

An experimental program was conducted to determine the collapse rate of slug-type vapor bubbles rising due to buoyancy through subcooled parent liquid in a vertical isothermal tube. The experimental apparatus included a vertical glass tube with an outer glass container providing a constant temperature water bath for the inner tube. The inner tube contained distilled, deaerated water, and water vapor bubbles were generated at the bottom of this tube with a pulsed electric heater. The parent liquid was uniformly subcooled with respect to the vapor bubble resulting in heat transfer controlled bubble collapse. Collapse rates and rise velocities were recorded by high-speed motion picture photography. Over a limited range of subcooling, the bubble collapse was well behaved, and a simple, quasi-steady boundary layer heat transfer analysis adapted from slug flow over a flat plate correlated the experimental results with a high degree of accuracy. Experimental results were obtained with tubes having inside diameters of 0.0127, 0.0218, and 0.0381 m and for a range of subcooling from 0.5 to 9.0 K.

Introduction

Cylindrical or slug-type vapor bubbles are frequently encountered in low velocity two-phase flow, and the existence of such vapor pockets is of importance in all associated transport calculations. Consequently, the collapse rate of such bubbles is of interest since this affects the net vapor generation and heat transfer rates inside the tubes, and the present work reports agreement between a boundary layer analysis and experimental results obtained with distilled water vapor bubble/liquid systems.

Large water vapor pockets rising due to buoyancy in a vertical tube assume a slug configuration with a hemispherical upper cap, the main portion being essentially cylindrical and almost filling the tube radially. The bottom is somewhat irregularly shaped due to the wake-type flow. Such bubbles are sometimes referred to as Taylor bubbles, and a photograph of a typical bubble is shown in Fig. 1. It may be observed from this figure that the diameter at the top is somewhat smaller than that at the bottom. This is typical of all bubbles observed during this study.

While there is an extensive body of research literature devoted to spherical bubble collapse and bubble dynamics, very little has been presented for the present case. For a single component, two-phase system, the heat transfer controlled collapse of a vapor bubble proceeds at a rate governed by the energy transfer at the liquid interface necessary for removal of the latent heat of the vapor and its subsequent subcooling. Analytical investigations of this physical situation for a spherical bubble, or the closely related growth problem, have been conducted by Plesset and Zwick [1, 2],[1] Degarabedian [3], Forster [4], Forster and Zuber [5], and Akiyama [6] among others. Heat transfer controlled collapse of spherical bubbles has been investigated analytically and experimentally by Hewitt and Parker [7], by Florschuetz and Chao [8] under zero gravity conditions, and by Wittke and Chao [9] with translatory velocities due to reduced gravity. Previous investigations with a slug or cylindrical type bubble in a tube have been presented by White and Beardmore [10] and by Kouremenos [11] for rise velocity of non-collapsing air bubbles, and by Anderson, et al. [12] for tube surface heat transfer coefficients.

In the present paper attention is directed to the case of a collapsing vapor bubble rising due to buoyancy under standard gravity conditions. The collapse is controlled by heat transfer, and the appropriate integral-type boundary layer equations are unchanged from flow over a flat plate. In particular, the boundary layer flow of liquid over the vapor surface is modelled by slug flow. The solutions of these equations are compared with experimental data obtained during this study and reported herein.

Contributed by the Heat Transfer Division and presented at the Winter Annual Meeting, New York, N. Y., December 5-10, 1976. Revised manuscript received by the Heat Transfer Division May 23, 1977. Paper No. 76-WA/HT-24.

[1] Numbers in brackets designate References at end of paper.

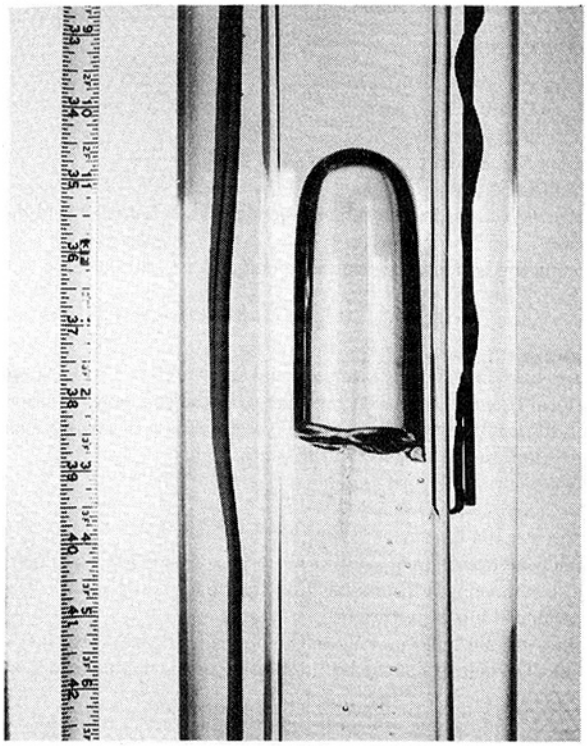

Fig. 1 Typical cylindrical bubble in a restraining circular tube

Experimental Investigation

High speed motion picture photography was employed to record vapor bubble collapse history as large cylindrical bubbles rose due to buoyancy in a uniformly subcooled parent liquid. Tests were conducted in three different cylindrical pyrex tubes with inside diameters of 1.27, 2.18, and 3.81 cm. These tubes were selected for internal diameter uniformity, and the length of each tube was approximately 1 m. Bubble generation was accomplished with a small nichrome-wire heater mounted in the bottom of the tube and submerged in the parent liquid.

The entire system temperature was controlled by mounting the tube in a heated water bath. The bath temperature was monitored with a six-point copper-constantan thermocouple probe. Temperature stratification over the bath depth was limited to a maximum of 0.5 K. This stratification resulted when convective cooling was used to obtain the desired experimental conditions. This maximum value of 0.5 K was associated with the 9 K subcooled condition. Less stratification occurred with lower subcooling. The actual stratification over the total length traversed by the bubble during the time it was studied was less than one-half of this maximum since the histories all took place in a vertical distance of less than ½ m.

Prior thermometric calibration and correlation of the tube fluid temperature with the bath thermocouples was obtained with a removable inside-tube thermocouple probe. This eliminated the need of a temperature probe and resulting flow obstruction inside the tube during actual runs. Experimental run time was on the order of 1 s. Bath and tube fluid temperature changes during these short periods were found experimentally to be negligible. Thermocouples were calibrated between the ice and steam points.

With the tube filled with distilled, deaerated water and mounted in the bath, the system temperature was raised to the saturation value by means of the bath heater and the tube heater. The entire system was allowed to cool slowly by natural convection until the desired experimental temperature was reached. At this point, a single bubble was generated which collapsed due to heat transfer as it traversed the tube length.

Photographic recording of bubble collapse histories was accomplished with a Wollensak model WF4-ST, Fastax, 16 mm, high-speed movie camera together with its associated control equipment, power supply, and timing signal generator. The filming speed was approximately 1000 frames per s, and the timing signal generator was operated at 100 Hz providing a time signal at about every tenth frame. Photographic data reduction utilized a model 900 Motion Analyzer projector manufactured by L-W Photo, Inc., of Van Nuys, California, which featured a highly corrected lens suitable for quantitative data reduction. Length scales were placed in the tube for vertical and horizontal length calibration. Once the optical distortion was established, the scale was removed and known tube diameters were used as reference lengths.

Bubble collapse data reduction was accomplished by measurement of the photographic image of the vapor configuration at preselected time intervals. During most of the collapse period the bubble could be treated as a tapered cylinder with a hemispherical cap, necessitating only a minimum number of measurements for calculation of the vapor volume. These were the cylinder diameter at the bottom, total length including hemispherical cap, and cap diameter. During final stages of collapse, the configuration was approximately hemispherical, progressing to a somewhat spherical shape. This final collapse, however, represented only a small fraction of the bubble volume change and was not considered as a part of this investigation since the bubble configuration at this time was so markedly different from that for most of the volume change period.

Analytical Correlation

As a bubble rises due to buoyancy inside a tube of otherwise quiescent liquid, liquid above the bubble must flow over the bubble upper surface and then along the sides in the annular space between

Nomenclature

A_a = annular cross-sectional area
A_b = cross-sectional area of cylindrical portion of the vapor bubble
A_1 = area over which fluid velocity is constant
A_2 = area over which fluid velocity varies
D_b = bubble diameter
D, D_t = tube diameter
$\bar{h}$ = average heat transfer coefficient
h_L = heat transfer coefficient based on L
h_x = heat transfer coefficient based on x
L = length of cylindrical portion of bubble
Nu_L = Nusselt number based on bubble length
Nu_x = Nusselt number based on x
Pr = Prandtl number
$\dot{q}$ = heat flux
R_b = bubble radius
R_t = tube radius
Re_L = Reynolds number based on L
Re_x = Reynolds number based on x
$\Delta T = -(T - T_0)$
T = temperature
T_0 = saturation temperature
T_∞ = free stream temperature
t = time
V = volume
V_0 = initial volume
V_b = bubble bulk rise velocity (of center of mass)
$V_{\ell,b}$ = bulk average fluid velocity
V_r = relative velocity
$(V_2)_{\mathrm{avg}}$ = average liquid velocity in the boundary layer
$V_\infty(x)$ = fluid free stream velocity
x = distance along cylindrical portion of the bubble
y = distance perpendicular to bubble profile
α = thermal diffusivity
δ = local boundary layer thickness, momentum
δ_t = local boundary layer thickness, thermal
ϵ = dummy variable of integration
ν = kinematic viscosity

the vapor bubble and the tube wall. For a slowly collapsing bubble where the radial dimension is essentially invariant during the collapse, a quasi-steady boundary layer analysis can be applied to this nonsteady problem. The mathematical model chosen is adapted from laminar flow boundary layer theory, the outer surface of the cylindrical bubble being approximated by a flat plate of length equal to that of the bubble and width equal to the bubble circumference. The bubble radius of curvature is an order of magnitude greater than the boundary layer thickness, thereby rendering the flat plate model suitable. The analysis parallels that for slug flow in liquid metal heat transfer.

The configuration shown in Fig. 2 represents a cross-sectional view of a collapsing bubble having a bulk rise velocity, V_b. This bulk rise velocity is that of the center of mass of the vapor bubble. The rising bubble results in flow over the hemispherical upper cap followed by an annular flow bounded by the tube inner wall and the vapor bubble. Following a suggestion by Rohsenow [13] it is assumed that the shear stress in the liquid at the liquid-vapor interface is negligible, and consequently slip-flow exists at this surface. This is a result of the order-of-magnitude difference between the kinematic viscosity of the liquid and that of the vapor. At the tube wall, however, the no-slip boundary condition applies, and a typical velocity boundary layer forms due to the retarding influence of the wall shear stress.

The quasi-steady velocity boundary layer, which is assumed to begin at $x = 0$, develops as the fluid travels along the length of the tube wall adjacent to the bubble. The location $x = 0$ is determined volumetrically using the geometrical model of a hemisphere mated to a cylinder as shown in Fig. 2. For purposes of determining the fluid free stream velocity, $V_\infty(x)$, the liquid flow rate is assumed to be constant at any cross-section along this length. This neglects any contribution due to radial bubble collapse resulting from phase change, but photographic studies indicate that such radial collapse was negligible. Thus V_∞ increases with x as required by the continuity equation, and the local value of this parameter can be added to the bubble rise velocity to yield an appropriate quasi-steady free stream velocity for use in the heat transfer equation.

Free Stream Velocity. Application of the continuity equation to the liquid region of Fig. 2, Detail A results in

$$V_\infty = \frac{A_b V_b - A_2 (V_2)_{\text{avg}}}{A_1} \tag{1}$$

where it is assumed that there is no radial movement of the bubble surface. A_b is the cross-sectional area of the cylindrical portion of the vapor bubble, and V_b is the rise velocity of the vapor bubble. Both of these terms are obtainable for a given bubble collapse from high-speed motion pictures. The average liquid velocity in the boundary layer, $(V_\infty)_{\text{avg}}$, is obtained by integrating the product of velocity and area through the velocity boundary layer and then dividing by the liquid flow area within this boundary layer. Using the customary third order velocity profile

$$\frac{V(\epsilon)}{V_\infty} = \frac{3}{2}\left(\frac{\epsilon}{\delta}\right) - \frac{1}{2}\left(\frac{\epsilon}{\delta}\right)^3 \tag{2}$$

which satisfies the four known boundary conditions for flow over a flat plate with constant V_∞ (this condition being approximately true for the present problem) yields the following average velocity at a given length location within the momentum boundary layer

$$(V_2)_{\text{avg}} = 0.05\, V_\infty \left(\frac{25R_t - 16\delta}{2R_t - \delta}\right) \tag{3}$$

Substitution of this into equation (1) and subsequent rearrangement gives

$$V_\infty = \frac{A_b V_b}{A_1 - 0.05 A_2 \left(\dfrac{25R_t - 16\delta}{2R_t - \delta}\right)} \tag{4}$$

which relates the fluid velocity outside of the velocity boundary layer to measurable parameters (R_t, A_b, and V_b) and the boundary layer thickness δ which together with R_t fixes A_1 and A_2. Expressing A_1 and A_2 in terms of the tube and bubble diameters and the boundary layer thickness results in

$$V_\infty = A_b V_b \left\langle \frac{\pi}{4}\left[(D_t - 2\delta)^2 - D_b{}^2\right] - 0.05\left(\frac{\pi}{4}\right)\left[D_t{}^2 - (D_t - 2\delta)^2\right]\left(\frac{25R_t - 16\delta}{2R_t - \delta}\right)\right\rangle^{-1} \tag{5}$$

where D_b is the average diameter of the slightly tapered cylindrical section.

Using the bulk average liquid velocity in the annular flow

$$V_{\ell,b} = \frac{A_b V_b}{A_a} \tag{6}$$

where A_a is the annular cross-sectional area $(\pi/4)(D_t{}^2 - D_b{}^2)$ to form the local Reynolds number, together with the conventional integral analysis result for the boundary layer thickness in steady, incompressible, laminar flow over a flat plate, yields

$$\delta = \frac{4.64x}{(A_b V_b x/A_a \nu)^{1/2}} \tag{7}$$

which is an approximation for δ since $V_{\ell,b}$ is used for V_∞. The fluid free stream velocity at any position can be found by substitution of equation (7) into equation (5).

Since the liquid is moving in the opposite direction to the vapor bubble, the velocity of the liquid relative to the vapor surface is

$$V_r = V_\infty + V_b \tag{8}$$

Energy Equation. The quasi-steady thermal boundary layer is also assumed to begin at $x = 0$ and to increase in thickness (from the bubble wall) with increasing bubble length. Under the assumptions of slug flow and a third order temperature profile, expressions for the local thermal boundary layer thickness

$$\frac{\delta_t}{x} = 2.828\,(\text{Re}_x \text{Pr})^{-1/2} \tag{9}$$

and the length-averaged Nusselt number

$$\text{Nu}_L = \frac{\bar{h}L}{k} = 1.0608\,(\text{Re}_L \text{Pr})^{1/2} \tag{10}$$

result where the Reynolds number is calculated with the relative velocity V_r. These equations are developed for slug velocity profile flow of liquid metal over a flat plate in undergraduate heat transfer texts.

Equation (10) is used to predict the bubble collapse rate and compared with the experimental collapse data for each bubble history.

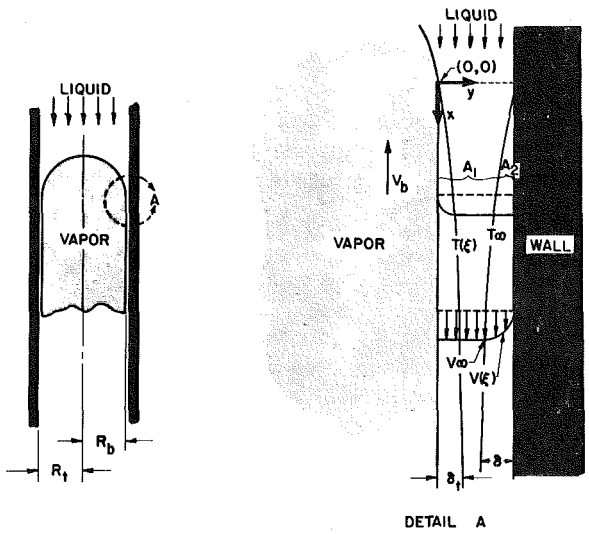

Fig. 2 Model for analysis

The comparison is carried out as follows: For given initial bubble size, rise velocity, T_0, and T_∞, the initial heat transfer coefficient $\bar{h}$ is calculated using equation (10). This, together with the cylindrical portion of the bubble surface area and the temperature difference, is used to calculate the total heat transfer Q for a small time increment. The collapse length of the bubble for that time increment is determined by multiplying this total heat transfer by the vapor specific volume and dividing by the product of the latent heat of vaporization and A_b. During the time increment, the vertical displacement of the bubble results in a reduction of the hydrostatic pressure. Using the perfect gas equation of state, the increase in volume due to this pressure reduction is calculated and added algebraically to the volume reduction due to the heat transfer. This process is repeated to generate the collapse curve, i.e., volume versus time history, using the customary precautions to ascertain that the time increment for each subcalculation is sufficiently small.

To carry out these calculations the rise velocity, T_0 and T_∞ are assumed constant and are obtained experimentally for each bubble. The relative velocity (V_r) used to determine Re_l for use in equation (10) is that at the end of the bubble, $x = L$. While this is the maximum value of $V_r = V_\infty + V_b$, it should be noted that this velocity is a rather weak function of x as can be seen by examining equation (4), that is, for the present problem R_t is an order of magnitude greater than δ. This allows V_r to be treated as a constant to obtain equations (9) and (10).

Results

Photographic data for the collapse of 22 bubbles ranging in initial volume from 3.15 to 106.8 cm^3 and ranging in subcooling from 0.5 to 9.0 K were obtained and reduced. A majority of these (16 bubbles) were obtained with the 2.18-cm dia tube; two were obtained with the 3.81-cm tube; and four were for the 1.27-cm tube. Typical experimental results are presented in Figs. 3–5. In each of these figures the circular data points represent experimental results, and the solid black line on each figure is the theoretical collapse rate obtained by application of the analysis result, equation (10). Figs. 3 and 4 cover most of the range of subcooling used in the experimental program and are typical of the results obtained with the 2.18-cm tube. Fig. 4 represents the degree of experimental repeatability obtained; these data were obtained under intentionally repeated test conditions. Fig. 5 is typical of the results using the 1.27-cm tube and the 3.18-cm tube. The comparison between experiment and theory for all experiments is remarkably good when compared with usual phase change results. When the subcooling was somewhat greater than 9.0 K in our experiments (the exact value for this was not determined), the vapor bubble did not rise in the tube. Since this situation does not fit the actual model, it is not recommended that the analysis be used for cases where the collapse rate causes zero or negative bubble rise velocity.

The percent error between the theoretical collapse rate of equation (10) and the experimental measurements had a mean value of 3.4 percent and a standard deviation of 12 percent. This error analysis did not include the 9.0 K subcooling data. It is very possible that the measurement techniques could introduce errors of this magnitude.

The major error involved in the experimental study is that of determining the time dependent vapor bubble volume. Measurements included the cylindrical portion bottom diameter, upper diameter, and overall length. Errors resulted from: (i) lack of precise vapor-liquid interface definition and (ii) lack of exact conformance to the tapered cylinder and hemispherical cap model. It is estimated that the volume determination was within ±10 percent and this error completely overshadows errors in other measurements involved.

The flat plate analysis which is compared with individual collapse histories in Figs. 3–5 neglects the heat transfer along the upper cap surface and in the wake region. A more exact solution should include these effects. To examine the relative magnitude of error introduced by these omissions, an approximation of the heat transfer from the cap surface can be obtained with the usual correlation equation for forced flow over a sphere, $\overline{\mathrm{Nu}}_D = 0.37\ \mathrm{Re}_D^{0.6}$. In the present application, the appropriate velocity for the Reynolds number is the integrated average velocity of the liquid flow over the cap. A number

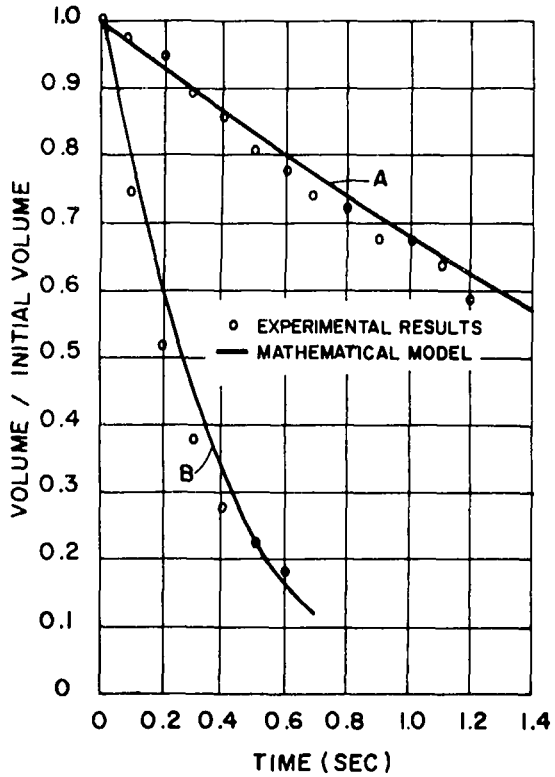

Fig. 3 Comparison of experimental and analytical collapse of a bubble in an 0.0218-m ID tube: (A) Bubble 13-c, 0.50 K subcooling; (B) Bubble 13-f, 3.20 K subcooling

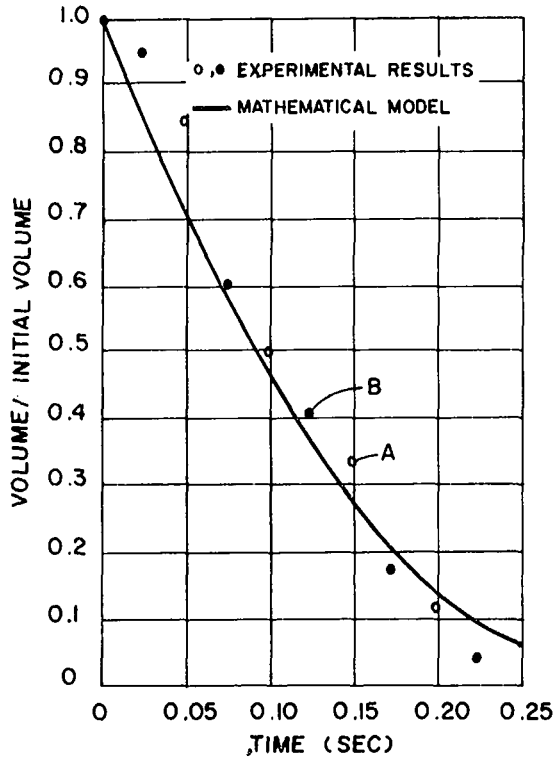

Fig. 4 Comparison of experimental and analytical collapse of two bubbles in an 0.0218-meter ID tube for subcooling of 9.00 K: (A) Bubble 8-b-2; (B) Bubble 8-b-3

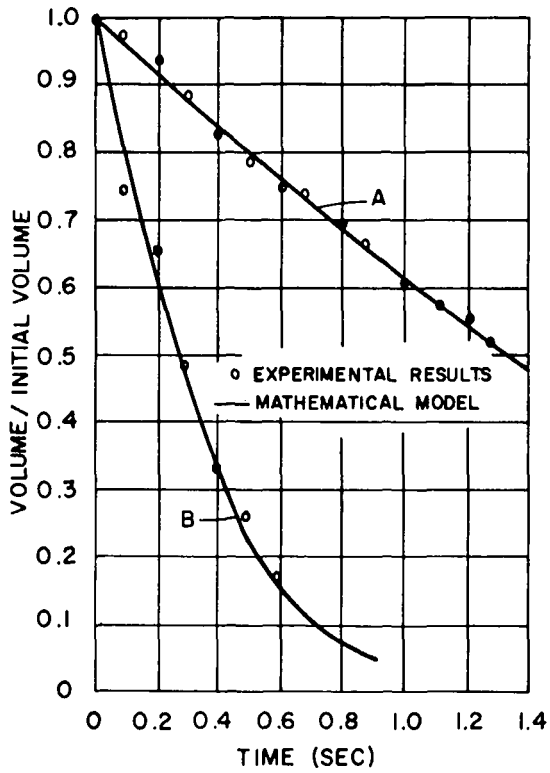

Fig. 5 Comparison of experimental and analytical collapse of bubbles: (A) Bubble 12-b, 0.0381-m ID tube, 1.00 K subcooling (B) Bubble 14-e, 0.0127-m ID tube, 2.31 K subcooling

of calculations were carried out for the conditions of the experiments of this study; in general, the ratio of $\dot{q}_{cap}/\dot{q}_{cyl}$ approaches 10 percent when the ratio of cylindrical length to bubble diameter is on the order of ⅓ in the 3.81-cm tube, ¼ in the 2.18-cm tube, and 1/10 in the 1.27-cm tube. This ratio of $\dot{q}_{cap}/\dot{q}_{cyl}$ drops markedly with increasing length-to-diameter ratio. At length-to-diameter ratios less than 0.5, however, the bubble loses its cylindrical configuration, and no flat plate analysis should be considered. This was the criterion used in comparing experimental collapse history with theory.

The application of the flat plate analysis should be limited to cases where laminar flow exists over the bubble length and where there is no overlap of the thermal and velocity boundary layers developing along the vapor surface and the tube wall, respectively. Appendix Table A-3 tabulates experimental and some calculated results, including maximum Reynolds numbers, δ, and δ_t for thirteen vapor bubbles studied. (Of the 22 bubbles photographed, only thirteen were completely analyzed with regard to calculated parameters due to time limitations.)

In the small diameter tube (1.27 cm) the combination of $\delta_t + \delta$ was greater than the liquid thickness which indicates that interaction between the thermal and velocity boundary layers existed at the start of collapse. Two comments should be made on this situation:

1 The velocity boundary layer, δ, is measured from the glass and the thermal boundary layer, δ_t, is measured from the vapor. Therefore, this interaction will occur in a region where both are relatively slowly changing functions.

2 The scale readability of measuring length from the photographic images made the values of $D_t - D_b$ questionable for the small tube.

Both effects may require additional study to provide more information. However, the integral solution method did seem to adequately model this case, and is recommended for estimation of cylindrical water vapor bubble collapse rate under the following conditions:

(i) inside tube pressure near atmospheric;
(ii) tube inside diameters from 1 to 4 cm;
(iii) subcooling to 9 K;
(iv) bubble cylindrical length-to-diameter ratio not less than 0.5 at end of collapse prediction;
(v) laminar flow over entire bubble length.

Conclusions

The heat transfer controlled collapse of large, cylindrically shaped water vapor bubbles rising due to buoyancy effects inside a vertical tube with constant wall temperature is dependent upon tube diameter and fluid subcooling. This collapse rate can be predicted with a very high degree of accuracy by a simple energy balance at the liquid-vapor interface which relates the convective heat transfer to the change of latent heat of vaporization within the bubble due to volume change.

The simple integral boundary layer analysis for slug-flow of liquid over a flat plate yields a valid convective heat transfer coefficient in the usual form of a length controlled Nusselt number as a function of the Reynolds and Prandtl numbers. The appropriate velocity for determination of the Reynolds number is the relative velocity between the vapor and the liquid. Application of the boundary layer result requires that the bubble translatory velocity, which is treated as a constant, be known. Further, the continuously decreasing bubble length and the corresponding continuously changing heat transfer coefficient necessitates a computer-type solution for the complete collapse. A major contribution of this effort is that the collapse phenomenon is shown to be boundary layer heat transfer controlled.

Acknowledgments

The authors wish to express their sincere appreciation to the referees who reviewed the sessions paper manuscript, to those who reviewed the Journal paper manuscript, and especially to Dr. B. T. Chao, Technical Editor of the Journal of Heat Transfer, for their collective efforts and suggestions for improvements of this paper. Also,

Table A-1 Experimental data

Bubble	Inside Tube Diameter cm	in	Bubble Diameter* cm	in	Initial Length** cm	ft	Bubble Rise Velocity cm/sec	ft/sec	ΔT*** °C	°F
8b-2	2.18	(0.86)	1.80	(0.71)	13.08	(0.429)	30.02	(0.985)	9.00	(16.2)
8b-3	2.18	(0.86)	1.80	(0.71)	15.64	(0.513)	34.47	(1.131)	9.00	(16.2)
8b-4	2.18	(0.86)	1.80	(0.71)	14.63	(0.480)	22.01	(0.722)	9.00	(16.2)
12-b	3.81	(1.50)	3.02	(1.19)	7.13	(0.234)	22.56	(0.74)	1.00	(1.8)
12-d	3.81	(1.50)	3.02	(1.19)	4.42	(0.1449)	21.12	(0.693)	2.70	(4.86)
13-c	2.18	(0.86)	1.80	(0.71)	6.64	(0.2179)	15.12	(0.496)	0.50	(0.9)
13-d	2.18	(0.86)	1.80	(0.71)	3.28	(0.1075)	14.72	(0.483)	1.67	(3.0)
13-e	2.18	(0.86)	1.80	(0.71)	4.85	(0.1591)	11.89	(0.390)	2.70	(4.86)
13-f	2.18	(0.86)	1.80	(0.71)	5.94	(0.1950)	13.56	(0.445)	3.20	(5.76)
14-b	1.27	(0.50	1.12	(0.44)	3.08	(0.1010)	10.97	(0.360)	0.55	(0.99)
14-c	1.27	(0.50)	1.12	(0.44)	3.16	(0.1035)	10.36	(0.340)	1.20	(2.16)
14-d	1.27	(0.50)	1.12	(0.44)	5.32	(0.1745)	9.51	(0.312)	2.17	(3.90)
14-e	1.27	(0.50)	1.12	(0.44)	11.19	(0.367)	10.12	(0.332)	2.31	(4.16)

*Diameter is average of measurements at top and bottom
**Rise velocity is that of center of mass of vapor
***ΔT is subcooling, i.e., $T_o - T$

Table A-2 Experimental collapse data

Bubble	Time (sec)	V/V_o[1]	Bubble	Time (sec)	V/V_o
12-b	0	1.0	12-d	0	1.0
	0.1	0.969		0.1	0.907
	0.2	0.939		0.2	0.780
	0.3	0.871		0.3	0.642
	0.4	0.826			
	0.5	0.773			
	0.6	0.743			
	0.7	0.728			
	0.8	0.683			
	0.9	0.653			
	1.0	0.608			
	1.1	0.577			
	1.2	0.555			
	1.3	0.517			
13-c	0	1.0	13-d	0	1.0
	0.1	0.982		0.1	0.812
	0.2	0.948		0.2	0.709
	0.3	0.897		0.3	0.658
	0.4	0.855		0.4	0.607
	0.5	0.812			
	0.6	0.778			
	0.7	0.744			
	0.8	0.727			
	0.9	0.684			
	1.0	0.676			
	1.1	0.642			
	1.2	0.591			
	1.3	0.608			
13-e	0	1.0	13-f	0	1.0
	0.1	0.793		0.1	0.749
	0.2	0.654		0.2	0.518
	0.3	0.529		0.3	0.383
	0.4	0.425		0.4	0.287
	0.5	0.367		0.5	0.229
	0.6	0.278		0.6	0.181

[1] V/V_o is ratio of volume to initial volume

Table A-2 (Cont'd)

Bubble	Time (sec)	V/V_o	Bubble	Time (sec)	V/V_o
14-b	0	1.0	14-c	0	1.0
	0.1	0.906		0.1	0.765
	0.2	0.832		0.2	0.631
	0.3	0.795		0.3	0.464
	0.4	0.683		0.4	0.397
	0.5	0.572		0.5	0.347
	0.6	0.646		0.6	0.246
	0.7	0.572			
	0.8	0.534			
	0.9	0.497			
	1.0	0.460			
	1.1	0.441			
	1.2	0.386			
14-d	0	1.0	14-e	0	1.0
	0.1	0.795		0.1	0.742
	0.2	0.570		0.2	0.656
	0.3	0.386		0.3	0.485
	0.4	0.263		0.4	0.342
	0.5	0.161		0.5	0.265
				0.6	0.175
8b-2	0	1.0	8b-3	0	1.0
	0.05	0.841		0.025	0.948
	0.10	0.495		0.075	0.610
	0.15	0.362		0.125	0.412
	0.20	0.113		0.175	0.171
	0.25	0.016		0.225	0.039
8b-4	0	1.0			
	0.05	0.780			
	0.10	0.622			
	0.15	0.501			
	0.20	0.272			
	0.25	0.151			
	0.30	0.098			
	0.35	0.030			
	0.40	0.017			

Table A-3 Calculated data

Bubble	Re_L	Pr	δ (cm)	δ_t (cm)	$(D_t - D_b)$ (cm)
3b-2	322,000	1.86	1.069×10^{-1}	4.78×10^{-2}	3.80×10^{-1}
8b-3	524,000	1.86	1.003×10^{-1}	4.48×10^{-2}	3.80×10^{-1}
8b-4	403,000	1.86	1.069×10^{-1}	4.78×10^{-2}	3.80×10^{-1}
12-b	159,000	1.75	8.30×10^{-2}	3.82×10^{-2}	7.90×10^{-1}
12-d	82,000	1.78	7.16×10^{-2}	3.27×10^{-2}	7.90×10^{-1}
13-c	109,000	1.75	9.33×10^{-2}	4.30×10^{-2}	3.80×10^{-1}
13-d	54,000	1.76	6.55×10^{-2}	3.01×10^{-2}	3.80×10^{-1}
13-e	59,000	1.78	9.26×10^{-2}	4.23×10^{-2}	3.80×10^{-1}
13-f	55,000	1.79	1.17×10^{-1}	5.35×10^{-2}	3.80×10^{-1}
14-b	52,000	1.75	6.27×10^{-2}	2.89×10^{-2}	1.50×10^{-1}
14-c	59,000	1.76	6.04×10^{-2}	2.77×10^{-2}	1.50×10^{-1}
14-d	72,000	1.77	9.20×10^{-2}	4.21×10^{-2}	1.50×10^{-1}
14-e	179,000	1.77	1.227×10^{-1}	5.62×10^{-2}	1.50×10^{-1}

Re_L, δ, and δ_t are maximum values based on initial bubble length. Properties are based on film temperature.

we wish to acknowledge support of Tennessee Technological University during the experimental research program.

References

1 Plesset, M. S., and Zwick, S. A., "A Non-Steady Heat Diffusion Problem With Spherical Symmetry," *Journal of Applied Physics*, Vol. 23, 1952, p. 95.

2 Plesset, M. S., and Zwick, S. A., "The Growth of Vapor Bubbles in Superheated Liquids," *Journal of Applied Physics*, Vol. 25, 1954, p. 493.

3 Dergarabedian, P., "The Rate of Growth of Vapor Bubbles in Superheated Water," *Journal of Applied Physics*, Vol. 20, 1953, p. 537.

4 Forster, H. K., "On the Conduction of Heat Into a Growing Vapor Bubble," *Journal of Applied Physics*, Vol. 25, 1954, p. 1067.

5 Forster, H. D., and Zuber, N., "Growth of a Vapor Bubble in a Superheated Liquid," *Journal of Applied Physics*, Vol. 25, 1954, p. 474.

6 Akiyama, M., "Spherical Bubble Collapse in Uniformly Subcooled Liquid," *Bulletin of the Japanese Society of Mechanical Engineers*, Vol. 8, No. 32, 1965, p. 683.

7 Hewitt, H. C. and Parker, J. D., "Bubble Growth and Collapse in Liquid Nitrogen," JOURNAL OF HEAT TRANSFER, TRANS. ASME, Series C, Vol. 90, No. 1, 1968, p. 22.

8 Florschuetz, L. W., and Chao, B. T., "On The Mechanics of Vapor Bubble Collapse," JOURNAL OF HEAT TRANSFER, TRANS. ASME, Series C, Vol. 87, No. 2, 1965, p. 209.

9 Wittke, D. D. and Chao, B. T., "Collapse of Vapor Bubbles with Translatory Motion," JOURNAL OF HEAT TRANSFER, TRANS. ASME, Series C, Vol. 89, No. 1, 1967, p. 17.

10 White, E. T., and Beardmore, R. H., "The Velocity of Rise of Single Cylindrical Air Bubbles Through Liquids Contained in Vertical Tubes," *Chemical Engineering Science*, Vol. 17, 1962, p. 351.

11 Kouremenos, "Über die strömung einzelner zylinderförmiger gasblasen in vertikalen kreisrohren," PhD dissertation, Eidgenössischen Technischen Hochschule, Zürich, 1967.

12 Anderson, G. H., Haselden, G. G., and Mantzourznis, B. G. "Two Phase (Gas-Liquid) Flow Phenomena—IV," *Chemical Engineering Science*, Vol. 17, 1962, p. 751.

13 Rohsenow, W. M., Private communication, Jan., 1970.

APPENDIX

Tables A-1 to A-3 contain both experimental and calculated data for thirteen vapor bubbles that were analyzed. Since experimental measurements were taken with British Engineering Units, these have been retained in the Appendix and are shown in parentheses in Table A-1.

K. A. Joudi
Research Student.

D. D. James
Lecturer.

Department of Mechanical Engineering,
UMIST, Manchester, U.K.

Incipient Boiling Characteristics at Atmospheric and Subatmospheric Pressures

Experimental data are reported for incipient boiling of water, refrigerant R-113, and methanol from a flat horizontal stainless steel surface of known surface roughness. The work was carried out over a pressure range of 1, 0.5, and 0.25 atm. Overshoot temperatures at incipience for R-113 and methanol were systematically investigated and found to exist for all pressures employed. The overshoot in temperature at incipience did not occur for water within the experimental range covered. Surface temperature fluctuations were found to increase in amplitude with decreasing pressure, reaching a maximum at incipience. In general, these temperature fluctuations became less pronounced as fully developed nucleate boiling became established. An abnormal occurrence of transition from single-phase free convection to film boiling is also reported.

Introduction

An understanding of the factors which influence the onset of boiling is of importance in the design and operation of cooling systems associated with high heat flux units. Transition from single-phase convection to nucleate boiling occurs when the liquid layer adjacent to a heating surface becomes superheated. Corty and Foust [1][1] observed that the immediate past history of the boiling surface had a pronounced effect on the superheat required for incipience. They described and classified the phenomenon for ether, normal pentane and refrigerant R-113 and reported superheats far in excess of those normally required to initiate boiling. The phenomenon of large temperature overshoots preceding the initiation of boiling bubbles was termed "hysteresis" and similar trends have been reported by various investigators. Turton [2] reported large temperature overshoots—as high as 100 and 120°F—for refrigerant R-11 boiling from a stainless steel tube at pressures above atmospheric and under the influence of increased gravity. An excess value for incipient superheat of between 25–30°F was found by Abdelmessih, et al. [3] for refrigerant R-11 boiling in a stainless steel tube under forced flow conditions. The superheat was found to be independent of the fluid velocity in the range tested. Marto and Rohsenow [4] reported temperatures as high as 135°F for the onset of nucleate boiling for liquid sodium in pool boiling and found that the value of temperature overshoot depended on the surface finish. Similar overshoots in temperature have been reported by Chen [5] for flow boiling of liquid potassium. Small temperature differences of a few degrees obtained with increasing and decreasing heat flux near the incipience value have been reported by numerous authors for various liquids and conditions and these temperature differences have been attributed to hysteresis effects.

Analytical predictions of incipient superheat, critical bubble radius, and heat flux have been comprehensively reviewed by Cole [6] for both the heterogeneous case and nucleation from heated surfaces.

From graphical calculations Bergles and Rohsenow [7] proposed the following equation:

$$(q/A)_i = 15.6p^{1.156}(T_w - T_s)^{2.3/p^{0.0234}} \quad (1)$$

which relates incipient heat flux to saturation temperature difference and system pressure. This equation was in good agreement with their data for forced convection boiling of water in stainless steel and nickel tubes. Davis and Anderson [8] derived an expression relating incipient heat flux and superheat which reduced to the following:

$$(q/A)_i = \frac{K_\ell \lambda \rho_v}{8(1 + \cos\theta)\sigma T_s}(T_w - T_s)^2 \quad (2)$$

for systems of low surface tension or higher pressures. This expression reduces to that derived by Sato and Matsumura [9] and by Rohsenow [10] for a hemispherical bubble nucleus.

The foregoing studies were conducted at atmospheric pressure and above. The present experimental investigation provides information on the behavior of liquids during incipient boiling at atmospheric and subatmospheric pressures.

Description of the Equipment

The experimental apparatus and instrumentation are shown

[1] Numbers in brackets designate References at end of paper.

Contributed by the Heat Transfer Division for publication in the JOURNAL OF HEAT TRANSFER. Manuscript received by the Heat Transfer Division February 10, 1977.

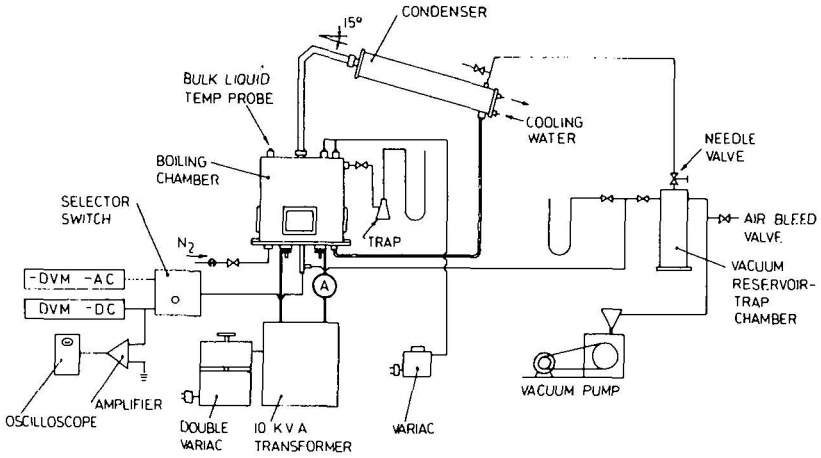

Fig. 1 Schematic diagram of experimental apparatus

schematically in Fig. 1. Test liquids were boiled from an electrically heated horizontal rectangular stainless steel plate elevated 31 mm from the base of the pool. The test surface assembly was housed in a cubical stainless steel chamber with clear inside dimensions of 210 mm on all sides. Plate glass windows were incorporated on four sides for observation purposes. An auxiliary heater made of resistance wire in a silica glass tube and regulated by a variac surrounded the test surface assembly. This was used to bring the test liquid to boiling and maintain it at saturation temperature during low heat flux operation. Hot vapors passed to a stainless steel condenser through a 25-mm stainless steel tube. The condenser contained three independent, elongated "U" shaped cooling passages made of 25-mm stainless steel tubes housed in a rectangular stainless steel shell. The unit was mounted at 15 deg to the horizontal to facilitate flow of condensate which was returned to the boiling chamber, through the base plate, by glass tubing.

The test surface was fitted with a 6-mm thick "pure natural" rubber backing piece which provided thermal insulation as well as sealing. These items were then placed onto an Araldite block which fitted over two gold plated brass electrodes (Fig. 2). Thermocouples spot welded to the back of the test surface passed through the rubber backing and out through a 6-mm stainless steel tube. The wires were sealed after passing through a glass "T" piece, the vertical leg of which was connected to a vacuum pump, which thus pulled down the test surface onto the rubber and the Araldite block.

Low pressure operation was achieved by evacuating the system from the cold end of the condenser which reduced loss of vapor to a negligible level. Pressure inside the chamber was regulated by a throttling needle valve connected to a vacuum reservoir-trap chamber. A pressure difference was continually maintained between the system and the underside of the sample, so that positive pressure always existed on top of the boiling surface.

The Heating Surface

The test surface was made of type EN58E stainless steel measuring nominally 100 × 50 × 1.6 mm. To each end was brazed a copper terminal provided with two holes by means of which it was fastened to the gold-plated brass electrode. The copper terminals were highly

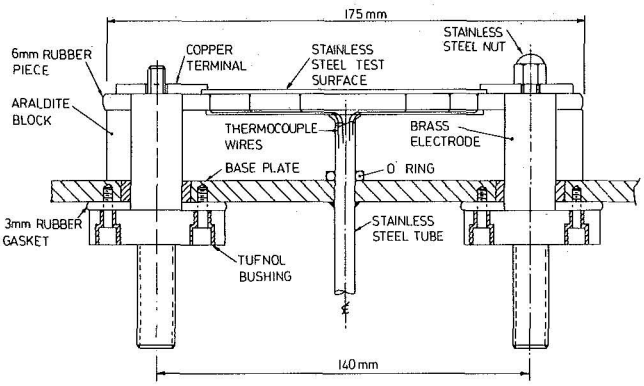

Fig. 2 Schematic diagram of test surface assembly

polished and then gold plated to eliminate tarnishing and oxidation. Extreme care was taken to ensure that the test surface remained free from localized corrosion due to water, and contamination due to methanol, by nitrogen sparging of the liquids before and during the tests. Inside the boiling chamber, double deionized "Analar" water and distilled pure methanol were bubbled with a nitrogen column positioned remotely from the test surface so as not to interfere with the boiling process. This procedure was not required for refrigerant R-113 with which no contamination occurred.

The stainless steel surface was finished with vaqua blasting, which consists of the impingement on the surface at high pressure of an alumina particle suspension in water. This technique yielded a consistent and reproducible surface micro-roughness of 0.94 μm C.L.A. (37 μ in.) in all directions and rendered a homogeneous surface texture for the whole surface. An examination of electron micrographs of the surface taken at 5 K magnification over several locations revealed the existence of a variety of cavity shapes and sizes and included numerous irregular shaped re-entrant cavities. The long free edges of

Nomenclature

K = thermal conductivity
p = pressure
q/A = heat flux
T = temperature
θ = bubble contact angle
λ = heat of vaporization
ρ = density
σ = surface tension

Subscripts

i = incipient boiling condition
ℓ = liquid condition
s = saturation condition
v = vapor condition
w = heated surface condition

the sample were polished to a near mirror finish to eliminate nucleation from these areas.

Instrumentation and Measurement

Heating of the test surface was accomplished by the passage of a heavy current at low voltage from a 10 kVA transformer regulated by a double variac. Current was measured by an ammeter through a current transformer, and voltage was measured directly across the heating section using two thermocouple wires welded at the extreme edges of the stainless steel surface i.e., at the dimensionless distances of ±0.5 on each side of the specimen center line. The exact distance between these voltage tappings was determined with a vernier microscope and this dimension was used in the calculations. The potential drop across the surface was observed on a digital voltmeter. Conduction losses to the copper terminals were calculated using a one-dimensional model with internal heat generation, assuming that the copper temperature at the stainless steel interface, was equal to the liquid saturation temperature. Using the bulk liquid saturation temperature as a basis for calculation provides the condition for maximum possible end losses.

The surface temperature was determined from the average indication of 10 Chromel-Alumel thermocouples attached to the base of the test specimen. The thermocouples were situated so as to provide a temperature distribution across the length and width of the sample, as indicated in Fig. 3(*a*). All were connected to a selector switch and the emf generated was displayed on a digital voltmeter. The boiling surface temperature was calculated from the average measured base temperature using the one-dimensional heat conduction equation with internal heat generation. This average value was used as one boundary condition in the solution of this equation together with the assumption of zero temperature gradient at the base of the specimen. Typical temperature distributions are presented in Fig. 3(*b*). At low heat inputs and during incipience, temperatures in the immediate vicinity of the edges were in general lower than those existing over the mid 80–85 percent region. Under these conditions, the average temperature over this region only was used in the calculations.

Bulk liquid temperature was obtained from a thermocouple situated in a glass tube immersed in the liquid and passing through the top plate of the boiling chamber. System saturation pressure was measured by a pressure tapping on the side of the chamber connected to a mercury-in-glass manometer and system pressure variation was controlled to within ±3 mm Hg.

Temperature history traces were recorded by an oscilloscope together with a Polaroid camera. A single thermocouple situated at the center of the test specimen was used for this purpose. The emf generated by this thermocouple was also observed by means of a digital voltmeter. The thermocouple signal was filtered and amplified before being introduced into the oscilloscope. It was found necessary to employ separate filters at the input to the amplifier and the oscilloscope because of the large 50 cps a-c picked up by the thermocouple.

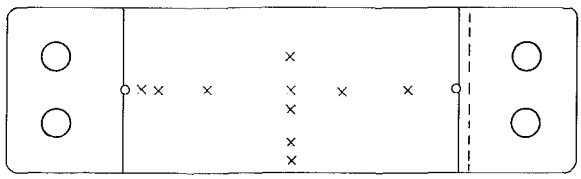

Fig. 3(*a*) Thermocouple distribution over the heating surface—× temperature thermocouple; 0 voltage tapping

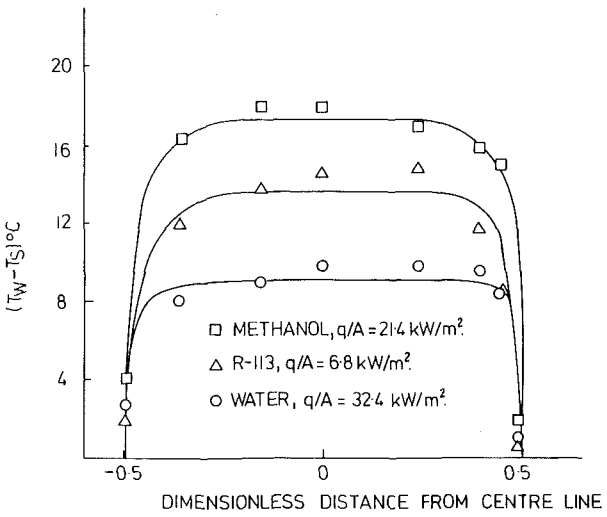

Fig. 3(*b*) Temperature distribution over the heating surface

Experimental Procedure

The test liquid was brought to boiling temperature by the auxiliary heater at the desired operating pressure, and was boiled until the whole system was in equilibrium. The heater was then turned down and current was passed through the test specimen. Power was raised gradually and at each level of heat input, equilibrium was established before readings were recorded. During incipience, temperatures were never constant at any one location nor indeed the same across the surface. Such variations at incipience are not generally reported in the literature. This may be due to the fact that in most investigations, particularly involving flat surfaces, the surface temperature is deduced from extrapolating the temperatures indicated by thermocouples situated in a vertical axis within a copper heating cylinder, the top surface of which comprises the boiling test surface. This represents a single indirect damped measurement whereas in the present work, although some damping inevitably occurs due to the thermal capacity of the test specimen, surface temperature was obtained by a more direct means utilizing several thermocouples at various locations. Equilibrium at incipience was considered to be established, for the worst case, when each thermocouple slowly fluctuated within ±0.5°C and the variation across the central 80 percent of the plate was no more than 3°C. Current and voltage readings were then recorded, as were the surface and bulk liquid temperatures together with the system pressure.

After the first appearance of bubbles (incipience), power was turned off and the plate allowed to cool to the liquid saturation temperature. The power input was then reset to a level higher than that previously attained and the surface temperature was observed to rise rapidly to a maximum value before dropping sharply as bubbles erupted over the surface. The values of temperature immediately before and after the eruption were recorded, together with other relevant measurements. This process was repeated at successively higher power levels.

Discussion of Results

In this work the overshoot of temperatures associated with incipient boiling have been measured for a range of fluids which include water, R-113, and methanol. Also, boiling surface temperature fluctuations have been observed during incipience for the experimental range which covered the following pressures: atmospheric, 0.5 atm, and 0.25 atm.

It was found that the overshoot phenomenon occurred only for R-113 and methanol for all pressures investigated, and significant temperature excesses were required to initiate boiling. Incipience occurred in the form of a cloud of bubbles appearing at an arbitrary point on the heating surface and spreading quickly to cover the whole of the heating surface area. The "explosion" of bubbles quenched the surface and was immediately followed by stable and separate bubble columns.

Fig. 4(*a*) shows a typical eruption of R-113 at atmospheric pressure

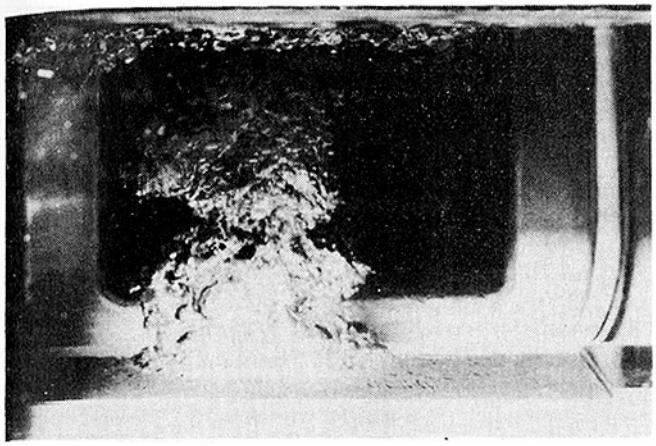

Fig. 4(*a*) Advance of incipient boiling eruption—q/A = 15 kW/m^2

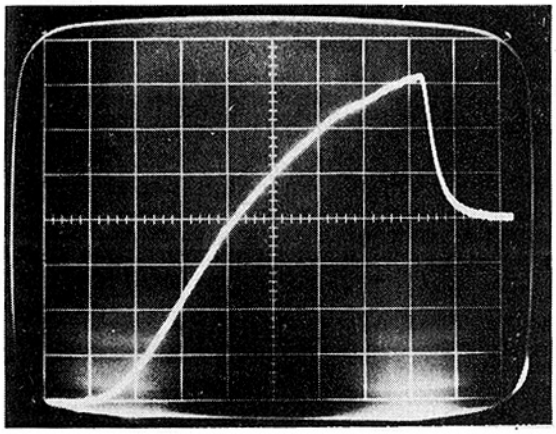

Fig. 4(*b*) Temperature history of boiling eruption, vertical scale 2.5°C/major division, horizontal scale 2 s/major division

Fig. 4 A typical boiling eruption at incipience for R-113 at atmospheric pressure

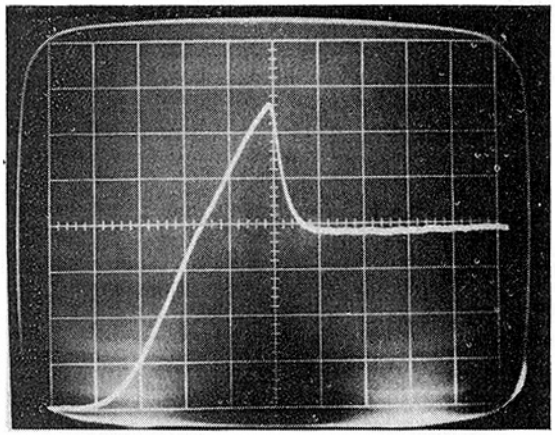

Fig. 5(*a*) Normal boiling eruption: $(T_w - T_s)_{peak}$ = 21°C, q/A = 30 kW/m^2; vertical scale 3.5°C/major division, horizontal scale 2 s/major division

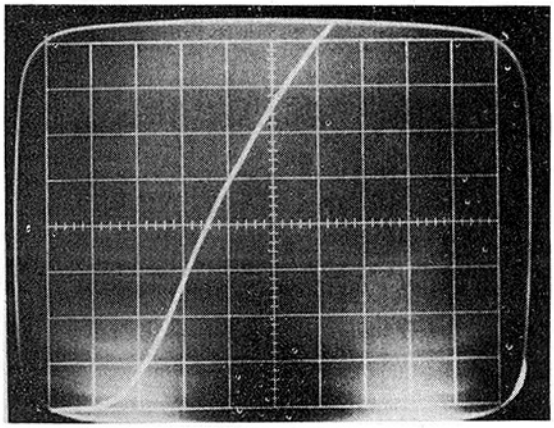

Fig. 5(*b*) Transition from free convection to film boiling: $(T_w - T_s)_{peak}$ = 53°C, q/A = 30 kW/m^2; vertical scale 3.5°C/major division, horizontal scale 2 s/major division

occurring on an otherwise freely convecting surface. Fig. 4(*b*) is the corresponding temperature history of this event. As the power was increased, the surface temperature was observed to rise from that of liquid saturation, to an overshoot value before finally relaxing to a steady boiling temperature as the surface was quenched with the advance of the boiling eruption. The surface temperature prevailing under steady boiling conditions is seen to be significantly less than that required for the onset of incipience. The rate at which the surface temperature dropped to a steady value in established nucleate boiling is indicated by the sudden drop in temperature.

Fig. 5(*a*) shows a normal temperature history for an eruption at 0.5 atm for R-113. Figs. 5(*b*) and 5(*c*), however, show an interesting abnormal event of transition from single phase free convection to transition-film boiling, which was found to occur at 0.5 atm and for R-113 only. This was occasionally observed after the surface had been submerged in the working fluid at saturation temperature for periods of 10–20 min in-between tests. The power input in Figs. 5(*a*) and 5(*b*) are the same (approximately 30 kW/m^2) but that of Fig. 5(*c*) is higher (approximately 40 kW/m^2). When the power input to the heat transfer surface was increased to a level which would normally have produced a temperature difference sufficient to cause boiling, on these particular occasions the surface temperature continued to rise and peak temperature differences of 53 and 33°C were recorded from the digital voltmeter indication. When the eruption occurred, film boiling ac-

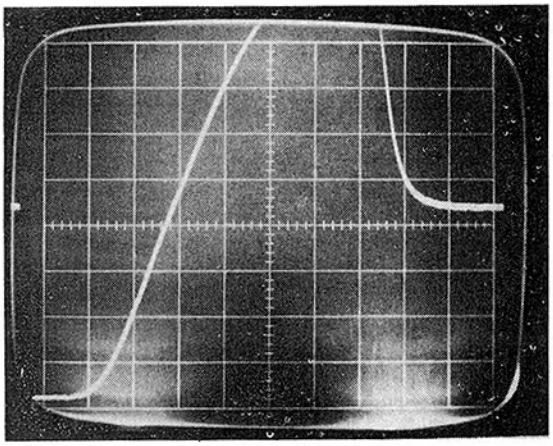

Fig. 5(*c*) Transition from free convection to film boiling: $(T_w - T_s)_{peak}$ = 33°C, q/A = 40 kW/m^2; vertical scale 3.5°C/major division horizontal scale 2 s/major division

Fig. 5 Normal incipience and transition from free convection to film boiling for R-113 at 0.5 atm

tually covered a portion of the surface momentarily. The film then diminished in size as the temperature relaxed to the normal boiling temperature and nucleate boiling prevailed. The duration of film boiling in the localized area was 2–5 s depending on the maximum temperature attained before the eruption. It would appear, therefore, that the nucleate boiling regime is by-passed and the mode of heat transfer is changed from free convection directly into transition-film boiling over a localized area due to the high temperature difference. However, since the heat flux is not high enough to sustain this mode of boiling, the surface temperature drops and steady nucleate boiling becomes established. Hall [11] recently reviewed experiments with subcooled water in which attempts to show a sudden transition from liquid conduction to film boiling failed for a wide range of pressures. The transition observed here is not in contradication, since R-113 possesses entirely different properties from water and it occurred at 0.5 atm only. Turton [2] also observed very high overshoot temperatures of 100 and 121°F with R-11 although this work was carried out at pressures higher than atmospheric and under increased gravity.

The observations for methanol, boiling at atmospheric pressure, 0.5 atm, and 0.25 atm are similar to those of Fig. 4. It was observed that the position on the surface at which the incipient eruption commenced was arbitrary, and although in some cases bubbles formed on the thin vertical edge they in no way influenced the phenomenon observed here. The eruptions start spontaneously from random locations on the surface and it is not possible to determine whether they are preceded by the appearance of the isolated bubbles normally associated with incipience.

Data for heat flux versus incipient temperature difference are presented in Fig. 6 for R-113 and Fig. 7 for methanol, together with the predictions of equation (2). The predictions underestimate the value of incipient boiling wall superheat, and are in keeping with the expectations of Rohsenow [10] for low velocity forced convection and pool boiling. It will be observed that the overshoot temperatures for each liquid at all pressures investigated may be represented by a single curve which gives the temperature difference required to initiate boiling at each heat flux. Overshoot temperature differences (defined as the difference between the overshoot and the normal incipience temperature values) are observed to decrease with decreasing pressure. The heat flux required to initiate boiling for methanol is nearly 2.5 times that required for R-113 and the overshoot temperatures for the same pressure in methanol are nearly 1.25 times those in R-113.

The phenomenon of temperature overshoot at incipience was not encountered with water for the range of pressures investigated. As the power input was raised the free convection regime changed and a few isolated bubbles appeared, becoming more numerous with further increase in power. However, it was observed that as the system pressure was reduced, the incipient water bubbles became intermittent in generation, unpredictable in location and duration, deformed in shape, and greatly enlarged. The number of incipient bubbles at any one heat flux was greatly reduced with decreasing pressure. These changes in bubble behavior caused surface temperature fluctuations that increased in amplitude as the pressure decreased. At 0.5 atm these fluctuations subsided as the heat flux increased and fully developed boiling with numerous bubbles became established. A similar trend in surface temperature fluctuation was reported by Turton [2] for water boiling on the outside surface of a stainless steel tube at pressures higher than atmospheric and also under the influence of increased gravity. In the current investigation it was found that the temperature fluctuations were so severe at 0.25 atm, even during fully developed nucleate boiling, that the recording of meaningful data on surface temperature after incipience was impossible. In addition, it was observed that a pattern of repeated temperature build-up followed by an extremely sharp and fast temperature drop, was associated with the relatively prolonged absence followed by the sudden appearance of large incipient bubbles. The bubbles quench the surface by removing the superheated layer which is built up during their absence and cause temperature drops of 6–10°C in a manner similar to the boiling eruptions.

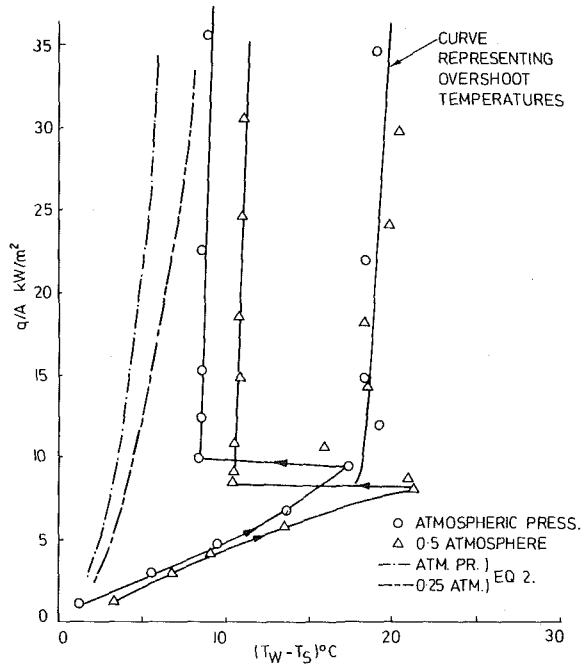

Fig. 6 Incipient boiling and temperature overshoots for R-113

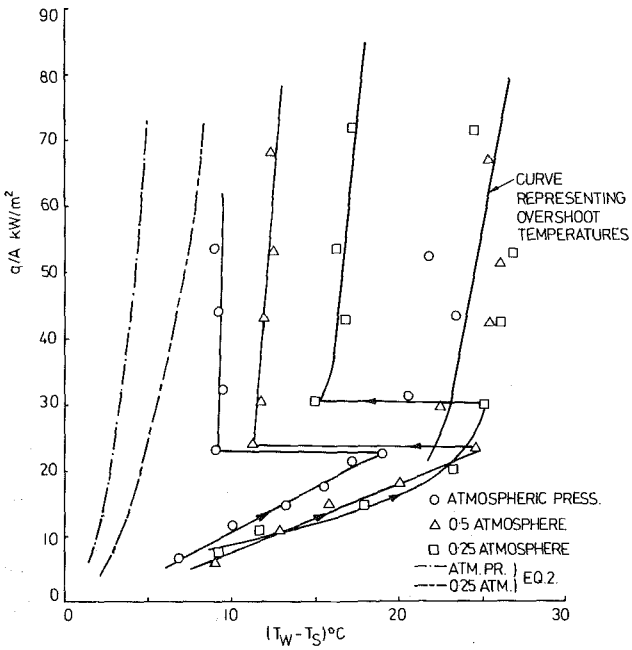

Fig. 7 Incipient boiling and temperature overshoots for methanol

Temperature fluctuations for the three liquids over the range of pressures were very slow and small in the single-phase free convection regime and only slightly increased in amplitude with increasing heat flux and decreasing pressure. Maximum amplitude of fluctuation in any one thermocouple was at the point where bubbles were just about to appear. The worst case of ±1.5°C occurred at a pressure of 0.25 atm with water. Incipience data for water at the pressures investigated are presented in Fig. 8, and are compared with the predictions of equations (1) and (2). Both equations underestimate the wall superheat

required to initiate boiling. Bergles and Rohsenow [7] attribute this trend to the absence of very large cavities which would be activated first at the lower values of superheat. However, with the surface employed in these experiments (C.L.A. = 0.94 μm) such cavities with good vapor trapping characteristics had been found to be numerous. Increasing temperature variations with decreasing pressure for the free convection regime are also indicated. At 0.25 atm, the two bounding lines represent the maximum and minimum temperatures observed.

Conclusions

1 Overshoot temperature differences far in excess of normal boiling temperature differences were required to initiate boiling of refrigerant R-113 and methanol. These overshoot temperature differences tended to decrease with decreasing pressure. Large superheats for incipience appear to be characteristic of organic liquids of low surface tension and relatively low thermal conductivity compared with water.

2 Using refrigerant R-113 at 0.5 atm and under certain conditions a transition from natural convection directly into film boiling appears possible.

3 An appreciable reduction in the number of bubbles occurs at reduced pressure. The higher temperature differences associated with nucleate boiling at reduced pressure may be attributable to this reduced bubble population. This is in agreement with the observations of others of lower temperature differences with increasing pressure.

4 Severe surface temperature fluctuations were found to occur, in particular at subatmospheric pressures at which bubble population was significantly reduced.

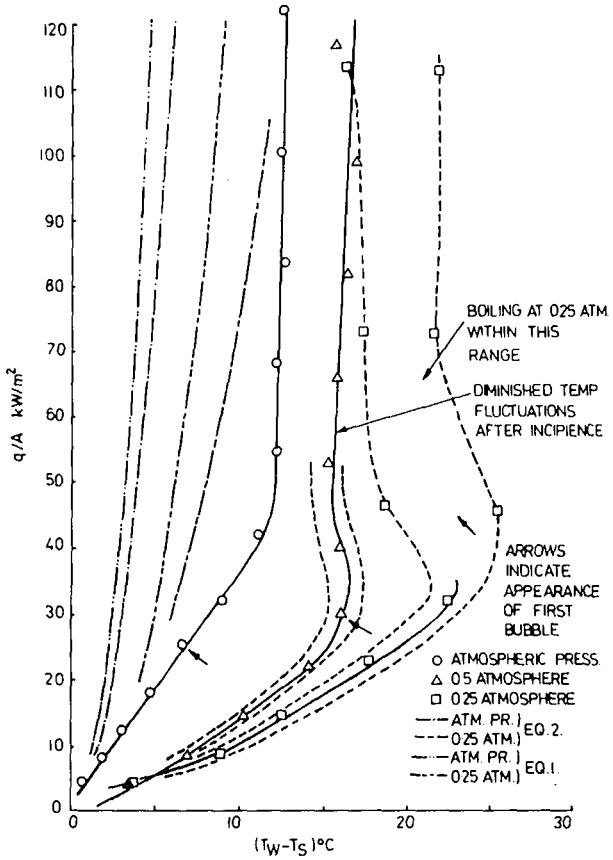

Fig. 8 Free convection and incipience of water

Acknowledgments

Acknowledgment is made to the Science Research Council, who supported this work. One of the authors K. A. Joudi is grateful to the University of Basrah for the award of a Gulbenkian Foundation Scholarship.

References

1. Corty, C., and Foust, A. S., "Surface Variables in Nucleate Boiling," *Chem. Eng. Prog. Symp. Ser.*, Vol. 51, No. 16, 1955, pp. 1–12.

2 Turton, J. S., "The Effects of Pressure and Acceleration on the Pool Boiling of Water and Arcton 11," *Int. J. of Heat and Mass Transfer*, Vol. 11, 1968, pp. 1295.

3 Abdelmessih, A. H., Fakhri, A., and Yin, S. T., "Hysteresis Effects in Incipient Boiling Superheat of Freon 11," 5th International Heat Transfer Conference JSME, Vol. Iv, 1974, p. 165.

4 Marto, P. J., Rohsenow, W. M., "Effects of Surface Conditions on Nucleate Pool Boiling of Sodium," JOURNAL OF HEAT TRANSFER, TRANS. ASME, Series C, Vol. 88, 1966, p. 196.

5 Chen, J. C., "Incipient Boiling Superheats in Liquid Metals," JOURNAL OF HEAT TRANSFER, TRANS. ASME, Series C, Vol. 90, 1968, p. 303.

6 Cole, R., "Boiling Nucleation," *Advances in Heat Transfer*, J. P. Hartnett and T. F. Irvine Jr., eds., Vol. 10, Academic Press, 1974.

7 Bergles, A. E., and Rohsenow, W. M., "The Determination of Forced-Convection Surface-Boiling Heat Transfer," JOURNAL OF HEAT TRANSFER, TRANS. ASME, Series C, Vol. 86, 1964, p. 365.

8 Davis, E. J., and Anderson, G. H., "The Incipience of Nucleate Boiling in Forced Convection Flow," *AIChE Journal*, Vol. 12, No. 4, 1966, p. 774.

9 Sato, T., and Matsumura, H., "On the Conditions of Incipient Subcooled-Boiling With Forced Convection," *Bulletin of JSME*, Vol. 7, No. 29, 1964, p. 392.

10 Rohsenow, W. M., "Nucleation With Boiling Heat Transfer," Fluids Engineering, Heat Transfer, Lubrication Conference, Detroit, Mich., ASME Paper No. 70-HT-18, 1970.

11 Hall, W. B., "Heat Transfer Problems in Nuclear Reactor Safety," *Proceedings of the Institute of Mechanical Engineers.*, Vol. 190, 1976, p. 215.

Y. Mori
Professor.

K. Hijikata
Assoc. Researcher.

I. Kuriyama
Graduate Student.

Department of Physical Engineering,
Tokyo Institute of Technology,
Meguro, Tokyo, Japan

Experimental Study of Bubble Motion in Mercury With and Without a Magnetic Field

The behavior and hydrodynamical performance of a single bubble rising through mercury with and without magnetic field has been studied experimentally. A new method to measure the rise velocity and the shape of bubble with an electrical triple probe is proposed. When there is no magnetic field, a bubble changes its shape from spherical to elliptic and then to a spherical cap shape, as its equivalent radius R_m changes from 0.1 to 3 mm. The experimental results are found to agree well with the theories reported so far. In the case of a magnetic field, it is found that the effect of intensity of magnetic field B on the rise velocity depends largely on the radius of a bubble. When R_m = 3 mm, the rise velocity decreases monotonically with the increase of B. However, when R_m = 1 mm, the rise velocity increases once but it then starts to decrease afterwards with the increase of B.

Introduction

The most promising method to reject heat from the nuclear fusion reactor at present is to use liquid lithium in the blanket of the reactor in consideration of producing tritium. However, this method has such disadvantages as the large flow resistance due to the strong magnetic field and the deterioration of heat transfer coefficient. To reduce these defects, we propose a new heat rejecting method using a two-phase flow. In this configuration, a cooling pipe cooled by helium flow is installed to extract heat from lithium. Adding to that, helium bubbles are properly injected into liquid lithium to avoid local overheating of lithium and blanket walls. Tritium produced in liquid lithium is taken away by helium bubbles. By this method, it becomes possible to reject an adequate heat from the blanket of the nuclear fusion reactor.

In the multipurposed high temperature helium gas cooled reactor, the energy is used not only for electric power generation but also for steel-making, various chemical industries, and coal gasification. Therefore, it is required that heat exchangers between the primary and secondary loops be used in the high temperature region of 900–1000°C and have a high overall heat transfer coefficient. The following can be considered as one of such heat exchangers, where helium of the primary loop flows in the tube installed in the liquid metal vessel and the gas in the secondary loop rises up as bubbles in the liquid metal which works as an intermediate heat exchange medium. In the research and development of the heat exchangers mentioned previously, it is essential to clarify the heat transfer and hydrodynamical performances of two-phase flows in liquid metals. However, they have scarcely been studied so far. As a primary step to clarify these points, this paper reports experimental results of the behavior and hydrodynamical performance of bubbles in mercury which is used as the liquid metal with and without a magnetic field.

In the case without a magnetic field, many studies have been carried out on the movement of bubbles rising in liquids, especially in water. There is a study by Haberman and Morton [1][1] over a wide Reynolds number region. Haberman and Morton and Peebles and Garber, et al. [2] used several other liquids but not liquid metals. Theoretical solutions have been obtained for several cases: by Rybczynski and Taylor [3] in the small Reynolds number region, by Moore [4] in the large Reynolds number region, and by Davis, et al. [5] for spherical cap bubbles. However, as its performance depends not only on Reynolds number but also on the surface tension, the behavior of the bubble in the liquid metal should be different from that in water and, therefore, the performance should differ. In addition, since liquid metal is not transparent, it is not possible to observe the behavior of bubbles and, therefore, we have seen no experimental studies of the motion of bubble so far except for one paper by Davenport, et al. [6], who studied the behavior of very big bubbles in mercury.

Contributed by the Heat Transfer Division for publication in the JOURNAL OF HEAT TRANSFER. Manuscript received by the Heat Transfer Division October 12, 1976

[1] Numbers in brackets designate References at end of paper.

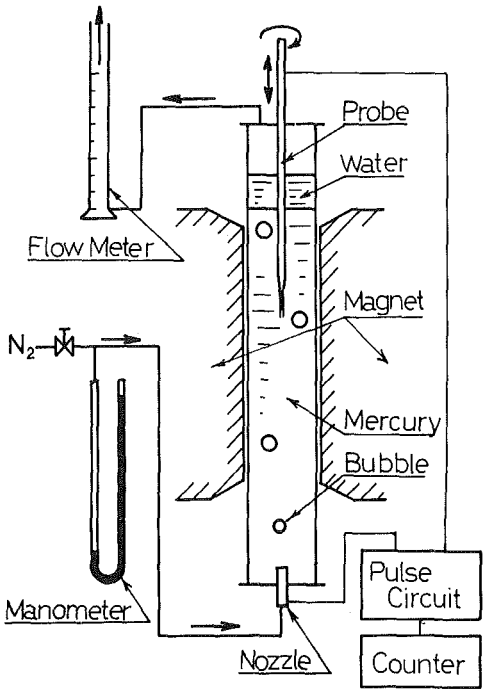

Fig. 1 Experimental apparatus

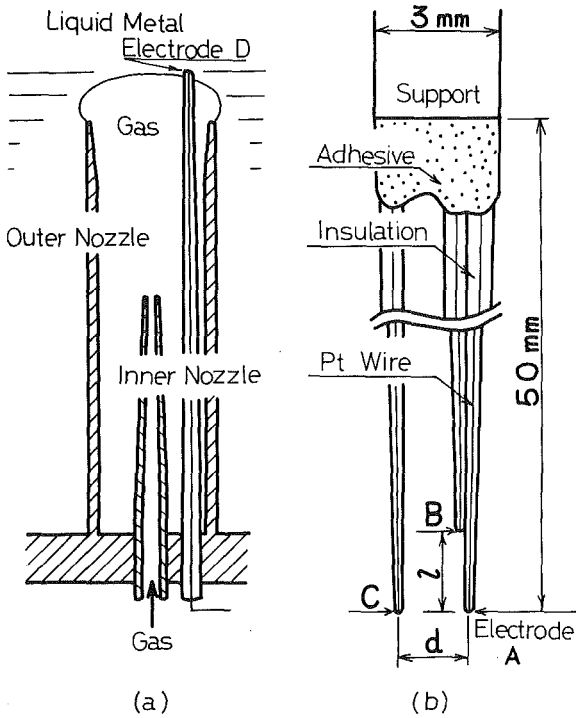

Fig. 2 Schemata of nozzle and probe

On the other hand, few studies on the hydrodynamical behavior of bubbles in an electrically conducting liquid with a magnetic field have been reported. The theoretical studies that have been reported so far in this related field are on the flow field around a nonconducting solid sphere [7] under aligned [8] and transverse [9] magnetic fields in the small Reynolds and Hartman numbers region. Experimental studies of the motion of solid sphere under the transverse magnetic field in the large Reynolds number region by Tsinober, et al., and Kalis, et al., whose results are reviewed by Lielausis [7]. As the bubbles change shape in accordance with the intensity of the magnetic field, their hydrodynamical behavior is considered to be different and more complex than that of solid spheres.

From these points of view, the primary purposes of this paper are to assure a method of accurately measuring bubble shapes and their rise velocities in mercury with an electrical triple probe. The second is to obtain the hydrodynamical relations among the drag coefficient, the shapes of bubble, Weber number and Reynolds number without a magnetic field by using this method and to compare our experimental results with the theoretical results reported so far. As the third step, the results obtained by measuring the behavior of a single bubble in a transverse magnetic field are discussed.

Experimental Apparatus

The diagram of the experimental apparatus used to measure the behavior of bubbles in mercury is shown in Fig. 1. A glass mercury-container, 500-mm high with a 75-mm ID, is installed at the center of a uniform magnetic field that has a height of 300 mm, a width of 85 mm, and a depth of 100 mm. The bubbles in the mercury travel across this magnetic field, whose intensity can be set on several discrete values between 0 and 1.5 T. About 250–300 mm of the container was filled with mercury. The bubbles were blown into the mercury from the bubble blowing nozzle installed at the bottom of the container and the bubbles rose up through the mercury. In the present experiment, the bubbles were of nitrogen. The electrical triple probe installed at the upper part of the mercury container was traversed up and down in mercury. In the present study, the shapes and rise velocity of the bubbles were obtained by a statistical calculation of the signals obtained from the electrical triple probe under the assumption of the uniformity of the bubble equivalent diameter. For this purpose, a nozzle that generates bubbles of uniform diameter was developed. This nozzle, shown in Fig. 2 (*a*), consists of two coaxial nozzles. The diameter of a bubble was determined by the outer nozzle diameter and the number of bubbles generated per unit time was determined by the inner nozzle diameter. The diameter of the outer nozzle used was 0.2–6 mm and that of the inner nozzle 10 μm. The generation rate of bubbles was determined by fixing the interval between the succeeding bubbles so as not to affect each other [11]. The rate of bubble

Nomenclature

a = radius of bubble in x-direction
B = intensity of magnetic field
b = radius of bubble in y-direction
C_D = drag coefficient = $8gR_m/3U^2$
d = distance between electrodes A and C
g = acceleration of gravity
H = height of bubble
J = ratio of intersecting probabilities
K = nondimensional parameter related to a, b, d, and θ
L = distance between nozzle and probe
ℓ = distance between electrodes A and B
M = nondimensional physical property = $g\eta^4/\rho\sigma^3$
N = interaction parameter = $2\gamma B^2R_m/\rho U$
Re = Reynolds number = $2UR_m\rho/\eta$
R_m = equivalent radius of bubble
Δt = delay time
U = rise velocity of bubble
V = volume of bubble
We = Weber number = $2\rho U^2R_m/\sigma$
x = distance along magnetic field
y = distance normal to x and z axes
z = vertical distance
α = angle of rise
γ = electrical conductivity
ρ = density
η = viscosity
σ = surface tension
θ = angle between x axis and line connecting electrodes A and C
χ_x = aspect ratio = $2a/H$
χ_y = aspect ratio = $2b/H$

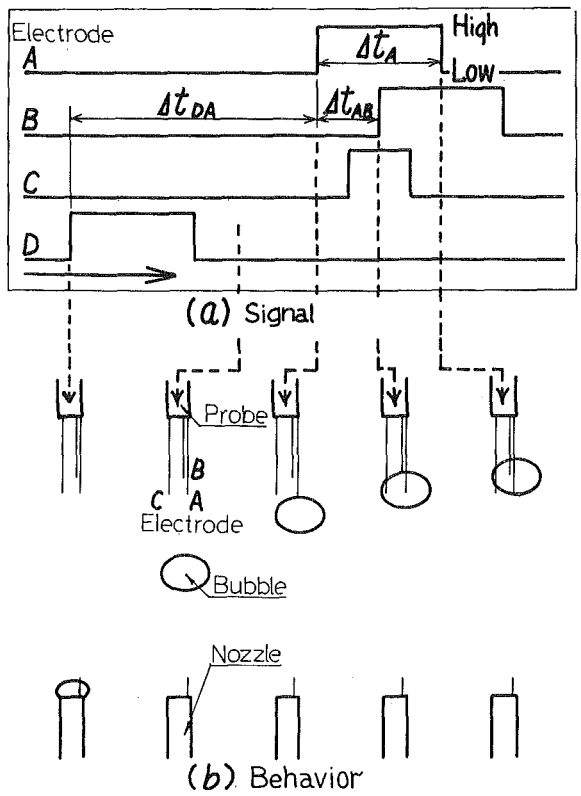

Fig. 3 Behavior of bubble and signals from electrodes

generation was measured by the platinum wire electrode placed between the inner nozzle and the outer nozzle.

The outline of the electrical triple probe used in the experiment is shown in Fig. 2 (*b*). The probe consists of two electrodes A and B, which are placed in the same direction as that of the bubbles movement, and the electrode C placed parallel to the electrode A. The angle θ between the direction of the magnetic field and a line connecting the electrodes A and C in a horizontal plane can be varied arbitrarily by rotating the probe around its axis. The electrode of platinum wire is coated with glass but the end point is exposed. In the present study, probes of various sizes were prepared according to the bubble diameters; the distance d between the electrodes A and C was 1–5 mm, the distance ℓ between the electrodes A and B was 1–2 mm, the diameter of the platinum wire for the electrode was 0.03 mm, and the outer diameter of the coating glass of the electrode was less than 0.1 mm. The bubble shape and its rise velocity were obtained from the output signals from the three electrodes A, B, C, and the electrode D set in the bubble generating nozzle.

Principle of Measurement

The shape and rise velocity of the bubble in mercury could not be measured from visual observations since mercury is opaque. However, if the position of the probe relative to the bubble center when the bubble comes up to the horizontal plane including the electrodes A and C is assumed to be statistically random and if the shape and rise velocity of the bubble is assumed to be same for all the bubbles in an experiment, the bubble shape and rise velocity can be obtained by treating the three signals statistically. Although the details of the method of measurement have already been reported [10] for bubbles having axisymmetric shapes, there is a need for developing a new and different method of measurement for the cases with a transverse magnetic field since bubbles are considered to be deformed from the axisymmetric shape.

The output signals from the electrodes A, B, and C of the triple probe and the electrode D installed in the nozzle are assumed as in Fig. 3 (*a*) corresponding to the relative positions of the probe and the bubble as shown in Fig. 3 (*b*). The electric circuit for the electrodes is so designed as for the output signal to be of a low level when the electrode is in mercury, and to be of a high level when in the bubble.

Bubble Rise Velocity U and Angle of Rise α. Except the region of several centimeters above the nozzle, the rise velocity is considered to be constant and terminal. By traversing the triple probe in the vertical direction as to change the distance L between the electrodes A and D, the region where the bubble has its terminal velocity is obtained. The terminal rise velocity of the bubble U may be given as follows,

$$U(L) = dL/d\Delta t_{DA} \tag{1}$$

where Δt_{DA} is the time needed for the bubble to reach the electrode A from the electrode D. A different velocity U' can also be calculated from the following relation,

$$U' = \ell/\Delta t_{AB} \tag{2}$$

where Δt_{AB} is the time needed for the bubble to reach the electrode B from the electrode A. Due to such effect as that of spiral motion of the bubble, the standard deviation of Δt_{AB} is between 10 and 20 percent. The value of U and U' do not always agree and, generally, U' takes larger value than U. The difference of U and U' is considered to be mainly caused by the fact that the bubble would not always rise vertically in the mercury. Assuming that the bubble rises with the angle α between the vertical axis and its own rising direction and that its velocity is taken as U_r, the component to the vertical direction is $U_r\cos\alpha$ which is equal to the velocity U given by equation (1). On the other hand, the orthographic projection of the length ℓ between the electrodes A and B to the rising direction of the bubble is $\ell\cos\alpha$, and as the time required for the bubble going through this distance is Δt_{AB}, U_r is equal to $\ell\cos\alpha/\Delta t_{AB}$. Consequently, the relation among U_r, U, and U' can be expressed as follows

$$U_r = \ell\cos\alpha/\Delta t_{AB} = U'\cos\alpha,\ U = U_r\cos\alpha \tag{3}$$

Therefore,

$$U/U' = \cos^2\alpha \tag{4}$$

By making use of the measured values of U and U' and of equation (4), the angle of rise α can be calculated.

Shape of Bubbles Observed From Above. The direction of the magnetic field in the horizontal plane is taken along x axis and the directions normal and vertical to it are taken along the y and z axes, respectively. The center of the nozzle is taken as an original point. We now assume that the shape of a bubble can be written in the form of the following elliptic equation when x_0, y_0 and z_0 are the distances from the center of the ellipsoid to the bubble surface.

$$\frac{x_0^2}{a^2} + \frac{y_0^2}{b^2} + \frac{4z_0^2}{H^2} = 1 \tag{5}$$

As the triple probe can rotate around its axis, an angle between the line connecting the electrodes A and C and the x axis in the horizontal plane is indicated by θ.

The ratio J of P_{and}, the probability that the bubble intersects both electrodes to P_{or}, the probability that the bubble intersects at least one of the electrodes, can be obtained as a function of (a/d, b/d, θ). The value of a/d and b/d can be determined uniquely by measuring the values of J for two angles of θ, then a and b can be obtained from the measured value of d. When the center of the bubble is completely taken at random relative to the electrodes A and C, the following equations hold.

$$J = \left\{\frac{\pi}{\sin^{-1}[\sqrt{1-(2K)^{-2}}] - \sqrt{1-(2K)^{-2}}/2K} - 1\right\}^{-1}$$

$$K = \left\{d^2\left(\frac{\cos^2\theta}{a^2} + \frac{\sin^2\theta}{b^2}\right)\right\}^{-1/2}. \tag{6}$$

If $\theta = 0$ and $\pi/2$, then $K_0 = a/d$ and $K_{\pi/2} = b/d$, respectively. Thus, a and b can be separated completely, and, furthermore, they can be

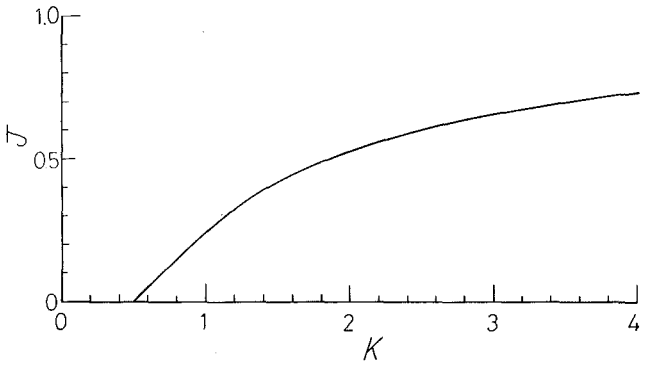

Fig. 4 Relation between J and K

determined from the measurements of J_0 and $J_{\pi/2}$ by using d and equation (6) which is shown in Fig. 4.

Equivalent Radius and Height of Bubble. The equivalent radius of a bubble is defined by the following relation from the measured volume under the assumption that the bubble is spherical.

$$R_m = (3V/4\pi)^{1/3} \tag{7}$$

The volume of the bubble V at atmospheric pressure is obtained from the measured flow rate of gas and the rate of bubble generation measured by the electrode D. The volume at the triple probe is calculated from the correction of the pressure by the mercury head. On the other hand, the bubble height H can be also calculated from the following geometrical relation among R_m, a, b, and H. This relation was obtained from integrating equation (5).

$$H = 2R_m{}^3/ab \tag{8}$$

If the center of bubble is assumed to be completely at random when the bubble intersects the triple probe and also if the bubble is to rise up vertically, the probability that the time needed for the probe to pass through the bubble, $\Gamma(\Delta t_A)$, is less than Δt_A (signal width from electrode A) may be given as follows.

$$\Gamma(\Delta t_A) = (U\Delta t_A/H')^2 \tag{9}$$

The relation between $\Gamma(\Delta t_A)$ and Δt_A is first obtained from experiment and then, by drawing the most suitable quadratic curve correlating these experiment values, the value of the bubble height H' can be obtained from the curve and by use of U and equation (9). In the present experiment H' of equation (9) is only employed here to check H of equation (8).

Experimental Results and Discussions

Preliminary Experiments. Preliminary experiments were to check the validity of the assumption in the preceding chapter and the accuracy of the experimental setup. The intersecting frequency of bubbles to an electrode in a horizontal plane was measured under the condition of no magnetic field. Consequently, its uniformity together with the uniformity of the bubble diameter was ascertained. The rise velocity of the bubble given by equation (1) was made sure to be constant through the whole region excluding the part close to the nozzle. The deviation of Δt_{AB} was observed to be about five times that of Δt_{DA}. This can be explained by the spiral motion of the bubble.

In our experiments, the values of the bubble height obtained from equations (8) and (9) agree within the accuracy of about 30 percent. This is due to the shape and spiral motion of bubbles.

Cases Without a Magnetic Field. In the case without a magnetic field, the hydrodynamical behavior of a gas bubble in liquid metal in the gravitational field can be expressed by the following four nondimensional parameters as the density and viscosity of gas can be generally neglected [12]:

Reynolds number : $\mathrm{Re} = 2UR_m\rho/\eta$

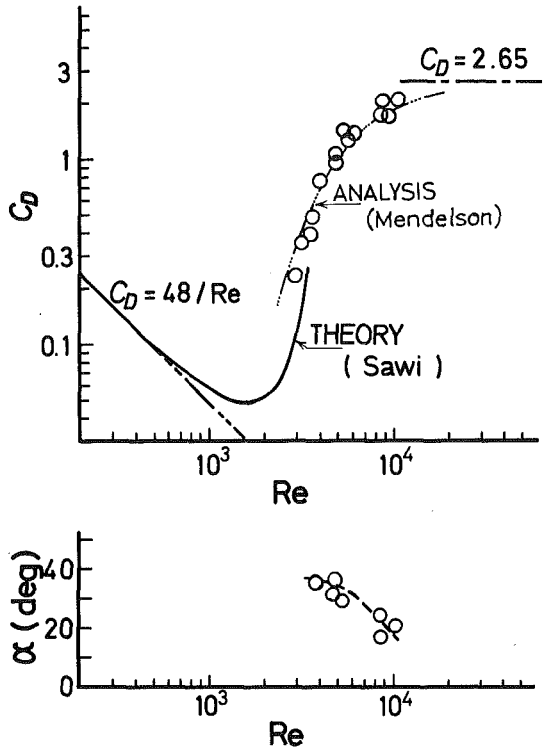

Fig. 5 Relations among C_D, α, and Re

Weber number : $\mathrm{We} = 2U^2R_m\rho/\sigma$

drag coefficient : $C_D = 8gR_m/3U^2$

aspect ratio : $\chi_x = 2a/H$, $\chi_y = 2b/H$ $(\chi = \chi_x = \chi_y)$ (10)

The following nondimensional parameter introduced by Schmidt [13] is often used instead of We:

$$M = g\eta^4/\rho\sigma^3 = 3\mathrm{We}^3C_D/4\mathrm{Re}^4$$

$M = 3.94 \times 10^{-14}$ for mercury is much different from 2.57×10^{-11} for water. According to the theoretical analysis [12] reported so far, the aspect ratio χ is equal to unity ($\chi = 1$) and C_D is a function of Re for $\mathrm{We} \ll 1$, and its functions are $C_D = 16/\mathrm{Re}$ for $\mathrm{Re} \ll 1$, and $C_D = 48/\mathrm{Re}$ for $\mathrm{Re} \gg 1$.

Once we start to increase with the increase of Re, the deformation of the bubble begins. For large Re, the dynamic pressure is predominant and C_D is independent of Re, We having a constant value of 2.65 [5]. In the intermediate Reynolds number region, Moore [4] and Sawi [14] made theoretical analyses in consideration of the deformation of the bubble and reported the following relations.

$$C_D = (48/\mathrm{Re})\cdot G_1(\chi) \tag{12}$$

$$\mathrm{We} = G_2(\chi) \tag{13}$$

whose functions $G_1(\chi)$ and $G_2(\chi)$ are given in their papers.

The realizable size of the stable bubble rising in mercury based on our experimental results is a diameter of about 0.5–5 mm and their Re covers 10^3–10^4. In this Reynolds number region, the hydrodynamical behavior of bubble changes considerably. In the smaller Reynolds number region of near 10^3, $\chi = 1.0$ and $C_D = 48/\mathrm{Re}$. With the increase of Re, the bubble deforms from the spherical shape and begins to rise spirally upward. Then, C_D, which depends only on M, starts to increase with Re. With the further increase of Re, the bubble begins to have a shape of a spherical cap and starts to rise vertically. The results of the present experiments are shown in Fig. 5, where R_m included in Re is calculated from equation (7), U from equation (1), C_D and Re from equation (10) and α from equation (4). In defining

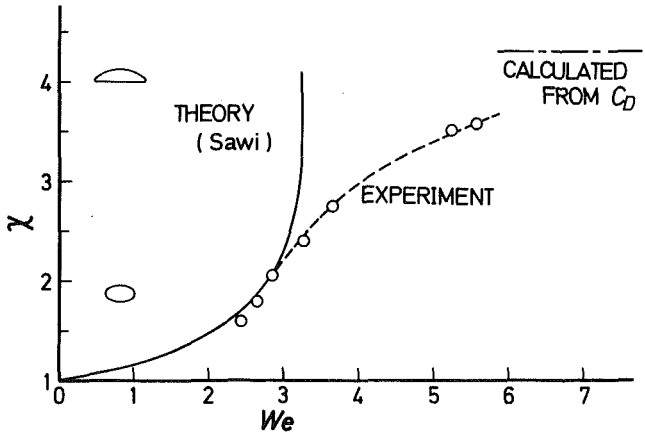

Fig. 6 Relation between χ and We

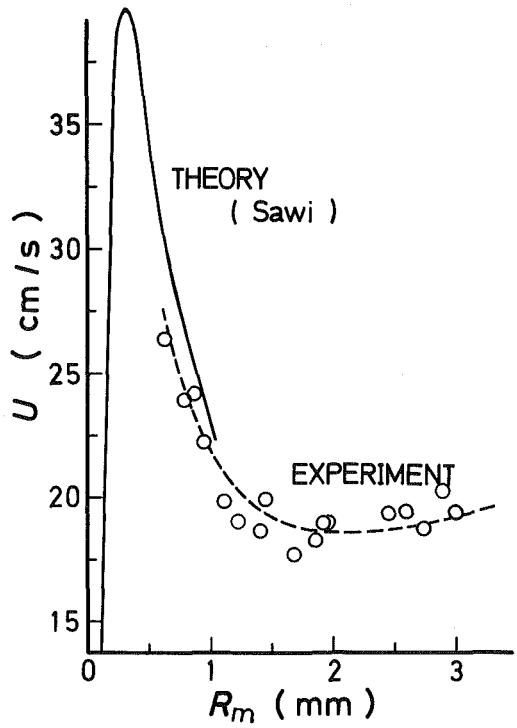

Fig. 7 Relation between U and R_m

C_D, the vertical component of the rise velocity U is used in consideration of a well-accepted usage. As seen from Fig. 5, the realizable region of bubbles in mercury is transitional between the region of the spherical bubble ($C_D = 48/\mathrm{Re}$) and that of the spherical cap bubble ($C_D = 2.65$). In this transitional region, symmetrical and asymmetrical deformations, and the spiral upward motion of the bubble play an important role. The theoretical curve suggested by Sawi [14] in consideration of slight symmetrical deformation is shown in Fig. 5 for $M = 3.7 \times 10^{-14}$, which is little different from that of mercury. This curve is in good agreement with our experimental results for rather small Reynolds number region. With the increase of Re, due to the asymmetrical deformation and intense spiral motion, a deviation appears between them. With the further increase of Re, the experimental result of C_D approaches the constant value of 2.65.

On the other hand, Mendelson [15] considered that the behavior of rising bubble is similar to the behavior of surface waves, and gave the following equation by using Eötvös number $E = 4g\rho R_m{}^2/\sigma$,

$$C_D = \frac{8}{3}\frac{E}{4+E} \tag{14}$$

The relation between Re and C_D is obtained from equation (14) by using equation (10) as follows.

$$\mathrm{Re} = \left\{\frac{M}{6C_D}\left(1-\frac{3}{8}C_D\right)^3\right\}^{-1/4} \tag{15}$$

As shown with a three-dotted chain line in Fig. 5, equation (15) agrees very well with our experimental results. However, as in this Re region the deformation and spiral motion of the bubble gives the essential effect on the hydrodynamical performance, it should not be hastily concluded that equation (15) would be in general applicable to the bubble motion in liquid metal, and a more detailed hydrodynamical study based on a physically acceptable model and applicable to MHD problems may be required.

The relation between We and the aspect ratio χ is shown in Fig. 6, where the solid line indicates the theory by Sawi given in equation (13). The theory is found to be applicable up to about $\chi = 2.0$, after when We tends to be saturated. The experimental results indicate a different tendency in larger χ region.

For more direct and easier understanding, the relation between the rise velocity of bubble U and the equivalent radius R_m is shown in Fig. 7, where circles indicate the experimental results and the solid line expresses the theory by Sawi [14]. U increases proportionally to R_m at the beginning, but, it then starts to decrease once a symmetric deformation begins. With the further increase of R_m, the spiral motion induced by the asymmetric flow separation increases. However, this spiral motion begins to decrease when a further deformation of bubble starts to take place due to the increase of R_m, and U begins to increase again. Then large bubbles come to have a spherical cap shape and the drag coefficient becomes constant. This means that U begins to increase in proportion to $\sqrt{R_m}$.

From this result, it is concluded that the behavior of bubbles in liquid or even in liquid metal such as mercury or lithium, is predicted partly from the theory by Sawi [14] or Moore [4] in the intermediate Reynolds number region and mostly from our experiment.

Cases With a Magnetic Field. As shown in Fig. 7, when bubbles rise in mercury in the gravitational field, the effect of the deformation of bubble and the structure of wake play a very important role. When the deformation of bubble becomes three-dimensional due to the transverse magnetic field applied, the rise velocity U is thought to change in a very complicated way according to the equivalent radius R_m and the intensity of the magnetic field B. The following interaction parameter N is now introduced to write the intensity of the magnetic field B in a nondimensional form.

$$N = 2\gamma B^2 R_m/\rho U \tag{16}$$

χ_x and χ_y change due to the magnetic field applied in x-direction.

For a bubble of $R_m = 2.88$ mm with a shape of spherical cap, the relation between C_D/C_{D_0} and N is shown in Fig. 8, where C_{D_0} is the drag coefficient in the case of $N = 0$. The dots denote the experimental results while the broken line shows the result obtained by Tsinober, et al., and Kalis, et al. [7] for a solid sphere in a transverse magnetic field. For larger bubbles, the general tendency of C_D/C_{D_0} is similar to the case of a solid sphere but tends to take a constant value when N is large. This is due to a stable wake of a spherical cap bubbles. However, the different tendency between a bubble and a sphere is considered to be due to the three-dimensional deformation of bubble.

The rise velocity of a bubble of $R_m = 1.18$ mm, whose spiral motion is remarkable, is shown in Fig. 9 against the intensity of the magnetic field B. Unlike in the case of $R_m = 2.88$ mm, the rise velocity once increases with B (C_D/C_{D_0} decreases), and it then starts to decrease. In the figure U' and U_r, obtained from equations (3) and (4), respectively, are also indicated. The angle of rise α of this size of bubble is large corresponding to the large difference between U' and U when $B = 0$. The angle of rise α decreases monotonously with the increase of the intensity of the magnetic field B. The bubbles rise up vertically when B is about 1.5 T. On the other hand, the ratio of the number of

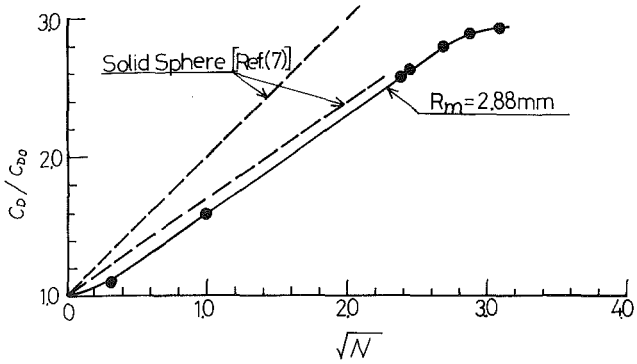

Fig. 8 Relation between C_D/C_{D_0} and $\sqrt{N}$

bubbles that intersects either of the electrodes A and C to the number of bubbles generated from the nozzle increases monotonously with the increase of B. In the neighborhood of B = 1.5 T when the nozzle is set a little below the lower edge of the magnetic pole face, up to about 90 percent of the bubbles generated reach the electrode A, while for B = 0 only 15 percent intersects the electrode. This indicates that bubbles rise vertically with the increase of the intensity of magnetic field. From these results, it is understood that in case of bubbles of R_m = 1.18 mm the spiral motion of bubble is prevented by the magnetic field and the bubble rises vertically. This explains the reason why U increases slightly, thus C_D decreases with the increase of B in the small B region.

Using the intensity of the magnetic field B, as a parameter, the relation between the rise velocity U and the equivalent radius R_m is shown in Fig. 10. The bubbles of R_m = 1.93 mm have a tendency that is intermediate between that of bubbles of R_m = 2.88 mm in Fig. 8 and those of R_m = 1.18 mm in Fig. 9. A similar tendency is seen for bubbles of R_m = 0.87 mm and R_m = 1.18 mm.

Conclusion

A method of accurately measuring the bubble shape and their rise velocity with an electrical triple probe in nontransparent liquid such as liquid metal is proposed. The hydrodynamical behavior of the bubble in mercury is experimentally studied for both cases with and without a magnetic field and the following conclusions have been obtained.

1 The rise velocity, the equivalent radius and the horizontal radii of the bubble are accurately obtained over a wide realizable Reynolds number region.

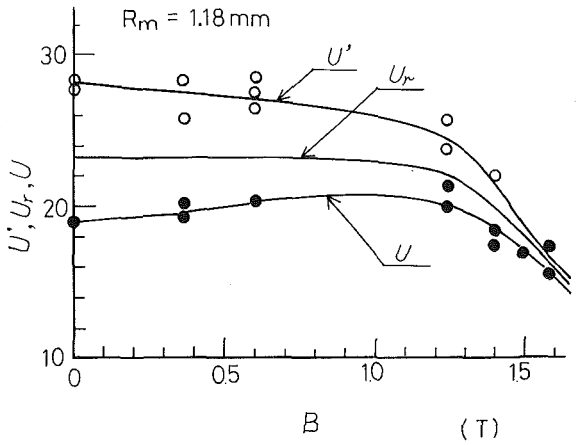

Fig. 9 Relations among U', U_r, U, and B

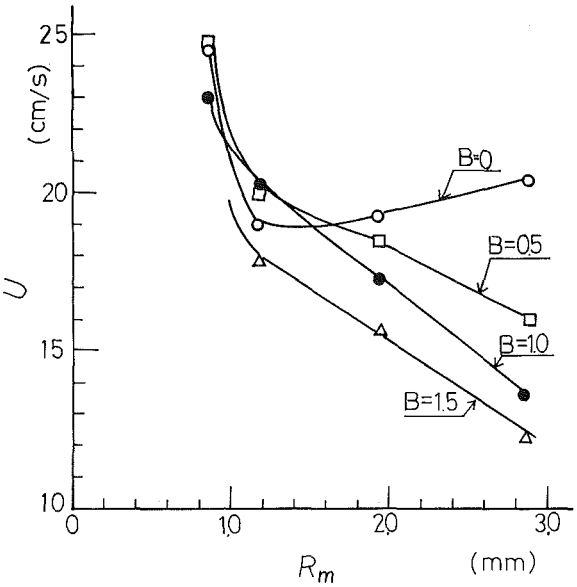

Fig. 10 Relation between U and R_m

2 The results obtained for the case without a magnetic field show that the hydrodynamical characteristics of the bubble are divided into three regions according to the Reynolds number and, with the increase in the bubble diameter, the bubble shape changes from spherical shape to flat and the rise velocity decreases. However, with a further increase in the diameter, the bubble comes to have a semispherical shape and the rise velocity starts to increase with the diameter. The drag coefficient and the aspect ratio of the bubble are expressed by the Reynolds number and the Weber number, and, the relations among them agree well with the theoretical prediction made by Sawi.

3 In a magnetic field, the effect of the magnetic field plays a large part depending on the bubble radius. The bubble of about R_m = 3 mm, whose shape is nearly a spherical cap, has a tendency similar to that of a solid sphere in a magnetic field. On the contrary, the rise velocity of a small bubble of about R_m = 1 mm, whose spiral motion is very strong in no magnetic field, shows a temporary increase with the increase of the intensity of the magnetic field. This is thought that the spiral motion is prevented by the magnetic field.

Acknowledgment

This research was partly supported by the Fundamental Studies on Two-phase Flow Characteristics for Thermal Design of Fusion Reactor Blanket supported by the Ministry of Education of Japanese Government.

References

1 Haberman, W. L., and Morton, R. K., "An Experimental Investigation of the Drag and Shape of Air Bubbles Rising Various Liquids," David Taylor Model Basin Re., No. 802, 1953.

2 Peebles, F. N., and Garber, H. J., "Studies on the Motion of Gas Bubbles in Liquids," *Chem. Eng. Prog.*, Vol. 18, 1964, pp. 88–97.

3 Taylor, T. D., and Acrivos, A., "On the Deformation and Drag of a Falling Viscous Drop at Low Reynolds Number," *Journal of Fluid Mechanics.*, Vol. 18, 1964, pp. 466–476.

4 Moore, D. W., "The Velocity of Rise of Distorted Gas Bubbles in a Liquid of Small Viscosity," *Journal of Fluid Mechanics*, Vol. 23, 1965, pp. 749–766.

5 Davis, R. M., and Taylor, G. I., "The Mechanics of Large Bubbles Rising Through Extended Liquids and Through Liquids in Tubes," *Process Royal Society*, Series A, Vol. 200, 1950, pp. 375–390.

6 Davenport, W. C., "Behaviour of Spherical Cap Bubbles in Liquid Metals," *J. Iron Steel Inst.* London, Vol. 205, 1967, pp. 1034–1042.

7 Lielausis, O., "Liquid-Metal Magnetohydrodynamics," *Atomic Energy Review*, Vol. 13, 1975, pp. 527–581.

8 Chester, W., "The Effect of a Magnetic Field on Stokes Flow in a Conducting Fluid," *Journal of Fluid Mechanics*, Vol. 3, 1957, pp. 304–308.

9 Gotoh, K., "Stokes Flow of an Electrically Conducting Fluid in a Uniform Magnetic Field," *J. of Phys. Soc. Japan*, Vol. 15, 1960, pp. 696-705.
10 Hijikata, K., Mori, Y., and Watabe, S., "Bubble Dynamics in Mercury," *Process 1975 Joint JSMA-ASME Applied Mechanics, Western Conference*, Honolulu, Hawaii, JSME B-12, 1975.
11 Harmathy, T. Z., "Velocity of Large Drops and Bubbles in Media of Infinite or Restricted Extent," *AICHE Journal*, Vol. 6, 1960, pp. 281–288.
12 Harper, J. F., "The Motion of Bubbles and Drops Through Liquids," *Advances in Applied Mechanics*, Vol. 12, Academic Press, New York, 1972, pp. 59–129.
13 Schmidt, E., "Fortschritte der Warmetechnischen Forschung," *VDI Z.* Vol. 77, 1933, pp. 1159–1160.
14 Sawi, M. E., "Distorted Gas Bubbles at Large Reynolds Number," *Journal of Fluid Mechanics*, Vol. 62, 1974, pp. 163–183.
15 Mendelson, H. D., "The Prediction of Bubble Terminal Velocities From Wave Theory," *AIChE Journal*, Vol. 13, 1967, pp. 250–253.

V. K. Dhir
J. N. Castle
Ivan Catton

Chemical, Nuclear, and Thermal Engineering Department, School of Engineering and Applied Science, University of California, Los Angeles, Calif.

Role of Taylor Instability on Sublimation of a Horizontal Slab of Dry Ice[1]

Sublimation of a horizontal slab of dry ice (≃190 K) placed beneath a pool of warm water or benzene (278–340 K) has been observed experimentally. Data for the heat transfer coefficient have been obtained in both steady and quasi-static states. The heat transfer coefficient for this pseudo film boiling process is found to be strongly dependent on the pool temperature. In the temperature range of stable film boiling, the heat transfer coefficient depends on the laminar or turbulent nature of the gas film. However, when the pool temperatures are such that a stable film can no longer be maintained, and the overlying liquid starts to freeze at the interface, the heat transfer coefficient data are correlated with the parameter $c_p \Delta T_f / h_{sf}$ for the liquid. Post-experiment visual observations of the dry ice surface show the presence of valleys and ridges arranged in a nearly square array spaced about one Taylor wavelength apart. An application of the present study to the fast reactor hypothetical accident situations in which a pool of molten fuel may be formed on horizontal steel surfaces is discussed.

Introduction

The Taylor instability concept has been applied in the past to describe many diverse physical phenomena such as maximum and minimum pool boiling heat fluxes, film condensation on the underside of a plate or tube, bacteria growth patterns on horizontal surfaces, and so on. The objective of this paper is to apply the same concept to study the heat flux from a liquid pool to a melting surface underneath, when the density of the melted phase is less than the pool density and the two fluid phases are immiscible.

In 1950, Taylor [1][2] discussed the instability of the horizontal interface between two ideal incompressible fluids of infinite depth. He showed that the irregularities at the interface tended to grow if the acceleration was directed from the heavier fluid to the less dense fluid placed underneath. Bellman and Pennington [2] extended Taylor's analysis to take into account the interfacial surface tension and the viscosities of the two fluids. For a simple case in which only surface tension at the interface was considered, they obtained analytical expressions for the "fastest growing" unstable wavelength and its growth rate.

Zuber [3] in 1959, made the first successful attempt to apply the hydrodynamic instability concepts to the maximum and minimum pool boiling heat fluxes on horizontal infinite heaters. Zuber argued that the steady cyclic release of bubbles at discrete locations in film boiling was a classical example of Taylor instability. He proposed that near the minimum heat flux the bubble-releasing nodes lie on a square grid with spacing bounded between the wavelengths of the fastest growing and "critical" Taylor waves. Using the two-dimensional wavelength for the fastest growing wave at the interface of two inviscid fluids of infinite depth and assuming that two bubbles were released per cycle, Zuber was able to obtain an expression for the minimum heat flux from purely hydrodynamic considerations.

Subsequently, Berenson [4, 5] made several careful observations of the minimum heat fluxes for carbon tetrachloride and pentane boiling on flat plates. Berenson rederived Zuber's expression for the minimum heat flux by restricting the bubble spacing to the fastest growing Taylor wavelength and by determining the bubble growth rate from experimental data rather than time averaging it over the amplitude as Zuber had done originally. However, Berenson kept Zuber's original assumptions of a two-dimensional Taylor wave growing at the interface of two inviscid liquids of infinite depth and a release of two bubbles per cycle.

Employing a simple geometrical model of the film boiling process, Berenson also obtained an expression for the film boiling heat transfer coefficient near the minimum. An expression for the minimum tem-

[1] This work was supported by the Reactor Safety Research Division of the Nuclear Regulatory Commission under Agreement No. AT(04-3)-34 P.A. 223, Mod. 5.

[2] Numbers in brackets designate References at end of paper.

Contributed by the Heat Transfer Division and presented at the Winter Annual Meeting, New York, N. Y., December 5-10, 1976 of THE AMERICAN SOCIETY OF MECHANICAL ENGINEERS. Revised manuscript received by the Heat Transfer Division April 8, 1977. Paper No. 76-WA/HT-67.

perature difference between the heater and the saturation temperature of the liquid to sustain film boiling was then obtained from the expressions for the minimum heat flux and the heat transfer coefficient.

Shortly after Berenson's work, results of experimental observations of film boiling of water and Freon-11 on a 20 cm square horizontal plate made out of aluminum were reported by Hosler and Westwater [6]. The observed minimum heat flux and minimum temperature to sustain film boiling were found to be significantly higher than Berenson's prediction. However, Berenson's prediction for the heat transfer coefficient in film boiling was found to be only slightly lower than the data. Hosler and Westwater's study was the first of its kind which provided photographic observation of the possible existence of the Taylor wave pattern during film boiling. From the photographs, the maximum bubble diameter at departure was observed to be 0.73λ. The classical picture of the bubble release pattern taken by Hosler and Westwater was further discussed by Lienhard and Schrock [7]. They showed that two different square arrays with their border points related to one another could be drawn through the bubbles. They suggested that the bubble release pattern appeared disordered because of the phase angle drift between the bubble-releasing nodes or due to possible horizontal movement of the bubbles as they rise through the pool.

Recently Sernas, et al. [8] showed that a three-dimensional fastest growing wave of wavelength $\sqrt{2}\lambda$ will, in fact, also give rise to a square grid with a spacing equal to the wavelength, λ, of a two-dimensional wave. In a square grid of size λ one bubble would be released alternately from each of the nodes and antinodes during one cycle, whereas in a $\sqrt{2}\lambda$ grid, four such bubbles will be released per cycle. Justification for the use of an infinite depth of the vapor blanket and for assuming the two fluids to be inviscid, while calculating the Taylor wavelength during film boiling, has been provided by Lienhard and Dhir [9].

The aim of the present study is to show how Taylor instability may govern the heat transfer from a liquid pool to a subliming solid surface underneath. The physical situation is created by placing a slab of dry ice underneath a pool of warm water or benzene. The results of this study may be helpful in making preliminary assessment of the wall heat transfer during a hypothetical core disruptive accident in a LMFBR when a pool of molten UO_2 may form on a steel surface. Although, heat transfer from molten UO_2 to steel would result in melting rather than sublimation of steel, the basic mechanism should remain the same as long as the lower liquid is lighter than the upper liquid and the two liquids are immiscible.

Pseudo Film Boiling Heat Transfer Models

Visual observations made after placing a horizontal slab of dry ice beneath a pool of warm water showed that the solid surface was immediately covered with a shiny gas blanket from which CO_2 bubbles started to leave in a very regular fashion. The interface wave pattern oscillated initially, but soon the surface became uneven and a standing wave pattern was established. During each cycle, the interface was found to grow, collapse, and regrow at the same location rather than alternate between nodes and antinodes as observed in film boiling on flat plates and cylinderical heaters. Fig. 1 shows the bubble-release phenomenon from a horizontal slab of dry ice. The regrowth of the interface at the nodes of the detached bubbles can be seen very clearly in the picture, whereas the antinodes which coincide with the valley on the surface remain inactive.

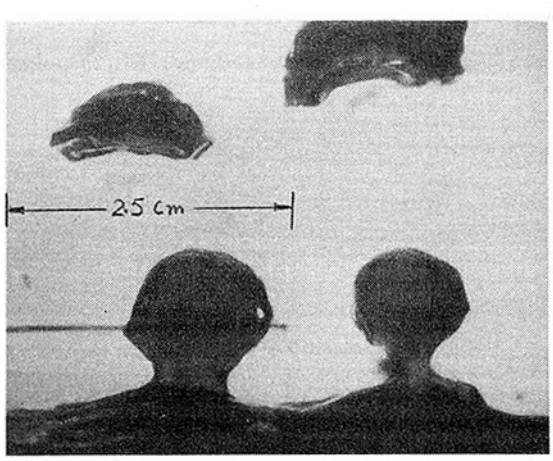

Fig. 1 Pseudo film boiling on a slab of dry ice

Laminar Film. As long as the temperature difference between the heater and the sublimation temperature of the dry ice is such that a cyclic release of CO_2 bubbles can be maintained, a stable gas film will blanket the dry ice surface. In order to derive an expression for the heat transfer coefficient in the pseudo film boiling process, we assume a geometrical model similar to that of Berenson [4]. The two geometrical models are shown in Fig. 2. In classical film boiling, two bubbles, one each from a node and an antinode, are released per λ^2 area per cycle. However, in the pseudo film boiling process only one bubble is released from the nodes per λ^2 area per cycle. The antinodes which coincide with the local valley in the solid surface do not contribute any bubbles. The reason that no bubbles are released from the valleys is probably that the interface there cannot overcome the pressure due to negative curvature. The valleys and ridges in the surface are, in turn, created by uneven sublimation of the solid surface underneath a growing bubble and a thin film. We also make certain other assumptions regarding various thermal and hydrodynamic parameters. Some of these assumptions are similar to those of Berenson and are:

(i) The temperature in the overlying pool of liquid is uniform and the temperature at the liquid-gas interface is the same as that of the liquid.

(ii) The dry ice surface is at its sublimation temperature and a negligible amount of heat is conducted into the slab. This assumption

Nomenclature

c_p = specific heat of the liquid
c_v = constant volume specific heat of the gas
D = bubble diameter
g = gravitational acceleration
h = heat transfer coefficient
h_{sf} = liquid latent heat of fusion
h_{sg} = latent heat of sublimation
k_g = thermal conductivity of the gas
Nu = Nusselt number, $h\lambda/k_g$
q = heat flux, subscript min denotes minimum heat flux
Re = Reynolds number, $q\lambda/\mu_g h_{sg}$
r = radius
T, T_H, T_C = temperature, subscripts H and C denote temperatures of the liquid and the solid surface, respectively
$\overline{U}$ = mean film velocity in the radial direction
V = velocity in the vertical direction
V_s = gas evolution velocity at the solid surface
Δp = pressure difference
ΔT = difference between the pool temperature and sublimation temperature of dry ice at one atmosphere, subscript min denotes minimum temperature
ΔT_f = difference between the pool temperature and the freezing temperature of the liquid
y = ordinate perpendicular to solid surface
δ = gas film thickness
λ = wavelength of the fastest growing two-dimensional Taylor wave, $2\pi\sqrt{3}\sqrt{\sigma/g(\rho_f - \rho_g)}$
μ_g = gas viscosity
ρ_f, ρ_g = liquid and gas densities, respectively
σ = surface tension between liquid and gas
τ_w = wall shear stress

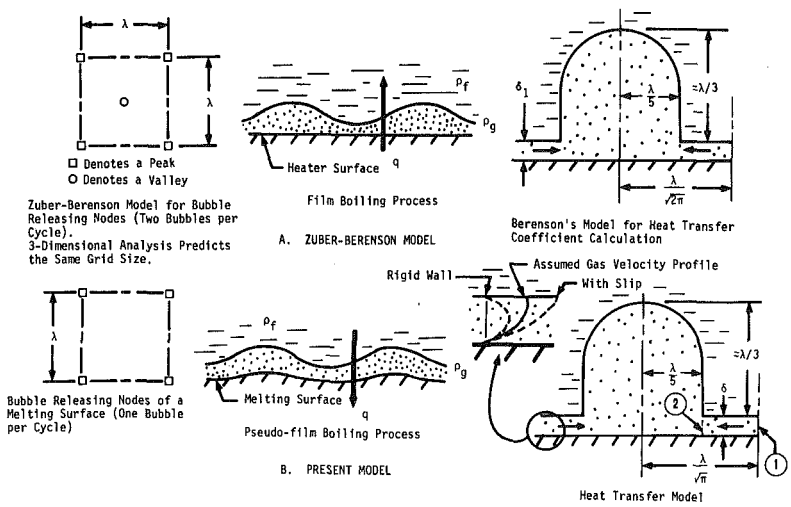

Fig. 2 Film boiling models

will be true if the dry ice slab had been in storage for some time prior to experiments.

(iii) The gas film is thin and the gas velocity in the film is small so that the inertia of the film can be neglected. The gas evolution velocity at the surface of the solid is also very small so that the temperature distribution in the film can be assumed to be linear.

(iv) The flow of gas in the film is laminar. A no-slip condition exists at the solid surface. The choice of the right boundary condition at the liquid-gas interface is not easy. Thus, we decide a priori that conditions between slip and no-slip exist at the liquid-gas interface.

(v) The effect of evolution of gas at the surface of the solid in reducing shear stress and heat transfer at the wall is small. We will check this assumption and assumption (iii) after we have completed the analysis.

(vi) The kinetic energy of the gas is small in comparison with the enthalpy change.

(vii) The gas properties are evaluated at an average temperature of the liquid and the dry ice surface.

(viii) The gas flows radially into the bubble and the bubble spacing is unaffected by the gas flow.

(ix) The average bubble diameter is 0.4λ and the average bubble height prior to break-up is about 0.3λ. Hosler and Westwater [6] observed that the maximum bubble diameter was 0.73λ; however, the average diameter could be considerably less. Fig. 1 suggests that 0.4λ is a realistic bubble diameter.

Now, we replace the area feeding one bubble by an equivalent circular area of radius $\lambda/\sqrt{\pi}$, with a center coinciding with the center of the bubble area ($r = 0.2\lambda$) as projected on the solid surface. The configuration details are given in Fig. 2(*b*). For a film of constant thickness, δ, a simple energy balance at the surface of the solid gives the gas evolution velocity in the vertical direction as[3,4]

$$V_s = \frac{k_g \Delta T}{\delta \rho_g h_{sg}} \tag{1}$$

The mean film velocity, $\overline{U}$, in the radial direction is related to the gas evolution velocity, V_s, through the relation

$$\rho_g 2\pi r \delta \overline{U} = (\lambda^2 - \pi r^2)\rho_g V_s \qquad \text{or} \qquad \frac{\overline{U}}{V_s} = \frac{\lambda^2 - \pi r^2}{2\pi r \delta} \tag{2}$$

Combining equations (1) and (2), the mean radial gas velocity can be written as

$$\overline{U} = \frac{k_g \Delta T}{\rho_g h_{sg} \delta} \frac{\lambda^2 - \pi r^2}{2\pi r \delta} \tag{3}$$

The mean radial velocity for a no-slip condition at the surface of the solid and a condition between a rigid boundary and slip boundary at the liquid-gas interface can be written in terms of the radial pressure gradient as

$$\overline{U} = \frac{1}{7.5} \frac{dp}{dr} \frac{\delta^2}{\mu_g} \tag{4}$$

Elimination of $\overline{U}$ from equations (3) and (4) results in

$$\frac{dp}{dr} = 7.5 \frac{\mu_g k_g \Delta T}{\rho_g h_{sg} \delta^4} \frac{\lambda^2 - \pi r^2}{2\pi r} \tag{5}$$

For a constant δ, the integration of equation (5) between points 1 ($r = \lambda/\sqrt{\pi}$) and 2 ($r = 0.2\lambda$) shown in Fig. 2(*b*) gives

$$(\Delta p)_{1-2} = 7.5 \frac{\mu_g k_g \Delta T}{\rho_g h_{sg} \delta^4} \frac{\lambda^2}{\pi} (0.300) \tag{6}$$

The hydrostatic pressure difference between points 1 and 2 can be written as

$$(\Delta p)_{1-2} = 0.3\lambda(\rho_f - \rho_g)g - \frac{2\sigma}{0.2\lambda} \tag{7}$$

From equations (6) and (7), the pressure can be eliminated to give

$$0.3\lambda(\rho_f - \rho_g)g - \frac{2\sigma}{0.2\lambda} = \frac{7.5\mu_g k_g \Delta T}{\rho_g h_{sg} \delta^4} \frac{\lambda^2}{\pi}. \tag{8}$$

The wavelength for the fastest growing two-dimensional Taylor wave in inviscid liquids of infinite depth is

$$\lambda = 2\pi\sqrt{3}\sqrt{\sigma/g(\rho_f - \rho_g)} \tag{9}$$

Use of equation (9) in (8) gives

$$\delta = 2.44 \left[\frac{\mu_g k_g \Delta T}{\rho_g h_{sg} g(\rho_f - \rho_g)} \sqrt{\frac{\sigma}{g(\rho_f - \rho_g)}} \right]^{1/4} \tag{10}$$

The foregoing equation for δ has been arrived at by considering that all the heat supplied to a unit cell is transferred through the film covering the area between the adjacent bubbles only, and no heat is transferred through the bubble itself. Thus, to obtain an average film thickness, which will give the same total heat transfer as the foregoing equation, δ should be multiplied by the ratio of the total area of a unit cell to the area not occupied by the bubble. This results in

[3] Symbols are explained in the Nomenclature section.

[4] The gas density at the surface will actually be slightly higher than the mean gas density used in equation (1). However, as seen from equation (4) it does not effect our subsequent analysis.

$$\delta = 2.77\left[\frac{\mu_g k_g \Delta T}{\rho_g h_{sg} g(\rho_f - \rho_g)}\sqrt{\frac{\sigma}{g(\rho_f - \rho_g)}}\right]^{1/4} \tag{11}$$

Finally, an expression for the heat transfer coefficient in the laminar film is obtained as:[5]

$$h = \frac{k_g}{\delta} = 0.36\left[\frac{k_g{}^3 h_{sg}\rho_g(\rho_f - \rho_g)g}{\mu_g \Delta T\sqrt{\sigma/g(\rho_f - \rho_g)}}\right]^{1/4} \tag{12}$$

Equation (12) for the pseudo film boiling process predicts a heat transfer coefficient 15 percent below Berenson's prediction for film boiling on infinite flat plates. The decrease in heat transfer coefficient in the pseudo film boiling process considered here is due to the presence of a thicker vapor film resulting from release of only one bubble per λ^2 per cycle as compared to release of two bubbles in classical film boiling.

At this point we digress for a while and check the validity of our assumptions (iii) and (v). The steady-state energy equation in the film can be written as

$$\rho c_p V\frac{dT}{dy} = k_g\frac{d^2T}{dy^2} \tag{13}$$

In equation (13), V is the velocity in the vertical direction and is maximum at the surface of the solid. As seen from equation (2), the ratio of radial to gas evolution velocity, $\overline{U}/V_s$, varies significantly along the flow path, being minimum at $r = \lambda/\sqrt{\pi}$ and maximum at $r = 0.2\lambda$. To carry out an order of magnitude analysis, we first obtain an average value of $\overline{U}/V_s$ over the surface area feeding one bubble.

$$\left.\frac{\overline{U}}{V_s}\right|_{\text{avg}} = \frac{1}{\lambda^2 - (0.2\lambda)^2\pi}\int_{0.2\lambda}^{\lambda/\sqrt{\pi}}\frac{\lambda^2 - \pi r^2}{\delta}\,dr$$

or

$$\left.\frac{\overline{U}}{V_s}\right|_{\text{avg}} = 0.21\frac{\lambda}{\delta} \tag{14}$$

The velocity in equation (13) can be nondimensionalized by choosing $\overline{U}_{\text{avg}}$ as a velocity scale and λ as the length scale. Using the same symbols for y and δ in both dimensional and nondimensional form and defining

$$\text{Re} \equiv \frac{q\lambda}{\mu_g h_{sg}}$$

$$\theta \equiv \frac{T - T_c}{T_H - T_C}$$

equation (13) becomes

$$\frac{\delta}{0.21}\frac{d\theta}{dy} = \frac{1}{\text{RePr}}\frac{d^2\theta}{dy^2} \tag{15}$$

$$\frac{\delta}{0.21}\quad\frac{1}{\delta}\qquad\frac{1}{\text{RePr}}\qquad\frac{1}{\delta^2}$$

$$1\qquad 0(10^{-2})\quad 0(10^4)$$

Typically, the wavelength may be about 2.5 cm, and the gas film thickness approximately 5×10^{-3} cm. The order-of-magnitude analysis of equation (15) then shows that for δ of the order of 10^{-2} and RePr of the order of 10 or 100, the convective term on the left-hand side is at least two orders of magnitude smaller than the conductive term. Thus, for an inertialess film in which Re is small, the neglect of the convective term in the energy equation imposes little error and our assumption of linear temperature profile in the film is valid.

The effect on shear stress of the evolution of the gas at the surface of the solid is also expected to be small. As seen from Schlichting [10, pp. 369–376], for small film Reynolds number, the effect of uniform blowing with $V_s/\overline{U}|_{\text{avg}}$ of the order of 10^{-2}, will be to reduce the drag by only a few percent.

In the present work we have not attempted to obtain expressions for the minimum heat flux and the minimum temperature to sustain pseudo film boiling on a horizontal surface, but will use Berenson's predictions to compare our results. Based on carbon-tetrachloride and pentane data, the expressions for the minimum heat flux and the minimum temperature were given by Berenson as:

$$q_{\min} = 0.09\,\rho_g h_{fg}\left[\frac{g(\rho_f - \rho_g)}{(\rho_f + \rho_g)}\right]^{1/2}\left[\frac{\sigma}{g(\rho_f - \rho_g)}\right]^{1/4} \tag{16}$$

and

$$\Delta T_{\min} = 0.127\frac{\rho_g h_{fg}}{k_g}\left[\frac{g(\rho_f - \rho_g)}{(\rho_f + \rho_g)}\right]^{2/3} \times\left[\frac{\mu_g}{g(\rho_f - \rho_g)}\right]^{1/3}\left[\frac{\sigma}{g(\rho_f - \rho_g)}\right]^{1/2} \tag{17}$$

Turbulent or Ripply Film. As the liquid pool temperature is increased, its viscosity will decrease exponentially. Now a slip condition at the liquid-gas interface would be more appropriate. Relaxation of the interfacial boundary condition will result in a lower value of δ, and consequently in a higher heat transfer coefficient. The direct effect of the increased ΔT, across the film, would be to enhance the heat flux for the same h. The cumulative effect of increased h and ΔT will be a larger gas volume flux, and possibly an increased gas velocity in the film. An increased gas velocity may cause the film to become turbulent, thereby causing the temperature distribution in the upper portion of the film to become uniform. The gas film, with increased velocity and a slip condition at the gas-liquid interface, is also more susceptible to Kelvin-Helmholtz type instability. The presence of small capillary waves on the film may tend to improve the heat transfer process. Under such conditions the pressure drop in the film will not be directly proportional to the average radial velocity but will depend on the radial velocity raised to a certain exponent. For a constant Prandtl number, the heat transfer coefficient for a ripply or turbulent film may be expected to be correlated by a relation of the type

$$\frac{h\lambda}{k_g} = f(\text{Re}) \tag{18}$$

The functional dependence of the heat transfer coefficient on the Reynolds number will be determined from the experimental data.

Partial Direct Liquid-Solid Contact. When the liquid temperature is above its freezing temperature but is not high enough to sustain a stable film between the liquid and the solid, a direct liquid-solid contact will be established. For such liquid temperatures the mode of heat transfer will very much depend on whether the liquid-solid interface temperature is below or above the freezing temperature of the overlying liquid. The spontaneous interface temperature when two plane surfaces are brought in direct contact, can be written as

$$\frac{T_I - T_C}{T_H - T_I} = \sqrt{\frac{k_H\rho_H c_H}{k_C\rho_C c_C}} \tag{19}$$

For a water temperature, $T_H = 295$ K, and a dry ice temperature, $T_C = 194$ K, the instantaneous interface temperature is obtained from equation (19) as

$$T_I = 236\text{ K}$$

This temperature is 37 K below the freezing temperature of water. Similarly for benzene at 295 K, the interface temperature is

$$T_I = 224\text{ K}$$

This temperature is about 54 K below the freezing temperature of benzene. Thus, for pool temperatures of about 295 K, both water and benzene are expected to freeze at the interface on collapse of the vapor film. The freezing of the liquid would, however, be inhibited by the motion generated by the gas evolving at the interface.

[5] Equation (12) does not contain a correction to h_{sg} for the sensible heat of the gas. This is done to facilitate comparison of predictions with the data, where the sensible heat of the gas was accounted for separately. However, the correction is small.

Neglecting any heat conduction through the frozen crust of the liquid, the overall heat transfer coefficient will depend on the interplay of such parameters as the temperature of the bulk of the liquid, its specific heat, freezing temperature, latent heat of fusion, crystal growth rate, and the fractional area and heat transfer coefficient of the surface not covered by the solid crust. Assuming that the heat transfer coefficient in the area not covered by the solid crust is approximately given by our expression for the laminar film, the functional dependence of the average heat transfer coefficient can be written as

$$\frac{h}{0.36(k_g{}^3\rho_g h_{sg}(\rho_f-\rho_g)/\mu_g\Delta T\sqrt{\sigma/g(\rho_f-\rho_g)})^{1/4}} = f\left(\frac{c_p\Delta T_f}{h_{sf}}, \phi\chi\right) \quad (20)$$

where

$$\phi = \frac{\text{interfacial crust growth rate determined from crystallization theory}}{\text{heat transfer controlled solidification rate}}$$

and

$$\chi = \frac{\text{surface area not covered by the interfacial crust}}{\text{total surface area}}$$

For the liquids used in this study ϕ is generally a large number and as such may not influence the heat transfer process significantly. Thus, we may expect the heat transfer coefficient to depend on $c_p\Delta T_f/h_{sf}$ and χ, and will determine the functional dependence from the experiments.

Experimental Apparatus and Procedure

Experiments for heat transfer from a pool of warm water or benzene to the dry ice slab placed underneath were performed both in the steady-state (pool temperature held nearly constant) and quasi-static state (pool temperature varying with time). The test apparatus is shown in Fig. 3. The dry ice slab (20 × 20 × 2.5 cm) was supported on a thick sheet of styrofoam. The liquid pool was formed in a thin sheet-metal cylinder covered on the sides with a foam insulation and open at both ends. A sponge rubber gasket with a loading collar was attached to the sheet-metal cylinder. This was done to avoid any leakage of liquid when the cylinder was placed on the dry ice surface and was filled with water. Provision for placing a cartridge heater in the cylinder was also made so that in steady-state experiments the pool temperature could be maintained constant by adjusting power to this heater. The pool temperature was measured by a copper-constantan thermocouple placed about ½ cm above the dry ice surface and connected to a Houston X-Y recorder.

Prior to each experiment, the dry ice test surface was visually examined to avoid use of an originally uneven surface. In some cases, the temperature of the interior of the dry ice slab was also measured before starting the experiment. These measurements showed that generally the dry ice temperature as obtained from the vendor was about 5 K below its sublimation temperature at 1 atm pressure. The dry ice slab was then placed on the styrofoam base plate and leveled so that the test surface was as nearly horizontal as possible. The sheet-metal cylinder was then placed on the dry ice surface and lead weights were placed on the loading collar. About 2 kg of distilled water or reagent grade benzene was then heated on a hot plate. The temperature and precise weight of the test liquid were noted and the test liquid poured into the sheet-metal cylinder. In the experiments, the pool height above the dry ice surface varied from about 11 to 14 cm.

In the steady-state experiments the heat transfer rate from the pool was estimated and power to the cartridge heater was adjusted accordingly. The X-Y recorder was then started and temperature of the liquid pool was recorded as a function of time. The rising CO_2 gas bubbles kept the pool well stirred and changing the position of the thermocouple to different parts of the pool showed little temperature variation (<0.25 K). The power input to the heater was then used to calculate the rate at which energy was transferred to the dry ice. If the initial setting on the power was slightly wrong, the energy loss from the pool was corrected by noting the time rate of change of the pool temperature and an average pool temperature was then used in the heat transfer calculations. However, if the initial setting was off by a significant margin, a new test with a modified power was made. Error analysis showed that the heat flux calculations were accurate to within ±3 percent.

In the quasi-static tests, the heater was not used and the heat transfer calculations were made by noting the rate of change of enthalpy of the liquid. The rate of change of enthalpy of the liquid was calculated by knowing its mass, specific heat, and the rate of change of temperature with time. The quasi-static total heat flux calculations are believed to be accurate within ±1½ percent.

The observations of the temperature of the gas leaving the pool free surface showed that the gas essentially left at the pool temperature. Thus, a correction for the sensible heat content of the escaping gas was made to the heat flux calculations. The correction to the heat flux for CO_2 lost by diffusion at the gas-liquid interface was found to be small [11]. Also, the temperature rise of the pool due to heat of solution of CO_2 in water is expected to be small. For a water pool at 298 K and saturated with CO_2, the temperature rise due to heat of solution will be about 0.3 K. In reality, water will not be saturated with CO_2 and the effect of heat of solution will be even less.

During the course of the experiments, it was observed that a significant amount of heat was lost from the pool by convection and evaporation at the free surface. The heat loss data were obtained by carrying out simulated experiments without the presence of dry ice slab. In these experiments nitrogen gas was released at the bottom of the pool from small holes drilled in a plexiglass tube and allowed to bubble through the liquid. The gas flow rate and the rate of change of the pool enthalpy with time were noted. From this information the heat loss curves for different pool temperatures and gas flowrates were obtained and the raw data were corrected using an iterative procedure. The raw and the corrected data are tabulated in reference [12]. The overall error in computing the heat transfer coefficient from the heat flux data, after a correction for heat loss has been made, is expected to be less than ±6 percent. A countercheck on the accuracy of the heat flux calculations by noting the weight change of the dry ice slab could not be made because of uncontrolled loss of CO_2 at the dry ice slab sides exposed to the atmosphere.

The mass transfer from the surface caused the originally smooth surface to become uneven with time. This in turn resulted in exposure of more dry ice surface area to the liquid pool. The net effect of the increased surface area was to increase with time the total heat transferred from the pool to the dry ice slab. For this reason, the data used in this study are only for early periods of time (less than 4 min) when the melting surface was nearly smooth but the surface wave pattern had been established.

Results and Discussion

On postexperiment examination, the dry ice surface exposed to the liquid for a large period of time (≃15 min) was found to be very uneven. The ridges and valleys on the surface showed a very definite pattern and were found to be arranged in a near square grid pattern spaced about a Taylor wavelength apart. The pattern was, however, distorted near the ends of the container. Fig. 4 shows a photograph of one such surface exposed to a pool of water maintained at a constant temperature of about 298 K. A three-dimensional standing wave pattern is clearly visible. From the scale in the picture, it is gratifying to note that the distance between rows of alternating peaks and valleys is about 2.8 cm, whereas for water at 298 K Taylor instability theory predicts the wavelength of the fastest growing two-dimensional Taylor wave to be 2.85 cm. Physical measurement of the distance between consecutive peaks and valleys in the plane of the picture was also found on the average to be 2.8 cm. Existence of the nodes of a Taylor wave in a near square grid with absence of the nodes in the valley is clearly evident in the picture. The peaks on the dry ice surface correspond to the nodes where a bubble grew and departed at regular

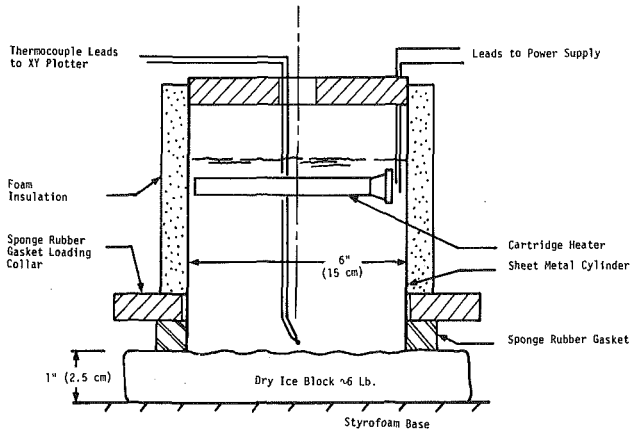

Fig. 3 Test apparatus

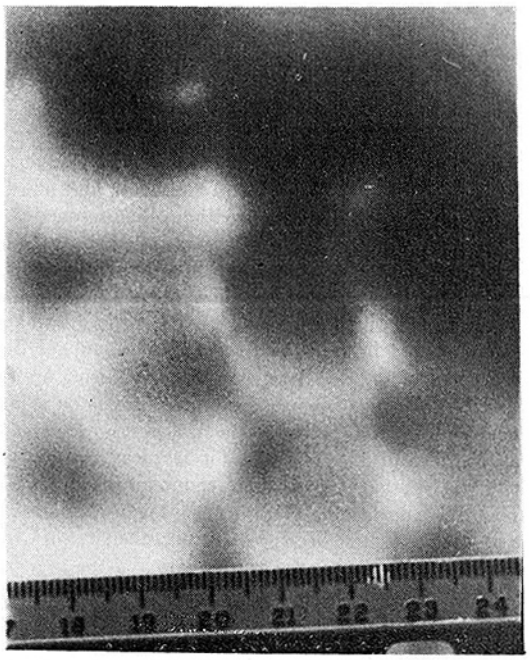

Fig. 4 Three-dimensional Taylor wave pattern on the dry ice surface

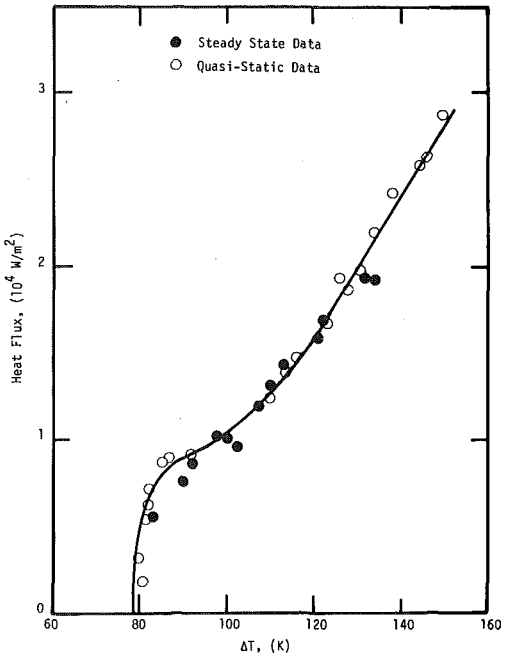

Fig. 5 Variation of heat flux with temperature for dry ice-water system

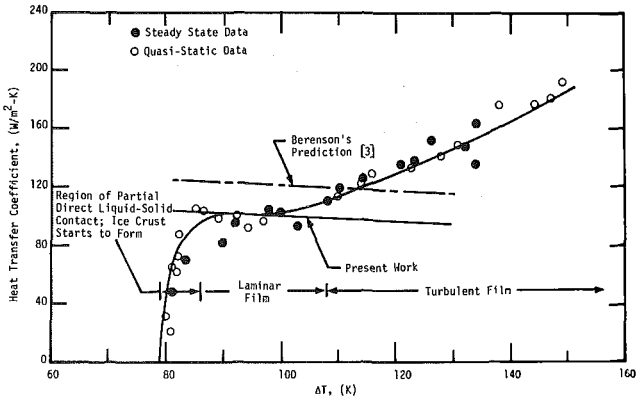

Fig. 6 Variation of heat transfer coefficient with temperature for dry ice-water

intervals. Because of very small heat transfer to the dry ice beneath a growing bubble, the sublimation rate of the dry ice is relatively small at bubble releasing nodes. This effect accumulated over a period of time gives rise to formation of conspicuous peaks and valleys. The height difference between the peaks and valleys seemed to reach a steady-state limit ($\simeq\lambda/3$) after about 15 min. However, this time was strongly dependent on the pool temperature.

The water steady-state and quasi-static heat flux data are plotted in Fig. 5, as a function of the temperature difference between water and the sublimation temperature of the dry ice. No distinguishable difference exists between the steady-state and quasi-static data, though the steady-state data tend to show larger variability because of increased uncertainty associated with the heat flux calculations as well as the evenness of the dry ice surface. The curve faired through the data shows a knee at $\Delta T = 87$ K or at a water temperature of about 281 K. Visual observations showed that at or below this temperature a stable gas film was no longer sustained and a partial direct contact of water with the dry ice surface was established. The heat flux associated with the pseudo film boiling process quickly drops to zero after the gas film breaks down and the water approaches its freezing temperature. Near the freezing temperature of the overlying liquid, a frozen crust of the overlying liquid completely covers the dry ice surface. Now, CO_2 gas does not escape normally from the dry ice surface, but moves laterally beneath the crust and leaves through the open area around the edges. The heat conducted to the dry ice through the crust further thickens the crust without any change in the temperature of the overlying liquid. In the experiments, the heat flux was measured by noting the rate of change of sensible heat of the overlying liquid and no attempt was made to measure the growth rate of the crust. Though there is definitely some heat transfer to the dry ice at the freezing temperature of the overlying liquid, it is not associated with the pseudo film boiling process. The nonlinear nature of the heat flux curve above the knee indicates the temperature dependence of the stable film boiling heat transfer coefficient.

The heat transfer coefficient data are plotted in Fig. 6. In this figure the predictions for the laminar film heat transfer coefficient based on Berenson's formulation as well as our equation (12) are also shown. In the stable film boiling, the heat transfer coefficient is weakly dependent on temperature for ΔT varying from 87 to 108 K. In this range, the data are very well correlated by our prediction based on laminar film model, while Berenson's prediction is about 15 percent higher. At temperature differences larger than 108 K, the heat transfer

coefficient is strongly dependent on temperature. In this region the heat transfer coefficient is probably increased by the turbulent or ripply nature of the film and we should hope to correlate the data with the gas film flow Reynolds number. For water temperatures corresponding to ΔT less than 87 K, the heat transfer coefficient decreases rapidly with decreasing pool temperature.

The quasi-static heat transfer coefficient data for benzene are plotted in Fig. 7. For ΔT greater than 97 K (benzene temperature = 291 K), the heat transfer coefficient depends weakly on temperature and the data are correlated well with our equation (12). The stable gas film breaks down at ΔT = 97 K and for a ΔT less than 97 K the heat transfer coefficient drops to zero as the benzene temperature approaches its freezing temperature (278 K). While plotting in Figs. 6 and 7 the heat transfer coefficient predicted by equation (12), the values of surface tension between water and air and benzene and air have been used. The dependence of the heat transfer coefficient on the physical properties of the overlying liquid is such that laminar film heat transfer coefficient for water and benzene differ by only about 20 percent. Thus, a large error will not be made if water and benzene data in the narrow temperature range 90 K < ΔT < 120 K is treated as one entity.

From the data plotted in Figs. 5–7, the minimum heat flux and minimum ΔT needed to sustain a stable gas film between the liquid and the dry ice surface can be ascertained. In the following we compare these values for the pseudo film process with Berenson's equations (16) and (17). The minimum heat flux given by Berenson's prediction is about twice as large as observed in the present experiments for water and about one and a half times as large as observed in the present experiments for benzene. The lower value of the minimum heat flux in the present physical situation does not come as a surprise because of the observed two-fold reduction in the number of bubbles released per cycle as compared to film boiling. Lack of data on the bubble growth rate and the bubble release frequency inhibits us from making any strong conclusions about the minimum heat flux for the pseudo film boiling process. Nevertheless, the functional dependence on the physical properties should be the same as for film boiling. The observed values of ΔT_{min} are about 40 percent lower than Berenson's prediction for water and about 14 percent lower than Berenson's prediction for benzene. The empirical constant in equation (17) was arrived at from film boiling heat transfer data for pentane and CCl_4. In boiling experiments, it is very difficult to keep the heater surface completely free of an oxide layer which can influence ΔT_{min}. In the present experiments, the dry ice surface is very clean and lower values of ΔT_{min} do not come as a surprise. The value of the numerical constant in equation (17) which is representative of the pseudo film boiling process can only be obtained if an expression similar to equation (16) for the minimum heat flux is developed first. However, if the numerical constants in equations (16) and (17) are multiplied by 0.62 and 0.73, respectively, the observed values of q_{min} and ΔT_{min} for pseudo film boiling process will lie within ±20 percent of the predictions.

The nondimensionalized heat transfer data for stable film boiling are plotted in Fig. 8 as a function of Reynolds number. The dominant wavelength, λ, which determines the spacing of the bubbles has been chosen as the characteristic length. This wavelength is weakly dependent on pool temperature and in the present experiments it is about 2.85 cm for water and about 2.0 cm for benzene. For Re < 40, the heat transfer coefficient is independent of the Reynolds number. However, for Re > 40, the dimensionless heat transfer coefficient is seen to vary as $(Re)^{0.5}$. This is probably due to ripply or turbulent nature of the film. The dimensionless heat transfer coefficient for constant Prandtl number (Pr ≃ 0.7) can be written as

$$\frac{h\lambda}{k_g} = 245 \qquad \text{for Re} < 40 \tag{21}$$

$$\frac{h\lambda}{k_g} = 37.5\,(\text{Re})^{0.5} \qquad \text{for Re} > 40 \tag{22}$$

The value of the transition Reynolds number in the gas film is considerably less than that in pipes. This could be the result of the presence of a near slip condition at the liquid-gas interface which does not help to dampen capillary waves at the interface. Interestingly, similar values for the transition Reynolds number and a similar functional dependence on Reynolds number of the turbulent heat transfer coefficient were obtained by Carpenter and Colburn [13] during high shear film condensation of steam in pipes. The Carpenter-Colburn correlation reduces to the form of equation (22) when τ_w is replaced by $\mu_g \overline{U}/\lambda$.

Distilled water and benzene heat transfer coefficient data for the partial direct liquid-solid contact region are plotted in Fig. 9 with $c_p \Delta T_f / h_{sf}$ as abscissa. Meaningful data for the equilibrium fraction of the interface area not covered by the frozen liquid could not be obtained because of experimental difficulties. The data show a considerable scatter and the correlation with $c_p \Delta T_f / h_{sf}$ alone is not clearly established. Further work is needed to understand this complex region of interfacial crust formation. Visual observations in the partial direct liquid-solid contact region showed that invariably liquid will locally come in contact with dry ice surface and will freeze in the form of a thin flake. The water-ice crystals grew on the dry ice surface and were probably weakly linked with the solid surface. The crystals were seen to be moved around locally by the escaping gas for a very short period of time before they grew in size and became stationary above the dry ice surface.

Equation (12) can be used to predict the magnitude of the pool wall heat transfer in a similar situation when the solid surface placed un-

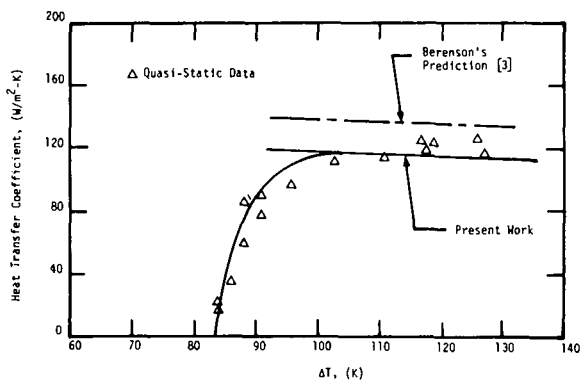

Fig. 7 Variation in heat transfer coefficient with temperature for dry ice-benzene

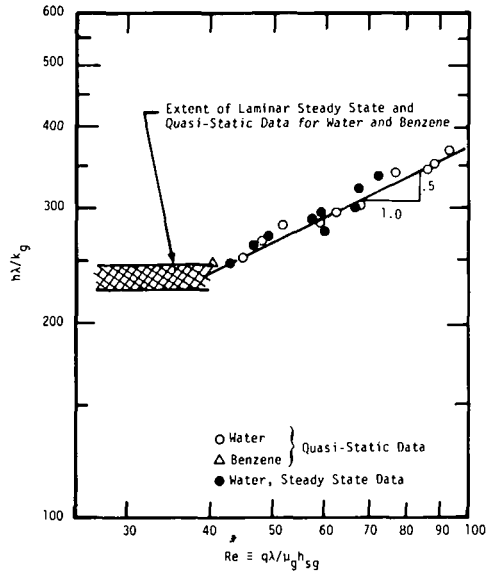

Fig. 8 Dependence of pseudo film boiling heat transfer coefficient on Reynolds number

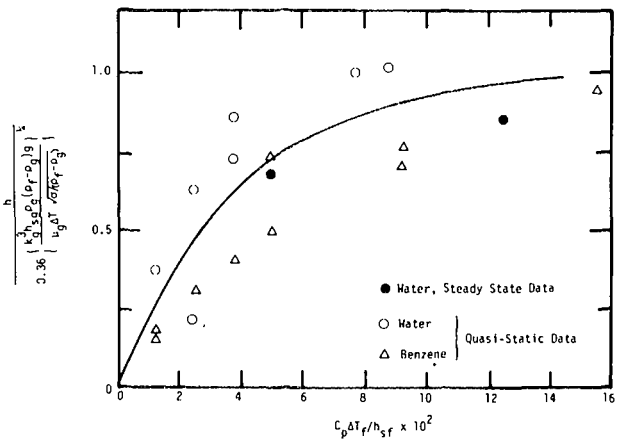

Fig. 9 Variation of heat transfer coefficient in the region of partial freezing of the pool

derneath a heavier liquid melts rather than sublimes. However, it would be necessary to check a priori that freezing of the overlying liquid does not occur at the pool-wall interface and various other assumptions used in deriving this equation are satisfied. If, during a hypothetical core meltdown accident in a LMFBR, a pool of molten UO_2 at 3100 K is considered to be formed on a steel surface held adiabatically at 1700 K, and properties of the gas and overlying liquid are replaced by those of liquid steel and molten UO_2, respectively; the heat transfer coefficient from equation (12) is evaluated to be 57 kW/m^{2}K. This heat transfer coefficient corresponds to an extremely high heat flux of about 80 MW/m^2. However, a real test of these high heat fluxes can only come from future experiments using simulant fluids.

Conclusions

1 Vaporization of a less dense material under a heavier liquid has been shown to be governed by the Taylor instability.

2 Heat transfer data for pseudo film boiling of CO_2 underneath a pool of water or benzene have been obtained for a wide range of pool temperatures.

3 Taylor instability theory has been shown to successfully predict heat transfer to the subliming interface when the gas film is laminar.

Table 1 Comparison of q_{min} and ΔT_{min} data with Berenson's prediction

	$q_{min} \times 10^{-4}$ W/m^2		ΔT_{min}, K	
Liquid	Present	Berenson	Present	Berenson
Distilled water	0.85	1.75	87	144
Benzene	1.14	1.50	97	114

4 The data for the turbulent film have been correlated successfully with the film flow Reynolds number. However, correlation of the partial direct liquid-solid contact regime data with the parameter $c_p\Delta T_f/h_{sf}$ has met with only partial success.

References

1 Taylor, G. I., "The Instability of Liquid Surfaces When Accelerated in a Direction Perpendicular to Their Planes, Part I," *Proceedings Royal Society London*, A-201, 1950, p. 192.

2 Bellman, R., and Pennington, R. H., "Effects of Surface Tension and Viscosity on Taylor Instability," *Quart. Appl. Math.*, Vol. 12, 1954, p. 151.

3 Zuber, N., "Hydrodynamics Aspects of Boiling Heat Transfer," AEC Report No. AECU-4439, Physics and Mathematics, 1959.

4 Berenson, P. J., "Film Boiling Heat Transfer From a Horizontal Surface," JOURNAL OF HEAT TRANSFER, TRANS. ASME, Series C, Vol. 83, No. 1, 1961, pp. 351–362.

5 Berenson, P. J., "Experiments on Pool-Boiling Heat Transfer, *International Journal of Heat and Mass Transfer*, Vol. 5, No. 10, 1962, pp. 985–999.

6 Hosler, E. R., and Westwater, J. W., "Film Boiling on a Horizontal Plate," *ARS Journal*, Vol. 32, No. 4, Apr. 1962, p. 553.

7 Lienhard, J. H., and Schrock, V. E., "The Effect of Pressure, Geometry, and the Equation of State Upon the Peak and Minimum Boiling Heat Flux," JOURNAL OF HEAT TRANSFER, TRANS. ASME, Series C, Vol. 85, No 3, 1963, pp. 261–272.

8 Sernas, V., Lienhard, J. H., and Dhir, V. K., "The Taylor Wave Configuration During Boiling From a Flat Plate," *International Journal of Heat and Mass Transfer*, Vol. 16, No. 9, 1973.

9 Dhir, V. K., and Lienhard, J. H., "Taylor Stability of Viscous Fluids With Application to Film Boiling," *International Journal of Heat and Mass Transfer*, Vol. 16, No. 11, Nov. 1973.

10 Schlichting, H., *Boundary Layer Theory*, Sixth ed., McGraw-Hill, New York, 1968.

11 Stewart, P. B., and Munjal, P. K., "The Solubility of Carbon Dioxide in Distilled Water, Synthetic Sea Water and Synthetic Sea Water Concentrations," Sea Water Conversion Laboratory, Report No. 69-2, University of California, Berkeley, July 1969.

12 Dhir, V. K., Castle, J. N., and Catton, I., "Pool Wall Heat Transfer Studies," UCLA-ENG-Report 7780, to be published.

13 Carpenter, F. S., and Colburn, A. P., "The Effect of Vapor Velocity on Condensation Inside Tubes," *Proceedings of the General Discussion of Heat Transfer*, the Institute of Mechanical Engineers and ASME, July 1951, pp. 20–26.

R. R. Gilpin

Assoc. Professor,
University of Alberta,
Edmonton, Alberta, Canada

The Effect of Cooling Rate on the Formation of Dendritic Ice in a Pipe With No Main Flow

Dendritic ice forms in a pipe when there is no main flow through the pipe during the freezing process. This ice form occurs because the quiescent water supercools considerably below 0°C before ice nucleation occurs. It has been shown that growth of dendritic ice can cause blockage of a water pipe [1][1] much sooner than would have been predicted if the ice grew as a solid annulus. The extent of the dendritic growth is largely determined by the temperature distribution that exists in the pipe at the time of ice nucleation. In this paper the factors effecting the temperature distribution and thus the extent of dendritic ice growth are examined to determine the conditions under which blockage by dendritic ice is likely to occur. The factors that are important are the cooling rate the pipe is exposed to, the ice nucleation temperature, and the type of thermal boundary condition the pipe wall provides.

Introduction

In utility systems used in cold regions water pipes are often unavoidably exposed to subfreezing environments. One way to prevent freezing in these pipes is to continually heat and circulate the water. A question arises, however, as to the time that one of these pipes may stand with no flow through it before it will be blocked by ice to the extent that flow cannot be restarted.

It is generally assumed that when a pipe is exposed to a subfreezing environment and ice begins to form it will grow as a solid cylindrical annulus extending in from the pipe wall. When calculations are made of the time required for a pipe to become blocked by ice, this assumption is normally used [2]. A recent study [1] has, however, shown that an entirely different ice morphology may occur in a pipe if there is no main flow through the pipe during the freezing process. In this case the stagnant water in the pipe will undergo a substantial supercooling before ice nucleation occurs. Thus when ice growth does occur it is growing into supercooled water which results in the formation of dendritic ice. This ice form consists of thin plate-like crystals of ice interspersed in the water medium. For water that has cooled $(T_f - T_n)$ below the freezing point, T_f, when ice nucleates the amount of supercooling enthalpy in the water is $C_w(T_f - T_n)$. During the dendritic ice growth phase this enthalpy is consumed by the growth of ice and at the end of the phase the water has returned to T_f. The quantity of the dendritic ice that is formed can therefore be related to the amount of supercooling by $C_w(T_f - T_n)/L$ where L is the latent heat of fusion. Only after this dendritic growth phase is complete will the normally assumed solid annulus of ice begin to grow in from the pipe wall.

It was shown in reference [1] that the dendritic ice crystals can form a dense enough matrix in the pipe that flow cannot be restarted in the pipe subsequent to their growth. For this dendritic ice blockage to occur, only a small fraction of the total water volume in the pipe need be frozen. On the other hand, an annular ice growth will only cause a complete pipe blockage when the entire water volume in the pipe is frozen. As a consequence of this difference the total amount of cooling and thus the time required to form a dendritic ice blockage is much less than that required for a complete blockage to occur due to an annular ice growth. It is therefore of considerable practical interest to determine the conditions under which a dendritic ice blockage may occur.

Reference [1] was confined to a study of the effects of dendritic ice when it grew in a pipe in which the water and pipe wall were at a uniform temperature at the time of ice nucleation. This situation would occur for a pipe subjected to a very slow rate of cooling. For a pipe experiencing a finite cooling rate, a temperature distribution will exist in the pipe at the time of ice nucleation. It might be anticipated that this temperature distribution will be a controlling factor in determining the subsequent distribution of dendritic ice growth in the pipe. For example, for a very high rate of cooling the zone of supercooled water may be confined to a thin zone adjacent to the pipe wall. The dendritic ice growth, which occurs only in the supercooled water, would not in that case result in a pipe blockage. The objective of the present study was to quantify the conditions of cooling under which

[1] Numbers in brackets designate References at end of paper.

Contributed by the Heat Transfer Division for publication in the JOURNAL OF HEAT TRANSFER. Manuscript received by the Heat Transfer Division February 25, 1977.

a dendritic ice blockage of a pipe can be expected.

The temperature distribution in a pipe that is being cooled will be determined by the natural convection processes occurring in the pipe. In this regard a number of experimental studies have been made of the natural convection that occurs during the cooling of a horizontal cylindrical container of water.

A cylinder with a wall temperature that was uniform around the circumference and was changing at a constant rate was studied by Deaver and Eckert [3]. Similar studies were done for a cylinder with a unifoirm wall heat flux by Maahs [4]. Numerical simulations have also been done for the uniform wall temperature case by Takeuchi and Cheng [5]. These studies apply for situations in which fluid properties are temperature independent in which case the cylinder experiences a quasi-steady temperature change; that is, temperature differences in the cylinder remain constant with time. Complicating factors that arise in cooling a cylinder of water to the freezing point are that the water passes through its maximum density point at 4°C immediately prior to freezing and as well the viscosity of water is strongly temperature dependent near 0°C. Experimental measurements [6] and numerical simulations [7] of a cylinder cooling through 4°C show that the inversion of the convective patterns that occurs causes a transient behavior that persists for some time after the inversion. These experimental and numerical studies were done only in the temperature range above 0°C. For the purposes of this study, it was necessary to extend these measurements into the supercooled regime to determine the temperature differences that exist in a pipe at the time of ice nucleation.

Since the quantity of dendritic ice that forms in supercooled water is controlled by the amount of supercooling, the temperature at which ice nucleates will also be an important factor in this study. A large number of studies have been made of ice nucleation temperatures. The main conclusion from these studies as summarized in [8, 9] is that ice nucleation in normal tap water is likely to occur on small particles, most likely insoluble mineral particles, in the water. Also the effectiveness of these particles as nucleation sites depends on the length of time they have been in contact with water and on the temperature of the water during this contact period. The nucleation temperature of a sample of water will therefore depend on its previous history. Measurements [8] made on tap water normally showed nucleation temperatures in the range 5–6°C for water from the cold water tap. Nucleation temperatures were up to 1°C colder for water from the hot water tap. Fresh water samples from lakes and streams had nucleation temperatures in the range 3–5°C. The nucleation temperatures have generally been found to be independent of the material of the container in which the tests were done, and essentially independent of the rate of cooling of the water for cooling rates less than 1°C/min [9].

Experimental Apparatus

A schematic of the typical cooling arrangement for testing a given size cylinder is shown in Fig. 1. Each end of the copper cylinder is blanked off with a pair of plexiglass flanges with an air gap between them. On the exterior of the cylinder is soldered a double helix of copper coolant tubes. The coolant is circulated in opposite directions through the two helii so as to maintain a uniform temperature along the length and around the circumference of the cylinder. The inside diameters of the cylinders tested with a uniform wall temperature were 25.4, 52.2, and 99.2 mm. In addition, three sizes—56.9, 94.5, and 137 mm—of plexiglass cylinders were tested. For the plexiglass cylinders the copper cooling jacket with its coolant tubes was made to fit tightly over the exterior of the plexiglass cylinder. The heat transfer to the water in this case was controlled by the thermal resistance provided by the wall of the plexiglass cylinder. This thermal resistance is constant around the cylinder. It will be seen that this arrangement produced an approximation to a uniform heat flux boundary condition. For most of the cylinders the temperature instrumentation consisted simply of a thermocouple on the center line of the cylinder and one against the wall at the top of the cylinder. These thermocouples were used to give a measure of the temperature differences existing in the cylinders for various cooling conditions. In the largest cylinder, 137 mm ID, six thermocouples were used to give a more complete profile of temperature along a vertical section through the cylinder.

The coolant which circulates around the cylinder wall was pumped from a controlled temperature bath, the temperature of which could be programed to vary in the desired fashion. For the uniform wall temperature experiments the temperature of the coolant was programed to decrease at a constant rate starting from room temperature. For the nonuniform wall temperature cylinders two cooling conditions were used. One was a constant rate of temperature decrease and the other was a step decrease from room temperature to some temperature below freezing. For a step change in the cooling jacket temperature the water in the cylinder experienced an approximately exponential decline toward this temperature. In the tests the cylinder filled with normal tap water would be allowed to come to equilibrium at room temperature. The cooling would then be commenced while temperatures in the cylinder were recorded. The water in the cylinder would cool till some point in the cylinder reached the ice nucleation temperature and then the growth of dendritic ice would occur. After the dendritic ice growth was complete photographs would be taken of the extent of its growth. In most of the photographs a uniform light field was applied at one end of the cylinder and the photograph taken from the other. The end view of the cylinder as seen in the photographs is shown on the right of Fig. 1.

Results

The complete cooling and dendritic ice formation process will first be illustrated for a 137-mm plastic cylinder. The water in the cylinder was initially at equilibrium at 15°C when the environment temperature was suddenly dropped to −10°C. Fig. 2 shows the time histories of the water temperatures at the center line and adjacent to the cylinder wall at the top and bottom of the cylinder. This figure shows clearly the inversion process occurring near 4°C. When the inversion is complete the temperature at the top of the cylinder becomes the cold spot in the cylinder and the temperatures at the center line and at the bottom are essentially equal. This behavior is quite different from that occurring for the uniform wall temperature cylinder as has been examined in references [6, 7]. In that case the uniformity of the wall temperature insures that the temperatures at the top and bottom of the cylinder remain equal throughout the cooling process. It will be seen that this results in much smaller temperature differentials developing in the cylinder. In the test run shown in Fig. 2 ice was ar-

Nomenclature

C = constant in the equation for critical cooling rate
C_w = heat capacity of water
L = latent heat of fusion
g = acceleration of gravity
h_{eff} = effective heat transfer coefficient of pipe wall, k_p/t_p
k_p = thermal conductivity of plastic
k_w = thermal conductivity of water
t = time
t_p = thickness of plastic wall
Bi = Biot number $k_pD/(k_wt_p)$
D = internal diameter of cylinder
H = cooling rate at cylinder center line
Ra = Rayleigh number $g|\beta|D^5H/(\alpha^2\nu)$
T_ℓ = temperature at cylinder center line
T_f = freezing temperature (0°C)
T_n = ice nucleation temperature
α = thermal diffusivity of water
β = volumetric coefficient of expansion of water
τ = characteristic time ($\alpha t/D^2$)
ν = kinematic viscosity of water
ΔT = difference in temperature between top and center line of cylinder
ΔT_c = temperature difference for conduction only $HD^2/(16\alpha)$

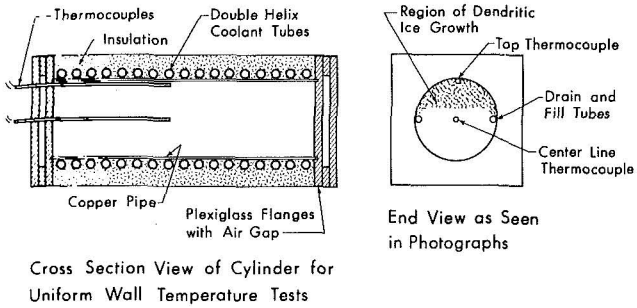

Fig. 1 Experimental arrangement for observing dendritic ice growth in a cylinder

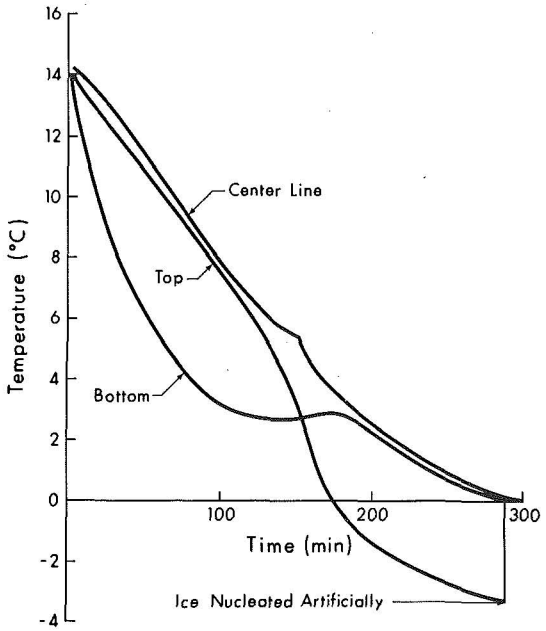

Fig. 2 Temperatures in a horizontal cylinder during cooling from 15°C until ice nucleates

tificially nucleated at −3.4°C so that photographs could be taken during the dendritic ice growth process. This artificial nucleation was produced by subjecting the cylinder to a small mechanical shock, that is, by tapping the exterior of the cylinder. Fig. 3 shows temperature profiles and photographs taken of the dendritic ice growth during its formation. It will be noted that most of the dendritic ice growth is completed in 5–10 min. If the supercooling had been allowed to continue to the normal nucleation temperature of −5 to −6°C the dendritic growth would have taken 20 s or less. In Fig. 3(*a*) the temperature profile on a vertical section through the cylinder is shown immediately prior to ice nucleation. Nucleation occurs at the top of the cylinder in cold water adjacent to the cylinder wall. A photograph taken immediately after nucleation is shown on the left of Fig. 3(*a*). The dendritic ice spreads from the nucleation site down toward the center of the cylinder and as well it grows down along the cylinder walls in the cold boundary layer region. During the process of growth the water temperature returns to a uniform temperature of 0°C.

By comparing the temperature profile in Fig. 3(*a*) with the final extent of the dendritic ice growth in Fig. 3(*d*) it can be seen that the dendritic growth progressed toward the center of the cylinder approximately to the −0.7°C temperature level. Previous studies [10] of dendritic ice growth in a container with an initial uniform supercooling have shown that for supercoolings less than about −2.0°C natural convection occurs in the melt ahead of the dendritic growth front. This natural convection tends to carry the supercooling enthalpy of the melt toward the growing dendrites. The result is that the dendritic growth does not entirely fill the container unless its initial supercooling is greater than about 2.0°C.

As an approximate guide it was found that if the supercooling at the cylinder center line was greater than 2°C when nucleation occurred, then complete blockage of the cylinder could be expected. Figs. 4(*a*), 4(*b*), and 4(*c*) are photographs showing the final extent of dendritic ice growth in a cylinder in which ice has been nucleated artificially at different times during the cooling process. The cooling rate and other conditions were the same for each case. It can be seen that a progression toward complete blockage occurs as the center line temperature approaches −2°C at the time of nucleation.

For nucleation occurring at a given temperature, say −5°C, the temperature difference between the top and the center line of the cylinder will determine whether the cylinder will be blocked by dendritic ice. That is, if due to the conditions of cooling experienced by the cylinder, a temperature difference of greater than 3°C exists the top of the cylinder, where nucleation occurs, will reach −5°C when the center is still above −2°C. Thus complete blockage would not occur. Alternately under a slower cooling rate where the temperature difference was less, complete blockage would occur. Figs. 4(*d*), 4(*e*), and 4(*f*) show the extent of blockage that results in a cylinder when the cylinder is cooled at different rates. In each of these tests the ice nucleation occurred naturally in the range −5.1 to −5.5°C. It can be seen that for the lowest cooling rate a complete blockage of the cylinder results. Note that all photographs other than that in Fig. 4(*d*) were taken at a shutter exposure at which the dendritic ice completely

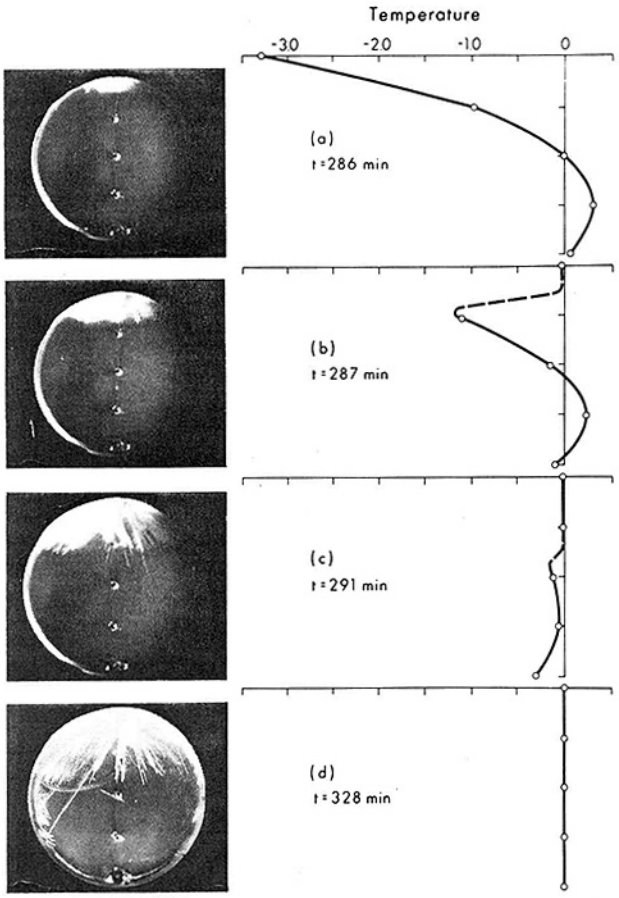

Fig. 3 The extent of dendritic ice growth and the temperature profile along a vertical section through the cylinder at various times during the dendritic ice growth phase

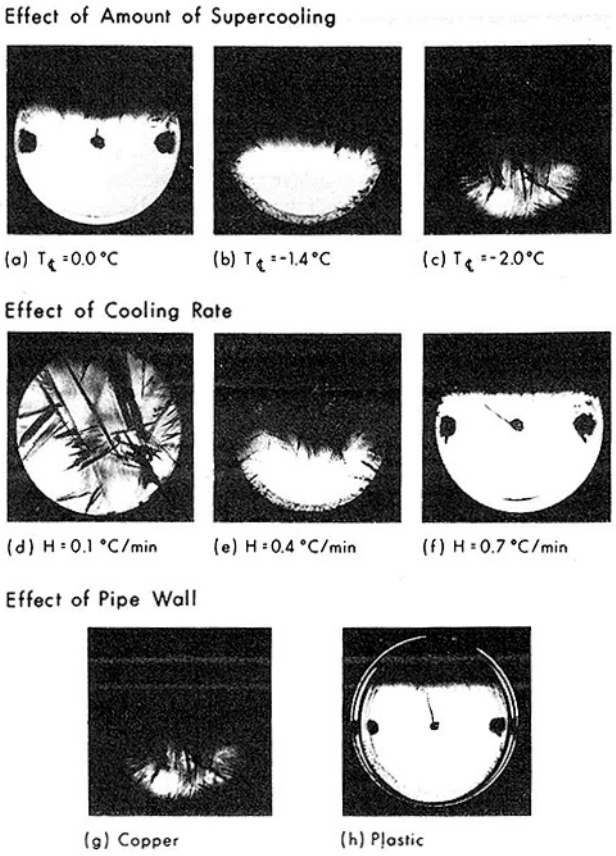

Fig. 4 The effects of various factors on the extent of dendritic ice growth in a cylinder: (*a*), (*b*), and (*c*) show the effect of the amount of supercooling existing at the cylinder center line at the time of ice nucleation; (*d*), (*e*), and (*f*) show the effect of cooling rate for a constant nucleation temperature, ≈ −5°C; (*g*) and (*h*) show the effect of the type of pipe wall (note all the photographs except (*d*) were taken at the same light exposure—for the photograph in (*d*) the light level was increased to reveal the structure of the ice in the pipe)

blocked off the light. To reveal the structure of the dendritic ice in Fig. 4(*d*) a much brighter light source and a longer exposure time were used. This photograph shows that the dendritic ice blockage is produced by a maze of interlacing ice crystals and is not a solid plug of ice as would be produced by the growth of an annulus of ice in from the pipe wall. In Figs. 4(*e*) and 4(*f*) it can be seen that the extent of the dendritic ice blockage becomes progressively less for pipes experiencing higher cooling rates. The decreased blockage occurring at the higher cooling rates also coincided with a larger temperature differential occurring between the center line and the top of the cylinder.

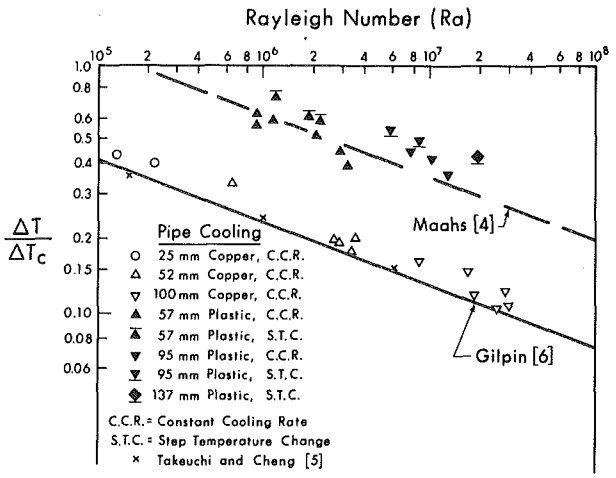

Fig. 5 Temperature differences existing in the pipes for various diameters and cooling conditions

In addition to the cooling rate and the cylinder diameter, the type of pipe wall is also important in determining the temperature differential and thus the extent of the dendritic blockage. The effect of the pipe wall is shown in Figs. 4(*g*) and 4(*h*). The cooling rates and the nucleation temperatures for the two cases shown are approximately the same; however, the cylinder in Fig. 4(*g*) was copper and that in Fig. 4(*h*) was plastic. It will be seen later that the effect of the pipe wall is due to the type of thermal boundary condition it provides for the water in the pipe.

In order to predict the conditions under which dendritic ice growth is likely to result in blockage of a pipe an examination must first be made of the temperature differentials that are likely to exist in a pipe at the time of ice nucleation. Fig. 5 shows an accumulation of these data for various cylinder diameters tested and for various cooling conditions.

In the figure the measured temperature difference between the top of the cylinder and the center line is normalized by the temperature difference ΔT_c that would have existed if only conduction heat transfer was occurring, $\Delta T_c = HD^2/16\alpha$. This ratio is proportional to the inverse of the Nusselt number. The Rayleigh number used was based on the rate of cooling as in reference [7].

$$\mathrm{Ra} = \left(\frac{g|\beta|}{\alpha^2\nu}\right) D^5 H$$

The cooling rate, H, was taken as the measured rate of decrease of the center line temperature at the time of nucleation.

A quasi-steady boundary layer model was developed in reference [6] for a uniform wall temperature cylinder cooled at a constant rate. The correlation given by this model,

$$\frac{\Delta T}{\Delta T_c} = 7.4\ \mathrm{Ra}^{-1/5} \tag{1}$$

is shown in Fig. 5. Results of numerical simulations made in reference [5] for the same problem are shown to give essentially the same values. The experimental measurements made in this study show that this quasi-steady approximation provides a good first approximation to the temperature differences measured for the copper cylinder. All the results fall in a band between the theory and a line at about 30 percent larger temperature difference. The slightly higher temperature differences actually recorded may be attributed to the interruption of the quasi-steady circulation patterns caused by the inversion process at 4°C and also the rapid variation of the physical properties of water occurring between 4°C and the nucleation temperature.

Temperature differences recorded in the plastic cylinders are also shown in Fig. 5. These measurements approximate a correlation derived from the results of Maahs [4] for a constant heat flux cylinder,

$$\frac{\Delta T}{\Delta T_c} = 19.4\ \mathrm{Ra}^{-1/5} \tag{2}$$

Biot numbers were calculated for the plastic cylinders based on the thermal resistance of the cylinder walls, that is,

$$\mathrm{Bi} = \frac{h_{\mathrm{eff}} D}{k_w} = \frac{k_p D}{k_w t_p}$$

In this expression the effective heat transfer coefficient, h_{eff}, of the pipe wall is k_p/t_p where k_p is the conductivity of the plastic and t_p is the wall thickness. Theoretically the results obtained for the plastic cylinders should approach the uniform wall temperature results for large enough Biot numbers. Biot numbers calculated for the plastic test cylinders were quite large, in the range 7–25; however, the measured temperature differences were still in much closer agreement with the constant heat flux limit than the uniform wall temperature limit. This evidence would suggest that the constant heat flux limit is probably closer to the actual situation for most cases, the only ex-

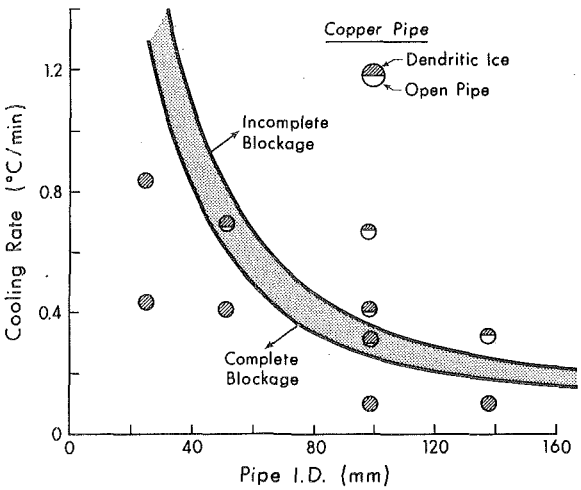

Fig. 6 The critical condition for dendritic blockage to occur in a copper (uniform wall temperature) pipe—nucleation temperature near −5°C

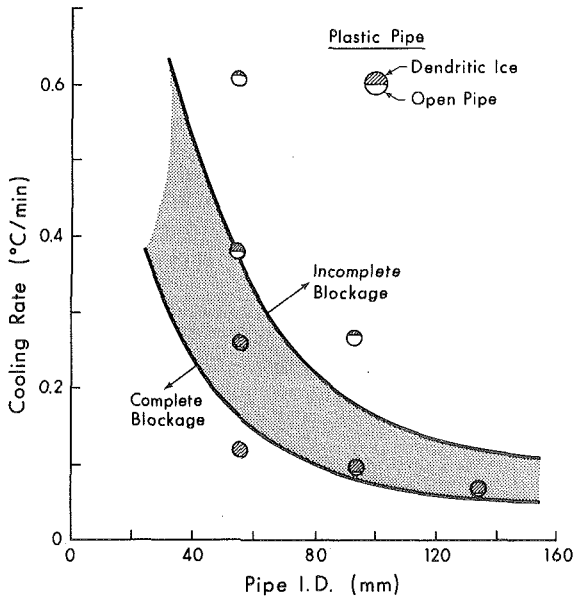

Fig. 7 The critical condition for dendritic blockage to occur in a plastic (uniform heat flux) pipe—nucleation temperature near −5°C

ceptions being those where the Biot number is extremely high such as the case of a copper pipe with a vigorous convective heat transfer from its exterior.

Transient effects probably also have a significant effect on the temperature differences measured in the plastic cylinders. This can be seen from the fact that for cases where the cooling jacket temperature underwent a step change the temperature differences in the cylinder are larger than in the cases where a constant cooling rate was used. This difference occurred even when the cooling rate of the water in the cylinder, as indicated by the Rayleigh number, was the same. In spite of these variations, all the results for the plastic cylinders can be bound within a band approximately ±30 percent of the quasi-steady constant heat flux correlation.

Qualitatively it was previously observed that at a high rate of cooling the dendritic ice growth in a pipe does not block its entire cross section. A complete blockage of the pipe in that case would occur at a much later time in the freezing process when an annulus of solid ice had grown in from the pipe wall closing off the cross section. The critical condition for a dendritic ice closure of the cross section was that the center of the pipe must have cooled to −2°C or lower at the time when the top of the cylinder reaches the nucleation temperature, T_n. Using this temperature difference with the correlations in equations (1) and (2) the critical condition or band of conditions can be specified. The expression for the critical cooling rate is of the form

$$H = C\left(\frac{-2 - T_n}{D}\right)^{5/4} \tag{3}$$

Taking into consideration the range of temperature differences measured and using the properties of water in the supercooled regime numerical values of C can be calculated. For the uniform wall temperature pipe C is in the range 21–29 when D is the pipe ID in mm, H is the cooling rate in °C/min, and the nucleation temperature is in °C. Similarly for the plastic wall pipe C is in the range 6.3–13.7.

Using −5°C as the nucleation temperature the critical conditions for the uniform wall temperature and uniform heat flux pipes have been plotted in Figs. 6 and 7, respectively. Also shown on these figures are symbols indicating the extent of dendritic ice growth observed for various pipe diameters and for various cooling rates. The observations made with the copper pipes are plotted with the uniform wall temperature criterion and those for the plastic pipes are plotted with the uniform heat flux criterion. For all these observations the ice nucleated naturally in the pipe within the temperature range −4.8 to 5.7°C. It can be seen that the observed extent of dendritic growth is consistent with the derived conditions for its blockage of the pipe. One concern about using the expressions of the form in equation (3) is that they strictly apply only to the case where a quasi-steady cooling of the pipe is occurring. Takeuchi and Cheng [5] have made some numerical calculations of the temperatures in a pipe for which cooling is suddenly started from a uniform temperature condition. Their results show that for characteristic times, $\tau = \alpha t/D^2$, greater than about 0.02 the temperature differences are within 20 percent of their quasi-steady values. Since the density maximum in water at 4°C will interrupt the quasi-steady cooling process, an estimate of the characteristic time can be made using the time taken to cool the water from 4°C to the nucleation temperature, that is,

$$\tau = \frac{\alpha(4 - T_n)}{HD^2}$$

Calculations of τ for various points on the critical curves in Figs. 6 and 7 show that the characteristic time at nucleation is greater than 0.02 for all diameters of pipe less than about 120 mm. This means that for larger diameter pipes transient cooling effects will become important. For small pipes quasi-steady conditions exist even though the critical cooling rates are much larger for these pipes. This occurs because the characteristic time increases as the inverse square of the pipe diameter.

The use of the foregoing theory for precise predictions would require a detailed knowledge of the ice nucleation temperature and its statistical variation for the type of water in the pipe in question. For most cases these measurements would not be available; however, the theory could still be used with typical nucleation temperatures to estimate, within a factor of two or three, the conditions under which a dendritic ice blockage is possible.

Discussion and Conclusions

In calculating the time that a pipe exposed to a subfreezing environment can be left without a main flow through it, it is necessary to know the type of ice blockage that can be expected in the pipe. The two types of ice blockage that can occur are: (*a*) a blockage of the pipe cross section by dendritic ice forming as a result of supercooling in the water, and (*b*) a subsequent blockage of the pipe by the growth of a solid annulus of ice in from the pipe wall. Since the dendritic ice blockage can occur early in the freezing history of the pipe when only a small fraction of the water in the pipe is frozen, it is essential to know the conditions under which such a dendritic ice blockage will occur.

From this study some general conclusions can be made about these conditions. First, small diameter pipes are much more likely to be

blocked by dendritic ice than large pipes. This is a direct result of the fact that the temperature differences occurring during cooling in the large pipes are much greater than those existing in the smaller pipe sizes. Second, the slower the cooling rate that the pipe is exposed to the more likely it is to be blocked by dendritic ice. At high cooling rates only the water near the pipe wall, primarily the top of the pipe, experiences a supercooling. The dendritic ice, which forms only in the supercooled water, does not therefore block the cross section of the pipe. Blockage of the pipe would only occur in this case when the solid annulus of ice had closed off the cross section.

A third factor that has an important effect on the temperature distribution in a cooling pipe and thus on the growth of dendritic ice in it is the thermal boundary condition provided by the pipe and its surroundings. This difference in thermal boundary conditions explains the difference in dendritic ice growth observed in the copper as opposed to the plastic pipes. Measurements showed that the temperature differences existing in a pipe with a uniform wall temperature were about 60 percent less than those that existed in a pipe with a uniform heat flux for the same rate of cooling. As a consequence, at a given cooling rate, the copper pipes, which had an approximately uniform wall temperature during cooling, were much more susceptible to a dendritic ice blockage than the plastic pipes were. The plastic pipes approximated a uniform heat flux conditon.

The final factor that has an important effect on the extent of the dendritic ice growth in a pipe is the ice nucleation temperature. The nucleation temperature determines the amount of supercooling and thus the amount of dendritic ice that forms. The typical nucleation temperature observed for tap water in these tests was around −5°C. This observation would appear to be consistent with other reported results for tap water [8]. Studies are continuing to obtain a better statistical sampling of nucleation temperatures.

It was found that these various factors could be related by an expression of the form of

$$H = C\left(\frac{-2 - T_n}{D}\right)^{5/4}$$

which gives the maximum cooling rate for which a dendritic ice blockage of a pipe is likely to occur. In this expression the constant, C, is dependent on the thermal boundary conditions imposed by the pipe. In deriving this expression it was assumed that a quasi-steady cooling process was occurring at the time that ice nucleated. Theoretical considerations would suggest that transient effects may become important for cylinder diameters greater than about 120 mm.

As has been pointed out the larger diameters of plastic pipe are the least likely to be blocked by dendritic ice; however, even for this type of pipe a 120 mm ID pipe would experience a dendritic ice blockage for cooling rates less than 3.5°C/hr. For most naturally occurring conditions it is difficult to image a situation that would produce a larger cooling rate than this. It would therefore appear that in general, blockage of a pipe by dendritic ice is a probable event. This means that the commonly used assumption of an annular growth of ice probably leads to a gross overestimation of the time required for a blockage to occur for most naturally occurring cooling conditions.

Acknowledgment

This work was supported by the National Research Council of Canada.

References

1 Gilpin, R. R., "The Effects of Dendritic Ice Formation in Water Pipes," *International Journal of Heat and Mass Transfer*, Vol. 20, 1977, p. 693.

2 ASHRAE, *Handbook of Fundamentals*, American Society of Heating, Refrigeration and Air Conditioning Engineers, 1974, p. 305.

3 Deaver, F. K., and Eckert, E. R. G. "An Interferometric Investigation of Convective Heat Transfer in a Horizontal Fluid Cylinder With Wall Temperature Increasing at a Uniform Rate," *Proceedings of the Fourth International Heat Transfer Conference*, Vol. 4, Paper NC1.1, ASME, New York, 1970.

4 Maahs, H. G., "Transient Natural Convection Heat Transfer in a Horizontal Cylinder," PhD thesis, University of Washington, 1964.

5 Takeuchi, M., and Cheng, K. C., "Transient Natural Convection in Horizontal Cylinders With Constant Cooling Rate," *Wärme-und Stoffübertragung*, Vol. 9, 1976, p. 215.

6 Gilpin, R. R., "Cooling of a Horizontal Cylinder of Water Through Its Maximum Density Point at 4°C," *International Journal of Heat and Mass Transfer*, Vol. 18, 1975, p. 1307.

7 Cheng, K. C., and Takeuchi, M., "Transient Natural Convection of Water in a Horizontal Pipe With Constant Cooling Rate Through 4°C," JOURNAL OF HEAT TRANSFER, TRANS. ASME, Series C, Vol. 98, 1976, p. 581.

8 Dorsey, N. E. "The Freezing of Supercooled Water," *Transactions of the American Philosophical Society*, Vol. 38, 1948, p. 247.

9 Hobbs, P. V., *Ice Physics*, Clarendon Press, Oxford, 1974, p. 496.

10 Gilpin, R. R. "The Influence of Natural Convection on Dendritic Ice Growth," *Journal of Crystal Growth*, Vol. 36, 1976, p. 101.

R. J. Pederson
E. M. Sparrow

Department of Mechanical Engineering,
University of Minnesota,
Minneapolis, Minn.

Heat Transfer From a Cylinder in Crossflow Situated in a Turbulent Pipe Flow

Experiments to measure the average heat transfer characteristics for a cross-flow cylinder situated in a pipe flow have been performed for various degrees of blockage. Three cylinders, respectively with diameters of one-fifth, one-third, and one-half that of the pipe, were employed. The experiments were carried out with both water and air as working fluids. Measurements were also made of the turbulence level in the flow approaching the cylinder. The measured heat transfer results were compared with literature information for a cylinder of large length-diameter ratio situated in cross-flow in an unbounded low-turbulence flow (i.e., the ideal case of a cylinder in cross-flow) and were found to be substantially higher. A number of schemes were investigated for correlating the cylinder-in-pipe results with those for the ideal case. As an outcome of these correlation efforts, adaptations of available ideal cylinder relations are presented from which cylinder-in-pipe results can be predicted with good accuracy.

Introduction

Forced convection heat transfer to or from a circular cylinder in cross-flow is widely encountered in engineering practice. As documented in [1, 2],[1] there is an extensive literature devoted to this subject which, in the main, is concerned with a cylinder of large length-diameter ratio situated in an unbounded flow. These conditions, together with a low level of turbulence in the approach flow, characterize the ideal case of a cylinder in cross-flow.

In practice, however, cross-flow cylinders are frequently situated in the ducts of heat exchangers and, in general, do not conform to the conditions of the ideal case. In such applications, the turbulence level may be appreciable and, in addition, the presence of the cylinder in conjunction with the confining effect of the duct walls can give rise to substantial blockage. In some instances, the interactions between the cylinder and the walls induce complex three-dimensional flows. These interactions and their effects are accentuated for smaller values of the cylinder length-diameter ratio, as is the effect of velocity profile nonuniformities in the flow approaching the cylinder.

The present research is concerned with the heat transfer characteristics of a cylinder in cross-flow situated in a turbulent fully developed pipe flow. The heat transfer coefficients for such a cylinder are expected to differ from those predicted by the available correlations for an ideal cylinder in cross-flow owing to the factors discussed in the foregoing paragraph. The flow field induced by the presence of the cylinder is particularly complex because the free flow area (i.e., the clearance between the cross-flow cylinder and the pipe wall) varies as a function of circumferential position around the wall of the pipe. As a consequence, the flow about the cylinder and in the wake is three-dimensional. In addition, the free stream turbulence level (~4 percent) of the fully developed pipe flow approaching the cylinder is sufficiently high to augment the heat transfer coefficients relative to those for a low turbulence approach flow [2].

The research has two objectives. The first is the measurement of heat transfer coefficients for a cross-flow cylinder situated in a pipe flow for various degrees of blockage, for a wide range of the Reynolds number, and for a moderate range of the Prandtl number. The second objective is the correlation of the cylinder-in-pipe results with those for the ideal cylinder in cross-flow. The motivation for such a correlation effort is to provide a computationally convenient method for future evaluation of cylinder-in-pipe heat transfer results by using the available relations for the heat transfer coefficient for the ideal cross-flow case. Two correlation formats will be employed. In one, the Nusselt number will be modified by a geometrical factor which involves the ratio of the cylinder and pipe diameters. In the other, a reference velocity accounting for blockage is introduced in the Reynolds number in lieu of the actual pipe mean velocity.

Three cross-flow cylinders were employed during the course of the research, respectively, with diameters of one-fifth, one-third, and one-half that of the pipe. The cylinders were designed to provide an isothermal surface for the forced convection heat transfer. Experiments were carried out for both air and water as working fluids, with

[1] Numbers in brackets designate References at end of paper.

Contributed by the Heat Transfer Division for publication in the JOURNAL OF HEAT TRANSFER. Manuscript received by the Heat Transfer Division January 25, 1977.

respective bulk Prandtl numbers of about 0.7 and 5.2 at the temperature level of the tests. The range of the Reynolds number, based on the mean velocity of the pipe flow, cylinder diameter, and bulk fluid properties, extended from 1000 to 62,000. The corresponding range of the pipe Reynolds number was from 5000 to 290,000. These experiments yielded average heat transfer coefficients and average Nusselt numbers.

To supplement the heat transfer experiments, measurements were made of the turbulence level in the flow approaching the cylinder. A hot-film anemometer was used for this purpose. The turbulence measurements in air were accomplished using standard methods, but those in water required special procedures for data acquisition and evaluation in order to cope with the problem of probe contamination. Consideration will be given to the role of turbulence level in the correlation of cylinder-in-pipe heat transfer results with those for the ideal cross-flow cylinder.

The heat transfer characteristics of a cylinder in cross-flow situated in a duct have been investigated to a moderate extent in the published literature, but no measurements have been reported for the flow configuration considered here. It appears that the main effort has been directed to the case of a cylinder in a rectangular duct under conditions where the flow is essentially two-dimensional [3–5].

The Experiments

Experimental Apparatus. The experimental apparatus was designed so that the test section and the flow metering section could be used with either water or air as the working fluid. For the water experiments, these components were incorporated into a closed-loop flow circuit. The air experiments were performed in the open-loop mode.

The test section was a continuous length of *pvc*[2] piping, 520 cm (17 ft) long and 7.25 cm (2.85 in.) in internal diameter, which housed the cross-flow cylinder whose heat transfer characteristics were to be investigated. To insure hydrodynamic development of the flow approaching the cylinder, it was positioned about 50 pipe dia downstream of the inlet cross section. The experiments were performed with the test section horizontal and with the crossflow cylinder oriented with its axis coincident with the horizontal diameter of the test section.

As noted earlier, three cross-flow cylinders were employed during the course of the experiments, with diameters equal to one-fifth, one-third, and one-half that of the test section pipe. Each cylinder consisted of an annular copper sheath which surrounded a cartridge-type electrical heating element. Continuous thermal contact between the casing of the heater cartridge and the sheath was assured by soldering. The respective copper sheaths had wall thicknesses of 0.254, 0.572, and 1.025 cm (0.1, 0.225, and 0.404 in.).

The arrangement for mounting the respective cylinders in the test section was devised to minimize extraneous heat losses from the ends of the cylinder. Such heat losses were a matter of concern in the airflow experiments (owing to the relatively low convective heat transfer coefficients), but are negligible in the water experiments. For the air experiments, each end of the cylinder was supported by an annular ring of min-K insulation which was, in turn, positioned by a fixture installed in the wall of the test section. The thermal conductivity of the min-K insulation is approximately equal to that of quiescent air. Inasmuch as the min-K cannot be effectively used in the presence of water and since heat losses are very small, end supports made of *pvc* were employed in the water experiments. Further information about the mounting of the cross-flow cylinders is available in [6].

The test section was surrounded along its entire length by a wooden trough filled with insulation. Silica aerogel powder, whose thermal conductivity is about two-thirds that of air, was employed to insulate the test section over a 30-cm length (12 in.) in the neighborhood of the location of the cross-flow cylinder. Fibrous wood insulation was used for the other parts of the test section. The minimum thickness of the insulation was about 9 cm (3½ in.).

For the water experiments, the test section was part of a closed loop whose components may be identified by tracing the path of the flowing fluid. Water discharged by the circulating pump is ducted to a heat exchanger which serves to remove heat imparted by the heated cross-flow cylinder and by mechanical dissipation throughout the loop. From the heat exchanger, the water is piped to the test section. To eliminate flow nonuniformities caused by bends situated in the intervening pipeline, a set of screens (15 layers, 9½ mesh per cm) is positioned just upstream of the test section inlet. After traversing the test section, the flow enters the return leg which delivers it to the metering section. Flow metering is accomplished via a calibrated orifice, and the metering section consists of straight pipe lengths of 30 and 10 dia, respectively, upstream and downstream of the orifice, plus flanges and pressure taps. From the exit of the metering section, the flow passes to the pump intake.

The loop is equipped with a pump by-pass line and a control valve, which are employed in setting the flow rate. It also contains an elevated standpipe fitted with a sight glass for monitoring and maintaining the liquid level in the system and for eliminating air prior to the initiation of a data run.

The air experiments were conducted utilizing an open loop system consisting of the test section, the flow metering section, and a centrifugal blower. These components were arranged in series along a straight path, without elbows or bends. The experiments were performed in the suction mode, with air being drawn into the test section inlet from the laboratory room.

Instrumentation. Temperature measurements were made at six surface locations on each of the cross-flow cylinders. At the centerspan of each cylinder (i.e., half way between the ends), thermocouple junctions were positioned at 0, 90, 180, and 270 deg from the forward stagnation point. In addition, junctions were positioned at 135 and 225 deg, respectively, offset from the centerspan by 1.27 and 2.54 cm (½ and 1 in.). The thermocouples were fabricated from 36 gage (0.0127 cm, 0.005 in.) teflon-coated copper and constantan wire, with the junctions being made by a special spot welding technique which resulted in a 0.018 cm (0.007 in.) spherical bead.

[2] Polyvinyl chloride.

Nomenclature

A = cylinder surface area
D = pipe diameter
DEV = statistic giving deviation from ideal case
d = cylinder diameter
h = average heat transfer coefficient, equation (1)
k = thermal conductivity
N_B = Nusselt-Prandtl group, equation (7)
N_F = Nusselt-Prandtl group, equation (6)
N' = correlation variable involving N
Nu = Nusselt number, hd/k
Pr = Prandtl number
Q = average rate of heat transfer
Re = Reynolds number, $\overline{U}d/\nu$
Re* = reference-velocity Reynolds number, U^*d/ν
Re′ = correlation variable involving Re or Re*
SPD = data spread statistic
T_B = fluid bulk temperature
T_F = film temperature
T_W = cylinder surface temperature
Tu = turbulence level, equation (22)
$\overline{U}$ = pipe mean velocity
U^* = reference velocity
ν = kinematic viscosity

Subscripts

B = bulk fluid properties
F = film properties

These thermocouples were laid in carefully machined spanwise grooves in the surface of the copper sheath. The grooves extended along the entire length of the cylinder. Each thermocouple was installed so that the copper wire was lead away to one end of the cylinder and the constantan wire was lead away to the other end. This separated lead wire arrangement enabled the groove depth and width to be held to a minimum. Once installed, the thermocouples were fixed in place with copper oxide cement, and the cement was carefully worked to conform smoothly to the contour of the copper sheath.

The fluid bulk temperatures at the inlet and exit of the test section were measured by L-shaped thermocouple probes. It was established, both by computation and experiment, that the bulk temperature of the flow approaching the cross-flow cylinder differed only slightly from the inlet bulk temperature. At the very most, the deviation was a few tenths of a percent of the cylinder wall-to-bulk temperature difference. Furthermore, initial traverses had shown the inlet fluid temperature to be uniform to within the resolving power of the instrumentation.

All thermocouples were made from calibrated wire. The thermocouple emf's were read and recorded by a digital voltmeter.

The rate of flow through the test section was measured with one of three orifices that had been fabricated according to ASME specifications. The orifices were calibrated by the weigh tank method. To provide a check on the orifice flow rate determinations and to facilitate the calibration of the hot-film anemometer, an L-shaped impact probe was installed near the downstream end of the test section. The impact opening was positioned at the center line of the cross section and a static tap implanted in the pipe wall.

A thermo systems hot film probe situated 15.3 cm (6 in.) upstream of the cross-flow cylinder was employed to measure the center-line turbulence intensity of the flow approaching the cylinder. (The probe was removed from the test section during the heat transfer runs.) The probe was calibrated in situ. The calibration for the airflow case followed standard procedures. However, in the case of water, an innovative approach had to be devised to cope with the effects of contamination. These effects were manifested as a decrease of the bridge voltage with time, as the contaminants accumulated. The calibration procedure is described in detail in Appendix E of [6].

Experimental Procedure. The procedures employed in the execution of the experiments are presented in [6]. Of particular importance in the water runs were the steps taken to eliminate air from the system. For the water runs, the bulk temperature of the flow approaching the cylinder was maintained at approximately 32°C (90°F) for all of the data runs, which corresponds to a bulk Prandtl number of 5.2. The cylinder heat transfer rates (i.e., power input to the heater) were adjusted so that the wall-to-bulk temperatures were in the range 8 to 9°C (14 to 16°F). For the air runs, the test section bulk temperature corresponded to that of the laboratory room. The wall-to-bulk temperature differences were maintained in the range 16 to 20°C (29 to 36°F).

With regard to the Reynolds number range, the upper end was fixed by the respective capacities of the pump and blower. The cutoff value at the lower end was selected to avoid significant heat conduction losses from the ends of the cross-flow cylinder.

Data Reduction. The average heat transfer coefficient for the cross-flow cylinder was evaluated from the defining equation

$$h = (Q/A)/(T_W - T_B) \tag{1}$$

In cognizance of the precautions taken to eliminate conduction end losses, the heat transfer rate Q was determined from the electric power input to the heater imbedded in the cylinder. For the evaluation of the cylinder surface area A, it was necessary to take account of the fact that the line of contact between the cylinder and the inner wall of the test section pipe is curved rather than straight. The final expression for A involves the complete elliptic integral of the first kind ([6, Appendix F]).

The cylinder wall temperature T_W was determined by averaging the six measured surface temperatures for each data run. For the experiments with water, variations among the measured temperatures for a given run were less than ±7.5 percent of the mean wall-to-bulk temperature difference; for the air experiments, the corresponding variations were ±0.6 percent. The relatively larger temperature variations for the case of water reflect the conflict between the heat conduction in the copper sheath and the variations of the convective heat transfer coefficient.

On the basis of information available in the literature, it can be inferred that the aforementioned surface temperature variations do not significantly affect the average Nusselt number results. In the cross-flow experiments of [7] for the case of uniform heat flux, measured deviations fromthe mean surface temperature on the order of 35 percent of the wall-to-bulk temperature difference were encountered. These experiments covered the Reynolds number range between 10,000 and 50,000. On the other hand, it was found in [8] that the average Nusselt numbers for uniform wall temperature and uniform wall heat flux differed by 10–15 percent at a Reynolds number of about 10,000 (the largest Re value of the experiments). It may, therefore, be concluded that the present results do not differ significantly from those for uniform wall temperature.

The bulk temperature T_B appearing in equation (1) is that of the flow approaching the cross-flow cylinder. As mentioned earlier, the change in bulk temperature between the test section inlet and the cross-flow cylinder is negligible, so that T_B was evaluated from the measurements of the inlet temperature.

The experimentally determined average heat transfer coefficients were recast in dimensionless form in terms of the Nusselt number

$$\mathrm{Nu} = hd/k \tag{2}$$

where d is the diameter of the cross-flow cylinder. For the presentation of the results, either of two Reynolds numbers, Re or Re*, will be employed, where

$$\mathrm{Re} = \overline{U}d/\nu, \qquad \mathrm{Re}^* = U^*d/\nu \tag{3}$$

The quantity $\overline{U}$ is the mean velocity of the flow approaching the cylinder, whereas U^* is a reference velocity used in relating the present results with those for the ideal cylinder in cross-flow.

The properties appearing in the dimensionless groups were evaluated either at the film temperature $T_F = \frac{1}{2}(T_W + T_B)$ or at the bulk temperature, and corresponding identifying subscripts F and B are appended.

Results and Discussion

The presentation of results will begin with the basic Nusselt number—Reynolds number data, both in terms of film and bulk properties. Next, the results are compared with literature representations for the ideal cylinder in cross-flow. This comparison serves to motivate a correlation effort aimed at bringing together the present cylinder-in-pipe results with those for the ideal cylinder. A number of correlation schemes are examined, and the most effective schemes are identified. Finally, the role of turbulence level as an explicit correlation parameter is discussed.

To facilitate the interpretation of the results, a common set of data symbols is employed in all of the figures. These symbols are exhibited in Table 1, where d/D is the ratio of the diameters of the cross-flow cylinder and the pipe.

Nusselt Number Results. The basic heat transfer results are presented in Figs. 1 and 2, where the Nusselt number is plotted as a function of the Reynolds number. These figures correspond, respectively, to the use of film and bulk fluid properties. The overall range of the Reynolds number extends from about 1000 to 70,000, and the Nusselt number increases monotonically with Reynolds number. A power law dependence of the form $\mathrm{Nu} \sim \mathrm{Re}^{\ell}$ can be fitted to the data, with $\ell \sim 0.6$, but curve fitting will be deferred until the data have been brought together in a more compact form.

Further examination of these figures indicates that at a given Reynolds number, there is a tendency for the Nusselt number to increase as the cylinder diameter increases. This characteristic is more marked for the water data than for the air data. The expected separation of the water and air data is also in evidence. Comparison of Figs.

Table 1 Data symbols

Symbol	Fluid	d/D
○	air	1/5
□	air	1/3
△	air	1/2
●	water	1/5
■	water	1/3
▲	water	1/2

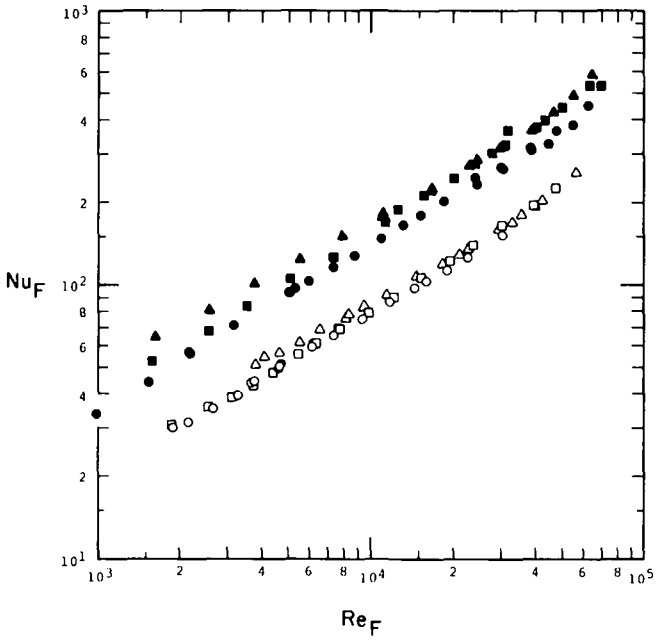

Fig. 1 Nusselt number results based on film properties

Table 2 Constants for equations (4) and (5)

(a) Equation (4)

Re_F	C_1	m
35 to 5×10^3	0.655	0.471
5×10^3 to 5×10^4	0.166	0.633
5×10^4 to 2×10^5	0.0208	0.814

(b) Equation (5)

Re_B	C_2	n
40 to 10^3	0.51	0.5
10^3 to 2×10^5	0.26	0.6
2×10^5 to 10^6	0.076	0.7

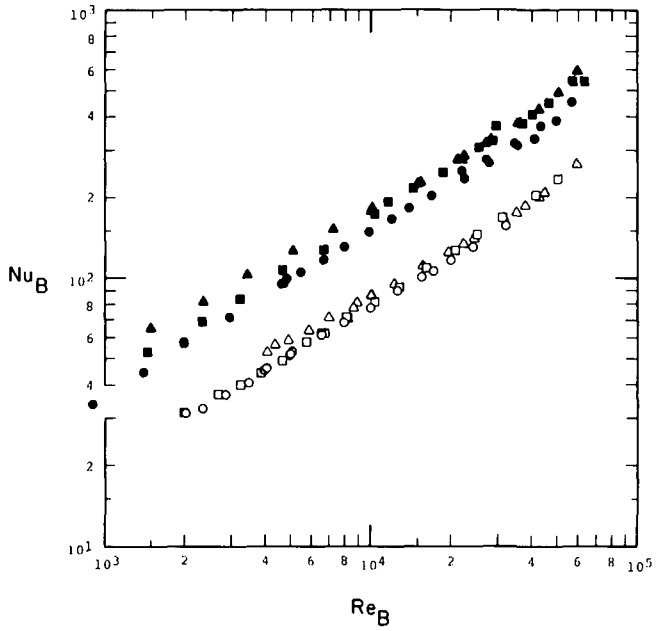

Fig. 2 Nusselt number results based on bulk properties

1 and 2 shows that the data spread is about the same in both figures, so that no clear preference for either film or bulk properties is indicated.

Next, it is relevant to compare the present Nusselt number results with those for the ideal cylinder in cross-flow. An examination of the literature reveals that there are many candidate representations of the available data for the ideal cross-flow case, but that none have gained universal acceptance. The representations of [2, 1], respectively, based on film and bulk properties, appear well founded and are used here. They are

$$\mathrm{Nu}_F\mathrm{Pr}_F^{-1/3} = C_1\mathrm{Re}_F{}^m \tag{4}$$

$$\mathrm{Nu}_B\mathrm{Pr}_B{}^{-0.37}(\mathrm{Pr}_W/\mathrm{Pr}_B)^{1/4} = C_2\mathrm{Re}_B{}^n \tag{5}$$

equation (4) is, in actuality, an adaptation of that of [2], which was specific to air ($\mathrm{Pr}\sim0.7$). In accordance with a widely employed generalization (e.g., [9]), the $\mathrm{Pr}_F{}^{-1/3}$ factor was appended and the constants C_1 adjusted accordingly. The values of C_1, m, C_2, and n appropriate to equations (4) and (5) are listed in Table 2. In addition, to facilitate a more compact presentation, it is convenient to define

$$\mathrm{N}_F \equiv \mathrm{Nu}_F\mathrm{Pr}_F{}^{-1/3} \tag{6}$$

$$N_B \equiv \mathrm{Nu}_B\mathrm{Pr}_B{}^{-0.37}(\mathrm{Pr}_W/\mathrm{Pr}_B)^{1/4} \tag{7}$$

The data of the present experiments and the representations for the ideal cylinder in cross-flow are brought together in Figs. 3 and 4, respectively, for film and bulk properties. The solid lines in the respective figures correspond to equations (4) and (5).

From an examination of these figures, it is clear that the Nusselt numbers for a cylinder situated in a pipe are substantially higher than those for an ideal cylinder in cross-flow. There are two factors which contribute to this behavior. One of these is the blockage effect, which gives rise to relatively high velocities around the circumference of the cylinder. The other is free stream turbulence, the level of which is quite high in a pipe flow (~4 percent) as contrasted to the low values (a few tenths of a percent) encountered in quality wind tunnels.

The Prandtl number factors that appear in the N_F and N_B groupings serve to integrate the water and air data, but the systematic in-

crease of the Nusselt number with increasing cylinder diameter has not been affected.

Correlation Criteria. For computational convenience in applications, it is highly desirable to correlate the cylinder-in-pipe Nusselt numbers with those for the ideal cross-flow cylinder. A number of correlation schemes will be examined. To help assess the degree of success of the various correlations, graphical comparisons will be made. In addition, two statistical measures of the quality of the correlation will be presented. The first of these indicates the spread of the data, and the second measures the deviation of the data from the representation for the ideal cylinder. These statistics will be, respectively, denoted by *SPD* and *DEV*.

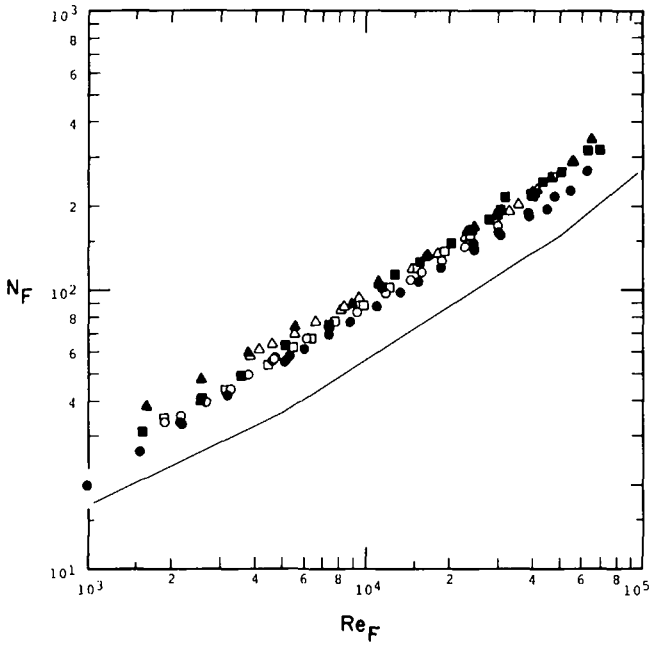

Fig. 3 Comparison of cylinder-in-pipe Nusselt numbers with those for the ideal cross-flow case, film properties

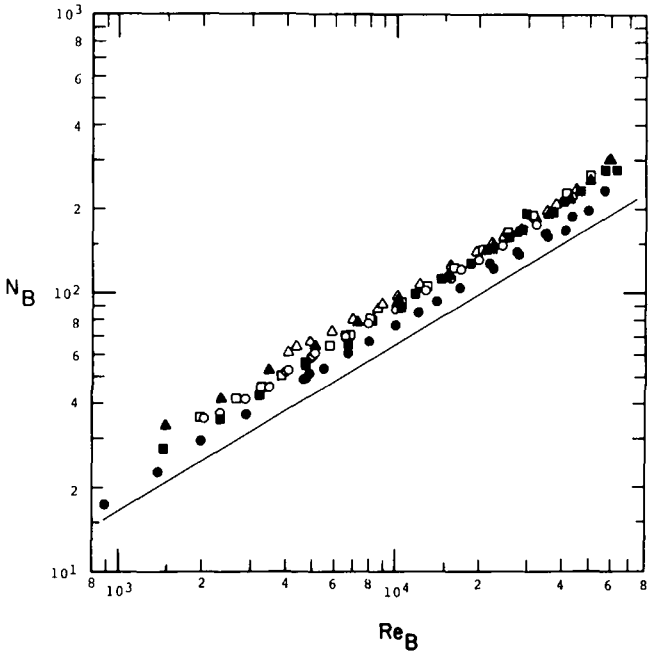

Fig. 4 Comparison of cylinder-in-pipe Nusselt numbers with those for the ideal cross-flow case, bulk properties

Let any candidate pair of correlation variables be denoted by N' and Re', where N' involves the Nusselt and Prandtl numbers (e.g., N_F or N_B), and suppose that the data have been rephrased in terms of these variables. As a first step in evaluating the spread in the data, a least squares curve of the form

$$N' = C_3(\mathrm{Re}')^{\ell} \tag{8}$$

is passed through the data (without regard to the ideal cylinder results). If the value of N' predicted by equation (8) for a given Re' is denoted by N'_p and the corresponding experimental value is N'_e, then the spread of the data is defined as

$$SPD = [\Sigma((N'_e/N'_p) - 1)^2/(K - 2)]^{1/2} \tag{9}$$

where the sum is extended over all K data points for the three cylinders and two Prandtl numbers ($K = 118$). The quantity $(K - 2)$ is the number of degrees of freedom associated with the data after the two constants C_3 and ℓ have been determined. Thus, *SPD* is an estimate of the standard deviation of the data about its least squares fit in the form of equation (8).

The desired end result is that the data, when phrased in terms of N' and Re', closely approximate either

$$N'_F = C_1(\mathrm{Re}'_F)^m \tag{10a}$$

for film properties, or

$$N'_B = C_2(\mathrm{Re}'_B)^n \tag{10b}$$

for bulk properties. The constants C_1, m, C_2, and n are those for the ideal cylinder, equations (4) and (5) and Table 2. For a given value of Re', equation (10*a*) or (10*b*), whichever is appropriate, can be employed to provide the predicted value of N' corresponding to the ideal cylinder relationship. If this predicted value is denoted by N'_i ($i \sim$ ideal) and if the experimental value for the same Re' is denoted by N'_e, then the deviation *DEV* can be defined by

$$DEV = [\Sigma((N'_e/N'_i) - 1)^2/(K - 2)]^{1/2} \tag{11}$$

This statistic is a measure of the ability of the ideal cylinder relationship to predict the data.

When the value of the deviation *DEV* is very close to that of spread *SPD*, then the ideal cylinder representation qualifies as a least squares fit of the data. In addition, the smaller the value of *SPD*, the better the fit. The success of a given correlation scheme will be judged by its ability to minimize the values of *SPD* and *DEV*, as well as on its ability to make them equal.

To serve as a baseline for the subsequent correlation efforts, the spread and deviation statistics for the uncorrelated results of Figs. 3 and 4 are presented as the initial entries in Table 3. Clearly, there are significant differences between *SPD* and *DEV* in both cases.

The correlation effort to be described in the subsequent sections will be carried out without explicit consideration of the effects of turbulence level. The role of turbulence level as a correlation parameter will be discussed later in the paper.

Correlation Based on Film Properties. In [3], a film-property correlation relating the results for a cylinder in a rectangular duct with those for the ideal cross-flow case was achieved by dividing the Nusselt number by the factor $(1 + \sqrt{d/w})$, where w is the duct width. As an adaptation of that approach, w will be replaced by D and the correlation variables N' and Re' defined as

$$N'_F = N_F/(1 + \sqrt{d/D}), \qquad \mathrm{Re}'_F = \mathrm{Re}_F \tag{12}$$

where N_F is expressed by equation (6). A presentation of the data in terms of these variables is shown in Fig. 5 along with a solid line representing the ideal cylinder relationship. As seen from the figure as well as from the *SPD* and *DEV* statistics listed in Table 3, the correlation is very successful.

Notwithstanding this success, efforts were also made to correlate on the basis of a reference velocity via the definitions

$$N'_F = N_F, \qquad \mathrm{Re}'_F = \mathrm{Re}^*_F \tag{13}$$

in which Re^*_F is based on a reference velocity U^*. A procedure for finding U^*, designated as the point matching approach, will now be described.

For each cylinder, the Nu_F value for each data run was introduced into the ideal cylinder relation (4) and a value of Re_F was calculated. This Re_F was compared with the actual Re_F for the data run, and the ratio was identified as $U^*/\overline{U}$ for that run, where the use of U^* in lieu of $\overline{U}$ gives rise to exact agreement between equation (4) and the data run. This procedure was repeated for all the data runs for a given cylinder, and the individual $U^*/\overline{U}$ were averaged. For the three cylinders, the average values of $U^*/\overline{U}$ were found to be 1.89, 2.12, and 2.30, respectively, for d/D = 1/5, 1/3, and 1/2. The trend whereby the reference velocity increases with blockage is physically reasonable.

The data were rephrased in terms of the variables of equation (13) and evaluated using the aforementioned values of $U^*/\overline{U}$. The rephrased data are plotted in Fig. 6 along with the ideal cylinder relationship (solid line). From the figure, it is seen that the correlation is not as successful as that of Fig. 5, as is corroborated by Table 3. The reason for the somewhat unsatisfactory outcome evidenced in Fig. 6 is that the individual $U^*/\overline{U}$ ratios which contribute to the respective averages show a marked dependence on Reynolds number ([6, Fig. 5.6]).

Table 3 Correlation statistics (percent)

Identification	SPD	DEV
Fig. 3	7.90	61.3
Fig. 4	8.88	38.6
Fig. 5	4.85	5.78
Fig. 6	4.95	8.06
Fig. 7	6.08	14.3
Fig. 8	5.98	5.96
Eqs. (15), (16), (17)	7.61	10.3
Eqs. (15, (16), (18)	10.9	11.5
Eqs. (15), (19)	6.37	18.7
Eqs. (15), (20)	7.14	26.7
Eqs. (15), (21)	6.69	28.2

On the basis of the foregoing, it was concluded that there was little to be gained in further examination of the reference velocity approach when used in conjunction with a film-property correlation. The correlation represented by equation (12) and evidenced in Fig. 5 appears to be entirely satisfactory.

Correlation Based on Bulk Properties. The first bulk-property correlation scheme to be examined is the analogue of the film-property correlation (12), that is,

$$N'_B = N_B/(1 + \sqrt{d/D}), \qquad Re'_B = Re_B \tag{14}$$

where N_B is expressed by equation (7). The representation of the data in terms of these variables is presented in Fig. 7 along with the ideal cylinder relationship. It is evident from both the figure and from Table 3 that the correlation is not very successful. This outcome is not altogether unexpected, since the correlation variables were first devised in connection with film properties rather than with bulk properties [3].

The reference velocity concept will now be used as a basis for correlation. First, the point matching approach will be employed. The description of this approach, as presented in the paragraph following equation (13), continues to apply here, except that equation (5) is used in lieu of equation (4). The individual $U^*/\overline{U}$ ratios for the data runs corresponding to a given cylinder diameter were found to be substantially less dependent on Reynolds number than in the film-property correlation. This lesser dependence stems from the fact that the exponent n in equation (5) has a constant value over the entire Reynolds number range of the experiments (see Table 2(b)).

The average values of $U^*/\overline{U}$ for the respective d/D = 1/5, 1/3, and 1/2 are 1.46, 1.74, and 1.90. Then, with the correlation variables

$$N'_B = N_B, \qquad Re'_B = Re^*_B \tag{15}$$

the data and the ideal cylinder representation are presented in Fig. 8. The correlation is seen to be very good, and it is especially worthy

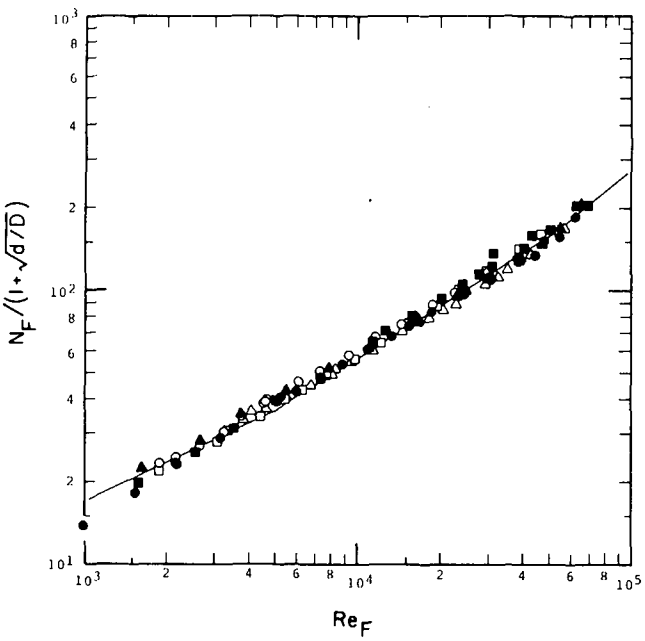

Fig. 5 Correlation based on replacing Nu with Nu/(1 + $\sqrt{d/D}$), film properties

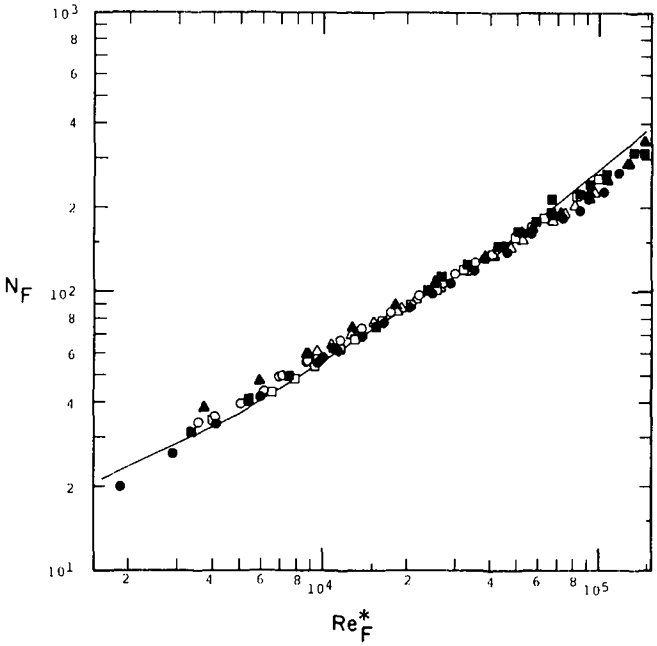

Fig. 6 Correlation based on the use of a reference velocity determined via the point matching approach, film properties

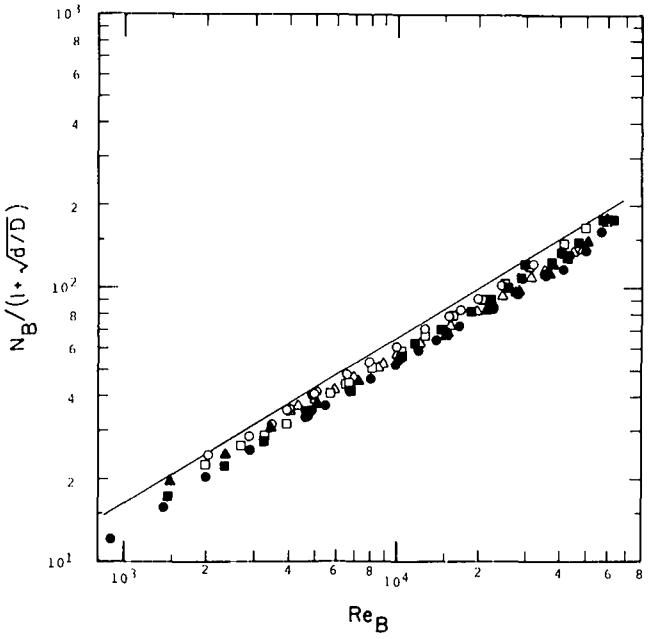

Fig. 7 Correlation based on replacing Nu with Nu/(1 + $\sqrt{d/D}$), bulk properties

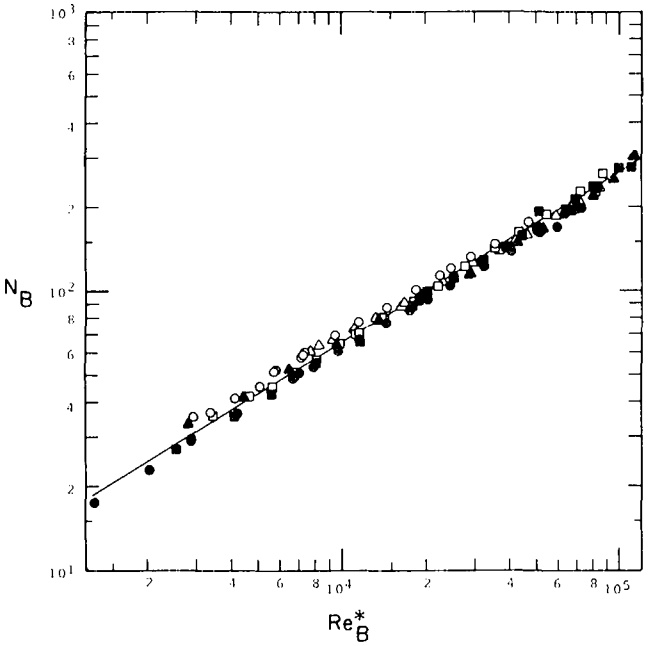

Fig.8 Correlation based on the use of a reference velocity determined via the point matching approach, bulk properties

of note that the *SPD* and *DEV* statistics (Table 3) are essentially identical. Thus, the ideal cylinder representation serves as a least squares fit of the data.

Other reference velocities proposed by investigators of related problems will now be reviewed. One approach involves the definition of an effective flow cross sectional area A^* such that

$$U^* = (A_d/A^*)\overline{U} \tag{16}$$

where A_d and $\overline{U}$, respectively, represent the flow cross section and mean velocity of the unobstructed duct. In [1, 4], A^* was defined as

$$A^* = \frac{\text{duct volume} - \text{cylinder volume}}{\text{cylinder diameter}} \tag{17}$$

Both the duct and cylinder volumes correspond to the streamwise length of the cylinder. Alternatively, in heat exchanger practice (e.g., [1]), A^* is defined as

$$A^* = \text{minimum flow cross section} \tag{18}$$

By employing the reference velocities evaluated from equation (16) in conjunction with equations (17) and (18), the data were recast in terms of the correlation variables of equation (15). These results have been plotted in Figs. 5.9 and 5.10 of [6]. These figures are not presented here owing to space limitations, but the correlation statistics *SPD* and *DEV* are listed in Table 3. It is seen that while the A^* definition of equation (17) gives a better correlation than does that of equation (18), it is not as effective as the point matching approach.

Other U^* definitions that were examined are those of [10, 11, and 5], which are, respectively,

$$U^* = \overline{U}(1 + 1.333(d/D)^2 + 0.318C_D(d/D)) \tag{19}$$

$$U^* = \overline{U}(1 + \sqrt{d/D})^{1/2} \tag{20}$$

$$U^* = \overline{U}(1 + 1.18(d/D)^2)^3 \tag{21}$$

where in (20) and (21) the pipe diameter D has been substituted in place of the duct width w that appeared in the original forms of these equations. In (19), the cylinder drag coefficient C_D was evaluated at the average Reynolds number of the experiments. The N'_B, Re'_B graphs corresponding to equations (19)–(21) are available as Figs. 5.11–5.13 of [6], where generally unsatisfactory correlation is in evidence. Table 3 clearly reflects this outcome.

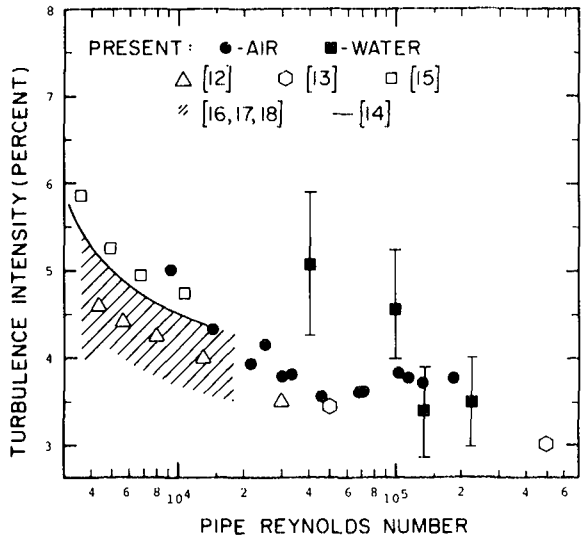

Fig. 9 Turbulence intensity at center line of pipe

On the basis of the foregoing, it may be concluded that the most satisfactory bulk-property correlation is that based on reference velocities obtained from the point matching approach.

Role of Turbulence Level. A basic consideration in any correlation effort is the question of whether the effect of turbulence level need be displayed explicitly. Prior investigators of related problems have not included turbulence effects in their data representations. As noted earlier, center-line turbulence measurements were performed as part of the present investigation. The results are reported in Fig. 9 in terms of the turbulence intensity parameter Tu defined as

$$Tu = \frac{\text{root-mean-square axial fluctuations}}{\text{time-averaged axial velocity}} \tag{22}$$

where both numerator and denominator are evaluated at the pipe

center line. The abscissa is the pipe Reynolds number based on the center-line velocity. The figure also includes data from a number of other investigations which encompass a variety of measurement techniques (hot wire anemometer, hot film anemometer, laser-Doppler velocimeter).

The water data (black squares) provide perspective on the effects of probe contamination. The data points at the two higher Reynolds numbers were taken shortly after the probe had been cleaned, and these data are in good agreement with the air results. The other two data points for water were taken after three hours of operation subsequent to cleaning and are believed to be strongly affected by contamination.

Excluding the contamination-affected points, the general agreement among the data in Fig. 9 is worthy of note, especially in view of the diversity of measurement techniques that were employed. On this basis, it can be concluded that the turbulence level for pipe flows is a well-defined and reproducible property. Furthermore, since the pipe-flow turbulence level is not an independent parameter, there is no special need to correlate its effect. Even if such a correlation were to be sought, there is insufficient reliable information to enable its fruition.

Concluding Remarks

It has been demonstrated that the cylinder-in-pipe Nusselt number results of the present experiments can be correlated with those for the case of an ideal cylinder in cross-flow. On the basis of the correlations, cylinder-in-pipe Nusselt numbers can be predicted by employing adaptations of the ideal cylinder representations. For film properties, equation (4) is applicable provided that Nu_F is replaced by $Nu_F/(1 + \sqrt{d/D})$. In the case of bulk properties, equation (5) is to be used with Re^*_B replacing Re_B. The reference velocity $U^*/\overline{U}$ can be obtained from a curve passed through the points $U^*/\overline{U} = 1, 1.46, 1.74$, and 1.90, respectively, for $d/D = 0, 1/5, 1/3$, and $1/2$.

References

1 Zukauskas, A., "Heat Transfer From Tubes in Crossflow," *Advances in Heat Transfer*, Academic Press, New York, Vol. 8, 1972, p. 93.

2 Morgan, V. T., "The Overall Convective Heat Transfer From Smooth Circular Cylinders," *Advances in Heat Transfer*, Academic Press, New York, Vol. 11, 1975, p. 199.

3 Robinson, W., Han, L. S., Essig, R. H., and Heddleson, C. F., "Heat Transfer and Pressure Drop Data for Circular Cylinders in Ducts and Various Arrangements," Ohio State University Research Foundation, Report 41, 1951.

4 Perkins, H. C., and Leppert, G., "Forced Convection Heat Transfer From a Uniformly Heated Cylinder," JOURNAL OF HEAT TRANSFER, TRANS. ASME, Series C, Vol. 84, 1962, p. 257.

5 Akilbayev, Z. S., Isatayev, S. I., Krashtalyev, P. A., and Masleyeva, N. V., *Probl. Teploenerg. Prikl. Teplofiz.*, Vol. 3, 1966, p. 180.

6 Pederson, R. J., "Heat Transfer From a Cylinder in Crossflow Situated in a Turbulent Tube Flow," PhD thesis, University of Minnesota, 1976.

7 Perkins, H. C., Jr., "Forced Convection Heat Transfer From a Uniformly Heated Cylinder," PhD thesis, Stanford University, 1963.

8 Boulos, M. I., and Pei, C. T., "Dynamics of Heat Transfer From Cylinders in a Turbulent Air Stream," *International Journal of Heat and Mass Transfer*, Vol. 17, 1974, p. 767.

9 Kays, W. M., *Convective Heat and Mass Transfer*, McGraw-Hill, New York, 1966, p. 228.

10 Vincenti, W. G., and Graham, D. J., "The Effect of Wall Interference Upon the Aerodynamic Characteristics of an Airfoil Spanning a Closed-Throat Circular Wind Tunnel," NACA Report 849, 1946.

11 Knudsen, J. G., and Katz, D. L., *Fluid Dynamics and Heat Transfer*, McGraw-Hill, New York, 1958.

12 Pennell, W. T., Sparrow, E. M., and Eckert, E. R. G., "Turbulence Intensity and Time-Mean Velocity Distributions in Low Reynolds Number Pipe Flows," *International Journal of Heat and Mass Transfer*, Vol. 15, 1972, p. 1067.

13 Laufer, J., "The Structure of Turbulence in Fully Developed Pipe Flow," NACA Technical Report 1174, 1954.

14 Bourke, P. J., Pulling, D. T., Gill, L. E., and Denton, W. H., "The Measurement of Turbulent Velocity Fluctuations and Turbulent Temperature Fluctuations in a Supercritical Region by a Hot-Wire Anemometer and a Cold-Wire Resistance Thermometer," Symposium on Heat Transfer and Fluid Dynamics of Near Critical Fluids, Paper No. 9, Institution of Mechanical Engineers, London, 1968.

15 Pike, E. B., Jackson, D. A., Bourke, P. J., and Page, D. I., "Measurement of Turbulent Velocities from the Doppler Shift in Scattered Layer Radiation," *Journal of Scientific Instruments*, Vol. 1, 1968, p. 727.

16 Goldstein, R. J., and Hagen, W. F., "Turbulent Flow Measurements Utilizing the Doppler Shift of Scattered Layer Radiation," *Physics of Fluids*, Vol. 10, 1967, p. 1349.

17 Goldstein, R. J., Adrian, R. J., and Kreid, D. K., "Turbulent and Transition Pipe Flow of Dilute Polymer Solutions," *I and E Fundamentals*, Vol. 8, 1969, p. 498.

18 Goldstein, R. J., and Kreid, D. K., "Fluid Velocity Measurement From the Doppler Shift of Scattered Layer Radiation," Heat Transfer Laboratory, Department of Mechanical Engineering, University of Minnesota, Minneapolis, Minn., Report No. 85, 1968.

K. S. Rao[2]
V. W. Nee
K. T. Yang

University of Notre Dame
Notre Dame, Ind.

Mass Diffusion From a Point Source in a Neutral Turbulent Shear Layer[1]

An investigation of the diffusion of pollutants in neutral surface layer of atmosphere is analyzed here based on a simple phenomenological differential field theory of turbulent shear flows. The variation of the effective turbulent viscosity is governed by a rate equation. The analytical model studied in this work consists of mass diffusion from a continuous crosswind point source at ground level in a turbulent shear layer. The system of governing equations is solved by finite-differences giving the pollutant distributions, eddy diffusivities, and velocity profiles at various downstream locations for various initial and boundary conditions. The computed diffusion data are presented and compared favorably with the available experimental results.

Introduction

One of the fundamental characteristics of turbulent motion is diffusion. The study of this phenomenon has attracted much interest for quite a long time with a wide range of approaches from very empirical to purely mathematical. Recently, increased attention has been focused on this problem especially for its social relevance as related to air pollution. In the atmospheric surface layer, the diffusion of pollen, radioactive materials, dust, bacteria and viruses, smoke and gases produced by factories, etc., are affected profoundly by the action of turbulent diffusion.

The analysis of this problem is generally difficult. The nonlinear and indeterminate nature of the governing mean equations of motions prohibits exact analysis for all problems of turbulent flow. The presence of the concentration field here in the turbulent diffusion problem will introduce an added difficulty in the coupled fluctuating velocity and concentration fields. For the calculation of turbulent diffusion from a point source, the Gaussian model has been used most frequently. Several parameters have to be selected in order to compute the concentration field [1, 2].[3] The gradient-transfer theory, with its rationale provided by the mixing-length hypothesis, is also a familiar approach to the theoretical study of atmospheric diffusion problems. In this theory, based on Eulerian description, the mean mass flux terms are related to the mean concentration gradients through the introduction of the coefficients of turbulent diffusion.

For the ground-level source, there is an increase in the mixing action as the vertical growth of the plume proceeds, and this increase is associated with the height in the flow field. Therefore, the effective turbulent diffusivity will be more adequately specified as a function of height above the ground instead of a constant. Up to now, the understanding of this effective turbulent diffusivity variation under various flow conditions is not as extensive as that of the turbulent or eddy viscosity. To capitalize on the current knowledge on eddy viscosity or the Reynolds stress, the usual approach is to utilize an extension of the Reynolds analogy to turbulent mass transfer. In the conventional constant turbulent Schmidt number treatment, the variation of the turbulent diffusivity is rigidly controlled by the turbulent viscosity variation. In order to let the eddy diffusivity vary in height, as well as in the downstream direction, a general differential field treatment of the turbulent viscosity is desirable.

The present analysis is based on a nonlocal phenomenological differential field theory proposed by Nee and Kovasznay [3] for quasi-parallel turbulent shear flows. It is formulated by taking into account the relevant mechanisms of the turbulent motion. A rate equation is used to govern the variation of the effective turbulent viscosity, and it has only two universal constants to be determined from experiments. If, in addition, the "law of wall" is regarded as universal, then the number of universal constants for wall turbulence is reduced to one. Further elaborations and refinements are still possible at, of course, the expense of simplicity. This approach has been applied with success to the study of the diffusion of a line source in a neutral surface layer by Rao, Nee, and Yang [4] and also in temperature-stratified surface layers [5].

The analytical model studied in this work deals with mass diffusion from a continuous point source at ground level in a two-dimensional turbulent boundary layer. Among the various known approaches, the "K-theory" is particularly pertinent to the present analysis. The commonly used assumptions in the "K-theory" include constant turbulent mass diffusivity coefficients and/or some simple power law velocity profile. In the present approach, however, the turbulent mass diffusivity coefficients are allowed to vary as a function of height, and

[1] This research was supported by the EPA under Grant R801945.

[2] Present address: National Oceanic and Atmospheric Administration, Oak Ridge, Tenn.

[3] Numbers in brackets designate References at end of paper.

Contributed by the Heat Transfer Division for publication in the JOURNAL OF HEAT TRANSFER. Manuscript received by the Heat Transfer Division August 9, 1976.

the velocity as well as the mass concentration fields are obtained from a differential field calculation.

Laboratory investigations of mass diffusion from continuous sources located at the solid boundary of a two-dimensional boundary layer were reported by Davar [6], Malhotra and Cermak [7], Poreh [8], and others.

Theoretical Formulation

The neutral meteorological micro-scale surface layer over a homogeneous terrain is considered as a two-dimensional turbulent boundary layer with a zero pressure gradient. The flow velocity corresponds to the strong wind conditions in the atmosphere and the boundary layer approximations can therefore be introduced in the equation of motion. For the velocity range of the wind under usual weather conditions, the effects of compressibility can be neglected. The present analysis is for the case where the averaged mean motion of the wind is steady. The diffusion model studied here consists of a continuous point source of constant strength G at ground level, emitting a dynamically passive pollutant which diffuses within the surface layer. The solid boundary is assumed to be perfectly reflecting with respect to the diffusive matter. The mean concentration field is three-dimensional, though the mean flow field is considered here as two-dimensional.

The continuity and momentum equations for the mean flow field can then be written as

$$\frac{\partial U}{\partial x} + \frac{\partial V}{\partial y} = 0 \tag{1}$$

$$U\frac{\partial U}{\partial x} + V\frac{\partial U}{\partial y} = \frac{\partial}{\partial y}\left(\nu\frac{\partial U}{\partial y} - \overline{u'v'}\right) \tag{2}$$

The Reynolds stress is expressed as the product of the mean velocity gradient and the eddy viscosity ϵ_M:

$$-\overline{u'v'} = \epsilon_M \frac{\partial U}{y} \tag{3}$$

The total turbulent viscosity, $n(x, y) = \nu + \epsilon_M(x, y)$, is assumed to be governed by a rate equation, proposed by Nee and Kovasznay [3], as follows:

$$U\frac{\partial n}{\partial x} + V\frac{\partial n}{\partial y} = \frac{\partial}{\partial y}\left(n\frac{\partial n}{\partial y}\right) + A(n-\nu)\frac{\partial U}{\partial y} - \frac{Bn(n-\nu)}{y^2} \tag{4}$$

The effects of convection, diffusion, generation, and decay are each represented in the rate equation by appropriate terms involving only two universal constants, $A = 0.133$ and $B = 0.8$. A detailed discussion on the formulation of the rate equation and value of these constants can be found in reference [3]. From this equation, the well-known "Prandtl's mixing length theory" can be derived as a limiting case inside the wall region, where the convection and diffusion effects are negligible.

The mean equation for the three-dimensional concentration field in the boundary layer can be written as

$$U\frac{\partial C}{\partial x} + V\frac{\partial C}{\partial y} = \frac{\partial}{\partial y}\left(D\frac{\partial C}{\partial y} - \overline{v'c'}\right) + \frac{\partial}{\partial z}\left(D\frac{\partial C}{\partial z} - \overline{w'c'}\right) \tag{5}$$

Introducing the concept of eddy diffusivity of mass for the concentration field, we have,

$$-\overline{v'c'} = \epsilon_{Dy}\frac{\partial C}{\partial y} \tag{6}$$

$$-\overline{w'c'} = \epsilon_{Dz}\frac{\partial C}{\partial z} \tag{7}$$

where ϵ_{Dy} and ϵ_{Dz} are the principal diagonal components of the eddy diffusivity tensor in y- and z-directions, respectively.

The molecular Schmidt number and turbulent Schmidt numbers characterizing mass diffusivity in the vertical and lateral directions are introduced here respectively as,

$$\mathrm{Sc} = \nu/D \tag{8}$$

$$\mathrm{Sc}_{ty} = \epsilon_M/\epsilon_{Dy}$$

$$\mathrm{Sc}_{tz} = \epsilon_M/\epsilon_{Dz} \tag{9}$$

The total turbulent diffusivity of mass $n_D(x, y, z) = D + \epsilon_D(x, y, z)$, can be related to the turbulent viscosity distribution, $n(x, y)$, through the definition of Schmidt number as follows:

$$n_{Dy} = \nu\left[\frac{1}{\mathrm{Sc}} + \left(\frac{n}{\nu} - 1\right)\Big/\mathrm{Sc}_{ty}\right] \tag{10}$$

$$n_{Dz} = \nu\left[\frac{1}{\mathrm{Sc}} + \left(\frac{n}{\nu} - 1\right)\Big/\mathrm{Sc}_{tz}\right] \tag{11}$$

The concentration, rate, momentum, and continuity equations for the mean flow form a closed system of parabolic partial differential equations for prescribed values of the Schmidt numbers. Given the boundary and initial conditions, a direct forward integration using a digital computer can be performed to determine the distributions of the variables U, V, n, n_D, and C at any downstream location. The boundary conditions on the solid boundary are

$$\text{at } y = 0, \quad U = V = 0, \quad n = \nu$$

$$n_D\frac{\partial C}{\partial y} = 0 \qquad \text{for } x > x_c \tag{12}$$

where x_c is the value of x at the location of the source. The last condition in (12) expresses the zero mass flux through the solid boundary. The boundary conditions far away from the wall are the usual free stream conditions,

$$y \to \infty,\ U \to U_\infty,\ n \to \nu,\ C \to 0 \tag{13}$$

Nomenclature

C = mean concentration
$C_{\max}$ = maximum value of local concentration profile
c' = instantaneous turbulent component of concentration
D = molecular diffusivity of mass
G = constant strength of point source
$k \equiv 0.41$, Von Kármán's constant
$n \equiv \epsilon_M + \nu$, total turbulent viscosity
$n_D \equiv \epsilon_D + D$, total turbulent diffusivity of mass
$N \equiv n/\nu$
$N_D \equiv n_D/\nu$
$\mathrm{Sc} \equiv \nu/D$, molecular Schmidt number
$\mathrm{Sc}_t \equiv \epsilon_M/\epsilon_D$, turbulent Schmidt number
$u_* \equiv$ friction velocity
$u_c \equiv u_*$ at $n = n_0$
u', v', w' = instantaneous turbulent components of velocity in x-, y-, and z-directions, respectively
U, V = mean velocity components in x- and y-directions, respectively
U_∞ = ambient velocity
x = downstream distance measured from the origin of turbulent boundary layer
x_c = value of x where the source is located
x_i = value of x where the initial concentration profile is specified
x_0 = value of x where the initial velocity and turbulent viscosity profiles are specified
x_s = downstream distance measured from the location of the source
$X = xu_c/\nu$
$Y \equiv yu_c/\nu$
y = distance measured from and normal to the ground; vertical coordinate
$Z \equiv zu_c/\nu$
z = distance measured normal to the x-y plane; lateral coordinate
δ = velocity boundary layer thickness
η = vertical characteristic length scale of the diffusion plume
ϵ_D = eddy diffusivity of mass
ϵ_M = eddy viscosity
ν = kinematic viscosity
σ = lateral characteristic length scale of the diffusion plume

For mass diffusion from a ground-level point source, the maximum concentration occurs at $y = z = 0$. And in a two-dimensional mean flow, the lateral concentration distribution is symmetrical about the plane $z = 0$. These conditions can be expressed by the equation

$$\text{at } z = 0, \quad \frac{\partial C}{\partial z} = 0 \tag{14}$$

Also, as

$$z \to \infty, C \to 0 \tag{15}$$

The initial conditions are given as

$$U(x_0, y) = U_0(y), \quad n(x_0, y) = n_0(y), \quad C(x_0, y, z) = C_0(y, z) \tag{16}$$

In equation (16), x_0 is the value of x where the numerical computations commence.

The constant strength of the source, G, defined as the quantity of diffusing matter per unit time, can be obtained as the integral form of equation (5):

$$G = 2\int_0^\infty \int_0^\infty U(x, y) \cdot C(x, y, z)\, dy\, dz = \text{constant} \tag{17}$$

To calculate the concentration field, the values of the Schmidt numbers in equations (10) and (11) must be specified. No universal agreement regarding the variation of the turbulent Schmidt numbers is known, as can be seen from the divergent views in the experimental investigations [6, 7, 9–12].

In order to maintain turbulent mass diffusion coefficients as functions of space without the usual severe restriction of forcing them to be constants, the Reynolds analogy is adopted here to relate turbulent mass diffusivity coefficients to the eddy viscosity, which is a function of space variables and governed by the rate differential equation.

With the foregoing considerations in mind, the turbulent Schmidt number Sc_{ty} is assumed to have the value of 0.9 according to the experiments of Poreh [8] and the value of Sc_{tz} is 0.45 according to the experiments of Davar [6] and Malhotra and Cermak [7]. The assumption of constant Schmidt number is adopted here as a first approximation for its simplicity and convenience. More sophisticated model can be incorporated.

Finite Difference Solution

An explicit finite difference scheme has been developed to solve the governing equations together with the initial and boundary conditions. The outputs of this computing program give the eddy diffusivities, velocity, and concentration profiles at various downstream locations. The inputs of the program can be easily adjusted to any given source and weather conditions.

Since the details of the general finite difference numerical method have already been given by Rao, Nee, and Yang [4], only that portion concerning the three-dimensional diffusion problem is presented here.

The finite difference form of the nondimensional diffusion equation (5) is expressed as follows:

$$\begin{aligned} C_{i+1,j,k} = {} & C_{i,j,k} - \frac{\Delta x}{2\Delta y}\frac{V_{i,j}}{U_{i,j}}(C_{i,j+1,k} - C_{i,j-1,k}) \\ & + \frac{\Delta x}{4(\Delta y)^2}\frac{1}{Sc_{ty}}\frac{(N_{i,j+1} - N_{i,j-1})}{U_{i,j}}(C_{i,j+1,k} - C_{i,j-1,k}) \\ & + \frac{\Delta x}{(\Delta y)^2}\left(\frac{1}{Sc} + \frac{(N_{i,j-1})}{Sc_{ty}}\right)\frac{C_{i,j+1,k} - 2C_{i,j,k} + C_{i,j-1,k}}{U_{i,j}} \\ & + \frac{\Delta x}{(\Delta z)^2}\left(\frac{1}{Sc} + \frac{(N_{i,j-1})}{Sc_{tz}}\right)\frac{C_{i,j,k+1} - 2C_{i,j,k} + C_{i,j,k-1}}{U_{i,j}} \end{aligned} \tag{18}$$

In the present computations, a uniform grid spacing of $\Delta x = \Delta y/2 = \Delta z/2$ is used with the boundary layer thickness divided into 15 cells (Fig. 1). The procedure of numerical integration, the stability criteria, and the computing time required are discussed in detail by Rao [13].

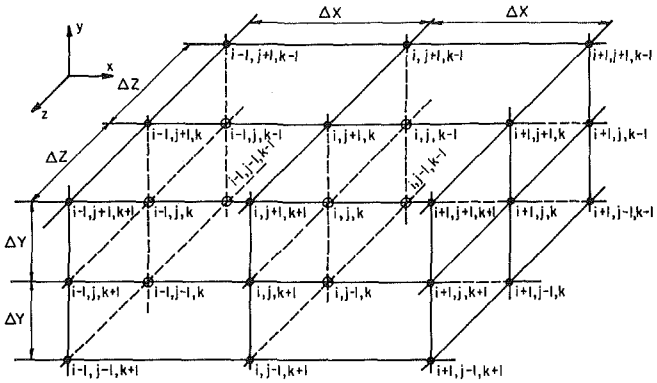

Fig. 1 Three-dimensional uniform grid scheme

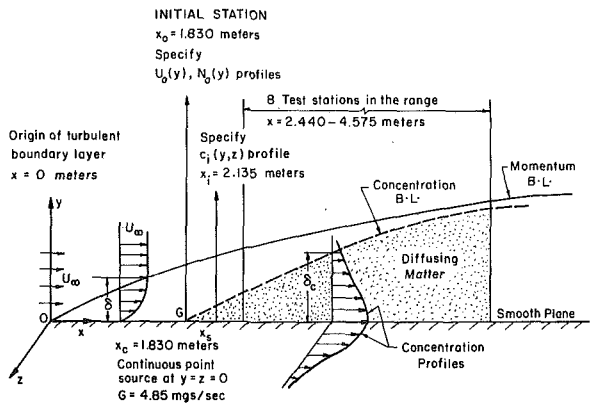

Fig. 2 Schematic diagram of flow conditions

The finite difference code is flexible enough to allow for arbitrary changes in wall temperature T_w or roughness and other boundary conditions in the flow direction by the specification of $T_w(x)$ and a roughness shift of the mean velocity. For the purpose of comparing the results of the present analysis with the experimental data, calculations have only been made here based on the flow conditions of available experiments, namely, the work of Davar [6] and Malhotra and Cermak [7] for the neutral case. A schematic diagram of the flow conditions is shown in Fig. 2.

From the measured data [6, 7], the initial profiles of the velocity and mass concentration are known. However, the needed initial turbulent viscosity profile is not available from the experiment and consequently the quasi-similarity profile of Nee and Kovasznay [3] which agrees well with the measurements of Townsend [14] and Klebanoff [15] for the flat-plate turbulent boundary layer is utilized here [4].

As discussed in the previous analysis [3, 4, 16], the present theory is employed to predict the flow field above the sublayer and up to the free stream. It is, however, important to mention here that the law of wall provides only a functional form of the mean velocity, and the friction velocity u_*, which appears in the law of the wall profile is calculated directly from the present theory.

For a ground-level point source, the concentration distribution at any location will have a maximum value along the line of symmetry which can be expressed with sufficient accuracy by a third order polynomial as demonstrated in [4].

Discussion of Results

The diffusion plume over the distance calculated is completely submerged in the boundary layer, and it can be regarded as a good

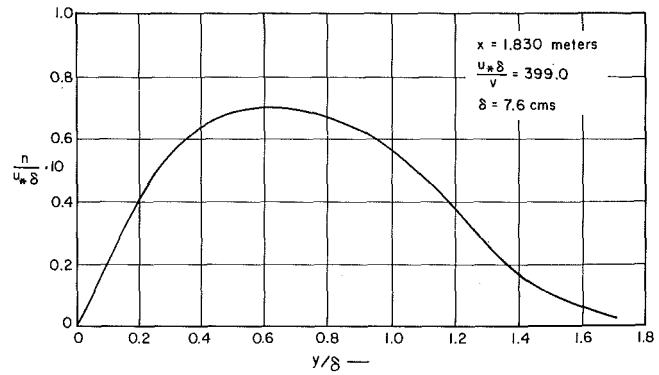

Fig. 3 Calculated eddy viscosity variation across the boundary layer

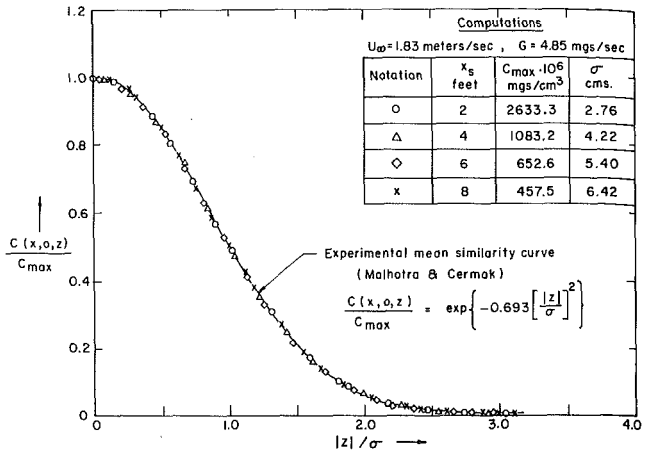

Fig. 5 Lateral concentration distribution—similarity profile

model for approximation of the atmospheric diffusion from a ground-level source [8]. Calculations have been made on the flow conditions of available experimental data given in [6, 7]. A typical variation of the eddy viscosity across the boundary layer is shown in Fig. 3. The vertical concentration distribution at several downstream locations is plotted nondimensionally in Fig. 4 as $C(x, y, 0)/C_{max}$ versus y/η. Here $\eta(x)$ is the vertical similarity length of the diffusion plume defined by

$$C(x, \eta\ 0)/C_{max}(x, 0, 0) = 0.5 \tag{19}$$

The calculated diffusion data have a good fit to the curve given by the equation

$$\frac{C(x, y, 0)}{C_{max}} = \left(\exp -0.693 \frac{y}{\eta(x_s)}^{1.8}\right) \tag{20}$$

The corresponding experimental mean similarity curve, due to Malhotra and Cermak [7], is also shown in Fig. 4 for comparison. This curve is described by the equation

$$\frac{C(x, y, 0)}{C_{max}} = \left(\exp -0.693 \frac{y}{\eta(x_s)}^{1.4}\right) \tag{21}$$

The lateral concentration distribution at several downstream locations is plotted nondimensionally in Fig. 5 as $C(x, 0, z)/C_{max}$ versus z/σ, where $\sigma(x_s)$ is the lateral similarity length of the diffusion plume defined by

$$C(x, 0, \sigma)/C_{max}(x, 0, 0) = 0.5 \tag{22}$$

The calculated diffusion data show an excellent agreement to the experimental mean similarity curve [7] described by the equation

$$\frac{C(x, 0, z)}{C_{max}} = \left(\exp -0.693 \frac{z}{\sigma(x_s)}^{2}\right) \tag{23}$$

The similarity scales of the diffusion plume namely, η, σ, and C_{max}, are functions of x_s, the downstream distance from the source. Field measurements indicated that the peak concentration at any point downwind of a continuous source varies directly as the strength of the source and approximately inversely as the mean wind velocity, while the time-mean height and width of a continuously generated cloud show little variation with mean wind speed [2]. Within the range of the experimental variables, the laboratory data [6, 7] also support this statement. In Fig. 6, the computed values of η, σ, and $U_\infty \cdot C_{max}$ at several stations are plotted against the downstream distance x_s. The variations of these parameters can be given as

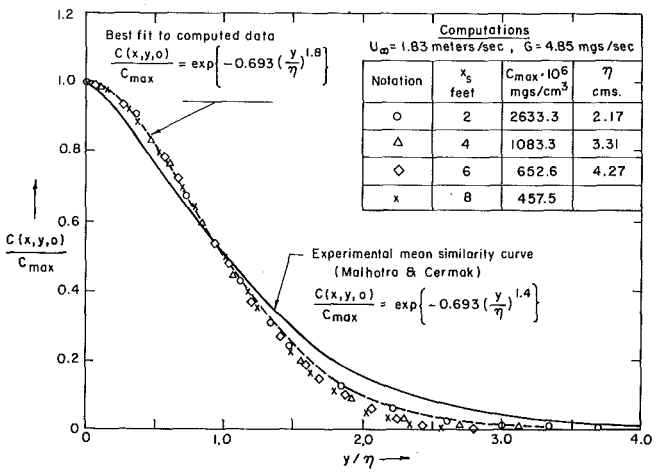

Fig. 4 Vertical concentration distribution—similarity profile

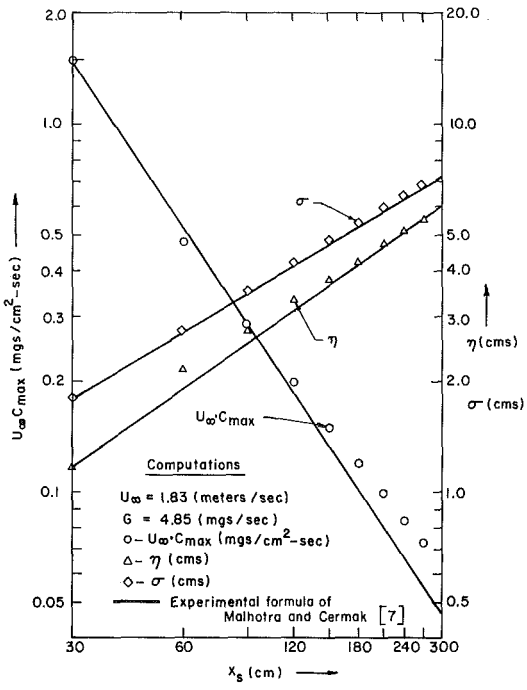

Fig. 6 Variation of the similarity scales with distance from the point source

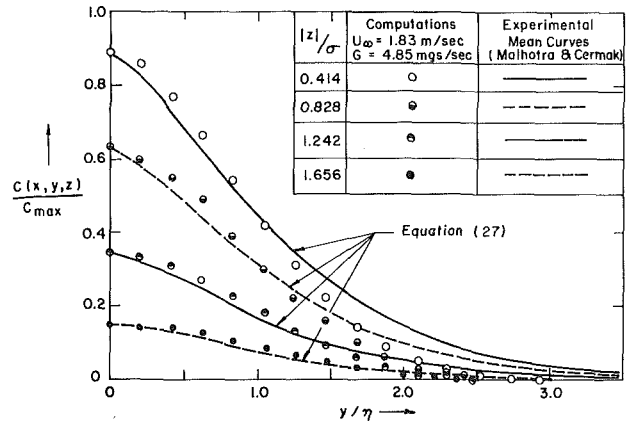

Fig. 7 Vertical concentration profiles at various lateral distances

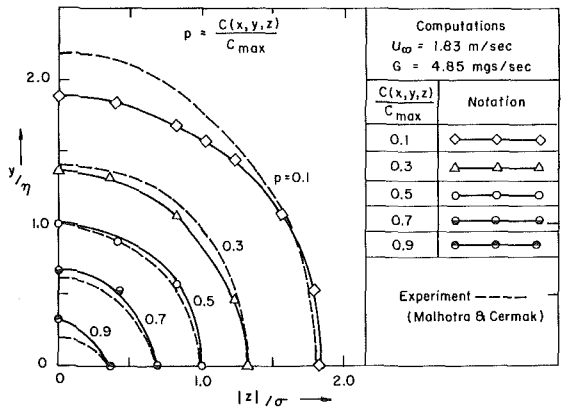

Fig. 9 Nondimensional isoconcentration contours over plume cross section

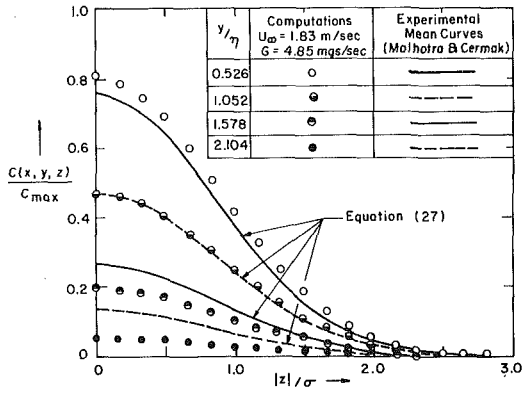

Fig. 8 Lateral concentration profiles at various heights

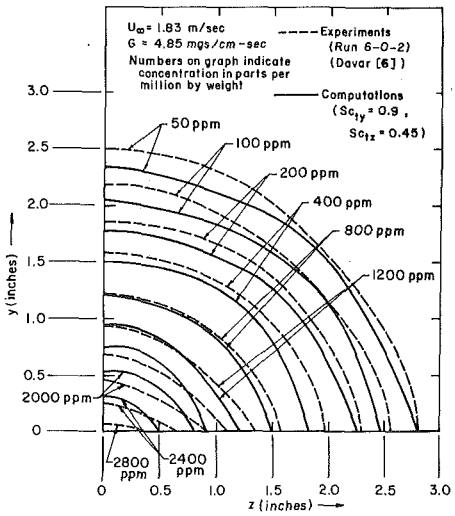

Fig. 10 Isoconcentration contours over the plume cross section at x_s = 2 ft

$$\eta(x_s) = 0.121(x_s)^{0.69}$$

$$\sigma(x_s) = 0.223(x_s)^{0.61}$$

$$U_\infty \cdot C_{\max}(x_s) = 132.34(x_s)^{-1.35} \tag{24}$$

The corresponding experimental correlations [7], also shown in Fig. 6, are given by the equations,

$$\eta(x_s) = \text{const} \cdot (x_s)^{0.71}$$

$$\sigma(x_s) = \text{const} \cdot (x_s)^{0.60}$$

$$U_\infty \cdot C_{\max}(x_s) = \text{const} \cdot x_s^{-1.47} \tag{25}$$

The rate of decay of the computed peak concentrations is slightly smaller than that in the experiments; otherwise, the calculated and experimental variations of the diffusion characteristics, equations (24) and (25), show good agreement. Here, the maximum error occurs only near the far downstream where $C_{\max}$ is very small and the experimental precision is marginal.

In Fig. 7, the relative concentration, $C(x, y, z)/C_{\max}$, is plotted as a function of the dimensionless height y/η, for several values of the lateral distance parameter $|z|/\sigma$. In Fig. 8, the relative concentration is shown as a function of $|z|/\sigma$, for several values of the height parameter y/η. The calculated concentration distributions can be described by a dimensionless universal curve,

$$\frac{C(x, y, z)}{C_{\max}} = \exp\left\{-0.693\left[\left(\frac{y}{\eta}\right)^{1.8} + \left(\frac{z}{\sigma}\right)^2\right]\right\} \tag{26}$$

The corresponding experimental mean curves, shown in Figs. 7 and 8, are described by the following universal distribution due to Malhotra and Cermak [7]:

$$\frac{C(x, y, z)}{C_{\max}} = \exp\left\{-0.693\left[\left(\frac{y}{\eta}\right)^{1.4} + \left(\frac{z}{\sigma}\right)^2\right]\right\} \tag{27}$$

It can be seen that the calculated distributions agree well with the experimental curves except near the outer edges of the diffusion plume where the concentration level makes accurate measurements difficult to achieve.

The nondimensional isoconcentration contours over the plume cross section are shown in Fig. 9. The computed and experimental contours show good agreement except for small values of the relative concentration at the outer edge of the boundary layer, as already indicated.

In Figs. 10 and 11, the calculated isoconcentration data, over the plume cross sections at x_s = 2 ft and x_s = 4 ft, respectively, are compared in the half plane with the corresponding dimensional mean isoconcentration contours given by Davar [6] from diffusion experiments. Both the computed and experimental contours behave similarly over the plume cross section with the maximum deviation being less than 10 percent over the range of calculations.

In Fig. 12, the calculated vertical and lateral spreads of the plume are shown as configurations of the 0.25 C_{max} and 0.75 C_{max} lines to demonstrate the capability of the present approach in mapping the

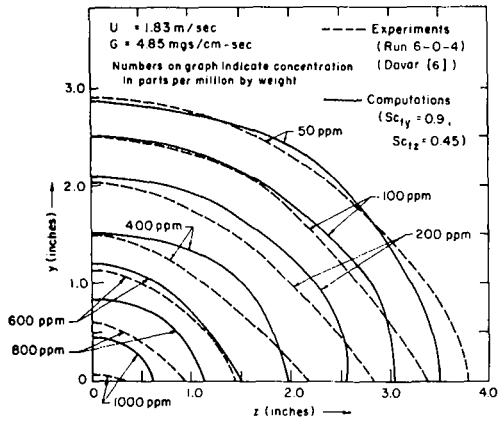

Fig. 11 Isoconcentration contours over the plume cross section at x_s = 4 ft

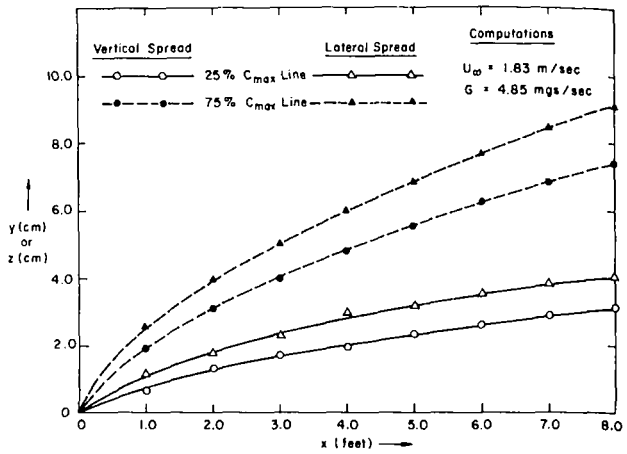

Fig. 12 Calculated vertical and lateral spreads of point source plume

entire concentration field over the range of calculations.

In conclusion, the overall agreement with the experimental measurements gives a good indication of the usefulness of the differential field-calculation approach and the Reynolds-analogy approximation in this type of problem.

References

1 Pasquill, F., *Atmospheric Diffusion*, Van Nostrand, New York, 1953.

2 Sutton, O. G., *Micrometeorology*, McGraw-Hill, New York, 1953.

3 Nee, V. W., and Kovasznay, L. S. G., "A Simple Theory of the Turbulent Shear Flows," *The Phys. Fluids*, Vol. 13, 1969, pp. 473–484.

4 Rao, K. S., Nee, V. W., and Yang, K. T., "Mass Diffusion From a Line Source in a Neutral Turbulent Shear Layer," *Proceedings of the 23rd Heat Transfer and Fluid Mechanics Institute*, Northridge, Calif., 1972.

5 Rao, K. S., Nee, V. W., and Yang, K. T., "Diffusion in a Thermally Stratified Turbulent Boundary Layer," *Heat Transfer*, Vol. 74, Tokyo, CT. 1.8, V-34.

6 Davar, K. S., "Diffusion From a Point Source Within a Turbulent Boundary Layer," PhD dissertation, Civil Engineering Department, Colorado State University, 1961.

7 Malhotra, R. C., and Cermak, J. E., "Mass Diffusion in Neutral and Unstably Stratified Boundary Layer Flows," *International Journal of Heat and Mass Transfer*, Vol. 7, 1968, pp. 169–186.

8 Poreh, M., "Diffusion From a Line Source in a Turbulent Boundary Layer," PhD dissertation, Colorado State University, 1961.

9 Blom, J., "Experimental Determination of the Turbulent Prandtl Number in a Developing Temperature Boundary Layer," Thesis, Technological University, Eindhoven, The Netherlands, 1970.

10 Johnson, D. S., "Turbulent Heat Transfer in a Boundary Layer With Discontinuous Wall Temperature," PhD dissertation, The Johns Hopkins University, 1955.

11 Kestin, J. and Richardson, P. D., "Heat Transfer Across Turbulent Incompressible Boundary Layers," *International Journal of Heat and Mass Transfer*, Vol. 6, 1963, pp. 147–189.

12 Monin, A. S., and Yaglom, A. M., *Statistical Hydrodynamics I*, Nauka Press, Moscow; English Translation TT 66-34191, U. S. Department of Commerce, 1965.

13 Rao, K. S., "Mass Diffusion in a Neutral or Thermally Stratified Turbulent Shear Layer," PhD dissertation, University of Notre Dame, 1971.

14 Townsend, A. A., "The Structure of the Turbulent Boundary Layer," *Proceedings Cambridge Phil. Soc.*, Vol. 47, 1951, pp. 375–395.

15 Klebanoff, P. S., "Characteristics of Turbulence in a Boundary Layer With Zero Pressure Gradient," NACA Tech. Note 3178, 1954.

16 Nee, V. W., and Kovasznay, L. S. G., "The Calculation of the Incompressible Turbulent Boundary Layers by a Simple Theory," *Proceedings Computation of Turbulent Boundary Layers*, AFOSR-IFP, Stanford Conference, 1968.

C. K. Hsieh
Assoc. Professor.
Assoc. Mem. ASME

R. W. Coldewey
Graduate Student.

Mechanical Engineering Department,
University of Florida,
Gainesville, Fla.

The Natural Convection of Air Over a Heated Plate With Forward-Facing Step

An experimental study of free convection flow of air over a vertically oriented, isothermal, heated plate with a forward-facing step was done. The step height was varied from 0.3175 to 0.9525 cm, and the distance of the step from the leading edge was varied from 7.62 to 15.24 cm. Temperature profiles were measured with a thermocouple probe, and velocity profiles were measured by photographing the trajectories of small dust particles carried along with the flow. For comparison purposes the same measurements were made for a flat plate. The results are nondimensionalized for comparison with the theoretical velocity and temperature profiles for a flat plate. A discussion of how the temperature and velocity profiles deform as the fluid passes over the step and the effect of step size and location on profile shape is included. The experimentally obtained temperature profiles are used to calculate the dimensionless heat-transfer coefficient. This coefficient is characterized in terms of the size and location of the step.

Introduction

The widespread use of printed circuit boards in electronics in recent years has suggested a new class of surfaces important for heat transfer studies. This involves protrusion of steps from a vertically oriented flat plate as shown in Fig. 1. The study of free convection from such a configuration requires the solution of a set of four simultaneous partial differential equations subjected to boundary conditions. The fact that these equations are coupled, further complicates the problem. As a result, an analytical solution cannot be made without relying on numerical techniques. As an alternative to this approach, an experimental study was attempted and presented in this paper to show velocity fields, temperature fields, and finally, the heat transfer coefficients expressed in pertinent dimensionless groups.

The physical model used in the study is shown schematically in Fig. 1. An isothermally heated plate of temperature T_w, having an upstream facing step, is vertically suspended in the atmosphere of temperature T_∞, pressure p_∞. The X axis is chosen along the plate surface while the Y axis is in the direction of the step. The leading length L of the plate was varied in the experiment from 7.62 to 15.24 cm. These lengths correspond to 1/6-1/3 of the plate length required to reach turbulent flow, thus laminar flow is assured in the study. The step height t was varied from 0.3175 to 0.9525 cm, which was indeed small as compared to the size of horizontal plates previously studied in the literature.

Description of Experiment

Velocity Measurement. An inexpensive method of dust trajectory technique was employed to measure the velocity field. The method calls for injecting extremely fine dust particles into the air stream and pumping the dust laden air into a test chamber in which the test object is located. Owing to the dust suspended in the air, the movement of the air becomes visible if illuminated with high intensity flashing light. The movement of the dust particles can also be photographed and recorded as dotted lines in photographs. From the length of the dust traces as well as the period of the light flashes, the flow velocity could be calculated. From the location of the plane of focus of the camera, the position of the flow field could further be selected to minimize the end effects of plates.

The method has been previously used by Eichhorn [1][1] to study free convection from a vertical, isothermal, flat plate. At low Grashof number (3.36×10^6), Eichhorn's measured velocity showed a systematic deviation from Ostrach's theory [2] in the region outside the

Contributed by the Heat Transfer Division of The American Society of Mechanical Engineers and presented at the ASME-AIChE Heat Transfer Conference, St. Louis, Mo., August 9–11, 1976. Revised manuscript received by the Heat Transfer Division February 22, 1977. Paper No. 76-HT-15.

[1] Numbers in brackets designate References at end of paper.

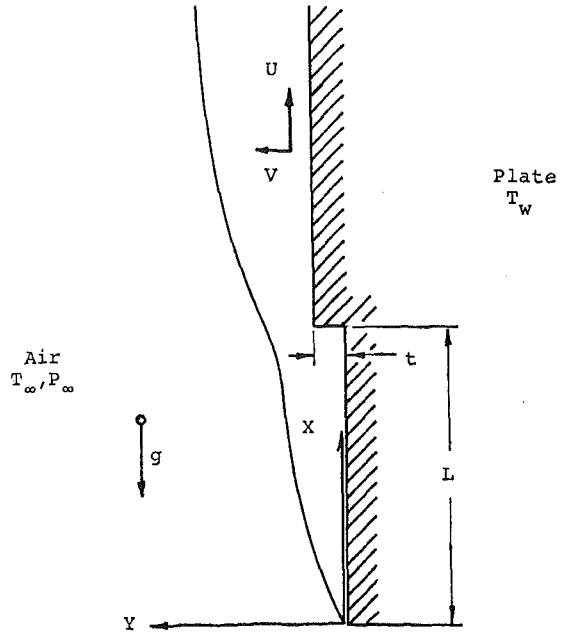

Fig. 1 Physical model

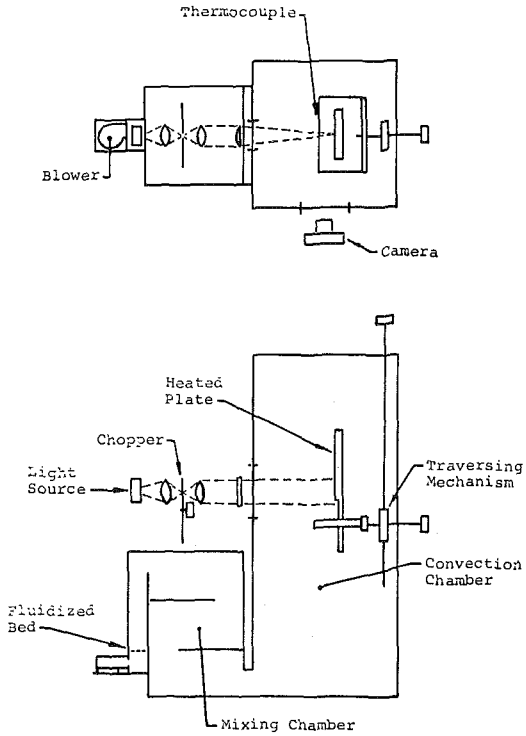

Fig. 2 Test apparatus schematic

maximum velocity in the boundary layer. For his comparison, the kinematic viscosity was based on a reference temperature, $T_r = T_w + 0.17\,(T_w - T_\infty)$. Refinements in the experimental apparatus were later made by Aihara, et al. [3], Aihara and Saito [4], and Brodowicz and Kierkus [5]. However, bodies of different orientations and configurations were tested in their studies, thus providing no further verification of Eichhorn's observation. Their modifications of Eichhorn's method are nevertheless significant in correcting some experimental techniques in which Eichhorn has difficulties. Some of their modifications include the use of a stirred, fluidized bed to obtain a positive injection of the zinc stearate dust into the test chamber. A modified photographic technique was also devised. Whereas Eichhorn used a lens with a magnification of nearly 18 and was thus limited to a field of view of 2.04 × 1.36 mm, the other investigators used a lower magnification, thus gaining a much larger field of view. The capability of photographing steamlines in a relatively large area by time exposure could also be achieved. Nevertheless, this lower magnification also brought about a much greater depth of field, giving rise to difficulties in determining the particle location in the view field.

The apparatus and methods used in this study are basically similar to those of Aihara, et al., but with further refinements and modifications. Fig. 2 is a schematic diagram showing the experimental setup. Its construction is briefly described in the following.

The experimental apparatus consisted essentially of three components, namely, the convection chamber, the mixing chamber and the optics. The convection chamber was a wood framed, plywood box of dimensions 91.44 × 91.44 × 213.36 cm. Long, glass covered ports were cut on the wall to allow illumination and photography of the dust particles near the test object which was mounted at the center of the chamber by supporting posts. To minimize possible electrostatic effects on the dust particles, the interior of the chamber was lined with an electrically conducting screen grounded to the heated plate and other metal parts in the chamber. Sheets of black paper were also used to cover the interior walls of the chamber to improve picture contrast in photographs.

The test plate was constructed of aluminum and had dimensions 30.48 × 45.72 × 0.635 cm. Step plates of different thicknesses could be attached to the heated front plate by screws (see Fig. 3). A layer of aluminum foil and a generous coat of silicon vacuum grease were applied between the plates to minimize contact resistance. Both the front plate and the step plate were instrumented with copper-constantan thermocouples mounted with copper oxide cement in grooves milled in the plate surface. This plate assembly was electrically heated by coils of 0.0254-cm nichrome wire and the temperature adjusted by a variac. In operation it was found that the variation in plate temperature was no more than 1.2°C, resulting in a variation of $(T_w - T_\infty)$ of less than 3 percent. This was considered as satisfactory to meet the assumption of constant wall temperature. The surfaces of the plates were also polished to enhance the light reflection on the dust particles while minimizing the temperature nonuniformity resulting from the high intensity light projected onto the plate.

Nomenclature

d = distance on image
Gr = Grashof number, $\beta g(T_w - T_\infty)x^3/\nu^2$
g = gravitational acceleration
L = distance of step from the leading edge of plate
ℓ = distance on image
M = magnification factor
N = chopper speed
Nu = Nusselt number
n = number of images
S = number of slots in chopper disk
T_r = reference temperature
T_w = wall temperature
T_∞ = ambient temperature
t = step size
U = velocity in X-direction
X, Y = coordinates
β = volume expansivity
δ_{FP} = boundary layer thickness for flat plate
ζ = dimensionless parameter, equation (2)
η = dimensionless parameter, equation (3)
θ = dimensionless parameter, $(T - T_\infty)/(T_w - T_\infty)$
ν = kinematic viscosity

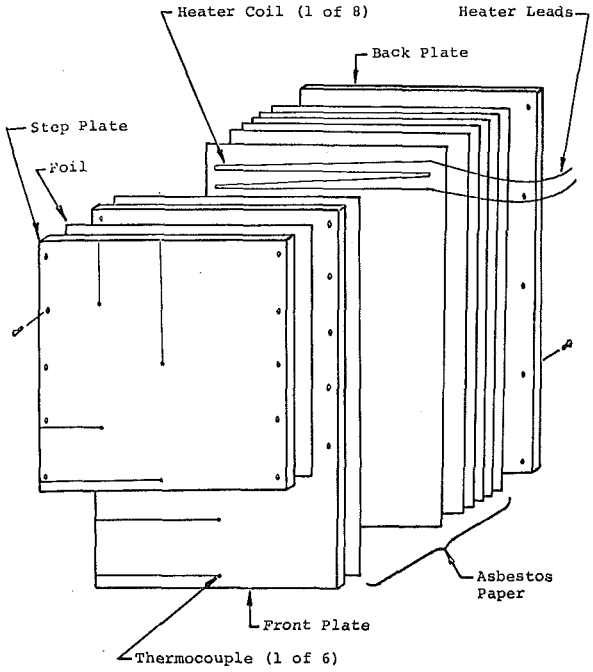

Fig. 3 Heated plate assembly

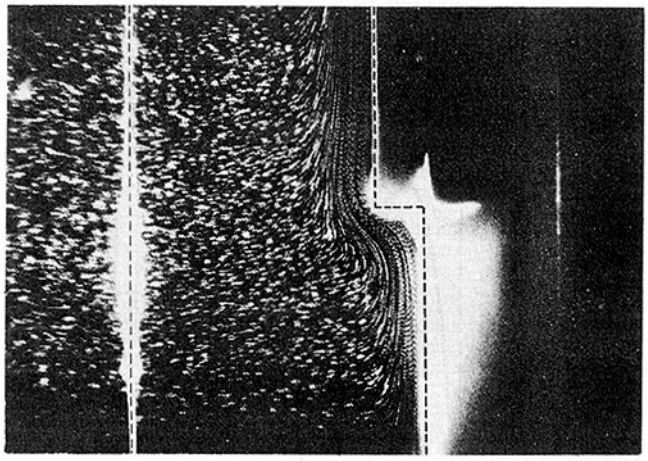

Fig. 4 Dust particle traces

The zinc stearate dust (less than 6 microns in size) was introduced into the convection chamber through an opening at the bottom of the chamber. Air was forced by a blower up through a fine net on which the zinc stearate dust was rested and the dust laden air was pumped through a mixing chamber on its way to the convection chamber (see Fig. 2). The mixing chamber served the dual purposes of minimizing the forced draft induced by the room air disturbance while settling out larger dust particles in the air. A trial and error method was used to control the dust amount in the air by blocking off a portion of the blower intake.

The optics consists primarily of an illumination system used to flash lights incident on the dust particles. The system consists of a set of lenses, an aperture, a chopper and a lamp all mounted on an optical bench. A 1000-W Eppley Laboratory calibration lamp was used for the light source. A 600-rpm synchronous motor fitted with a circular disk of on-off ratio of 1:2 was used as a chopper. Two biconvex lenses and a plano-convex cylindrical lens were set to form an intense focal field of 1.27 × 12.7 cm on the test plate. The camera used was a 35-mm single lens reflex Nikon F with an f1.2 lens. An extension ring was also used to focus down to close distances. Kodak Tri-X film was used in the photography. The normal speed of this film is ASA 400, not sensitive enough to show a clear image of dust on films. Thus a special processing with HC-110 developer was used to effectively increase the film speed rating to 4000. Tests showed that an aperture setting of f2 and exposure time of 1/8 s gave best results for recording the dust trajectory. If photographs of streamlines were desired, times up to one second were found satisfactory.

Since length measurement, both for position and velocity, were to be taken from the photographs, the magnification of the photographic image had to be precisely known. For this purpose, a reference length was included in all pictures. It was a 7.62×10^{-3}-cm wire hung vertically a known distance in front of the plate. This distance could be used to determine the magnification. As another reference, beads were strung on the wire at a known distance apart. This wire appears to the left of the stepped plate in Fig. 4, one of the photographs taken in this study. Throughout the study, no local turbulence was observed inside the field of view.

To obtain the dust particle position from the photographs the developed film was projected onto a large screen. The magnification was determined by measuring the reference distances on the projected image and comparing them with the corresponding real distances. The particle's distance from the plate leading edge and plate surface was measured on the projected image and scaled down to real values of X and Y, respectively, by dividing by M, the magnification. The distance d of n images of the same particle was measured from the projection and the average particle speed over the measured path was obtained from the equation

$$U = \frac{3SNd}{M(3n - 2)} \tag{1}$$

where S is the number of slots in the disk, N the disk speed in revolutions per second, and M the magnification.

Temperature Measurement. A thermocouple probe was used to measure the temperature distribution in the boundary layer. A 7.62×10^{-3}-cm dia copper-constantan thermocouple was stretched across two balsa wood slats to form a fork-shaped probe to measure the temperature. Since these wooden slats should stay outside the flow field, the thermocouple wire could not be made without a wide span. The balsa wood conveniently provided the needed spring action to keep the thermocouple from sagging at the measuring point. The measuring fork was mounted on an $X - Y$ translation stage which allowed for adjusting the thermocouple position from outside the convection chamber. The mechanism was located behind the test plate in order to minimize disturbance of the flow field. Counters were also installed to register positions of the thermocouple. The translation mechanism was designed to permit a precision measurement of the thermocouple position to 4.572×10^{-2} cm. To measure the ambient temperature in the chamber, two additional thermocouples were also stretched in front of the leading and trailing edges of the plate.

In operation, a step was mounted on the plate. The convection chamber was sealed and the plate heaters turned on. After about 12 hr the temperature would reach steady state, the plate at about 71°C and the air at about 27°C. Next the blower was turned on and dust was slowly blown into the chamber for approximately 15 min until a good quantity of dust was observed suspended in the chamber. At this time the blower was turned off and a period of time, usually 30 min to an hour, was allowed for the larger dust particles to settle out and for the air to be warmed back to a steady temperature. After this time period the chopper and light source were turned on and a series of photographs taken of the flow field over the step. The temperature field was measured with the thermocouple probe and the ambient and plate temperature readings were monitored periodically to insure stability.

Results and Discussion

Velocity Profiles. Because of the small step size present on the flat plate, it seems desirable to first measure the velocity profile on

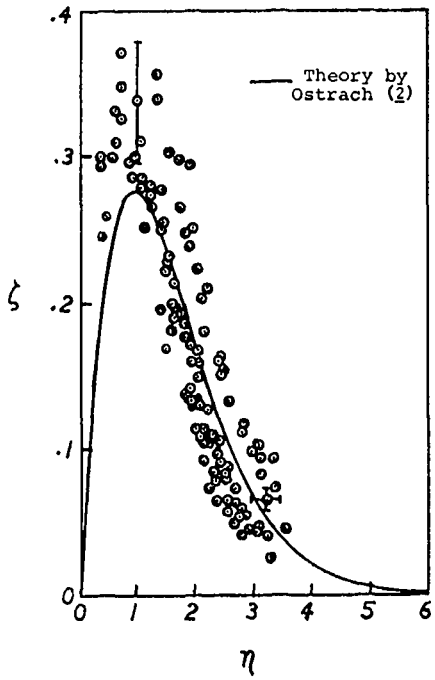

Fig. 5 Flat plate velocity profile

a flat plate in order to reveal the characteristics of the method. Following Ostrach [2], the dimensionless velocity was defined as

$$\zeta = \frac{U}{2\sqrt{\beta g(T_w - T_\infty)X}} = \frac{UX/\nu}{2\sqrt{\mathrm{Gr}_x}} \tag{2}$$

Similarly, a dimensionless distance normal to the vertical plate was defined by

$$\eta = \left[\frac{\beta g(T_w - T_\infty)}{4\nu^2 X}\right]^{1/4} \quad Y = \frac{\mathrm{Gr}_x^{1/4}}{4}\frac{Y}{X} \tag{3}$$

The property values in these equations were evaluated at $T_r = T_w + 0.17\ (T_w - T_\infty)$ following Eichhorn [1]. Fig. 5 is a plot of velocity profile on an isothermal, flat plate. The solid curve in the figure represents the theoretical profile developed by Ostrach (Pr = 0.72). The limits of uncertainty of the data are also indicated on the plot (see reference [6] for error analysis). As is seen in the figure, the experimental data conform fairly well with the theory over most of the range of η except that the experimental peak velocity is up to 36 percent greater than the theoretical value. This could be ascribed to one deficiency inherent in the method. At locations very close to the plate surface, the flow velocity was nearly zero and sharp images of the dust trajectories could not be observed (see Fig. 4). On the other hand, there was entrainment of air into the boundary layer toward the outer edge of the layer. This resulted in a parabolic trajectory of the dust particle there. The problem was further complicated by the fact that the flow velocity was very low at the edge of the boundary layer, causing the dust paths to follow continuous streaks, and making it impossible to calculate velocities.

Having gained this experience, velocity profiles on stepped plates were next measured. To facilitate correction, the data were grouped using nondimensionalized parameter X/L to identify X position. The step size t was nondimensionalized as t/δ_{FP} where δ_{FP} is the local theoretical boundary layer thickness evaluated at $X = L$ for an isothermal, flat plate. For the present study,

$$\delta_{FP} = 4.5L\left(\frac{4}{\mathrm{Gr}_L}\right)^{1/4} \tag{4}$$

Fig. 6 presents the dimensionless velocity profile on stepped plates for X/L ranging from 0.83 to 1.17 and t/δ_{FP} ranging from 0.25 to 0.72. The solid curves, representing theoretical curves for a flat plate, are also given to serve as contrast. In each row of figures, the left two profiles show the velocities below the step; right two, above the step. (For a more comprehensive data presentation covering other X/L values, the interested reader is referred to reference [6].)

It is of interest to note from the figures how the velocity profiles change in the immediate vicinity of the step. Depending upon the magnitude of t/δ_{FP}, at some distance below the step, the velocity profile closely resembles that obtained experimentally for the flat plate, including peak velocities higher than theoretical. As the step is approached, the peak velocity decreases and the thickness of the boundary layer increases as the fluid decelerates in the X-direction and accelerates in the Y-direction to move over the step. Immediately after crossing the step, the fluid near the wall has a relatively high velocity but as it continues up the plate the profile tends back to that of the flat plate.

A careful examination of the figures for t/δ_{FP} equal 0.61 and 0.72 reveals something peculiar happening. Curves for $t/\delta_{FP} = 0.61$ have the highest peak velocity among all step sizes tested. In contrast to what one might normally expect, the large step size increases the peak velocity markedly in the upstream direction. Because of this large peak velocity, the drop of this velocity as well as the thickening of the boundary layer when the flow crosses over the step is the most pronounced of those observed. This step size even has an effect on the flow in the downstream direction, as the observed large peak velocity as well as the thickened boundary layer persist even for X/L reaching 1.17. Contrary to what would be expected, the next larger step ($t/\delta_{FP} = 0.72$) has a lesser effect upon the flow than was experienced for $t/\delta_{FP} = 0.61$. The peak velocity is not as high, and, when the flow crosses the step, the relative decrease in velocity and increase in boundary layer thickness is not nearly as large as for the smaller step. A check of the experimental data revealed no differences in the experiment other than a slightly lower temperature (about 3.8°C). However, this difference was not sufficient to cause such a dramatic change. These observations suggest that the low pressure region in the downstream direction does have a marked effect on the total flow field, while an excessive buildup of the step size hinders the flow. A critical t/δ_{FP} might exist between 0.61 and 0.72.

Temperature Profiles. The measured temperature data were nondimensionalized by using

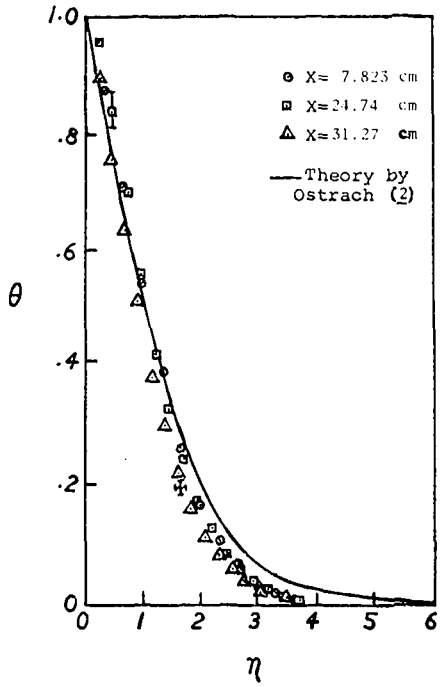

Fig. 7 Flat plate temperature profile

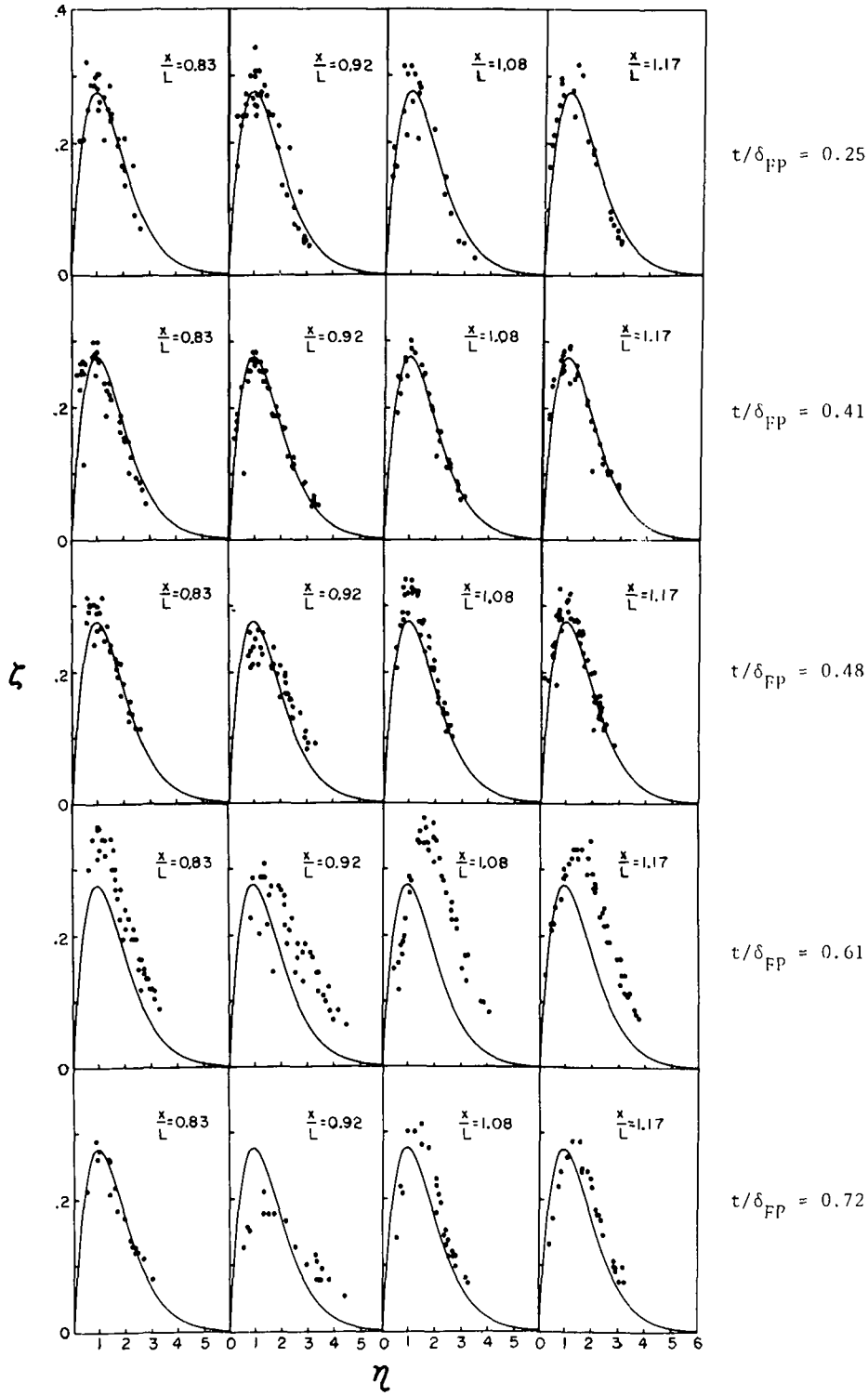

Fig. 6 Velocity profiles on stepped plates

$$\theta = \frac{T - T_\infty}{T_w - T_\infty}$$

Again for the purpose of comparison, temperature profiles for flow over a flat plate were first measured and compared with the theoretical solution by Ostrach [2]. Fig. 7 shows the result where the experimental uncertainty is again identified. Agreement is found good for η ranging from 0 to 2. For points of η greater than 2 the measured values of θ are generally lower than the predicted. Also, the measured thermal boundary layer thickness seems to be smaller than predicted, thus indicating that the thermal boundary layer is not as thick as the hydrodynamic boundary layer for the study made.

The temperature profiles for stepped plates are presented in Fig. 8, noting that the X/L values are slightly different for data presented in the two right columns of the figure (see reference [6] for more data). As is consistent with the velocity profiles, at some distance below the

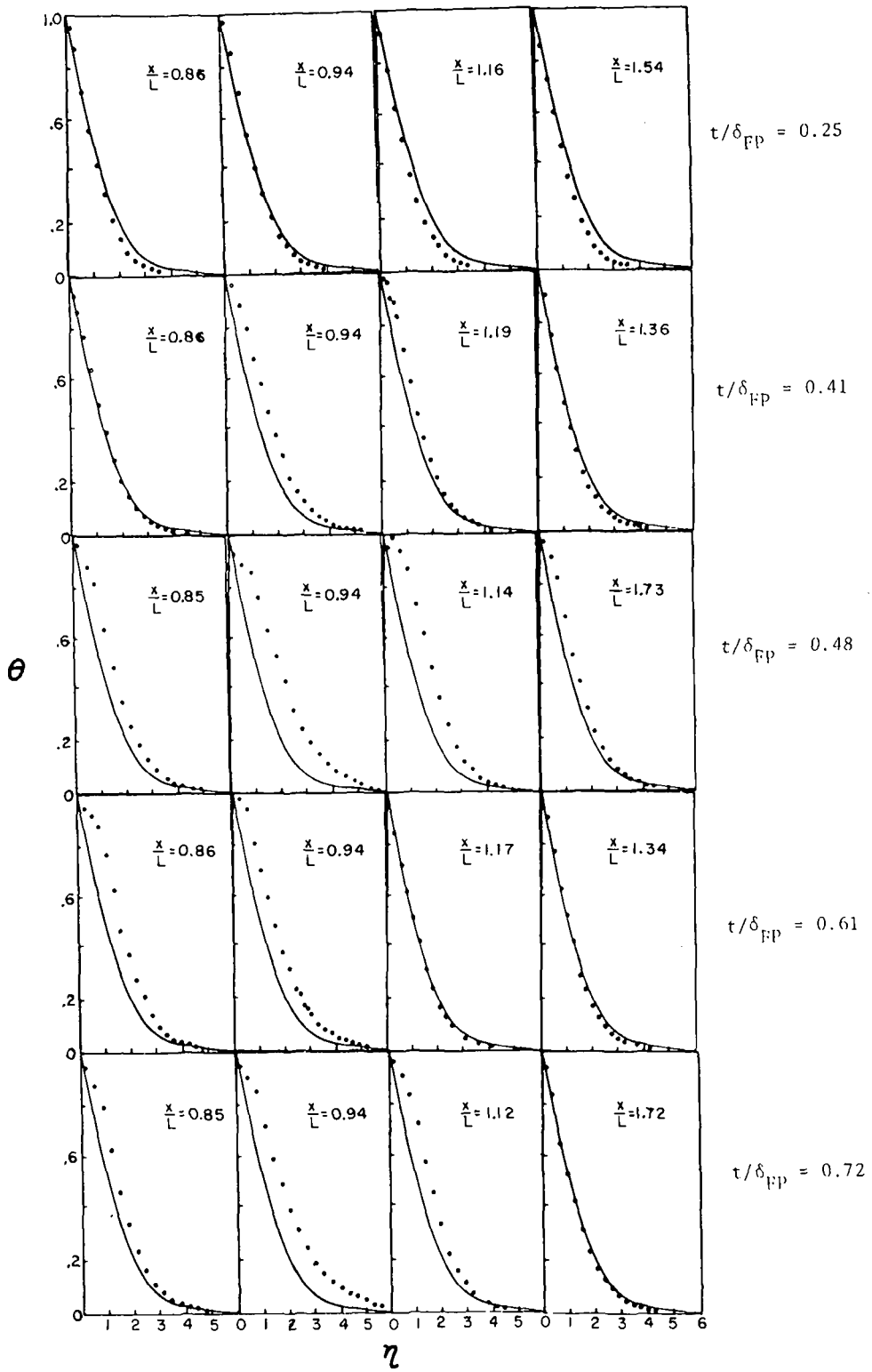

Fig. 8 Temperature profiles on stepped plates

step, the temperature profile generally resembles that obtained for the flat plate. Close to the step the warmer fluid that was near the wall starts moving outward to cross the step. The gradient of temperature is thus decreased while the boundary layer is thickened. Then as the fluid crosses the step and the boundary layer thickness decreases, the temperature gradient becomes steeper, consequently increasing heat transfer. Once again as the fluid moves downstream, the profile tends to return to the similar flat plate profile.

A large step size appears to have an effect on the upstream temperature profiles. For X/L ranging from 0.51 to 0.55 (not shown, see [6]) the temperature gradient near the wall is not as steep as for a flat plate. Farther downstream from the step, for $t/\delta_{FP} = 0.48$, the temperature profile does not return to that of a flat plate, even for $X/L = 1.73$ [6]. A close examination of this figure reveals that the change of temperature gradient at the wall as well as the increase in thermal boundary layer thickness is the largest of those tested. As noted earlier

in the discussion of velocity profiles, there was a peculiar change in the flow characteristics for t/δ_{FP} changing from 0.61 to 0.72. There is no apparent difference of this sort for the temperature profiles at $t/\delta_{FP} = 0.61$ and 0.72.

The temperature curves were subsequently used together with the equation

$$\frac{\mathrm{Nu}_x}{\mathrm{Gr}_x{}^{1/4}} = -0.707 \left(\frac{\delta\theta}{\delta\eta}\right)_w \tag{5}$$

to find the local heat transfer coefficient expressed in Nu_x. The correlation between $\mathrm{Nu}_x/\mathrm{Gr}_x{}^{1/4}$ and X/L, for Grashof numbers ranging from 2×10^5 to 8×10^7, can be expressed as (6)

$$\frac{\mathrm{Nu}_x}{\mathrm{Gr}_x{}^{1/4}} = \left[0.657 - 0.830\left(\frac{t}{\delta_{FP}}\right)\right] \times (1 - X/L)^{1/5} \quad 0.25 \le t/\delta_{FP} \le 0.61 \tag{6}$$

$$\frac{\mathrm{Nu}_x}{\mathrm{Gr}_x{}^{1/4}} = \left[-0.289 + 0.721\left(\frac{t}{\delta_{FP}}\right)\right] \times (1 - X/L)^{1/5} \quad 0.61 \le t/\delta_{FP} \le 0.72 \tag{7}$$

for $X/L < 1$, and

$$\frac{\mathrm{Nu}_x}{\mathrm{Gr}_x{}^{1/4}} = \left[0.808 - 1.327\left(\frac{t}{\delta_{FP}}\right)\right] \times (X/L - 1)^{1/5} \quad 0.25 \le t/\delta_{FP} \le 0.48 \tag{8}$$

$$\frac{\mathrm{Nu}_x}{\mathrm{Gr}_x{}^{1/4}} = \left[-0.707 + 1.832\left(\frac{t}{\delta_{FP}}\right)\right] \times (X/L - 1)^{1/5} \quad 0.48 \le t/\delta_{FP} \le 0.61 \tag{9}$$

$$\frac{\mathrm{Nu}_x}{\mathrm{Gr}_x{}^{1/4}} = \left[1.446 - 1.672\left(\frac{t}{\delta_{FP}}\right)\right] \times (X/L - 1)^{1/5} \quad 0.61 \le t/\delta_{FP} \le 0.72 \tag{10}$$

for $X/L > 1$. The thermophysical properties used in the correlation were evaluated at $T_r = T_w + 0.17(T_w - T_\infty)$ for $T_w = 71°\mathrm{C}$ and $T_\infty = 27°\mathrm{C}$. Uncertainty in the heat transfer parameter ($\mathrm{Nu}_x/\mathrm{Gr}^{1/4}$) was calculated to be less than 20 percent (see reference [6] for complete error analysis).

These equations demonstrate that the heat transfer parameter decreases with increase of (X/L) until the step is reached, where this parameter is zero. Further downstream from the step, the heat transfer parameter gradually increases with distance and reaches flat plate value for small step sizes. It is noted that, since the step size is small in the study, heat transfer contribution due to the step surfaces has been ignored in the analysis.

References

1 Eichhorn, R., "An Analytical Investigation of Combined Free and Forced Convection and a New Method to Measure Free Convection Velocity Profiles," PhD thesis, University of Minnesota, 1959.

2 Ostrach, S., "An Analysis of Laminar Free-Convection Flow and Heat Transfer About a Flat Plate Parallel to the Direction of the Generating Body Force," NACA Report—No. 1111, 1953.

3 Aihara, T., Yamada, Y., and Endo, S., "Free Convection Along the Downward-Facing Surface of a Heated Horizontal Plate," *International Journal of Heat and Mass Transfer*, Vol. 15, 1972, p. 2535.

4 Aihara, T., and Saito, E., "Free Convection Heat Transfer From a Horizontal Torus," JOURNAL OF HEAT TRANSFER, TRANS. ASME, Series C, Vol. 94, 1972, p. 95.

5 Brodowicz, K., and Kierkus, W. T., "Experimental Investigation of Laminar Free Convection Flow in Air above Horizontal Wire With Constant Heat Flux," *International Journal of Heat and Mass Transfer*, Vol. 9, 1966, p. 81.

6 Coldewey, R. W., "The Natural Convection of Air Over a Heated Plate With Forward-Facing Step," MS thesis, University of Florida, 1974.

G. B. Lewis
Ethicon Inc.,
Division of Johnson and Johnson,
Somerville, N. J.
Assoc. Mem. ASME

J. L. Novotny[1]
Mem. ASME

K. T. Yang
Department of Aerospace and Mechanical Engineering,
University of Notre Dame,
Notre Dame, Ind.
Fellow ASME

An Experimental Study of Natural Convection Mass Transfer Along a Vertical Plate With Surface Injection

Laminar isothermal natural-convection mass transfer along a porous vertical plate in an aqueous sodium chloride solution with uniform surface injection of pure water at the plate surface is investigated experimentally by means of a Mach-Zehnder interferometer. Grashof numbers for the mass transfer system range from 0.253×10^4 to 0.858×10^7; the surface injection velocities are from 0.519×10^{-4} cm/s to 0.937×10^{-3} cm/s; and Schmidt numbers cover a range from 582 to 643. Steady concentration profiles and rate of surface mass transfer have been obtained, and are compared with the theoretical result based on a similarity solution with matched surface concentration distribution, Grashof and Schmidt numbers, and surface injection rate.

Introduction

Laminar natural convection heat transfer phenomena at high Grashof numbers have been extensively analyzed in the literature based on the boundary layer equations, and the results are well substantiated by experimental data. Corresponding natural convection problems in mass transfer or combined heat and mass transfer have been similarly treated analytically, and good examples are the analyses of Seville and Churchill [1][2] and Gebhart and Pera [2]. Unfortunately, very few experimental data are available for comparison with such analyses. For the vertical-plate geometry, we have the interferometric data of Adams and McFadden [3] who studied the sublimation of a heavy organic vapor from a heated vertical surface, the liquid data of DenBouter, DeMunnik, and Heertjes [4] also for the combined heat and mass transfer problem, and the pure mass transfer data of Lloyd, Sparrow, and Eckert [5], using an electrochemical technique. Also pertinent are the horizontal plate data of Goldstein, Sparrow, and Jones [6] based on the naphthalene sublimation technique. It is noted that with the exception of the data of Adams and McFadden [3], none of these data includes detailed concentration and/or temperature profiles. Furthermore the authors are not aware of any experimental work dealing with the effect of surface injection in similar problems, even though general analyses are available for the vertical plate heat transfer problem with surface injection [7, 8].

This paper describes an experimental study of laminar isothermal natural-convection mass transfer along a porous vertical plate in an aqueous sodium chloride solution with uniform injection of pure water at the plate surface. Steady concentration profiles and local rates of mass transfer have been measured by a Mach-Zehnder interferometer. These results are compared with that based on a similarity solution with matched surface concentration distribution, Schmidt number, local Grashof number and surface injection rate.

Experimental Apparatus

A schematic diagram of the experimental apparatus and the auxiliary equipment is shown in Fig. 1. The experiments were conducted in a stainless steel cylindrical tank, 76-cm ID and 152-cm long. The tank was mounted with its axis vertical and with an open top. There were four ports evenly spaced around the circumference of the tank at a distance of 45.7 cm from its bottom. Special stainless steel holders to support the optically flat glass windows were mounted in two opposite ports by bolts and properly sealed. The holders provided approximately a 20-cm gap in the tank between the two opposite optical flats and a field of view 8.3 cm in diameter. Plexiglas disks were fabricated for the remaining two ports to serve as observation windows. A stirrer was also installed in the test tank to aid in mixing the solutions and reducing temperature gradients during the interferometric tests.

The vertical test plate was 11.2-cm wide, 21.3-cm long, and 0.63-cm thick, made of nickel Foametal (marketed by General Electric) having a porosity of approximately 40 percent. It was mounted on an alu-

[1] Deceased.
[2] Numbers in brackets designate References at end of paper.

Contributed by The Heat Transfer Division of THE AMERICAN SOCIETY OF MECHANICAL ENGINEERS and presented at the National Heat Transfer Meeting, St. Louis, Mo., August 9–11, 1976. Revised manuscript received by the Heat Transfer Division March 10, 1977. Paper No. 76-HT-14.

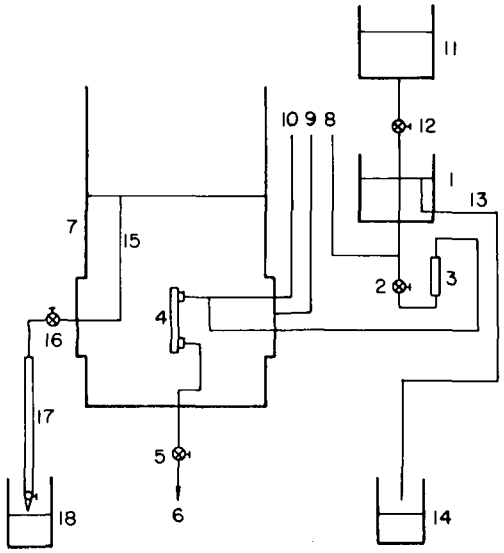

1. Feed Vessel
2. Needle Valve
3. Flowmeter
4. Foametal Plate Assy.
5. Needle Valve
6. Outlet
7. Environmental Tank
8. Feed Vessel Sight Tube
9. Tank Sight Tube
10. Pressure Tap Sight Tube
11. Supply Vessel
12. Needle Valve
13. Feed Vessel Overflow Line
14. Polyethylene Container
15. Tank Overflow Line
16. Needle Valve
17. Burette
18. Beaker

Fig. 1 Schematic diagram of the experimental apparatus

minum holder coated with a corrosion-resistant paint, and sealed with Silastic at the edges. The holder provided a hollow interior about 0.5-cm thick behind the test plate so that a uniform flow could be fed through the plate to generate the natural convection process. Manifolds were used for inflow and outflow; and had eight 6-mm holes connected to the hollow interior behind the plate and also two plastic tube fittings for connection to the plate flow system. A piece of Plexiglas with three needles mounted in it at 7.6-cm intervals was attached to the side of the holder frame. These needles were used as precise reference points to determine exact locations along the plate in the interferometric measurements. The plate-holder assembly was bolted to a structural system which permitted manual rotating and leveling of the test plate in the field of view of the interferometer, when placed in position in the tank.

The mass transfer medium in the test tank was an aqueous sodium chloride solution and pure water was fed through the Foametal test plate. This concentration difference generated the natural convection flow adjacent to the plate. The pure water was fed into the test system from an overhead cylindrical polyethylene feed vessel, 27.9 cm in diameter and 35.6 cm in height. Polyethylene tubing of 0.64-cm ID was used to connect the feed vessel to the inlet manifold on the plate holder through one of the Plexiglas tank windows. A needle valve and a flowmeter were installed directly below the feed vessel to control and record the rate of water flow. Inside the test tank, the tubing was coiled twice, and a glass wedge-fitting was installed to divide the flow prior to its entry into the inlet manifold. The coils provided approximately 2.5 m of tubing in which the temperature of the incoming flow could be brought to that of the tank solution.

To control the flow of pure water into the test plate, overflow systems and fluid level sight tubes were incorporated in the experimental apparatus. The overflow in the main test tank ran into one of three calibrated burettes, and provided a check on the flow through the test plate. The fluid levels in the test tank and the feed vessel were monitored by sight tubes and accurately measured by a microscope, which also monitored the fluid head representing the pressure at the inlet of the test plate assembly.

As mentioned previously, the main measurement device used in this experimental study was a Mach-Zehnder interferometer with 10.2-cm optical components. A compensating chamber in the reference arm of the interferometer was used to compensate for the increased optical path length due to the width of the sodium chloride solution and the glass in the test arm. The compensating chamber duplicated the optical characteristics of the test section by providing the same essential geometry, optical plates, and the solution at the same hydrostatic pressure. The fringe patterns were photographed with a Graflex camera. The image of a machinist's scale and a counter was also superimposed on the image of the plate holder in the interferograms. Other instrumentations used in this study are given in [9]. It suffices to indicate here that temperatures in the test tank, feed vessel and room were monitored by means of three 30 gauge copper-constantan thermocouples and a self-balancing potentiometer; and concentration of the dilute sodium chloride solution by a calibrated conductivity cell with platinum electrodes, as well as by platinum conductivity probes.

Experimental Procedure

Because of the small pore size of the Foametal plate, it was necessary to use extreme care in the preparation and storage of all water used in the experiments. Water was first run through a softener, then distilled, immediately demineralized, and subsequently filtered

Nomenclature

a_1, a_2, a_3 = constants in similarity solution
D = diffusion coefficient, cm^2/s
f = dimensionless stream function, equation (11)
$\mathrm{Gr}_{wx} \equiv g\alpha x^3 (w_{Aw} - w_{A\infty})/\nu^2$
g = gravitational acceleration, cm/s^2
$H \equiv g\alpha L^3(w_A - w_{A\infty})/\nu^2$
L = overall height of test plate, cm
m = constant in equation (8)
$\dot{m}$ = mass flux, gm/s cm^2
n = exponent in similarity solution
Sc = Schmidt number
Sh_x = local Sherwood number, $\dot{m}_A x/[\rho D(w_{Aw} - w_{A\infty})]$
u = velocity in the x-direction, cm/s
$\bar{u} \equiv uL/\nu$
v = velocity in the y-direction, cm/s
$\bar{v} \equiv \bar{v}L/\nu$
w = mass fraction, gm/gm
x = vertical coordinate measured from the leading edge, cm
$\bar{x} \equiv x/L$
y = normal coordinate measured from the plate surface, cm
$\bar{y} \equiv y/L$
$\alpha \equiv -\frac{1}{\rho}\left(\frac{\partial \rho}{\partial w_A}\right)_{T,p}$
η = dimensionless similarity variable, equation (12)
ν = kinematic viscosity, cm^2/s
ξ = dimensionless similarity variable, equation (16)
ρ = fluid density, gm/cm^3
ϕ = dimensionless stream function, equation (16)
$\chi \equiv (w_A - w_{A\infty})/(w_{Aw} - w_{A\infty})$
ψ = dimensionless stream function, equation (11)

Subscripts

A = component A of a binary mixture (NaCl)
w = wall conditions
∞ = conditions in the ambient

Superscript

$(')$ = derivatives with respect to the independent variable

through 1.2-micron pore-size membranes. It was then stored in polyethylene containers. Water used in the plate-flow system was prepared in the same manner, except it was filtered twice. The solutions used in the experiments were prepared with a reagent grade sodium chloride of certified purity and purified water. The purity of the water was always assured by resistance measurement with a conductivity bridge. The procedure was first to dissolve the salt thoroughly in approximately 12–15 l of water in a container. The contents were then added to a known volume of tank water. Using the microscope and sight tube to determine the volume change, the bulk concentration in the tank could be calculated. The solution was mixed thoroughly by stirring for at least 6 hr, and the interferometric testing was not begun until 24 hr had elapsed. The bulk concentration was checked by the electrolytic resistance measurements.

To prepare for the interferometric study, the test tank was first degreased with toluene and acetone, and thoroughly cleaned and rinsed with purified water. The plate assembly was cleaned in a similar manner. The appropriate tubing connections in the complete flow system were then made and the three sight tubes were leveled and aligned. The large tank and the feed vessel were then filled with water and the system was run for an initial period of 24–48 hr to insure ridding the air bubbles from the tubes and the plate-holder assembly. The Foametal plate was then calibrated for the flow-pressure drop behavior by means of the overflow system.

Immediately following the calibration of the porous plate, the interferometric testing was initiated. The interferometer was aligned in much the same manner as outlined by Eckert, Drake, and Soehngen [10] and the midplane of the Foametal plate was then focused on the ground glass screen of the camera by means of a surface locating probe and a suspended plumb-line. At this time, the desired amount of salt was added to the water already in the tank and the solution thoroughly mixed, as described previously. The image of the scale and counter was superimposed on that of the plate assembly. Prior to each run, the spacing of the fringes was adjusted, and the fringes were aligned perpendicular to the plate surface.

The flow rate to the plate was then set to match the overflow rate from the tank, and the timer was started. Each run lasted between 45 and 90 min depending on the position of the plate in the interferogram. When steady-state conditions prevailed, a single exposure was taken of the fringe field. In addition, the flowmeter reading, the emf readings of the thermocouples and the fluid levels in the sight tubes were recorded. When the flow-pressure drop readings deviated from the original calibration curve, this signified permeability change due to corrosion and clogging and the run was consequently aborted. The bulk concentration of the tank solution was checked after each set of four or five runs. Because the amount of water added during the runs was very small relative to the tank solution volume, the change in bulk concentration during a set of runs was negligible. The interferometer and test equipment were located in an isolated end of the laboratory behind a heavy velvet curtain, and all testing was performed at night to reduce vibrations in the fringe patterns caused by external disturbances.

Experimental Results

Errors associated with the interferometer measurements were analyzed in this investigation, and details are given in [9]. It suffices to indicate that these errors were of the order of 5 percent, except for cases of high surface injection rates where they could approach 10 percent. In particular, the end effects were evaluated with an approach given by Eckert and Soehngen [11] and Goldstein [12] and the associated error was found to be well within one percent in the concentration gradients. Temperature variations in the experiments were found to be extremely small, and they had little effects on the results. This was substantiated by taking and examining interferograms prior to mass transfer tests by running pure water through the entire test system with controlled temperature differences between the water in the feed vessel and that in the tank. Calculations of the dimensionless quantities in this study were based on property values for the sodium chloride solution interpolated from tabulated values given in the following references: equivalent conductance [13, 14], density

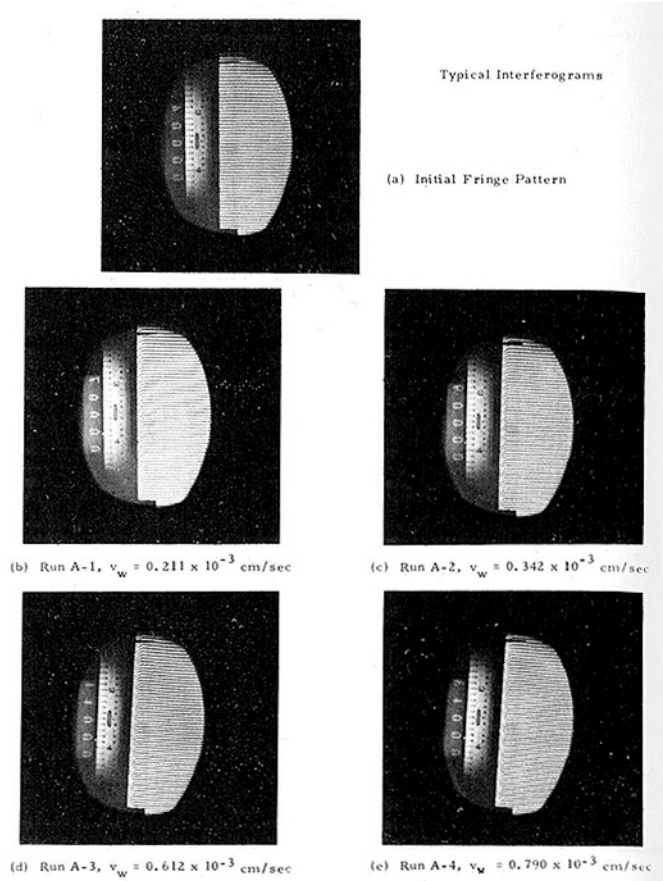

Fig. 2 Typical interferograms: (*a*) initial fringe pattern; (*b*) run A-1, $v_w = 0.211 \times 10^{-3}$ cm/s; (*c*) Run A-2, $v_w = 0.342 \times 10^{-3}$ cm/s; (*d*) Run A-3, $v_w = 0.612 \times 10^{-3}$ cm/s; (*e*) Run A-4, $v_w = 0.790 \times 10^{-3}$ cm/s

[14, 15], diffusion coefficient [13], viscosity [14, 15], and refractive index [16].

A few of the typical interferograms are presented in Fig. 2, which show clearly the effect of the wall velocity on the concentration profiles. At the low injection rates the fringe patterns resemble those for ordinary natural convection heat transfer. The change in the profiles with increasing injection to the characteristic S-shaped form is readily apparent.

Some selected data are shown in Tables 1 and 2. Table 1 lists the ambient conditions and the surface injection velocity for the various

Table 1 Ambient NaCl solution properties and surface injection velocities

RUN	$w_{A\infty} \times 10^4$	T(oC)	Sc	$v_m (\frac{cm}{sec}) \times 10^4$
A-3	0.810	22.9	620	6.12
C-1	0.793	22.2	643	0.533
M-1	0.810	23.6	597	0.553
M-2	0.810	23.6	597	0.951
M-3	0.810	23.6	597	1.24
M-4	0.810	23.7	594	2.06
M-5	0.810	23.6	597	4.67
M-7	0.810	23.5	601	9.37
P-5	1.548	23.8	591	4.81

Table 2 Results of interferogram analyses

x(cm)	$w_{Aw} \times 10^6$	$(\frac{dw_A}{dy})_w \times 10^4$	n	$Gr_{wx} \times 10\text{-}4$
RUN A-3				
12.07	8.38	0.55	0.14	100
14.89	6.06	0.546	0.14	194
18.03	4.14	0.517	0.14	354
RUN C-1				
12.24	63.3	0.634	0.33	22.2
15.10	62.4	0.641	0.33	44.2
17.81	58.2	0.688	0.33	90.7
RUN M-1				
2.94	68.7	0.649	0.28	0.253
5.96	67.7	0.587	0.28	2.27
8.69	63.9	0.568	0.28	9.03
RUN M-2				
2.93	64.7	0.742	0.18	0.333
5.91	63.1	0.628	0.18	2.99
8.84	60.9	0.555	0.18	11.3
RUN M-3				
2.99	63.6	0.727	0.17	0.377
5.92	60.9	0.644	0.17	3.38
8.64	60.3	0.563	0.17	10.8
RUN M-4				
2.94	54.7	0.964	0.15	0.543
5.71	51.8	0.796	0.15	4.41
8.20	50.3	0.740	0.15	13.7
RUN M-5				
2.99	34.6	0.849	0.026	1.00
5.87	34.8	0.656	0.026	7.57
8.22	33.4	0.554	0.026	21.4
RUN M-7				
3.10	16.0	0.434	0.048	0.56
5.73	11.8	0.408	0.048	10.5
8.23	13.3	0.354	0.048	30.4
RUN P-5				
3.20	65.3	1.81	0.041	2.39
5.64	64.3	1.26	0.041	13.2
7.79	63.5	1.15	0.041	34.8

runs analyzed, and Table 2 provides the direct results of the interferogram analyses in terms of w_{Aw}, $(\partial w_A/\partial y)_w$, and the local mass transfer Grashof number Gr_{wx} at various x-locations in each run. The local Grashof number ranges from 0.253×10^4 to 0.858×10^7. A total of 22 runs were carried out, and the interested reader is referred to [9] for the remaining data not shown here.

It should be noted that theoretically the surface injection rate and the surface concentration variation can be independently specified for a given mass transfer problem. The fact that this was not done in this investigation was due to the specific experimental apparatus. Particularly, the contamination of the pure water inside the test plate due to back diffusion of the salt solution could not be controlled in the experiments. Consequently, in addition to the surface injection velocity, the measured surface concentration variation must also be considered as a boundary condition for the mass transfer problem in any theoretical calculations.

Comparison With A Local Similarity Solution

No theoretical solution to the problem treated in this experimental study was available in the literature. A similarity solution was attempted for the mass transfer problem, and the result can be used to compare with the experimental data on a local-similarity basis. Such a comparison not only gives another indication of the validity of a local similarity solution, but also provides a basis for discussing the physical phenomenon.

Dimensionless boundary-layer equations for steady, laminar, two-dimensional, isothermal natural convection mass transfer on a vertical plate for a two component and constant-property boundary layer with negligible dissipation and coupling effects can be written as

$$\frac{\partial \bar{u}}{\partial \bar{x}} + \frac{\partial \bar{v}}{\partial \bar{y}} = 0 \tag{1}$$

$$\bar{u}\frac{\partial \bar{u}}{\partial \bar{x}} + \bar{v}\frac{\partial \bar{u}}{\partial \bar{y}} = H + \frac{\partial^2 \bar{u}}{\partial \bar{y}^2} \tag{2}$$

$$\bar{u}\frac{\partial H}{\partial \bar{x}} + \frac{g\alpha L^3}{\nu^2}\bar{u}\frac{dw_A}{d\bar{x}} + \bar{v}\frac{\partial H}{\partial \bar{y}} = \frac{1}{\mathrm{Sc}}\frac{\partial^2 H}{\partial \bar{y}^2} \tag{3}$$

with the boundary conditions

$$\left.\begin{aligned} &\bar{y} = 0 \quad \bar{u} = 0 \quad \bar{v} = \bar{v}_w(\bar{x}) \quad H = H_w(\bar{x}) \\ &\bar{y} \to \infty \quad \bar{u} \to 0 \quad H \to 0 \end{aligned}\right\} \tag{4}$$

Here we seek the functionals $w_{A\infty}(\bar{x})$, $\bar{v}_w(\bar{x})$, and $H_w(\bar{x})$ which would permit a similarity solution to the foregoing governing equations. The technique used follows closely that of Yang [17] and Yang, Novotny, and Cheng [18], and only the results will be shown here. For

$$\frac{g\alpha L^3}{\nu^2} w_{Aw} = a_3 + a_1 a_2 (m+1)\left(\frac{4\bar{x}}{a_2}\right)^n \tag{5}$$

$$\frac{g\alpha L^3}{\nu^2} w_{A\infty} = a_3 + a_1 a_2 m \left(\frac{4\bar{x}}{a_2}\right)^n \tag{6}$$

$$H_w(\bar{x}) = a_1 a_2 \left(\frac{4\bar{x}}{a_2}\right)^n \tag{7}$$

where all a's are constants, and

$$m = \frac{g\alpha L^3}{\nu^2}\left(\frac{d\bar{x}}{dH_w}\right)\frac{dw_{A\infty}}{d\bar{x}} \tag{8}$$

Equations (1)–(3) are reducible to the following ordinary equations

$$\left.\begin{aligned} &f''' + (n+3)ff'' - 2(n+1)f'^2 + a_1\chi = 0 \\ &\frac{1}{\mathrm{Sc}}\chi'' + (n+3)f\chi' - 4nf'\chi - 4mnf' = 0 \end{aligned}\right\} \tag{9}$$

with the boundary conditions from (4)

$$\left.\begin{aligned} &f(0) = f_w \qquad f'(0) = 0 \qquad \chi(0) = 1 \\ &f'(\infty) = \chi(\infty) = 0 \end{aligned}\right\} \tag{10}$$

where f is the dimensionless stream function defined by

$$\bar{u} = \frac{\partial \psi}{\partial \bar{y}} \qquad \bar{v} = -\frac{\partial \psi}{\partial \bar{x}} \qquad \psi(\bar{x}, \bar{y}) = a_2\left(\frac{4\bar{x}}{a_2}\right)^{(n+3)/4} f(\eta) \tag{11}$$

and the prime refers to derivatives respect to η defined by

$$\eta = \left(\frac{4x}{a_2}\right)^{(n-1)/4}\bar{y} \tag{12}$$

The surface mass transfer characteristics are then given by

$$\frac{\mathrm{Sh}_x}{(\mathrm{Gr}_{wx}/4)^{1/4}} = -\frac{\chi'(0) + (n+3)\mathrm{Sc}\dfrac{w_{Aw}}{w_{Aw} - w_{A\infty}} f_w}{a_1^{1/4}} \tag{13}$$

Note that this definition includes both the diffusive and convective fluxes. If only the diffusive flux were included, the corresponding Sherwood number would then be similar to that commonly used for natural convection heat transfer problems. Also, equation (13) is only compatible with the similarity solution with $a_3 = 0$, unless $n = 0$, for which case a_3 is an arbitrary constant.

For the pure mass transfer problem considered here, $m = 0$, and $a_1 = 1$ without any loss of generality. The Schmidt number is high (~600), and as a result, asympototic equations for $\mathrm{Sc} \to \infty$ can be used as a good approximation. Thus, equations (9) and (10) reduce to

$$\left.\begin{aligned} &\phi''' + \chi = 0 \\ &\chi'' + (n+3)\phi\chi' - 4n\phi'\chi = 0 \end{aligned}\right\} \tag{14}$$

With the boundary conditions

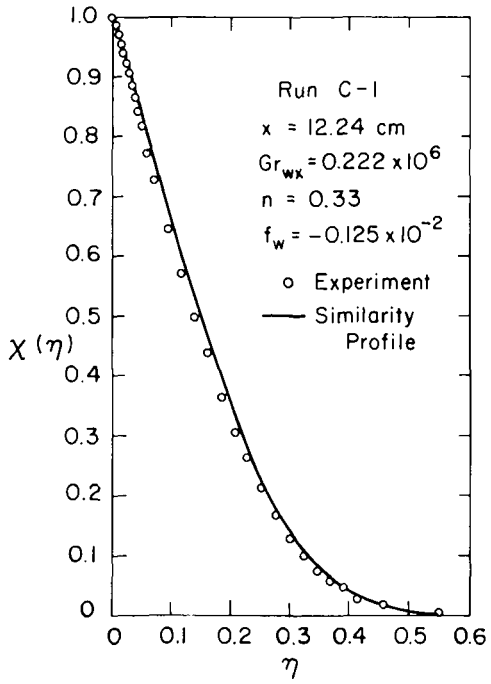

Fig. 3 Concentration profile for Run C-1

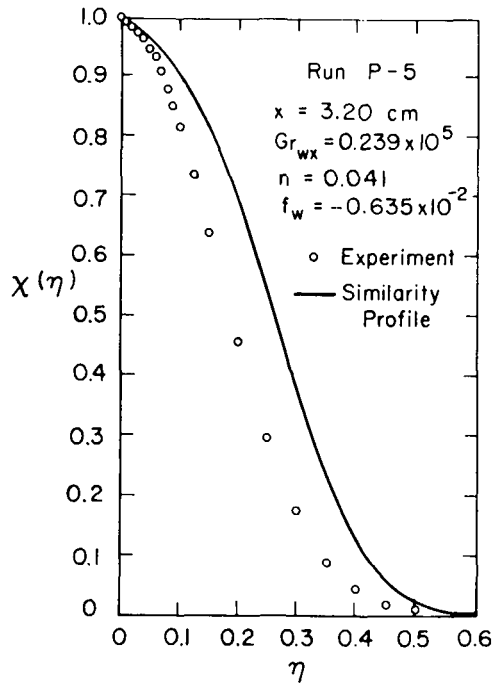

Fig. 5 Concentration profile for Run P-5

$$\left.\begin{aligned} &\phi(0) = \mathrm{Sc}^{1/2}(1+\mathrm{Sc})^{1/4} f_w \qquad \phi'(0) = 0 \quad \chi(0) = 1 \\ &\phi''(\infty) = 0 \quad \chi(\infty) = 0 \end{aligned}\right\} \tag{15}$$

where prime refers to derivatives with respect to ξ, and

$$\left.\begin{aligned} &\phi(\xi) = \mathrm{Sc}^{1/2}(1+\mathrm{Sc})^{1/4} f(\eta) \qquad \chi(\xi) = \chi(\eta) \\ &\xi = \left(\frac{\mathrm{Sc}^2}{1+\mathrm{Sc}}\right)^{1/4} \eta \end{aligned}\right\} \tag{16}$$

Note that the boundary condition $\phi'(\infty) = 0$ is here replaced by $\phi''(\infty)$ since the solution sought here represents an inner solution. Numerical solutions to equations (14) and (15) were used to compare with the experimental data on a local basis.

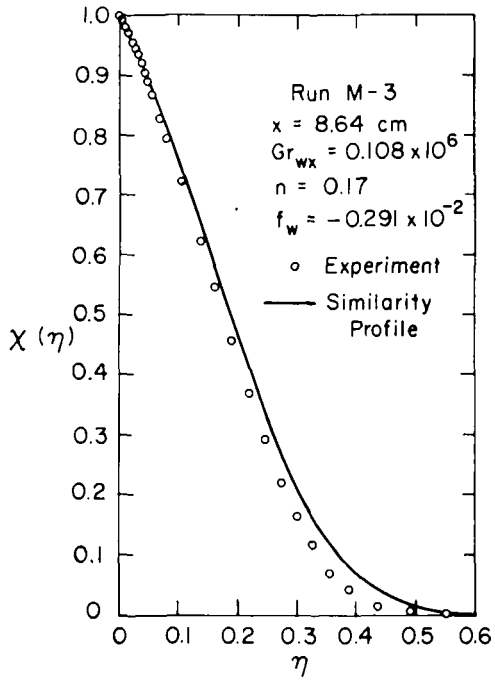

Fig. 4 Concentration profile for Run M-3

For such a comparison, it is necessary to establish the input parameters from the experimental data for use in the local similarity solution. A least-square technique was used to fit the three $(w_{A\infty} - w_{Aw})$ values in a given run, as shown in Table 2, by a curve of the form $\sim \bar{x}^n$, so that a value of n could be determined. It was found that in all runs the data of $(w_{A\infty} - w_{Aw})$ only differed from that of the least-square curve by no more than 0.6 percent. The constant a_2, which in this case represents the level of the mass transfer Grashof number, was then calculated from equations (5) and (6):

$$a_2 = \left[\frac{g\alpha L^3}{\nu^2}(w_{Aw} - w_{A\infty}) \Big/ (4\bar{x})^n\right]^{1/(1-n)} \tag{17}$$

The corresponding f_w could then be determined from equations (11) and differentiation with respect to $\bar{x}$, or

$$f_w = -\frac{1}{n+3}\bar{v}_w \left(\frac{4\bar{x}}{a_2}\right)^{(1-n)/4} \tag{18}$$

where $\bar{v}_w$ is the dimensionless injection velocity $v_w L/\nu$, which is positive for injection. Once the local value of f_w was known, the similarity solution could then be obtained numerically with the n value determined for the run and Sc of f_w was known and calculated from the property values.

Figs. 3–6 show typical comparisons of the concentration profiles for a wide range of f_w values, as a function of the similarity variable η given by $\eta = (y/L)(a_2/4\bar{x})^{(1-n)/4}$. It is apparent from the figures that the experimental data exhibit the same trends predicted by the present local similarity solution. It is also apparent that the similarity profiles are in good agreement with the data at low injection rates, but show increasingly large deviations from the experimental data as injection rate increases. In all cases, the local similarity solution underestimates the surface concentration gradient $-\chi'(0)$.

In the limit $f_w \to 0$, the similarity solution meets all the conditions of the experimental situation with the same value of n, and consequently, the local similarity solution is quite accurate in the range of low injection rates. As injection rate increases, the behaviors of the injection rate variation along the plate are quite different. The higher injection rate in the upstream locations, as called for in the similarity solution according to equation (18), carried a large amount of low

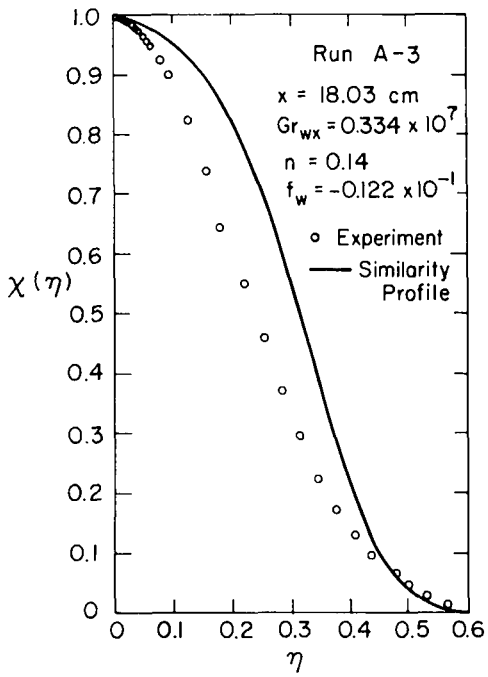

Fig. 6 Concentration profile for Run A-3

concentration fluid upward and would consequently lead to lower concentration at any given y, when compared to the case of uniform injection of the experiments. As a result, the similarity solution deviates increasingly from the experimental situation as injection rate increases and in all cases of f_w, underestimates the dimensionless surface concentration gradient $-\chi'(0)$.

The apparent relation between the surface concentration and the surface injection rate as shown in Table 2 needs some clarification. As pointed out previously, in the mass transfer problem these two quantities should be independent inputs. The reason that they are not in the experiments is because of the specific experimental apparatus and procedure used. There was always back diffusion of the salt into the plate between the runs and the Foametal plate retained a certain level of concentration before the next run commenced. As a result, this contamination affected the subsequent surface concentration variation. For low injection rates, the surface concentration level was high. As the injection rate increases, more pure water with zero concentration came through the plate, thus leading to lower concentrations at the surface. However, this back-diffusion phenomenon should not affect the validity of the experimental data, since the mass transfer was uniquely determined by the injection rate and the surface concentration variation.

To further compare the experimental data with the local similarity solution, the Sherwood numbers in the form of $Sh_x/(Gr_{wx}/4)^{1/4}$ were determined from both the experimental data and the similarity solution in accordance with equation (13) for the M-series of runs. The results at several locations are shown in Table 3, together with the corresponding f_w values. Note that all local Sherwood numbers are negative, indicating that the net surface mass flux is going into the fluid from the surface against the direction of decreasing concentration. The primary reason is that in all the experimental runs the surface convective flux overshadows the diffusive flux.

Upon initial observation, it is very surprising that while the surface gradients $-\chi'(0)$ are not predicted well by the local similarity solution at large injection rates, the surface mass fluxes predicted by the local similarity solution are quite accurate throughout the injection rate range dealt with in the experiments. The reason here is that we are dealing with basically an injection-dominated mass transfer problem. The diffusive flux as represented by $\chi'(0)$ in equation (13) only plays

Table 3 Comparison of the experimental and theoretical values of $-Sh_x/(Gr_{wx}/4)^{1/4}$

RUN	x(cm)	$-f_w \times 10^2$	$-Sh_x/(Gr_{wx}/4)^{1/4}$	
			Experimental	Theoretical
M-1	2.94	0.111	8.63	8.31
M-2	5.91	0.213	11.6	11.6
M-3	8.64	0.291	14.0	14.1
M-4	2.94	0.356	11.6	11.7
M-5	5.87	0.840	10.6	11.1
M-7	8.23	1.710	2.64	2.81

a minor role in the mass transfer process. At low injection rates, $\chi'(0)$ is accurate, but so is the convective flux term. At high injection rates, $\chi'(0)$ is inaccurate, but it only contributes a small amount to the net surface mass flux.

Another feature of the data depicted in Table 3 is that the surface mass flux increases to a maximum and then decreases as the injection rate increases. This behavior is believed to be directly related to the present experimental investigation. It can readily be understood if we examine again equation (13). The convective flux term is largely determined by the product of w_{Aw} and f_w. At low flow rates, w_{Aw} decreases only slightly as injection rate and f_w increase. As a result, the surface mass flux increases. We reach a maximum when these two effects balance each other. As the injection rate further increases, the w_{Aw} decreases much more rapidly than the increase in f_w, and consequently the surface mass flux drops off. In fact, it is fully expected that as the injection rate becomes very high, the surface concentration will approach zero and the surface mass flux will also tend to be zero.

Conclusion

An experimental study was carried out for mass transfer along a vertical plate with surface injection of pure water into an environment of a dilute aqueous sodium chloride solution. Concentration profiles and surface concentration gradients were measured by a Mach-Zehnder interferometer. The results are compared with a local similarity solution with matched surface concentration variation, local injection rate and Grashof number, and Schmidt number. The following conclusions can be drawn:

1 Some typical experimental data of surface concentration variations and surface concentration gradients are presented in tabulated form so that they could be used as a base for developing predictive theories.

2 The local similarity solution predicts well the concentration profiles for low injection rates. However, the prediction becomes increasingly worse as the injection rate increases. Also, throughout the range of injection rates used in the experiments, the local similarity solution underestimates the surface concentration gradients, the difference being larger for higher injection rates.

3 In contrary, the local similarity solution is quite accurate in predicting the surface mass flux even in the range of high injection rates where predictions of surface concentration gradient are inaccurate. The resson for this is that the surface mass flux is predominantly governed by the convective flux.

4 For the surface concentration variations encountered in the experiments, the surface mass flux increases to a maximum and then decreases, as the injection rate increases. As the injection rate becomes very large, the surface mass flux tends to zero in the limit.

5 No simple dimensionless correlation was found for the local Sherwood number in the present investigation.

Acknowledgment

This study was supported in part by the Office of Naval Research under Contract No 0014-68-A-0152.

References

1 Saville, D. A., and Churchill, S. W., "Simultaneous Heat and Mass Transfer in Free Convection Boundary Layers," *Journal of the American Institute of Chemical Engineers*, Vol. 16, 1970, pp. 268–273.

2 Gebhart, B., and Pera, L., "The Nature of Vertical Natural Convection Flows Resulting From the Combined Buoyancy Effects of Thermal and Mass Diffusion," *International Journal of Heat and Mass Transfer*, Vol. 14, 1971, pp. 2025–2050.

3 Adams, J. A., and McFadden, P. W., "Simultaneous Heat and Mass Transfer in Free Convection With Opposing Body Forces," *Journal of the American Institute of Chemical Engineers*, Vol. 12, 1966, pp. 642–647.

4 Den Bonter, J. A., DeMunnik, B., and Heertjes, P. M., "Simultaneous Heat and Mass Transfer in Laminar Free Convection From a Vertical Plate," *Chemical Engineering Science*, Vol. 23, 1968, pp. 1185–1190.

5 Lloyd, J. R., Sparrow, E. M., and Eckert, E. R. G., "Local Natural Convection Mass Transfer Measurements," *Journal of Electrochemical Society*, Vol. 119, 1972, pp. 702–707.

6 Goldstein, R. J., Sparrow, E. M., and Jones, D. C., "Natural Convection Mass Transfer Adjacent to Horizontal Plates," *International Journal of Heat and Mass Transfer*, Vol. 16, 1973, pp. 1025–1035.

7 Sparrow, E. M., and Cess, R. D., "Free Convection With Blowing or Suction," JOURNAL OF HEAT TRANSFER, TRANS. ASME, Series C, Vol. 83, 1961, pp. 287–289.

8 Eichhorn, R., "The Effect of Mass Transfer on Free Convection," JOURNAL OF HEAT TRANSFER, TRANS. ASME, Series C, Vol. 82, 1960, pp. 260–263.

9 Lewis, G. B., "Natural Convection Heat and Mass Transfer Along a Vertical Plate," PhD dissertation, University of Notre Dame, Aug. 1972.

10 Eckert, E. R. G., Drake, R. M., and Soehngen, E., "Manufacture of a Zehnder-Mach Interferometer," Air Force Report 5721, ASTI No. 34235, 1948.

11 Eckert, E. R. G., and Soehngen, E., "Studies on Heat Transfer in Laminar Free Convection With the Zehnder-Mach Interferometer" Air Force Report 5747, ASTI No. 44580, 1948.

12 Goldstein, R. J., "Interferometric Study of the Steady State and Transient Free Convection Thermal Boundary Layers in Air and Water About a Uniformly Heated Vertical Flat Plate," PhD thesis, University of Minnesota, 1959.

13 *International Critical Tables*, Vols. III, V, and VII, McGraw-Hill, New York, 1930.

14 Kauffman, D. W., *Sodium Chloride*, Reinhold, New York, 1960.

15 Dorsey, N. E., *Properties of Ordinary Water Substance*, Reinhold, New York, 1940.

16 Kruis, A., "Die Aquivalent Dispersion Von. starken Elektrolyten in Losung I. Die Messung der Konzentrationsabhangigheit der Aquivalentrefraktion in Sicht baren," *Zeitschrift für Physik und Chemie*, Vol. 34, Abt. B, 1936, pp. 13–50.

17 Yang, K. T., "Possible Similarity Solutions for Laminar Free Convection on Vertical Plates and Cylinders," *Journal of Applied Mechanics*, Vol. 27, 1960, pp. 230–236.

18 Yang, K. T., Novotny, J. L., and Cheng, Y. S., "Laminar Free Convection From a Nonisothermal Plate Immersed in a Temperature Stratified Medium," *International Journal of Heat and Mass Transfer*, Vol. 15, 1972, pp. 1097–1109.

J. H. Merkin

Lecturer,
Department of Applied Mathematics,
University of Leeds,
Leeds, England

Free Convection Boundary Layers on Cylinders of Elliptic Cross Section

Numerical results are presented for free convection boundary layers over horizontal cylinders of elliptic cross section when the major axis is both horizontal and vertical and when the cylinder is isothermal and has constant heat flux. The particular case of a circular cylinder is considered and these results are compared with the various series expansions suggested for solving the equations.

Introduction

There is, at present, a good deal of information about laminar free convection boundary layers over isothermal bodies for which the flow is similar. For more general body shapes various approximate methods have been suggested, perhaps the most reliable of these being series expansion techniques which expand in powers of some variable related to the distance around the cylinder. The disadvantage of such methods is that it is impossible to estimate their overall accuracy. In [1],[1] the author described a method of solving the full partial differential equations for the free convection boundary layer over cylinders of general rounded cross-sectional form which could be used to give reliable results over the whole of the cylinder; the particular example considered there was of a circular cylinder. These numerical results can then be used as a check on those given by the various series expansions. Those considered are a Blasius series, as described by [2, 3] which uses the natural boundary-layer variables, a Görtler-type expansion, given by [4], in which a transformation of variables is first made, and a series based on a local similarity solution, as given by [5, 6].

The numerical solution is also used to give results for the heat transfer from isothermal cylinders of elliptic cross section of various eccentricities in both cases when the major axis is horizontal and vertical. Also given are surface temperatures on these cylinders when they have constant heat flux. These latter results are obtained from essentially the same numerical method as given in [1], modified slightly to account for the derivative boundary condition on the cylinder.

Equations of Motion

With the usual assumptions, the equations for the free convection boundary layer on a horizontal cylinder are

$$\frac{\partial u}{\partial x} + \frac{\partial v}{\partial y} = 0 \tag{1}$$

$$u\frac{\partial u}{\partial x} + v\frac{\partial u}{\partial y} = g\beta(T - T_0)\sin\phi + \nu\frac{\partial^2 u}{\partial y^2} \tag{2}$$

$$u\frac{\partial T}{\partial x} + v\frac{\partial T}{\partial y} = \kappa\frac{\partial^2 T}{\partial y^2} \tag{3}$$

with boundary conditions

$u = v = 0$, $T = T_1$ (isothermal) or

$$\frac{\partial T}{\partial y} = -q \text{ (constant heat flux) on } y = 0$$

$$u \to 0, \qquad T \to T_0 \qquad \text{as } y \to \infty \tag{4}$$

Here ϕ is the angle made by the outward normal from the cylinder with the downward vertical. A full description of the coordinate system used is given in Fig. 1. From equation (1) a stream function ψ can be defined in the usual way, and then the equations made nondimensional by introducing nondimensional variables $X = x/a$ and for the isothermal case $\theta = (T - T_0)/\Delta T$, $\bar{\psi} = \psi/\nu \mathrm{Gr}^{-1/4}$, $Y = (y/a)\mathrm{Gr}^{1/4}$ with the Grashof number given by $\mathrm{Gr} = g\beta\Delta T a^3/\nu^2$, and in the constant heat flux case $\theta = (T - T_0)\mathrm{Gr}^{1/5}/aq$, $\bar{\psi} = \psi/\nu\mathrm{Gr}^{-1/5}$, $Y = (y/a)\mathrm{Gr}^{1/5}$ with the Grashof number now given by $\mathrm{Gr} = g\beta q a^4/\nu^2$. a is a typical length scale, taken as the radius for the circular cylinder and the length of the semimajor axis for an elliptic cross section.

To deal with bodies with rounded lower ends for which $\sin\phi/X \to A_0$ (a constant) as $X \to 0$, a further transformation is necessary, namely $\bar{\psi} = Xf(X, Y)$. The resulting equations are

$$\frac{\partial^3 f}{\partial Y^3} + \frac{\sin\phi}{X}\theta + f\frac{\partial^2 f}{\partial Y^2} - \left(\frac{\partial f}{\partial Y}\right)^2 = X\left(\frac{\partial f}{\partial Y}\frac{\partial^2 f}{\partial X \partial Y} - \frac{\partial f}{\partial X}\frac{\partial^2 f}{\partial Y^2}\right) \tag{5}$$

[1] Numbers in brackets designate References at end of paper.

Contributed by the Heat Transfer Division for publication in the JOURNAL OF HEAT TRANSFER. Manuscript received by the Heat Transfer Division December 30, 1976.

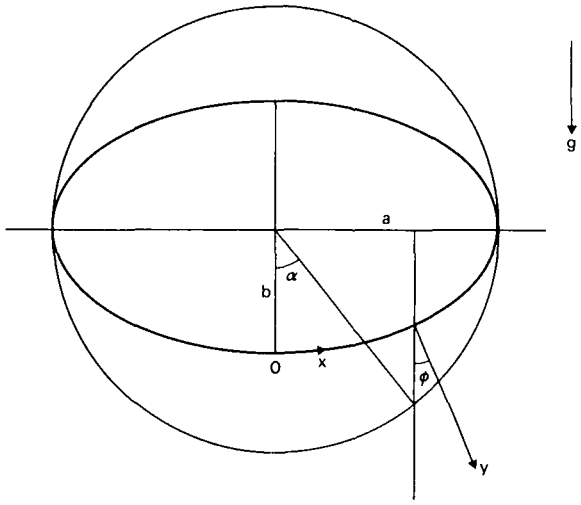

Fig. 1

$$\frac{1}{\Pr}\frac{\partial^2\theta}{\partial Y^2} + f\frac{\partial\theta}{\partial Y} = X\left(\frac{\partial\theta}{\partial X}\frac{\partial f}{\partial Y} - \frac{\partial\theta}{\partial Y}\frac{\partial f}{\partial X}\right) \tag{6}$$

with boundary conditions

$$f = \frac{\partial f}{\partial Y} = 0, \qquad \theta = 1 \text{ (isothermal)},$$

$$\frac{\partial\theta}{\partial Y} = -1 \text{ (constant heat flux) on } Y = 0$$

$$\frac{\partial f}{\partial Y} \to 0, \qquad \theta \to 0 \qquad \text{as } Y \to \infty \tag{7}$$

For cylinders of circular cross section $\sin\phi = \sin X$. For cylinders of elliptic cross section there are two orientations to consider, one when the major axis is horizontal and the other when it is vertical. Following [5], we will call these the blunt and slender orientations, respectively. Here X and $\sin\phi$ are given parametrically in terms of a parameter α, as shown in Fig. 1, by

$$X = \int_0^\alpha (1 - e^2\sin^2\lambda)^{1/2}\,d\lambda, \qquad \sin\phi = \frac{b}{a}\frac{\sin\alpha}{\sqrt{1 - e^2\sin^2\alpha}}$$

for the blunt orientation, and

$$X = \int_0^\alpha (1 - e^2\cos^2\lambda)^{1/2}\,d\lambda, \qquad \sin\phi = \frac{\sin\alpha}{\sqrt{1 - e^2\cos^2\alpha}}$$

for the slender orientation. b is the length of the semiminor axis and e is the eccentricity, given by $e^2 = 1 - (b/a)^2$, so that $A_0 = b/a$ for the blunt orientation and $A_0 = (a/b)^2$ for the slender orientation.

Equations (5) and (6) were solved numerically by the method described in [1]. This involved first differencing in the X-direction and averaging the other terms. This leads to two nonlinear ordinary differential equations in the Y-direction which are written in finite-difference form and the resulting nonlinear algebraic equations solved iteratively by the Newton-Raphson method. The numerical solution starts at $X = 0$ with profiles as given by the local similarity solution there, i.e., with $\sin\phi/X$ replaced by A_0 and proceeds round the cylinder up to the highest point. A step length of 0.1 in the Y-direction was used and the outer boundary condition was applied at $Y = 20$. This was found to give sufficiently accurate results.

Values of the heat transfer Q, given by

$$Q = -a\frac{\mathrm{Gr}^{-1/4}}{\Delta T}\left(\frac{\partial T}{\partial y}\right)_0 = -\left(\frac{\partial\theta}{\partial Y}\right)_0$$

are given in Tables 1 and 2 for blunt and slender orientations, respectively, for various values of b/a.

For the constant heat flux case the method has to be modified slightly to allow for the derivative boundary condition on the cylinder, and results for the surface temperature $\theta(X, 0)$ in this case are given in Tables 3 and 4 for the blunt and slender orientations, respectively. The values of X for various α are not repeated in Tables 3 and 4 as they are the same as in Tables 1 and 2 for the corresponding value of b/a.

Graphs of θ and of $\partial f/\partial Y$, which is related to the streamwise velocity component u by $u = (\nu/a)\,\mathrm{Gr}^{2/5}X\,(\partial f/\partial Y)$, as calculated by the numerical solution at various values of X for $b/a = \frac{1}{2}$ are given for the blunt orientation in Fig. 2 and for the slender orientation in Fig. 3.

Table 1 Heat transfer Q—blunt orientation, Pr = 1 (isothermal cylinder)

	b/a = 0.1		b/a = 0.25		b/a = 0.5		b/a = 0.75	
α	X	Q	X	Q	X	Q	X	Q
0	0.000	0.2369	0.000	0.2979	0.000	0.3542	0.000	0.3920
0.2	0.199	0.2382	0.199	0.2994	0.199	0.3555	0.199	0.3925
0.4	0.390	0.2421	0.390	0.3039	0.392	0.3593	0.395	0.3940
0.6	0.565	0.2490	0.567	0.3118	0.574	0.3657	0.585	0.3961
0.8	0.718	0.2599	0.723	0.3240	0.740	0.3747	0.766	0.3986
1.0	0.843	0.2767	0.853	0.3418	0.887	0.3861	0.937	0.4004
1.2	0.936	0.3031	0.954	0.3673	1.014	0.3984	1.099	0.4006
1.4	0.993	0.3497	1.027	0.4008	1.124	0.4081	1.253	0.3975
1.6	1.019	0.4142	1.080	0.4244	1.226	0.4088	1.403	0.3897
1.8	1.052	0.3731	1.136	0.4070	1.329	0.3958	1.555	0.3766
2.0	1.120	0.3206	1.217	0.3670	1.443	0.3713	1.711	0.3585
2.2	1.222	0.2748	1.326	0.3241	1.576	0.3407	1.875	0.3364
2.4	1.356	0.2361	1.465	0.2840	1.729	0.3081	2.049	0.3112
2.6	1.516	0.2030	1.627	0.2476	1.900	0.2752	2.232	0.2838
2.8	1.697	0.1735	1.809	0.2136	2.085	0.2418	2.424	0.2535
3.0	1.891	0.1444	2.003	0.1791	2.281	0.2056	2.622	0.2186
π	2.032	0.1206	2.145	0.1504	2.422	0.1746	2.763	0.1873

Nomenclature

a = length of semimajor axis of ellipse
b = length of semiminor axis of ellipse
e = eccentricity of ellipse
g = acceleration of gravity
q = prescribed (constant) heat flux
T = temperature of fluid
T_0 = temperature of ambient fluid
T_1 = prescribed (constant) cylinder temperature
$\Delta T = T_1 - T_0$
u = velocity component in the x-direction
v = velocity component in the y-direction
x = coordinate measuring distance round the cylinder
y = coordinate measuring distance normal to the cylinder
Gr = Grashof number
$\overline{Q}$ = average heat flux
Pr = Prandtl number
β = thermal expansion coefficient
κ = thermal conductivity
ν = kinematic viscosity
ϕ = angle between outward normal and downward vertical

Table 2 Heat transfer Q—slender orientation, Pr = 1 (isothermal cylinder)

	b/a = 1		b/a = 0.75		b/a = 0.5		b/a = 0.25	
α	X	Q	X	Q	X	Q	X	Q
0	0.000	0.4212	0.000	0.5150	0.000	0.5953	0.000	0.8359
0.2	0.200	0.4204	0.151	0.4828	0.102	0.5826	0.055	0.7682
0.4	0.400	0.4182	0.306	0.4733	0.215	0.5519	0.131	0.6617
0.6	0.600	0.4145	0.469	0.4596	0.345	0.5159	0.236	0.5788
0.8	0.800	0.4093	0.641	0.4436	0.494	0.4819	0.371	0.5187
1.0	1.000	0.4025	0.824	0.4271	0.663	0.4522	0.530	0.4745
1.2	1.200	0.3942	1.014	0.4108	0.847	0.4270	0.709	0.4409
1.4	1.400	0.3843	1.211	0.3952	1.041	0.4058	0.902	0.4149
1.6	1.600	0.3727	1.411	0.3804	1.240	0.3878	1.102	0.3943
1.8	1.800	0.3594	1.610	0.3661	1.439	0.3724	1.300	0.3779
2.0	2.000	0.3443	1.805	0.3519	1.631	0.3589	1.489	0.3646
2.2	2.200	0.3270	1.993	0.3373	1.810	0.3465	1.664	0.3538
2.4	2.400	0.3073	2.173	0.3212	1.973	0.3342	1.816	0.3447
2.6	2.600	0.2847	2.343	0.3022	2.117	0.3204	1.942	0.3363
2.8	2.800	0.2581	2.503	0.2784	2.242	0.3019	2.039	0.3266
3.0	3.000	0.2252	2.656	0.2463	2.351	0.2731	2.108	0.3084
π	3.142	0.1963	2.763	0.2145	2.411	0.2407	2.145	0.2785

Table 3 Cylinder temperature $\theta(X, 0)$—blunt orientation, Pr = 1 (constant heat flux)

α	b/a = 0.1	b/a = 0.25	b/a = 0.5	b/a = 0.75
0	3.1647	2.6351	2.2943	2.1158
0.2	3.1565	2.6287	2.2903	2.1144
0.4	3.1318	2.6097	2.2784	2.1105
0.6	3.0903	2.5780	2.2590	2.1046
0.8	3.0316	2.5335	2.2331	2.0978
1.0	2.9554	2.4767	2.2022	2.0916
1.2	2.8612	2.4093	2.1694	2.0885
1.4	2.7512	2.3365	2.1404	2.0912
1.6	2.6466	2.2756	2.1238	2.1030
1.8	2.6101	2.2543	2.1290	2.1271
2.0	2.6403	2.2835	2.1623	2.1664
2.2	2.7375	2.3621	2.2255	2.2228
2.4	2.8943	2.4844	2.3180	2.2983
2.6	3.1316	2.6455	2.4399	2.3960
2.8	3.3575	2.8472	2.5959	2.5228
3.0	3.6868	3.1107	2.8055	2.6979
π	4.0251	3.3829	3.0253	2.8856

Results and Discussion

The numerical integration of equations (5) and (6) can be carried out up to the top of the cylinder, given by $\alpha = \pi$, without encountering a singularity. Furthermore, at this point, the boundary layer has nonzero thickness and there is no flow reversal, see Figs. 2 and 3. In forced convection flows a singularity is found in the solution of the boundary layer equations with the skin friction behaving like $(X_s - X)^{1/2}$, where X_s is the separation point. The solution cannot be continued past $X = X_s$ and this point is identified with the boundary layer leaving the surface to form a wake behind the cylinder. Thus the mechanism by which the free convection boundary layer leaves the surface of the cylinder to form a buoyant plume is quite different to

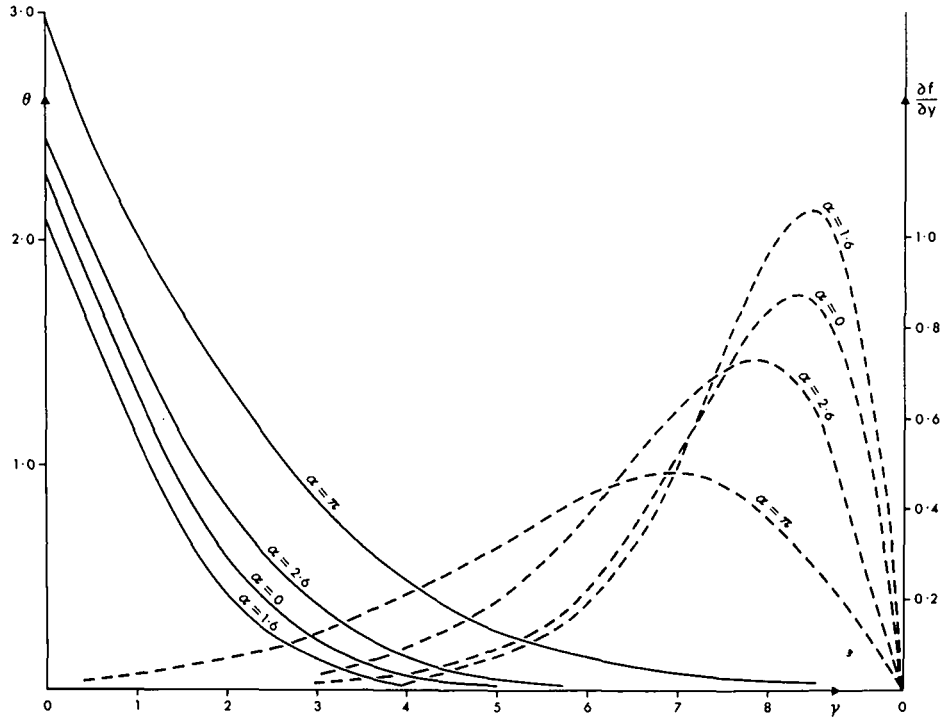

Fig. 2

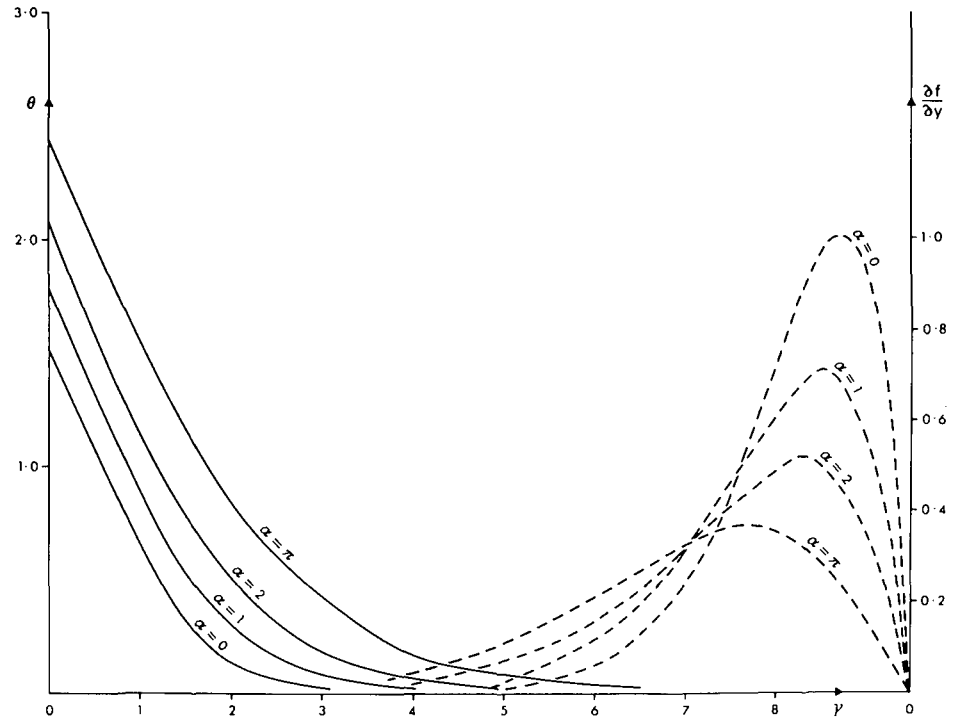

Fig. 3

that of ordinary boundary-layer separation. We can suggest an explanation of this type of separation as follows. There will be two boundary layers, one on each side of the cylinder, which will collide at the top and so be forced up off the surface to form the buoyant plume. Experimental observations by [7] show this form of separation by the collision of two free convection boundary layers; [7] also report no flow reversal, again in general agreement with the foregoing discussion.

In this collision region, where the boundary layer leaves the surface, the tangential and streamwise velocity components will be of about the same size, so we would expect it to have streamwise extent of the order of the thickness of the boundary layer. Although the boundary-layer model will not be appropriate in the immediate vicinity of the top of the cylinder, results are presented there to show that the numerical integration of the equations can be carried out up to that point, whereas in the forced convection case the numerical integration of the boundary-layer equations cannot proceed beyond the separation point, which is reached before the top of the cylinder.

Various series expansion methods have been suggested for solving equations (5) and (6), and Table 5 gives the values of Q as obtained by these series as compared with those from the numerical solution for a circular cylinder with Pr = 0.7, the former being taken from [5] with the corrected values for the Görtler series taken from [8]. It should be noted that the length scale used for the results given in Table 5 is the diameter of the circle $2a$ whereas it is a in the other tables. From Table 5 it can be seen that the Blasius series [2, 3] is better than the Görtler series [4] for evaluating Q. The Blasius series gives an overestimate and the Görtler series, an underestimate for Q. It also appears from the results in Table 5 that the series expansion based on a local similarity solution recently suggested by Lin and Chao [5] is an improvement on the other series. For example, at 150 deg from the front stagnation point this latter series is about 1 percent in error, while the Blasius and Görtler series are about 3 and 8 percent in error, respectively.

The results in Table 1 show that for the blunt orientation Q first increases, with a corresponding decrease in boundary-layer thickness, while for the slender orientation Q decreases and the boundary layer thickens all the way round the cylinder. We can calculate the average heat transfer $\overline{Q}$, given by

$$\overline{Q} = \frac{1}{X_0}\int_0^{X_0} Q(X)dX$$

where X_0 is the value of X at the highest point on the cylinder, given parametrically by $\alpha = \pi$. Values of $\overline{Q}$ are given in Table 6 from which it can be seen that the slender orientation gives a higher value of $\overline{Q}$

Table 4 Cylinder temperature $\theta(X, 0)$—slender orientation, Pr = 1 (constant heat flux)

α	b/a = 1	b/a = 0.75	b/a = 0.5	b/a = 0.25
0	1.9963	1.7808	1.5147	1.1562
0.2	1.9994	1.7872	1.5315	1.2096
0.4	2.0046	1.8053	1.5759	1.3233
0.6	2.0135	1.8333	1.6377	1.4469
0.8	2.0261	1.8687	1.7071	1.5634
1.0	2.0428	1.9090	1.7779	1.6687
1.2	2.0637	1.9524	1.8468	1.7626
1.4	2.0894	1.9974	1.9118	1.8455
1.6	2.1205	2.0432	1.9722	1.9182
1.8	2.1578	2.0897	2.0278	1.9815
2.0	2.2025	2.1374	2.0789	2.0360
2.2	2.2562	2.1874	2.1264	2.0823
2.4	2.3218	2.2423	2.1719	2.1213
2.6	2.4035	2.3064	2.2189	2.1584
2.8	2.5097	2.3883	2.2744	2.1852
3.0	2.6597	2.5064	2.3554	2.2237
π	2.8245	2.6407	2.4539	2.2771

Table 5 Heat transfer Q—circular cylinder Pr = 0.7 (isothermal cylinder)

X (in degrees)	Numerical	Lin & Chao	Blasius	Görtler
0	0.4402	0.4402	0.4402	0.4402
10	0.4395	0.4393	0.4396	0.4397
20	0.4377	0.4375	0.4379	0.4380
30	0.4348	0.4346	0.4350	0.4351
40	0.4307	0.4304	0.4309	0.4308
50	0.4255	0.4252	0.4256	0.4254
60	0.4190	0.4186	0.4192	0.4187
70	0.4113	0.4109	0.4116	0.4105
80	0.4024	0.4018	0.4029	0.4010
90	0.3922	0.3913	0.3930	0.3898
100	0.3806	0.3794	0.3819	0.3769
110	0.3677	0.3659	0.3697	0.3620
120	0.3532	0.3508	0.3563	0.3449
130	0.3370	0.3338	0.3417	0.3251
140	0.3190	0.3145	0.3260	0.3019
150	0.2986	0.2923	0.3091	0.2740
160	0.2752	0.2700	0.2928	
170	0.2475			
180	0.2121			

Table 6 Average heat transfer $\bar{Q}$ (isothermal cylinder) Pr = 1

Orientation	b/a	$\bar{Q}$
blunt	0.1	0.2373
blunt	0.25	0.2938
blunt	0.50	0.3340
blunt	0.75	0.3496
	1	0.3551
slender	0.75	0.3799
slender	0.50	0.4075
slender	0.25	0.4325

than the blunt orientation for a particular value of b/a, so we can conclude that the slender orientation is a more efficient way of transferring heat to the fluid from the cylinder.

Table 3 shows that in the constant heat flux case the cylinder temperature first decreases for the blunt orientation while for the slender orientation it increases all the way round the cylinder. It can also be seen from Figs. 2 and 3 that, as in the isothermal case, for the blunt orientation the boundary-layer thickness first decreases while for the slender orientation the boundary layer thickens all the way round the cylinder.

References

1 Merkin, J. H., "Free Convection Boundary Layer on an Isothermal Horizontal Cylinder," Presented at the ASME-AIChE Heat Transfer Conference, St. Louis, Mo., Aug. 1976.

2 Chiang, T., and Kaye, J., "On Laminar Free Convection From a Horizontal Cylinder," *Proceedings 4th National Congress of Applied Mechanics*, 1962, p. 1213.

3 Chiang, T., Ossin, A., and Tien, C. L., "Laminar Free Convection From a Sphere," JOURNAL OF HEAT TRANSFER, TRANS. ASME, Series C, Vol. 86, 1964, p. 537.

4 Saville, D. A., and Churchill, S. W., "Laminar Free Convection in Boundary Layers Near Horizontal Cylinders and Vertical Axisymmetric Bodies," *Journal of Fluid Mechanics*, Vol. 29, 1967, p. 391.

5 Lin, F. N., and Chao, B. T., "Laminar Free Convection Over Two-Dimensional and Axisymmetric Bodies of Arbitrary Contour," JOURNAL OF HEAT TRANSFER, TRANS. ASME, Series C, Vol. 96, 1974, p. 435.

6 Chao, B. T., and Lin, F. N., "Local Similarity Solutions for Free Convection Boundary Layer Flows," JOURNAL OF HEAT TRANSFER, TRANS. ASME, Series C, Vol. 97, 1975, p. 294.

7 Pera, L., and Gebhart, B., "Experimental Observations of Wake Formation Over Cylindrical Surfaces in Natural Convection Flows," *International Journal of Heat and Mass Transfer*, Vol. 15, 1972, p. 175.

8 Lin, F. N., and Chao, B. T., "Addendum to Laminar Free Convection Over Two-Dimensional and Axisymmetric Bodies of Arbitrary Contour," JOURNAL OF HEAT TRANSFER, TRANS. ASME, Series C, Vol. 98, 1976, p. 344.

J. D. Felske
Asst. Professor,
Department of Mechanical Engineering,
Massachusetts Institute of Technology,
Cambridge, Mass.

C. L. Tien
Professor,
University of California,
Berkeley, Calif.

The Use of the Milne-Eddington Absorption Coefficient for Radiative Heat Transfer in Combustion Systems

The applicability of the Milne-Eddington absorption coefficient approximation is discussed in relation to the calculation of radiative transport involving the two distinct types of species produced in combustion systems—gases and soot particles. The approximation is found to apply well to hydrocarbon soot particles and as a result analytical closed-form solutions are derived for the radiative heat transfer inside one-dimensional slab shaped soot clouds. (The applicability of the gray approximation to soot is also discussed.) For the calculation of total band radiation from gases, however, the Milne-Eddington approximation is found to be questionable. The meaning of its assumption is discussed in light of an established Curtis-Godson wide band scaling approximation. Its usefulness for real gases is then assessed through the calculation and comparison of slab radiation by both techniques.

Introduction

The determination of radiation heat transfer through nongray nonhomogeneous absorbing-emitting media presents a formidable computational problem. Approaches to this problem which allow a compact mathematical and computational formulation always involve a "separability" type of approximation. These approximations, as the name indicates, allow the mathematical separation of the dependency on frequency and the dependency on pathlength of the various functions which are required to characterize the medium—such as the absorption coefficient, the mean spectral transmittance or the total band absorptance. Two such approximations of particular usefulness are the Milne-Eddington absorption coefficient assumption and the Curtis-Godson scaling approximation. Both have the effect of allowing the frequency integration to be completed first leaving only the pathlength integration to be made afterwards.

The Curtis-Godson approximation [1][1] attains this separation by assuming that the functions required for the nonhomogeneous pathlength have the same functional form as their homogeneous counterparts with the nonhomogeneity of the path being accounted for by simply scaling the independent variables. This approximation has been verified for gases for both narrow bands of rotational lines [1] and, more recently, for entire vibrational-rotational wide bands [2–4].

The Milne-Eddington absorption coefficient approximation, on the other hand, takes the absorption coefficient to be directly separable into a product of a function only of frequency with a function only of the path variables. This means that:

$$k_\nu(T, P) = \alpha_1(\nu)\beta_1(T, P) \tag{1}$$

where k_ν is the spectral absorption coefficient, ν is the wavenumber, T the temperature, P the pressure, α_1 the frequency function, and β_1 the pathlength function. The use of this approach in the calculation of slab radiation has been often suggested [5–9], and it allows a very elegant mathematical treatment of the problem [5, 7]. However the applicability of such an assumption to real systems is still questionable.

The purpose of the present paper is twofold. First, it is to investigate the applicability of this latter method to systems containing the typical absorbing-emitting gases and soot particles produced by combustion. Second, it is to complete the analytical development for nonhomogeneous slab radiation in the cases where it is found to apply.

[1] Numbers in brackets designate References at end of paper.

Contributed by the Heat Transfer Division for publication in the JOURNAL OF HEAT TRANSFER. Manuscript received by the Heat Transfer Division September 7, 1976.

The analytical developments will be for systems in nonradiative equilibrium since in real situations other modes of heat transfer are always present. As such, typical temperature profiles will be assumed and closed form solutions will then be derived.

Hydrocarbon Soots

Soot is generated in flames due to the incomplete combustion of the fuel [10]. The nucleation and growth of soot particles is not well understood at this time, but some general observations have been made regarding their production [10–19]. In typical gaseous diffusion flames, the volume fraction of soot (volume of soot per total volume of combustion products) has been experimentally determined to be on the order of 10^{-7} to 10^{-6} [11, 15]. The soot can be in the form of spherical particles, agglomerated masses, or long filaments [10, 14, 15] and its size generally ranges from 50 angstroms to 0.3 microns in diameter with agglomerated masses sometimes being even larger [10, 14, 15]. These characteristics, and the simplifications they allow in theoretical developments, will be employed throughout the present considerations of the radiative properties of and the radiative transfer within clouds of soot particles.

The Milne-Eddington Absorption Coefficient for Soot. From the Mie theory [20], the important parameters which determine the radiative properties of soot are the size parameter:

$$w_i = \frac{\pi D_i}{\lambda} \tag{2}$$

where D_i is the diameter of the assumed spherically shaped ith particle and λ is the wavelength of radiation, and the optical constants of the particle:

$$m = n - i\kappa \tag{3}$$

where m is the complex index of refraction, n the refractive index, $i = \sqrt{-1}$, and κ the absorption index. These optical constants are functions of the chemical composition of the soot [12, 16, 17] because the number and type of electrons (free or bound) varies with this composition. They are also inherently functions of wavelength.

In combustion systems, the characteristic wavelength of the radiation (say, the wavelength at the maximum of the Planck blackbody function) is usually 2 microns or larger. As a result, the characteristic size parameters of the soot particles, w_i, are generally less than 0.5 (and are typically much less than 0.25). This allows for a vast simplification of the general Mie scattering theory [20] in that the small particle (Rayleigh) limit results may be employed.

For absorbing particles such as soot, n ranges from about 1.4 to 3.5 and κ from about 0.37 to 2.2 for infrared wavelengths between 1 and 7 microns [16, 17]. Both n and κ increase only slightly with wavelength, and appear to be essentially independent of temperature [16, 17]. Because the values of the size parameter and the optical constants are in the ranges discussed previously, it can be shown that scattering will be negligible as compared to absorption. Hence, under typical conditions in flames, the soot behaves like a gas in the sense that the scattering of radiation is unimportant. Consequently the radiative participation of the soot particles, as reflected by their extinction efficiencies, is reduced to simplify their absorption behavior:

$$A_\lambda = \frac{24\pi D}{\lambda} \frac{n\kappa}{[(n^2 - \kappa^2) + 2]^2 + 4n^2\kappa^2} \tag{4}$$

where A_λ is the spectral absorption efficiency. The foregoing is the first term in the power series for A_λ. The next term is of the order of $(\pi D/\lambda)^3$ and is therefore indeed negligible for the range of particle sizes being considered.

Another important simplification resulting from the above characteristics of soot particles is that the distribution of sizes of the particles is unimportant. This is readily seen by considering the spectral absorption coefficient for an ensemble of small absorbing particles having an arbitrary size distribution $F(D)$. The number of particles per unit volume in the range D to $D + dD$ for such a distribution is $F(D)dD$. Using the definition of the extinction efficiency [20] and equation (4), the absorption coefficient becomes:

$$k_{\lambda s} = \int_0^\infty A_\lambda \frac{\pi D^2}{4} F(D)dD = \frac{36\pi}{\lambda} f_v \frac{n\kappa}{[(n^2 - \kappa^2) + 2]^2 + 4n^2\kappa^2} \tag{5}$$

where f_v is the total volume fraction of soot particles present:

$$f_v = \int_0^\infty V(D)F(D)dD \tag{6}$$

and $V(D)$ is the volume of a particle of diameter D.

In the infrared, the function of the optical constants in equation (5) is only a weak function of λ. As a result, the variation of $k_{\lambda s}$ with λ is continuous and has the form:

$$k_{\lambda s} = \frac{\text{const}}{\lambda^\delta} \tag{7}$$

where δ is close to one [13, 23].

Therefore, the radiative properties of small hydrocarbon soot particles can be reasonably represented by a single function—their absorption coefficient—which is of the Milne-Eddington type. From equation (1) there follows:

Nomenclature

a_2, a_3 = pre-exponential constants used in approximating E_2, E_3
A_λ = spectral absorption efficiency of an absorbing particle
b_3 = exponential constant used in approximating E_2, E_3
c_0 = a constant determined by soot properties
C_0 = band type parameter
$C_1 = 0.59544 \times 10^{-12}$ W-cm^2
$C_2 = 1.4388$ K-cm
E_n = the nth exponential integral function
f_v = volume fraction of soot particles
I = intensity
I_b = Planck blackbody intensity
k = absorption coefficient
L = total length of path
m = complex refractive index
n = refractive index
P = pressure
Q = heat flux
T, T_0 = general and reference temperatures
u = dimensionless mass pathlength
w_i = Mie size parameter
x = mass pathlength
y = perpendicular distance from edge of slab
α = integrated band intensity
α_1 = Milne-Eddington frequency function
β_1 = Milne-Eddington path function
κ = absorption index
λ = wavelength
ν = wavenumber
ν_0 = wavenumber of band head or band center
ρ = density
σ = $(2C_1\pi^5)/(15C_2^4)$, Stefan-Boltzmann constant
τ = optical depth parameter
ϕ = dimensionless T^4 distribution
ω = band width parameter

Subscripts

h = equivalent homogeneous value
L = value corresponding to end of path of length L
M = value at extremum of temperature distribution
net = the net value
s = soot
λ = wavelength
ν = wavenumber
o = reference or standard value

Superscripts

$-$ = traveling in the negative y-direction
$+$ = traveling in the positive y-direction
Bars = appropriate mean values

$$\alpha_1(\lambda) = \frac{1}{\lambda} \tag{8}$$

and

$$\beta_1(f_v) = c_0 f_v \tag{9}$$

where c_0 is a constant determined by the properties of the soot and can be estimated from experimental data [16, 17] to be on the order of 3–7.

Radiative Transfer in a Soot Cloud Slab. Since the absorption coefficient for soot particles can be considered to be of the Milne-Eddington type, then the net heat flux traveling in the positive y-direction at any point $\tau(y)$ within a one-dimensional nonhomogeneous slab can be written as [7]:

$$Q_{\text{net}}{}^+(\tau) = 2\pi \int_0^\infty I_\lambda{}^+(0) E_3[\alpha_1(\lambda)\tau] d\lambda - 2\pi \int_0^\infty I_\lambda{}^-(\tau_L) \times E_3[\alpha_1(\lambda)(\tau_L - \tau)] d\lambda + 2\pi \int_0^\infty \int_0^\tau I_{b\lambda}(t) E_2[\alpha_1(\lambda)(\tau - t)] \times \alpha_1(\lambda) dt d\lambda - 2\pi \int_0^\infty \int_\tau^{\tau_L} I_{b\lambda}(t) E_2[\alpha_1(\lambda)(\mathrm{t} - \tau)] \alpha_1(\lambda) dt d\lambda \tag{10}$$

where

$$t(y') = \int_0^{y'} \beta_1 dy'' \tag{11}$$

$$\tau(y) = \int_0^y \beta_1 dy' \tag{12}$$

$$\tau_L = \int_0^L \beta_1 dy \tag{13}$$

$I_\lambda{}^+(0)$ and $I_\lambda{}^-(L)$ are the assumed diffuse spectral intensities incident on the ends of the slab, $I_{b\lambda}$ is the Planck function, and E_2 and E_3 are the second and third exponential integral functions, respectively:

$$E_n(x) = \int_0^1 \mu^{n-2} \exp(-x/\mu) d\mu \tag{14}$$

Extensive consideration was given to equation (10) as it might apply to banded radiation for various band shapes [7]. For soot clouds, however, the radiation is continuous in nature, as given by equations (1), (8), and (9), and hence a different treatment is required.

Approximating the Planck function by Wien's distribution:

$$I_{b\lambda} \simeq \frac{2C_1}{\lambda^5} \exp(-C_2/\lambda T) \tag{15}$$

and the exponential integral functions by [24]:

$$E_n(x) = a_n \exp(-b_n x) \tag{16}$$

where $a_2 = 3/4$, $a_3 = 1/2$, $b_3 = 3/2$ and noting [25]:

$$\int_0^\infty \lambda^{-n} \exp(-A/\lambda) d\lambda \doteq \frac{(n-2)!}{A^{n-1}} \tag{17}$$

allows equation (10) to be written for a soot cloud slab bounded by black walls as:

$$Q_{\text{net}}{}^+(\tau) = 4\pi 3! C_1 a_3 \left\{ \left[\frac{C_2}{T(0)} + b_3\tau \right]^{-4} - \left[\frac{C_2}{T(1)} + b_3(\tau_L - \tau) \right]^{-4} \right\} + 4\pi 4! C_1 a_2 \left\{ \int_0^\tau \left[\frac{C_2}{T(t)} + b_3(\tau - t) \right]^{-5} dt - \int_\lambda^{\tau_L} \left[\frac{C_2}{T(t)} + b_3(t - \tau) \right]^{-5} dt \right\} \tag{18}$$

The approximations, however, always cause an underprediction of the heat flux. A comparison between the limits of the above equation and the exact results for the optically thin and thick cases with and without bounding walls respectively indicates that both limits can be satisfied if equation (18) is divided by 0.924. Hence it is suggested that this corrective factor be used in general so as to give the following governing equation:

$$Q_{\text{net}}{}^+(\tau) = \sigma \left\{ \frac{T^4(0)}{\left[1 + \frac{T(0) b_3 \tau}{C_2} \right]^4} - \frac{T^4(1)}{\left[1 + \frac{T(1) b_3(\tau_L - \tau)}{C_2} \right]^4} \right\} + \frac{6\sigma}{C_2} \left\{ \int_0^\tau \left[\frac{1}{T(t)} + \frac{b_3(\tau - t)}{C_2} \right]^{-5} dt - \int_\tau^{\tau_L} \left[\frac{1}{T(t)} + \frac{b_3(t - \tau)}{C_2} \right]^{-5} dt \right\} \tag{19}$$

where σ is the Stefan-Boltzmann constant.

The above may be numerically integrated for any given path-length distribution of temperature and soot concentration. In addition, a closed form result can be obtained by assuming the temperature distribution is a known function of t in the form:

$$\frac{1}{T\left(\frac{t}{\tau_L}\right)} = A + B\left(\frac{t}{\tau_L}\right) + C\left(\frac{t}{\tau_L}\right)^2 \tag{20}$$

Noting that [25]:

$$F_n(b, c, q; x) = \int \frac{dx}{X^n(x)} = \frac{[2(n-1)]!}{[(n-1)!]^2} \left(\frac{c}{q}\right)^{n-1} \times \left\{ \frac{2cx + b}{q} \sum_{r=1}^{n-1} \left(\frac{q}{cX(x)} \right)^r \left[\frac{(r-1)!r!}{(2r)!} \right] + G(b, c, q; x) \right\} \tag{21}$$

where

$$\left.\begin{aligned} X(x) &= a + bx + cx^2 \\ q &= 4ac - b^2 \end{aligned}\right\} \tag{22}$$

and

$$\left.\begin{aligned} G(b, c, q; x) &= \frac{2}{\sqrt{q}} \tan^{-1}\left[\frac{2cx + b}{\sqrt{q}} \right] && q > 0 \\ G(b, c, q; x) &= \frac{-2}{\sqrt{-q}} \tanh^{-1}\left[\frac{\sqrt{-q}}{2cx + b} \right] && q < 0 \end{aligned}\right\} \tag{23}$$

equation (19), upon substitution of equation (20), may be directly integrated to give:

$$Q_{\text{net}}{}^+(\tau) = \sigma \left\{ \frac{T^4(0)}{\left[1 + \frac{T(0) b_3 \tau}{C_2} \right]^4} - \frac{T^4(1)}{\left[1 + \frac{T(1) b_3(\tau_L - \tau)}{C_2} \right]^4} \right\} + 6(C_2/\tau_L)^4 \sigma \left\{ F_5\left(b', c', q'; \frac{t}{\tau_L} = \frac{\tau}{\tau_L}\right) - F_5\left(b', c', q'; \frac{t}{\tau_L} = 0\right) + F_5\left(b'', c'', q''; \frac{t}{\tau_L} = \frac{\tau}{\tau_L}\right) - F_5\left(b'', c'', q''; \frac{t}{\tau_L} = 1\right) \right\} \tag{24}$$

where

$$\left.\begin{aligned} a' &= (C_2 A + b_3\tau)/\tau_L & a'' &= (C_2 A - b_3\tau)/\tau_L \\ b' &= (C_2 B - b_3\tau_L)/\tau_L & b'' &= (C_2 B + b_3\tau_L)/\tau_L \\ c' &= C_2 C/\tau_L & c'' &= C_2 C/\tau_L \\ q' &= 4a'c' - b'^2 & q'' &= 4a''c'' - b''^2 \\ X'\left(\frac{t}{\tau_L}\right) &= a' + b'\left(\frac{t}{\tau_L}\right) + c'\left(\frac{t}{\tau_L}\right)^2 \\ X''\left(\frac{t}{\tau_L}\right) &= a'' + b''\left(\frac{t}{\tau_L}\right) + c''\left(\frac{t}{\tau_L}\right)^2 \end{aligned}\right\} \tag{25}$$

The families of profiles which equation (20) describe are shown in Figs. 1 and 2. Equation (20) may be rewritten in the following forms:

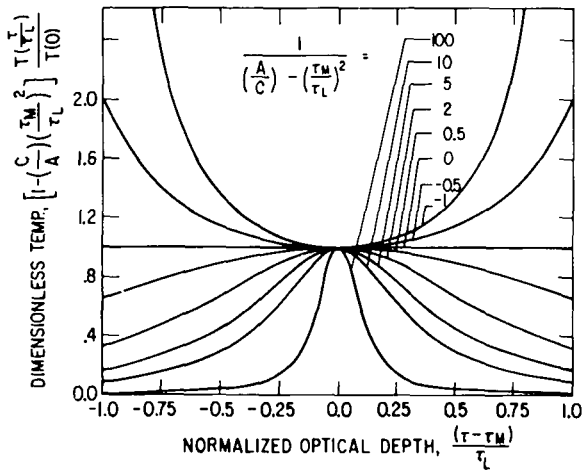

Fig. 1 Family of symmetric temperature profiles

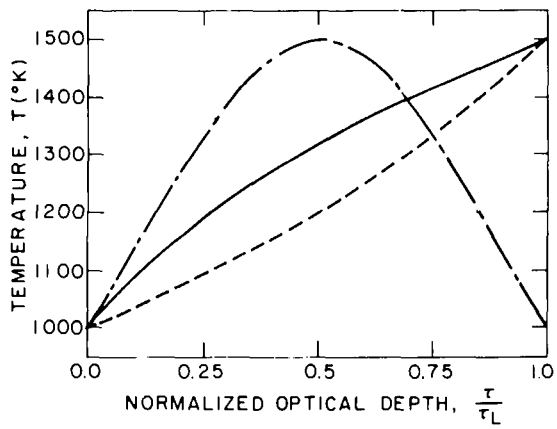

Fig. 3 - - - symmetric temperature distribution with $T(0) = T(1) = 1000$ K, $T(1/2) = 1500$ K; $\tau_M/\tau_L = 0.5$; - - - - linear $1/T$ temperature distribution with $T(0) = 1000$ K, $T(1) = 1500$ K — linear T^4 temperature distribution with $T(0) = 1000$ K, $T(1) = 1500$ K

$$\left[1-\left(\frac{C}{A}\right)\left(\frac{\tau_M}{\tau_L}\right)^2\right]\frac{T\left(\frac{t}{\tau_L}\right)}{T(0)} = \frac{1}{1+\left[\frac{1}{\left(\frac{A}{C}\right)-\left(\frac{\tau_M}{T_L}\right)^2}\right]\left(\frac{t-\tau_M}{\tau_L}\right)^2} \quad \text{for } C \neq 0 \qquad (20a)$$

$$\frac{T\left(\frac{t}{\tau_L}\right)}{T(0)} = \frac{1}{1+\left[\frac{T(0)}{T(1)}-1\right]\left(\frac{t}{\tau_L}\right)} \quad \text{for } C = 0 \qquad (20b)$$

where the temperature in the first case has an extremum at $\tau = \tau_M$. In Fig. 1 the coefficient C is different from zero and, depending upon the values of the coefficients, the distribution will lie along one of the curves defined by equation (20a). It will not encompass the entire length of the curve, but rather any section of it which is one unit wide. In Fig. 2 the coefficient C equals zero and the curves defined by equation (20b) are plotted for various values of $T(0)/T(1)$. Fig. 3 shows plots of the temperature distributions for a symmetric case of Fig. 1, for a linear $1/T$ distribution of the type in Fig. 2, and for a linear T^4 distribution. The temperature limits are characteristic of diffusion flames of hydrocarbon fuels [10–19].

Fig. 4(a) presents the variation of heat flux with position and optical depth for the symmetric temperature distribution of Fig. 3. The slab is bounded by black walls. As expected, the symmetric temperature distribution produces asymmetric net heat flux distributions. When the soot is optically thin ($\tau_L \sim 10^{-6}$ cm) the net flux goes to zero everywhere since the bounding walls have identical temperatures and

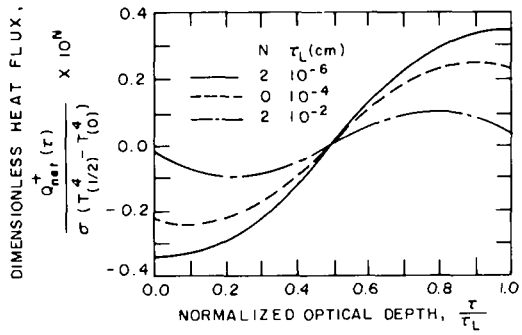

Fig. 4(a) Flux distribution for non gray slab bounded by black walls—symmetric temperature distribution

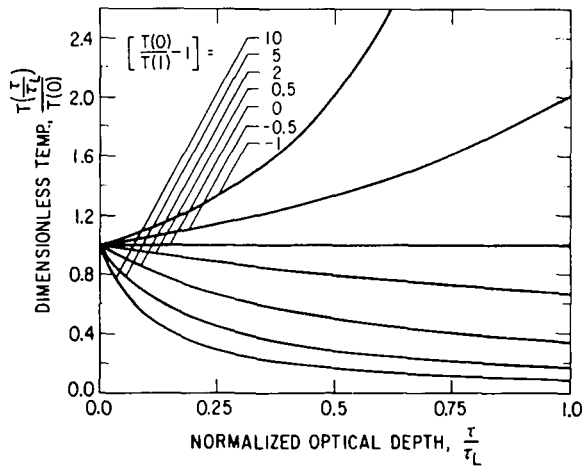

Fig. 2 Family of linear $1/T$ temperature profiles

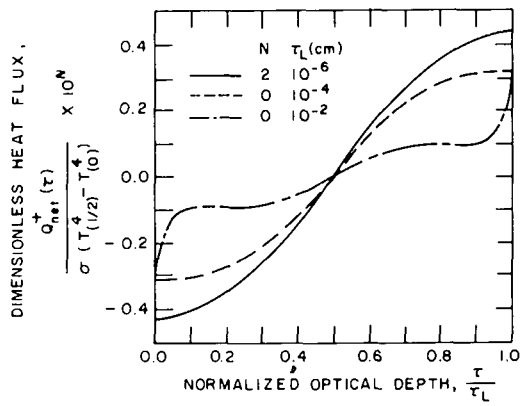

Fig. 4(b) Flux distribution for an unbounded non gray slab—symmetric temperature distribution

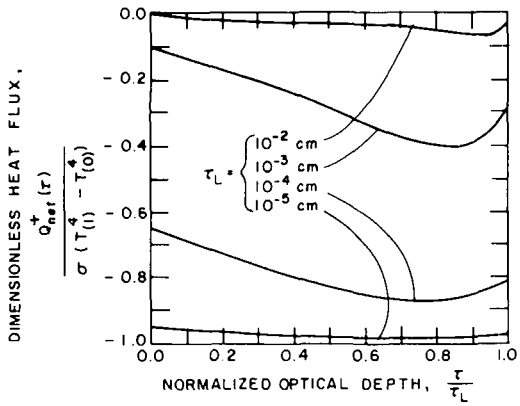

Fig. 5(*a*) Flux distribution for non gray slab bounded by black walls—linear 1/*T* temperature distribution

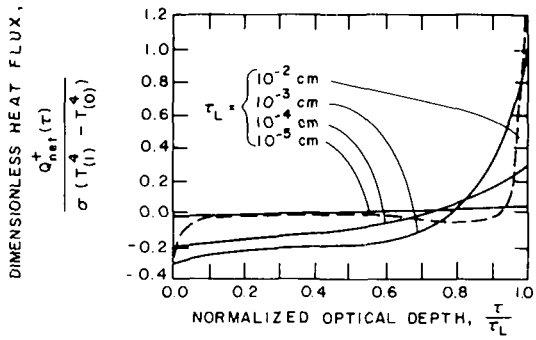

Fig. 5(*b*) Flux distribution for an unbounded non gray slab—linear 1/*T* temperature distribution

the soot only weakly absorbs and emits radiation-becoming essentially nonparticipating. When the soot is optically thick ($\tau_L \sim 10^{-2}$ cm) the net flux again tends to zero everywhere since the soot is now so strongly absorbing that radiant energy is only exchanged throughout local regions wherein the temperature is essentially uniform. Intermediate values of optical depth yield the highest fluxes since the nonisothermal nature of the soot (which is the driving force for the net flux) can be felt throughout the slab.

Fig. 4(*b*) is for the same conditions as Fig. 4(*a*) except the slab is not bounded by black walls. The unbounded slab solution is obtained by setting the first term in equation (24) equal to zero. The trends are similar to those in Fig. 4(*a*) in that optically thin ($\tau_L \sim 10^{-6}$ cm) and optically thick ($\tau_L \sim 10^{-2}$ cm) regions can be identified in which the net flux *interior* to the slab tends to zero. However, since the slab is unbounded, the net fluxes at the *edges* of the slab do not tend to zero for large optical depths but rather approach the blackbody flux at the slab edge temperature. This is because the other hemisphere of radiation is absent at the slab edge when no bounding wall is present. For intermediate optical depths the fluxes are greater throughout the slab and at the edges. For the edges this means that radiation from the hot inner zones of the slab is escaping from the slab in significant amounts.

Fig. 5(*a*) shows the variation of heat flux with position and optical depth for the linear 1/*T* distribution of Fig. 3. The slab is bounded by black walls. The flux is greatest in absolute value for the optically thin region since the medium approaches the nonparticipating limit and hence the two walls of *different* temperature can have their maximum interaction. An extremum value with respect to position in the slab is produced by the tradeoff between wall and medium contributions to the total radiation. The extrumum shifts towards the hotter wall as the optical depth increases. For the optically thick region, the flux everywhere tends to zero for reasons previously discussed.

Fig. 5(*b*) is for the same conditions as Fig. 5(*a*) except the slab is not bounded by black walls. Comments made regarding Fig. 4(*b*) also apply to Fig. 5(*b*) except that fluxes at intermediate optical depths aren't always the largest. This is because the temperature distribution is not a symmetric one having a maximum. Also, the crossover from negative to positive flux values is shifted towards the hot edge—indicating the dominance of the higher temperature radiation.

The Gray Approximation for Soot. If the soot could be considered gray ($\alpha_1(\lambda) = \text{const.} = \bar{\alpha}_1$), a large body of existing work concerning radiative equilibrium could be immediately used. Also, analysis in general would become much simpler. For example, the following nonradiative equilibrium results can be derived in which the temperature distribution is quite arbitrary.

Assuming the soot to be gray and the slab boundaries to be black allows equation (10) to be written as:

$$Q_{net}^+(\tau) = 2\sigma[T^4(1) - T^4(0)]\left\{-E_3(\bar{\alpha}_1(\tau_L - \tau)) + \bar{\alpha}_1\tau_L\int_0^{\tau/\tau_L}\phi\left(\frac{t}{\tau_L}\right)E_2\left[\bar{\alpha}_1\tau_L\left(\frac{\tau}{\tau_L} - \frac{t}{\tau_L}\right)\right]d\left(\frac{t}{\tau_L}\right) - \bar{\alpha}_1\tau_L\int_{\tau/\tau_L}^1\phi\left(\frac{t}{\tau_L}\right)E_2\left[\bar{\alpha}_1\tau_L\left(\frac{t}{\tau_L} - \frac{\tau}{\tau_L}\right)\right]d\left(\frac{t}{\tau_L}\right)\right\} \quad (26)$$

where

$$\phi\left(\frac{t}{\tau_L}\right) = \frac{T^4\left(\frac{t}{\tau_L}\right) - T^4(0)}{T^4(1) - T^4(0)} \quad (27)$$

If the fourth power of the temperature distribution can be represented by a power series in the optical depth, as any physically meaningful temperature distribution will be, then:

$$\phi\left(\frac{t}{\tau_L}\right) = \sum_{n=1}^{\infty} a_n\left(\frac{t}{\tau_L}\right)^n \quad (28)$$

and the integrals in equation (25) have the form:

$$In = \int_a^b\left(\frac{t}{\tau_L}\right)^n E_2\left[\bar{\alpha}_1\tau_L\left|\frac{\tau}{\tau_L} - \frac{t}{\tau_L}\right|\right]d\left(\frac{t}{\tau_L}\right) \quad (29)$$

which are easily determined through successive integration by parts. For example, when the distribution is linear just the first term in the series remains and only a single integration by parts is required. The result for this case with $a_1 = 1$ is:

$$Q_{net}^+(\tau) = -\frac{2\sigma}{\bar{\alpha}_1\tau_L}[T^4(1) - T^4(0)]\left\{\frac{2}{3} - E_4[\bar{\alpha}_1(\tau_L - \tau)] - E_4(\bar{\alpha}_1\tau)\right\} \quad (30)$$

If the soot slab is not bounded by walls and the intensity incident on it is negligible then equation (26) becomes:

$$Q_{net}^+(\tau) = 2\sigma T^4(0)\{E_3[\bar{\alpha}_1(\tau_L - \tau)] - E_3(\bar{\alpha}_1\tau)\} + 2\bar{\alpha}_1\tau_L\sigma[T^4(1) - T^4(0)]\left\{\int_0^{\tau/\tau_L}\phi\left(\frac{t}{\tau_L}\right) \times E_2\left[\bar{\alpha}_1\tau_L\left(\frac{\tau}{\tau_L} - \frac{t}{\tau_L}\right)\right]d\left(\frac{t}{\tau_L}\right) - \int_{\tau/\tau_L}^1\phi\left(\frac{t}{\tau_L}\right)E_2\left[\bar{\alpha}_1\tau_L\left(\frac{t}{\tau_L} - \frac{\tau}{\tau_L}\right)\right]d\left(\frac{t}{\tau_L}\right)\right\} \quad (31)$$

The integrals of equation (29) are again required. And, for the linear distribution, the foregoing equation easily reduces to:

$$Q_{net}^+(\tau) = 2\sigma T^4(1)E_3[\bar{\alpha}_1(\tau_L - \tau)] - 2\sigma T^4(0)E_3(\bar{\alpha}_1\tau) - \frac{2\sigma}{\bar{\alpha}_1\tau_L}[T^4(1) - T^4(0)]\left\{\frac{2}{3} - E_4[\bar{\alpha}_1(\tau_L - \tau)] - E_4(\bar{\alpha}_1\tau)\right\} \quad (32)$$

In Table 1 is shown the variation of the net heat flux with position

Table 1 Distributions of $Q_{net}^{+}(\tau)/\sigma[T^4(0) - T^4(1)]$ for gray and nongray soot absorption between black walls—linear $T^4(\tau)$; $\bar{\alpha}_1 = 3609\ cm^{-1}$

	$\bar{\alpha}_1\tau_L = 0.1$		$\bar{\alpha}_1\tau_L = 1.0$		$\bar{\alpha}_1\tau_L = 10.0$	
τ/τ_L	gray	nongray	gray	nongray	gray	nongray
0	0.912	0.902	0.495	0.456	0.067	0.071
0.2	0.939	0.932	0.612	0.576	0.128	0.129
0.4	0.952	0.949	0.666	0.638	0.133	0.126
0.6	0.952	0.952	0.666	0.644	0.133	0.118
0.8	0.939	0.940	0.612	0.592	0.128	0.109
1.0	0.912	0.912	0.495	0.465	0.067	0.056

and optical depth for the linear T^4 distribution of Fig. 3. The gray slab is bounded by black walls. As expected the flux is greatest for the smallest optical depth and decreases to zero as the depth gets large. The distributions are symmetric and are quite flat except for mid-range optical depths. This coincides with the solution for a gray slab in radiative equilibrium where the resulting T^4 temperature distributions are, to a fair approximation, linear for small and large optical depths. Table 2 is for the same conditions as Table 1 except the slab is not bounded by black walls. Flux values increase with increasing optical depth and the fluxes at the edges of the slab approach black body fluxes at the slab edge temperature as $\bar{\alpha}_1\tau_L \to \infty$.

Whether the gray solutions are useful for determining soot radiation depends on: (1) whether the flux distribution has the same character for both the gray and nongray cases, and (2) if a mean coefficient can be specified a priori.

Regarding the specification of a mean coefficient, for the optically thin region the Planck mean coefficient is appropriate:

$$k_P = \int_0^\infty k_\lambda I_{b\lambda} d\lambda \Big/ \int_0^\infty I_{b\lambda} d\lambda \tag{33}$$

Substituting equations (1), (8), and (9) and using Planck's distribution instead of Wien's approximation for $I_{b\lambda}$ yields:

$$k_P = \left[\int_0^\infty \xi^4 (e^\xi - 1)^{-1} d\xi \Big/ \int_0^\infty \xi^3 (e^\xi - 1)^{-1} d\xi \right] (c_0/C_2) f_v T = 3.83 (c_0/C_2) f_v T \tag{34}$$

where the integrals can be identified with the Riemann zeta functions [32]. For the optically thick region, the Rosseland mean coefficient is appropriate:

$$k_R = \int_0^\infty \frac{\partial I_{b\lambda}}{\partial T} d\lambda \Big/ \int_0^\infty \frac{1}{k_\lambda} \frac{\partial I_{b\lambda}}{\partial T} d\lambda \tag{35}$$

Substituting equations (1), (8), and (9) and using Planck's distribution for $I_{b\lambda}$ yields:

$$k_R = \left[\int_0^\infty \xi^4 e^\xi (e^\xi - 1)^{-2} d\xi \Big/ \int_0^\infty \xi^3 e^\xi (e^\xi - 1)^{-2} d\xi \right] (c_0/C_2) f_v T = 3.60 (c_0/C_2) f_v T \tag{36}$$

where the Riemann zeta functions were again used.

Table 1 Distributions of $Q_{net}^{+}(\tau)/\sigma[T^4(1) - T^4(0)]$ for gray and nongray soot absorption without walls—linear $T^4(\tau)$; $\bar{\alpha}_1 = 3609\ cm^{-1}$

	$\bar{\alpha}_1\tau_L = 0.1$		$\bar{\alpha}_1\tau_L = 1.0$		$\bar{\alpha}_1\tau_L = 10.0$	
τ/τ_L	Gray	Nongray	Gray	Nongray	Gray	Nongray
0	−0.121	−0.110	−0.467	−0.432	−0.313	−0.316
0.2	−0.101	−0.095	−0.425	−0.419	−0.143	−0.162
0.4	−0.067	−0.067	−0.315	−0.327	−0.133	−0.129
0.6	−0.017	−0.023	−0.119	−0.139	−0.126	−0.103
0.8	0.048	0.038	0.194	0.180	−0.053	−0.022
1.0	0.129	0.117	0.698	0.697	1.180	1.190

The two results are identical in form and differ only slightly in their constant coefficients. This suggests that the form,

$$\bar{k} = C(c_0/C_2) f_v T \tag{37}$$

might be appropriate for all optical depths with C lying between 3.60 and 3.83. It should be noted that although the spectral absorption coefficient is independent of temperature, the mean coefficient is linearly proportional to T. This is a result of the nongray nature of the soot ($k_\lambda \propto 1/\lambda$). Because of this temperature dependence, the determination of a mean coefficient characteristic of the entire slab requires the specification of an appropriate average temperature. If the soot concentration is constant, then equation (26) indicates the following parameter is important:

$$\bar{\alpha}_1\tau_L = \int_0^L \bar{k} dy = C(c_0/C_2) f_v \int_0^L T dy \tag{38}$$

This suggests the following mean temperature:

$$\bar{T} = (1/L) \int_0^L T dy \tag{39}$$

Noting that $\tau_L = c_0 f_v L$, then

$$\bar{\alpha}_1 = (C/C_2)\bar{T} \tag{40}$$

Using equation (19), calculations were made for various τ_L for a slab having the linear T^4 distribution of Fig. 3. The results were compared with the gray solutions of equations (29) and (31) where $\bar{\alpha}_1$ was determined from the foregoing equation. A range of values (3.6 to 4.0) was used for the constant C and it was found that the predictions were always within 10 percent of one another. However, no connection could be made between the result which compared best with the nongray solution and the range of optical thickness under consideration. Hence it is suggested than an average value of C, say 3.72, be used for the gray approximation for all optical depths. Calculations using this value of C are given in Tables 1 and 2. It is seen that the gray and nongray solutions have similarly shaped distributions and that using the gray coefficient prescribed by equation (40) yields surprisingly good agreement with the nongray result.

Combustion Gases

In contrast to the continuous spectral distribution of soot particle radiation, radiation from combustion gases is banded in nature. In the infrared, each vibration-rotation wide band is composed of a large number of individual lines, each of which corresponds to a unique transition from one quantized energy sate to another. However, even for the simplest case of radiation from an isolated collision broadened spectral line [1], the absorption coefficient is not describable in terms of the Milne-Eddington form. In fact this is the reason why Curtis-Godson scaling approximations have been introduced for both line and band radiation. Nevertheless, the over-riding mathematical and computational versatility of the Milne-Eddington form entices one to try and fit existing line and band models into its mold, thereby greatly simplifying total line and band calculations for nonhomogeneous gases [33, 7].

One approximation which is applicable in many practical gas radiation calculations is to neglect the effects of the band find structure when doing wide band calculations. This assumption is particularly useful in conjunction with the exponential wide band model [26, 27] since it tends to compensate for underpredictions inherent in the same model. As a result, the mean spectral absorption coefficient under this assumption and for this model becomes [8]:

$$\bar{k}_\nu = \frac{\alpha\rho}{\omega} \exp(-C_0|\nu - \nu_0|/\omega) \tag{41}$$

where ρ is the density of the gas species, α is the integrated band intensity, ω the band width parameter, $C_0 = 2$ for a symmetrical band having a center at ν_0 and $C_0 = 1$ for bands with upper or lower wavenumber heads at ν_0. The quantities α and ω are functions of the temperature and the physical constants of the particular molecular species. For nonhomogeneous paths it is quite tempting to assume that ω is relatively constant, assigning it the value $\bar{\omega}$. Equation (41)

then indicates that the absorption coefficient for the gas would indeed be of the Milne-Eddington form with:

$$\alpha_1(\nu) = \exp(-C_0|\nu - \nu_0|/\bar{\omega}) \tag{42}$$

and

$$\beta_1(T, P) = \frac{\alpha(T)}{\bar{\omega}}\rho(T, P) \tag{43}$$

For an unbounded nonhomogeneous gas slab whose emission is dominated by a single wide band having an absorption coefficient given by equation (41), the energy flux emitted into the negative y-direction at $y = 0$ can be obtained by using the analysis of [34]:

$$Q^-(0) = \pi \int_0^L I_{b\nu 0} \frac{d}{dy}\left\{\omega_h\left[E_1(u_h) - E_3(u_h) + \ln(u_h) + \frac{1}{2} + \gamma\right]\right\} dy \tag{44}$$

where $\gamma = 0.577216$, and the subscripts h indicate that the following equivalent homogeneous scaled parameters are to be used [2]:

$$u_h = \frac{\alpha_h x}{\omega_h}; \qquad \alpha_h = \frac{1}{x}\int_0^y \alpha\rho dy'; \qquad \omega_h = \frac{1}{\alpha_h x}\int_0^y \omega\alpha\rho dy' \tag{45}$$

in which

$$x = \int_0^y \rho dy' \tag{46}$$

If the Milne-Eddington assumption is used, equation (44) can be written as:

$$Q^-(0) = \pi \int_0^L I_{b\nu 0}\left[\frac{1}{u(y)}(1 - e^{-u(y)}) + E_2(u(y))\right]\alpha(y)\rho(y)dy \tag{47}$$

where

$$u = \frac{1}{\bar{\omega}}\int_0^y \alpha\rho dy' \tag{48}$$

The function of u in the integrand is monotonically decreasing in u having a value of 2 at $u = 0$ while asymptotically going to 0 as u approaches infinity. Hence it is a monotonically increasing function of $\bar{\omega}$ whose gradient increases with increasing $\bar{\omega}$. Since ω itself is given by [27]:

$$\omega = \omega_0(T/T_0)^{1/2} \tag{49}$$

then the integrand will increase in its sensitivity to the assumed value of $\bar{\omega}$ as the mean temperature of the gas body increases. Consequently the accuracy of this approach in predicting heat flux from systems such as flames (where both the mean temperature and the temperature range are large) hinges crucially on being able to accurately specify the proper value of $\bar{\omega}$, hopefully by being able to specify a priori a mean temperature characteristic of the slab, $\bar{T}$.

To determine if there exists a scaling prescription for this parameter, calculations were performed using equations (44) and (47) from which the required value of $\bar{\omega}$ (and hence $\bar{T}$) could be determined such that the Milne-Eddington approach would yield the correct value of the heat flux. The results are presented in Table 3. The average temperature, $\bar{T}_2$, required by the Milne-Eddington assumption to predict the same heat flux as the nonhomogeneous slab band absorptance technique was found by iteration and is given in the table. Also listed is the integrated average temperature, $\bar{T}_{A2}$, which would be an easy scaling prescription to use in determining $\bar{\omega}$ a priori.

The results indicate that when the percentage change in temperature in the slab, $(T_{max} - T_{min})/T_{min}$, is on the order of 50 percent or less (the first four cases in the table) then a meaningful average value of ω can be prescribed. However, when this percentage change is large (as in the case of flames) the approach fails. This is seen from the remaining entries in Table 3. In these cases the required average temperature nearly always lies outside the actual temperature range within the slab, being always too high.

Because of this failure a second approach was tried in which ω was taken to be constant only in the exponential term in equation (41) and was allowed to have its normal variation in the pre-exponential factor. This results in equation (47) still defining the heat flux but with:

$$u = \int_0^y (\alpha\rho/\omega)dy' \tag{48(a)}$$

The average temperatures, $\bar{T}_1$, required in these cases for agreement with the nonhomogeneous slab band absorptance calculations are also listed in Table 3. Again the approach fails for slabs having large temperature variations.

Finally, the Milne-Eddington assumption was compared with the calculations of Chan and Tien [28] for gases confined between black parallel plates. (It should be noted that the pressure broadening was large enough in these cases such that fine structure effects were indeed negligible.) From the comparison it was found that if one used the actual values of the optical depth parameters, then the temperature distributions in the slab could not be adequately determined. (In fact, they can never be precisely determined since the method always predicts an antisymmetric emissive power distribution for this case [7] whereas the real gas calculation is not bound by this restriction [28].) Even when trying only to predict the correct reduction in heat flux due to the presence of the gases, errors on the order of 20 percent were experienced when the average temperature was used to compute $\bar{\omega}$.

The conclusion to be drawn from all these considerations is that

Table 3 Slab calculations by the Milne-Eddington assumption and by the nonhomogeneous slab band absorptance method

Run[1]	Band; gas	P_i	u eq. (48a)	$\bar{T}_1$(K)	$\bar{T}_2$(K)	$\bar{T}_{A2}$(K)	$\frac{Q^-(0)_{actual}}{Q^-(0)_{approx}}$
122-9	2.7 H_2O	0.472	7.54	1000	1000	1000	1.00
122-4	2.7 H_2O	0.528	7.27	1128	1144	1120	1.00
1125-5(6)	2.7 H_2O	0.786	11.1	1141	1156	1125	1.01
122-8	2.7 H_2O	0.517	7.07	1115	1123	1110	1.00
12-10	2.7 H_2O	0.69	16.4	1325	1130	762	1.32
9-13	2.7 H_2O	0.47	10.6	1536	1277	769	1.41
12-1	2.7 H_2O	0.45	8.90	1054	980	817	1.36
Gaussian	4.3 CO_2	1.00	1840.0	5007	5284	1097	2.14
Linear I	4.3 CO_2	1.00	1380.0	1275	1719	750	1.30
Linear II	4.3 CO_2	1.00	489.0	1831	2163	1500	1.10

[1]122-9 T = 1005 K, 122-4 (1000 K at 9 cm) to (1240 K at 60 cm), 1125-5(6) (1015 K at 0 cm) to 1250 K at 60 cm), 122-8 (1000 K at 0 cm) to (1220 K at 30 cm) to (1000 K at 60 cm), 12-10 (389 K at 0 cm) to (1117 K at 10.5 cm) to (417 K at 48.56 cm), 9-13 (444 K at 0 cm) to (1102 K at 38.8 cm) to (411 K at 48.56 cm), 12-1 (467 K at 0 cm) to (1086 K at 9.8 cm) to (559 K at 48.56 cm), Gaussian: $T = 300 + 1300 \exp(-7.49 \times 10^{-4} y^2)$, Linear I: (500 K at 0 cm) to (10000 K at 50 cm), Linear II: (1000 K at 0 cm) to (2000 K at 50 cm).

for gas bodies having large temperature variations, the Milne-Eddington form achieved by taking only ω as constant is not reliable. However, a constant properties method has been proposed [34] which appears to be quite accurate for highly nonisothermal paths of large optical depth. It that method α, ρ and ω are taken to be constant whereas in the present study only ω is explicitly so considered, with α happening to be constant in the calculations since only fundamental bands were considered. Both sets of assumptions lead to the Milne-Eddington form. The former yields better results, however, since it preserves the offsetting effects resulting from the variations of density and bandwidth with temperature. That is, in the colder regions of a gas mixture the higher density, ρ, tends to increase self-absorption whereas the smaller bandwidth, ω, tends to reduce self-absorption. Since the present study takes only ω to be constant the variation of ρ results in significant self-absorption in the cold regions without any compensation. Consequently the flux is always underpredicted, as is shown by the last column in Table 3.

Conclusion

It has been shown that the Milne-Eddington absorption coefficient approximation is applicable without restriction to radiative transfer within clouds of small hydrocarbon soot particles but must be applied with caution to the calculation of transfer within combustion gases. As such, closed form solutions have been derived for the net radiative heat flux within soot cloud slabs for both the realistic $1/\lambda$ variation of the absorption coefficient and also for the gray case. In addition, order of magnitude bounds on the applicability of the constant bandwidth assumption to gases have been given along with a means for practically using it in situations where it does apply.

Acknowledgment

This research was supported by the National Science Foundation in the Fire Research Program, Research Applied to National Needs (RANN), through Grant GI-43.

References

1 Goody, R. M., *Atmospheric Radiation I. Theoretical Basis*, Oxford University Press, Oxford, 1964.

2 Chan, S. H., and Tien, C. L., "Total Band Absorptance of Non-Isothermal Infrared-Radiating Gases," *Journal of Quantitative Spectroscopy and Radiative Transfer*, Vol. 9, 1969, pp. 1261-1271.

3 Edwards, D. K., and Morizumi, S. J., "Scaling of Vibration-Rotation Band Parameters for Nonhomogeneous Gas Radiation," *Journal of Quantitative Spectroscopy and Radiative Transfer*, Vol. 10, 1970, pp. 175-188.

4 Cess, R. D., and Wang, L. S., "A Band Absorptance Formulation for Non-isothermal Gaseous Radiation," *International Journal of Heat and Mass Transfer*, Vol. 13, 1970, pp. 547-555.

5 Gille, J., and Goody, R., "Convection in a Radiating Gas," *Journal of Fluid Mechanics*, Vol. 20, 1964, pp. 47-79.

6 Wang, L. S., "The Role of Emissivities in Radiative Transport Calculations," *Journal of Quantitative Spectroscopy and Radiative Transfer*, Vol. 8, 1968, pp. 1233-1240.

7 Crosbie, A. L., and Viskanta, R., "Effect of Band or Line Shape on the Radiative Transfer in a Nongray Planar Medium," *Journal of Quantitative Spectroscopy and Radiative Transfer*, Vol. 10, 1970, pp. 487-509.

8 Edwards, D. K., and Balakrishnan, A., "Slab Band Absorptance for Molecular Gas Radiation," *Journal of Quantitative Spectroscopy and Radiative Transfer*, Vol. 12, 1972, pp. 1379-1387.

9 Nelson, D. A., "A Study of Band Absorption Equations for Infrared Radiative Transfer in Gases: I. Transmission and Absorption Functions for Planar Media," *Journal of Quantitative Spectroscopy and Radiative Transfer*, Vol. 14, 1974, pp. 69-80.

10 Gaydon, A. G., and Wolfhard, H. G., *Flames, Their Structure, Radiation, and Temperatures*, Third ed., Chapman and Hall, London, 1970.

11 Sato, T., Kunitomo, T., Yoshi, S., and Hashimoto, T., "On the Monochromatic Distribution of the Radiation From the Luminous Flame," *Bulletin of the Japanese Society of Mechanical Engineers*, Vol. 12, 1969, pp. 1135-1143.

12 Stull, V. R., and Plass, G. N., "Emissivity of Dispersed Carbon Particles," *Journal of the Optical Society of America*, Vol. 50, 1960, pp. 121-129.

13 Siddall, R. G., and McGrath, I. A., "The Emissivity of Luminous Flames," *Ninth Symposium (International) on Combustion*, 1963, pp. 102-110.

14 Erickson, W. D., Williams G. C., and Hottel, H. C., "Light Scattering Measurements on Soot in a Benzene-Air Flame," *Combustion and Flame*, Vol. 8, 1964, pp. 127-132.

15 Kunugi, M., and Jinno, H., "Determination of Size and Concentration of Soot Particles in Diffusion Flames by a Light-Scattering Technique," *Eleventh Symposium (International) on Combustion*, 1966, pp. 257-266.

16 Howarth, C. R., Foster, P. J., and Thring, M. W., "The Effect of Temperature on the Extinction of Radiation by Soot Particles," *Third International Heat Transfer Conference, American Institute of Chemical Engineering*, Vol. 5, 1966, pp. 122-128.

17 Dalzell, W. H., and Sarofim, A. F., "Optical Constants of Soot and Their Application to Heat-Flux Calculations," JOURNAL OF HEAT TRANSFER, TRANS. ASME, Series C, Vol. 91, 1969, pp. 100-104.

18 Lowes, T. M., and Newall, A. J., "The Emissivities of Flame Soot Dispersions," *Combustion and Flame*, Vol. 16, 1971, pp. 191-194.

19 Kunitomo, T., "Mean Emissivity of a Luminous Flame (Spray Combustion of a Liquid Fuel)," *Heat Transfer-Japanese Research*, Vol. 1, 1972, pp. 57-64.

20 Mie, G., "Optics of Turbid Media," *Annalen der Physik*, Vol. 25, 1908, pp. 377-445.

21 Van der Hulst, H. C., *Light Scattering by Small Particles*, Wiley, New York, 1957.

22 Kerker, M., *The Scattering of Light and Other Electromagnetic Radiation*, Academic Press, New York, 1969.

23 Hottel, H. C., "Radiant Transmission," Chapter IV, McAdams, W. H., *Heat Transmission*, McGraw-Hill, New York, 1942.

24 Sparrow, E. M., and Cess, R. D., *Radiation Heat Transfer*, Wadsworth, Belmont, Calif., 1966.

25 Selby, S. M., *CRC Standard Mathematical Tables, 20th Edition*, The Chemical Rubber Company, Cleveland, Ohio, 1972.

26 Edwards, D. K. and Menard, W. A., "Comparison of Models for Correlation of Total Band Absorption," *Applied Optics*, Vol. 3, 1964, pp. 621-625.

27 Edwards, D. K., and Balakrishnan, A., "Thermal Radiation by Combustion Gases," *International Journal of Heat and Mass Transfer*, Vol. 16, 1973, pp. 25-40.

28 Chan, S. H., and Tien, C. L., "Infrared Radiative Heat Transfer in Nongray Nonisothermal Gases," *International Journal of Heat and Mass Transfer*, Vol. 14, 1971, pp. 19-26.

29 Simmons, F. S., "Band Models for Nonisothermal Radiating Gases," *Applied Optics*, Vol. 5, 1966, pp. 1801-1811.

30 Weiner, M. M., and Edwards, D. K., "Non-Isothermal Gas Radiation in Superposed Vibration-Rotation Bands," *Journal of Quantitative Spectroscopy and Radiative Transfer*, Vol. 8, 1968, pp. 1171-1183.

31 Weiner, M. M., "Radiant Heat Transfer in Non-Isothermal Gases," PhD dissertation, University of California, Los Angeles, 1966.

32 Abromowitz, M., and Stegun, I. A., *Handbook of Mathematical Functions*, U.S. Government Printing Office, Washington, D.C., 1964.

33 Wilson, K. H., and Greif, R., "The Separability Approximation in Non Homogeneous Gases," *Journal of Quantitative Spectroscopy and Radiative Transfer*, Vol. 11, 1971, pp. 1245-1263.

34 Edwards, D. K., and Balakrishnan, A., "Self-Absorption of Radiation in Turbulent Molecular Gases," *Combustion and Flame*, Vol. 20, 1973, pp. 401-417.

W. P. Schimmel, Jr.
Member of the Technical Staff,
Heat Transfer and Fluid Mechanics Division,
Sandia Laboratories,
Albuquerque, N.Mex.
Mem. ASME

J. V. Beck
Professor,
Michigan State University,
East Lansing, Mich.
Mem. ASME

A. B. Donaldson
Member of the Technical Staff,
Initiating and Pyrotechnic Components Division,
Sandia Laboratories,
Albuquerque, N.Mex.

Effective Thermal Diffusivity for a Multimaterial Composite Laminate[1]

This paper discusses the development of an "effective thermal diffusivity" which can be used to estimate the temperature response at the insulated rear surface of a multilayer composite to a step in temperature at the front surface of the composite. An example is considered using the effective value along with the mathematics of a single layer problem, and results thereof are compared with both those of an exact solution, and those which use an effective diffusivity computed from a "lumped" parameter model.

Introduction

Exact solutions for linear thermal conduction problems in multilayered media are generally very tedious in terms of matrix manipulation [1, 2].[2] Some authors have proposed an alternate method of solution for interfacial temperatures of a large class of problems from the solution of a single adjoint problem [3]. In addition to these two types of solutions, one always has the option of attempting a Laplace transform solution as outlined in [4]. In practice, if the number of layers involved is greater than two, the inversion of the resulting solution in the transform space becomes very complex. Finally, it is possible to utilize a numerical technique such as in a finite difference or finite element computer code to determine temperature-time profiles throughout the multilayer composite.

The foregoing techniques are all useful when detailed information about the transient temperature behavior of the composite is desired. There are situations, however, when one is concerned only with the temperature at a boundary or at the interface between two adjacent layers. Examples of this would be the thermal protection of internal components of a reentry vehicle which is subjected to atmospheric heating or the problem of maintaining the interior of a container below a certain specified temperature limit when the container is immersed in a fire. For these two examples and a host of others, it is excessive to solve for the entire temperature field throughout the composite insulating system for all times. The actual region of interest is, in fact, the rear surface of the system. In cases of this type, the concept of an "effective thermal diffusivity," i.e., a single parameter based upon the material properties which can be used to approximate the thermal response at some specified point, is useful in preliminary heat transfer studies.

This effective thermal diffusivity can then be used to avoid a detailed solution of the entire temperature field for transient problems in a manner analogous to the "effective thermal conductivity" used in steady-state conduction problems. The effective thermal diffusivity can be used with a Fourier series or numerical solution for a single effective layer. It should be pointed out that no single parameter is capable of describing exactly the temperature response at *all* points in the composite. In spite of this, the savings of effort in utilizing an effective thermal diffusivity for cases such as those described previously make it a worthwhile tool.

In the present work, a general technique for specifying the effective thermal diffusivity is outlined for arbitrary front surface heating conditions. A two-layer eigenvalue formulation is also developed and shown to agree with the general formulation for a temperature step boundary condition. Then, by example, results from the effective thermal diffusivity model are compared to those of an exact solution for the rear surface temperature response of a composite subjected to a front surface temperature step. For completeness, comparison is also made to results of a lumped model, which is not capable of considering material orientation.

Theory

General Problem. An expression for the effective thermal diffusivity of an n-layer composite laminate will be developed by the process of superposition and mathematical induction.

First, consider a single infinite slab of thickness L which is initially at temperature T_i and which is exposed to a heat flux of arbitrary time-dependence but finite total energy at its front surface (surface 1). That is

$$Q = \int_0^\infty q dt < \infty \tag{1}$$

The rear surface (surface 2) is insulated. The thermal properties are

[1] This work was supported in part by the United States Energy Research and Development Agency and in part by the National Science Foundation under Grant No. GK-41495.

[2] Numbers in brackets designate References at end of paper.

Contributed by the Heat Transfer Division and presented at the Winter Annual Meeting, Houston, Texas, November 30–December 5, 1975 of THE AMERICAN SOCIETY OF MECHANICAL ENGINEERS. Revised manuscript received by the Heat Transfer Division May 17, 1977. Paper No. 75-WA/HT-90.

assumed to be temperature independent. From equation (13) of [5], an expression for the thermal diffusivity of the slab is

$$\alpha = \frac{QL}{(\theta_1 - \theta_2)\rho C}; \qquad \theta_1 \neq \theta_2 \tag{2}$$

where θ_j is the temperature integral defined by

$$\theta_j = \int_0^\infty (T_i - T_j)dt \tag{3}$$

where $j = 1$ for the heated surface (surface 1) and $j = 2$ for the insulated surface (surface 2). Note that although the integral in equation (3) extends to infinity, in practice, it need only be evaluated for a large but finite time.

Next consider a two-layer laminate consisting of a material extending from $x = 0$ to $x = L_1$ and a second layer from $x = L_1$ to $x = L_1 + L_2$ (the $x = 0$ surface is heated). Equation (2) can now be written for the second layer

$$\alpha_2 = \frac{L_2^2(T_f - T_i)}{(\theta_2 - \theta_3)} \tag{4}$$

where the following relation was used

$$\frac{Q_2}{\rho_2 C_2} = L_2(T_f - T_i) \tag{5}$$

and T_f is the final temperature of the composite. This relation is derived from an energy balance on the second layer. Since the total energy added at the front surface of the second layer is Q_2 and the rear surface is insulated, an energy balance gives $Q_2 = \rho_2 C_2 L_2(T_f - T_i)$.

Consider now the solution of the first layer as the sum of the two solutions. First, a heat flux of $Q_1 + Q_2$ is imposed on the $x = 0$ surface with the $x = L_1$ surface insulated (case a). Second, $x = 0$ is assumed insulated with Q_2 occurring at $x = L_1$ (case b). The sum of cases a and b is $Q_1 + Q_2$ at $x = 0$ with Q_2 at $x = L_1$. As in equation (5)

$$\frac{Q_1}{\rho_1 C_1} = L_1(T_f - T_i) \tag{6}$$

From equation (2) the result of case a in the foregoing is

$$\theta_1{}^a - \theta_2{}^a = \frac{(Q_1 + Q_2)L_1}{\rho_1 C_1 \alpha_1} \tag{7}$$

Substituting equation (5) and (6) into (7) results in

$$\theta_1{}^a - \theta_2{}^a = \frac{(\rho_1 C_1 L_1 + \rho_2 C_2 L_2)L_1(T_f - T_i)}{\rho_1 C_1 \alpha_1} \tag{8}$$

and for case b, a similar analysis yields

$$\theta_1{}^b - \theta_2{}^b = \frac{\rho_2 C_2 L_2 L_1(T_f - T_i)}{\rho_1 C_1 \alpha_1} \tag{9}$$

The sum of equations (8) and (9) is the solution to the physical problem for the first layer

$$\theta_1 - \theta_2 = \frac{(\rho_1 C_1 L_1 + 2\rho_2 C_2 L_2)L_1(T_f - T_i)}{\rho_1 C_1 \alpha_1} \tag{10}$$

Equation (4) can be rewritten

$$\theta_2 - \theta_3 = \frac{L_2^2(T_f - T_i)}{\alpha_2} \tag{11}$$

The sum of equations (10) and (11) is

$$\theta_1 - \theta_3 = \left[\frac{L_1^2}{\alpha_1} + \frac{2L_1L_2}{\alpha_1}\frac{\rho_2 C_2}{\rho_1 C_1} + \frac{L_2^2}{\alpha_2}\right](T_f - T_i) \tag{12}$$

which relates the integrals of the temperatures at the heated and insulated surfaces. An effective thermal diffusivity α_{eff} and an effective length, L_{eff} are now defined by a similar equation relating θ_1 and θ_3.

$$\theta_1 - \theta_3 = \frac{L_{\text{eff}}^2}{\alpha_{\text{eff}}}(T_f - T_i) \tag{13}$$

A comparison of equations (12) and (13) then gives the ratio of $L_{\text{eff}}^2/\alpha_{\text{eff}}$ as

$$\frac{L_{\text{eff}}^2}{\alpha_{\text{eff}}} = \left[\frac{L_1^2}{\alpha_1} + \frac{2L_1L_2}{\alpha_1}\left(\frac{\rho_2 C_2}{\rho_1 C_1}\right) + \frac{L_2^2}{\alpha_2}\right] \tag{14a}$$

which can also be written as

$$\frac{L_{\text{eff}}^2}{\alpha_{\text{eff}}} = \frac{L_1^2}{\alpha_1}\left[1 + \frac{2}{C^+} + A^+\right] \tag{14b}$$

where A^+ and C^+ are the dimensionless ratios

$$C^+ \equiv L_1\rho_1 C_1/L_2\rho_2 C_2 \tag{15a}$$

$$A^+ = \alpha_1 L_2^2/\alpha_2 L_1^2 \tag{15b}$$

The ratio of $L_{\text{eff}}^2/\alpha_{\text{eff}}$ in (14b) divided by the same quantity for the materials reversed in order (i.e., material 2 now is heated at $x = 0$) is

$$R = \frac{1 + 2(C^+)^{-1} + A^+}{1 + 2A^+C^+ + A^+} \tag{15}$$

This ratio shows that there is a pronounced order effect unlike the lumped model to be discussed. The order effect is essential in most cases to give a satisfactory response at the heated surface. One case in which there is no order effect is for

$$A^+(C^+) = 1$$

since $R = 1$ for this case. The ratio R approaches zero for $C^+ \to \infty$ while $A^+ > 0$; R approaches infinity for $C^+ \to 0$ while $0 < A^+ < \infty$.

For three layers, the same procedure results in

$$\frac{L_{\text{eff}}^2}{\alpha_{\text{eff}}} = \frac{L_1^2}{\alpha_1} + \frac{L_2^2}{\alpha_2} + \frac{L_3^2}{\alpha_3} + 2\left[\left(\frac{L_1L_2}{\alpha_1}\right)\left(\frac{\rho_2 C_2}{\rho_1 C_1}\right) + \left(\frac{L_1L_3}{\alpha_1}\right)\left(\frac{\rho_3 C_3}{\rho_1 C_1}\right) + \left(\frac{L_2L_3}{\alpha_2}\right)\left(\frac{\rho_3 C_3}{\rho_2 C_2}\right)\right] \tag{16}$$

By mathematical induction, the general expression for an n-layer composite laminate is

Nomenclature

C = specific heat (J/kg-K)
C_{2n} = function defined by equation (22)
D_{2n} = function defined by equation (23)
E_n = eigenfunction error term
F_0 = Fourier modulus ($\alpha t/L^2$)
$f_n{}^*$ = initial value function, equation (25)
L = thickness (m)
L_{eff} = effective single layer thickness for the multilayer problem (m)
L_j = thickness of jth layer (m)
n = summation index
Q = time-integrated heat flux (J/cm^2)
Q_j = Q in jth layer
q = heat flux (W/cm^2)
T_f = final uniform temperature (K)
T_i = initial uniform temperature (K)
T_j = temperature in the jth layer (K)
T_0 = magnitude of temperature step (K)
t = time (s)
x = distance coordinate (m)
Z^2 = function defined by equation (35)
α_j = thermal diffusivity in the jth layer (cm^2/s)
α_{eff} = effective single layer thermal diffusivity for the multilayer problem
β_n = eigenvalue
$\gamma_{21} = \frac{\lambda_1}{\lambda_2}\sqrt{\frac{\alpha_2}{\alpha_1}}$
$\eta = \beta_n L_2/\sqrt{\alpha_2}$
θ_j = temperature integral in equation (3)
λ_j = thermal conductivity in the jth layer (W/m-K)
ρ = density (kg/m^3)
$\xi = \beta_n L_1/\sqrt{\alpha_1}$

$$\frac{L_{\text{eff}}^2}{\alpha_{\text{eff}}} = \left\{ \sum_{i=1}^{n} \frac{L_i^2}{\alpha_i} + 2 \sum_{i=1}^{n-1} \frac{L_i}{\alpha_i} \sum_{j=i+1}^{n} \frac{\rho_j C_j L_j}{\rho_i C_i} \right\} \tag{17}$$

In the following section, an alternative eigenvalue analysis will be used to derive the same expression as equation (14) for the two-layer problem. This lends credibility to the superposition analysis for more than two layers for which the eigenvalue technique becomes cumbersome.

Two-Layer Eigenvalue Analysis. In this section, a technique, for the special case of a two-layer composite developed by Schimmel and Donaldson [6], will be summarized to show that it leads to an expression identical to equation (14). The overall thickness of the system is $L_1 + L_2$ and the interface between the two layers is at L_1. The front surface is subjected to a temperature step at $t = 0$ while the rear surface is adiabatic for all time. Although the temperature step boundary condition is not as general as the arbitrary heat flux boundary condition of the preceding section, it does satisfy the condition of approaching zero heat flux at long time, since the rear boundary is insulated. The temperature response at the rear surface ($x = L_1 + L_2$) of a single material which is initial at T_i to the foregoing boundary conditions is

$$\frac{T(L_1 + L_2, t) - T_i}{T_0 - T_i} = 1 - \frac{4}{\pi} \sum_{n=0}^{\infty} \frac{(-1)^n e^{-(2n+1)^2 \pi^2 F_0/4}}{2n+1} \tag{18}$$

where the Fourier modulus is defined by

$$F_0 \equiv \frac{\alpha t}{(L_1 + L_2)^2} \tag{19}$$

Now the object is to determine an appropriate value of $\alpha_{\text{eff}}/L_{\text{eff}}$ to use in equation (18) for the case of two-layers. In this manner, the actual thermal diffusivities (and lengths) of the materials are suppressed and one works with some fictitious parameter for the calculation of the rear surface temperature response.

Using the temperature step front surface and adiabatic rear surface boundary conditions with temperature and heat flux matching conditions in the interface, the exact rear surface response of a two-layer composite is given by [1]

$$\frac{T_2(L_1 + L_2, t) - T_i}{T_0 - T_i} = 1 - \sum_{n=0}^{\infty} f_n^* e^{-\beta_n^2 t} \left[{}^{2t}\left[C_{2n} \cos \frac{\beta_n (L_1 + L_2)}{\sqrt{\alpha_2}} + D_{2n} \sin \frac{\beta_n (L_1 + L_2)}{\sqrt{\alpha_2}} \right] \right] \tag{20}$$

where the coefficients f_n^*, C_{2n}, and D_{2n} are

$$f_n^* = \frac{\frac{\lambda_1}{\alpha_1} \int_0^{L_1} \sin \frac{\beta_n x}{\sqrt{\alpha_1}} dx + \frac{\lambda_2}{\alpha_2} \int_{L_1}^{L_1+L_2} \left[C_{2n} \cos \frac{\beta_n x}{\sqrt{\alpha_2}} + D_{2n} \sin \frac{\beta_n x}{\sqrt{\alpha_2}} \right] dx}{\frac{\lambda_1}{\alpha_1} \int_0^{L_1} \sin^2 \frac{\beta_n x}{\sqrt{\alpha_1}} dx + \frac{\lambda_2}{\alpha_2} \int_{L_1}^{L_1+L_2} \left[C_{2n} \cos \frac{\beta_n x}{\sqrt{\alpha_2}} + D_{2n} \sin \frac{\beta_n x}{\sqrt{\alpha_2}} \right]^2 dx} \tag{21}$$

$$C_{2n} = \sin \frac{\beta_n L_1}{\sqrt{\alpha_1}} \cos \frac{\beta_n L_1}{\sqrt{\alpha_2}} - \gamma_{21} \cos \frac{\beta_n L_1}{\sqrt{\alpha_1}} \sin \frac{\beta_n L_1}{\sqrt{\alpha_2}} \tag{22}$$

$$D_{2n} = \sin \frac{\beta_n L_1}{\sqrt{\alpha_1}} \sin \frac{\beta_n L_1}{\sqrt{\alpha_2}} + \gamma_{21} \cos \frac{\beta_n L_1}{\sqrt{\alpha_1}} \cos \frac{\beta_n L_1}{\sqrt{\alpha_2}} \tag{23}$$

where

$$\gamma_{21} = \frac{\lambda_1}{\lambda_2} \sqrt{\frac{\alpha_2}{\alpha_1}} = \sqrt{\frac{\lambda_1 \rho_1 C_1}{\lambda_2 \rho_2 C_2}} \tag{24}$$

Equations (20)–(23) could also be expressed in terms of Laplace transforms yielding the same transcendental equation for the eigenvalues. It was felt, however, that this additional step might over complicate the logical thought progression in the analysis, so it was not done.

The eigenvalues, β_n, are determined from the boundary condition at the rear surface and can be written

$$C_{2n} \sin \frac{\beta_n (L_1 + L_2)}{\sqrt{\alpha_2}} = D_{2n} \cos \frac{\beta_n (L_1 + L_2)}{\sqrt{\alpha_2}} \tag{25}$$

Since the coefficients C_{2n} and D_{2n} are given by equations (22) and (23), equation (25) involves a single unknown, β_n, which is given by the roots of the transcendental equation

$$\cos \xi \cos \eta - \gamma_{21}^{-1} \sin \xi \sin \eta = 0 \tag{26}$$

where

$$\xi = \frac{\beta_n L_1}{\sqrt{\alpha_1}} \tag{27a}$$

and

$$\eta = \frac{\beta_n L_2}{\sqrt{\alpha_2}} \tag{27b}$$

The corresponding eigenvalue equation for a single layer problem can be written as

$$\cos z = 0, \qquad z = \frac{\beta_n L_{\text{eff}}}{\sqrt{\alpha_{\text{eff}}}} \tag{28}$$

The object at this point is to select $L_{\text{eff}}/\sqrt{\alpha_{\text{eff}}}$ so that the smallest eigenvalues, β_n, found from equations (26) and (28) are nearly identical. For $F_0 > 0.3$, the $n = 0$ corresponding to β_0 in the summation of equation (18) is at least 100 times larger than the next largest term. Thus, except for the smallest values of F_0, the temperatures found for the single layer with effective values of α and L would be expected to agree fairly well with the exact temperature given by a two-layer analysis. Utilizing the polynomial expansions for the sine and cosine functions, equations (26) and (28) become

$$1 - \frac{1}{2!}\left[\xi^2 + \frac{2\xi\eta}{\gamma_{21}} + \eta^2 \right] + \frac{1}{4!}\left[\xi^4 + \frac{4\xi^3\eta}{\gamma_{21}} + 6\xi^2\eta^2 + \frac{4\xi\eta^3}{\gamma_{21}} + \eta^4 \right] - \ldots = 0 \tag{29}$$

$$1 - \frac{1}{2!}(z^2) + \frac{1}{4!}(z^4) - \ldots = \cos(z) = 0 \tag{30}$$

For these equations to yield approximately the same eigenvalues for small values of n, a comparison of the two equations yields,

$$z^2 = \xi^2 + \frac{2\xi\eta}{\gamma_{21}} + \eta^2 \tag{31}$$

Introducing the definition of z, ξ and η in equation (31) results in exactly the same relation for $L_{\text{eff}}^2/\alpha_{\text{eff}}$ as given by equation (14). The two methods thus yield the same result.

Effective Diffusivity-Lumped Model. For a simple calculation of effective thermal diffusivity, a first approximation is a ratio of effective thermal conductivity to effective volumetric "heat capacity." This model, which will be referred to as the lumped model, has the shortcoming that it is independent of material arrangement. The effective thermal conductivity for a series of parallel slabs is given by

$$\lambda_{\text{eff}} = \frac{\sum L_j}{\sum L_j/\lambda_j} = \frac{L}{\sum L_j/\lambda_j} \tag{32}$$

where L is the total thickness of the composite. In the steady-state case, this expression can be used to obtain the temperature at any position in the composite slab via a technique similar to the electrical analog. Note that the heat capacity does not influence the steady-state heat conduction problem analogous to a charged capacitor in the d-c electrical circuit.

In the transient situation, one can imagine a lumped heat capacity given by

$$(\rho C)_{\text{eff}} = \frac{\sum L_j(\rho C)_j}{\sum L_j} = \frac{1}{L}\sum L_j(\rho C)_j \tag{33}$$

Again there is some physical justification because this will predict an equilibrium temperature rise of an adiabatic system following a given energy input. The lumped effective thermal diffusivity is the ratio of these two quantities

$$\alpha_{\text{eff}} = \frac{\lambda_{\text{eff}}}{(\rho C)_{\text{eff}}} = \frac{L^2}{\sum(L_j/\lambda_j)\sum L_j(\rho C)_j} \tag{34}$$

or

$$\frac{L^2}{\alpha_{\text{eff}}} = \sum\frac{L_j}{\lambda_j}\sum L_j(\rho C)_j \tag{35}$$

Note that the model is indeed independent of material arrangement.

Results

The technique for solution of boundary-value problems in composite media using quasi-orthogonal function expansion [1] has been used to generate an "exact" solution on the digital computer. The example considered for comparison with the effective analysis consists of two 1.0-cm layers of a material with a large heat capacity (heat sink) and two 1.0-cm layers of low thermal conductivity (insulator). The thermal conductivity and diffusivity for the two materials are respectively 418.6 W/m-K and 0.3 cm^2/s for the heat sink and 0.042 W/m-K and 0.003 cm^2/s for the insulator. These property values are not intended to represent any particular real material although they are typical of some used in engineering applications. The reason for selecting these two grossly different materials is that this type configuration requires a large number of eigenvalues in the exact solution and thus should furnish a critical test of the effective solution.

There are six possible configurations of the four layers, each of which will be examined for agreement between the exact and the effective solution. Fig. 1 is a comparison for all six of the configurations, of the effective model with the lumped model for a temperature step at the front surface and an adiabatic rear surface. The temperatures presented are at the rear surface. Note that the rather unusual time scale factor corresponds to $\alpha_{\text{eff}}/L_{\text{eff}}^2$ for the "slowest" configuration namely that of two insulator layers followed by two heat sink layers. It is interesting that two configurations (ABBA and BAAB) have the same response curves. If the layer thicknesses were all not the same, this would not be the case. Later comparison with the exact solution confirms this somewhat surprising fact.

In order to determine the agreement between the effective solution and the exact solution, the time scales are modified by an appropriate scale factor in Figs. 2–6. This permits a critical examination of the effective diffusivity at small times. In each of the various configurations, the scale factor is equal to $\alpha_{\text{eff}}/L_{\text{eff}}^2$. The agreement for the "fastest" situation which is two layers of heat sink followed by two layers of insulator is seen in Fig. 2 to be excellent for all times. The lumped model however, is unable to predict any significant response at all in this time frame. The exact solution for all cases, was verified by a numerical finite difference calculation. The agreement is so close

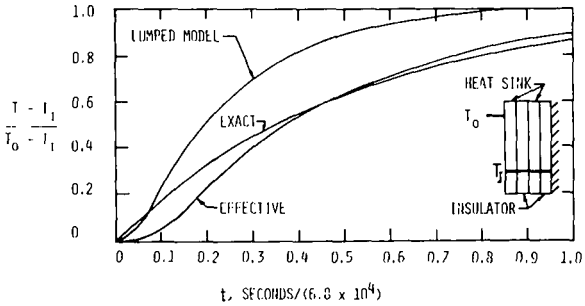

Fig. 3 Comparison of rear surface temperature history for heat sink/insulator/heat sink/insulator configuration

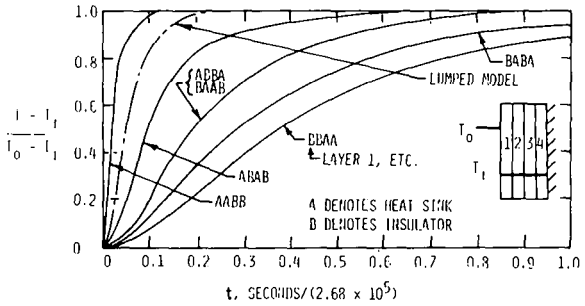

Fig. 1 Rear surface temperature history from the "effective model" and the "lumped model" for all configurations considered

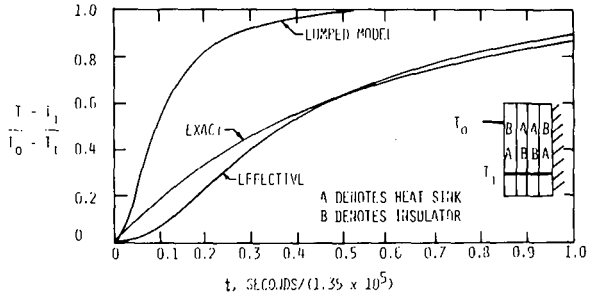

Fig. 4 Comparison of rear surface temperature history for either heat sink/insulator/insulator/heat sink configuration or insulator/heat sink/heat sink/insulator configuration

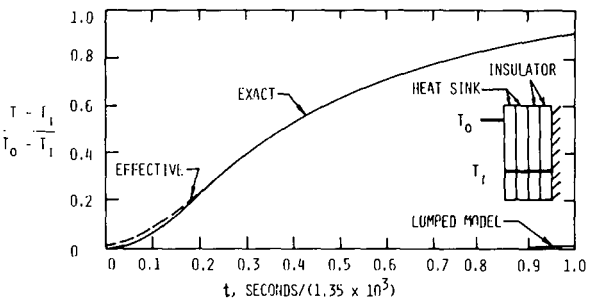

Fig. 2 Comparison of rear surface temperature history for the heat sink/heat sink/insulator/insulator configuration

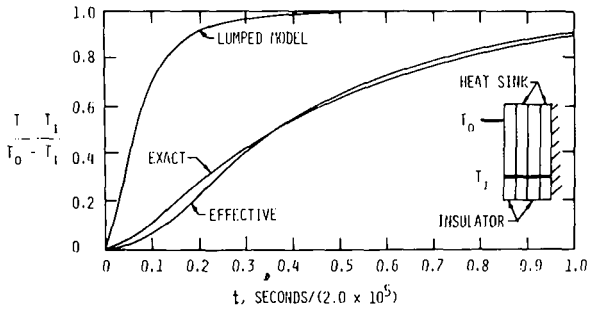

Fig. 5 Comparison of rear surface temperature history for insulator/heat sink/insulator/heat sink configuration

that no deviation between the two shows up on the scale used.

Figs. 3–6 show that the effective model disagreement to exact results is largest for small times as expected. The particular boundary condition considered tends to emphasize this small time inaccuracy. The important thing to notice in the figures is the ability of the effective model to predict trends and intermediate time behavior while the lumped model is greatly in error. The deviation between the effective results and the exact results is tentatively attributed to the fact that, although the effective model is orientation dependent, it still treats the thermal properties as being uniform over the composite and hence, cannot account for discreet property variation. It would be expected, that as the number of layers becomes large, the agreement between the effective model and the exact solution would improve.

In addition to the methods presented in this paper, there are a number of alternate ways of estimating an effective thermal diffusivity. One of these uses some parameter estimation techniques based upon least squares [7]. In this method, the sum of squares of differences between the temperature for both models (effective and exact) is calculated. This sum is then minimized with respect to the effective parameters.

Conclusions

The problem of thermal conduction in a multilayer composite laminate has been addressed by considering the composite to be equivalent to a single layer characterized by an effective thermal diffusivity. In the special case considered, the temperature response was determined for the insulated rear surface of a composite exposed to heating at its front surface. The effective diffusivity expression derived by a superposition analysis for the multilayer case was shown to be equal to that obtained by an eigenvalue analysis for the case of two layers.

This effective thermal diffusivity model represents a capability between the exact solution necessary for detailed design of thermal protection systems and the very approximate lumped model which is not capable of resolving various material arrangements, etc. Other boundary conditions should produce similar results and thus could be used in preliminary thermal studies.

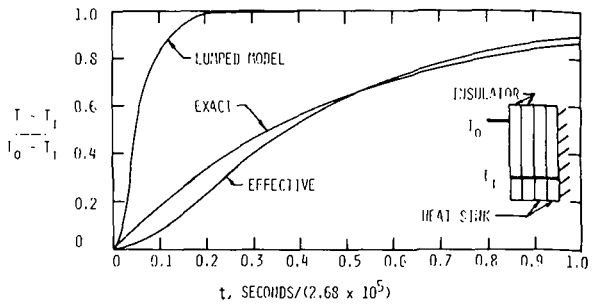

Fig. 6 Comparison of rear surface temperature history for insulator/insulator/heat sink/heat sink configuration

References

1 Tittle, C. W., "Boundary-Value Problems in Composite Media: Quasi-Orthogonal Functions," *Journal of Applied Physics*, Vol. 36, No. 4, 1965, pp. 1486–1488.

2 Bulavin, P. E., and Koshcheev, V. M., "Solution of Non-Homogeneous Heat Conduction Equation for Multi-Layered Bodies," *International Chemical Engineering*, Vol. 5, No. 1, 1965, pp. 112–115.

3 Goodman, T. R., "The Adjoint Heat-Conduction Problem for Solids," ASTIA-AD 254-769 (AFOSR-520), Apr. 1961.

4 Carslaw, H. S., and Jaeger, J. C., *Conduction of Heat in Solids*, Clarendon Press, Oxford, 1959.

5 Beck, J. V., and Al-Araji, S., "Investigation of a New Single Transient Method of Thermal Property Measurement," JOURNAL OF HEAT TRANSFER, TRANS. ASME Vol. 96, No. 3, 1974, pp. 59–64.

6 Schimmel, W. P., Jr., and Donaldson, A. B., "Determination of Effective Thermal Diffusivity for a Two-Layer Composite Laminate," *Advances in Thermal Conductivity*, University of Missouri-Rolla Press, Jan. 1975, pp. 405–415.

7 Beck, J. V., "Transient Determination of Thermal Properties," *Nuclear Engineering and Design*, Vol. 3, 1966, pp. 377–381.

K. Farnia
Coal Gasification Systems Operation,
Allis-Chalmers Corp.,
Milwaukee, Wisc.

J. V. Beck
Department of Mechanical Engineering,
Division of Engineering Research,
Michigan State University,
East Lansing, Mich.

Numerical Solution of Transient Heat Conduction Equation for Heat-Treatable Alloys Whose Thermal Properties Change With Time and Temperature

Changes in microstructure occur in as-received aluminum alloy (Al-2024-T351) when it is subjected to elevated temperatures (150–260°C). These changes, which are called precipitation hardening, in turn influence the thermal properties, making them time as well as temperature dependent. A computer-assisted transient experimental procedure has been developed to determine the values of thermal conductivity of as-received Al-2024-T351 under the influence of precipitation-hardening. Based on isothermal experimental data and related algebraic modeling of the thermal conductivity, a mathematical model in the form of two differential equations is proposed. Instantaneous values of volume fraction of precipitate and thermal conductivity can be predicted using this model. A method for the simultaneous numerical solution of the partial differential equation of conduction and the proposed differential equations of precipitation are also given. The influence of precipitation—hardening on temperature distribution and on values of thermal conductivity is shown graphically for several cases involving the Al-2024-T351 material.

1 Introduction

Design of heat transfer equipment using heat-treatable alloys such as aluminum alloy 2024-T351 (Al-2024-T351) can be difficult because metallurgical structural changes may occur during heating. These changes can result in increases as large as about 39 percent in values of thermal conductivity. The metallurgical changes can be related to precipitation-hardening of the alloy. To date, however, the literature does not contain a mathematical model to relate the thermal conductivity to the volume fraction of precipitate. An objective of this paper is to present a model through which the instantaneous value of volume fraction of precipitate, and subsequently the value of thermal conductivity of Al-2024-T351, can be predicted. A further objective is to demonstrate a numerical method for predicting the temperature history of Al-2024-T351 with time- and temperature-dependent thermal properties.

Although this paper presents data and a model specifically for as-received Al-2024-T351 material, the method of experimental investigation and mathematical modeling of the phenomena may be appropriate for other heat-treatable alloys which undergo similar metallurgical changes.

2 Experimental Study

Measurement of time- and temperature-dependent thermal properties of as-received Al-2024-T351 at elevated isothermal temperatures were first reported by Al-Araji [1, 2].[1] In order to: (1) verify his results, (2) use smaller departures from isothermal conditions, (3) use smaller time intervals between tests, and (4) develop a satisfactory

Contributed by the Heat Transfer Division for publication in the JOURNAL OF HEAT TRANSFER. Manuscript received by the Heat Transfer Division October 15, 1976.

[1] Numbers in brackets designate References at end of paper.

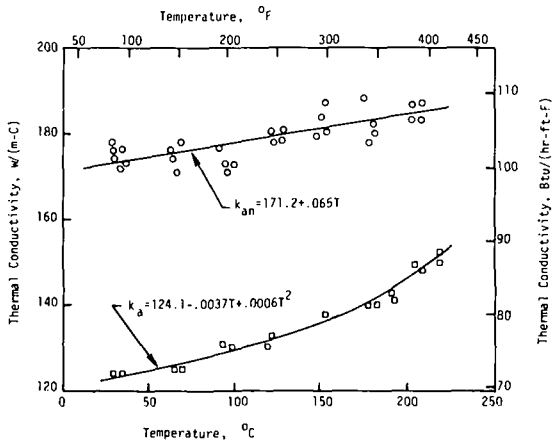

Fig. 1 Thermal conductivity values of as-received (no precipitation) and annealed Al-2024-T351

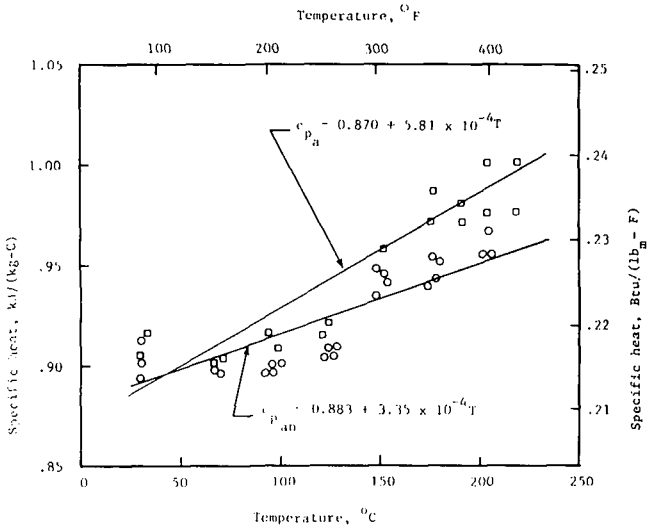

Fig. 2 Specific heat values of as-received (no precipitation) and annealed Al-2024-T351

mathematical model, further experimental and analytical work was done [3]. The new experimental results are similar, but there is one significant difference in the thermal conductivity values. In Al-Araji's work [1, 2], the thermal conductivity at any isothermal temperature appeared to start at a low value, increase to a maximum, and then gradually decrease to an equilibrium value which is still greater than the initial value. Al-Araji [1] modeled the experimental data of thermal conductivity only during the period when the conductivity was increasing. The mathematical model was an algebraic form and no relationship was postulated to relate the thermal conductivity and volume fraction of precipitate.

The Al-2024-T351 specimen used by Al-Araji [1] and in the present work is composed of 3.8–4.9-percent copper, 0.50-percent maximum silicon, 0.50-percent maximum iron, 0.3–0.9-percent manganese, 1.2–1.8-percent magnesium, 0.25-percent maximum zinc, 0.20-percent maximum zirconium plus titanium, 0.15-percent maximum titanium, 0.05-percent maximum others each, and 0.15-percent maximum others total, with the remaining balance being aluminum.

Al-Araji's [1] experimental strategy was to run tests: (1) first at room temperature, (2) then at the desired elevated temperature (these were the tests of primary interest), and (3) finally at room temperature again after all the other tests were completed. For each test, the energy input was provided by a copper calorimeter. An electronic device was used to carry out the necessary integrations.

In the present work, the same experimental strategy was followed. However, the energy input obtained from a d-c power source was introduced into a thin flexible heater sandwiched between two identical specimens. Another difference is that transient specimen temperatures were stored in the memory of an IBM 1800 computer during each test, which lasted only about 35 s. After each test the transient data were analyzed using the same computer. In addition, experiments were performed to determine the values of thermal conductivity of annealed Al-2024-T351 material as a function of temperature [3, 4].

Since an electric heater was used and the energy input was measured, the present method can be termed "direct." Al-Araji's method is comparative because the energy input was not measured directly; it was determined using the change in internal energy of a copper calorimeter. Direct methods are usually considered to be more accurate than comparative methods. The integration is also more accurately done in the present work using the IBM 1800 computer instead of the electronic integrator.

In both the present work and in that of Al-Araji, time variations in specific heat at isothermal temperatures were found to be small.

The primary objective of the present experimental study is to determine values of k and c_p for Al-2024-T351 alloy under three different conditions:

(a) As received properties with no precipitation. At low temperatures (below 150°C) the formation of precipitation is negligible; hence the values of k and c_p are affected only by the temperature level. For temperatures above 150°C precipitation occurs with time. For these temperatures, however, values of k and c_p with no precipitation are simply those at zero aging time. These were obtained from measurements within a 5-min period during which the specimens were rapidly heated to bring them from room temperature to a test temperature, such as 176.7°C. For this short time period it was assumed that negligible precipitation occurred. The experimental k and c_p values for this case are shown in Figs. 1 and 2. A least-squares technique was applied for these experimental data and the following functional relations were obtained:

$$k_a = 124.1 - 0.0037T + 0.0006T^2 \quad (1)$$

$$c_{p_a} = 0.870 + 5.81 \times 10^{-4}T \quad (2)$$

where k_a and c_{p_a} are values of thermal conductivity and specific heat, respectively, for Al-2024-T351 in the as-received condition. The units for k_a, c_{p_a}, and T are W/(m-C), kJ/(kg-C), and °C, respectively. These relations are valid in the range of 30–225°C.

Nomenclature

c_p = specific heat
k = thermal conductivity
k_0 = thermal conductivity at zero aging time
k_m = thermal conductivity at maximum aging time
k^+ = dimensionless thermal conductivity $= \dfrac{k(T, t) - k_0(T)}{k_m(T) - k_0(T)}$ obtained from equation (5a)
T = temperature
t = time
x = axial direction
η = volume fraction of precipitate
η_m = maximum volume fraction of precipitate
ρ = density
τ = time constant

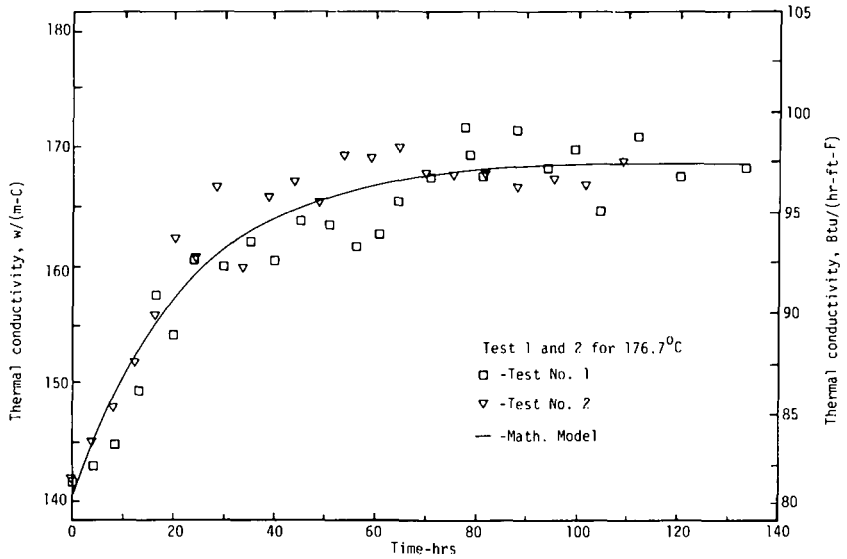

Fig. 3 Thermal conductivity as a function of time at 176.7°C for Al-2024-T351

(*b*) Annealed properties. Several Al-2024-T351 specimens were annealed at about 300°C and values of thermal conductivity as a function of temperature were then determined. The experimental values of k and c_p of annealed Al-2024-T351 are also shown in Figs. 1 and 2. A least-squares technique was also used to determine:

$$k_{an} = 171.2 + 0.065T \tag{3}$$

$$c_{p_{an}} = 0.883 + 3.35 \times 10^{-4}T \tag{4}$$

where the an subscript denotes values for annealed Al-2024-T351. The units are also given in the foregoing and the range of validity is 30–225°C. Notice from Fig. 1 that at 30°C annealed conductivity is about 40 percent larger than the as-received value.

The two specific heat curves shown in Fig. 2 (for annealed and as-received materials) are only slightly different. Small or negligible changes are expected. Below 150°C the difference in the measured values are due mainly to experimental errors. Above 150°C the difference is greater than the experimental variability; there is a 4-percent difference at about 200°C. Small, but noticeable and consistent, transient variations in the specific heat values were measured for the four test aging temperatures of 176.7, 190.5, 204.4, and 218.3°C [3]. The values for small times tended to be about 4 percent larger than for the later times while the standard deviation of the measured values was only about 1 percent. These time variations in the specific heat values were not expected and are not explainable at this time. In the range of 50 to 150°C a difference of less than 3 percent is noted in a comparison of the values of c_{p_a} and $c_{p_{an}}$ given in Fig. 2 with those reported in [10].

(*c*) As-received Al-2024-T351 with precipitation. Isothermal experiments were performed using as-received Al-2024-T351 material for the four temperatures of 176.7, 190.5, 204.4, and 218.3°C. At each isothermal temperature the test was repeated at least once; results of these tests are shown in Figs. 3 through 6. At each isothermal temperature the k values increase to a maximum with time and subsequently fluctuate about this maximum as time increases. A reasonably well-fitting mathematical model for thermal conductivity was found using nonlinear parameter estimation techniques [12] and related parameters were determined. The mathematical model for thermal conductivity of as-received Al-2024-T351 with isothermal precipitation is:

$$k(T, t) = k_0(T) + [k_m(T) - k_0(T)][1 - e^{-t/\tau(T)}] \tag{5a}$$

$$k_0(T) = 73.2 + 0.3725\ T \tag{5b}$$

$$k_m(T) = 148.2 + 0.1115\ T \tag{5c}$$

$$\tau(T) = \exp\left(-31.93 + 15.7\ \frac{1000}{T + 273}\right) \tag{5d}$$

where $k_0(T)$ is the k value at zero aging time, $k_m(T)$ is the k value at maximum aging time, and $\tau(T)$ is a time-constant. The unit for T is °C. These relations are valid for the range of 175–220°C. Both τ and t are in hours. The solid curves in Figs. 3–6 are plots of equation (5*a*) versus time.

3 Analytical Study

In practical applications, as-received Al-2024-T351 may be subjected to nonisothermal temperature conditions in the precipitation temperature range. For such cases, a model is proposed which is consistent with the isothermal algebraic mathematical model. The proposed model is in the form of two differential equations which describe the rate of volume fraction of precipitate during arbitrary thermal cycling; the model is:

$$\partial\eta(T, t)/\partial t = \frac{1}{\tau(T)}[\eta_m(T) - \eta(T, t)] \text{ if } \eta_m(T) > \eta(T, t) \tag{6a}$$

$$\partial\eta(T, t)/\partial t = 0 \qquad \text{if } \eta_m(T) \le \eta(T, t) \tag{6b}$$

where $\eta(T, t)$ is volume fraction of precipitate at temperature T and time t, $\tau(T)$ is the time-constant given in (5*d*), and $\eta_m(T)$ is the maximum volume fraction of precipitate at isothermal temperature.

Proposed equations (6*a*) and (6*b*) are based on a number of assumptions. These assumptions include: (1) for any isothermal temperature history, the volume fraction of precipitate can only increase or remain constant with time; (2) at any isothermal temperature, the volume fraction of precipitate reaches a maximum and subsequently remains unchanged as time increases; and (3) an instantaneous step change in temperature level does not affect the precipitation volume fraction. Following from these assumptions is the conclusion that the precipitation process is not reversible in the precipitation temperature range. The volume fraction of precipitation increases continuously or remains constant with time in the temperature range below 260°C. When the temperature of as-received Al-2024-T351 material is lowered, the rate of precipitation may go to zero if the cumulative amount of precipitation attained at a higher temperature surpasses the maximum volume fraction of precipitate at the lower temperature.

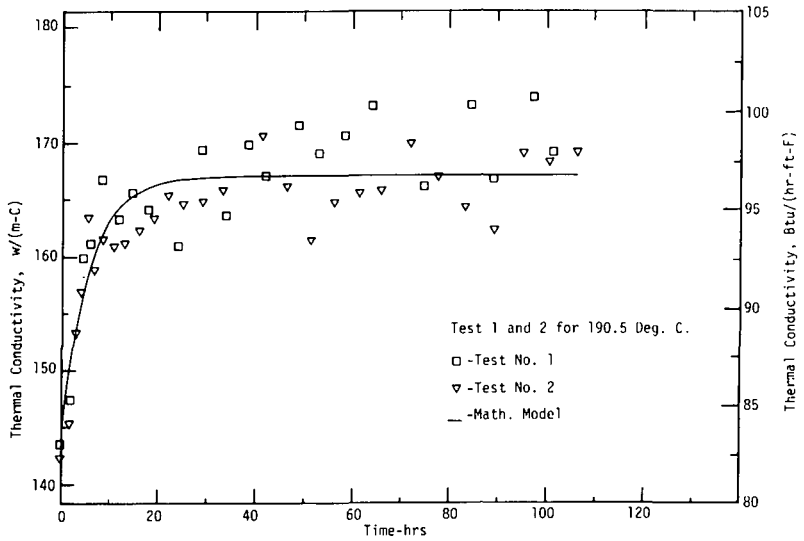

Fig. 4 Thermal conductivity as a function of time at 190.5°C for Al-2024-T351

For a detailed discussion of precipitation-hardening, see Hardy et al. [5], Turnbull [6], Panseri, et al. [7], and Kelly, et al. [8].

For complete precipitation, the value of η_m shown in equations (6*a*) and (6*b*) approaches unity. However, our experimental evidence indicates that the complete precipitation does not occur at any isothermal temperature unless the isothermal temperature is at least about 260°C. This is inferred from measured values of room temperature k of Al-2024-T351 specimens which had been previously aged at different isothermal temperatures. Based on these experimental data, the maximum volume fraction of precipitate $\eta_m(T)$ as a function of isothermal aging temperature T is:

$$\eta_m(T) = 8.68 \times 10^{-2} + 3.59 \times 10^{-3}T \tag{7}$$

which is valid for isothermal temperatures between 175 to 220°C, with T being in °C. $\eta_m(T)$ varies between 0.715 for 175°C to 0.877 for 220°C. It is interesting to note that, for $\eta_m(T) = 1.0$, a value of 254°C can be obtained from equation (7). The temperature 254°C is compared with the temperature 260°C, which has been suggested [10, 13] for annealing as-received Al-2024-T351 to obtain a stable microstructure.

Time- and temperature-dependent values of k are proposed to be related to the volume fraction of precipitate by:

$$k(T, t) = k_0(T) + [k_m(T) - k_0(T)]\eta(T, t)/\eta_m(T) \tag{8}$$

where $k_0(T)$, $k_m(T)$, $\eta(T, t)$, and $\eta_m(T)$ are given in equations (5*b*), (5*c*), (6*a*) or (6*b*), and (7), respectively.

4 Numerical Solution of Transient Conduction Equation Using Heat-Treatable Alloys

In predicting the temperature distribution of heat-treatable alloys, such as aluminum alloy 2024-T351, using the transient heat conduction equation

$$\frac{\partial}{\partial x}\left(k\frac{\partial T}{\partial x}\right) = \rho c_p \frac{\partial T}{\partial t} \tag{9}$$

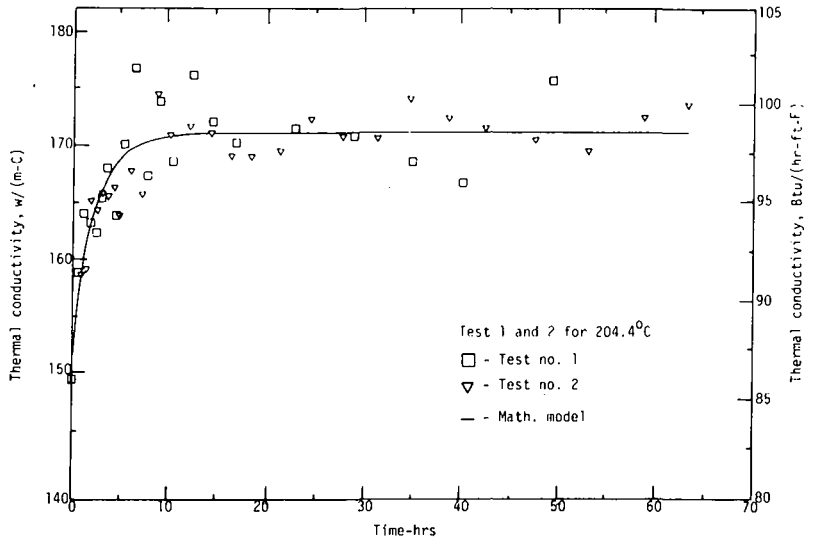

Fig. 5 Thermal conductivity as a function of time at 204.4°C for Al-2024-T351

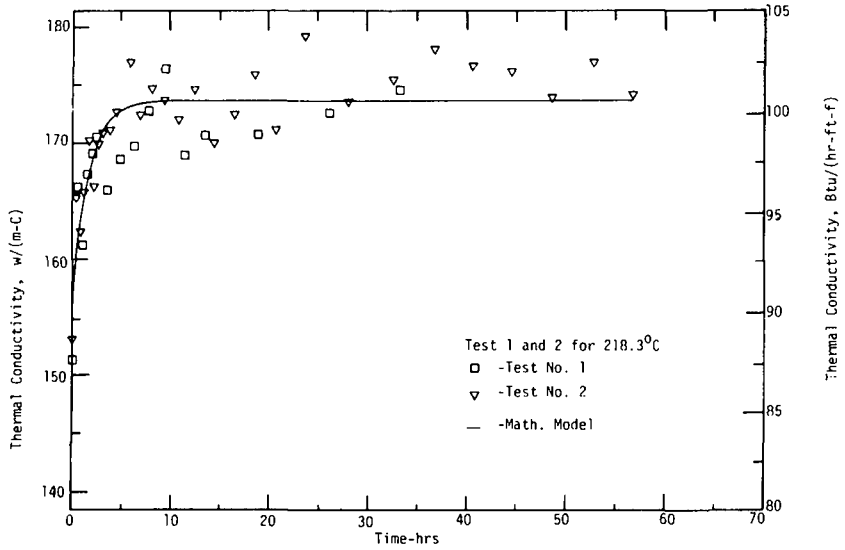

Fig. 6 Thermal conductivity as a function of time at 218.3°C for Al-2024-T351

one must consider the heat treatment history of the alloy in order to utilize the correct values of the thermal properties. If the alloy is annealed, the thermal properties introduced in equation (9) vary only with the material temperature. However, if the alloy is as-received, then the equation of precipitation given in (6*a*) or (6*b*) and the other related equation mentioned in connection with equation (8) should be solved simultaneously with equation (9).

In this section an example is given to: (1) present a numerical method of solution for transient temperature distributions in this alloy; and (2) demonstrate the effect of precipitation upon a temperature distribution. In the following discussion, the geometry is visualized as being a plate but it could also be a rod with heat transfer along its axis.

If the plate is relatively thin, so that the time-constant of heat transfer of the plate is relatively small compared with time-constant of precipitation τ, the precipitation distribution is nearly constant with position. On the other hand, if there are large temperature gradients in the plate either due to its relatively large thickness or to large-amplitude, high-frequency periodic heating, the plate could have significant differences in thermal conductivity through it due to the variation of precipitation across it.

The one-dimensional partial differential equation of conduction (9) was solved numerically for the aluminum alloy 2024-T351 material with the simple boundary conditions of $T(0, t) = 232.2°C$ (450°F) and $\partial T(L, t)/\partial t = 0$, and the initial condition of $T(x, 0) = 176.7°C$ (350°F). The thickness of the plate was chosen to be the large value of 0.6096 m (2 ft). This relatively large value of the thickness (or equivalently, length of a rod) is necessary to illustrate the influence of precipitation upon the spatial variation of the temperature distribution.

The k and c_p values of Al-2024-T351 material for the three cases of as-received with no precipitation, as-received with precipitation, and annealed properties are used in equation (9). Since the variation for c_p for the three aforementioned cases is small, equation (2) is used in equation (9) for c_p values. It should also be noted that as-received Al-2024-T351 material with no precipitation does not exist above about 150°C for protracted times because precipitation occurs. Therefore, solving the equation of conduction (9) for as-received Al-2024-T351 material with no precipitation is only a hypothetical case illustrating the extent of error one could make.

Values of thermal conductivity k for cases of as-received properties (no precipitation) and the annealed material are obtained using the pertaining equations given by (1) and (3).

The k values of as-received Al-2024-T351 with precipitation depend on the amount of precipitation; consequently, the values are time- and temperature-dependent. To calculate the instantaneous values of thermal conductivity, the amount of precipitation must be calculated. For cases in which the temperature of as-received Al-2024-T351 changes with time or position, equations of precipitation given by (6*a*) and (6*b*) and the conduction equation (9) must be solved simultaneously to determine the volume fraction of precipitate, thermal conductivity, and temperature.

One way to solve equation (9) numerically is to write an energy balance for node i at position $x_i = i\Delta x$ and time t_j. One result is:

$$(1-\beta)\left[k^j_{i-1/2}\frac{T^j_{i-1}-T^j_i}{\Delta x}-k^j_{i+1/2}\frac{T^j_i-T^j_{i+1}}{\Delta x}\right]+\beta\left[k^j_{i-1/2}\frac{T^{j+1}_{i-1}-T^{j+1}_i}{\Delta x}-k^j_{i+1/2}\frac{T^{j+1}_i-T^{j+1}_{i+1}}{\Delta x}\right]=(\rho c_p)^j_i\frac{T^{j+1}_i-T^j_i}{\Delta t} \quad (10)$$

where $k_{i-1/2}$ is the thermal conductivity evaluated at temperature $(T^j_{i-1} + T^j_i)/2$; similarly, $k^j_{i+1/2}$ is k value evaluated at $(T^j_i + T^j_{i+1})/2$.

Forward difference, backward difference, and Crank-Nicolson approximations can be specified by setting the value of β in equation (10) equal to 0.0, 1.0, and 0.5, respectively. Equation (10) can be rearranged so that all the unknown temperatures appear on one side (those at the time t_{j+1}) and all the known temperatures on the other. This rearrangement generates a set of linear tridiagonal algebraic equations. The algorithm given in [9] was used to solve these algebraic equations at each step.

The values of $k^j_{i-1/2}$ and $k^j_{i+1/2}$ are determined using the relationship given in equation (8). The value of $\eta_{i-1/2}$ for node $i - 1/2$ and time t_{j+1} was determined by approximating equation (6) using the fourth-order Runge-Kutta formulas [9] to obtain

$$\eta^{j+1}_{i-1/2} = \eta^j_{i-1/2} + (Rk_0 + 2Rk_1 + 2Rk_2 + Rk_3)/6 \quad (11)$$

where

$$Rk_0 = \Delta t\,(\eta^j_{m,i-1/2} - \eta^j_{i-1/2})/\tau^j_{i-1/2}$$

$$Rk_1 = \Delta t\,(\eta^{j+1/2}_{m,i-1/2} - \eta^j_{i-1/2} - Rk_0/2)/\tau^{j+1/2}_{i-1/2}$$

$$Rk_2 = \Delta t\,(\eta^{j+1/2}_{m,i-1/2} - \eta^j_{i-1/2} - Rk_1/2)/\tau^{j+1/2}_{i-1/2}$$

$$Rk_3 = \Delta t\,(\eta^{j+1}_{m,i-1/2} - \eta^j_{i-1/2} - Rk_2)/\tau^{j+1}_{i-1/2}.$$

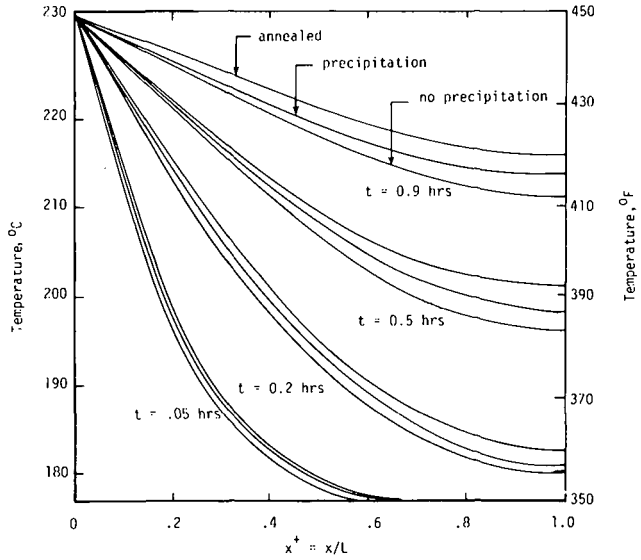

Fig. 7 Crank-Nicolson finite difference solution of conduction equation for Al-2024-T351 bar in cases of as received properties (no precipitation), as received with precipitation, and annealed conditions

For $\eta^{j}_{i+1/2}$, a similar expression is written with subscript $i + 1/2$. Note that the subscript $i - 1/2$ or $i + 1/2$ indicates that the components are calculated at a temperature $(T_{i-1} + T_i)/2$ or $(T_i + T_{i+1})/2$, respectively.

Equation (11) was used to calculate the volume fraction of precipitate at time t_{j+1}; subsequently the values of thermal conductivity were calculated by the relationship given in equation (8). These values were then utilized in equation (10) to obtain the temperature of the corresponding node at time t_{j+1}. If the time step Δt is small compared to the maximum time t, the effect of the past $k(T, t)$, $\eta_m(T)$, and $\tau(T)$ values (i.e., at t_j) used for one future (i.e., at t_{j+1}) temperature calculation is negligible.

The numerical results using the Crank-Nicolson method are given in Figs. 7–10. Fig. 7 shows temperature as a function of $x^+ = x/L$ for the three cases of as-received properties (no precipitation), as-received with precipitation, and annealed conditions for times 0.05, 0.2, 0.5, and 0.9 hr. The three aforementioned cases generate three distinct curves (temperature versus x^+) for any time t due to the differences in thermal conductivity k. The largest temperature difference for the three cases is obtained at $x^+ \approx 1$ (insulated surface) when time is between 0.8 and 1.6 hrs. The temperature history of the insulated surface for the three cases is shown in Fig. 8.

The thermal conductivity history of the Al-2024-T351 in cases of as-received with no precipitation and the annealed condition is shown in Fig. 9. At time zero, the value of k for the as-received Al-2024-T351 bar is 142 W/(m-C), while the corresponding value of k for the annealed condition is 183 W/(m-C). Due to a sudden change in temperature at the heated surface, there is an abrupt change in the value of k for as-received with no precipitation and the annealed condition, as shown in Fig. 9. These values for the as-received with no precipitation and the annealed condition at 232.2°C (450°F) are 156 and 186, respectively. The values of k at the insulated surface (for both cases) increase with time. Due to a higher thermal conductivity, the annealed Al-2024-T351 attains the final uniform temperature much faster than the as-received Al-2024-T351 bar with no precipitation.

Fig. 9 also shows the thermal conductivity history of the Al-2024-T351 with precipitation. The volume fraction of precipitate of this bar is given in Fig. 10. Prior to a step increase in temperature, the as-received Al-2024-T351 was held at 176.7°C for 25 hr. Before this time the bar was held at a low temperature at which negligible precipitation occurred. For 25 hr of isothermal aging at 176.7°C, the values of thermal conductivity (k) and the values of volume fraction of precipitate (η) increased with aging time. After this period, due to an abrupt change in temperature at the heated surface, there was also an abrupt change in the value of k and a rapid increase in the value of η, which are shown in Figs. 9 and 10, respectively. After the abrupt change, the values of k at the heated surface unlike the annealed and as-received with no precipitation cases changed with time because of the influence of the precipitation. It is important to note that the precipitation at the heated surface, due to a higher temperature, was completed more rapidly than the precipitation at the insulated surface. Hence the k values calculated for the heated surface approached a constant value sooner than the corresponding values of k obtained for the insulated surface.

5 Discussion and Accuracy

Important contributions of this paper are: (a) the conductivity

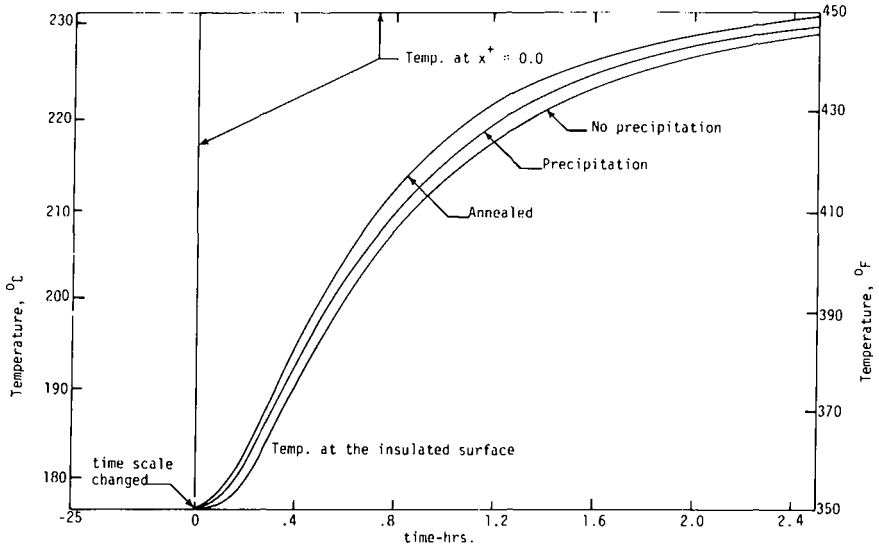

Fig. 8 Temperature history of the insulated surface of the Al-2024-T351 bar in cases of as received properties (no precipitation), as received with precipitation, and annealed conditions

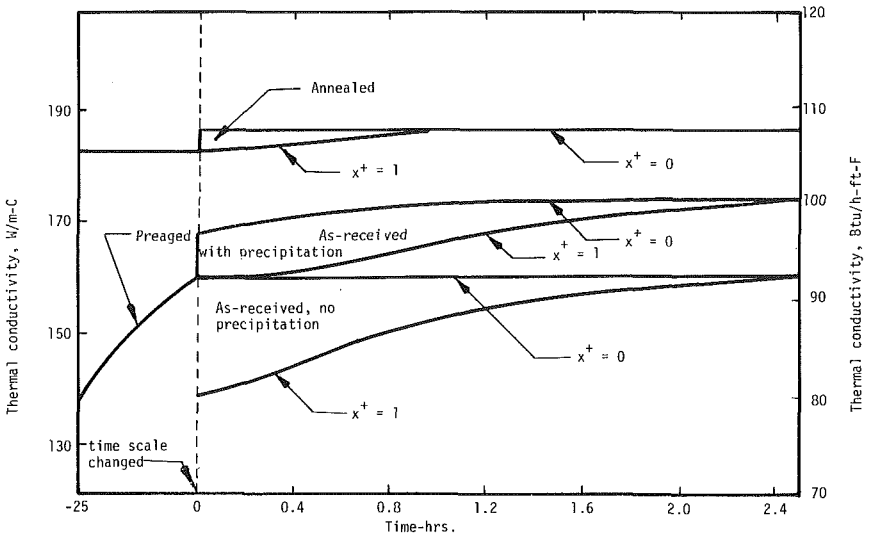

Fig. 9 Thermal conductivity history of the Al-2024-T351 bar in cases of as received properties (no precipitation), as-received with precipitation, and the annealed condition. The Al-2024-T351 bar was preaged at 176.7°C for 25 hr

model given by equations (6)–(8); (*b*) a method of solving the differential equation of precipitation with the transient heat conduction equation (9); and (*c*) a demonstration of the effect of precipitation on temperature distribution of an as-received Al-2024-T351 plate.

In order to provide further evidence that the isothermal aging data for thermal conductivity of as-received Al-2024-T351 is exponential with time, some experiments were performed to measure the electrical conductivity for specimens made from the same bar of the alloy. It has been suggested that the same functional relation would be expected because the Wiedemann-Franz ratio ($k/\sigma T$) tends to be independent of temperature for certain metals. (σ is the electrical conductivity and T is in K.) Data for two different isothermal temperatures are shown in Fig. 11. These experimental aging data appear to be exponential with time and a mathematical model similar to equation (5*a*) describes the data fairly well. The time constants for σ and k at 204.4°C are 2.10 and 2.23 hr, respectively. These two time constants and the shapes of the two corresponding curves are almost identical. This corroborates the exponential form of the isothermal aging data for thermal conductivity and the associated mathematical model.

Time variations of thermal conductivity of substances have been presented for mathematical forms other than the exponential [14]. To the best of our knowledge, however, for thermal conductivity of as-received Al-Cu alloys undergoing isothermal aging, our exponential form with its relationship to the volume fraction of precipitation is original.

The transient measurement facility used to determine the properties of the Al-2024-T351 material was initially tested by measuring

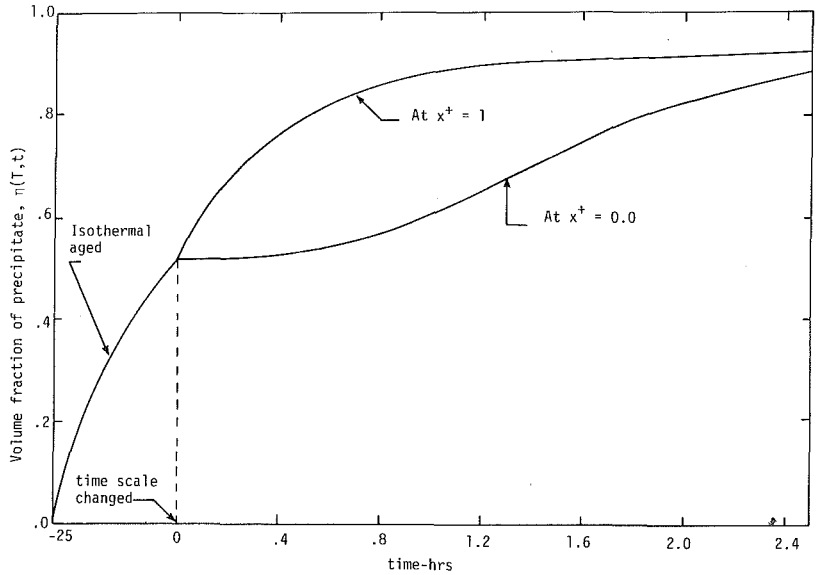

Fig. 10 Volume fraction of precipitate of as received Al-2024-T351 bar. The Al-2024-T351 bar was isothermally preaged at 176.7°C for 25 hr

the thermal properties of Armco Magnetic Ingot Iron as a reference material [3]. In the temperature range of 30 to 150°C, data obtained were compared with those given in reference [10]. Agreements within about 2 percent for k values and 5 percent for c_p were found.

A detailed error analysis for the experimental data for the Al-2024-T351 material is given in [3]. The thermal properties for the isothermal conditions as given herein have about the same accuracy as for the Armco iron mentioned above. The estimated standard deviations of the experimental data from the given smooth curves for c_{p_a}, $c_{p_{an}}$, k_a, k_{an}, and $k(T, t)$ are 0.019, 0.013, 1.45, 3.20, and 2.90, respectively. For arbitrary heating conditions further experimental work is needed to check the proposed model given by equation (5)–(8).

6 Conclusions

Repeated transient experiments were performed to obtain values of thermal conductivity for aluminum alloy 2024-T351 for cases of as-received properties (no precipitation), as-received material under the influence of precipitation-hardening, and annealed material. For all three cases, reasonable mathematical models were found. The mathematical models for thermal conductivity for the cases of as-received properties (no precipitation) and annealed materials are temperature-dependent only [10, 11]. The mathematical model for the case of as-received material under the influence of precipitation is both time- and temperature-dependent. The mathematical model for time/temperature-dependent thermal conductivity is significant because the proposed relationship has the physical basis of relating the thermal conductivity to the volume fraction of precipitation [5, 6]. Based on the isothermal mathematical model of time/temperature-dependent thermal conductivity (equation (5a)), two differential equations, namely equations (6a) and (6b), are proposed; these are useful not only for the isothermal case, but also for nonisothermal thermal processes. For the case of as-received Al-2024-T351 material under the influence of precipitation-hardening, the equation of precipitation and the one-dimensional partial differential equation of conduction, namely equations (6a) and (6b) and conduction equation (9), are solved numerically to determine the temperature history and corresponding volume fraction of precipitate. The solution of the equation of conduction for all three cases, solution of the equation of precipitation, and the thermal conductivity history of Al-2024-T351 material are shown graphically in Figs. 7 through 10 for particular boundary and initial conditions.

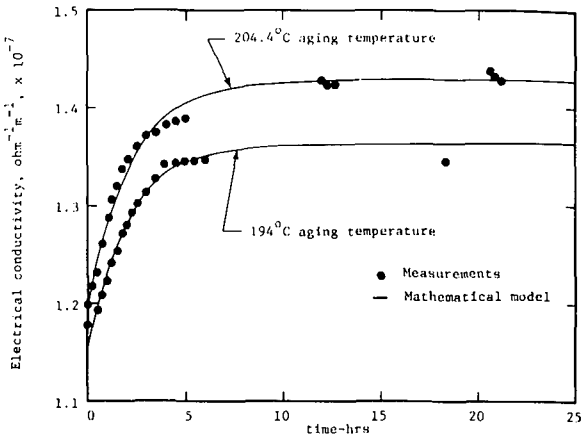

Fig. 11 Electrical conductivity as a function of aging time for Al-2024-T351

Acknowledgment

This research was supported by the National Science Foundation under Grant No. GK-41495.

References

1 Al-Araji, S. R., "Experimental Investigation of Transient Thermal Property Changes of Aluminum 2024-T351," PhD dissertation, Michigan State University, East Lansing, Mich., 1973.

2 Al-Araji, S., and Beck, J. V. "Heating Time and Heating Temperature Dependence of Thermal Conductivity of As-Received Aluminum Alloy 2024-T351," JOURNAL OF HEAT TRANSFER, TRANS. ASME, Series C, Vol. 97, 1975, pp. 148–149.

3 Farnia, K., "Computer-Assisted Experimental and Analytical Study of Time-Temperature-Dependent Properties of the Aluminum Alloy 2024-T351," PhD dissertation, Michigan State University, East Lansing, Mich. 1976.

4 Beck, J. V., and Al-Araji, S. "Investigation of a New Simple Transit Method of Thermal Property Measurement," JOURNAL OF HEAT TRANSFER, TRANS. ASME, Series C, Vol. 96, 1974, pp. 59–64.

5 Hardy, H. K., and Heal, T. J., "Nucleation-and-Growth Processes in Metals and Alloys," The Mechanism of Phase Transformation in Metals, Symposium, Belgrave Square, London, Institute of Metals, monograph and report series No. 18, 1956, pp. 1–46.

6 Turnbull, D. "Phase Changes," *Solid State Physics*, Vol. 3, 1956, pp. 225–306.

7 Panseri, C., and Federighi, T. "A Resistometric Study of Preprecipitation in an Aluminum . . . 1.4% Mg_2Si Alloy," *Institute of Metals Journal*, Vol. 94, 1966, pp. 99–105.

8 Kelly, A., and Nicholson, R. B., "Precipitation Hardening," *Progress in Material Science*, Vol. 13, 1966–1967, pp. 267–321.

9 Carnahan, B., Luther, H. A., and Wilkes, J. O., *Applied Numerical Methods*, Wiley, New York, 1969.

10 Touloukian, Y. S., ed., *Thermophysical Properties of High Temperature Solid Materials*, Vol. 2, 1966, MacMillan, New York, 1967.

11 Williams, D. R., and Blum, H. A., "The Thermal Conductivities of Several Metals," *Thermal Conductivity—Proceedings of the Seventh Conference*, Gaithersburg, Md, 1968, pp. 349–354.

12 Beck, J. V., and Arnold, K. J., *Parameter Estimation in Engineering and Science*, Wiley, New York, 1977.

13 Van Horn, K. R., *Aluminum*, Vol. 1, *Properties, Physical Metallurgy, and Phase Diagram*, Metals Park, Ohio, 1967.

14 Pacault, A., "The Kinetics of Graphitization," in *Chemistry and Physics of Carbon*, Vol. 7., P. L. Walker, ed., Marcel Dekker, Inc., New York, 1971.

S. Caspi
Post Graduate Research Engineer.

J. Y. Lee
Post Graduate Research Engineer.

T. H. K. Frederking
Professor.

Chemical, Nuclear, and Thermal Engineering Department,
University of California, Los Angeles,
Los Angeles, Calif.

Lambda—Transition (He II—He I) During Heat Flow at Supercritical Pressures

New boiling-like phenomena are reported which have been observed during heat-induced lambda transitions in liquid Helium-II at pressures above the thermodynamic critical pressure.

Introduction

Fluid phase transitions involving heat-induced changes from a more ordered to a less ordered phase (e.g., liquid to vapor) have been investigated extensively. The temperature range studied, cover phenomena all the way from high boiling points (e.g. H_2O) to cryo-liquids. Recent development work has even considered extensive use of superfluid liquid Helium II, e.g., [1].[1] Despite considerable research of utilization limits of near-saturated liquid He II [2–8] however, neither application in terrestrial advanced systems [1], nor resolution of basic phenomena has been straight forward. Near the λ-point of saturated liquid He^4 considerable difficulty in interpretation of data arises in part from possible coexistence of three phases (liquid He II, liquid He I, and vapor). Therefore, we have pressurized He II beyond its thermodynamic critical pressure, excluding vapor for a better resolution of phase change details. An applied heat flux induced the He II—He I transition locally, and led to new phenomena associated with the order-disorder transition (λ-transition) at supercritical pressures. The present brief communication has the purpose of presenting details of a new heat transfer response function obtained with an apparatus used previously for supercritical He I studies [11]. The function obtained is referred to briefly as He II "lambda curve."

Lambda-Curve

Fig. 1 plots the observed temperature of the heated solid (to an externally applied heat flux) as heat flux density q versus $\Delta T = T_H - T_\infty$; ($T_H$ "hot" wall temperature, T_∞ bulk fluid temperature); (q is per duct cross section to allow a comparison with references [9, 10]).

The lambda curve shows some properties reminiscent of boiling systems, despite the lack of a latent heat of phase change. Details though differ distinctly from classical "boiling curves." As q is increased (A-B in Fig. 1) Kapitza-resistance-dominated heat transfer conditions apparently are similar to natural convection with $[d \log q/d \log \Delta T] \approx 1$. At point B a sudden transition to a high ΔT (point C) occurs. Subsequently, upon continued heating ($dQ > 0$), a two-phase regime (C-D) is established with coexistence of He II and He I. This regime is characterized by a lowered heat transfer coefficient compared to regime (A-B). Upon further reduction of q, the two-phase regime was found to be extended beyond D-C down to point E. Finally, recovery toward the low ΔT-regime initiates at point E and is completed at point F. As q is reduced further, the system follows the previous characteristic function A-B from F to A.

The lambda curve incorporates the hysteresis loop F-B-C-E-F. This behavior is qualitatively quite similar to hysteresis phenomena of boiling curves of first order transitions. It incorporates a transition region with a negative slope of the thermal resistance curve. There are other properties of the lambda curve which depart significantly from boiling curves, for instance Kapitza resistance, lack of nucleate boiling, and the lack of latent heat of phase change. Further, it is noted that there exist order of magnitude differences between heat capacities of cryo-fluid He^4 and solid-materials (with the exception of paramagnetic solids and other less common cryo-vessel materials). The thermal conductivity of pure solids is quite large compared to He I (and He^4 gas at low T). Thus, cold He^4 I has a small thermal diffusivity. In contrast, He II has an excellent (apparent) thermal conductivity and diffusivity. Thus, during the lambda transition under consideration the rate of change of the heat flux with time is an important factor. Small constant rates of changes of the heater current with time are established in the runs with the present apparatus (sketched in insert of Fig. 1). In addition, a small mass flow rate of the order of magnitude 10^{-2} g/s was established. Oscillatory system disturbances were present in many runs at zero net mass flow. For all of these conditions however, relatively small changes (compared to

[1] Numbers in brackets designate References at end of paper.

Contributed by the Heat Transfer Division for publication in the JOURNAL OF HEAT TRANSFER. Manuscript received by the Heat Transfer Division January 13, 1977

data scatter) were found prior to point B, and at point B.

To resolve further details of the nature of the phase change, the transition heat flux density at point B (designated as q_λ) was measured as function of bulk fluid temperature (at constant system pressure). These results are displayed in Fig. 2. Full circles are data points obtained with the solid wall thermometer, squares denote data taken with a thermometer immersed in the fluid.

Both data sets are seen to be in good agreement with each other. Accordingly, a domain of supercritical fluid He II in the vicinity of the heater is converted quite fast into He I. Other thermal and geometric conditions are known to cause changes in limiting heat fluxes of near-saturated He II. This behavior exists also in the present runs, as far as system pressure changes are concerned. According to the evidence obtained, there is a well-defined transition function $q_\lambda(T_\infty)$ for each particular geometry and fluid state specification (e.g., isobaric operation). This feature is quite similar to the peak heat flux density of nucleate boiling in first order transitions. However, phenomena similar to nucleate boiling could not be found in our investigations. We turn now to a discussion of lambda point changes.

Lambda Temperature Depression

The present data are compared in Fig. 2 to literature data [9] reported for the vicinity of the lower triple point (low pressure lambda point of saturated liquid). Published data trends are seen to agree fairly well with results obtained in the present runs. Bhagat and Lasken [9] however, consider the possibility of a lambda temperature depression caused by an applied heat current. This type of lambda point depression does not appear to be present in other studies [10]. The reasonable agreement between the present data and reference [9] suggests the interpretation that no serious T_λ—depression may be present in both sets of data. Instead, there is a well-defined lambda transition heat flux density q_λ which is a function of bath temperature, pressure, and geometry. A possible lambda point depression however cannot be ruled out, outside of the scatter of the experimental data. Therefore, the data sets of Fig. 2 are considered indicative of an upper bound for this depression. At the order of $q_\lambda \approx 10$ mW/cm^2, the lambda point depression appears to be smaller than the order 1 mK. Another quantity of interest in this context is the thermodynamic limiting heat flux which precludes the existence of He II on the basis of thermodynamic energy arguments.

Thermodynamic Limit of Superfluidity

Numerical calculations of this limit have been carried out on the basis of superfluid thermodynamics, in order to assess a possible significance of thermodynamic limits for the interpretation of the present data. Attention is focussed upon Gibbs free energy density changes Δf in the presence of q. We evaluate the difference $(f_n - f)$ between the "normal" reference state and the He II superfluid state. The reference state at f_n is adopted from the thermodynamic two-fluid model (Gorter-Casimir model) for superfluid systems [12, 13], whose similarities have been emphasized in reference [14].

The normal state is an extension of the He I state adopted by Borelius [15] into the He II region. The calculations are based upon a simplified (mean field) calculation of Ginzburg and Pitaevskii [16] who utilize thermodynamic parametric functions α and β. In this form the present approach is referred to as Gorter-Casimir-Borelius (GCB) model.

A first order phase transition is characterized by discontinuities in the first derivatives of the Gibbs free energy (e.g., density ρ and entropy S). In contrast, the lambda transition under consideration shows continuous functions $S(T)$ and $\rho(T)$ for specified changes of state (e.g., saturated liquid, isobares). Second derivatives of f however, are no longer continuous (e.g., lambda-shaped specific heat). The He II free energy density of GCB is written along the line of the Ginzburg-Pitaevskii approach [16] for the special case of uniform counterflow of normal and superfluid as

$$f = f_n - \alpha(\rho_s/m) + (\beta/2)(\rho_s/m)^2 + \rho_s w^2/2 \qquad (1)$$

(ρ_s superfluid density, m mass of He^4 atom, $\overline{w} = \overline{v}_n - \overline{v}_s$, and v_n and

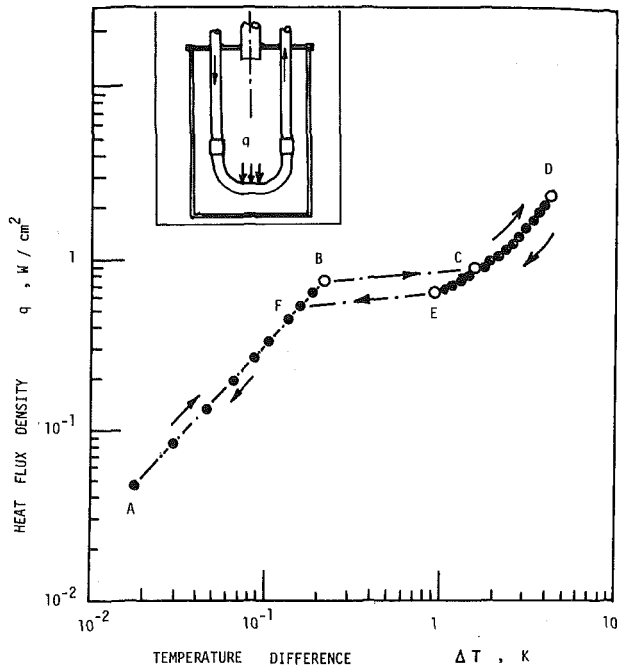

Fig. 1 "Lambda transition" function $q(\Delta T)$ at a bulk fluid temperature T_∞ = 2.00 K, a pressure P = 4.46 bar, and a mass flow rate of $1.57 \cdot 10^{-2}$ g/s; ($\Delta T = T_H - T_0$ denotes difference in T between wall and bulk fluid); insert: schematic of apparatus

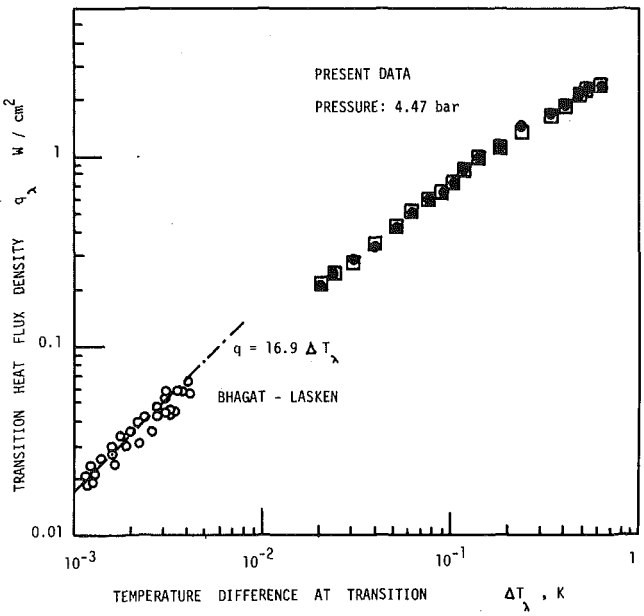

Fig. 2 "Lambda transition" heat flux density versus temperature difference; (squares: liquid thermometer; full circles: solid thermometer); results of Bhagat and Lasken from reference [9]

v_s denote normal and superfluid velocity, respectively.) Minimization of f for thermodynamic equilibrium $[(\partial f/\partial \rho_s)_T = 0]$ at constant T yields a superfluid equilibrium state density ($\Delta_{fe} = \alpha^2/(2\beta)$ for $w \to 0$, [subscript e])

$$\rho_s(w) = \rho_{se}[1 - (\rho_{se}/\Delta_{fe})(w^2/4)] \qquad (2)$$

As $w \to 0$, the equilibrium state value of ρ_s for quiescent He II is recovered ($\rho_s = \rho_{se}$). In equation (1) the Landau phase transition pa-

rameter may be expressed as

$$\alpha = 2m\Delta f_e/\rho_{se} \tag{3}$$

and

$$\beta = 2m^2\Delta f_e/\rho_{se}{}^2 \tag{4}$$

Other pertinent thermodynamic quantities are rate expressions at the limit of the superfluid state. The pertinent product for the uniform flow situation described by equation (1) is $(\rho_s w)$. This function has a maximum (subscript m) $[\partial(w\rho_s)/\partial w = 0]$ at a relative velocity

$$w_m = [(2/3)(\alpha/m)]^{1/2} = 2[\Delta f_e/(3\rho_{se})]^{1/2} \tag{5}$$

Once w_m has been exceeded, no stable values of He II counterflow will be available. (This situation is to some extent analogous to choking in nozzle flow of a compressible fluid.) After insertion of w_m and equilibrium state parameters into equation (1), we arrive at a normalized free energy density difference

$$(f_n - f)/\Delta f_e = 1 - (\rho_{se}/\Delta f_e)w^2/2 + (\rho_{se}/\Delta f_e)^2(w/2)^4$$
$$= 1 - (2/3)(w/w_m)^2 + (1/9)(w/w_m)^4 \tag{6}$$

At $T = 0$ K, w_m reaches its largest value $w_m(0)$. The related dimensionless free energy difference is $(f_n - f)/\Delta f_{e0} = 4/9$. At this limit, f has a point of inflection which signals the onset of a thermodynamically unstable flow regime beyond w_m. One possible reaction of the system to application of $w > w_m$ would be a "jump" from its last superfluid value toward the normal state, provided no other thermodynamic path is available. For further insight numerical values of (normalized) free energy differences have been obtained for various temperatures from the GCB-functions of reference [13]. They are displayed in Fig. 3. As the temperature is increased toward T_λ, the free energy density approaches f_n more and more. Further, w_m decreases to zero, as $T \to T_\lambda$.

Several conclusions concerning the free energy may be drawn from the present experimental evidence. There has been no support for easy accessibility of f_n via a discontinuity. Instead, a temperature increase along limiting states of the superfluid He II toward T_λ appears to be energetically more favorable. Further insight concerning this point may be obtained from a comparison of heat flux densities $q_m(w_m)$ with experimental results.

Comparison of Limiting Transport Rates

In line with the GCB-calculations [13], the maximum transport rate is written as (y_c condensate fraction ρ_L liquid density)

$$(\rho_s w)_m = (4/3)3^{-1/2}[\Delta f_e(\rho_{s_e}/\rho)y_c\rho_L]^{1/2} \tag{7}$$

Bhagat, et al. [17] have considered a special transport situation which may be expressed in terms of the entropy S_n per unit mass of normal fluid ($\rho S = \rho_n S_n$). If $(\rho_s w)$ has a meaningful limit $(\rho_s w)_m$ the related maximum heat flux density is [17] (for wall with $v_n \to 0$, critical value of $v_s \to w_m$)

$$q_m = (\rho_s w)_m S_n T \tag{8}$$

On the other hand, the simplified GCB-approach considered by Linnet, et al. [12] incorporates the approximation $(\rho_n/\rho) \sim (ST)$ with $S/S_\lambda = f(T/T_\lambda)$, and $S_\lambda = \gamma \cdot T_\lambda$ [15]. Accordingly, insertion of these GCB-functions in equation (8) in conjunction with equation (7) leads to a maximum heat flux density for uniform flow

$$q_m = \gamma T_\lambda{}^2(\rho_s w)_m = 3^{-1/2}(4/3)\gamma T_\lambda{}^2[\Delta f_e(\rho_{s_e}/\rho)y_c\rho_L]^{1/2} \tag{9}$$

Numerical values of $(\rho_s w)_m$ are displayed in Fig. 4 for a condensate fraction $y_c = 0.07$. This plot shows the monotonic decrease of the limiting transport rate toward zero at $T \to T_\lambda$. Entropy coefficients [γ-values] from reference [12] are listed in Table 1. The related energy $(\gamma T_\lambda{}^2)$ is shown in the insert of Fig. 4. Despite some apparent qualitative agreement the q_m—values resulting from $(\gamma T_\lambda{}^2)$ and $(\rho_s w)_m$ of Fig. 4 are not in the order of magnitude range of the present experimental studies.

A more encouraging agreement (by order of magnitude) appears to exist for a certain temperature range of film flow experiments [11]. These film data and the theoretical q_m—values appear to be upper

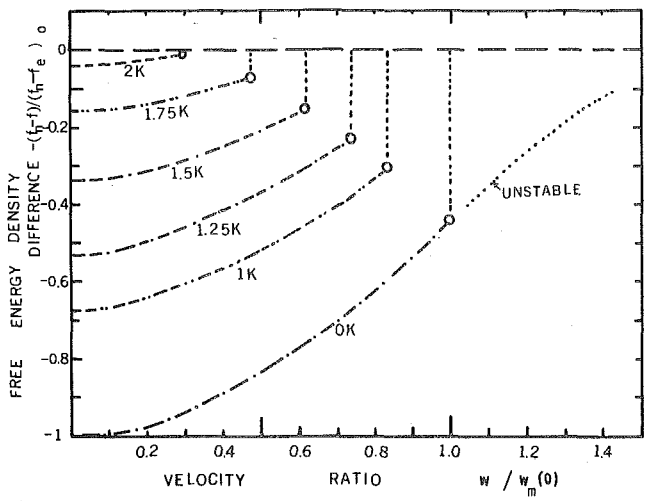

Fig. 3 Gibbs free energy density difference (normalized with respect to the value at $T = 0$ K as a function of the relative velocity ratio, ($w_m(0)$ = reference value at thermodynamic stability limit at $T = 0$ K; f_{e0} He II free energy density at $T = 0$ K)

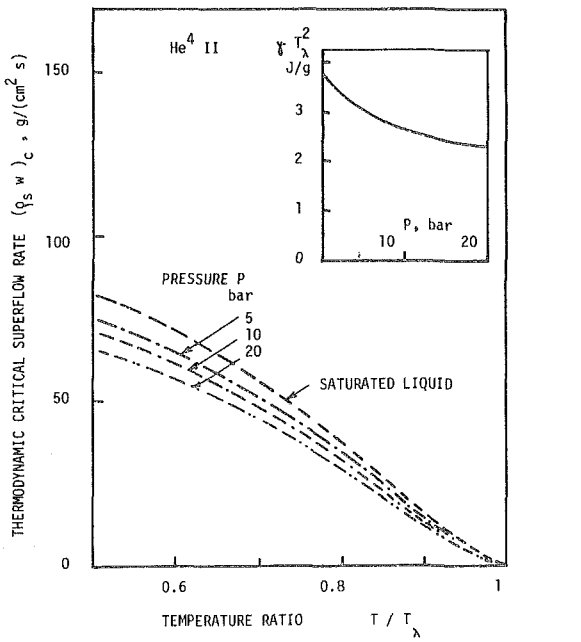

Fig. 4 Thermodynamic limiting mass transport rates of superflow (per unit cross sectional area of channel) as a function of temperature ratio; insert: characteristic thermal energies (per unit mass) at the lambda temperature versus pressure

Table 1 Entropy coefficient of He I

P, bar	Saturated He II	2.3	5.1	10.3	20.3
γ, $\frac{J}{gK^2}$	0.785	0.689	0.679	0.670	0.628

bounds for the present q_λ—results (point B of Fig. 1) and those of reference [7]. One possible cause for disagreement is the presence of convection modes which require an additional energy. This will decrease the state of order and (mean) values of w_m and $q_m(w_m)$. A further reduction in the state of order takes place in the two-phase regime (E-D) in which additional mixed convection patterns involving He I and He II appear to prevail.

Summary

A new thermal transport function $q(\Delta T)$ indicates for the lambda transition from He II to He I in the presence of heat flow the formation of He I—domains which impede transport rates, as soon as a limiting heat flux has been exceeded. This flux plays a role similar to the peak nucleate boiling flux of first order systems for cryo-system coolant operations. Details of this lambda curve appeared to have escaped attention previously [19, 20], as early studies explored He II limits with other geometries.

Theoretical estimates based on thermodynamics appear to be consistent with other findings [13]. When uniform flow is imposed, the theoretical results appear to be upper bounds to the data. This indicates convective motion. The motion is disordered in general. The transformation of the phase change due to this motion has been recognized early for well-defined restricted fluid spaces. The present results show in addition that instabilities play an important role in geometries more open than the configuration of reference [21].

Acknowledgment

Part of this work has been supported by the National Science Foundation.

References

1 Hilal, M. A., and McIntosh, G. E., "Cryogenic Design For Large Superconducting Energy Storage Magnets," *Advances in Cryogenic Engineering*, Vol. 21, 1976, pp. 69–77.

2 Matthews, D. W. B., and Leonard, A. C., "Vaporization Onset Heat Flux for Flat Plates in Saturated Liquid He II," *Advances in Cryogenic Engineering*, Vol. 19, 1974, pp. 417–426.

3 Goodling, J. S., and Irey, R. K., "Non-Boiling and Film Boiling Heat Transfer to a Saturated Bath of Liquid Helium," *Advances in Cryogenic Engineering*, Vol. 14, 1969, pp. 159–169.

4 Holdredge, R. M., and McFadden, P. W., "Boiling Heat Transfer for Cylinders in a Saturated Liquid Helium II Bath," *Advances in Cryogenic Engineering*, Vol. 11, 1966, pp. 507–515.

5 Broadwell, J. E., and Liepmann, W. H., "Local Boiling and Cavitation in Heat-Induced Counterflow of He II," *Physics of Fluids*, Vol. 12, 1969, pp. 1533–1535.

6 Eaton, Russell III, Lee, W. D., and Agee, F. J., "High-Heat-Flux Regime of Superfluid Cooling in Vertical Channels," *Physical Review*, Vol. A5, 1972, pp. 1342–1349.

7 Krafft, G., "Critical Heat Flux of Subcooled and Saturated Helium-II in Ling Tubes," *Proceedings of 4th International Cryogenic Engineering Conference*, Eindhoven 1972, IPC Science Technology Press Ltd., London, 1972, pp. 307–309.

8 Irey, R. K., *Heat Transport in Liquid Helium II, Heat Transfer at Low Temperatures*, Chapter 15, W. Frost, ed., Plenum Press, New York, 1975, pp. 325–355.

9 Bhagat, S. M., and Lasken, R. A., "Depression of T_λ by a Heat Current," *Physical Review*, Vol. A5, 1972, pp. 2297–2302.

10 Ahlers, G., Evenson, A., and Kornblit, A., "On the Depression of the Superfluid Transition Temperature in He^4 by a Heat Current," *Physical Review*, Vol. A4, 1971, pp. 804–806.

11 Caspi, S., Lee, J. Y., and Frederking, T. H. K., "Free Convection at Supercritical Pressure in Cryo-Fluid Helium-I," ASME Paper No. 76-WA/PID-14.

12 Linnet, C., PhD thesis, University of California, Los Angeles, 1971.

13 Linnet, C., Amar, R. C., Wang, Y. G., and Frederking, T. H. K., "Superfluid Thermodynamic Transport Limits for Liquid Helium II," *Advances in Cryogenic Engineering*, Vol. 19, 1974, pp. 365–372.

14 Mendelssohn, K., "States of Aggregation," *Physics Today*, No. 4, Apr. 1969, pp. 46–51.

15 Borelius, G., "Thermodynamic Analysis of the λ-Transition in Liquid Helium," *Physica Scripta*, Vol. 7, 1973, pp. 75–79.

16 Ginzburg, V. L., and Pitaevskii, L. P., "On the Theory of Superfluidity," *Soviet Physics, Journal of Experimental and Theoretical Physics*, Vol. 34, 1958, pp. 858–859.

17 Bhagat, S. N., and Winer, B. M., "Critical Heat Flux in Liquid Helium in the Neighborhood of the λ-Transition," *Physics Letters*, Vol. 27A, 1968, pp. 537–538.

18 Ahlers, G., "Critical Heat Flow in a Thick He II Film Near the Superfluid Transition," *Journal of Low Temperature Physics*, Vol. 1, 1969, pp. 159–172.

19 Madsen, R. A., and McFadden, P. W., "Heat Transfer to an Unsaturated Bath of Liquid Helium II," *Advances in Cryogenic Engineering*, Vol. 13, 1968, pp. 617–623.

20 Linnet, C., and Frederking, T. H. K., "Thermal Conditions at the Gorter-Mellink Counterflow Limit Between 0.01 and 3 bar," *Journal of Low Temperature Physics*, Vol. 21, 1975, pp. 447–462.

21 Peshkov, V. P., "Transformation of the λ-Transition in Helium to a Special Transition of the First Kind in the Presence of Heat Flow," *Soviet Physics, Journal of Experimental and Theoretical Physics*, Vol. 30, 1956, pp. 581–582.

journal of heat transfer

technical notes

Relationships Among Boundary Conditions and Nusselt Numbers for Thermally Developed Duct Flows

E. M. Sparrow[1] and S. V. Patankar[1]

Nomenclature

Bi = Biot number, $h_e r_0/k$
h = internal heat transfer coefficient, $q/(T_w - T_b)$
$\hat{h}$ = overall heat transfer coefficient, $q/(T_\infty - T_b)$
h_e = external heat transfer coefficient, $q/(T_\infty - T_w)$
k = thermal conductivity of fluid in tube
Nu = Nusselt number, $h(2r_0)/k$
$\hat{\text{Nu}}$ = Nusselt number, $\hat{h}(2r_0)/k$
Pe = Peclet number, $\bar{u}(2r_0)/\alpha$
q = local wall heat flux
R = dimensionless radial coordinate, r/r_0
r = radial coordinate
r_0 = tube radius
T = temperature
T_b = bulk temperature
T_w = wall temperature
T_∞ = temperature of external fluid environment
u = streamwise velocity
$\bar{u}$ = mean velocity
X = dimensionless streamwise coordinate, $(x/r_0)/\text{Pe}$
x = streamwise coordinate
α = thermal diffusivity
β = exponent in wall heat flux variation
θ = dimensionless temperature, equation (6)
λ = bulk temperature gradient, equation (6)

Introduction

Thermally developed pipe and duct flows are characterized by a heat transfer coefficient which is independent of the streamwise coordinate. There are four types of thermal boundary conditions that are compatible with the existence of a thermally developed regime. They are:

(a) uniform wall temperature, T_w = constant;
(b) uniform wall heat flux, q = constant;
(c) exponential variation of the wall heat flux, $q \sim e^{\beta x}$;
(d) convective heat transfer from the external surface of the duct to a fluid environment with heat transfer coefficient h_e and temperature T_∞, both of which are uniform.

Various subclasses of these boundary conditions can be formulated if circumferential variations are considered, but attention will be focused here on thermal boundary conditions which are circumferentially uniform.

The objective of this paper is to establish the interrelationships among the physical problems and results which correspond to these boundary conditions. An awareness of some of the interrelations is already in evidence in the literature, but nowhere have all of the foregoing cases (a)–(d) been tied together. It was felt that a synthesis which encompassed all thermally developed flows would simplify both analysis and correlation of results and would also have benefits in the teaching of duct-flow heat transfer.

The fully developed heat transfer characteristics for uniform wall temperature and uniform wall heat flux have been widely investigated, e.g., [1].[2] Although note has been taken of how these cases relate to the exponential heat flow case, these relationships remain less than common knowledge because:

(i) certain relevant papers have appeared in journals other than mainline heat transfer journals [2, 3];

(ii) relevant information has often been encapsulated into a single short paragraph in otherwise wide ranging papers [4, 5].

With regard to the external convection boundary condition, case (d), it has, in general, been studied in connection with the thermal entrance region, e.g., [6–9]. As a consequence, the fully developed heat transfer characteristics have not been investigated in detail and, in particular, the relationship between cases (d) and (c), which holds the key to the synthesis of all the cases, has not been noted.

For concreteness, we will be specifically concerned with flow in a circular tube, but the general conclusions are applicable to ducts of arbitrary cross section provided that circumferential uniformity is preserved. Furthermore, to facilitate the numerical work, the flow will be taken to be laminar, but the conclusions also carry over to turbulent flow.

Analysis and Results

The first step in the synthesis is to clearly set forth the interrelationships between cases (a)–(c). It is readily apparent that uniform heat flux is a specialization of the exponential variation, case (c), with $\beta = 0$. For uniform wall temperature, it will now be demonstrated that the wall heat flux distribution is also a special case of the exponential variation. From an energy balance for a streamwise length dx and with the definition of the local Nusselt number, one has

$$\dot{m} c_p dT_b = 2q\pi r_0 dx, \qquad \text{Nu} = [q/(T_w - T_b)](2r_0/k) \qquad (1)$$

[1] Department of Mechanical Engineering, University of Minnesota, Minneapolis, Minn.

Contributed by the Heat Transfer Division of THE AMERICAN SOCIETY OF MECHANICAL ENGINEERS. Manuscript received by the Heat Transfer Division February 11, 1977.

[2] Numbers in brackets designate References at end of technical note.

so that

$$dT_b/(T_b - T_w) = -(2\mathrm{Nu}/r_0\mathrm{Pe})dx \tag{2}$$

where Pe is the Peclet number. If this equation is integrated for uniform wall temperature and $\mathrm{Nu} \neq \mathrm{Nu}(x)$, it follows that

$$(T_w - T_b) \sim e^{-(2\mathrm{Nu}/r_0\mathrm{Pe})x} \tag{3}$$

Since Nu = 3.657 for laminar flow in an isothermal-walled tube, the substitution of equation (3) into the second of equations (1) yields

$$q \sim e^{-(7.314/r_0\mathrm{Pe})x} \tag{4}$$

which represents an exponential decay with $\beta = -7.314/r_0\mathrm{Pe}$.

The foregoing observations confirm that there are at least two values of the exponent β that are relevant to readily identifiable physical situations. Furthermore, the Nusselt numbers corresponding to exponentially varying heat flux with $\beta = 0$ and $\beta = -7.314/r_0\mathrm{Pe}$ can be associated directly with those for uniform wall heat flux and uniform wall temperature.

Attention will now be turned to the thermally developed regime for laminar flow in a circular tube which loses heat to (or gains heat from) an external environment having heat transfer coefficient h_e and temperature T_∞. This physical situation, although much more common in practice than either uniform wall temperature or uniform wall heat flux, has received relatively lesser attention in the literature. The primary objective of the analysis is to relate the heat flux distributions and Nusselt numbers for the external cooling/heating case with those for uniform wall temperature, uniform wall heat flux, and the general exponential heat flux variation $e^{\beta x}$.

The starting point of the analysis is the energy equation for constant property, hydrodynamically developed laminar pipe flow with negligible viscous dissipation and compression work. In terms of dimensionless coordinates $R = r/r_0$ and $X = (x/r_0)/\mathrm{Pe}$, the energy equation is

$$\frac{(u/\bar{u})}{2}\frac{\partial T}{\partial X} = \frac{1}{R}\frac{\partial}{\partial R}\left(R\frac{\partial T}{\partial R}\right) \tag{5}$$

For thermally developed conditions, it is appropriate to introduce a dimensionless temperature θ and bulk temperature gradient λ as follows

$$\theta(R) = (T - T_\infty)/(T_b - T_\infty),$$
$$\lambda = -(dT_b/dX)/(T_b - T_\infty) \tag{6}$$

The essential feature of the thermally developed regime is that θ is a function only of the radial coordinate R. With these, and with the Poiseuille velocity profile, equation (5) becomes

$$-(1 - R^2)\lambda\theta = \frac{1}{R}\frac{d}{dR}\left(R\frac{d\theta}{dR}\right) \tag{7}$$

With regard to the boundary conditions, let h_e represent the sum of the wall conductance and the external convective heat transfer coefficient, both referred to the *inside* surface area of the tube wall. Then, from an energy balance at $r = r_0 (R = 1)$, there results

$$(\partial\theta/\partial R)_1 = -\mathrm{Bi}\theta(1) \tag{8}$$

where the Biot number, Bi $(=h_e r_0/k)$, plays the role of a prescribable parameter. At the tube center line the temperature gradient is finite.

The solution of equation (7) subject to the boundary conditions is an eigenvalue problem for λ which was treated numerically. The resulting λ values are listed in Table 1 for the entire range of Biot numbers from zero to infinity. Over this range, λ increases monotonically from 0 to 7.314. As will now be demonstrated, the numerical values of λ are directly related to the results for the wall heat flux and the Nusselt number.

The wall heat flux q may be evaluated from Fourier's law, which gives

$$q = (k/r_0)(T_\infty - T_b)(-\partial\theta/\partial R)_1 \tag{9}$$

Since $(\partial\theta/\partial R)_1$ is independent of x, the streamwise variation of q is proportional to the variation of $(T_\infty - T_b)$. By integration of the second of equations (6), the latter variation is found to be proportional to $e^{-\lambda X}$, so that

$$q \sim e^{-(\lambda/r_0\mathrm{Pe})x} \tag{10}$$

This heat flux distribution is a subgroup of the general exponential variation $q \sim e^{\beta x}$ where, in accordance with Table 1, β is confined to the range

$$-7.314/r_0\mathrm{Pe} \leq \beta \leq 0 \tag{11}$$

Thus, the external cooling/heating case is actually a specialization of the general exponential heat flux variation, as are uniform wall heat flux and uniform wall temperature. Furthermore, the status of the uniform heat flux and uniform wall temperature cases is clearly revealed. In addition to being convenient boundary conditions for laboratory research, they are the true limiting cases for external convective cooling/heating, respectively, for small and large Biot numbers.

Attention may now be turned to the heat transfer coefficient and the Nusselt number. Two definitions of the heat transfer coefficient will be examined

$$h = \frac{q}{T_w - T_b}, \qquad \hat{h} = \frac{q}{T_\infty - T_b} \tag{12}$$

Whereas the first of these is the conventional definition for pipe flows, it is not very useful for the case of external cooling/heating since both q and T_w are unknowns. The second definition is of more direct applicability since it contains only q as an unknown. The corresponding Nusselt numbers are $\mathrm{Nu} = h(2r_0)/k$ and $\hat{\mathrm{Nu}} = \hat{h}(2r_0)/k$. From the fact that the heat flow path between the tube fluid and the environment is composed of series resistances, the relationship between Nu and $\hat{\mathrm{Nu}}$ is readily deduced as

$$2/\hat{\mathrm{Nu}} = 1/\mathrm{Bi} + 2/\mathrm{Nu} \tag{13}$$

Values of $\hat{\mathrm{Nu}}$ were evaluated from the relation

$$\hat{\mathrm{Nu}} = \lambda/2$$

which can be derived by integrating equation (7) across the section of the tube and using the definition of the bulk temperature, the dimensionless form of which is

$$\int_0^1 2(u/\bar{u})\theta R dR = 1 \tag{14}$$

Then, the values of Nu were determined from

$$\mathrm{Nu} = \hat{\mathrm{Nu}}/\theta(1) \tag{15}$$

equation (15) yields more accurate results for Nu than does equation (13) because it avoids the subtraction operation that must be performed in the latter.

Table 1 Results for the case of external cooling/heating

Bi	λ	Nu	$\hat{\mathrm{Nu}}$
0	0	4.364	0
0.1	0.3818	4.330	0.1909
0.25	0.8943	4.284	0.4471
0.5	1.615	4.221	0.8075
1	2.690	4.122	1.345
2	3.995	3.997	1.998
5	5.547	3.840	2.773
10	6.326	3.758	3.163
100	7.195	3.663	3.597
∞	7.314	3.657	3.657

Numerical values of Nu and $\hat{Nu}$ are listed in Table 1. Inspection of the table reveals that Nu is bounded between the values of 4.364 and 3.657, which respectively correspond to uniform wall heat flux and uniform wall temperature, thereby reaffirming their roles as limiting cases. The Nu values of Table 1 not only pertain to the case of external cooling/heating, but they are also applicable to the case of the general exponential heat flux variation $q \sim e^{\beta x}$ for the range of β delineated in equation (11).

The Nu values listed in Table 1 were compared to literature values representing the fully developed limits of entrance region analyses. In all cases where comparison was possible, excellent agreement was found to exist.

Concluding Remarks

It has been demonstrated that all the boundary conditions that are compatible with the existence of a thermally developed regime are tightly interrelated. In all cases, the wall heat flux varies exponentially in the streamwise direction. The uniform heat flux and uniform wall temperature cases serve as bounds on the heat flux variation and on the Nusselt number for convective cooling/heating at the external surface of the tube. These characteristics apply both to laminar and turbulent flows in circular and noncircular ducts, provided that the imposed boundary condition is circumferentially uniform.

For turbulent pipe flow, the fully developed Nusselt numbers for uniform heat flux and uniform wall temperature are nearly identical. Since the Nusselt number Nu for the external cooling/heating case is bounded between them, it can be regarded as known and no further analysis is needed. The overall Nusselt number $\hat{Nu}$ then follows immediately from equation (13).

Acknowledgment

This research was performed under the auspices of NSF Grant ENG-7518141.

References

1 Kays, W. M., *Convective Heat and Mass Transfer*, McGraw-Hill, New York, 1966.

2 Hall, W. B., Jackson, J. D., and Price, P. H., "Note on Forced Convection in a Pipe Having Heat Flux Which Varies Exponentially Along its Length," *Journal of Mechanical Engineering Science*, Vol. 5, 1963, pp. 48–52.

3 Hasegawa, S., and Fujita, Y., "Nusselt Numbers for Fully Developed Flow in a Circular Tube With Exponentially Varying Heat Flux," Memoirs of the Faculty of Engineering, Kyushu University, Fukuoka, Japan, Vol. 27, 1967, pp. 1–6.

4 Graber, H., "Heat Transfer in Smooth Tubes, Between Parallel Plates, in Annuli and Tube Bundles With Exponential Heat Flux Distributions in Forced Laminar or Turbulent Flow (in German)," *International Journal of Heat and Mass Transfer*, Vol. 13, 1970, pp. 1645–1703.

5 Shah, R. K., and London, A. L., "Thermal Boundary Conditions and Some Solutions for Laminar Duct Flow Forced Convection," JOURNAL OF HEAT TRANSFER, TRANS. ASME, Series C, Vol. 96, 1974, pp. 159–165.

6 Sideman, S., Luss, D., and Peck, R. E., "Heat Transfer in Laminar Flow in Circular and Flat Conduits With Constant Surface Resistance," *Applied Scientific Research*, Vol. A14, 1964–1965, pp. 157–171.

7 McKillop, A. A., Harper, J. C., and Bader, H. J., "Heat Transfer in Entrance-Region Flow With External Resistance," *International Journal of Heat and Mass Transfer*, Vol. 14, 1971, pp. 863–866.

8 Hsu, C. J., "Laminar Flow Heat Transfer in Circular or Parallel-Plate Channels With Internal Heat Generation and the Boundary Condition of the Third Kind," *Journal of the Chinese Institute of Chemical Engineers*, Vol. 2, 1971, pp. 85–100.

9 Javeri, V., "Simultaneous Development of the Laminar Velocity and Temperature Fields in a Duct for the Temperature Boundary Condition of the Third Kind," *International Journal of Heat and Mass Transfer*, Vol. 19, 1976, pp. 943–949.

Forced Convection Within Straight Noncircular Ducts[1]

V. O'Brien[2] and L. W. Ehrlich[2]

Introduction

Energy conscious Americans today are interested in increasing the efficiency of heat exchangers. Theoretical development can precede and guide experimental development, particularly when it reveals facts unsuspected from prior measurements. For instance, we show that fins do not necessarily increase average heat conductance although the heat transfer literature implies the contrary. Our numerical program can ultimately help optimize the design of longitudinal fins.

Experience with coupled second-order partial differential equations [1][3] has been applied to the equations for fully developed convective thermal fields within various noncircular straight ducts. The steady laminar flow is fully developed, and the velocity solutions are given in [2]. Uniform heat input per unit length of duct is assumed, but a variety of temperature boundary conditions can be applied at the wall. The versatile finite-difference simulations allow consideration of any duct, including those with longitudinal fins [3].

Mathematically, the linear solutions always exist under the specified conditions, but exact closed-form analytic solutions have been limited to special sections, which often require computer assistance for accurate evaluation. Alternatively we use the computer directly in an inexpensive general scheme. The absolute accuracy has been established for square and elliptical sections (three or four significant figures everywhere for a normalized mesh $h = 2^{-5}$) [2, 3].

Equations and Method of Solution

The reduced momentum equation for the parallel steady laminar flow is

$$\nabla^2 u^* = \left(\frac{\partial^2}{\partial X^2} + \frac{\partial^2}{\partial Y^2}\right) u^* = -1 \tag{1}$$

with the nonslip viscous boundary condition at the wall (W) $u^*|_W = 0$. Here, the normalized velocity is $u^* = u/\{\mu^{-1} b^2 dp/dz\}$; $\mathbf{X} = \mathbf{x}/b$; and b is the duct half-height. Neglecting axial heat conduction and frictional heating the normalized fully developed temperature field satisfies

$$\nabla^2 \theta^* = u^* \tag{2}$$

where either of two Dirichlet boundary conditions has been considered, (a) $\theta^*|_W = 0$ or (b) $\theta^*|_W = f(x, y)$. One could also consider a fourth-order equation

$$\nabla^4 \theta^* = -1 \tag{3}$$

which has to satisfy two θ^* boundary conditions, one from the velocity field and the other the temperature condition [4]. The temperature normalization is

$$\theta^* = (\theta - \bar{\theta}_W)/\{\alpha^{-1}\mu^{-1} b^4 \partial\theta/\partial z \; dp/dz\}$$

where θ is temperature and θ_W is the mean peripheral (wall) temperature.

The pair of equations (1) and (2) are solved by finite-difference numerical approximation [3]. Briefly, a square grid of mesh h is superimposed on the arbitrary region. The usual five-point difference approximation to ∇^2, of $0(h^2)$, is applied to each point not adjacent

[1] Supported by the Department of the Navy, Naval Sea Systems Command under Contract No. N00017-72-C-4401.

[2] Applied Physics Laboratory, The Johns Hopkins University, Laurel, Md.

[3] Numbers in brackets designate References at end of technical note.

Contributed by the Heat Transfer Division of THE AMERICAN SOCIETY OF MECHANICAL ENGINEERS. Manuscript received by the Heat Transfer Division January 27, 1977.

Numerical values of Nu and $\hat{Nu}$ are listed in Table 1. Inspection of the table reveals that Nu is bounded between the values of 4.364 and 3.657, which respectively correspond to uniform wall heat flux and uniform wall temperature, thereby reaffirming their roles as limiting cases. The Nu values of Table 1 not only pertain to the case of external cooling/heating, but they are also applicable to the case of the general exponential heat flux variation $q \sim e^{\beta x}$ for the range of β delineated in equation (11).

The Nu values listed in Table 1 were compared to literature values representing the fully developed limits of entrance region analyses. In all cases where comparison was possible, excellent agreement was found to exist.

Concluding Remarks

It has been demonstrated that all the boundary conditions that are compatible with the existence of a thermally developed regime are tightly interrelated. In all cases, the wall heat flux varies exponentially in the streamwise direction. The uniform heat flux and uniform wall temperature cases serve as bounds on the heat flux variation and on the Nusselt number for convective cooling/heating at the external surface of the tube. These characteristics apply both to laminar and turbulent flows in circular and noncircular ducts, provided that the imposed boundary condition is circumferentially uniform.

For turbulent pipe flow, the fully developed Nusselt numbers for uniform heat flux and uniform wall temperature are nearly identical. Since the Nusselt number Nu for the external cooling/heating case is bounded between them, it can be regarded as known and no further analysis is needed. The overall Nusselt number $\hat{Nu}$ then follows immediately from equation (13).

Acknowledgment

This research was performed under the auspices of NSF Grant ENG-7518141.

References

1 Kays, W. M., *Convective Heat and Mass Transfer*, McGraw-Hill, New York, 1966.

2 Hall, W. B., Jackson, J. D., and Price, P. H., "Note on Forced Convection in a Pipe Having Heat Flux Which Varies Exponentially Along its Length," *Journal of Mechanical Engineering Science*, Vol. 5, 1963, pp. 48–52.

3 Hasegawa, S., and Fujita, Y., "Nusselt Numbers for Fully Developed Flow in a Circular Tube With Exponentially Varying Heat Flux," Memoirs of the Faculty of Engineering, Kyushu University, Fukuoka, Japan, Vol. 27, 1967, pp. 1–6.

4 Graber, H., "Heat Transfer in Smooth Tubes, Between Parallel Plates, in Annuli and Tube Bundles With Exponential Heat Flux Distributions in Forced Laminar or Turbulent Flow (in German)," *International Journal of Heat and Mass Transfer*, Vol. 13, 1970, pp. 1645–1703.

5 Shah, R. K., and London, A. L., "Thermal Boundary Conditions and Some Solutions for Laminar Duct Flow Forced Convection," JOURNAL OF HEAT TRANSFER, TRANS. ASME, Series C, Vol. 96, 1974, pp. 159–165.

6 Sideman, S., Luss, D., and Peck, R. E., "Heat Transfer in Laminar Flow in Circular and Flat Conduits With Constant Surface Resistance," *Applied Scientific Research*, Vol. A14, 1964–1965, pp. 157–171.

7 McKillop, A. A., Harper, J. C., and Bader, H. J., "Heat Transfer in Entrance-Region Flow With External Resistance," *International Journal of Heat and Mass Transfer*, Vol. 14, 1971, pp. 863–866.

8 Hsu, C. J., "Laminar Flow Heat Transfer in Circular or Parallel-Plate Channels With Internal Heat Generation and the Boundary Condition of the Third Kind," *Journal of the Chinese Institute of Chemical Engineers*, Vol. 2, 1971, pp. 85–100.

9 Javeri, V., "Simultaneous Development of the Laminar Velocity and Temperature Fields in a Duct for the Temperature Boundary Condition of the Third Kind," *International Journal of Heat and Mass Transfer*, Vol. 19, 1976, pp. 943–949.

Forced Convection Within Straight Noncircular Ducts[1]

V. O'Brien[2] and L. W. Ehrlich[2]

Introduction

Energy conscious Americans today are interested in increasing the efficiency of heat exchangers. Theoretical development can precede and guide experimental development, particularly when it reveals facts unsuspected from prior measurements. For instance, we show that fins do not necessarily increase average heat conductance although the heat transfer literature implies the contrary. Our numerical program can ultimately help optimize the design of longitudinal fins.

Experience with coupled second-order partial differential equations [1][3] has been applied to the equations for fully developed convective thermal fields within various noncircular straight ducts. The steady laminar flow is fully developed, and the velocity solutions are given in [2]. Uniform heat input per unit length of duct is assumed, but a variety of temperature boundary conditions can be applied at the wall. The versatile finite-difference simulations allow consideration of any duct, including those with longitudinal fins [3].

Mathematically, the linear solutions always exist under the specified conditions, but exact closed-form analytic solutions have been limited to special sections, which often require computer assistance for accurate evaluation. Alternatively we use the computer directly in an inexpensive general scheme. The absolute accuracy has been established for square and elliptical sections (three or four significant figures everywhere for a normalized mesh $h = 2^{-5}$) [2, 3].

Equations and Method of Solution

The reduced momentum equation for the parallel steady laminar flow is

$$\nabla^2 u^* = \left(\frac{\partial^2}{\partial X^2} + \frac{\partial^2}{\partial Y^2}\right) u^* = -1 \tag{1}$$

with the nonslip viscous boundary condition at the wall (W) $u^*|_W = 0$. Here, the normalized velocity is $u^* = u/\{\mu^{-1} b^2 dp/dz\}$; $\mathbf{X} = \mathbf{x}/b$; and b is the duct half-height. Neglecting axial heat conduction and frictional heating the normalized fully developed temperature field satisfies

$$\nabla^2 \theta^* = u^* \tag{2}$$

where either of two Dirichlet boundary conditions has been considered, (a) $\theta^*|_W = 0$ or (b) $\theta^*|_W = f(x, y)$. One could also consider a fourth-order equation

$$\nabla^4 \theta^* = -1 \tag{3}$$

which has to satisfy two θ^* boundary conditions, one from the velocity field and the other the temperature condition [4]. The temperature normalization is

$$\theta^* = (\theta - \bar{\theta}_W)/\{\alpha^{-1}\mu^{-1} b^4 \partial\theta/\partial z \; dp/dz\}$$

where θ is temperature and θ_W is the mean peripheral (wall) temperature.

The pair of equations (1) and (2) are solved by finite-difference numerical approximation [3]. Briefly, a square grid of mesh h is superimposed on the arbitrary region. The usual five-point difference approximation to ∇^2, of $0(h^2)$, is applied to each point not adjacent

[1] Supported by the Department of the Navy, Naval Sea Systems Command under Contract No. N00017-72-C-4401.

[2] Applied Physics Laboratory, The Johns Hopkins University, Laurel, Md.

[3] Numbers in brackets designate References at end of technical note.

Contributed by the Heat Transfer Division of THE AMERICAN SOCIETY OF MECHANICAL ENGINEERS. Manuscript received by the Heat Transfer Division January 27, 1977.

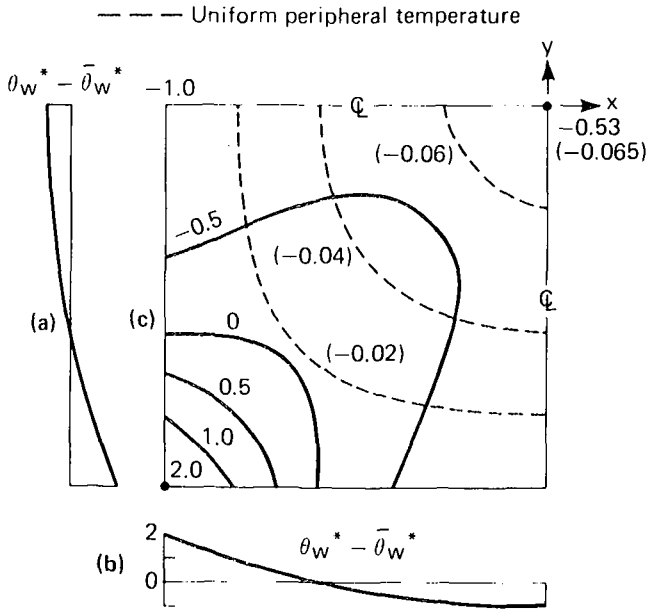

Fig. 1 Isotherms (c) for a square duct with parabolic temperature distributions (*a*), (*b*) on the sides (¼ of duct shown; dashed contours are for uniform peripheral temperature)

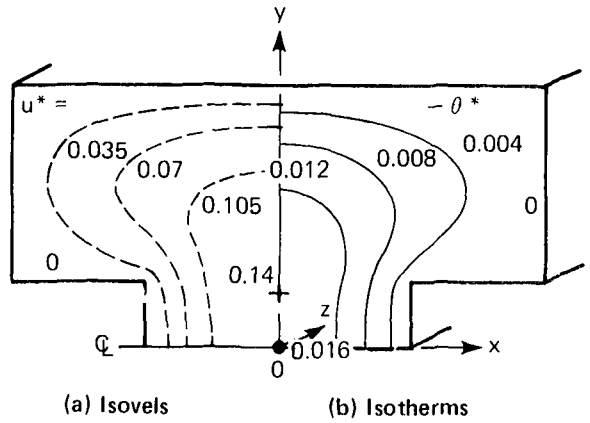

Fig. 3 Isovels and isotherms in a finned duct ($\theta^*|_W = 0$); ¼ of duct shown for each

to the boundary. Near a curved boundary, a Shortley-Weller approximation [5] is applied. Boundary mesh values are imposed. The resulting system of simultaneous equations is solved by direct method using the capacitance matrix approach [6].

Some Field Results

A **An Open (Finless) Square Duct.** Our finite-difference solutions have been tested by this duct section where analytic solutions exist [3, 4]. While the isotherms for the (2*a*) boundary condition resemble the isovels of u^*, the isotherms for equation (2*b*) can be considerably different, Fig. 1. The normal temperature gradients at the wall no longer resemble the velocity shear distribution if $\theta^*|_W \neq 0$. Instead of moderate flux input at the centers of the sides of the square and none at the corners (with $\theta^*|_W \neq 0$), there is a very high flux input at the corners and large opposite flux at the centers of the sides [3]. (Square ducts in square array might have the assumed $f(x, y)$.)

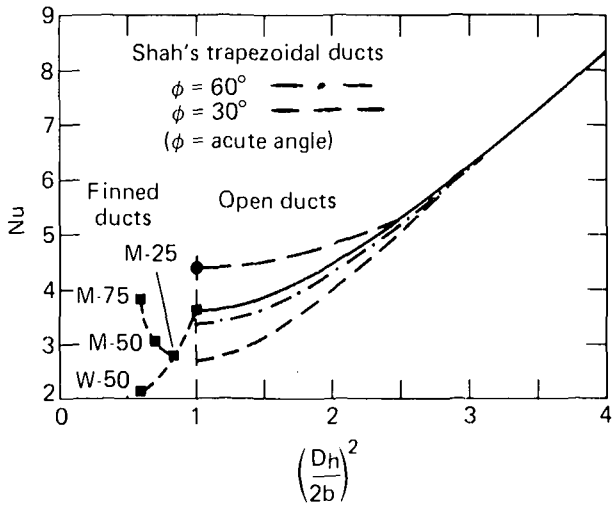

Fig. 4 Nusselt number Nu as a function of $(D_h/2(b))^2$ for ducts of various section (finned duct values labelled corresponding to Fig. 2): ellipses ——— rectangular ——

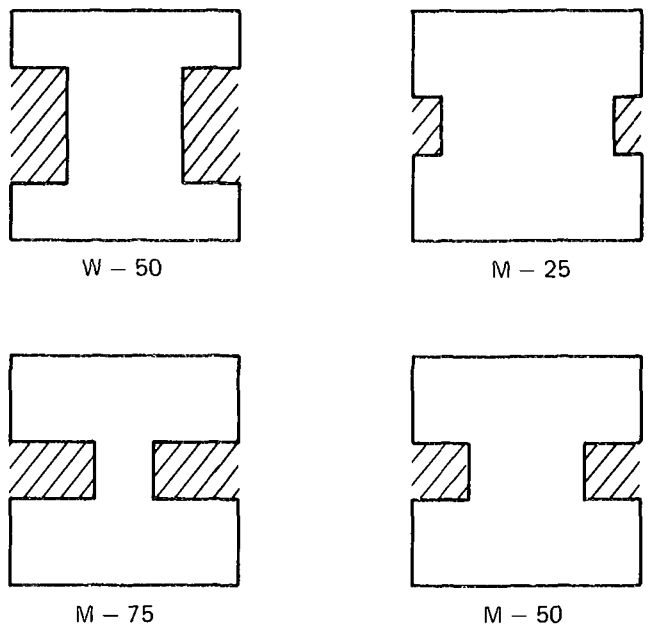

Fig. 2 Square ducts with fins (labels: *W* = wide, *M* = moderate width, number = percentage length relative to half-height)

B **A Square Duct With Two Side-Centered Longitudinal Fins.** Several finned square ducts have been considered, Fig. 2, the labels denoting widths and relative lengths of the fins. With uniform peripheral temperature (equation 2(*a*)) (implying infinite conductivity for the fins), the isotherms resemble the isovels, though the maximum velocity (much reduced from the open square) tends to split into two peaks displaced from the center of the duct, Fig. 3. The temperature extremum tends to remain at the center. The temperature gradient and velocity shear distributions along the fin surfaces and on the rest of the perimeter are rather similar; the highest values occur near the tips of the fins. The difference between fin tips and the rest of perimeter increases as the fin gets longer for a fixed width of fin.

Assigning temperatures along the fins (equation 2(*b*)), even though $\theta^*|_W = 0$ along the rest of the perimeter, causes considerable change in the local isotherm pattern and heat flux extrema (3).

Average Heat Transfer

The comparison of overall heat conductance of straight ducts is usually on the basis of a Nusselt number Nu based on the hydraulic diameter, $D_h = 4A/P$ where A is flow area and P the perimeter of the duct section. In the present notation

$$\mathrm{Nu} = \frac{\bar{h}D_h}{k} = \frac{(D_h)^2}{4b^2}\frac{\bar{u}^*}{\theta_b^*} \tag{4}$$

where $\bar{h}$ is the average conductance, k the thermal conductivity of the fluid, $\bar{u}^*$ is the mean u^* and θ_b^* is the (bulk) mixed-mean $A^{-1}\int_A u^*\theta^* dA$.

Our calculated results equations (1) and (2a) are plotted in Fig. 4, the data points on the left representing the finned square ducts. Three out of the four configurations show no improvement in average heat transfer. For moderate width fins, most Nu are in the range of Nu shown by Shah's recent approximate solutions for trapezoidal ducts with $(D_h/2b)$ slightly greater than one [7]. For our finned ducts the value of $(D_h/2b) < 1$ so the effect of the extended surface is overemphasized by equation (4).

On the other hand, exact and numerical solutions (for equation 2(b)) show that there exist perimeter temperature distributions which make $\theta_b^* = 0$ (and thus Nu = ∞). This is a physical impossibility but it does indicate significant changes in Nu are consistent with nonuniform peripheral temperature.

Conclusion

Nonuniform temperature on the periphery of the section has been shown to have a significant effect on local heat conductance and overall heat transfer. The physics of a "thermally active" fin requires matching a heat conduction solution within the wall (fin) material and heat convection in the duct. The boundary temperature distribution is determined as part of the solution. The finite-difference scheme is being extended to this real situation.

References

1 Ehrlich, L. W., "Solving the Biharmonic Equation as Coupled Finite-Difference Equations," *SIAM Journal of Numerical Analysis*, Vol. 8, 1971, pp. 278–287.

2 O'Brien, V., "Steady and Unsteady Flow in Noncircular Straight Ducts," *Journal of Applied Mechanics*, TRANS. ASME, Vol. 44, 1977, pp. 1-6.

3 O'Brien, V., "Developed Convective Thermal Fields in Noncircular Ducts," Johns Hopkins Applied Physics Laboratory Report, APL/JHU TG 1303 Sept. 1976.

4 Marco, S. M., and Han, L. S., "A Note on Limiting Laminar Nusselt Number in Ducts With Constant Temperature Gradient by Analogy to Thin-Plate Theory," TRANS. ASME, Vol. 77, 1955, pp. 625–630.

5. Shortley, G. H., and Weller, R., "The Numerical Solution of Laplace's Equation", *Journal of Applied Physics*, Vol. 9, 1938, pp. 334–348.

6 Buzbee, B. L., Dorr, F. W., George, J. A., and Golub, G. H., "The Direct Solution of the Discrete Poisson Equation on Irregular Regions," *SIAM Journal of Numerical Analysis*, Vol. 8, 1971, pp. 722-736.

7 Shah, R. K., "Laminar Flow Friction and Forced Convection Heat Transfer in Ducts of Arbitrary Geometry," *International Journal of Heat and Mass Transfer*, Vol. 18, 1975, pp. 849-862.

Mean Temperature Difference in Odd-Tube-Pass Heat Exchangers

R. Crozier, Jr.[1] and M. Samuels[2]

Nomenclature

A = surface area, ft^2
c = tube specific heat, Btu/lb°F
C = shell specific heat, Btu/lb°F
F = log mean temperature difference correction factor, dimensionless
L = constant ±1 depending on flow direction, dimensionless
LMTD = log mean temperature difference, °F
n = number of tube passes, dimensionless
P = exchanger effectiveness, dimensionless
Q = total heat transferred, Btu/hr
R = heat capacity ratio, dimensionless
t = tube fluid temperature, °F
T = shell fluid temperature, °F
tP = intermediate tube pass temperature, °F
U = overall heat transfer coefficient, Btu/hr ft^2 °F
w = tube flow rate, lb/hr
W = shell flow rate, lb/hr

Introduction

Logarithmic mean temperature difference correction factors (F) are required to determine the heat transfer area and thermal stability of shell and tube heat exchangers with multiple tube passes. F factors are available in the literature for exchangers with an even number of tube passes. Only one geometry, however, with an odd number of tube passes has been evaluated.

The quantity of heat transferred in a heat exchanger is the product of the overall heat transfer coefficient, the exchanger area and the appropriate mean temperature difference (MTD); that is, $Q = UA$ (MTD). For single pass exchangers the shell and tube fluids are in either counter or cocurrent flow and the appropriate MTD is the log-mean temperature difference (LMTD). In heat exchangers with multiple passes the shell and tube fluids are diverted and rerouted through the exchanger causing some tubes to be in counter, while others are in cocurrent flow. Because of this, the true mean temperature difference lies somewhere between the LMTD values for counter and cocurrent flow.

Literature

For heat exchangers with one shell and two tube passes Nagle [1][3] derived a correction factor (F); which when multiplied by the counter flow LMTD gives the true mean temperature difference for the multiple pass geometry. He expressed the heat exchanged as: $Q = UAF$ (LMTD). (Henceforth, we will denote an exchanger with X shell passes and Y tube passes as an X-Y exchanger.)

For 1–3 exchangers with two passes in counter current flow Fischer [2] developed a correlation for F in the form of an infinite series. Additional geometries with an odd number of tube passes have not been reported in the literature.

Gardner and Taborek [3] give an excellent summary of the state-of-the-art as it now exists.

Mathematical Model and Assumptions

The governing differential equations defining the heat transferred in a single shell, multiple tube pass heat exchanger were integrated numerically to determine the tube pass temperature profile, area and ultimately F. The following assumptions were employed in this work:

[1] University of Delaware, Newark, Del.; presently employed by E. I. Du Pont de Nemours & Co., Inc., Wilmington, Del.

[2] University of Delaware, Newark, Del.

Contributed by the Heat Transfer Division of THE AMERICAN SOCIETY OF MECHANICAL ENGINEERS. Manuscript received by the Heat Transfer Division July 19, 1976.

[3] Numbers in brackets designate References at end of technical note.

Average Heat Transfer

The comparison of overall heat conductance of straight ducts is usually on the basis of a Nusselt number Nu based on the hydraulic diameter, $D_h = 4A/P$ where A is flow area and P the perimeter of the duct section. In the present notation

$$\mathrm{Nu} = \frac{\bar{h}D_h}{k} = \frac{(D_h)^2}{4b^2}\frac{\bar{u}^*}{\theta_b^*} \tag{4}$$

where $\bar{h}$ is the average conductance, k the thermal conductivity of the fluid, $\bar{u}^*$ is the mean u^* and θ_b^* is the (bulk) mixed-mean $A^{-1}\int_A u^*\theta^* dA$.

Our calculated results equations (1) and (2a) are plotted in Fig. 4, the data points on the left representing the finned square ducts. Three out of the four configurations show no improvement in average heat transfer. For moderate width fins, most Nu are in the range of Nu shown by Shah's recent approximate solutions for trapezoidal ducts with $(D_h/2b)$ slightly greater than one [7]. For our finned ducts the value of $(D_h/2b) < 1$ so the effect of the extended surface is overemphasized by equation (4).

On the other hand, exact and numerical solutions (for equation 2(b)) show that there exist perimeter temperature distributions which make $\theta_b^* = 0$ (and thus Nu = ∞). This is a physical impossibility but it does indicate significant changes in Nu are consistent with nonuniform peripheral temperature.

Conclusion

Nonuniform temperature on the periphery of the section has been shown to have a significant effect on local heat conductance and overall heat transfer. The physics of a "thermally active" fin requires matching a heat conduction solution within the wall (fin) material and heat convection in the duct. The boundary temperature distribution is determined as part of the solution. The finite-difference scheme is being extended to this real situation.

References

1 Ehrlich, L. W., "Solving the Biharmonic Equation as Coupled Finite-Difference Equations," *SIAM Journal of Numerical Analysis*, Vol. 8, 1971, pp. 278–287.

2 O'Brien, V., "Steady and Unsteady Flow in Noncircular Straight Ducts," *Journal of Applied Mechanics*, TRANS. ASME, Vol. 44, 1977, pp. 1-6.

3 O'Brien, V., "Developed Convective Thermal Fields in Noncircular Ducts," Johns Hopkins Applied Physics Laboratory Report, APL/JHU TG 1303 Sept. 1976.

4 Marco, S. M., and Han, L. S., "A Note on Limiting Laminar Nusselt Number in Ducts With Constant Temperature Gradient by Analogy to Thin-Plate Theory," TRANS. ASME, Vol. 77, 1955, pp. 625–630.

5 Shortley, G. H., and Weller, R., "The Numerical Solution of Laplace's Equation", *Journal of Applied Physics*, Vol. 9, 1938, pp. 334–348.

6 Buzbee, B. L., Dorr, F. W., George, J. A., and Golub, G. H., "The Direct Solution of the Discrete Poisson Equation on Irregular Regions," *SIAM Journal of Numerical Analysis*, Vol. 8, 1971, pp. 722-736.

7 Shah, R. K., "Laminar Flow Friction and Forced Convection Heat Transfer in Ducts of Arbitrary Geometry," *International Journal of Heat and Mass Transfer*, Vol. 18, 1975, pp. 849-862.

Mean Temperature Difference in Odd-Tube-Pass Heat Exchangers

R. Crozier, Jr.[1] and M. Samuels[2]

Nomenclature

A = surface area, ft^2
c = tube specific heat, Btu/lb°F
C = shell specific heat, Btu/lb°F
F = log mean temperature difference correction factor, dimensionless
L = constant ±1 depending on flow direction, dimensionless
LMTD = log mean temperature difference, °F
n = number of tube passes, dimensionless
P = exchanger effectiveness, dimensionless
Q = total heat transferred, Btu/hr
R = heat capacity ratio, dimensionless
t = tube fluid temperature, °F
T = shell fluid temperature, °F
tP = intermediate tube pass temperature, °F
U = overall heat transfer coefficient, Btu/hr ft^2 °F
w = tube flow rate, lb/hr
W = shell flow rate, lb/hr

Introduction

Logarithmic mean temperature difference correction factors (F) are required to determine the heat transfer area and thermal stability of shell and tube heat exchangers with multiple tube passes. F factors are available in the literature for exchangers with an even number of tube passes. Only one geometry, however, with an odd number of tube passes has been evaluated.

The quantity of heat transferred in a heat exchanger is the product of the overall heat transfer coefficient, the exchanger area and the appropriate mean temperature difference (MTD); that is, $Q = UA$ (MTD). For single pass exchangers the shell and tube fluids are in either counter or cocurrent flow and the appropriate MTD is the log-mean temperature difference (LMTD). In heat exchangers with multiple passes the shell and tube fluids are diverted and rerouted through the exchanger causing some tubes to be in counter, while others are in cocurrent flow. Because of this, the true mean temperature difference lies somewhere between the LMTD values for counter and cocurrent flow.

Literature

For heat exchangers with one shell and two tube passes Nagle [1][3] derived a correction factor (F); which when multiplied by the counter flow LMTD gives the true mean temperature difference for the multiple pass geometry. He expressed the heat exchanged as: $Q = UAF$ (LMTD). (Henceforth, we will denote an exchanger with X shell passes and Y tube passes as an X-Y exchanger.)

For 1–3 exchangers with two passes in counter current flow Fischer [2] developed a correlation for F in the form of an infinite series. Additional geometries with an odd number of tube passes have not been reported in the literature.

Gardner and Taborek [3] give an excellent summary of the state-of-the-art as it now exists.

Mathematical Model and Assumptions

The governing differential equations defining the heat transferred in a single shell, multiple tube pass heat exchanger were integrated numerically to determine the tube pass temperature profile, area and ultimately F. The following assumptions were employed in this work:

[1] University of Delaware, Newark, Del.; presently employed by E. I. Du Pont de Nemours & Co., Inc., Wilmington, Del.

[2] University of Delaware, Newark, Del.

Contributed by the Heat Transfer Division of THE AMERICAN SOCIETY OF MECHANICAL ENGINEERS. Manuscript received by the Heat Transfer Division July 19, 1976.

[3] Numbers in brackets designate References at end of technical note.

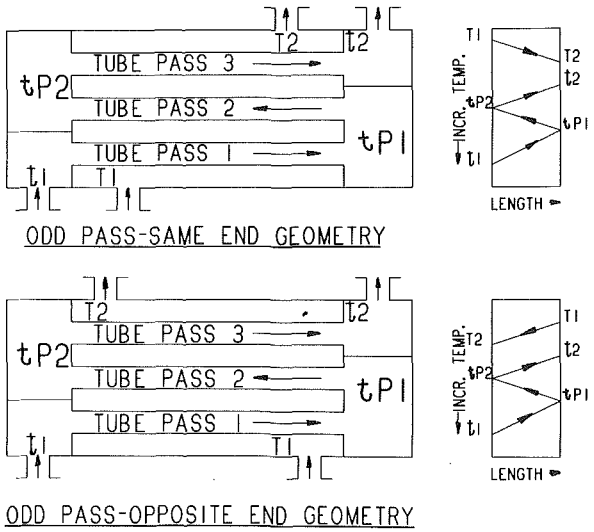

Fig. 1 Odd pass geometries—shell and tube exchangers

1 The flow rate of each fluid is constant.
2 There are no phase changes (evaporation or condensation) in the exchanger.
3 Heat losses are negligible.
4 The shell fluid temperature is an average isothermal temperature at any cross section.
5 There is an equal amount of heating surface in each pass.
6 The overall coefficient of heat transfer is constant.
7 The specific heat of each fluid is constant.

Fig. 1 illustrates a one shell, three tube pass heat exchanger and defines the odd tube pass nomenclature that will be used. The following derivation, however, covers any single shell, multiple tube pass heat exchanger.

Let t_1, t_2, t_n represent bulk temperatures in the first, second and nth tube passes respectively, and at the same cross section as T (shell temperature). For an n tube pass exchanger the tube side heat balances can be expressed as:

$$wcdt_1 = U_1 \frac{dA}{n}(T - t_1) \tag{1}$$

$$wcdt_2 = -U_2 \frac{dA}{n}(T - t_2) \tag{2}$$

and for the nth tube pass

$$wcdt_n = U_n \frac{dA}{n}(T - t_n) \tag{3}$$

Generalizing the preceding equations:

$$wcdt_i = L_i U_i \frac{dA}{n}(T - t_i) \tag{4}$$

Where $i = 1, \ldots, n$ and L_i is ± 1 depending on the direction of heat flow. That is, the numerical procedure used in this study requires the integration to proceed from left to right which necessitates the algebraic sign to change for each tube pass. For example, if the first pass temperature decreases then the second pass temperature must increase when integrating from left to right.

In the incremental area dA the shell temperature changes by $-dT$. Therefore, the shell side heat balance over the area dA is:

$$-\mathbf{WC}\, dT = U_1(T - t_1)\frac{dA}{n} + U_2(T - t_2)\frac{dA}{n} + \cdots + U_n(T - t_n)\frac{dA}{n} \tag{5}$$

For constant physical properties U is not a function of temperature and equation (5) can be rearranged as:

$$\frac{-U}{\mathbf{WC}} \int dA = \int \frac{n\,dT}{nT - (t_1 + t_2 + \ldots + t_n)} \tag{6}$$

where $T, t_1, t_2, \ldots, t_n$ are the dependent variables.

Numerical Procedure

To determine the required heat exchanger area, $n + 1$ coupled linear differential equations containing $n + 1$ unknown temperatures must be solved. The heat balance equations were numerically integrated using a Runge-Kutta procedure. To start the integration, all tube pass temperatures at one end of the exchanger must be defined. (In this study we shall call the temperature at the start or end of each tube pass the terminal tube temperature.) Unfortunately, the terminal tube temperatures are not initially known and the exchanger area must be determined by a trial-and-error procedure.

The trial-and-error algorithm is detailed in the following paragraphs. The terminal tube and shell temperatures (Fig. 1) on the left end of the exchanger are defined either by initial conditions, that is, tube and shell inlet temperatures (t_1, T_1) or an initial guess of the terminal tube temperature (tP_2). The exchanger area is then determined by integrating the governing equations from left to right in fixed increments of area.

Integration proceeds until the calculated exceeds the actual shell outlet temperature (T_2). That is, by integrating in fixed increments the calculated area is greater than the actual area. To minimize this error, the calculated area is reduced by one increment and rerun in increments of one square foot. When the actual and calculated shell temperatures are equal, the right end terminal tube temperatures are equated (tp_1). If they are not equal, the initial guess of tP_2 was in error and must be corrected.

With a new value of tP_2 the integration procedure is repeated until a converged solution is obtained. The solution has converged when the adjoining right end terminal tube temperatures are equal.

F is calculated by dividing the area obtained by using the counter flow LMTD definition by the integrated area (equation (6)).

Discussion of Results

Numerical Convergence. The use of 30 integration steps gives a calculated area which is only 0.4 percent higher than that obtained by using an infinite number of integration steps. This difference is well within the required accuracy for heat exchanger sizing and thus 30 integration steps were used in all subsequent calculations.

To check the accuracy of the numerical algorithm, computer values of F were checked against those predicted by Nagle's analysis. As shown in Fig. 2, the comparison is excellent and supports our results.

***F* values—Odd Tube Pass.** Fig. 1 defines two geometries with an odd number of tube passes. Unlike exchangers with an even number of tube passes, exchangers with an odd number of tube passes, will have more tubes in either cocurrent or countercurrent flow. "Same end" denotes an odd tube pass geometry with more cocurrent than countercurrent tube passes. Conversely, "opposite end" denotes an odd tube pass exchanger with more countercurrent than cocurrent tube passes.

Fig. 3 shows F as a function of the number of tube passes for three different exchanger geometries. For a fixed value of R and P, Fig. 3 shows F values for an even tube pass, and an odd tube pass with "same and opposite" end geometries. The "opposite end" geometry has more counter than cocurrent tube passes and therefore has higher F values than the even tube pass exchanger. The "same end" geometry has more cocurrent than countercurrent tube passes and, therefore, has lower F values than the even tube pass geometry. For a 1–3 exchanger the difference between the even and odd tube pass F values (odd-even difference) can exceed 5 percent, however, as the number of tube passes increase the odd-even difference decreases. That is, as the number of tube passes increase the F values for both odd and even tube pass geometries approach a limiting value based on an infinite number of tube passes.

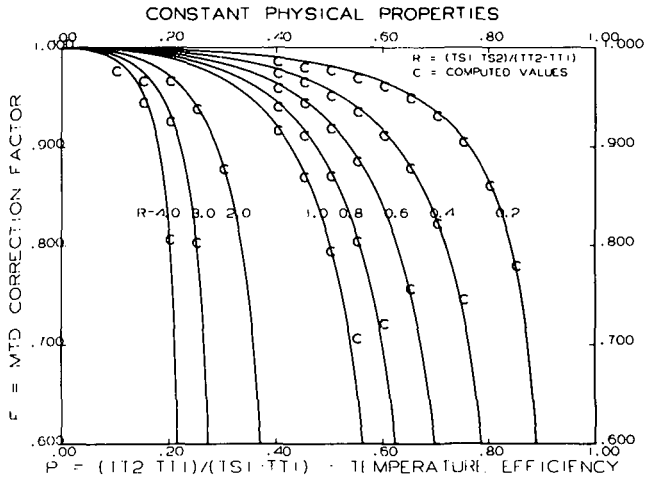

Fig. 2 MTD correction factor—1 shell pass, even tube passes

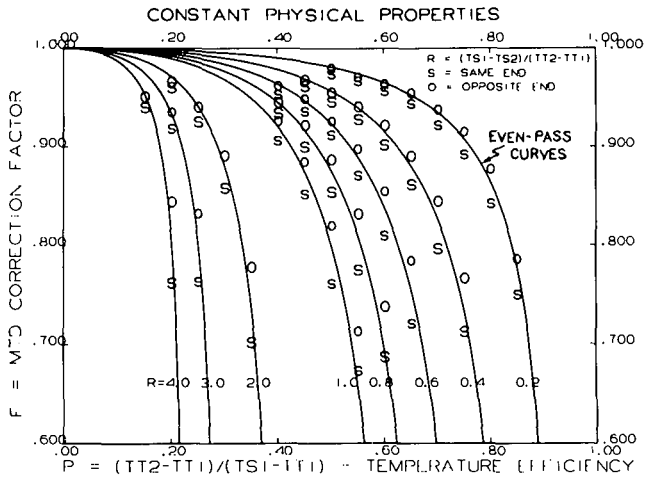

Fig. 4 MTD correction factor—1 shell pass, three tube passes

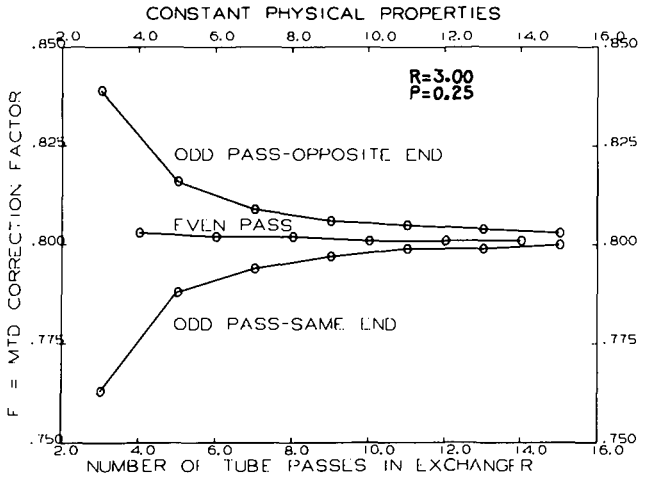

Fig. 3 MTD correction factor as a function of tube pass and exchanger geometry

Fig. 4 expands the data presented in Fig. 3 to include additional values of R and P. For a 1–3 exchanger, the following F values can be obtained from Fig. 3: (1) even tube pass $F = 0.805$, (2) odd-pass "opposite end" (0) $F = 0.835$, and (3) odd tube pass "same end" (S) $F = 0.760$. For $R = 3.0$ and $P = 0.25$ these same values can be found in Fig. 4. Therefore, the data presented in Fig. 4 are for a 1–3 exchanger and consist of "S" and "0" pairs of F values overlaid on even tube pass curves.

As shown in Fig. 4, the odd tube pass F values display the same functional relationship with R and P as the even tube pass geometries. A comparison of "opposite and same" end F values at a given R and P value, however, indicates that the odd-even difference is a function of R and P. As R and/or P decrease the odd-even difference decreases.

Graphs similar to Fig. 4 were constructed for 1–5, 1–7, and 1–9 geometries but for brevity are not presented. They displayed the same characteristics as the 1–3 geometry except the odd-even difference decreased as the number of tube passes increased (see Fig. 3).

In conclusion it has been shown that except for the one shell-three tube pass exchanger (1–3), even pass F values can be used for all odd tube pass geometries with a resulting error of less than two percent. For the 1–3 exchanger the difference between the odd and even pass F values can exceed five percent at large values of R and P and decreases as R and/or P decreases.

Acknowledgment

The authors acknowledge the support of this publication by E. I. du Pont de Nemours Co., Inc., Wilmington, Delaware.

References

1 Nagle, W. M. "Mean Temperature Differences in Multipass Heat Exchangers," *Ind. and Eng. Chem.*, Vol. 25, 1933, pp. 604–609.

2 Fischer, F. K., "Mean Temperature Difference Correction in Multipass Exchangers," *Ind. and Eng. Chem.*, Vol. 30, 1938, pp. 377–383.

3 Gardner, K., and Taborek, J., "Mean Temperature Difference—A Reappraisal," *AICHE HT & EC DIVISION*, 1976 National Heat Transfer Conference.

Analytical Solutions for Single- and Two-Phase Models of Packed-Bed Thermal Storage Systems

M. Riaz[1]

Nomenclature

c = specific heat
h_v = volumetric heat transfer coefficient
k = thermal conductivity
t = dimensionless time, τ/θ
x = dimensionless streamwise coordinate, ξ/λ
T = temperature
T_{in} = temperature at inlet of bed
v_a = velocity of air flow
v = velocity of thermal wavefront, $v_a \rho_a c_a / \rho_b c_b$

[1] Department of Electrical Engineering, University of Minnesota, Minneapolis, Minn.

Contributed by the Heat Transfer Division of THE AMERICAN SOCIETY OF MECHANICAL ENGINEERS. Manuscript received by the Heat Transfer Division February 17, 1977.

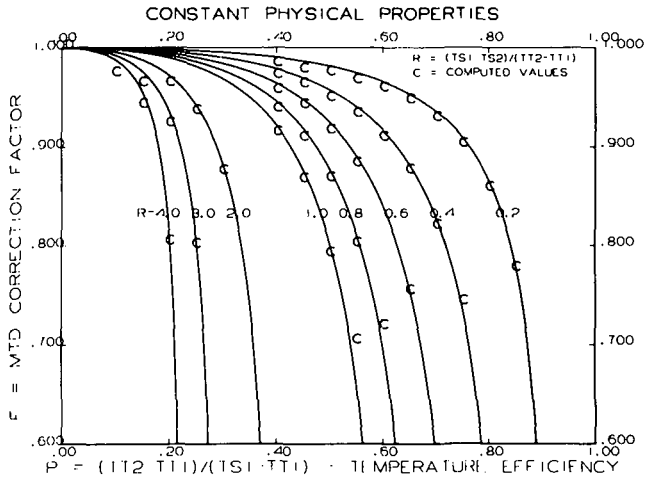

Fig. 2 MTD correction factor—1 shell pass, even tube passes

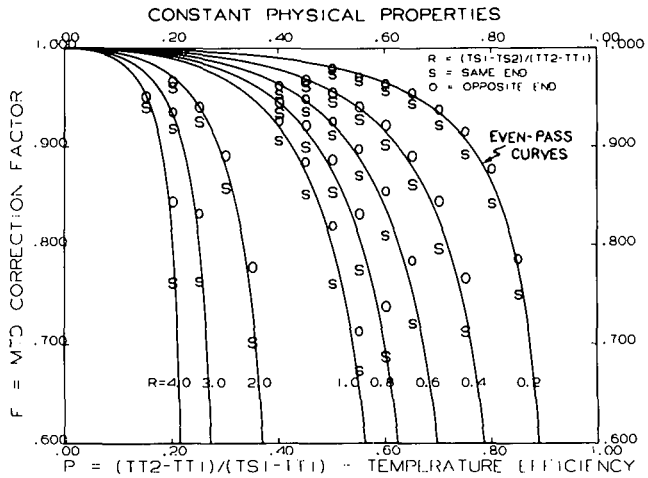

Fig. 4 MTD correction factor—1 shell pass, three tube passes

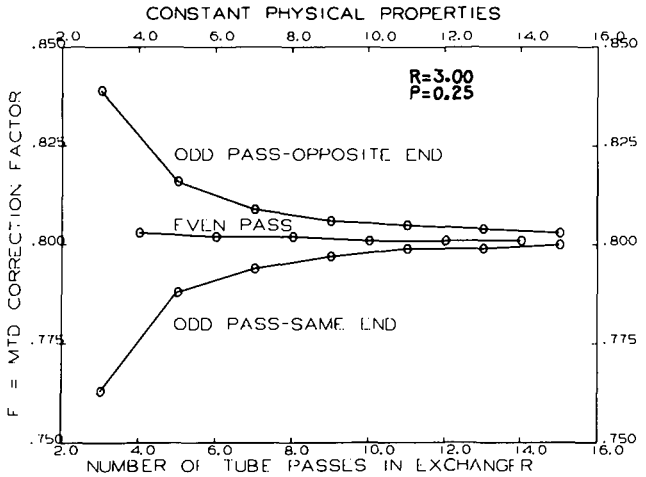

Fig. 3 MTD correction factor as a function of tube pass and exchanger geometry

Fig. 4 expands the data presented in Fig. 3 to include additional values of R and P. For a 1–3 exchanger, the following F values can be obtained from Fig. 3: (1) even tube pass $F = 0.805$, (2) odd-pass "opposite end" (0) $F = 0.835$, and (3) odd tube pass "same end" (S) $F = 0.760$. For $R = 3.0$ and $P = 0.25$ these same values can be found in Fig. 4. Therefore, the data presented in Fig. 4 are for a 1–3 exchanger and consist of "S" and "0" pairs of F values overlaid on even tube pass curves.

As shown in Fig. 4, the odd tube pass F values display the same functional relationship with R and P as the even tube pass geometries. A comparison of "opposite and same" end F values at a given R and P value, however, indicates that the odd-even difference is a function of R and P. As R and/or P decrease the odd-even difference decreases.

Graphs similar to Fig. 4 were constructed for 1–5, 1–7, and 1–9 geometries but for brevity are not presented. They displayed the same characteristics as the 1–3 geometry except the odd-even difference decreased as the number of tube passes increased (see Fig. 3).

In conclusion it has been shown that except for the one shell-three tube pass exchanger (1–3), even pass F values can be used for all odd tube pass geometries with a resulting error of less than two percent. For the 1–3 exchanger the difference between the odd and even pass F values can exceed five percent at large values of R and P and decreases as R and/or P decreases.

Acknowledgment

The authors acknowledge the support of this publication by E. I. du Pont de Nemours Co., Inc., Wilmington, Delaware.

References

1 Nagle, W. M. "Mean Temperature Differences in Multipass Heat Exchangers," *Ind. and Eng. Chem.*, Vol. 25, 1933, pp. 604–609.

2 Fischer, F. K., "Mean Temperature Difference Correction in Multipass Exchangers," *Ind. and Eng. Chem.*, Vol. 30, 1938, pp. 377–383.

3 Gardner, K., and Taborek, J., "Mean Temperature Difference—A Reappraisal," *AICHE HT & EC DIVISION*, 1976 National Heat Transfer Conference.

Analytical Solutions for Single- and Two-Phase Models of Packed-Bed Thermal Storage Systems

M. Riaz[1]

Nomenclature

c = specific heat
h_v = volumetric heat transfer coefficient
k = thermal conductivity
t = dimensionless time, τ/θ
x = dimensionless streamwise coordinate, ξ/λ
T = temperature
T_{in} = temperature at inlet of bed
v_a = velocity of air flow
v = velocity of thermal wavefront, $v_a \rho_a c_a / \rho_b c_b$

[1] Department of Electrical Engineering, University of Minnesota, Minneapolis, Minn.

Contributed by the Heat Transfer Division of THE AMERICAN SOCIETY OF MECHANICAL ENGINEERS. Manuscript received by the Heat Transfer Division February 17, 1977.

α = diffusivity, $k_b/\rho_b c_b$
θ = characteristic time
λ = characteristic distance
ρ = density
ξ = distance
τ = time

Subscripts

a = air (fluid)
b = bed (porous or packed solid)
1 = single-phase model
2 = two-phase model
eq = equivalent combined model

Introduction

Single- and two-phase models are commonly used to describe the dynamic behavior of rock-bed thermal storage systems. The classical Schumann two-phase model normally ignores axial conduction while the single-phase model is essentially a simple convection—conduction representation in which rock and air are at the same temperature. This note presents explicit analytical solutions for the response of these two models to a step change in inlet air temperature assuming that the semi-infinite bed is initially at a uniform temperature. The close agreement between the two responses, especially for large time, justifies the establishment of a combined equivalent model which accounts for both air-rock heat transfer and axial bed conductivity. The developed closed-form solutions for the transient response of the equivalent single-phase model of a packed bed provide a simple and convenient means for estimating the long-term dynamic performance of thermal storage systems without resorting to complex computer simulations.

Two-Phase Schumann Model

In the usual description of an air-rock packed bed as a one-dimensional two-phase linear model, an energy balance is performed on each of the fluid and solid phases yielding two coupled partial differential equations

$$\rho_a c_a v_a \frac{\partial T_a}{\partial \xi} = h_v(T_b - T_a) \qquad \text{(air)}$$

$$\rho_b c_b \frac{\partial T_b}{\partial \tau} = h_v(T_a - T_b) + k_b \frac{\partial^2 T_b}{\partial \xi^2} \qquad \text{(bed)} \qquad (1)$$

For an air system, it is justified to ignore the thermal capacity and conduction terms in the fluid phase equation. In addition, if axial conduction in the bed is also neglected (setting $k_b = 0$), the Schumann model of a packed bed is obtained [1][2] and is governed by two coupled equations normally written in dimensionless space-time variables x and t as

$$\frac{\partial T_a}{\partial x} = T_b - T_a = -\frac{\partial T_b}{\partial t} \qquad (2)$$

with the introduction of $\lambda_2 = v_a \rho_a c_a / h_v$ and $\theta_2 = \rho_b c_b / h_v$ as characteristic distance and time, respectively. For the single-blow operation in which a semi-infinite bed initially at a uniform reference temperature (chosen here, for convenience, to be zero) is suddenly subjected to a unit step of air inlet temperature, the solutions of equations (2) can be obtained [3] using Laplace transform methods as

$$T_b(x, t) = e^{-x} \int_0^t e^{-\lambda} I_0(2\sqrt{x\lambda}) d\lambda$$

$$T_a(x, t) = T_b + e^{-x-t} I_0(2\sqrt{xt}) \qquad (3)$$

where I_0 denotes a modified Bessel function of the first kind of zero order. Plots of the step responses were given originally by Anzelius [2] and Schumann [1], and, for an extended range of variables x and t, by Furnas [3]. Other analytical solutions have since been derived corresponding to various input conditions [4–6].

Single-Phase Conductivity Model

A single-phase conductivity model can be derived formally from the two-phase equations by letting the volumetric heat transfer coefficient h_v tend to infinity. In this limit, the air and bed temperatures coalesce to the same value T and equations (1) reduce to the single equation

$$\frac{\partial T}{\partial \tau} + v \frac{\partial T}{\partial \xi} = \alpha \frac{\partial^2 T}{\partial \xi^2} \qquad (4)$$

subject to a Danckwert type of inlet boundary condition, namely $\partial T/\partial_\xi = (v/\alpha)(T - T_{in})$. The parameter $v = v_a \rho_a c_a / \rho_b c_b$ represents the reduced velocity of a purely convective thermal wave and $\alpha = k_b/\rho_b c_b$ is the axial diffusivity of the bed. By introducing $\lambda_1 = \alpha/v$ as characteristic distance and $\theta_1 = \alpha/v^2$ as characteristic time, the equations of the single-phase model can be written in terms of dimensionless variables x and t as

$$\frac{\partial T}{\partial x} + \frac{\partial T}{\partial t} = \frac{\partial^2 T}{\partial x^2} \qquad \text{with} \quad \frac{\partial T}{\partial x} = T - T_{in} \qquad \text{at } x = 0 \qquad (5)$$

The solution of this equation for the unit step response can be shown, with the use of Laplace transform methods, to be expressible in the closed form

$$T(x, t) = \frac{1}{2} \operatorname{erfc}\left(\frac{x - t}{2\sqrt{t}}\right) + \sqrt{\frac{t}{\pi}} e^{-(x-t)^2/4t} - \frac{1}{2}(1 + x + t) e^x \operatorname{erfc}\left(\frac{x + t}{2\sqrt{t}}\right) \qquad (6)$$

in which erfc denotes the complementary error function. Plots of equation (6) as shown in Figs. 1 and 2 illustrate the space-time distribution of temperature inside the packed bed for the single blow case.

Comparison of the Two Models

By comparing these plots of equation (6) with those of Furnas [3], it can be verified that they are nearly identical. For values of time greater than ten, the curves practically coincide; for small values of t, the agreement between T of equation (6) and T_b of equation (3) is within ten percent; clearly, for small t, T_a differs appreciably from T or T_b as expressed by the second equation (3).

For large values of t, the following approximations hold

$$T(x, t) \cong 0.5 \operatorname{erfc}\left(\frac{x - t}{2\sqrt{t}}\right) \qquad (t > 10) \qquad (7)$$

and, at $x = t$,

$$\left.\begin{aligned} T &\cong 0.5[1 - (\pi x^3)^{-1/2}] \cong T_b \\ \frac{\partial T}{\partial x} &\cong -0.5(\pi x)^{-1/2} \\ T_a - T_b &\cong 0.5(\pi x)^{-1/2} \end{aligned}\right\} \qquad (8)$$

Equation (7) for the temperature profile may be visualized as constituting one half a complementary error function which moves in the x-direction at unity dimensionless velocity (or v actual) and which spreads out with increasing time. Equations (8) provide simple measures of the location and sharpness of the moving wavefront.

Clearly the single-phase model of a packed bed is simpler than the two-phase Schumann model. The closed-form solution for the transient step response as given by equation (6) makes it readily adapted for obtaining the response to arbitrary time-varying inlet temperatures through the use of convolution techniques. The unit impulse and ramp responses can be derived in closed forms by differentiating and integrating in turn equation (6) with respect to time so that:

$$T_\delta(x, t) = \frac{1}{\sqrt{\pi t}} e^{-(x-t)^2/4t} - \frac{1}{2} e^x \operatorname{erfc}\left(\frac{x + t}{2\sqrt{t}}\right) \qquad (9)$$

[2] Numbers in brackets designate References at end of technical note.

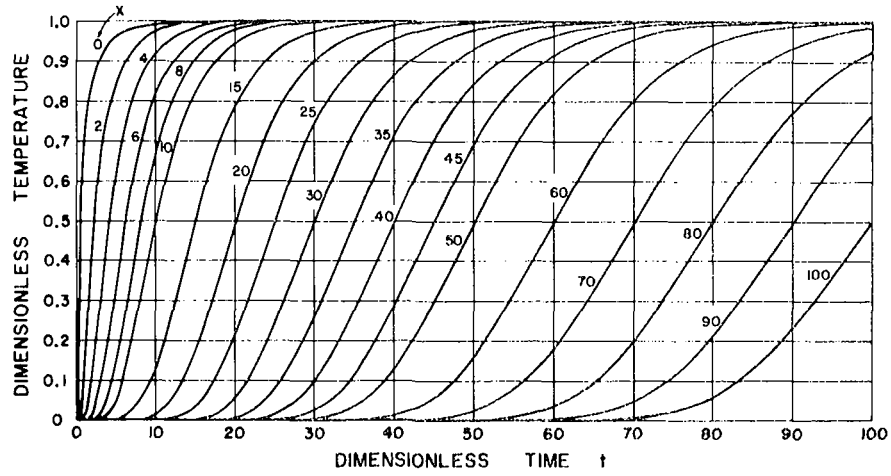

Fig. 1 Step response of packed bed (as a function of time)

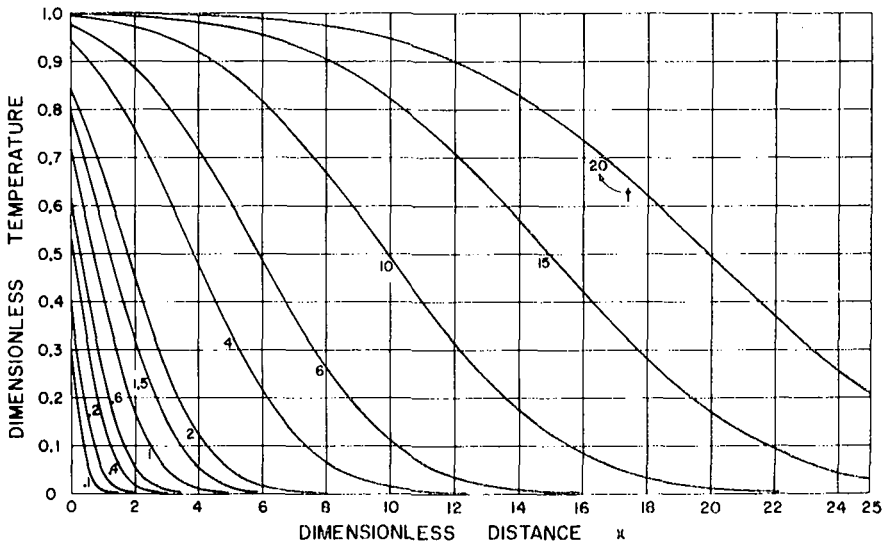

Fig. 2 Step response of packed bed (as a function of distance)

$$T_r(x,t) = -\frac{1}{2}(1+x-t)\,\mathrm{erfc}\left(\frac{x-t}{2\sqrt{t}}\right) - \frac{1}{2}\left(-1+t+xt+\frac{x^2}{2}+\frac{t^2}{2}\right)e^x\,\mathrm{erfc}\left(\frac{x+t}{2\sqrt{t}}\right) + \frac{1}{2}(2+x+t)\sqrt{\frac{t}{\pi}}\,e^{-(x-t)^2/4t} \quad (10)$$

Equivalent and Combined Models

The close agreement between the transient responses of the single- and two-phase models of a packed bed suggests that they are equivalent and can, therefore, be effectively combined. This equivalence, established differently by several authors [7–10], is predicated upon a physical interpretation of the heat transfer occurring in a packed bed in which the various individual dispersive mechanisms involved in stagnant bed conduction, air-rock heat transfer, and internal particle conduction act separately (i.e., they are statistically independent) and can be combined by superposition. In accordance with this view, the characteristic distance and time for a combined heat-transfer, conductivity model of a packed bed may be defined as the sum of the individual characteristic quantities associated with each model so that

$$\lambda_{eq} = \lambda_1 + \lambda_2 = \frac{v_a\rho_a c_a}{h_{eq}} = \frac{k_{eq}}{v_a\rho_a c_a}$$
$$\theta_{eq} = \theta_1 + \theta_2 = \frac{\rho_b c_b}{h_{eq}} = \frac{k_{eq}\rho_b c_b}{(v_a\rho_a c_a)^2} \quad (11)$$

where

$$\frac{1}{h_{eq}} = \frac{1}{h_v} + \frac{k_b}{(v_a\rho_a c_a)^2}$$
$$k_{eq} = k_b + \frac{(v_a\rho_a c_a)^2}{h_v} \quad (12)$$

These relations indicate that the effect of conductivity of the bed can be included in the Schumann model (this is especially relevant at low Reynolds numbers) by introducing the modified heat transfer coefficient h_{eq}. Similarly, in the single-phase model, the effect of air-rock heat transfer can be accounted for by introducing an effective thermal conductivity k_{eq}. To account for temperature gradients within the rock particles, the value of h_v may be reduced by a factor which in-

corporates the Biot number such as 1 + Bi/5 proposed by Jeffreson [10]. It is of interest to point out that the ratio $\lambda_{eq}/\theta_{eq} = v$ and is independent of both h_v and k_b.

Acknowledgment

This research was supported by the U. S. Energy Research and Development Administration under Contract No. EY-76-S-02-4002.

References

1 Schumann, T. E. W., "Heat Transfer: Liquid Flowing Through a Porous Prism," *Journal of the Franklin Institute*, Vol. 208, July 1929, p. 405-416.

2 Anzelius, A., "Über Erwärmung vermittels durchströmender Medien," *Z. angew. Math. Mech.*, Vol. 6, 1926, p. 291-294.

3 Jang, W. J., and Lee, C. P., "Dynamic Response of Solar Heat Storage Systems," ASME Paper No. 74-WA/HT-22, 1974.

4 Hung, F. T., and Nevins, R. G., "Unsteady-State Heat Transfer With a Flowing Fluid Through Porous Solids," ASME Paper No. 65-HT-10, 1965.

5 Arpaci, V. S., and Clark, J. A., "Dynamic Response of Fluid and Wall Temperatures During Pressurized Discharge for Simultaneous Time-Dependent Inlet Gas Temperature, Ambient Temperature, and/or Ambient Heat Flux," *Advances in Cryogenic Engineering*, Vol. 7, Plenum Press, 1962, p. 419-432.

6 Burch, D. M., Allen, R. W., and Peavy, B. A., "Transient Temperature Distributions Within Porous Slabs Subjected to Sudden Transpiration Heating," JOURNAL OF HEAT TRANSFER, TRANS. ASME, Series C, Vol. 98, May 1976, p. 221-225.

7 Furnas, C. C., "Heat Transfer From a Gas Stream to a Bed of Broken Solids," *Trans. A. Inst. Chem. E.*, Vol. 24, 1929, p. 142-169.

8 Hughes, P. J., Klein, S. A., and Close, D. J., "Packed Bed Thermal Storage Models for Solar Air Heating and Cooling Systems," JOURNAL OF HEAT TRANSFER, TRANS. ASME, Series C, Vol. 98, May 1976, p. 336-337.

9 Vortmeyer, D., and Schaeffer, R. J., "Equivalence of One- and Two-Phase Models for Heat Transfer Processes in Packed Beds: One Dimensional Theory," *Chemical Engineering Science*, Vol. 29, 1974, p. 485-491.

10 Jeffreson, C. P., "Prediction of Breakthrough Curves in Packed Beds," *AIChE Journal*, Vol. 18, Mar. 1972, p. 409-416.

Calculation of Shape Factors Between Rings and Inverted Cones Sharing a Common Axis

C. P. Minning[1]

Nomenclature

- x, y, z = Cartesian coordinates of dA_1
- x_2, y_2, z_2 = Cartesian coordinates of point on periphery of surface 2
- ℓ_1, m_1, n_1 = cosines (i.e., direction cosines) of angles between normal to dA_1 and x-, y-, and z-axes, respectively
- s = vertical distance between plane of dA_1 and cone vertex
  - > 0 if cone and plane of dA_1 do not intersect
  - $= 0$ if cone vertex and plane of dA_1 coincide
  - < 0 if cone and plane of dA_1 intersect
- h = vertical distance between plane of dA_1 and cone base
- R = radius of cone base $= (h - s)\tan\beta$
- r = radius of cone in plane of dA_1 (intersecting case only, $s < 0$) $= -s\tan\beta$
- ρ = radial coordinate in plane of dA_1
- ρ_0, ρ_i = outer and inner radii of surface 1, respectively
- ζ = distance between dA_1 and point on periphery of surface 2
- β = cone vertex half-angle
- ω = terminator angle defined in equation (5)
- γ = radius of cone $= (z_2 - s)\tan\beta$
- θ = angular position on A_2 with respect to x-axis

Introduction

In spacecraft thermal control calculations, it is often necessary to evaluate shape factors for diffuse radiant-energy exchange between a ring and an inverted cone (i.e., a cone whose vertex points toward the ring). Such a geometry is encountered, for example, in rocket plume-heating analyses.

Bobco [1][2] used a numerical integration scheme to evaluate the shape factor between a differential area on a ring and a cone which intersected the plane of the ring. Bobco's results were later extended by Edwards [2]. Comparable results for the situation where the cone and the plane of the ring do not intersect are not readily available in the literature.

The contour integral method is used in the present analysis to derive a closed-form expression for the shape factor from a differential area on a ring to an inverted cone for both the intersecting as well as nonintersecting cases. These expressions can then be integrated numerically to obtain the desired shape factors between the cone and finite-sized ring.

Analysis

Throughout this discussion, surface $2(A_2)$ is considered to be of finite size; surface 1 can be either a differential area (dA_1) or a finite-sized ring (A_1), depending on the problem under consideration.

Sparrow [3] has shown that the shape factor, $F_{dA_1-A_2}$, can be expressed as the sum of three contour integrals in the following manner:

$$F_{dA_1-A_2} = \ell_1 \int_C \frac{(z_2 - z)dy_2 - (y_2 - y)dz_2}{2\pi\zeta^2} + m_1 \int_C \frac{(x_2 - x)dz_2 - (z_2 - z)dx_2}{2\pi\zeta^2} + n_1 \int_C \frac{(y_2 - y)dx_2 - (x_2 - x)dy_2}{2\pi\zeta^2} \quad (1)$$

where

$$\zeta^2 = (x_2 - x)^2 + (y_2 - y)^2 + (z_2 - z)^2 \quad (2)$$

The letter C designates integration around the periphery of surface 2. For the problem of interest, the normal to dA_1 is parallel to the z-axis; therefore, $\ell_1 = m_1 = 0$, and $n_1 = 1$. Hence, only the last term in equation (1) is nonzero.

Configuration 1. Cone and Plane of dA_1 Intersect. The nomenclature for this geometry is illustrated in Fig. 1. Integration around the periphery of surface 2 is performed in the counterclockwise direction (as viewed from dA_1) in four steps, each step corresponding to one of the numbered boundaries shown in Fig. 1. For boundary 1: $x_2 = \gamma\cos\omega$, $y_2 = \gamma\sin\omega$, and $z_2 = (\gamma - r)/\tan\beta$. For boundary 2: $x_2 = R\cos\theta$, $y_2 = R\sin\theta$, and $z_2 = h$. For boundary 3: $x_2 = \gamma\cos\omega$, $y_2 = -\gamma\sin\omega$, and $z_2 = (\gamma - r)/\tan\beta$. For boundary 4: $x_2 = r\cos\theta$, $y_2 = r\sin\theta$, and $z_2 = 0$. For all boundaries, $x = \rho$, $y = 0$, and $z = 0$. Substitution of these expressions for x, y, z, x_2, y_2, and z_2 into equation (1) results in the following:

$$F_{dA_1-A_2} = \frac{\rho\sin\omega\tan^2\beta}{\pi}$$

[1] Member of Technical Staff, Hughes Aircraft Co., Space and Communications Group, El Segundo, Calif. Mem. ASME.

Contributed by the Heat Transfer Division of THE AMERICAN SOCIETY OF MECHANICAL ENGINEERS. Manuscript received by the Heat Transfer Division October 26, 1976.

[2] Numbers in brackets designate References at end of technical note.

corporates the Biot number such as 1 + Bi/5 proposed by Jeffreson [10]. It is of interest to point out that the ratio $\lambda_{eq}/\theta_{eq} = v$ and is independent of both h_v and k_b.

Acknowledgment

This research was supported by the U. S. Energy Research and Development Administration under Contract No. EY-76-S-02-4002.

References

1 Schumann, T. E. W., "Heat Transfer: Liquid Flowing Through a Porous Prism," *Journal of the Franklin Institute*, Vol. 208, July 1929, p. 405-416.

2 Anzelius, A., "Über Erwärmung vermittels durchströmender Medien," *Z. angew. Math. Mech.*, Vol. 6, 1926, p. 291-294.

3 Jang, W. J., and Lee, C. P., "Dynamic Response of Solar Heat Storage Systems," ASME Paper No. 74-WA/HT-22, 1974.

4 Hung, F. T., and Nevins, R. G., "Unsteady-State Heat Transfer With a Flowing Fluid Through Porous Solids," ASME Paper No. 65-HT-10, 1965.

5 Arpaci, V. S., and Clark, J. A., "Dynamic Response of Fluid and Wall Temperatures During Pressurized Discharge for Simultaneous Time-Dependent Inlet Gas Temperature, Ambient Temperature, and/or Ambient Heat Flux," *Advances in Cryogenic Engineering*, Vol. 7, Plenum Press, 1962, p. 419-432.

6 Burch, D. M., Allen, R. W., and Peavy, B. A., "Transient Temperature Distributions Within Porous Slabs Subjected to Sudden Transpiration Heating," JOURNAL OF HEAT TRANSFER, TRANS. ASME, Series C, Vol. 98, May 1976, p. 221-225.

7 Furnas, C. C., "Heat Transfer From a Gas Stream to a Bed of Broken Solids," *Trans. A. Inst. Chem. E.*, Vol. 24, 1929, p. 142-169.

8 Hughes, P. J., Klein, S. A., and Close, D. J., "Packed Bed Thermal Storage Models for Solar Air Heating and Cooling Systems," JOURNAL OF HEAT TRANSFER, TRANS. ASME, Series C, Vol. 98, May 1976, p. 336-337.

9 Vortmeyer, D., and Schaeffer, R. J., "Equivalence of One- and Two-Phase Models for Heat Transfer Processes in Packed Beds: One Dimensional Theory," *Chemical Engineering Science*, Vol. 29, 1974, p. 485-491.

10 Jeffreson, C. P., "Prediction of Breakthrough Curves in Packed Beds," *AIChE Journal*, Vol. 18, Mar. 1972, p. 409-416.

Calculation of Shape Factors Between Rings and Inverted Cones Sharing a Common Axis

C. P. Minning[1]

Nomenclature

- x, y, z = Cartesian coordinates of dA_1
- x_2, y_2, z_2 = Cartesian coordinates of point on periphery of surface 2
- ℓ_1, m_1, n_1 = cosines (i.e., direction cosines) of angles between normal to dA_1 and x-, y-, and z-axes, respectively
- s = vertical distance between plane of dA_1 and cone vertex
  - > 0 if cone and plane of dA_1 do not intersect
  - $= 0$ if cone vertex and plane of dA_1 coincide
  - < 0 if cone and plane of dA_1 intersect
- h = vertical distance between plane of dA_1 and cone base
- R = radius of cone base $= (h - s)\tan\beta$
- r = radius of cone in plane of dA_1 (intersecting case only, $s < 0$) $= -s\tan\beta$
- ρ = radial coordinate in plane of dA_1
- ρ_0, ρ_i = outer and inner radii of surface 1, respectively
- ζ = distance between dA_1 and point on periphery of surface 2
- β = cone vertex half-angle
- ω = terminator angle defined in equation (5)
- γ = radius of cone $= (z_2 - s)\tan\beta$
- θ = angular position on A_2 with respect to x-axis

Introduction

In spacecraft thermal control calculations, it is often necessary to evaluate shape factors for diffuse radiant-energy exchange between a ring and an inverted cone (i.e., a cone whose vertex points toward the ring). Such a geometry is encountered, for example, in rocket plume-heating analyses.

Bobco [1][2] used a numerical integration scheme to evaluate the shape factor between a differential area on a ring and a cone which intersected the plane of the ring. Bobco's results were later extended by Edwards [2]. Comparable results for the situation where the cone and the plane of the ring do not intersect are not readily available in the literature.

The contour integral method is used in the present analysis to derive a closed-form expression for the shape factor from a differential area on a ring to an inverted cone for both the intersecting as well as nonintersecting cases. These expressions can then be integrated numerically to obtain the desired shape factors between the cone and finite-sized ring.

Analysis

Throughout this discussion, surface $2(A_2)$ is considered to be of finite size; surface 1 can be either a differential area (dA_1) or a finite-sized ring (A_1), depending on the problem under consideration.

Sparrow [3] has shown that the shape factor, $F_{dA_1-A_2}$, can be expressed as the sum of three contour integrals in the following manner:

$$F_{dA_1-A_2} = \ell_1 \int_C \frac{(z_2 - z)dy_2 - (y_2 - y)dz_2}{2\pi\zeta^2} + m_1 \int_C \frac{(x_2 - x)dz_2 - (z_2 - z)dx_2}{2\pi\zeta^2} + n_1 \int_C \frac{(y_2 - y)dx_2 - (x_2 - x)dy_2}{2\pi\zeta^2} \quad (1)$$

where

$$\zeta^2 = (x_2 - x)^2 + (y_2 - y)^2 + (z_2 - z)^2 \quad (2)$$

The letter C designates integration around the periphery of surface 2. For the problem of interest, the normal to dA_1 is parallel to the z-axis; therefore, $\ell_1 = m_1 = 0$, and $n_1 = 1$. Hence, only the last term in equation (1) is nonzero.

Configuration 1. Cone and Plane of dA_1 Intersect. The nomenclature for this geometry is illustrated in Fig. 1. Integration around the periphery of surface 2 is performed in the counterclockwise direction (as viewed from dA_1) in four steps, each step corresponding to one of the numbered boundaries shown in Fig. 1. For boundary 1: $x_2 = \gamma\cos\omega$, $y_2 = \gamma\sin\omega$, and $z_2 = (\gamma - r)/\tan\beta$. For boundary 2: $x_2 = R\cos\theta$, $y_2 = R\sin\theta$, and $z_2 = h$. For boundary 3: $x_2 = \gamma\cos\omega$, $y_2 = -\gamma\sin\omega$, and $z_2 = (\gamma - r)/\tan\beta$. For boundary 4: $x_2 = r\cos\theta$, $y_2 = r\sin\theta$, and $z_2 = 0$. For all boundaries, $x = \rho$, $y = 0$, and $z = 0$. Substitution of these expressions for x, y, z, x_2, y_2, and z_2 into equation (1) results in the following:

$$F_{dA_1-A_2} = \frac{\rho\sin\omega\tan^2\beta}{\pi}$$

[1] Member of Technical Staff, Hughes Aircraft Co., Space and Communications Group, El Segundo, Calif. Mem. ASME.

Contributed by the Heat Transfer Division of THE AMERICAN SOCIETY OF MECHANICAL ENGINEERS. Manuscript received by the Heat Transfer Division October 26, 1976.

[2] Numbers in brackets designate References at end of technical note.

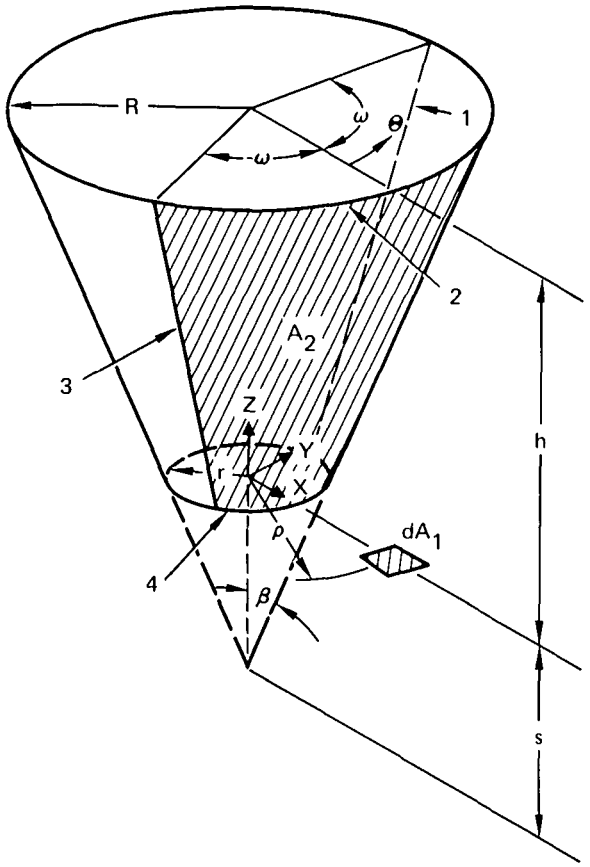

Fig. 1. Nomenclature for Configuration 1: cone and plane of dA_1 intersect ($s < 0$, $\rho \geq -s \tan \beta$)

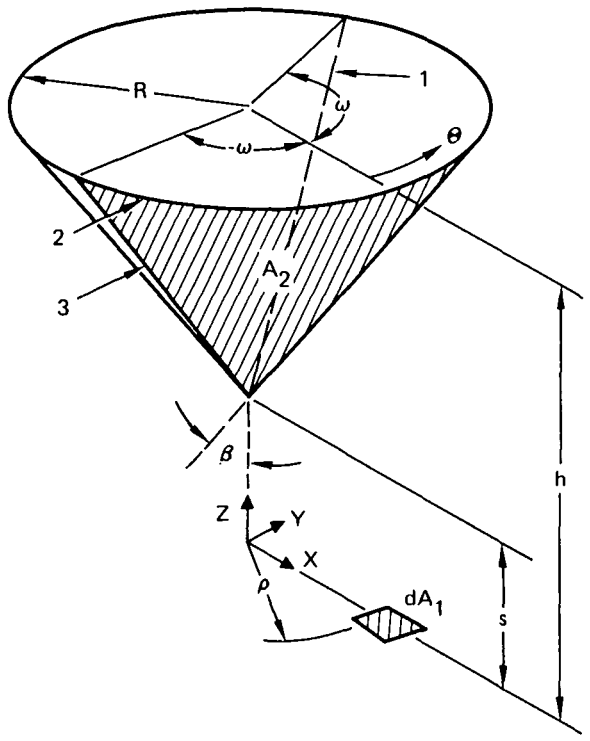

Fig. 2 Nomenclature for Configuration 2: cone and plane of dA_1 do not intersect ($s > 0$)

$$\times \int_r^R \frac{d\gamma}{\gamma^2(1+\tan^2\beta) - 2\gamma(\rho \tan^2\beta \cos\omega + r) + r^2 + \rho^2 \tan^2\beta} + \frac{R}{2\pi}\int_{-\omega}^{\omega} \frac{(R - \rho\cos\theta)d\theta}{R^2 + \rho^2 + h^2 - 2\rho R\cos\theta} - \frac{r}{2\pi}\int_{-\omega}^{\omega} \frac{(r - \rho\cos\theta)d\theta}{r^2 + \rho^2 - 2\rho r\cos\theta} \quad (3)$$

Configuration 2: Cone and Plane of dA_1 Do Not Intersect. The nomenclature for this geometry is shown in Fig. 2. Here, integration around the periphery of surface 2 is performed in the counterclockwise direction in three steps, each step corresponding to one of the numbered boundaries shown in Fig. 2. For boundary 1: $x_2 = \gamma \cos\omega$, $y_2 = \gamma \sin\omega$, and $z_2 = (\gamma/\tan\beta) + s$. For boundary 2: $x_2 = R\cos\theta$, $y_2 = R\sin\theta$, and $z_2 = h$. For boundary 3: $x_2 = \gamma\cos\omega$, $y_2 = -\gamma\sin\omega$, and $z_2 = (\gamma/\tan\beta) + s$. For all boundaries, $x = \rho$, $y = 0$, and $z = 0$. Substitution of these expressions into equation (1) then yields:

$$F_{dA_1-A_2} = \frac{\rho \sin\omega \tan^2\beta}{\pi} \times \int_0^R \frac{d\gamma}{\gamma^2(1+\tan^2\beta) - 2\gamma(\rho\tan^2\beta\cos\omega - s\tan\beta) + (\rho^2 + s^2)\tan^2\beta} + \frac{R}{2\pi}\int_{-\omega}^{\omega} \frac{(R - \rho\cos\theta)d\theta}{R^2 + \rho^2 + h^2 - 2\rho R\cos\theta} \quad (4)$$

The visible portion of A_2, as seen from dA_1, is defined by the terminator angle, ω which is given by [1].

$$\omega = \cos^{-1}\left(\frac{-s\tan\beta}{\rho}\right) \quad (5)$$

Equation (5) applies to both configurations under consideration provided that s, the separation distance, is considered a negative quantity when the cone and the plane of dA_1 intersect (i.e., Configuration 1). Note that $\rho \geq -s\tan\beta$ for Configuration 1.

Integration of equations (3) and (4), a considerable amount of algebraic manipulation, and introduction of the following trigonometric identity

$$\tan(\omega/2) = \sqrt{\frac{1-\cos\omega}{1+\cos\omega}} = \sqrt{\frac{\rho + s\tan\beta}{\rho - s\tan\beta}} \quad (6)$$

leads to the following expressions for $F_{dA_1-A_2}$.

Configuration 1: Cone and Plane of dA_1 Intersect.

$$F_{dA_1-A_2} = \frac{\sin\beta}{\pi}\tan^{-1}\left[h\sqrt{\frac{1+\tan^2\beta}{\rho^2 - s^2\tan^2\beta}}\right] + \frac{1}{\pi}\tan^{-1}\left[\sqrt{\frac{\rho - s\tan\beta}{\rho + s\tan\beta}}\right] + \frac{(h-s)^2\tan^2\beta - \rho^2 - h^2}{\pi\sqrt{[(h-s)^2\tan^2\beta + \rho^2 + h^2]^2 - 4\rho^2(h-s)^2\tan^2\beta}} \times \tan^{-1}\left[\sqrt{\frac{[(h-s)\tan\beta + \rho]^2 + h^2}{[(h-s)\tan\beta - \rho]^2 + h^2}\cdot\left(\frac{\rho + s\tan\beta}{\rho - s\tan\beta}\right)}\right] \quad (7)$$

Configuration 2: Cone and Plane of dA_1 Do Not Intersect.

$$F_{dA_1-A_2} = \frac{\omega}{2\pi} + \frac{\sin\beta}{\pi}\left\{\tan^{-1}\left[h\sqrt{\frac{1+\tan^2\beta}{\rho^2 - s^2\tan^2\beta}}\right] - \tan^{-1}\left[s\sqrt{\frac{1+\tan^2\beta}{\rho^2 - s^2\tan^2\beta}}\right]\right\} + \frac{(h-s)^2\tan^2\beta - \rho^2 - h^2}{\pi\sqrt{[(h-s)^2\tan^2\beta + \rho^2 + h^2]^2 - 4\rho^2(h-s)^2\tan^2\beta}} \times \tan^{-1}\left[\sqrt{\frac{[(h-s)\tan\beta + \rho]^2 + h^2}{[(h-s)\tan\beta - \rho]^2 + h^2}\cdot\left(\frac{\rho + s\tan\beta}{\rho - s\tan\beta}\right)}\right] \quad (8)$$

Note that both equations (7) and (8) yield the same expression for the condition $s = 0$, that is, when the cone vertex lies in the plane of dA_1.

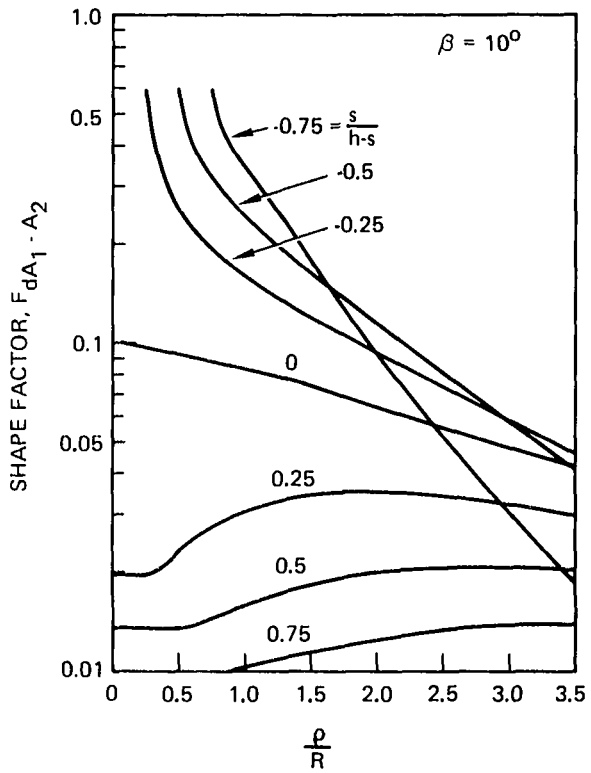

Fig. 3 Shape factors from a differential area to an inverted cone, $\beta = 10$ deg

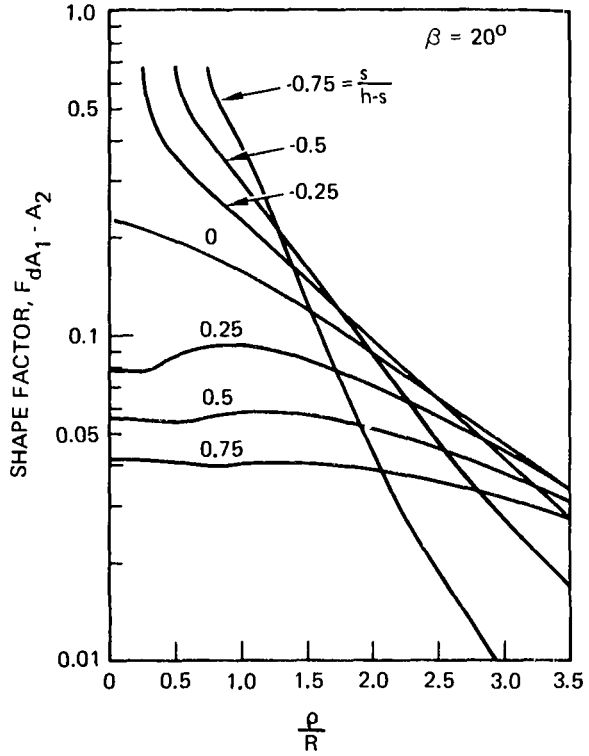

Fig. 4 Shape factors from a differential area to an inverted cone, $\beta = 20$ deg

Results and Discussion

Consider Configuration 1 (intersecting case) for the condition $\rho = -s \tan \beta$. For this special case, it is seen that equation (7) reduces to

$$\lim_{\rho \to -s \tan\beta} F_{dA_1-A_2} = \frac{1}{2}[1 + \sin \beta] \tag{9}$$

Now consider Configuration 2 (nonintersecting case) for the condition $\rho \leq s \tan \beta$. For this special case, $\omega = \pi$, and equation (8) reduces to

$$F_{dA_1-A_2} = \frac{1}{2}\left[1 + \frac{(h-s)^2 \tan^2 \beta - \rho^2 - h^2}{\sqrt{[(h-s)^2 \tan^2 \beta + \rho^2 + h^2]^2 - 4\rho^2(h-s)^2 \tan^2 \beta}}\right] \tag{10}$$

which is the familiar expression for the shape factor from an off-center differential area to a circular disk (i.e., the cone base).

Typical shape factors from a differential area to inverted 10 and 20 deg cones are shown in Figs. 3 and 4, respectively. Here, the parameter $s/(h-s)$ is the ratio of the separation distance to the vertical distance between the vertex and base of the cone, and the abscissa is the ratio of the radial coordinate of dA_1 to the radius of the cone base.

For $s > 0$ and $0 \leq \rho \leq s \tan \beta$, the shape factor from dA_1 to the cone is numerically equal to the shape factor from dA_1 to the cone base, because both subtend the same solid angle as seen from dA_1. When $\rho > s \tan \beta$, the shape factor from dA_1 to the cone at first increases (because the solid angle subtended by the cone increases), passes through a maximum, and then decreases with ρ. As the separation distance is increased, the shape factor decreases.

For $s < 0$, the shape factors decrease quite rapidly with distance from the cone surface. This rapid decrease becomes more severe as β is increased. Note that the cone and the plane of dA_1 intersect at $\rho = -s \tan \beta$ and that the shape factor is a maximum at this point. (A value of $\rho < -s \tan \beta$ would place dA_1 *inside* the cone, which is not the case under consideration here.)

For $s = 0$, it is seen that the shape factor is discontinuous at $\rho = 0$. This is due to the step increase in the solid angle subtended by the cone as ρ is increased from zero.

Shape factors between cones and plane annular rings of finite size can be determined by integrating equations (7) or (8) in the following manner

$$F_{A_1-A_2} = \frac{2}{\rho_0^2 - \rho_i^2} \int_{\rho_i}^{\rho_0} \rho F_{dA_1-A_2}\, d\rho \tag{11}$$

Because of the complex integrals involved in equation (11), integration is most easily performed through use of numerical methods such as Simpson's rule.

Acknowledgments

This paper is based on work performed under the sponsorship of Comsat General Corporation. Any views expressed in this paper will not necessarily be those of Comsat General.

References

1 Bobco, R. P., "Radiation From Conical Surfaces With Nonuniform Radiosity," *AIAA Journal*, Vol. 4, 1966, pp. 544–546.

2 Edwards, D. K., "Comments on Radiation From Conical Surfaces With Nonuniform Radiosity," *AIAA Journal*, Vol. 7, 1968, pp. 1656–1659.

3 Sparrow, E. M., "A New and Simpler Formulation for Radiative Angle Factors," JOURNAL OF HEAT TRANSFER, TRANS. ASME, Series C, Vol. 85, 1963, pp. 81–88.

A Residual Method With Lagrange Multipliers for Transient Heat Conduction Problems

T. R. Tauchert[1]

Introduction

Methods of weighted residuals [1–3][2] including the well-known Galerkin technique have been used extensively for obtaining approximate solutions to stationary heat conduction problems. Least-squares procedures, reviewed recently by Eason [4], have been employed also in the case of transient, linear conduction. A difficulty often encountered in applying interior residual methods involves selecting basis functions which satisfy boundary conditions. The purpose of this note is to describe a least-squares residual method which incorporates Lagrange multipliers for satisfaction of both initial and boundary conditions. The approach is valid for problems of transient conduction in anisotropic, initially nonhomogeneous and temperature-sensitive bodies of one or more dimensions.

General Formulation

The differential equation, initial condition, and boundary condition governing heat conduction in an anisotropic body occupying the bounded region $D + B$ may be expressed, respectively, as

$$(k^{rs}T_{,s})_{,r} - a\frac{\partial T}{\partial t} = -Q(x_k, t) \text{ in } D,\ t > 0 \tag{1}$$

$$T = F(x_k) \text{ in } D,\ t = 0 \tag{2}$$

$$n_r k^{rs} T_{,s} + hT = hG(x_k, t) \text{ on } B,\ t > 0 \tag{3}$$

where the thermal conductivity tensor k^{rs} and the heat capacity a may vary with position x_k and temperature T.

We seek an approximate solution of the general form

$$\overline{T}(x_1, x_2, \ldots, t) = \sum_i \sum_j \cdots \sum_\ell C_{ij\ldots\ell}\Phi_i^{(1)}(x_1)\Phi_j^{(2)}(x_2)\ldots\psi_\ell(t) \tag{4}$$

where $\Phi_i^{(1)}(x_1)$, $\Phi_j^{(2)}(x_2), \ldots, \psi_\ell(t)$ represent an arbitrary number of preselected linearly independent functions. In contrast to other interior methods of weighted residuals we do not require that these trial functions satisfy identically conditions (2) and (3). However, known information on the temperature response for the problem of interest or for a similar problem can often be used to advantage in selecting appropriate trial functions.

It is assumed that the nonhomogeneous terms $F(x_k)$ and $G(x_k, t)$ in equations (2) and (3) can be represented by truncated power series as

$$F(x_k) = \sum_i \sum_j \cdots [a_{ij\ldots}\Phi_i^{(1)}(x_1)\Phi_j^{(2)}(x_2)\ldots] \tag{5}$$

$$G(x_k, t) = \sum_i \sum_j \cdots \sum_\ell [b_{ij\ldots\ell}\Phi_i^{(1)}(x_1)\Phi_j^{(2)}(x_2)\ldots\psi_\ell(t)] \tag{6}$$

Substitution of equations (4)–(6) into conditions (2) and (3) yields, respectively, two sets of restrictions upon the coefficients $C_{ij\ldots\ell}$, say $f_{ij\ldots} = 0$ and $g_{i\ldots\ell} = 0$. These restrictions could be used to eliminate certain of the undetermined coefficients from the assumed solution (4). However the algebra involved in the elimination process often becomes extremely involved, and so instead we employ here the method of Lagrange multipliers. We, therefore, introduce a functional E defined as

$$E = \int_{t=0}^{t_0}\int_D \left[(k^{rs}\overline{T}_{,s})_{,r} - a\frac{\partial\overline{T}}{\partial t} + Q\right]^2 dVdt + \sum_i \sum_j \cdots \lambda_{ij\ldots} f_{ij\ldots} + \sum_i \cdots \sum_\ell \mu_{i\ldots\ell} g_{i\ldots\ell} \tag{7}$$

where $\lambda_{ij\ldots}$ and $\mu_{i\ldots\ell}$ are the Lagrange multipliers for the constraint conditions $f_{ij\ldots} = 0$ and $g_{i\ldots\ell} = 0$, respectively. Thus the square of the residual of the differential equation has been integrated over the region D and over the time interval $0 < t < t_0$, where t_0 is an arbitrarily chosen upper limit; clearly t_0 should be at least as large as the largest time of interest in the particular problem. For an approximate solution which satisfies the initial and boundary conditions and has a least-squared error, we require that

$$\frac{\partial E}{\partial C_{rs\ldots u}} = \frac{\partial E}{\partial \lambda_{rs\ldots}} = \frac{\partial E}{\partial \mu_{r\ldots u}} = 0 \tag{8}$$

In the case of a body with material properties which are independent of temperature, (8) represents a system of $n + m$ linear algebraic equations in the n coefficients $C_{ij\ldots\ell}$ and m Lagrange multipliers. For temperature-sensitive materials the system is nonlinear in the coefficients $C_{ij\ldots\ell}$.

Numerical Example

As a simple illustrative example, consider the heat flow in a slab $(0 < \zeta < 1)$ of material having a conductivity which varies linearly with temperature. The slab is assumed to have zero initial temperature; thereafter, the temperature on face $\zeta = 0$ remains zero, while the temperature on $\zeta = 1$ increases to unity. The associated boundary value problem may be written in terms of dimensionless quantities as

$$\frac{\partial}{\partial\zeta}\left[(1 + bT)\frac{\partial T}{\partial\zeta}\right] - \frac{\partial T}{\partial t} = 0 \tag{9}$$

$$T(\zeta, 0) = T(0, t) = 0,\ T(1, t) = 1 - e^{-\beta_N t} \tag{10}$$

Here the constant β_N may be assigned a very large finite value if one wishes to approximate an instantaneous temperature rise on $\zeta = 1$ at $t = 0$.

For an approximate solution we let

$$\overline{T}(\zeta, t) = \sum_j \sum_\ell C_{j\ell}\zeta^j e^{-\beta_\ell t} \tag{11}$$

in which case (8) leads to a system of equations of the general form

$$\sum_i \sum_j \sum_k \sum_\ell \sum_m \sum_n D_{suijk\ell mn}C_{ij}C_{k\ell}C_{mn} + \sum_i \sum_j \sum_k \sum_\ell E_{suijk\ell}C_{ij}C_{k\ell} + \sum_i \sum_j F_{suij}C_{ij} + \sum_j G_{uj}\lambda_s + \sum_\ell H_{s\ell}\mu_u = 0 \tag{12}$$

where the quantities $D_{suijk\ell mn}, E_{suijk\ell}, \ldots, H_{s\ell}$ are easily determined. The coefficients C_{ij} and the Lagrange multipliers λ_s and μ_u are found by solving these nonlinear algebraic equations. An efficient Fortran program for this purpose is the Harwell Subroutine NS01A.[3]

Numerical results were computed first for the limiting case of a temperature-independent conductivity ($b = 0$). Approximate temperature profiles, obtained using 12 coefficients $C_{j\ell}$ ($j = 1, 2, 3$ and $\beta_\ell = 0, \pi^2, 4\pi^2, 800$)[4] and $t_0 = 0.5$, are compared with the exact solution

---

[1] Professor, Department of Engineering Mechanics, University of Kentucky, Lexington, Ky. Mem. ASME.

[2] Numbers in brackets designate References at end of technical note.

Contributed by the Heat Transfer Division of THE AMERICAN SOCIETY OF MECHANICAL ENGINEERS. Manuscript received by the Heat Transfer Division May 16, 1977.

[3] Harwell Subroutine Library, Atomic Energy Research Establishment-R.5947, Harwell, England, 1968.

[4] The values of β_ℓ used in the approximate solutions for both the temperature-independent and temperature-dependent cases were taken equal to the lowest three characteristic roots $(0, \pi^2, 4\pi^2)$ of the exact solution for the temperature-insensitive problem. Also β_N was arbitrarily taken equal to 800.

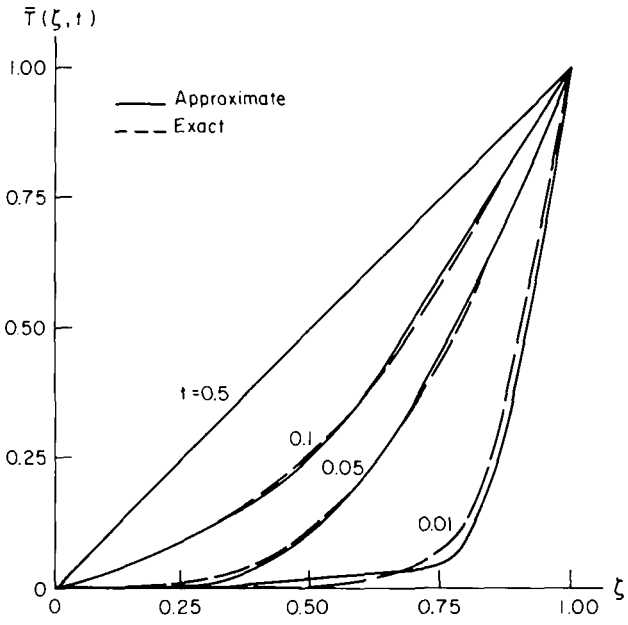

Fig. 1 Temperature profiles for a slab with temperature-independent properties

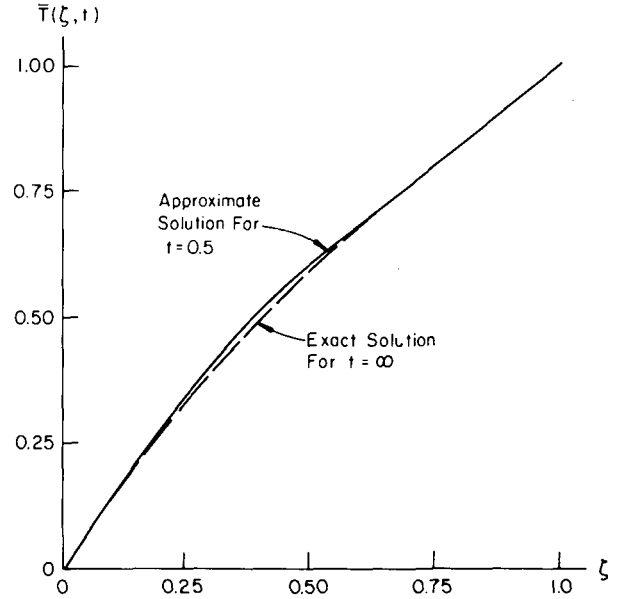

Fig. 2 Temperature profile for a slab in which the thermal conductivity varies linearly with temperature

(based upon $\beta_N = \infty$) to this problem in Fig. 1. The agreement is seen to be quite good, particularly for values of time $t > 0.01$. When additional terms ($j = 4, \ldots; \beta_\ell = 9\pi^2, \ldots$) were included in the approximate solution (11), or when t_0 was increased ($t_0 = 1$) the computed temperature distributions changed only slightly.

In the case of a material having a conductivity which varies linearly with temperature, b = 1, the exact steady-state solution to the foregoing problem is given by $T = \sqrt{1 + 3\zeta} - 1$. Fig. 2 provides a comparison between this exact distribution and the approximate solution evaluated at a large time, $t = 0.5$. The values of j, β_ℓ, and t_0 given earlier were used in this example also, and good agreement between the two solutions again is observed.

In conclusion it is noted that by employing Lagrange multipliers to satisfy initial and boundary conditions, it has been possible to select very simple basis functions for the assumed solution. Applications of the present formulation to transient heat conduction problems involving more than one spatial coordinate have been carried out with similar success.

References

1 Becker, M., *The Principles and Applications of Variational Methods*, M.I.T. Press, Cambridge, Mass., 1964.

2 Ames, W. F., *Nonlinear Partial Differential Equations in Engineering*, Academic Press, New York, 1965.

3 Finlayson, B. A., *The Method of Weighted Residuals and Variational Principles*, Academic Press, New York, 1972.

4 Eason, E. D., "A Review of Least-Squares Methods for Solving Partial Differential Equations," *International Journal for Numerical Methods in Engineering*, Vol. 10, 1976, pp. 1021–1046.

The Effect of Surface Suction on Condensation in the Presence of a Noncondensable Gas

I. Antonir[1] and A. Tamir[2]

Nomenclature

C = air concentration in the bulk of the steam, percent mole
h_x = local overall heat transfer coefficient, cal/s-cm^2 − °C, $q_x/(T_\infty - \bar{T})$
$\bar{h}$ = mean overall heat transfer coefficient, cal/s-cm^2 − °C, $\Sigma^n h_x/n$
$\bar{h}_{\min}$ = corresponds to $\bar{h}$ in the absence of surface suction
m = steam condensation rate, g mole/s
m_s = steam suction rate, g mole/s
n = number of observations per run
p = total pressure, mm Hg
q_x = local condensation flux, cal/cm^2-s
T_0 = water temperature at spray nozzle outlet, °C
T_∞ = steam bulk temperature
$\bar{T}$ = local average temperature in the transverse section of the sheet [4], °C

Introduction

The phenomenon of the presence of small quantities of a noncondensable gas in a condensing vapor is well known. During condensation, the noncondensable gas tends to accumulate at the condensation surface and reduce the heat transfer drastically [1].[3] There exists a technical difficulty in eliminating the small quantities of a noncondensable gas and hence the significance of developing means to improve the condensation rate in the presence of a noncondensable gas.

The present study investigates the technique of local surface suction where a mixture of steam and air is continuously sucked from the vicinity of the condensing surface. A theoretical study by Tamir and Taitel [2] where the suction rate was inversely proportional to the

[1] Graduate Student, Department of Chemical Engineering, Ben-Gurion University of the Negev, Beer-Sheva, Israel.

[2] Assoc. Professor, Department of Chemical Engineering, Ben-Gurion University of the Negev, Beer-Sheva, Israel.

[3] Numbers in brackets designate References at end of technical note.

Contributed by the Heat Transfer Division of THE AMERICAN SOCIETY OF MECHANICAL ENGINEERS. Manuscript received by the Heat Transfer Division January 31, 1977.

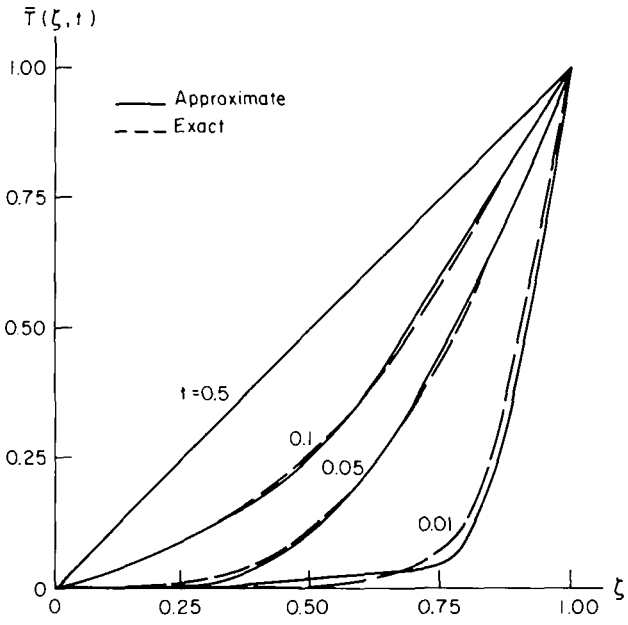

Fig. 1 Temperature profiles for a slab with temperature-independent properties

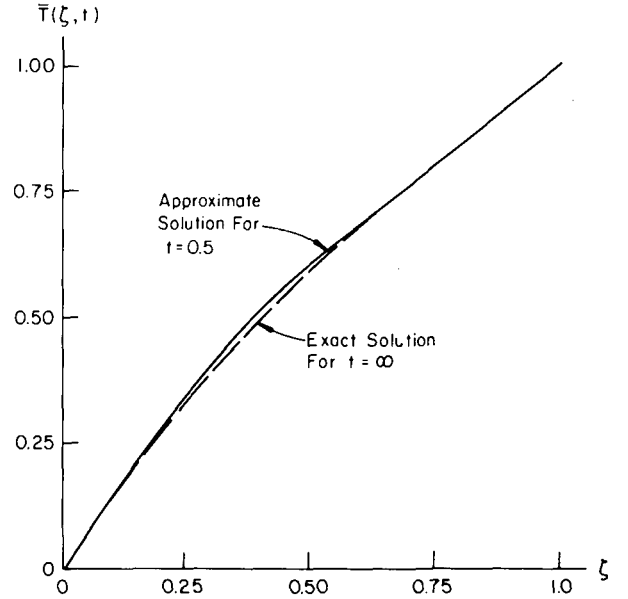

Fig. 2 Temperature profile for a slab in which the thermal conductivity varies linearly with temperature

(based upon $\beta_N = \infty$) to this problem in Fig. 1. The agreement is seen to be quite good, particularly for values of time $t > 0.01$. When additional terms ($j = 4, \ldots; \beta_\ell = 9\pi^2, \ldots$) were included in the approximate solution (11), or when t_0 was increased ($t_0 = 1$) the computed temperature distributions changed only slightly.

In the case of a material having a conductivity which varies linearly with temperature, b = 1, the exact steady-state solution to the foregoing problem is given by $T = \sqrt{1 + 3\zeta} - 1$. Fig. 2 provides a comparison between this exact distribution and the approximate solution evaluated at a large time, $t = 0.5$. The values of j, β_ℓ, and t_0 given earlier were used in this example also, and good agreement between the two solutions again is observed.

In conclusion it is noted that by employing Lagrange multipliers to satisfy initial and boundary conditions, it has been possible to select very simple basis functions for the assumed solution. Applications of the present formulation to transient heat conduction problems involving more than one spatial coordinate have been carried out with similar success.

References

1 Becker, M., *The Principles and Applications of Variational Methods*, M.I.T. Press, Cambridge, Mass., 1964.

2 Ames, W. F., *Nonlinear Partial Differential Equations in Engineering*, Academic Press, New York, 1965.

3 Finlayson, B. A., *The Method of Weighted Residuals and Variational Principles*, Academic Press, New York, 1972.

4 Eason, E. D., "A Review of Least-Squares Methods for Solving Partial Differential Equations," *International Journal for Numerical Methods in Engineering*, Vol. 10, 1976, pp. 1021–1046.

The Effect of Surface Suction on Condensation in the Presence of a Noncondensable Gas

I. Antonir[1] and A. Tamir[2]

Nomenclature

C = air concentration in the bulk of the steam, percent mole
h_x = local overall heat transfer coefficient, cal/s-cm^2 − °C, $q_x/(T_\infty - \bar{T})$
$\bar{h}$ = mean overall heat transfer coefficient, cal/s-cm^2 − °C, $\Sigma^n h_x/n$
$\bar{h}_{\min}$ = corresponds to $\bar{h}$ in the absence of surface suction
m = steam condensation rate, g mole/s
m_s = steam suction rate, g mole/s
n = number of observations per run
p = total pressure, mm Hg
q_x = local condensation flux, cal/cm^2-s
T_0 = water temperature at spray nozzle outlet, °C
T_∞ = steam bulk temperature
$\bar{T}$ = local average temperature in the transverse section of the sheet [4], °C

Introduction

The phenomenon of the presence of small quantities of a noncondensable gas in a condensing vapor is well known. During condensation, the noncondensable gas tends to accumulate at the condensation surface and reduce the heat transfer drastically [1].[3] There exists a technical difficulty in eliminating the small quantities of a noncondensable gas and hence the significance of developing means to improve the condensation rate in the presence of a noncondensable gas.

The present study investigates the technique of local surface suction where a mixture of steam and air is continuously sucked from the vicinity of the condensing surface. A theoretical study by Tamir and Taitel [2] where the suction rate was inversely proportional to the

[1] Graduate Student, Department of Chemical Engineering, Ben-Gurion University of the Negev, Beer-Sheva, Israel.

[2] Assoc. Professor, Department of Chemical Engineering, Ben-Gurion University of the Negev, Beer-Sheva, Israel.

[3] Numbers in brackets designate References at end of technical note.

Contributed by the Heat Transfer Division of THE AMERICAN SOCIETY OF MECHANICAL ENGINEERS. Manuscript received by the Heat Transfer Division January 31, 1977.

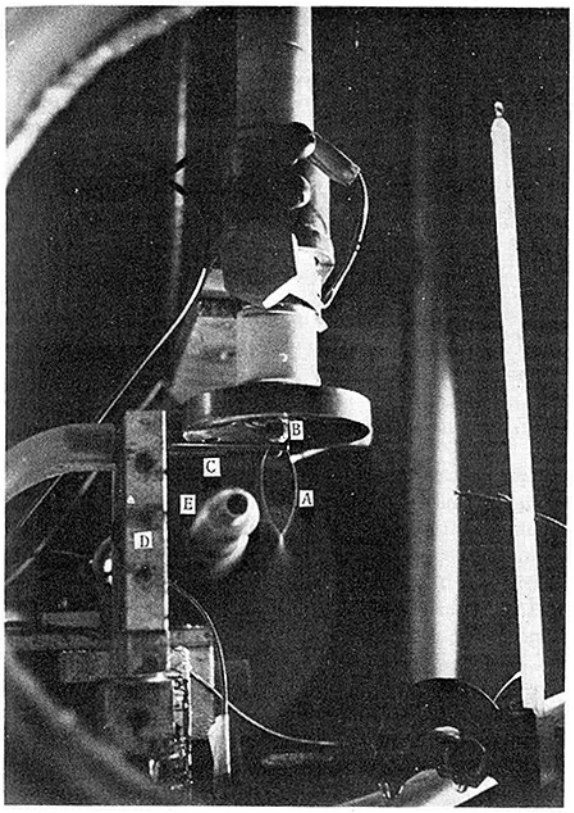

Fig. 1 Fan-shaped sheet and suction device

square of the distance along the condensing surface [2] showed a significant improvement in the condensation rate of steam by suction of small quantities of steam-air mixtures. An additional objective of this work is to explore theoretical predictions concerning the effect of the total pressure on the heat transfer in the presence of noncondensables.

Principles of the Experimental Method, Its Precision and Treatment of the Data

The effect of the surface suction is studied by measuring the local overall heat-transfer coefficients, h_x, to a fan-shaped sheet of water (Fig. 1 (*A*)) in direct contact condensation of steam on its surface in the presence of noncondensables. h_x combines both the conduction resistance in the liquid and the gas-side resistance. The thin laminar sheet with a continuously decreasing thickness is generated when water flows through a special spray nozzle *B*. Illumination of the sheet by a monochromatic light produces interference lines [3, 4] with changing density dependent on the sheet thickness due to condensation. The thickness variation can be translated to h_x. A detailed description of the flow in a fan-shaped sheet, its characteristics, and the theory of the interferometric determinations of h_x are given in references [3–5]. The apparatus used in a previous steam condensation study [4] was adapted for this work. Modifications which are detailed in [5] were made in order to apply surface suction and measure the air content of steam. Surface suction is performed perpendicular to the sheet surface by means of two stainless steel arms *C* located symmetrically at both sides of the sheet and parallel to it. Two holes of 0.0306 cm^2 each were made at the inner face of the suction tubes (blocked at both ends). The latter were mounted on a device *D* which made it possible to regulate the distance between the arms and their position with respect to the nozzle outlet. The distance between the arms was fixed at 1.3 mm. This was found to be the minimal distance which did not cause any distortion of the sheet. The suction arms were nearest to the nozzle exit *B* less than 5 mm because the noncondensable accumulation at this region is the highest which would require minimum suction rate. The distance was determined from an interferogram by means of a microscope. The determination of the suction rate is carried out by passing air-steam mixtures through a rotameter by means of which the suction rate is maintained constant. In principle, the amount of steam in the mixture is measured by its condensation in trap cooled by liquid nitrogen and the air is determined by measuring the change of the pressure in a bulb due to the introduction of the air into it. Air content in the bulk of the steam is similarly determined by sucking air-steam samples through an 8-mm dia pipe *E* located at about 100 mm from the water sheet *A*. Repeated analysis gave results in agreement between 2 and 5 percent where the higher figure corresponds to the lower air concentration (1.16 percent in mole fraction).

An experimental run usually yields five interferometric photographs each providing 15–40 local values of h_x and hence each run provides 100–200 local values. The use of the interferometric technique for determining h_x dictates limitations on the operating variables. The net effect is that the measurements are confined to a narrow range of distances from the nozzle. An analysis of the propagation of errors which has been carried out [5] yielded that $\Delta h_x/h_x$ is in the order 0.3. This is not unusual in the determination of local heat transfer coefficients. The major conclusion drawn by considering the random scatter of h_x in a run and the aforementioned facts is that each run may be reliably described by a single value of the mean overall heat-transfer coefficient $\bar{h}$.

Results and Discussion

Table 1 summarizes the operating conditions and the maximum values of $\bar{h}$ obtained in the presence of suction. The rest of the values appear in Figs. 3 and 4. In all the experiments the water flowrate was kept at 2.42 g/s corresponding to a sheet velocity of 2050 cm/s. The detailed results are given in [5].

Fig. 2 demonstrates the effect of the air concentration in the steam on the mean overall heat transfer coefficient at three levels of steam pressures and in the absence of surface suction. The prominent observation is that at constant air concentration $\bar{h}$ decreases with a decrease in the total pressure. In other words, the effect of the noncondensable gases is enhanced toward low pressures which is consistent with the theoretical result first predicted by Sparrow and Lin [1].

Fig. 3 demonstrates the effect of the local surface suction on $\bar{h}$ at various constant levels of air concentration. The major conclusion drawn is that there is a remarkable increase in the heat transfer coefficient due to surface suction. Table 1 shows the ratio between the maximum heat transfer coefficient $\bar{h}$, usually obtained at the

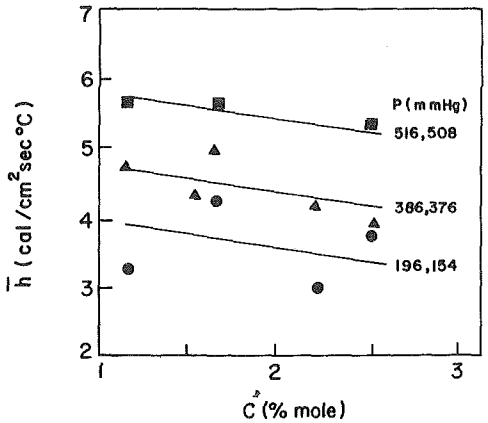

Fig. 2 Mean overall heat transfer coefficients as a function of air concentration in the absence of surface suction

Table 1 Summary of operating conditions and the main results

C percent mole	P mm Hg	T_∞ °C	T_0 °C	$m_s \times 10^4$ mole/s	$\bar{h}_{max}$ cal/cm² s °C	$\bar{h}_{max}/\bar{h}_{min}$	$\frac{m_s}{m_s+m}100$
1.16	508	89	42	8.6	8.68	1.54	6.84
	376	80	36.5	9.4	9.21	2.01	7.98
	154	62.5	32.5	7.4	8.01	2.47	9.04
1.54	386	83	38	12.4	13.63	3.13	9.95
1.67	516	89	42	7.9	8.84	1.58	6.35
	376	81	41	23.8	13.14	2.68	19.31
	196	65.7	33.2	6.3	9.54	2.24	7.21
2.24	376	79.5	36.5	4.8	9.60	2.29	4.31
	196	64.9	33.5	7.3	10.51	3.50	8.53
2.57	516	89	40.7	13.1	11.33	2.14	9.82
	376	81.5	35.8	11.3	9.81	2.50	9.07
	196	65.6	34.0	6.8	9.18	2.47	7.94

higher suction rate to the minimal value, $\bar{h}_{min}$, obtained in the absence of suction. The ratio varies between 1.5 and 3.5, indicating the high efficiency of surface suction. The corresponding percentage of steam suction rate from the total main flow of steam reaching the condensing surface, $m_s + m$, under conditions of maximal heat transfer coefficients are also reported in Table 1. From Fig. 3, it is not possible to determine unequivocally the direction of the effect of the surface suction. In other words, does it act asymptotically toward a constant value of $\bar{h}$ (as indicated in Fig. 4 at 376 mm Hg and $C = 1.16$ percent or at 516 mm Hg for $C = 1.67$ percent) or is the effect proportional to the suction rate at all range of values? It is also not possible to conclude whether the effect of the suction is identical at different pressures and at a constant air concentration. However, the positive effect of the suction is undoubtedly proven.

Fig. 4 demonstrates the effect of surface suction on $\bar{h}$ at three pressures and at various air concentrations tested at each pressure. The results indicate that at a certain pressure and within the explored experimental range of the air concentrations, the suction effect on $\bar{h}$ is probably identical and independent of the air concentration.

The role of the suction on increasing the mean overall heat transfer coefficient may be explained qualitatively as follows: the total resistance, $1/\bar{h}$, in the fan-shaped sheet is composed of the liquid-side resistance, $1/h_L$, and the gas-side resistance $1/h_g$, so that $1/\bar{h} = 1/h_L + 1/h_g$. All experiments were conducted at the same water flowrate, and as previously noted, the measurements were confined to a narrow length of the sheet. Hence, the liquid side resistance in the measurements section may be approximated by a mean value $1/h_L$. The gas-side resistance is caused by build-up of the noncondensable gas at the condensing surface, which in turn reduces the partial pressure of the condensing vapor. Hence, the vapor-liquid interfacial temperature is reduced and consequently so is the thermal driving force to the heat

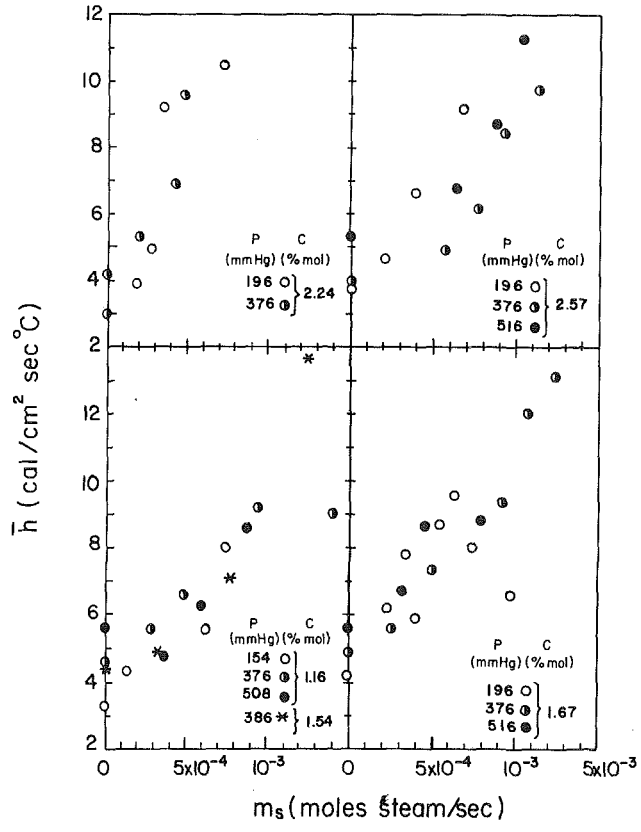

Fig. 3 Effect of steam suction rate on the mean heat transfer coefficient at constant values of air concentrations

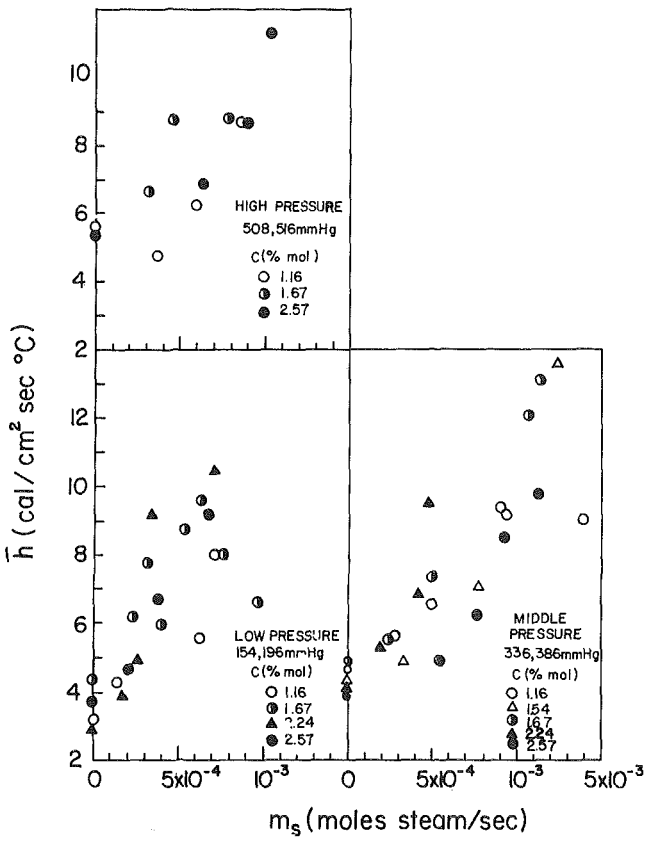

Fig. 4 Effect of steam suction rate on the mean heat transfer coefficient at constant values of air concentrations

transfer. It is quite evident that a change in the interfacial temperature would be caused by a change in the noncondensable concentration at the condensing surface. This can be achieved by affecting the rate of removal of the noncondensable gases from the interface. According to the mechanism suggested by Sparrow and Lin [1], the removal of the noncondensable gases from the interface is achieved by diffusive flow to the bulk of the vapor. As demonstrated in the present investigation, this flow can be enhanced by superposing a convective component in the form of surface suction.

Concluding Remarks

The experiments indicate that local surface suction is very efficient and that heat transfer coefficients may be increased by a factor of 1.5–3.5 by the application of surface suction. It is also shown that in the absence of surface suction, the effect of the noncondensable gas is enhanced toward low pressures, which is consistent with previous theoretical predictions [1].

Acknowledgments

We gratefully acknowledge the support by the Bat-Sheva de Rothschild Fund in order to carry out this work. Thanks are also due to Mr. M. Golden for his technical support.

References

1 Sparrow, E. M., and Lin, S. H., "Condensation Heat Transfer in the Presence of a Non-Condensable Gas," JOURNAL OF HEAT TRANSFER, Series C, Vol. 86, 1964, pp. 430–436.

2 Tamir, A., and Taitel, Y., "Improving Condensation Rate by Interfacial Suction and Forced Convection in the Presence of Non-Condensable Gases," *Israel Journal of Technology*, Vol. 9, 1971, pp. 69–81.

3 Dombrowski, N., Hasson, D., and Ward, D. E., "Some Aspects of Liquid Flow Through Fan Spray Nozzles," *Chem. Eng. Sci.*, Vol. 12, 1960, pp. 35–50.

4 Hasson, D., Luss, D., and Navon, U., "An Experimental Study of Steam Condensation on Laminar Water Jets," *International Journal of Heat and Mass Transfer*, Vol. 7, 1964, pp. 983–1001.

5 Antonir, I., "Improving Condensation Rates in the Presence of Non-Condensable Gases in a Fan Spray Sheet," MSc thesis, Ben-Gurion University of the Negev, Beer-Sheva, Israel, 1976.

Free Convection Effects on the Stokes Problem for an Infinite Vertical Plate

V. M. Soundalgekar[1]

An exact analysis of Stokes' problem (also Rayleigh's problem) for the flow past an impulsively started infinite vertical plate is presented. The effects of externally heating or cooling the plate by free convection currents are studied. It is observed that the velocity decreases due to more heating of the plate and increases due to more cooling of the plate. The skin friction increases due to greater heating of the plate and decreases owing to greater cooling of the plate. More cooling of the plate may cause reverse type of flow near the plate in the case of air.

Nomenclature

C_p = specific heat at constant temperature
g = acceleration due to gravity
G = Grashof number $(\nu g\beta\ (T_w' - T_\infty')/U_0^3)$
K = thermal conductivity
P = Prandtl number $(\mu C_p/K)$
T' = temperature of the fluid near the plate
T_∞' = temperature of the fluid at infinity
T_w' = temperature of the plate
t = dimensionless time $(t'U_0^2/\nu)$
t' = time
u = velocity of the fluid (u'/U_0)
U_0 = velocity of the plate
x', y' = coordinates along and normal to the plate
x, y = dimensionless coordinates $(y = y'U_0/\nu)$
ν = kinematic viscosity
β = coefficient of volume expansion
$\eta = y/2\sqrt{t}$
ρ = density
θ = dimensionless temperature $(T' - T_\infty'/(T_w' - T_\infty'))$
τ' = skin friction
τ = dimensionless skin friction
erfc = complementary error function

1 Introduction

The flow of an incompressible viscous fluid past an impulsively started infinite horizontal plate, in its own plane, was studied first by Stokes [1].[2] It is also known as Rayleigh's problem in the literature. Because of its practical importance, it has been extended to bodies of different shapes by a number of researchers. Amongst them are Illingworth [2], Stewartson [3], Hall [4], and Elliott [5]. Illingworth considered the flow of a compressible gas with variable viscosity near an impulsively started vertical plate and the problem was solved by the method of successive approximation. Elliott generalized Illingworth's problem by assuming a time-dependent velocity and temperature for the plate, but neglected the viscous dissipative heat. However, in both these papers, only mathematical results were derived and no physical situation was discussed. In fact, in such types of problems, from the engineering point of view, the physical aspects are very important. In the remaining two papers, the flow past an impulsively started semi-infinite horizontal plate has been considered. Stewartson studied it by analytical methods, whereas Hall analyzed the problem by finite-difference method.

So in order to present the physical situation of the flow past an impulsively started infinite vertical plate, we have again considered the problem for incompressible fluid with constant properties.

Now in this type of flow, we can consider two physical situations: (1) the temperature of the plate is the same as that of the fluid extended to infinity; (2) the plate temperature differs from the temperature of the fluid at infinity. The second case is more important from both the physical and practical point of view. If the difference between the plate temperature T_w' and that of the fluid at infinity T_∞', viz. $T_w' - T_\infty'$ is appreciable, then free convection currents are induced in the vicinity of the plate. Such a physical situation has not been studied in the literature and hence it is presented here. This problem has a variety of physical applications, e.g., filtration processes, the drying of porous materials in textile industries, etc.

Mathematical Analysis

Here x'-axis is taken along the infinite plate, in the vertical direction and the y'-axis is taken normal to the plate. Initially, the temperature of the plate is the same as that of the fluid. At time $t > 0$, the plate starts moving impulsively in its own plane with a velocity U_0, and its temperature is instantaneously raised or lowered to T_w' which is thereafter maintained constant. All the fluid properties are assumed constant except that the influence of the density variation with temperature is considered only in the body force term. Then the flow is governed by the following system of nondimensional equations:

[1] Asst. Professor, Indian Institute of Technology, Bombay, India.

Contributed by the Heat Transfer Division of THE AMERICAN SOCIETY OF MECHANICAL ENGINEERS. Manuscript received by the Heat Transfer Division December 30, 1976.

[2] Numbers in brackets designate References at end of technical note.

transfer. It is quite evident that a change in the interfacial temperature would be caused by a change in the noncondensable concentration at the condensing surface. This can be achieved by affecting the rate of removal of the noncondensable gases from the interface. According to the mechanism suggested by Sparrow and Lin [1], the removal of the noncondensable gases from the interface is achieved by diffusive flow to the bulk of the vapor. As demonstrated in the present investigation, this flow can be enhanced by superposing a convective component in the form of surface suction.

Concluding Remarks

The experiments indicate that local surface suction is very efficient and that heat transfer coefficients may be increased by a factor of 1.5–3.5 by the application of surface suction. It is also shown that in the absence of surface suction, the effect of the noncondensable gas is enhanced toward low pressures, which is consistent with previous theoretical predictions [1].

Acknowledgments

We gratefully acknowledge the support by the Bat-Sheva de Rothschild Fund in order to carry out this work. Thanks are also due to Mr. M. Golden for his technical support.

References

1 Sparrow, E. M., and Lin, S. H., "Condensation Heat Transfer in the Presence of a Non-Condensable Gas," JOURNAL OF HEAT TRANSFER, Series C, Vol. 86, 1964, pp. 430–436.

2 Tamir, A., and Taitel, Y., "Improving Condensation Rate by Interfacial Suction and Forced Convection in the Presence of Non-Condensable Gases," *Israel Journal of Technology*, Vol. 9, 1971, pp. 69–81.

3 Dombrowski, N., Hasson, D., and Ward, D. E., "Some Aspects of Liquid Flow Through Fan Spray Nozzles," *Chem. Eng. Sci.*, Vol. 12, 1960, pp. 35–50.

4 Hasson, D., Luss, D., and Navon, U., "An Experimental Study of Steam Condensation on Laminar Water Jets," *International Journal of Heat and Mass Transfer*, Vol. 7, 1964, pp. 983–1001.

5 Antonir, I., "Improving Condensation Rates in the Presence of Non-Condensable Gases in a Fan Spray Sheet," MSc thesis, Ben-Gurion University of the Negev, Beer-Sheva, Israel, 1976.

Free Convection Effects on the Stokes Problem for an Infinite Vertical Plate

V. M. Soundalgekar[1]

An exact analysis of Stokes' problem (also Rayleigh's problem) for the flow past an impulsively started infinite vertical plate is presented. The effects of externally heating or cooling the plate by free convection currents are studied. It is observed that the velocity decreases due to more heating of the plate and increases due to more cooling of the plate. The skin friction increases due to greater heating of the plate and decreases owing to greater cooling of the plate. More cooling of the plate may cause reverse type of flow near the plate in the case of air.

Nomenclature

C_p = specific heat at constant temperature
g = acceleration due to gravity
G = Grashof number $(\nu g\beta\ (T_w' - T_\infty')/U_0^3)$
K = thermal conductivity
P = Prandtl number $(\mu C_p/K)$
T' = temperature of the fluid near the plate
T_∞' = temperature of the fluid at infinity
T_w' = temperature of the plate
t = dimensionless time $(t'U_0^2/\nu)$
t' = time
u = velocity of the fluid (u'/U_0)
U_0 = velocity of the plate
x', y' = coordinates along and normal to the plate
x, y = dimensionless coordinates $(y = y'U_0/\nu)$
ν = kinematic viscosity
β = coefficient of volume expansion
$\eta = y/2\sqrt{t}$
ρ = density
θ = dimensionless temperature $(T' - T_\infty'/(T_w' - T_\infty'))$
τ' = skin friction
τ = dimensionless skin friction
erfc = complementary error function

1 Introduction

The flow of an incompressible viscous fluid past an impulsively started infinite horizontal plate, in its own plane, was studied first by Stokes [1].[2] It is also known as Rayleigh's problem in the literature. Because of its practical importance, it has been extended to bodies of different shapes by a number of researchers. Amongst them are Illingworth [2], Stewartson [3], Hall [4], and Elliott [5]. Illingworth considered the flow of a compressible gas with variable viscosity near an impulsively started vertical plate and the problem was solved by the method of successive approximation. Elliott generalized Illingworth's problem by assuming a time-dependent velocity and temperature for the plate, but neglected the viscous dissipative heat. However, in both these papers, only mathematical results were derived and no physical situation was discussed. In fact, in such types of problems, from the engineering point of view, the physical aspects are very important. In the remaining two papers, the flow past an impulsively started semi-infinite horizontal plate has been considered. Stewartson studied it by analytical methods, whereas Hall analyzed the problem by finite-difference method.

So in order to present the physical situation of the flow past an impulsively started infinite vertical plate, we have again considered the problem for incompressible fluid with constant properties.

Now in this type of flow, we can consider two physical situations: (1) the temperature of the plate is the same as that of the fluid extended to infinity; (2) the plate temperature differs from the temperature of the fluid at infinity. The second case is more important from both the physical and practical point of view. If the difference between the plate temperature T_w' and that of the fluid at infinity T_∞', viz. $T_w' - T_\infty'$ is appreciable, then free convection currents are induced in the vicinity of the plate. Such a physical situation has not been studied in the literature and hence it is presented here. This problem has a variety of physical applications, e.g., filtration processes, the drying of porous materials in textile industries, etc.

Mathematical Analysis

Here x'-axis is taken along the infinite plate, in the vertical direction and the y'-axis is taken normal to the plate. Initially, the temperature of the plate is the same as that of the fluid. At time $t > 0$, the plate starts moving impulsively in its own plane with a velocity U_0, and its temperature is instantaneously raised or lowered to T_w' which is thereafter maintained constant. All the fluid properties are assumed constant except that the influence of the density variation with temperature is considered only in the body force term. Then the flow is governed by the following system of nondimensional equations:

[1] Asst. Professor, Indian Institute of Technology, Bombay, India.

Contributed by the Heat Transfer Division of THE AMERICAN SOCIETY OF MECHANICAL ENGINEERS. Manuscript received by the Heat Transfer Division December 30, 1976.

[2] Numbers in brackets designate References at end of technical note.

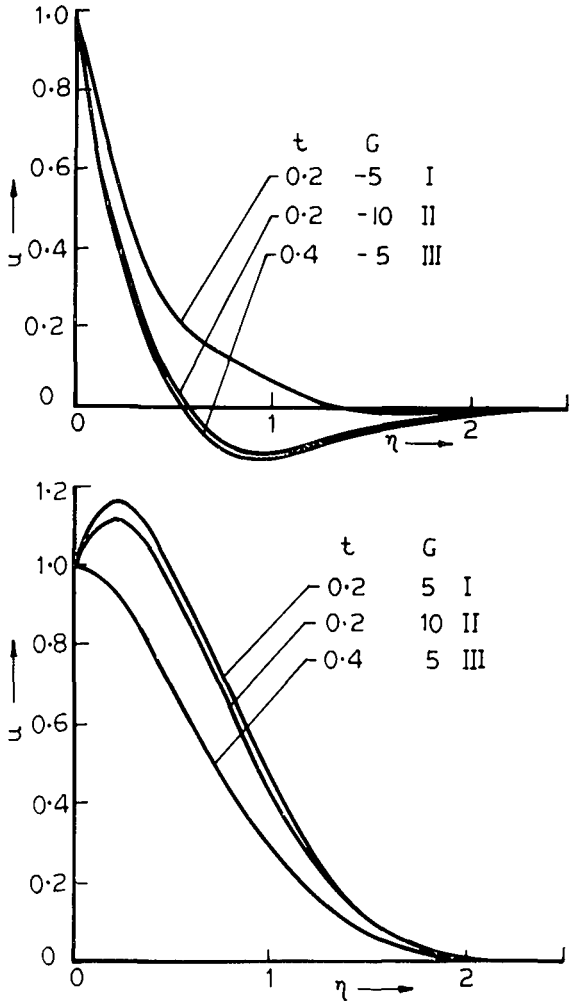

Fig. 1 Velocity profiles, P = 0.71

$$\frac{\partial u}{\partial t} = \frac{\partial^2 u}{\partial y^2} + G\theta \tag{1}$$

$$P\frac{\partial \theta}{\partial t} = \frac{\partial^2 \theta}{\partial y^2} \tag{2}$$

$$\begin{aligned} t \le 0, \quad & u(y,t) = 0, \quad && \theta(y,t) = 0 \\ t > 0, \quad & u(0,t) = 1, \quad && \theta(0,t) = 1 \\ t > 0, \quad & u(\infty,t) = 0, \quad && \theta(\infty,t) = 0 \end{aligned} \tag{3}$$

The nondimensional quantities are defined in the Nomenclature.

By usual Laplace-transform technique, the solutions are as follows:

For $P \neq 1$,

$$\theta = \operatorname{erfc}(\eta\sqrt{P}) \tag{4}$$

$$u = \operatorname{erfc}(\eta) + \frac{Gt}{P-1}\left[(1+2\eta^2)\operatorname{erfc}(\eta) - (1+2\eta^2 P)\operatorname{erfc}(\eta\sqrt{P}) - \frac{2\eta}{\sqrt{\pi}}\left(e^{-\eta^2} - \sqrt{P}e^{-P\eta^2 P}\right)\right] \tag{5}$$

and for $P = 1$,

$$u = \operatorname{erfc}(\eta) + Gt\left[\frac{2}{\sqrt{\pi}}\eta e^{-\eta^2} - 2\eta^2 \operatorname{erfc}(\eta)\right] \tag{6}$$

The velocity profiles are shown in Fig. 1. The free convection currents are in existence due to the temperature difference $T_w' - T_\infty'$ and hence $T_w' - T_\infty'$ may be positive, zero, or negative. Therefore, the Grashof number $G(= \nu g\beta(T_w' - T_\infty')/U_0^3)$ will assume positive, zero, or negative values. From the physical point of view, $G < 0$ corresponds to an externally heated plate as the free convection currents are carried toward the plate. Then $G > 0$ corresponds to an externally cooled plate and $G = 0$ corresponds to the absence of the free convection currents.

The velocity profiles for $P = 0.71$ are shown in Fig. 1. We conclude from this figure that greater cooling of the plate causes a rise in the velocity and greater heating of the plate causes a fall in the velocity.

Physically, the increase or decrease in the velocity owing to cooling or heating of the plate can be explained as follows.

In the process of externally cooling the plate, the free convection currents travel away from the plate. As the fluid is also moving with the plate in the upward direction, the free convection currents tend to help the velocity to increase. But in the case of heating of the plate, as the free convection currents are traveling toward the plate, the motion is opposed by these currents and hence there is a decrease in velocity.

From (4), we conclude that there is a fall in temperature of fluid, with increasing Prandtl number.

Knowing the velocity field, we can now calculate the skin friction which is given by

$$\tau = \tau'/\rho U_0^2 = -\left(\frac{du}{dy}\right)_{y=0} \tag{6}$$

From equations (5) and (6), τ has been calculated and its numerical values are entered in Table 1 for $P = 0.71$ and $P = 7$ and for both $G \gtrless 0$. It is interesting to note that greater cooling of the plate causes a fall in the skin friction for air and when $G = 4$, $t = 0.4$, the value of the skin friction becomes negative which shows that after some time there occurs a reverse type of flow near the moving plate. Physically this is also true as the motion of the fluid is due to plate moving in the upward direction against the gravitational field. Thus it can be expected that even at small time value, more cooling of the plate ($G > 4$) may cause separation of the flow. However, when the plate is being heated by free convection currents, ($G < 0$) and when G is small, there is a fall in the value of skin friction when time increases. But greater heating of the plate causes a rise in the value of skin friction for air and skin-friction increases as time increases.

In the case of water, though the skin friction decreases owing to greater cooling of the plate by the free convection current, the rate of decrease is not so high as in the case of air, and hence, for $G > 0$, the separation may be expected after a long time as compared to the one in the case of air. Owing to greater heating of the plate, there is a rise in the value of skin friction though the rate of increase is not so high as in the case of air.

But it is important to note that the skin friction is higher when the plate is being heated by the free-convection currents than when it is cooled by free convection currents.

Knowing the temperature field, we now study the rate of heat transfer. In terms of the Nusselt number, it is defined by

Table 1 Values of skin friction

P	G/t	0.2	0.4
0.71	2	0.7130	0.1134
	4	0.1640	−0.6111
	5	−0.1122	−1.0517
	−2	1.8046	1.5495
	−4	2.3599	2.3832
	−5	2.6158	2.8353
7.0	2	0.8834	0.5238
	4	0.7572	0.1047
	−2	1.5144	1.3095
	−4	1.7663	1.5314

$$\mathrm{Nu} = \frac{1}{2\sqrt{t}} \frac{d\theta}{d\eta}\bigg|_{\eta=0}$$
$$= \frac{\sqrt{\mathrm{P}}}{\sqrt{\pi t}} \qquad \text{from (4)}$$

Hence, the rate of heat transfer is directly proportional to $\sqrt{\mathrm{P}}$ and inversely proportional to $\sqrt{t}$.

References

1. Stokes, G. C., "On the Effect of the Internal Friction of Fluids on the Motion of Pendulums," *Camb. Phil. Trans.*, IX, Vol. 8, 1951.
2. Illingworth, C. R., "Unsteady Laminar Flow of Gas Near an Infinite Flat Plate," *Proceedings Cambridge Philosophical Society*, Vol. 46, 1950, p. 603.
3. Stewartson, K., "On the Impulsive Motion of a Flat Plate in a Viscous Fluid," *Quart. Appl. Math. and Mech.*, Vol. 4, 1951, p. 182.
4. Hall, M. G., "Boundary Layer Over an Impulsively Started Flat Plate," *Proceedings of the Royal Society* (London), Vol. 310A, 1969, p. 401.
5. Elliott, L., "Unsteady Laminar Flow of Gas Near an Infinite Flat Plate," *Zeit. Angew. Math. Mech.*, Vol. 49, 1969, p. 647.

ERRATUM

Erratum: Tsai-tse Kao, "Non-Fourier Heat Conduction in Thin Surface Layers," published in the May 1977 issue of the JOURNAL OF HEAT TRANSFER, pp. 343–345.

Equation (13) should read:

$$\theta(\delta,p) = \frac{1}{p} e^{-\delta/2[\epsilon+\sqrt{\epsilon^2+4(p^2+2p)}]}$$

All capital P's in equations (17), (18), (19), (25), (26) and (28) should be lower case.

Equation (27): $e^{-\epsilon/2\delta}$ should be $e^{-\delta\epsilon/2}$

The × sign should remain in the last line only.

journal of heat transfer

discussion

Analysis of Conduction-Controlled Rewetting of a Vertical Surface[1]

M. E. Sawan,[2] H. M. Temraz,[3] and G. M. Zaki.[3] The authors presented an analysis for the rewetting of a vertical slab assuming wet and dry regions only and a constant heat transfer coefficient. They also considered that conduction takes place only in a thin layer in the slab surface for large Peclet numbers. However this is accepted if Region V is small compared to the slab half thickness, δ. The boundary condition that $\theta \to 0$ as $y \to \infty$ (equation (37)) does not guarantee that the temperature gradient is zero at $y = \delta$ as required by symmetry unless Region V is very small compared to δ. However, Thompson[4] showed that Region V may reach 40 percent of δ and dependence on the initial temperature.

The authors found a deviation of 20 percent between their model and the numerical solution of Coney [9], and claimed inadequacy of Duffey's results. We think that comparison between Duffey's analysis [5] and experimental data in Fig. 6 of reference [5] shows reasonable agreement. The agreement between the experimental data and any theoretical model is possible provided that a proper value for the heat transfer coefficient is used. No accurate or direct measurements for the heat transfer coefficient during the rewetting process are available. We have investigated this point obtaining a correlation for the heat transfer coefficient h which gives good agreement of available experimental data with the model of Duffey. Therefore, we think that the mathematical models for the rewetting process should essentially define the value of the heat transfer coefficient to be used in conjunction with the model.

The authors obtained two formulas, equations (50) and (52), for low and high Peclet numbers and established a continuous function for the whole range of Peclet numbers. This expression, equation (53), is one of an infinite number of smooth functions satisfying both limits of equations (50) and (52). No systematic method for developing equation (53) was presented. We have obtained a smooth expression for the whole range of Peclet numbers assuming a zero temperature gradient at $y = \delta$ as required by symmetry, while the other conditions are similar to equations (35) and (36). The model accounts for inlet subcooling and heat generation. It is developed for different cladding geometries. In the simple case of no heat generation and zero subcooling in slab geometry our results reduce to the two-dimensional solution of Duffey [5].

[1] By C. L. Tien and L. S. Yao, published in May 1975 issue of the JOURNAL OF HEAT TRANSFER, TRANS. ASME, Series C, Vol. 97, pp. 161–165.

[2] Faculty of Engineering, Alexandria University, Egypt.

[3] heat Transfer and Desalination Group, Atomic Energy Establishment, Cairo.

[4] Thompson, T. S., "On the Process of Rewetting a Hot Surface By a Falling Liquid Film," AECL—4316, 1973.

Authors' Closure

The comments of Sawan, et al., indicate a misunderstanding of the analysis for capital P in the paper. The solution is of an asymptotic nature. The boundary condition that $\theta \to 0$ as $y \to \infty$, equation (37), is the matching condition between Regions II and V. It can be derived straightforwardly by following the well-established asymptotic matching principle [16]. Its mathematical meaning is that the temperature matching condition for a finite $\tilde{y}$ at the boundary between Regions II and V can be applied at $y \to \infty$ when $P \to \infty$, where $y = (P/2\delta)\tilde{y}$. The physical location to which equation (37) applies is still at the boundary of Regions II and V. It is worthy to point out that one of the advantages of applying the Wiener-Hopf technique in a rewetting problem is that the wet-front velocity can be obtained directly from the surface temperature distribution of the vertical slab. It is unnecessary to go through a complicated mathematical procedure to find the temperature distribution inside the slab. It has been demonstrated by Yao, et al. [17] that the temperature distribution inside the slab of a rewetting problem is similar to that of a moving slab in two adjacent temperature chambers. Region II (labeled as Region I in [17]) is an undisturbed region. Its temperature is a constant equal to T_0, and the temperature gradient is zero in Region II. Therefore, the symmetric condition is indeed satisfied at $\tilde{y} = \delta$ as long as the size of Region V is smaller than δ. They also showed [17] that the shape of Region V (Region IV in [17]) is a parabola with its vertex translated slightly to the negative $\tilde{x}$-axis. The size of Region V is smaller than δ when $P > 8$. This suggests that the solution for large Peclet numbers is applicable when $P > 8$.

Several solutions of the two-dimensional transient-conduction equation for the rewetting problem have been cited in the paper. Unfortunately, most of them including that of Duffey and Porthouse [5] only took one or two terms from an infinite convergent series in order to give a closed-form correlation, thus yielding an incorrect functional dependence of the wet-front velocity on temperature. It has long been recognized that one or two terms of an infinite series are insufficient to represent the actual solution of the transient-conduction equation. In particular, Horvay [18] showed that the infinite series diverges when P is not small. The solution for a small Peclet number presented in the paper has been shown to approach the one-dimensional solution when the Biot number is also small. Furthermore, the wet-front velocity for small P which has been verified by an integral method [19] is quite different from the one obtained by taking one term of an infinite series. For large P, the wet-front velocity cannot be predicted by a one-dimensional analysis due to the competition of the effects of conduction and convection. The case for large P is currently being studied by use of the integral method in order to include the effects of precursory cooling and fuel-stored energy.

The data correlated in Fig. 6 of Duffey and Porthouse's paper [5] is first a special case and second based on an effective Biot number which makes the heat transfer coefficient in the wet-front zone dependent upon the mass flow rate of the coolant. This is contrary to the conclusions of Thompson's study [6] which indicates that the

sputtering heat transfer coefficient is independent of the mass flow rate. The effect of mass flow rate on rewetting velocity enters only through precursory cooling ahead of the wet front [20]. In the absence of any direct measurements, several investigators have treated the heat transfer coefficient as a fitting parameter to correlate the experimental data with different rewetting models. Recent experimental study by Dua and Tien [21] indicates that the heat transfer in the sputtering region can be best represented based on an average of maximum and minimum heat fluxes of pool boiling. Thus defining a value of the heat transfer coefficient to be used in conjunction with a given model of rewetting is not only unnecessary but unrealistic also.

It is recognized that an infinite number of smooth functions satisfying the asymptotic solutions in the two limiting cases of very small and very large Peclet numbers are possible. In fact, the recent studies by Dua and Tien [20, 22] very clearly emphasize this point by first giving the equation of a family of matching functions and later picking up a specific semianalytical matching based on how closely this choice either represents a numerical solution in the intermediate range of Peclet numbers [20] or correlates the experimental data in this range [22].

Additional References

16 Van Dyke, M., *Perturbation Methods in Fluid Mechanics*, Academic Press, New York and London, 1964.

17 Yao, L. S., Tien, C. L., and Berger, S. A., "Thermal Analysis of a Fast-Moving Slab in Two Adjacent Temperature Chambers," JOURNAL OF HEAT TRANSFER, TRANS. ASME, Series C, Vol. 98, No. 2, 1976, pp. 327–329.

18 Horvay, G., "Temperature Distribution in a Slab Moving From a Chamber at One Temperature to a Chamber at Another Temperature," JOURNAL OF HEAT TRANSFER, TRANS. ASME, Series C, Vol. 83, 1961, pp. 391–402.

19 Yao, L. S., "Rewetting of a Vertical Surface With Internal Heat Source," Paper No. AIChE-8, 16th National Heat Transfer Conference, St. Louis, Mo., Aug. 1976.

20 Dua, S. S., and Tien, C. L., "Two-Dimensional Analysis of Conduction-Controlled Rewetting With Precursory Cooling," JOURNAL OF HEAT TRANSFER, TRANS. ASME, Series C, Vol. 98, 1976, pp. 407–413.

21 Dua, S. S., and Tien, C. L., "An Experimental Study of Rewetting With Precursory Cooling," in preparation.

22 Dua, S. S., and Tien, C. L., "A Generalized Two-Parameter Relation for Conduction-Controlled Rewetting of a Hot Vertical Surface," to appear in *International Journal of Heat and Mass Transfer*.

ERRATUM

Erratum: R. B. Holmberg, "Heat and Mass Transfer in Rotary Heat Exchangers With Nonhygroscopic Rotor Materials," published in the May 1977 issue of the JOURNAL OF HEAT TRANSFER, pp. 196–202.

Page 200, left-hand column, line 6:
0.8220 instead of 0.8222.
Page 200, right-hand column, line 2:
0.555 instead of 0.5631
0.554 instead of 0.5617